THE UNIVERSITY OF CHICAGO

THE ROLE OF IRON IN THE SURFACE REDOX EVOLUTION OF EARLY EARTH AND MARS

A DISSERTATION SUBMITTED TO

THE FACULTY OF THE DIVISION OF THE PHYSICAL SCIENCES

IN CANDIDACY FOR THE DEGREE OF

DOCTOR OF PHILOSOPHY

DEPARTMENT OF THE GEOPHYSICAL SCIENCES

BY

ANDREW WINSTON HEARD

CHICAGO, ILLINOIS

JUNE 2021

DEDICATION

This thesis is dedicated to my parents, for the work ethic they instilled in me, and the support they gave me in pursuing a vocation that has taken me thousands of miles away from the countryside where I grew up; to Jyotsna, for keeping me grounded and sane; and to Rob Setchell, without whom I would be an engineer, and far less happy.

TABLE OF CONTENTS

Supplementary files available online:

Chapter 2 – Compiled Fe and S Isotope Records

Chapter 4 – Videos Showing X-ray CT Internal Structure of Griquatown Formation Stromatolites

ABSTRACT

The oxygenation of Earth's atmosphere 2.43 billion years ago (Ga) in the 'Great Oxidation Event' (GOE), set Earth on the trajectory to being able to support complex life. Planetary surface oxidation set the stage for atmospheric oxygenation, so understanding when, where, and how Earth's surface was oxidized is fundamental to understanding habitability. In this work we explore aspects of early Earth and Mars surface redox evolution, emphasizing novel uses of iron geochemistry.

We first address controversial evidence for atmospheric oxygenation at around 2.95 Ga. In a study of an ancient weathering horizon, we show that continental weathering took place under an anoxic atmosphere, despite widespread evidence for the coincident oxygen production in the oceans.

Next, we show that oxic and sulfidic iron sinks in the oceans both grew in the runup to the GOE and resolve a resolve a longstanding controversy about the iron isotope record of Archean pyrites. An increase in pyrite burial after 2.65 Ga, likely driven by increased volcanic sulfur supply to sulfur-starved early oceans, might have driven the iron cycle in high-productivity ocean environments to become a net source of environmental oxygen that overwhelmed nearby iron oxidation buffers.

We also investigated columnar stromatolites in the shallowest facies of an iron formation deposited prior to the GOE. Combined geochemical and textural evidence suggest that these stromatolites were formed where iron-rich waters inundated a shallow shelf occupied by cyanobacterial communities, providing a unique snapshot of a ground zero site for early oxygen production.

Lastly in our investigation of ancient Earth, we consider an alternative model for the deposition iron formations, long assumed to be an oxide-rich sedimentary sink in the early oceans, that instead elevates the role of ferrous iron silicates. We determine the equilibrium iron isotope behavior of

the ferrous silicate greenalite and find surprising similarity between the iron isotope systematics of greenalite and ferrihydrite, a representative hydrous ferric oxide.

For Mars, we first consider the impacts of long-term processes that affected the surface volatile budget. We indirectly quantify the post 3.5 Ga loss of CO_2 from Mars by independently constraining the loss of hydrogen and oxygen to space, and to surface oxidation, and inferring carbon loss from the oxygen loss unexplained by depletion of the Mars hydrosphere. We find that the late surface oxidation sink on Mars is small, and oxygen loss can by predominantly attributed to water, necessitating a missing Martian (sub)surface CO_2 sink.

Finally, we conducted new experiments to constrain the kinetics of iron photooxidation and tested whether this process can quantitatively oxidize iron from solution. By modeling iron photooxidation in Gale Crater Lake, we find that it supports iron deposition rates consistent with sedimentary textures, relaxing the need for other chemical oxidants. Taking lessons from chemical trends seen on pre-GOE Earth, we show that extensive iron oxidation can explain the iron and manganese systematics of Gale Lake sediments and produce manganese rich residual fluids that explain localized elemental enrichments observed by Curiosity.

ACKNOWLEDGEMENTS

First and foremost, I thank my advisor, Nicolas Dauphas, for always pushing me to always make my science the best version of itself, for being generous with both time and ideas, and for teaching me the importance of finding good scientific questions to ask. Also, I thank my PhD committee members Jake Waldbauer, Philipp Heck, and Mike Pellin, for keeping me on track and acting as a great sounding board for my research as it has progressed over the years. I also have to thank everyone in the Origins Lab, past and present for the technical and personal support they have given me, particularly Nicole Nie, for teaching me everything I know in the lab, Sarah Aarons, for providing me frequent sanity checks, and Justin Hu, for always being on hand to help me troubleshoot the mass spec. There are also many people I have to thank in the Department of Geophysical Sciences at large. Thanks to Edwin Kite for being sharing numerous ideas, and opportunities for collaboration, and for consistently asking me questions that change the way I think for the better. Thank you to Gerry Olack, for letting me treat the 3rd floor labs like a second home, while providing sage advice and comic relief in equal measure. Thanks also to Sarah Lippert, Jolene Hanchar, and David Taylor, for the administrative support provided to me over the years that went above and beyond. And I am grateful also to Malte Jansen for answering all of my physical oceanography questions. Finally, I need to thank a large number of collaborators at various institutions who helped make my PhD come together. Thank you to Olivier Rouxel, Romain Guilbaud, Ian Butler, Axel Hofmann Tom Ireland, Liping Qin, Xiaoqing He, Hari Tsikos, Ercan Alp, Michael Hu, Jiyong Zhao, Barbara Lavina, Jena Johnson, Isaac Hinz. Last, but by no means least, thank you to Andrey Bekker, for taking a chance on me when I asked to join in with fieldwork in South Africa, for always posing the hard questions, for providing countless samples, and for becoming a friend in science I hope to keep working with for many years to come.

LIST OF FIGURES

Introduction:

Chapter 1:

Chapter 3:

Chapter 7:

LIST OF TABLES

INTRODUCTION

Early Earth

On Earth today, the atmosphere contains 21 % free oxygen (O_2). All known complex multicellular life on Earth, which is currently our single datapoint for life in the universe, requires O_2 for cellular respiration to generate energy. The oxygenation of Earth's atmosphere is thus one of the key factors that makes the Earth habitable to complex life today; and understanding the history of O_2 on our planet is a critical step in developing theories that explain if, and how, habitability can develop on other planetary bodies, in our solar system and beyond. Earth's atmosphere was not always O_2-rich. Earth history is punctuated by major transitional episodes where the redox state of the atmosphere dramatically changed. The first, and most significant of these was what has come to be known as the 'Great Oxidation Event' (Holland, 2002), or 'GOE', which took began approximately 2.4 billion years ago (Ga) (Bekker et al., 2004; Gumsley et al., 2017; Luo et al., 2016), a little over half of Earth's 4.5-billion-year history ago (Fig. 0.1). Earth was a very different planet when the GOE took place to the Earth as we know it now. There were no plants and no animals. The days and nights were shorter, and the Moon, prior to is long tidal retreat, loomed larger in the night sky. Major uncertainties remain about the growth of emerged lands throughout time, but it is likely that Earth, currently 70 % covered by oceans, was even more of water world, with small, largely submerged continents (Korenaga et al., 2017). Chemistry on the surface of the early Earth would have looked dramatically different in the absence of O_2. This thesis investigates in detail the geochemistry one of one element, iron (Fe), during major transitions in planetary surface redox conditions. Iron is the most abundant metal with multiple redox states present in the rocky crusts of Earth and Mars, and therefore, its potential to be affect, and be affected by, changes in surface redox conditions is immense. Throughout this thesis, we will employ novel

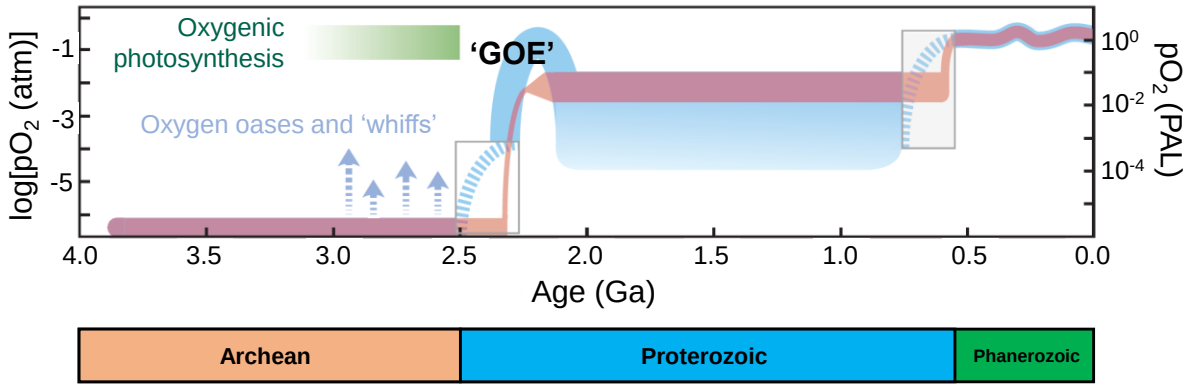

Figure 0.1. Evolution of Earth's atmospheric O_2 partial pressure (pO_2) through time, adapted from Lyons et al. (2014), with permission from Springer Nature. This thesis explores the redox evolution of Fe in the oceans in the time period preceding the Great Oxidation Event (GOE).

geochemical, isotopic, and modeling approaches that illustrate how Fe was both an important participant in, and serves a star geological witness for, the redox evolution of the surfaces of Earth, and as we also explore later on, Mars.

To understand the oxidation of the Earth's surface in the GOE and role Fe played in this event, it is useful to consider more generally the conditions of Earth's surface during its relative youth. The Earth's last major stage of accretion ended around 4.5 Ga, following an impact between the proto-Earth and a Mars-sized body referred to as Theia, which resulted in the formation of the Moon from the debris of this impact (Canup et al., 2021). The Earth was entirely molten in the aftermath of the Moon-forming impact, thanks to the conversion of kinetic and gravitational energy of accretion and metal core segregation to thermal energy. However, by 4.4 Ga at the latest, the Earth had cooled sufficiently that continental crust had formed, along with liquid water oceans; as evidenced by the heavy oxygen isotope composition of detrital zircons as old as 4.4 Ga recovered from the Jack Hills Conglomerate in Western Australia (Mojzsis et al., 2001; Wilde et al., 2001). However, the oldest rocks at Earth's surface are the 4.02 Ga Įdì whaà gneisses from the Acasta Gneiss Complex in the Slave Craton of Canada (Bowring and Williams, 1999). This means that at

least the first 400 million years Earth's history with continents and oceans is currently unaccounted for in the geological record.

It is highly likely that life evolved during these early dark ages of Earth history in the Hadean Eon (4.5-4.0 Ga), because the oldest sedimentary rock sequence on Earth, from the 3.8-3.7 Ga Isua Supracrustal Belt in Greenland, already contains evidence for biological activity, including: (i) graphite with a light carbon isotope composition (negative $\delta^{13}C$) consistent with biological carbon fixation (Rosing, 1999); (ii) iron formations (IFs), Fe-rich chemically precipitated sediments that bear signs of both partial marine Fe oxidation, potentially by photosynthetic life, and contributions of organic carbon to their carbonate composition (Craddock and Dauphas, 2011; Dauphas et al., 2004; Moorbath et al., 1973); (iii) hematite-encased filament and tube structures that bear morphological similarities to modern-day Fe-oxidizing bacteria (Dodd et al., 2017); and (iv) putative stromatolites, macroscopic laminated sedimentary features associated with the accumulation of layers of microbial mats (Nutman et al., 2016). A critical review of the origins of or earliest evidence for life on Earth is not included in this study, but these examples emphasize that life likely pre-dates the rock record on Earth.

The sedimentary rock record of the Early Earth also confirms that there were permanent liquid water oceans for as long as we have had a rock record. This in itself, is somewhat remarkable because solar luminosity at 4.0 Ga was approximately 75 % of the value it is today (Fig. 0.2), and prior to the gradual brightening of the Sun over time, the Earth should have been permanently glaciated, for at least the entirety of the Archean Eon (4.0-2.5 Ga). Archean ocean temperatures remain uncertain, and recently published triple oxygen isotope systematics in Archean cherts now hint at clement temperatures similar to the modern Earth (Liljestrand et al., 2020), while earlier studies favor high temperature (> 55 °C) conditions in the oceans around 3 billion years ago

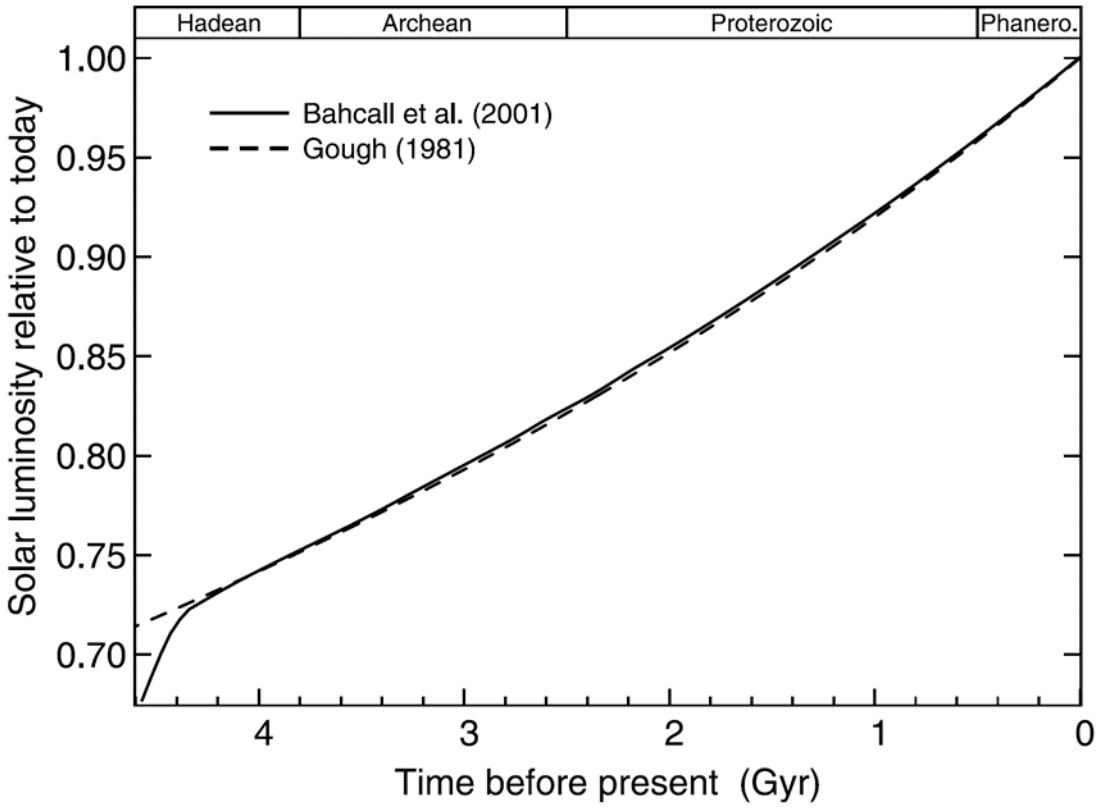

Figure 0.2. Evolution of Solar luminosity over time, relative to present day solar luminosity, from (Feulner, 2012, Reviews of Geophysics; DOI: 10.1029/2011RG000375). The solid (Bahcall et al., 2001) and dashed (Gough, 1981) curves refer to two different solar evolution models. At the beginning of the Archean Eon, solar luminosity was < 75 % of the present-day value, and persistent above-freezing temperatures on Earth throughout this time period indicate that the Archean atmosphere provided far strong greenhouse forcing the current 400 ppm CO_2 atmosphere on Earth.

(Knauth and Lowe, 2003; Marin-Carbonne et al., 2014). The sustained presence of liquid water at Earth's surface throughout its early history despite lower solar luminosity in the past, has become known as the Faint Young Sun Paradox, and the problem it posed for understanding planetary climate was first recognized by Sagan and Mullen (1972).

Solutions to the Faint Young Sun Paradox first and foremost require that the atmospheric greenhouse effect was far stronger early in Earth history, although changes in planetary albedo, or calls for revised astrophysical models for solar evolution, have also been appealed to in some studies (reviewed by Feulner, 2012). The greenhouse atmosphere compositions that have been

proposed as solutions to the Faint Young Sun Paradox typically assume a higher partial pressure of CO_2, the dominant greenhouse gas in the modern atmosphere, as a background condition (Feulner, 2012). However, a lack of the Fe carbonate mineral siderite ($FeCO_3$) in Archean fossil weathering horizons (paleosols) places a thermodynamic upper limit on Archean pCO_2 on the order of tens of millibars (Rye et al., 1995), which is below the level required to warm the planet above freezing under lower solar luminosity (Kuhn and Kasting, 1983). Sagan and Mullen (1972) initially argued for a reducing greenhouse gas atmosphere containing a few ppm of ammonia (NH_3), as a warming agent that could also have providing sufficiently reducing atmospheric conditions to be consistent with early origins of life experiments conducted by Miller and Urey (Miller, 1953; Miller and Urey, 1959). However, NH_3 is photochemically unstable under solar UV radiation (Kasting, 1982; Kuhn and Atreya, 1979). Sagan and Chyba (1997) later contended that high-latitude organic solids could form a protective haze for ammonia (Yung and Pinto, 1978), but this haze could potentially offset the warming effect of ammonia by blocking incoming shortwave radiation. Methane (CH_4) is another potent greenhouse gas that would sustain reducing atmospheric conditions and enable warming, but dependent on CO_2/CH_4 ratios, high altitude organic haze formation and adverse cooling effects again become a potential hindrance (Haqq-Misra et al., 2008). Warming from collision-induced absorption in a H_2-N_2 atmosphere with a total N_2 pressure of 2-3 bars is another potential pathway to warming the early Earth within strict geological pCO_2 constraints (Wordsworth and Pierrehumbert, 2013). However, what constraints are available for pN_2 during the Archean indicate most likely lower partial pressures than the 0.78 bar level of the modern atmosphere (Som et al., 2012). In summary, the Faint Young Sun Paradox cannot currently be considered solved, beyond stating that a solution must exist to explain the persistent stability of liquid water throughout the Archean Eon (Feulner, 2012). One line of

evidence that a reducing greenhouse component such CH_4 forms an integral part of this solution, is that the first universally accepted Snowball Earth event, that saw the planet's surface become entirely glaciated from equator to poles, came in the immediate aftermath of the rise of atmospheric O_2 during the GOE (Evans et al., 1997; Gumsley et al., 2017; Kopp et al., 2005; Young et al., 1998). The tantalizing coincidence of these two events has led to the general conclusion that rising O_2 destroyed a significant CH_4 component in the atmosphere that had provided a strong greenhouse effect and maintained clement conditions on Earth's surface in spite of the faint young Sun.

The volume, subaerial extent, and elevation of the continental crust are also physical parameters that are not well constrained for the Archean Earth. Emerged lands exert several significant controls on the physicochemical environment of Earth's surface. Chemical weathering of fresh continental crustal rocks continuously exposed by subaerial erosion processes both helps to regulate atmospheric CO_2 via the carbonate-silicate weathering feedback, and adds solutes, including bio-limiting nutrient elements, to continental runoff that is delivered to the oceans. Emerged lands enable subaerial volcanic eruptions to add reactive gases directly into the atmosphere, altering its composition and globally distributing volatile species that can be aerosolized and ultimately redeposit at Earth's surface. And submerged continental crust that surrounds emerged lands creates shallow, often warm, marine shelf environments, where volumetrically significant carbonate deposition can take place, closing the loop of the carbonate-silicate weathering cycle.

The growth of the continental crust since Earth's formation has been modeled variously as a stepwise, steady, decelerating, or cyclical process (reviewed in Hawkesworth et al., 2020), and a major source of uncertainty lies in the continental crust formation process itself. Today, continental

crust is formed at subduction zone plate margins, but most geodynamic models fail to produce subduction-driven tectonics on an early Earth with a hotter mantle, potentially delaying the start of modern-style plate tectonics until after 3.0 Ga (Foley, 2018). Recently, however, new models have produced subduction like-processes on early Earth by improving the microscale physics of shear within plates (Foley, 2018). Coincidentally, a Ti isotopic dataset from the Acasta gneiss complex in Canada, which hosts the oldest rocks on Earth, has revealed a magmatic transition around 3.8 Ga characterized by the appearance of calc-alkaline differentiation signatures (Aarons et al., 2020). This style of magmatism only occurs today at subduction zones, lending support to an early, if localized, onset of subduction and modern-like crust formation processes not long after the rock record begins.

There are numerous lines of evidence for a major episode of crustal thickening and emergence starting in the Neoarchean (2.8-2.5 Ga). Age-frequency distributions of zircon crystallization, and the occurrence of subaerial large igneous provinces (LIPs) feature temporal increases around 2.7 and 2.5 Ga (Kump and Barley, 2007; Voice et al., 2011). Meanwhile, the strontium (Sr) isotope record of marine carbonates suggests a shift towards a more continental weathering-dominated Sr supply to the oceans at 2.5 Ga (Veizer and Compston, 1976), and triple O isotope data from shales also indicate a shift to a more continentally influenced hydrological cycle at around 2.5 Ga (Fig. 0.3) (Bindeman et al., 2018). Modeling suggests this episode of increased emergence would have been facilitated in part by mantle cooling, and thickening of the continental lithosphere (Flament et al., 2008; Korenaga et al., 2017).

Reconstructions of the chemical composition of the emerged crust also vary greatly. Many studies have considered the record of fine-grained terrigenous sediments, shales, to provide spatial and temporal averages of their provenance regions, and therefore the selected trace elemental

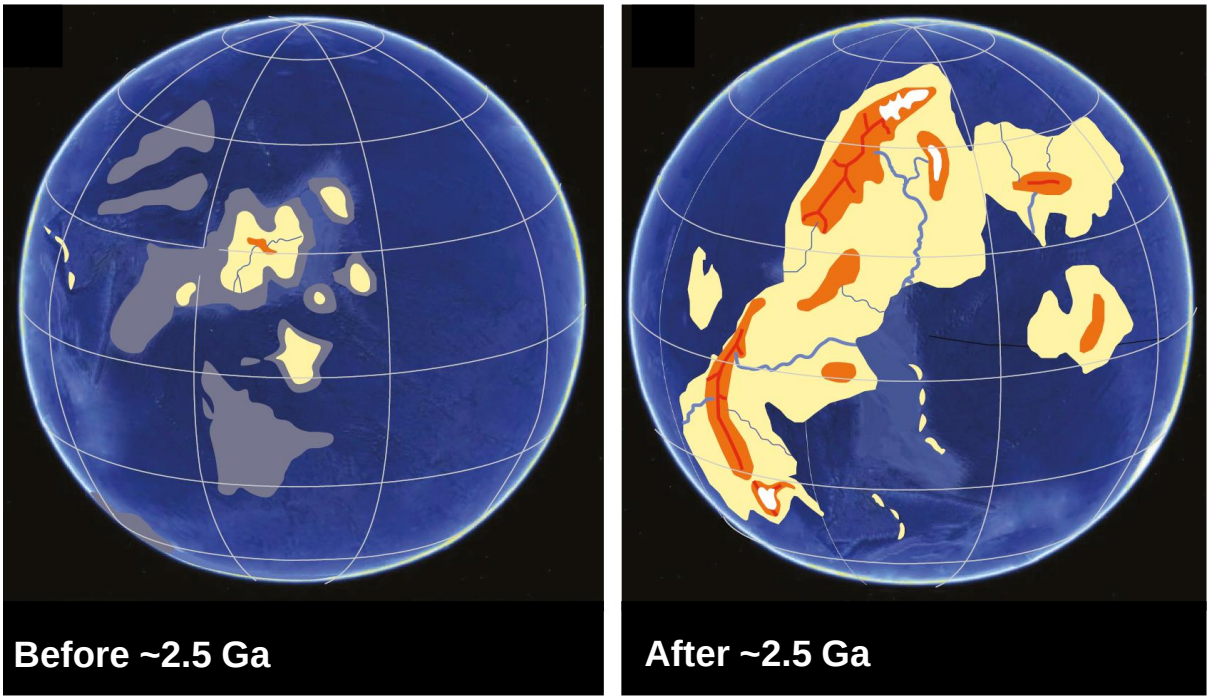

Figure 0.3. Conceptualized change in continental emergence before (left) and after (right) 2.5 Ga, adapted from Bindeman et al. (2018), with permission from Springer Nature. The increased emergence of the continents around the time of the GOE may have impacted surface geochemical cycling by increasing continental weathering fluxes, and enabling a shift to a modern proportion of subaerial *vs.* submarine volcanic gas emission (Gaillard et al., 2011; Kump and Barley, 2007), which has been implicated in oxidizing the Earth's atmosphere.

composition of shales through time has been used as a proxy for the composition of the continental crust (*e.g.* Chen et al., 2020; Greber et al., 2017; Greber and Dauphas, 2019; Ptáček et al., 2020; Smit and Mezger, 2017; Tang et al., 2016; Taylor and McLennan, 1995, 1985). Most early attempts at a chemical reconstruction concluded that the early crust was dominated by mafic rocks (Fe- and Mg-rich and Si-poor) (Smit and Mezger, 2017; Tang et al., 2016; Taylor and McLennan, 1995, 1995). However, in the last few years this model has been reconsidered in light of Ti isotopic data that track crustal differentiation and show little change in the shale record through time (Greber et al., 2017; Millet et al., 2016). Additionally, improved filtering and selection of the trace element proxies used for crustal reconstruction have revealed that several earlier proxy studies used elemental groups that are either prone to fluid alteration or do not resolve multicomponent

mixtures effectively, casting many of the mafic-dominated model interpretations into doubt (Greber and Dauphas, 2019; Ptáček et al., 2020). As we learn more about the diversity of Ti isotope behavior in different crustal settings, interpretations of the shale record may require further revision, but the most rigorous geochemical approaches available to date suggest the continents may have been very compositionally similar to the modern crust since at least 3.5 Ga (Greber et al., 2017; Greber and Dauphas, 2019; Keller and Harrison, 2020; Ptáček et al., 2020). Chapter 1 of this thesis briefly touches on the crustal composition problem by highlighting the potential usefulness of paleosols (fossil weathering horizons) as natural laboratories for ancient weathering where the viability of different crustal composition proxies can be tested.

In contrast to the major unknowns that still surround many of the basic physical conditions of Earth's surface throughout much of the Archean Eon, the geochemical record provides a detailed picture of Earth surface chemistry and how it was fundamentally different prior to the Great Oxidation Event (GOE) that drove the earliest permanent oxygenation of the atmosphere at around 2.43-2.32 Ga (Bekker et al., 2004; Gumsley et al., 2017; Luo et al., 2016). This thesis is concerned with understanding the role and record of iron (Fe) during the redox evolution of Earth's surface in the runup to the GOE. However, to fit Fe into the broader context of the GOE, we must first review the evidence for the GOE and the reducing atmospheric and ocean conditions that preceded it, and the major geochemical forces that worked to drive Earth in the direction of permanent surface oxidation.

The earliest suggestion that the ancient atmosphere was reducing was made in the 1960s, based on the preservation detrital grains of the minerals uraninite (UO_2), and pyrite (FeS_2) in conglomerate rocks (Roscoe, 1969). Both uraninite and pyrite are unstable in the presence of O_2, and their preservation in a conglomerate, a coarse-grained clastic rock formed by subaerial erosion in the

presence of running water, indicated that the atmosphere under which these grains were eroded did not contain appreciable oxygen (Rasmussen and Buick, 1999; Roscoe, 1969). By the time the term 'Great Oxidation Event' was finally formalized in the early 2000s (Holland, 2002), a wealth of geochemical evidence indicated that a transition in atmospheric redox conditions took place near the Archean-Proterozoic boundary (2.5 Ga), including: loss of the aforementioned redox-sensitive detrital mineral grains from conglomerates and sandstone (Rasmussen and Buick, 1999; Roscoe, 1969); retention of Fe in paleosols (ancient weathering horizons) that suggested the oxidation of Fe^{2+} to insoluble Fe^{3+} under an oxidizing atmosphere (Rye and Holland, 1998); the first occurrences of rusty red sandstone deposits, again, reflecting the subaerial oxidation of Fe; and the disappearance of sulfur (S) isotope mass-independent fractionation (S-MIF) from sedimentary sulfides and sulfate (Farquhar et al., 2000). S-MIF is thought to be generated by UV photochemical reactions in the upper atmosphere. Photolysis reactions disproportionate volcanically-derived SO_2 into S_8 and H_2SO_4 aerosols that subsequently carry distinct S isotopic compositions with excesses or deficits in ^{33}S relative to the expectations of mass-dependent isotope fractionation(Farquhar et al., 2001; Farquhar and Wing, 2003). State of the art photochemical models indicate that pO_2 below a threshold value of $<10^{-5}$ × the present atmospheric O_2 level (PAL; 0.21 atm) is required for the generation and preservation of S-MIF in the rock record (Pavlov and Kasting, 2002). When pO_2 exceeds 10^{-5} × PAL, photolysis converts all volcanically sourced SO_2 into sulfate, and no separately fractionated reservoirs bearing distinct S-MIF can be preserved. The constraint provided by the present/absence of S-MIF is the gold standard quantitative constraint on atmospheric O_2 levels, and age constraints from high-resolution stratigraphy currently place the beginning of the GOE in the interval 2.43-2.32 Ga based on the disappearance of S-MIF (Bekker et al., 2004; Gumsley et al., 2017; Luo et al., 2016). Recently, an

exciting new study has revealed the canonical Great Oxidation 'Event' may have been more of a protracted, 200 million year 'episodes', as Poulton et al. (2021) report the discovery that S-MIF returned to Paleoproterozoic successions in South Africa in the time period from 2.32-2.22 Ga. These compelling new data will change the way we think about the dynamics of atmospheric oxygenation that were initiated at the beginning of the canonical GOE. However, the focus of this thesis is on the evolution of the Fe cycle hundreds of millions of years prior to this episode, so the newfound protracted nature of the GOE has limited bearing on our findings.

Reducing conditions in the atmosphere had profound implications for the oceans prior to GOE, because the chemistry of ocean waters dramatically changes when they are not pervasively oxygenated (Fig. 0.4). In the modern global oceans, dissolved O_2 sourced from equilibration with a 0.21 bar atmospheric reservoir, and produced *in situ* by photosynthetic primary production, is by far the dominant redox active chemical species. Geologically abundant reductants, most notably Fe^{2+} and sulfide (S^{2-}, normally in H_2S and HS^-) are rapidly oxidized by O_2 and thus cannot accumulate in most oceanic settings. Only one of O_2, Fe^{2+}, and sulfide, can exist in any appreciable quantity in natural environments because they react with one another to form Fe^{3+} oxides (O_2 + Fe^{2+}), sulfate (SO_4^{2-}; O_2 + sulfide), and pyrite (FeS_2; Fe^{2+} + sulfide) until only the most abundant reactant remains. The byproducts of these reaction pairs are either insoluble and sink from the oceans (Fe^{3+} oxides, pyrite), or behave conservatively in solution (sulfate). The result of this redox balance is that modern Earth surface environments are dominated by O_2, insoluble Fe^{3+} oxides, and dissolved sulfate. Before the GOE, the massive atmospheric O_2 pool that buffers the oceans to an oxygenated state was entirely absent, and the balance of ocean chemistry was shifted to a different dominant redox-active species.

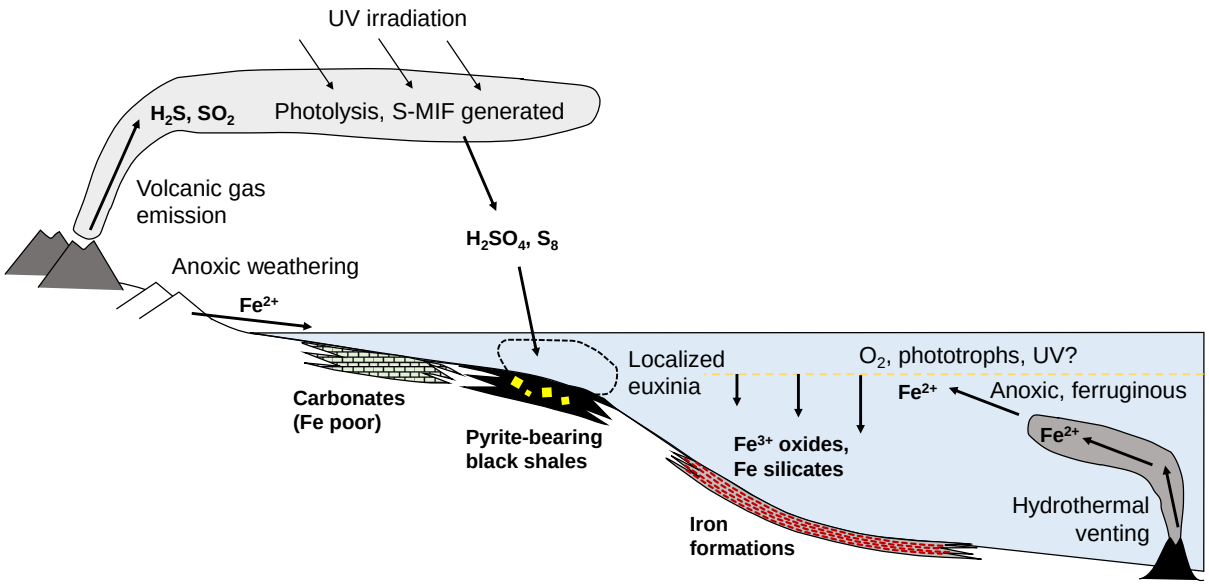

Figure 0.4. Schematic summary of major surface geochemical processes on the pre-GOE Earth. The anoxic oceans were enriched in highly soluble Fe^{2+}, sourced from anoxic continental weathering runoff and submarine hydrothermal vent fluids. Much of the Fe in the oceans was deposited in iron formations (IFs), after Fe^{2+} encountered near surface oxidants (O_2, anoxygenic photosynthetic bacteria, and/or UV photons), or saturated Fe silicate minerals Iron-poor carbonates formed in shallow waters where upwelled Fe^{2+} was effectively removed by these processes. Sulfur sourced from volcanic eruptions was processed in the atmosphere by UV-driven photolysis, depositing sulfate and elemental sulfur with S-MIF signatures into the oceans. Localized euxinia could develop where sulfur sources and high organic productivity in black shale-forming environments coincided, and these euxinic environments could bury some fraction of the surface Fe pool as pyrite.

The pre-GOE oceans were dominantly ferruginous, meaning they were characterized by being anoxic and Fe^{2+}-rich (Fig. 0.4) (Poulton and Canfield, 2011). This is evidenced most clearly in the Archean and Paleoproterozoic sedimentary rock record by the widespread present of iron formations (IFs); Fe- and Si-rich chemical sediments that formed by the precipitation of Fe minerals and amorphous silica from high-concentration dissolved pools of these elements (Bekker et al., 2010; Konhauser et al., 2017). Ferrous iron is highly soluble and thus mobile in marine settings, but when it becomes oxidized outside of strongly acidic pH conditions, Fe^{3+} is insoluble and rapidly precipitates. Thus, the most common interpretation of IFs is that they formed as a result of mobile dissolved Fe^{2+} being transported throughout largely reducing oceans, to oxidizing near-

surface marine environments that allow precipitation of Fe^{3+}-oxyhydroxide minerals (Fig. 0.4). These precipitates settled to the seafloor along with amorphous silica gels, and eventually underwent lithification. This is a highly simplified explanation of just one, if the most popular, model for IF deposition and it will be expanded up in detail at various points in this thesis (Chapters 2 to 5). However, at this point, the important concepts we must associate with IFs to understand the general picture of the pre-GOE oceans are: (i) an Fe^{2+} rich global ocean, which requires anoxic conditions at depth, and a steady Fe^{2+} source from continental runoff and hydrothermal fluids; and (ii), the existence of mechanisms to precipitate vast quantities of authigenic Fe minerals, likely through oxidation and possibly as a direct or indirect result of biological activity. These precipitation mechanisms must have been operating near the continental margins of the oceans because this is where the most voluminous 'Superior Style' IFs were deposited (Bekker et al., 2010; Konhauser et al., 2017). However, more localized volcanically associated 'Algoma Style' IFs are also quite common in the Archean Eon, and these indicate that precipitation mechanisms for Fe^{2+} were also available quite close to the seafloor hydrothermal sources of dissolved Fe^{2+} (Bekker et al., 2010; Konhauser et al., 2017).

A ferruginous global ocean state requires that that Fe^{2+} buffered away smaller sources of O_2 and H_2S in the pre-GOE oceans. Prior to the GOE, low O_2 was the norm. Meanwhile, H_2S is produced in the oceans by microbial sulfate reduction (MSR), which reduces sulfate (SO_4^{2-}) to hydrogen sulfide in order to oxidize organic carbon and derive energy from this reaction. Sulfur isotope records indicate that the pre-GOE oceans were sulfate-poor (discussed in Chapter 2) (Canfield, 2004; Crowe et al., 2014; Fike et al., 2015), so in general, MSR and production of H_2S was limited, and the larger marine Fe^{2+} pool effectively titrated it away in the form of pyrite. The sulfate supply to the oceans was so much smaller prior to the GOE because volcanic sulfur gases were the nearly

sole source of S to the oceans (Fig. 0.4) (Farquhar et al., 2000; Halevy et al., 2010; Olson et al., 2019; Scott et al., 2011), in contrast to the present, where O_2-driven oxidation of sulfide minerals in the continental crust supplies large quantities of sulfate to continental runoff. However, against the backdrop of generally ferruginous conditions, the pre-GOE oceans did contain spatially and temporally restricted occurrences of euxinic (anoxic and H_2S-rich) and oxic environments (Kendall et al., 2010). Euxinic conditions in several Neoarchean black shale deposits suggest that locally elevated sulfate supply, coincident with high organic productivity, occurred at times on the margins of some marine basins (Fig. 0.4) (Kendall et al., 2010; Olson et al., 2019; Reinhard et al., 2009; Scott et al., 2011). Meanwhile, shallow marine 'oxygen oases' have been identified in sedimentary sequences dating back to 2.95 Ga (Eickmann et al., 2018; Kurzweil et al., 2016; Ossa Ossa et al., 2018; Ostrander et al., 2019; Planavsky et al., 2014; Riding et al., 2014), and later occurrences of these closely coincide with instances of euxinia in the Neoarchean (Olson et al., 2019). The growing influence of locally euxinic and oxic conditions in the ancient oceans, starting hundreds of millions of years prior to the GOE, has only started to be fully recognized in the last two decades, and it is logical that these modern observations should lead us to re-evaluate the marine Fe cycle and the changes it underwent prior to and during the GOE. A large marine Fe^{2+} pool should have been a potent buffer for O_2 when it began to accumulate in the oceans and atmosphere and thus the evolution of the marine Fe^{2+} reservoir should play an important role in the story of what drove atmospheric oxygenation.

To generalize, the rise in atmospheric O_2 essentially requires that net geochemical O_2 source fluxes became larger than net geochemical O_2 buffers or sinks (Lyons et al., 2014). As free O_2 was ultimately only produced by oxygenic photosynthesis, conducted by cyanobacteria, there are two broad scenarios for the timing of the GOE. Either, it was spurred by a biological revolution,

wherein cyanobacteria evolved around 2.4 Ga (Fischer et al., 2016) and new photosynthetic O_2 production immediately overwhelmed all surface redox buffers in the atmosphere, exchangeable surface ocean, and emerged continental crust (Ward et al., 2016). Or, alternatively, oxygenic photosynthesis evolved up to hundreds of millions of years prior to the GOE, and surface O_2 buffers were eventually outpaced by O_2 sources, either due to declining buffering capacity, increasing cyanobacterial productivity, or both. Organic and inorganic geochemical data from rocks predating the GOE indicate at least local and low-level accumulations of O_2 in some regions of the surface oceans (Kurzweil et al., 2016; Ossa Ossa et al., 2018; Ostrander et al., 2019; Planavsky et al., 2014; Waldbauer et al., 2011), and perhaps briefly, the atmosphere (colloquially referred to as 'whiffs' of O_2; Anbar et al., 2007)), and have for the most part undermined the model for late-evolving cyanobacteria. However, this minority view still persists (Fischer et al., 2016; Johnson et al., 2013), bolstered by recent discoveries of new anoxygenic photosynthetic pathways (Daye et al., 2019), and the biological driver for the GOE is therefore considered carefully in a study of fossil microbial communities in Chapter 4.

Most research into the drivers of the GOE, however, has been directed towards understanding the change through time of the various sinks for O_2 or drivers of photosynthetic primary productivity (Lyons et al., 2014). All models for planetary oxidation can rely upon a favorable background process, the escape of hydrogen (H), to space over time. In a seminal study, Catling et al. (2001) showed that the photolysis of methane driven by stronger UV radiation from the young Sun, would have resulted in H escape rates to space orders of magnitude higher than modern ones. Hydrogen at Earth's surface is almost entirely present in its H^+ redox state, so atomic H escape from the upper atmosphere to space is a truly irreversible redox process affecting planets, and means that over time, planetary oxidation is inevitable. Whether the ultimate source of H to the upper

atmosphere is biogenic methane from the decomposition of cyanobacterial or anoxygenic bacterial organic matter, or mantle-derived thermogenic methane, the net result is oxidation of Earth's surface (Catling et al., 2001). Although only the case of cyanobacterial organic matter directly prescribes an accumulation of O_2, all of these H sources result in a gradual oxidation of the Earth and consumption of O_2 buffering capacity, for example through the oxidation of iron (Fe) or sulfur (S) in the crust or oceans.

Against the backdrop of irreversible H escape to space, changes in the O_2-buffering capacity of igneous processes are a popular long-term driver of planetary oxygenation. Igneous processes can affect the surface oxygen budget both in controlling the composition of the lava erupted to Earth's surface that then interacts with the atmosphere during chemical weathering; and in controlling the composition of volcanic gases emitted to the atmosphere. The volatile component of volcanism directly and quantifiably affects atmospheric composition and dominates discussion of volcanic impacts on atmospheric redox. A framework for thinking about the redox effect of volcanic degassing was introduced by Holland (2002), wherein the reducing power of global volcanic gas fluxes was formalized with a parameter now referred to as 'Holland's *f* ' that can be compared to a threshold level required for net oxidation of Earth's surface. Without indicating that such a change necessarily took place, Holland showed that a <0.5 log unit increase in the oxygen fugacity (f_{O2}) of volcanic gases would have been sufficient to drive the changes in Earth surface redox observed during the GOE. Subsequent work around this topic has sought to understand the feasibility of this process and its consistency with the igneous rock record. Two ways to increase the f_{O2} of volcanic gases through time are to change the redox state of the mantle or to change volcanic degassing processes.

The redox state of the mantle source for basaltic eruptions at different times in Earth history has been investigated numerous times using redox-sensitive trace element partitioning (*e.g.* Canil, 2002; Li and Lee, 2004), with the most up to date analysis suggesting that mantle f_{O2} increasing by ~0.44 log units between 4.0 Ga and 2.5 Ga (Aulbach and Stagno, 2016; Kadoya et al., 2020; Nicklas et al., 2019), similar to the threshold increase originally postulated by Holland (2002) as necessary to drive atmospheric oxygenation. Kadoya et al. (2020) calculated a 95 % probability that volcanic gases would have remained sufficiently reducing to prevent the rise of atmospheric O_2 until ~2.5 Ga, which roughly matches the timing for early whiffs of O_2 in the atmosphere (Anbar et al., 2007), and made an oxidizing transition in Earth surface environments possible from this time onwards.

Separately, a hypothesis has been proposed for a change in the redox state of volcanic gases emitted prior to the GOE due to a shift from predominantly submarine to increasingly subaerial volcanism (Gaillard et al., 2011; Kump and Barley, 2007). In this model, the shift in the location of volcanism systematically decreased the degassing pressure of sulfur gases, causing preferential speciation into the more oxidized SO_2 (S^{4+}) over H_2S (S^{2-}). This model is appealing because it satisfyingly connects the timing of Earth's oxygenation to an increase in continental emergence around 2.5 Ga, which is constrained by the frequency distribution of subaerial *vs.* submarine large igneous provinces (Kump and Barley, 2007), age distributions of continentally-derived detrital zircons (Voice et al., 2011), and triple oxygen isotope records of increased continentality in the meteoric water cycle (Bindeman et al., 2018). However, the sulfur-redox aspect of this model has recently been questioned, as it was shown that modern volcanic degassing, even in higher pressure mid ocean ridge settings, can release sufficiently oxidizing gases to support atmospheric oxygenation, and further decreases in pressure would have a limited effect in changing the overall

effect on the f_{O2} of the gas even if erupted at a subaerial volcano (Brounce et al., 2017). The other aspect of the subaerial-switch model for volcanically modulated atmospheric oxygenation is that subaerial degassing can increase the overall flux of S (with a sufficiently oxidizing redox state) to the atmosphere-ocean system (Gaillard et al., 2011; Olson et al., 2019), and therefore still result in a net increase in surface oxidation (explored in Chapter 3 of this thesis). There is therefore potential here for a change in the location of volcanic emissions to still be a viable mechanism to oxygenate the atmosphere, but further work is required to understand this quantitively, including better characterization of degassing controls in hydrous subduction zone melts (M. Brounce, personal communication).

Models that link atmospheric oxygenation to the intersection of inorganic geochemical processes and biological processes have also been proposed, on that basis that solid Earth processes play a role in controlling the availability of limiting nutrients to the oceans (Robbins et al., 2016). Two leading examples of this type of model deal with the availability of phosphorus (P), and nickel (Ni) in the Archean oceans. Phosphorus is considered the limiting nutrient required for marine photosynthetic primary productivity over geologic timescales and P limitation in the Archean oceans has been suggested based on an experimentally calibrated adsorption model linking the P/Fe ratio of Archean IFs to [P] in the contemporaneous seawater (Bjerrum and Canfield, 2002; Jones et al., 2015; Planavsky et al., 2010). Phosphorus drawdown due extensive adsorption to IFs, which themselves require reducing Fe^{2+}-rich global oceans (Reinhard et al., 2017), ties nutrient limitation to the redox state of the oceans in a circular manner and is not particularly informative for understanding the GOE. However, it is also possible that the continental weathering supply of P to the oceans increased from around 2.7 Ga, because the continental crust became ~50 % more P-rich, a result of progressive cooling and a decreasing degree of melting (Greber et al., 2017).

Meanwhile, the early the oceans were apparently rich in Ni, a crucial co-factor in an enzyme required for archaeal methanognensis, due to the weatherable crust containing a substantial component of Ni-rich ultramafic komatiite lavas, formed at high temperatures and high melt degrees (Konhauser et al., 2009). This initial Ni enrichment in seawater, and sharp decline around 2.7 Ga following the termination of extensive komatiitic crust formation, are both recorded in the Ni/Fe ratio of IFs. The decline in marine Ni starting around 2.7 Ga has been suggested to have led to an 'Ni famine' for methanogens, which could have decreased biogenic methane production and weakened the reducing power of the atmosphere in the runup to the GOE (Konhauser et al., 2015, 2009). Subsequently, it has been suggested that the Ni famine may have been delayed by a few 100 million years because whiffs of O_2 could have enabled leaching of Ni from continental sulfides (Wang et al., 2019). A concern for both the P and Ni models is that they specifically tie marine nutrient concentrations to a highly simplified adsorption model based on a single Fe precursor phase for IFs. The nature of this dominant precursor phase has recently been questioned (*e.g.* Rasmussen et al., 2015), and we explore this issue in Chapter 5. More generally, nutrient demands for marine microbes are not fixed numbers in time, and the current, highly qualitative nature of nutrient limitation models for the GOE means they should be regarded as speculative at best. Most importantly, a major increase in marine primary productivity as a driver for the GOE is not supported by the marine carbonate C isotope record, which indicates a fairly constant fractional consumption (~20 %) of marine C input by burial of organic carbon throughout the Archean eon (Hayes and Waldbauer, 2006; Holland, 2002; Lyons et al., 2014; Shields and Veizer, 2002).

Our understanding of the rise in atmospheric oxygen from around the end of the Archean eon is clearly not hindered by a shortage of explanatory models. In fact, finding ways to test the viability of these models more rigorously is arguably even more valuable than coming up with another new

hypothesis. Iron, as a major rock-forming element that forms distinct mineral phases in oxic (Fe^{3+} oxides and hydroxides), ferruginous (Fe carbonates and silicates) and euxinic (pyrite, FeS_2) environments, is the perfect witness to changes in planetary surface redox chemistry. Beyond this, Fe also plays an active role (if implicit) in many models of planetary oxidation.

With the dual significance of Fe as witness and active player in planetary redox processes in mind, the work we present in the following chapters is designed to provide some new constraints on aspects of Earth surface redox evolution preceding the GOE. In Chapter 1, we present a multi-proxy geochemical study of a 2.95 Ga paleosol (ancient weathering horizon), from which claims of early oxic weathering, have been made (Crowe et al., 2013), and present an alternative interpretation of this paleosol that does not require a dramatic overhaul of our understanding of atmospheric oxygenation. In Chapters 2 and 3, we use two novel and distinct stable Fe isotope-based approaches to reassess how the oxic and euxinic sinks for Fe in the early ferruginous oceans evolved over time. In Chapter 3 we particularly focus on in the timespan between early geologic evidence for oxygenic photosynthesis, and the GOE itself, and we show that with a new method of quantifying the relative sizes of O_2 sinks (burial of Fe^{3+} oxides) and indirect O_2 sources (burial of pyrite), we can test the viability of oxidizing the Earth's surface with volcanic S gases (Gaillard et al., 2011; Lyons and Gill, 2010; Olson et al., 2019). In Chapter 4, we investigate the interaction of Fe^{2+}-rich water and photosynthetic communities in a stromatolitic environment from ~2.45 Ga, in search of a smoking gun for the biological O_2 sources that ultimately powered the GOE. In Chapter 5, we conduct a preliminary study into the Fe isotopic systematics of greenalite, a reduced mineral proposed as an alternative primary precipitate for iron formations (Johnson et al., 2018; Rasmussen et al., 2015; Tosca et al., 2016), and test the assumption of widespread Fe^{3+} oxide

deposition in the early oceans, which underpins models of early ocean redox, and is used as the calibrant in major studies of nutrient availability.

All of these chapters lean heavily on the stable isotope systematics of Fe. Among the extant 'non-traditional' stable isotope systems used by geochemists today, Fe isotope systematics have received the richest and most detailed study (Dauphas et al., 2017). The ability of Fe isotopes to preserve the imprints of primary environmental redox reactions, and preserve these signatures through intensive reworking over billion years of metamorphism and alteration that all Precambrian rocks experienced, has made them an invaluable tool to early Earth geochemists for over two decades (Johnson et al., 2020). Each chapter in this thesis introduces the specific quirks and diagnostic behaviors of Fe isotopes in the specific geochemical environments we investigate. However, a unifying theme of this thesis is the recognition that a powerful isotopic tool can be made even more valuable when combined in novel ways with additional variables, ranging from a second Fe isotope ratio, to the morphological characteristics of a stromatolite. In doing so, we can start to distinguish between a dizzying array of ancient geochemical processes in a more precise and quantitative manner.

Early Mars

So far, our discussion of planetary surface evolution and oxidation has focused on Earth and, the first five chapters of this thesis explore some of the geochemical processes that set the stage for the Great Oxidation Event (GOE). For the last two chapters, we focus some aspects of the surface redox and volatile evolution of Mars. To do this in a way that makes the best use of lessons learned from Earth history, it is worth taking stock of some of the similarities, and differences, in the geochemical processes that affect the surface of these planets over the geological time (Fig. 0.5).

On Earth, the GOE was made possible in part by geochemical processes that are, to our knowledge, unique to Earth. Most notably, the GOE was ultimately driven by cyanobacterial oxygenic photosynthesis, which resulted in atmospheric *oxygenation*, opposed to mere planetary *oxidation*. Life is unique to Earth, as far as we know, so the process of oxygenic photosynthesis is a uniquely Earthly phenomenon that can't be used in general models of planetary surface evolution. While the search of evidence of past life on Mars is ongoing, with the beginning of the Perseverance rover mission at Jezero Crater, and this is arguably the most compelling question we have about Mars; the assumption must be that life did not arise there, until evidence proves others. Second, Earth's surface is constantly replenished by plate tectonics, which reveal the continued action of mantle convection to this day. No other planetary body in the solar system is known to have, or have had, a plate tectonic regime, which comes with major implications for volatile recycling and volcanic outgassing, weathering processes, and climate stability over billions of years. For example, clear evidence for past action of plate tectonics on Mars is absent, and major volcanism was restricted to the first <1 billion years of Mars history (Fig. 0.5)(Ehlmann et al., 2016). Early cooling of the mantle and core to produce a tectonically dead planet by around 4.0 Ga is also supported by evidence for cessation of the magnetic core dynamo around this time (Ehlmann et al., 2016; Lillis et al., 2013). Third, unlike the Earth, Mars, as a planet, is extremely arid. It is unclear whether geologic record of Mars supports a truly ocean-sized hydrological inventory at any time in its history, but if so, this large hydrosphere was lost early in Mars history (*e.g.* Alsaeed and Jakosky, n.d.; Carr and Head, 2003; Di Achille and Hynek, 2010; Head et al., 1999; Kurokawa et al., 2014; Malin and Edgett, 1999; Scheller et al., 2021). At present, the total volume of water accounted for at the surface of Mars is equivalent to a ~30 meter deep layer distributed uniformly over the surface (~30 m global equivalent layer, 'GEL'), and almost all of this water resides as ice

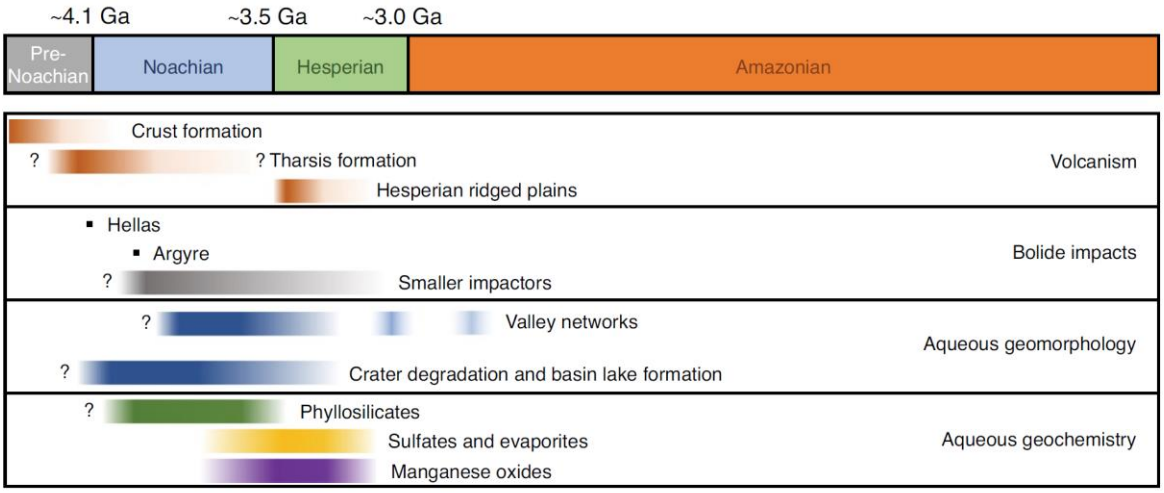

Figure 0.5. Overview of Martian epochs and estimated timing of various surface processes and features. From Wordsworth et al. (2021), reproduced with permission from Springer Nature. The early Hesperian epoch through to the present day are the focus of Chapter 6. Chapter 7 focuses on iron chemical sedimentation in lakes formed around 3.5 Ga, near the transition from wet, clay forming environments, to a more arid and oxidizing Mars surface.

in the polar caps (Carr and Head, 2015). Hydrogen isotope (D/H) ratio evolution on Mars over the past 4 billion years indicates substantial water loss has taken place, through a combination of escape to space and hydration of the crust (Alsaeed and Jakosky, 2019.; Krasnopolsky, 2015; Kurokawa et al., 2014; Mahaffy et al., 2015; Scheller et al., 2021). However, these processes of water loss diminish in efficacy heading toward to present, so Mars's hydrosphere has likely been of a similar order of magnitude to its present state for the majority of the last 4.5 billion years. Overall, at first glance, as a lifeless, tectonically dead, and extremely dry planet, Mars bears little similarity to Earth (Ehlmann et al., 2016). However, as we show in Chapters 6 and 7, which are concerned with some aspects of volatile cycling and surface redox processes on Mars, many of the same geochemical constraints and processes involved are factors that we also consider as important in the oxidation of Earth's surface.

First, Mars and Earth are both rocky planets, with a silicate mineral crust formed by primarily magmatic processes. The crusts of Mars and Earth are both iron (Fe) rich, Mars's probably more

so than Earth; and on both planets this is thus the most abundant rock-forming metal element with multiple redox states at surface conditions. Mars's crust is predominantly basaltic, like the oceanic crust of Earth, suggesting that felsic crust forming processes on Mars were not volumetrically significant (McSween et al., 2009). This is feasibly due to a lack of plate subduction that facilitates deep-seated flux melting of the mantle and extensive fractionation crystallization to evolved magmatic compositions on Earth. As with Earth, the oxidative weathering of the exposed Martian crust therefore should have acted as a potent sink for oxidized atmospheric species, and the extent of mobilization of Fe from the Martian crust may place constraints on the atmospheric redox state of early Mars.

Next, Mars also bears extensive geologic evidence for the long-lived presence of liquid water in its past (Fig. 0.5)(reviewed Ehlmann et al., 2016; Kite, 2019). So, like Earth, Mars's early surface geochemical history was influenced by water-rock interaction. While it is unclear whether Mars ever had global water oceans; river channels, large lakes within meteorite impact craters, and a putative inland sea, in the Eridania region, are well-documented (Fig. 0.5)(Dickson et al., 2009; Ehlmann et al., 2016; Grotzinger et al., 2014; Irwin et al., 2015, 2004; Kite et al., 2019; Michalski et al., 2017; Stucky de Quay et al., 2020). The chemical imprints of water on Mars are widespread; clay minerals, formed through sustained water-rock interaction and alteration of Martian basalt, are well-documented on Mars, particularly among older (Noachian, >3.56 Ga) terranes (Bishop et al., 2008; Cannon et al., 2017; Ehlmann et al., 2011; Ehlmann and Edwards, 2014; Mustard et al., 2008). Water-rock interactions on an anoxic early Mars resulted in Fe-depletion in weathering horizons (Liu et al., 2021) in a strikingly similar manner to that seen in pre-GOE paleosols on Earth (Holland, 1984; Rye and Holland, 1998). Ancient 'seafloor' deposits identified in the Eridiani region also hint at deep water hydrothermal venting to at least one large Martian water

body (Michalski et al., 2017). So, standing water bodies on early Mars were potentially Fe^{2+}-rich, much like the pre-GOE oceans, raising the possibility that we can apply lessons from the Archean chemical sedimentary record to better understand Martian sedimentary deposits and the environmental geochemical conditions they reveal.

Mars, like Earth, is also subject to the escape of hydrogen (H) to space (Fig. 0.6) (Jakosky et al., 2018). On billion-year timescales, H escape irreversibly oxidizes planetary surfaces (Catling et al., 2001). On Earth, H escape is implicated in the eventual rise of atmospheric O_2 (Catling et al., 2001), but prior to this, oxidizing power was deposited to the planetary surface through the formation of Fe^{3+} and possibly sulfate. It is unclear if Mars ever had a large atmospheric O_2 reservoir (Wordsworth et al., 2021), but abundant Fe^{3+} and sulfate at its present-day surface suggest (Burns, 1987a, 1987b; Hynek et al., 2002; Lammer et al., 2003; McSween et al., 2009; Morris et al., 2006; Niles and Michalski, 2009; Yen et al., 2005) that reduced Fe and sulfur species were important geologically long-lived oxidant sinks on early Mars. Potential mechanisms by which this surface oxidation may have taken place include aqueous Fe^{2+} photooxidation by UV radiation (Fig. 0.7) (Hurowitz et al., 2017, 2010; Nie et al., 2017; Schaefer, 1996; Tabata et al., 2021), which produces H_2 as a byproduct that can subsequently enter and then escape the atmosphere (this process is investigated in detail in Chapter 7, and was also implicated in the formation of terrestrial iron formations); and oxidation by O_2 and other reactive O species (Chevrier et al., 2006; Lanza et al., 2016; Mitra and Catalano, 2019; Smith et al., 2014; Wordsworth et al., 2021), produced through atmospheric photochemistry and associated with subsequent H escape. In Chapter 6, we will discuss how the impacts of volatile escape on Mars go far beyond slow surface oxidation and were likely the primary drivers of its surface evolution over 4 billion years. Unlike on Earth, where H escape is a minor process with respect to the planetary

surface H budget, on Mars, the time-integrated loss of H to space represents a substantial fraction of the total early Martian hydrosphere (Alsaeed and Jakosky, 2019.; Jakosky et al., 2018; Kurokawa et al., 2014; Mahaffy et al., 2015; Scheller et al., 2021).

Additionally, throughout Mars's entire history, it has been subject to a 'Faint Sun' problem similar to the one that underpins the 'paradox' of Archean Earth's climate stability (Ehlmann et al., 2016; Kite, 2019; Wordsworth et al., 2021). This fact was recognized in the original formalization of the Faint Young Sun Paradox by Sagan and Mullen (1972), however in the case of Mars, solar luminosity at all times in its history is insufficient to support stable liquid water at its surface without a strong greenhouse effect (Haberle et al., 2017). Mars orbits the Sun with a semimajor axis of 1.52 AU (where 1 AU is the average Earth-Sun distance), which due to the inverse-square relation, means that it receives less than half of the globally integrated insolation of Earth. Today, Mars has an average surface temperature of -60 °C. Beneath its 6 mbar CO_2 atmosphere, liquid water is unstable, freezing to ice and then subliming into atmospheric water vapor. It presents no Faint Young 'Paradox' in the modern day because it is precisely as frigid as one might expect from the dose of solar radiation it receives. However, Mars bears extensive geomorphic and sedimentological evidence for the past activity of large volumes of liquid water, that filled lakes and perhaps oceans, and crisscrossed the planet's surface with kilometer-scale river channels and the canyons. Therefore, early Mars's must have been warmed by a thick atmosphere with a strong greenhouse effect (*e.g.* Forget et al., 2013; Haberle et al., 2017; Kite, 2019; Kite et al., 2017; Ramirez et al., 2014; Ramirez and Craddock, 2018; Wordsworth and Pierrehumbert, 2013; Wordsworth, 2016).

In Chapter 6 of this thesis, we investigate how atmospheric and planetary surface oxidation depleted the Martian hydrosphere and atmosphere over the last 3.5 billion years (Fig. 0.6). This

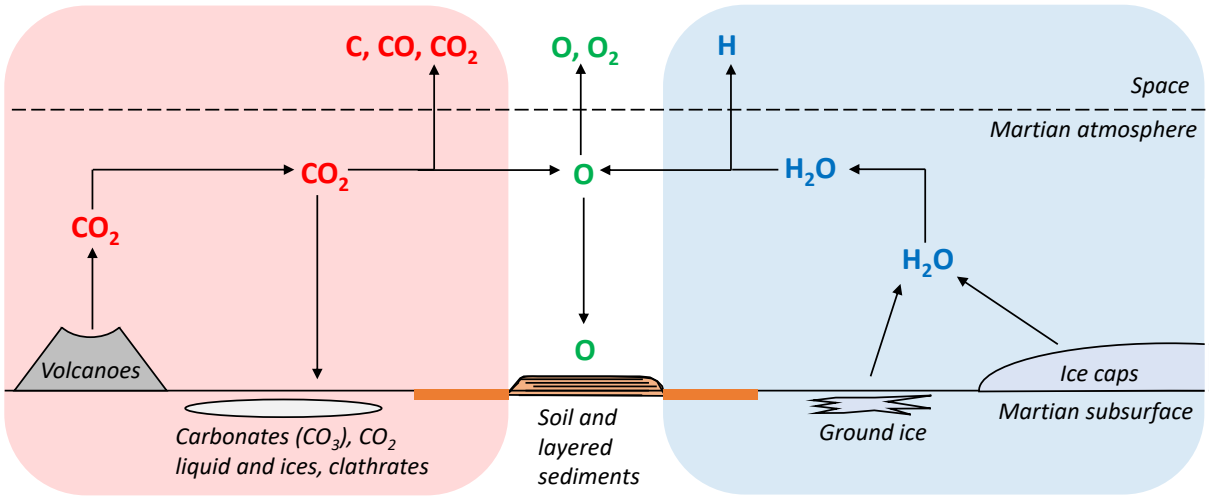

Figure 0.6. Overview of source and sink fluxes for Martian surface volatiles that we explore in detail in Chapter 6.

time interval in Mars history begins with widespread lakes of lakes and river channels indicative sustained surface liquid water stability and availability, which require an effective atmospheric greenhouse, and ends with the modern frigid, arid Mars. Understanding this transition, particularly the fate of what should have been an initially substantial (>0.25 bar) CO_2 atmosphere, requires us to consider both atmospheric escape processes and surface volatile sinks, but the problem of CO_2 loss from Mars becomes more and more difficult to answer the closer that evidence for stable liquid water is brought towards the present day, because sink process both become less effective and have less time over which to operate. This problem is compounded by a lack of evidence for major loss of C from Mars's atmosphere today (Barabash et al., 2007; Cui et al., 2019; Ramstad et al., 2018). To indirectly tackle this problem, our modeling focuses on the removal of O and H from Martian volatile reservoirs, making use of a wide variety of constraints, ranging from geochemical measurements of 3.5 billion-year-old sediments in Gale Crater made *in situ* by the Curiosity rover, to the escape rate of oxygen atoms form the top of the Martian atmosphere, measured by the Mars Atmosphere and Volatile Evolution Mission (MAVEN) orbiter. Because the finite supply of O in Martian volatile reservoirs was largely shared between H_2O and CO_2, we

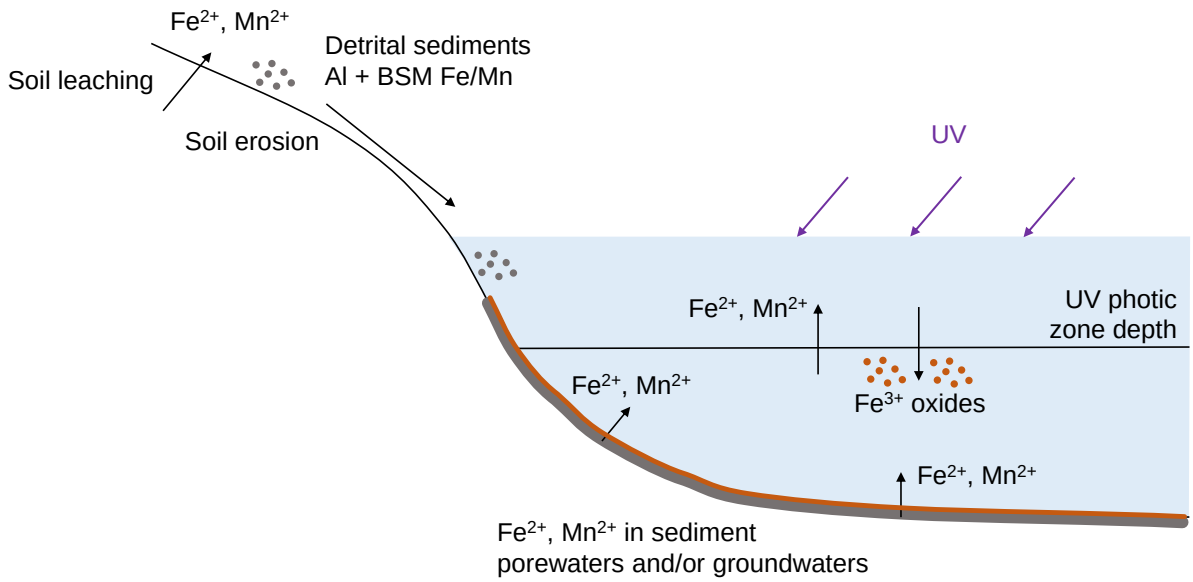

Figure 0.7. Schematic illustration of the Martian lake environments that we focus on in a study of Fe^{2+} photooxidation in Chapter 7. Presence of anoxic, ferruginous bottom waters, oxidizing conditions in a shallow water photic zone, and redox-decoupling of Fe and Mn during partial Fe^{2+} oxidation, are all familiar features of pre-GOE Earth geochemical models, and we show how applying lessons learned from the Archean Earth to early Mars can help understand the sedimentary rock record there.

show how the loss of Mars's hydrosphere, and the oxidation of Mars's surface, are the missing pieces in a global surface volatile mass balance that can be solved for ancient pCO_2 levels; and our results suggest that alternative pathways to ancient CO_2 sequestration should be explored to fully understand climate evolution on Mars since 3.5 Ga.

In the last chapter of this thesis, we move away from the global-scale, long-term evolution of Mars to take an in-depth look at aqueous Fe cycling in Martian water bodies. In Chapter 7, we focus on the role of UV photooxidation of Fe^{2+} as potentially significant process in driving chemical Fe sedimentation in Martian water bodies (Fig. 0.7) (Hurowitz et al., 2017, 2010; Nie et al., 2017; Schaefer, 1996; Tabata et al., 2021). This process has significant for the early Earth, as it has been proposed as one of the mechanisms that drove Fe oxide deposition in iron formations (IFs) (Anbar and Holland, 1992; Braterman et al., 1983; Cairns-Smith, 1978; François, 1986; Nie et al., 2017).

On Mars, however, this process takes on increased significance as the alternative, biological drivers of IF deposition were most likely not active. Our study in Chapter 7 includes an experimental redetermination of the quantum yield of Fe^{2+} photooxidation; this is the parameter that determines the kinetic efficiency of the photooxidation reaction under a given UV radiation flux; and we apply our new experimental constraints to understanding Fe^{3+} oxide deposition in Martian water bodies (Fig. 0.7). Our exploration of redox-sensitive element chemical sedimentation in Martian lakes also includes a reappraisal of the manganese (Mn) systematics of sedimentary rocks that have been mapped and characterized by the Curiosity rover at Gale Crater (Hurowitz et al., 2017; Lanza et al., 2016, 2014). We show how the decoupling of Mn from Fe in aqueous settings can be facilitated by Fe photooxidation, and apply the lessons learned from Mn/Fe systematics in terrestrial IFs to better understanding how Mn-rich sedimentary materials could have formed on Mars (Hiebert et al., 2018; Kurzweil et al., 2016; Planavsky et al., 2014; Tsikos et al., 2010). The huge geochemical archive of the pre-oxygenation Earth provides an invaluable reference when interpreting the sedimentary record on Mars. This chapter hopefully helps to emphasize that our understanding the Martian rock record will benefit immeasurably from planetary scientists familiarizing themselves with the ancient episodes of our own planet's history.

References

Aarons, S.M., Reimink, J.R., Greber, N.D., Heard, A.W., Zhang, Z., Dauphas, N., 2020. Titanium isotopes constrain a magmatic transition at the Hadean-Archean boundary in the Acasta Gneiss Complex. Sci. Adv. 6, eabc9959. https://doi.org/10.1126/sciadv.abc9959

Alsaeed, N.R., Jakosky, B.M., 2019 Mars Water and D/H Evolution from 3.3 Ga to Present. J. Geophys. Res. Planets 124, 1, 3344−3353. https://doi.org/10.1029/2019JE006066

Anbar, A.D., Duan, Y., Lyons, T.W., Arnold, G.L., Kendall, B., Creaser, R.A., Kaufman, A.J., Gordon, G.W., Scott, C., Garvin, J., Buick, R., 2007. A Whiff of Oxygen Before the Great Oxidation Event? Science 317, 1903–1906. https://doi.org/10.1126/science.1140325

Anbar, A.D., Holland, H.D., 1992. The photochemistry of manganese and the origin of banded iron formations. Geochim. Cosmochim. Acta 56, 2595–2603. https://doi.org/10.1016/0016-7037(92)90346-K

Aulbach, S., Stagno, V., 2016. Evidence for a reducing Archean ambient mantle and its effects on the carbon cycle. Geology 44, 751–754. https://doi.org/10.1130/G38070.1

Barabash, S., Fedorov, A., Lundin, R., Sauvaud, J.-A., 2007. Martian Atmospheric Erosion Rates. Science 315, 501–503. https://doi.org/10.1126/science.1134358

Bekker, A., Holland, H.D., Wang, P.-L., Rumble Iii, D., Stein, H.J., Hannah, J.L., Coetzee, L.L., Beukes, N.J., 2004. Dating the rise of atmospheric oxygen. Nature 427, 117–120. https://doi.org/10.1038/nature02260

Bekker, A., Slack, J.F., Planavsky, N., Krapež, B., Hofmann, A., Konhauser, K.O., Rouxel, O.J., 2010. Iron Formation: The Sedimentary Product of a Complex Interplay among Mantle, Tectonic, Oceanic, and Biospheric Processes. Econ. Geol. 105, 467–508. https://doi.org/10.2113/gsecongeo.105.3.467

Bindeman, I.N., Zakharov, D.O., Palandri, J., Greber, N.D., Dauphas, N., Retallack, G.J., Hofmann, A., Lackey, J.S., Bekker, A., 2018. Rapid emergence of subaerial landmasses and onset of a modern hydrologic cycle 2.5 billion years ago. Nature 557, 545. https://doi.org/10.1038/s41586-018-0131-1

Bishop, J.L., Dobrea, E.Z.N., McKeown, N.K., Parente, M., Ehlmann, B.L., Michalski, J.R., Milliken, R.E., Poulet, F., Swayze, G.A., Mustard, J.F., Murchie, S.L., Bibring, J.-P., 2008. Phyllosilicate Diversity and Past Aqueous Activity Revealed at Mawrth Vallis, Mars. Science 321, 830–833. https://doi.org/10.1126/science.1159699

Bjerrum, C.J., Canfield, D.E., 2002. Ocean productivity before about 1.9 Gyr ago limited by phosphorus adsorption onto iron oxides. Nature 417, 159–162. https://doi.org/10.1038/417159a

Bowring, S.A., Williams, I.S., 1999. Priscoan (4.00–4.03 Ga) orthogneisses from northwestern Canada. Contrib. Mineral. Petrol. 134, 3–16. https://doi.org/10.1007/s004100050465

Braterman, P.S., Cairns-Smith, A.G., Sloper, R.W., 1983. Photo-oxidation of hydrated Fe2+—significance for banded iron formations. Nature 303, 163–164. https://doi.org/10.1038/303163a0

Brounce, M., Stolper, E., Eiler, J., 2017. Redox variations in Mauna Kea lavas, the oxygen fugacity of the Hawaiian plume, and the role of volcanic gases in Earth's oxygenation. Proc. Natl. Acad. Sci. 114, 8997–9002. https://doi.org/10.1073/pnas.1619527114

Burns, R.G., 1987a. Ferric sulfates on Mars. J. Geophys. Res. Solid Earth 92, E570–E574. https://doi.org/10.1029/JB092iB04p0E570

Burns, R.G., 1987b. Gossans on Mars: Spectral features attributed to jarosite (No. 19870013984), NASA, Washington, Reports of Planetary Geology and Geophysics Program, 1986.

Cairns-Smith, A.G., 1978. Precambrian solution photochemistry, inverse segregation, and banded iron formations. Nature 276, 807–808. https://doi.org/10.1038/276807a0

Canfield, D.E., 2004. The evolution of the Earth surface sulfur reservoir. Am. J. Sci. 304, 839–861. https://doi.org/10.2475/ajs.304.10.839

Canil, D., 2002. Vanadium in peridotites, mantle redox and tectonic environments: Archean to present. Earth Planet. Sci. Lett. 195, 75–90. https://doi.org/10.1016/S0012-821X(01)00582-9

Cannon, K.M., Parman, S.W., Mustard, J.F., 2017. Primordial clays on Mars formed beneath a steam or supercritical atmosphere. Nature 552, 88. https://doi.org/10.1038/nature24657

Canup, R.M., Righter, K., Dauphas, N., Pahlevan, K., Ćuk, M., Lock, S.J., Stewart, S.T., Salmon, J., Rufu, R., Nakajima, M., Magna, T., 2021. Origin of the Moon. ArXiv210302045 Astro-Ph Physicsphysics.

Carr, M.H., Head, J.W., 2015. Martian surface/near-surface water inventory: Sources, sinks, and changes with time. Geophys. Res. Lett. 42, 726–732. https://doi.org/10.1002/2014GL062464

Carr, M.H., Head, J.W., 2003. Oceans on Mars: An assessment of the observational evidence and possible fate. J. Geophys. Res. Planets 108. https://doi.org/10.1029/2002JE001963

Catling, D.C., Zahnle, K.J., McKay, C.P., 2001. Biogenic Methane, Hydrogen Escape, and the Irreversible Oxidation of Early Earth. Science 293, 839–843. https://doi.org/10.1126/science.1061976

Chen, K., Rudnick, R.L., Wang, Z., Tang, M., Gaschnig, R.M., Zou, Z., He, T., Hu, Z., Liu, Y., 2020. How mafic was the Archean upper continental crust? Insights from Cu and Ag in ancient glacial diamictites. Geochim. Cosmochim. Acta, The continents: Origin, evolution and interactions with other reservoirs 278, 16–29. https://doi.org/10.1016/j.gca.2019.08.002

Chevrier, V., Mathé, P.-E., Rochette, P., Grauby, O., Bourrié, G., Trolard, F., 2006. Iron weathering products in a CO2 + (H2O or H2O2) atmosphere: Implications for weathering processes on the surface of Mars. Geochim. Cosmochim. Acta 70, 4295–4317. https://doi.org/10.1016/j.gca.2006.06.1368

Craddock, P.R., Dauphas, N., 2011. Iron and carbon isotope evidence for microbial iron respiration throughout the Archean. Earth Planet. Sci. Lett. 303, 121–132. https://doi.org/10.1016/j.epsl.2010.12.045

Crowe, S.A., Døssing, L.N., Beukes, N.J., Bau, M., Kruger, S.J., Frei, R., Canfield, D.E., 2013. Atmospheric oxygenation three billion years ago. Nature 501, 535–538. https://doi.org/10.1038/nature12426

Crowe, S.A., Paris, G., Katsev, S., Jones, C., Kim, S.-T., Zerkle, A.L., Nomosatryo, S., Fowle, D.A., Adkins, J.F., Sessions, A.L., Farquhar, J., Canfield, D.E., 2014. Sulfate was a trace constituent of Archean seawater. Science 346, 735–739. https://doi.org/10.1126/science.1258966

Cui, J., Wu, X.-S., Gu, H., Jiang, F.-Y., Wei, Y., 2019. Photochemical escape of atomic C and N on Mars: clues from a multi-instrument MAVEN dataset. Astron. Astrophys. 621, A23. https://doi.org/10.1051/0004-6361/201833749

Dauphas, N., John, S.G., Rouxel, O., 2017. Iron Isotope Systematics. Rev. Mineral. Geochem. 82, 415–510. https://doi.org/10.1515/9783110545630-012

Dauphas, N., Zuilen, M. van, Wadhwa, M., Davis, A.M., Marty, B., Janney, P.E., 2004. Clues from Fe Isotope Variations on the Origin of Early Archean BIFs from Greenland. Science 306, 2077–2080. https://doi.org/10.1126/science.1104639

Daye, M., Klepac-Ceraj, V., Pajusalu, M., Rowland, S., Farrell-Sherman, A., Beukes, N., Tamura, N., Fournier, G., Bosak, T., 2019. Light-driven anaerobic microbial oxidation of manganese. Nature 576, 311–314. https://doi.org/10.1038/s41586-019-1804-0

Di Achille, G., Hynek, B.M., 2010. Ancient ocean on Mars supported by global distribution of deltas and valleys. Nat. Geosci. 3, 459–463. https://doi.org/10.1038/ngeo891

Dickson, J.L., Fassett, C.I., Head, J.W., 2009. Amazonian-aged fluvial valley systems in a climatic microenvironment on Mars: Melting of ice deposits on the interior of Lyot Crater. Geophys. Res. Lett. 36. https://doi.org/10.1029/2009GL037472

Dodd, M.S., Papineau, D., Grenne, T., Slack, J.F., Rittner, M., Pirajno, F., O'Neil, J., Little, C.T.S., 2017. Evidence for early life in Earth's oldest hydrothermal vent precipitates. Nature 543, 60–64. https://doi.org/10.1038/nature21377

Ehlmann, B.L., Anderson, F.S., Andrews-Hanna, J., Catling, D.C., Christensen, P.R., Cohen, B.A., Dressing, C.D., Edwards, C.S., Elkins-Tanton, L.T., Farley, K.A., Fassett, C.I., Fischer, W.W., Fraeman, A.A., Golombek, M.P., Hamilton, V.E., Hayes, A.G., Herd, C.D.K., Horgan, B., Hu, R., Jakosky, B.M., Johnson, J.R., Kasting, J.F., Kerber, L., Kinch, K.M., Kite, E.S., Knutson, H.A., Lunine, J.I., Mahaffy, P.R., Mangold, N., McCubbin, F.M., Mustard, J.F., Niles, P.B., Quantin-Nataf, C., Rice, M.S., Stack, K.M., Stevenson, D.J., Stewart, S.T., Toplis, M.J., Usui, T., Weiss, B.P., Werner, S.C., Wordsworth, R.D., Wray, J.J., Yingst, R.A., Yung, Y.L., Zahnle, K.J., 2016. The sustainability of habitability on terrestrial planets: Insights, questions, and needed measurements from Mars for understanding the evolution of Earth-like worlds. J. Geophys. Res. Planets 121, 2016JE005134. https://doi.org/10.1002/2016JE005134

Ehlmann, B.L., Edwards, C.S., 2014. Mineralogy of the Martian Surface. Annu. Rev. Earth Planet. Sci. 42, 291–315. https://doi.org/10.1146/annurev-earth-060313-055024

Ehlmann, B.L., Mustard, J.F., Murchie, S.L., Bibring, J.-P., Meunier, A., Fraeman, A.A., Langevin, Y., 2011. Subsurface water and clay mineral formation during the early history of Mars. Nature 479, 53–60. https://doi.org/10.1038/nature10582

Eickmann, B., Hofmann, A., Wille, M., Bui, T.H., Wing, B.A., Schoenberg, R., 2018. Isotopic evidence for oxygenated Mesoarchaean shallow oceans. Nat. Geosci. 11, 133. https://doi.org/10.1038/s41561-017-0036-x

Evans, D.A., Beukes, N.J., Kirschvink, J.L., 1997. Low-latitude glaciation in the Palaeoproterozoic era. Nature 386, 262–266. https://doi.org/10.1038/386262a0

Farquhar, J., Bao, H., Thiemens, M., 2000. Atmospheric Influence of Earth's Earliest Sulfur Cycle. Science 289, 756–758. https://doi.org/10.1126/science.289.5480.756

Farquhar, J., Savarino, J., Airieau, S., Thiemens, M.H., 2001. Observation of wavelength-sensitive mass-independent sulfur isotope effects during SO2 photolysis: Implications for the early atmosphere. J. Geophys. Res. Planets 106, 32829–32839. https://doi.org/10.1029/2000JE001437

Farquhar, J., Wing, B.A., 2003. Multiple sulfur isotopes and the evolution of the atmosphere. Earth Planet. Sci. Lett. 213, 1–13. https://doi.org/10.1016/S0012-821X(03)00296-6

Feulner, G., 2012. The faint young Sun problem. Rev. Geophys. 50. https://doi.org/10.1029/2011RG000375

Fike, D.A., Bradley, A.S., Rose, C.V., 2015. Rethinking the Ancient Sulfur Cycle. Annu. Rev. Earth Planet. Sci. 43, 593–622. https://doi.org/10.1146/annurev-earth-060313-054802

Fischer, W.W., Hemp, J., Johnson, J.E., 2016. Evolution of Oxygenic Photosynthesis. Annu. Rev. Earth Planet. Sci. 44, 647–683. https://doi.org/10.1146/annurev-earth-060313-054810

Flament, N., Coltice, N., Rey, P.F., 2008. A case for late-Archaean continental emergence from thermal evolution models and hypsometry. Earth Planet. Sci. Lett. 275, 326–336. https://doi.org/10.1016/j.epsl.2008.08.029

Foley, B.J., 2018. The dependence of planetary tectonics on mantle thermal state: applications to early Earth evolution. Philos. Trans. R. Soc. Math. Phys. Eng. Sci. 376, 20170409. https://doi.org/10.1098/rsta.2017.0409

Forget, F., Wordsworth, R., Millour, E., Madeleine, J.-B., Kerber, L., Leconte, J., Marcq, E., Haberle, R.M., 2013. 3D modelling of the early martian climate under a denser CO2 atmosphere: Temperatures and CO2 ice clouds. Icarus 222, 81–99. https://doi.org/10.1016/j.icarus.2012.10.019
François, L.M., 1986. Extensive deposition of banded iron formations was possible without photosynthesis. Nature 320, 352–354. https://doi.org/10.1038/320352a0

Gaillard, F., Scaillet, B., Arndt, N.T., 2011. Atmospheric oxygenation caused by a change in volcanic degassing pressure. Nature 478, 229–232. https://doi.org/10.1038/nature10460

Greber, N.D., Dauphas, N., 2019. The chemistry of fine-grained terrigenous sediments reveals a chemically evolved Paleoarchean emerged crust. Geochim. Cosmochim. Acta 255, 247–264. https://doi.org/10.1016/j.gca.2019.04.012

Greber, N.D., Dauphas, N., Bekker, A., Ptáček, M.P., Bindeman, I.N., Hofmann, A., 2017. Titanium isotopic evidence for felsic crust and plate tectonics 3.5 billion years ago. Science 357, 1271–1274. https://doi.org/10.1126/science.aan8086

Grotzinger, J.P., Sumner, D.Y., Kah, L.C., Stack, K., Gupta, S., Edgar, L., Rubin, D., Lewis, K., Schieber, J., Mangold, N., Milliken, R., Conrad, P.G., DesMarais, D., Farmer, J., Siebach, K., Calef, F., Hurowitz, J., McLennan, S.M., Ming, D., Vaniman, D., Crisp, J., Vasavada, A., Edgett, K.S., Malin, M., Blake, D., Gellert, R., Mahaffy, P., Wiens, R.C., Maurice, S., Grant, J.A., Wilson, S., Anderson, R.C., Beegle, L., Arvidson, R., Hallet, B., Sletten, R.S., Rice, M., Bell, J., Griffes, J., Ehlmann, B., Anderson, R.B., Bristow, T.F., Dietrich, W.E., Dromart, G., Eigenbrode, J., Fraeman, A., Hardgrove, C., Herkenhoff, K., Jandura, L., Kocurek, G., Lee, S., Leshin, L.A., Leveille, R., Limonadi, D., Maki, J., McCloskey, S., Meyer, M., Minitti, M., Newsom, H., Oehler, D., Okon, A., Palucis, M., Parker, T., Rowland, S., Schmidt, M., Squyres, S., Steele, A., Stolper, E., Summons, R., Treiman, A., Williams, R., Yingst, A., Team, M.S., 2014. A Habitable Fluvio-Lacustrine Environment at Yellowknife Bay, Gale Crater, Mars. Science 343, 1242777. https://doi.org/10.1126/science.1242777

Gumsley, A.P., Chamberlain, K.R., Bleeker, W., Söderlund, U., Kock, M.O. de, Larsson, E.R., Bekker, A., 2017. Timing and tempo of the Great Oxidation Event. Proc. Natl. Acad. Sci. 114, 1811–1816. https://doi.org/10.1073/pnas.1608824114

Haberle, R.M., Catling, D.C., Carr, M.H., Zahnle, K.J., 2017. The Early Mars Climate System, in: The Atmosphere and Climate of Mars, Cambridge Planetary Science. Cambridge University Press, Cambridge, pp. 526–568.

Halevy, I., Johnston, D.T., Schrag, D.P., 2010. Explaining the Structure of the Archean Mass-Independent Sulfur Isotope Record. Science 329, 204–207. https://doi.org/10.1126/science.1190298

Haqq-Misra, J.D., Domagal-Goldman, S.D., Kasting, P.J., Kasting, J.F., 2008. A Revised, Hazy Methane Greenhouse for the Archean Earth. Astrobiology 8, 1127–1137. https://doi.org/10.1089/ast.2007.0197

Hawkesworth, C.J., Cawood, P.A., Dhuime, B., 2020. The Evolution of the Continental Crust and the Onset of Plate Tectonics. Front. Earth Sci. 8. https://doi.org/10.3389/feart.2020.00326

Hayes, J.M., Waldbauer, J.R., 2006. The carbon cycle and associated redox processes through time. Philos. Trans. R. Soc. B Biol. Sci. 361, 931–950. https://doi.org/10.1098/rstb.2006.1840

Head, J.W., Hiesinger, H., Ivanov, M.A., Kreslavsky, M.A., Pratt, S., Thomson, B.J., 1999. Possible Ancient Oceans on Mars: Evidence from Mars Orbiter Laser Altimeter Data. Science 286, 2134–2137. https://doi.org/10.1126/science.286.5447.2134

Hiebert, R.S., Bekker, A., Houlé, M.G., Rouxel, O.J., 2018. Depositional setting of the Late Archean Fe oxide- and sulfide-bearing chert and graphitic argillite in the Shaw Dome, Abitibi greenstone belt, Canada. Precambrian Res. 311, 98–116. https://doi.org/10.1016/j.precamres.2018.04.004

Holland, H.D., 2002. Volcanic gases, black smokers, and the great oxidation event. Geochim. Cosmochim. Acta 66, 3811–3826. https://doi.org/10.1016/S0016-7037(02)00950-X

Holland, H.D., 1984. The Chemical Evolution of the Atmosphere and Oceans, Princeton University Press, Princeton.

Hurowitz, J.A., Fischer, W.W., Tosca, N.J., Milliken, R.E., 2010. Origin of acidic surface waters and the evolution of atmospheric chemistry on early Mars. Nat. Geosci. 3, 323–326. https://doi.org/10.1038/ngeo831

Hurowitz, J.A., Grotzinger, J.P., Fischer, W.W., McLennan, S.M., Milliken, R.E., Stein, N., Vasavada, A.R., Blake, D.F., Dehouck, E., Eigenbrode, J.L., Fairén, A.G., Frydenvang, J., Gellert, R., Grant, J.A., Gupta, S., Herkenhoff, K.E., Ming, D.W., Rampe, E.B., Schmidt, M.E., Siebach, K.L., Stack-Morgan, K., Sumner, D.Y., Wiens, R.C., 2017. Redox stratification of an ancient lake in Gale crater, Mars. Science 356, eaah6849. https://doi.org/10.1126/science.aah6849

Hynek, B.M., Arvidson, R.E., Phillips, R.J., 2002. Geologic setting and origin of Terra Meridiani hematite deposit on Mars. J. Geophys. Res. Planets 107, 5088. https://doi.org/10.1029/2002JE001891

Irwin, R.P., Howard, A.D., Maxwell, T.A., 2004. Geomorphology of Ma'adim Vallis, Mars, and associated paleolake basins. J. Geophys. Res. Planets 109. https://doi.org/10.1029/2004JE002287
Irwin, R.P., Lewis, K.W., Howard, A.D., Grant, J.A., 2015. Paleohydrology of Eberswalde crater, Mars. Geomorphology, Planetary Geomorphology: Proceedings of the 45th Annual Binghamton Geomorphology Symposium, held 12-14 September 2014 in Knoxville, Tennessee, USA 240, 83–101. https://doi.org/10.1016/j.geomorph.2014.10.012

Jakosky, B.M., Brain, D., Chaffin, M., Curry, S., Deighan, J., Grebowsky, J., Halekas, J., Leblanc, F., Lillis, R., Luhmann, J.G., Andersson, L., Andre, N., Andrews, D., Baird, D., Baker, D., Bell, J., Benna, M., Bhattacharyya, D., Bougher, S., Bowers, C., Chamberlin, P., Chaufray, J.-Y., Clarke, J., Collinson, G., Combi, M., Connerney, J., Connour, K., Correira, J., Crabb, K., Crary, F., Cravens, T., Crismani, M., Delory, G., Dewey, R., DiBraccio, G., Dong, C., Dong, Y., Dunn, P., Egan, H., Elrod, M., England, S., Eparvier, F., Ergun, R., Eriksson, A., Esman, T., Espley, J., Evans, S., Fallows, K., Fang, X., Fillingim, M., Flynn, C., Fogle, A., Fowler, C., Fox, J., Fujimoto, M., Garnier, P., Girazian, Z., Groeller, H., Gruesbeck, J., Hamil, O., Hanley, K.G., Hara, T., Harada, Y., Hermann, J., Holmberg, M., Holsclaw, G., Houston, S., Inui, S., Jain, S., Jolitz, R., Kotova, A., Kuroda, T., Larson, D., Lee, Y., Lee, C., Lefevre, F., Lentz, C., Lo, D., Lugo, R., Ma, Y.-J., Mahaffy, P., Marquette, M.L., Matsumoto, Y., Mayyasi, M., Mazelle, C., McClintock, W., McFadden, J., Medvedev, A., Mendillo, M., Meziane, K., Milby, Z., Mitchell, D., Modolo, R., Montmessin, F., Nagy, A., Nakagawa, H., Narvaez, C., Olsen, K., Pawlowski, D., Peterson, W.,

Rahmati, A., Roeten, K., Romanelli, N., Ruhunusiri, S., Russell, C., Sakai, S., Schneider, N., Seki, K., Sharrar, R., Shaver, S., Siskind, D.E., Slipski, M., Soobiah, Y., Steckiewicz, M., Stevens, M.H., Stewart, I., Stiepen, A., Stone, S., Tenishev, V., Terada, N., Terada, K., Thiemann, E., Tolson, R., Toth, G., Trovato, J., Vogt, M., Weber, T., Withers, P., Xu, S., Yelle, R., Yiğit, E., Zurek, R., 2018. Loss of the Martian atmosphere to space: Present-day loss rates determined from MAVEN observations and integrated loss through time. Icarus. https://doi.org/10.1016/j.icarus.2018.05.030

Johnson, C., Beard, B., Weyer, S., 2020. The Ancient Earth, in: Johnson, C., Beard, B., Weyer, S. (Eds.), Iron Geochemistry: An Isotopic Perspective, Advances in Isotope Geochemistry. Springer International Publishing, Cham, pp. 215–360. https://doi.org/10.1007/978-3-030-33828-2_6

Johnson, J.E., Muhling, J.R., Cosmidis, J., Rasmussen, B., Templeton, A.S., 2018. Low-Fe(III) Greenalite Was a Primary Mineral From Neoarchean Oceans. Geophys. Res. Lett. 45, 3182–3192. https://doi.org/10.1002/2017GL076311

Johnson, J.E., Webb, S.M., Thomas, K., Ono, S., Kirschvink, J.L., Fischer, W.W., 2013. Manganese-oxidizing photosynthesis before the rise of cyanobacteria. Proc. Natl. Acad. Sci. 110, 11238–11243. https://doi.org/10.1073/pnas.1305530110

Jones, C., Nomosatryo, S., Crowe, S.A., Bjerrum, C.J., Canfield, D.E., 2015. Iron oxides, divalent cations, silica, and the early earth phosphorus crisis. Geology 43, 135–138. https://doi.org/10.1130/G36044.1

Kadoya, S., Catling, D.C., Nicklas, R.W., Puchtel, I.S., Anbar, A.D., 2020. Mantle data imply a decline of oxidizable volcanic gases could have triggered the Great Oxidation. Nat. Commun. 11, 2774. https://doi.org/10.1038/s41467-020-16493-1

Kasting, J.F., 1982. Stability of ammonia in the primitive terrestrial atmosphere. J. Geophys. Res. Oceans 87, 3091–3098. https://doi.org/10.1029/JC087iC04p03091

Keller, C.B., Harrison, T.M., 2020. Constraining crustal silica on ancient Earth. Proc. Natl. Acad. Sci. 117, 21101–21107. https://doi.org/10.1073/pnas.2009431117

Kendall, B., Reinhard, C.T., Lyons, T.W., Kaufman, A.J., Poulton, S.W., Anbar, A.D., 2010. Pervasive oxygenation along late Archaean ocean margins. Nat. Geosci. 3, 647–652. https://doi.org/10.1038/ngeo942

Kite, E.S., 2019. Geologic Constraints on Early Mars Climate. Space Sci. Rev. 215, 10. https://doi.org/10.1007/s11214-018-0575-5

Kite, E.S., Gao, P., Goldblatt, C., Mischna, M.A., Mayer, D.P., Yung, Y.L., 2017. Methane bursts as a trigger for intermittent lake-forming climates on post-Noachian Mars. Nat. Geosci. 10, 737–740. https://doi.org/10.1038/ngeo3033

Kite, E.S., Mayer, D.P., Wilson, S.A., Davis, J.M., Lucas, A.S., Quay, G.S. de, 2019. Persistence of intense, climate-driven runoff late in Mars history. Sci. Adv. 5, eaav7710. https://doi.org/10.1126/sciadv.aav7710

Knauth, L.P., Lowe, D.R., 2003. High Archean climatic temperature inferred from oxygen isotope geochemistry of cherts in the 3.5 Ga Swaziland Supergroup, South Africa. Bull. Geol. Soc. Am. 115, 566–580. https://doi.org/10.1130/0016-7606(2003)115<0566:HACTIF>2.0.CO;2

Konhauser, K.O., Pecoits, E., Lalonde, S.V., Papineau, D., Nisbet, E.G., Barley, M.E., Arndt, N.T., Zahnle, K., Kamber, B.S., 2009. Oceanic nickel depletion and a methanogen famine before the Great Oxidation Event. Nature 458, 750–753. https://doi.org/10.1038/nature07858

Konhauser, K.O., Planavsky, N.J., Hardisty, D.S., Robbins, L.J., Warchola, T.J., Haugaard, R., Lalonde, S.V., Partin, C.A., Oonk, P.B.H., Tsikos, H., Lyons, T.W., Bekker, A., Johnson, C.M., 2017. Iron formations: A global record of Neoarchaean to Palaeoproterozoic environmental history. Earth-Sci. Rev. 172, 140–177. https://doi.org/10.1016/j.earscirev.2017.06.012

Konhauser, K.O., Robbins, L.J., Pecoits, E., Peacock, C., Kappler, A., Lalonde, S.V., 2015. The Archean Nickel Famine Revisited. Astrobiology 15, 804–815. https://doi.org/10.1089/ast.2015.1301

Kopp, R.E., Kirschvink, J.L., Hilburn, I.A., Nash, C.Z., 2005. The Paleoproterozoic snowball Earth: A climate disaster triggered by the evolution of oxygenic photosynthesis. Proc. Natl. Acad. Sci. 102, 11131–11136. https://doi.org/10.1073/pnas.0504878102

Korenaga, J., Planavsky, N.J., Evans, D.A.D., 2017. Global water cycle and the coevolution of the Earth's interior and surface environment. Philos. Trans. R. Soc. Math. Phys. Eng. Sci. 375, 20150393. https://doi.org/10.1098/rsta.2015.0393

Krasnopolsky, V.A., 2015. Variations of the HDO/H2O ratio in the martian atmosphere and loss of water from Mars. Icarus 257, 377–386. https://doi.org/10.1016/j.icarus.2015.05.021

Kuhn, W.R., Atreya, S.K., 1979. Ammonia photolysis and the greenhouse effect in the primordial atmosphere of the earth. Icarus 37, 207–213. https://doi.org/10.1016/0019-1035(79)90126-X

Kuhn, W.R., Kasting, J.F., 1983. Effects of increased CO 2 concentrations on surface temperature of the early Earth. Nature 301, 53–55. https://doi.org/10.1038/301053a0

Kump, L.R., Barley, M.E., 2007. Increased subaerial volcanism and the rise of atmospheric oxygen 2.5 billion years ago. Nature 448, 1033–1036. https://doi.org/10.1038/nature06058

Kurokawa, H., Sato, M., Ushioda, M., Matsuyama, T., Moriwaki, R., Dohm, J.M., Usui, T., 2014. Evolution of water reservoirs on Mars: Constraints from hydrogen isotopes in martian meteorites. Earth Planet. Sci. Lett. 394, 179–185. https://doi.org/10.1016/j.epsl.2014.03.027

Kurzweil, F., Wille, M., Gantert, N., Beukes, N.J., Schoenberg, R., 2016. Manganese oxide shuttling in pre-GOE oceans – evidence from molybdenum and iron isotopes. Earth Planet. Sci. Lett. 452, 69–78. https://doi.org/10.1016/j.epsl.2016.07.013

Lammer, H., Lichtenegger, H.I.M., Kolb, C., Ribas, I., Guinan, E.F., Abart, R., Bauer, S.J., 2003. Loss of water from Mars:: Implications for the oxidation of the soil. Icarus 165, 9–25. https://doi.org/10.1016/S0019-1035(03)00170-2

Lanza, N.L., Fischer, W.W., Wiens, R.C., Grotzinger, J., Ollila, A.M., Cousin, A., Anderson, R.B., Clark, B.C., Gellert, R., Mangold, N., Maurice, S., Le Mouélic, S., Nachon, M., Schmidt, M., Berger, J., Clegg, S.M., Forni, O., Hardgrove, C., Melikechi, N., Newsom, H.E., Sautter, V., 2014. High manganese concentrations in rocks at Gale crater, Mars. Geophys. Res. Lett. 41, 2014GL060329. https://doi.org/10.1002/2014GL060329

Lanza, N.L., Wiens, R.C., Arvidson, R.E., Clark, B.C., Fischer, W.W., Gellert, R., Grotzinger, J.P., Hurowitz, J.A., McLennan, S.M., Morris, R.V., Rice, M.S., Bell, J.F., Berger, J.A., Blaney, D.L., Bridges, N.T., Calef, F., Campbell, J.L., Clegg, S.M., Cousin, A., Edgett, K.S., Fabre, C., Fisk, M.R., Forni, O., Frydenvang, J., Hardy, K.R., Hardgrove, C., Johnson, J.R., Lasue, J., Le Mouélic, S., Malin, M.C., Mangold, N., Martìn-Torres, J., Maurice, S., McBride, M.J., Ming, D.W., Newsom, H.E., Ollila, A.M., Sautter, V., Schröder, S., Thompson, L.M., Treiman, A.H., VanBommel, S., Vaniman, D.T., Zorzano, M.-P., 2016. Oxidation of manganese in an ancient aquifer, Kimberley formation, Gale crater, Mars. Geophys. Res. Lett. 43, 2016GL069109. https://doi.org/10.1002/2016GL069109

Li, Z.-X.A., Lee, C.-T.A., 2004. The constancy of upper mantle fO2 through time inferred from V/Sc ratios in basalts. Earth Planet. Sci. Lett. 228, 483–493. https://doi.org/10.1016/j.epsl.2004.10.006

Liljestrand, F.L., Knoll, A.H., Tosca, N.J., Cohen, P.A., Macdonald, F.A., Peng, Y., Johnston, D.T., 2020. The triple oxygen isotope composition of Precambrian chert. Earth Planet. Sci. Lett. 537, 116167. https://doi.org/10.1016/j.epsl.2020.116167

Lillis, R.J., Robbins, S., Manga, M., Halekas, J.S., Frey, H.V., 2013. Time history of the Martian dynamo from crater magnetic field analysis. J. Geophys. Res. Planets 118, 1488–1511. https://doi.org/10.1002/jgre.20105

Liu, J., Michalski, J.R., Tan, W., He, H., Ye, B., Xiao, L., 2021. Anoxic chemical weathering under a reducing greenhouse on early Mars. Nat. Astron. 1–7. https://doi.org/10.1038/s41550-021-01303-5

Luo, G., Ono, S., Beukes, N.J., Wang, D.T., Xie, S., Summons, R.E., 2016. Rapid oxygenation of Earth's atmosphere 2.33 billion years ago. Sci. Adv. 2, e1600134. https://doi.org/10.1126/sciadv.1600134

Lyons, T.W., Gill, B.C., 2010. Ancient Sulfur Cycling and Oxygenation of the Early Biosphere. Elements 6, 93–99. https://doi.org/10.2113/gselements.6.2.93

Lyons, T.W., Reinhard, C.T., Planavsky, N.J., 2014. The rise of oxygen in Earth's early ocean and atmosphere. Nature 506, 307–315. https://doi.org/10.1038/nature13068

Mahaffy, P.R., Webster, C.R., Stern, J.C., Brunner, A.E., Atreya, S.K., Conrad, P.G., Domagal-Goldman, S., Eigenbrode, J.L., Flesch, G.J., Christensen, L.E., Franz, H.B., Freissinet, C., Glavin, D.P., Grotzinger, J.P., Jones, J.H., Leshin, L.A., Malespin, C., McAdam, A.C., Ming, D.W., Navarro-Gonzalez, R., Niles, P.B., Owen, T., Pavlov, A.A., Steele, A., Trainer, M.G., Williford, K.H., Wray, J.J., Team, the M.S., 2015. The imprint of atmospheric evolution in the D/H of Hesperian clay minerals on Mars. Science 347, 412–414. https://doi.org/10.1126/science.1260291

Malin, M.C., Edgett, K.S., 1999. Oceans or seas in the Martian northern lowlands: High resolution imaging tests of proposed coastlines. Geophys. Res. Lett. 26, 3049–3052. https://doi.org/10.1029/1999GL002342

Marin-Carbonne, J., Robert, F., Chaussidon, M., 2014. The silicon and oxygen isotope compositions of Precambrian cherts: A record of oceanic paleo-temperatures? Precambrian Res. 247, 223–234. https://doi.org/10.1016/j.precamres.2014.03.016

McSween, H.Y., Taylor, G.J., Wyatt, M.B., 2009. Elemental Composition of the Martian Crust. Science 324, 736–739. https://doi.org/10.1126/science.1165871

Michalski, J.R., Dobrea, E.Z.N., Niles, P.B., Cuadros, J., 2017. Ancient hydrothermal seafloor deposits in Eridania basin on Mars. Nat. Commun. 8, 15978. https://doi.org/10.1038/ncomms15978

Miller, S.L., 1953. A Production of Amino Acids Under Possible Primitive Earth Conditions. Science 117, 528–529. https://doi.org/10.1126/science.117.3046.528

Miller, S.L., Urey, H.C., 1959. Organic Compound Synthes on the Primitive Eart: Several questions about the origin of life have been answered, but much remains to be studied. Science 130, 245–251. https://doi.org/10.1126/science.130.3370.245

Millet, M.-A., Dauphas, N., Greber, N.D., Burton, K.W., Dale, C.W., Debret, B., Macpherson, C.G., Nowell, G.M., Williams, H.M., 2016. Titanium stable isotope investigation of magmatic processes on the Earth and Moon. Earth Planet. Sci. Lett. 449, 197–205. https://doi.org/10.1016/j.epsl.2016.05.039

Mitra, K., Catalano, J.G., 2019. Chlorate as a Potential Oxidant on Mars: Rates and Products of Dissolved Fe(II) Oxidation. J. Geophys. Res. Planets 124, 2893–2916. https://doi.org/10.1029/2019JE006133

Mojzsis, S.J., Harrison, T.M., Pidgeon, R.T., 2001. Oxygen-isotope evidence from ancient zircons for liquid water at the Earth's surface 4,300 Myr ago. Nature 409, 178–181. https://doi.org/10.1038/35051557

Moorbath, S., O'nions, R.K., Pankhurst, R.J., 1973. Early Archaean Age for the Isua Iron Formation, West Greenland. Nature 245, 138. https://doi.org/10.1038/245138a0

Morris, R.V., Klingelhöfer, G., Schröder, C., Rodionov, D.S., Yen, A., Ming, D.W., de Souza, P.A., Wdowiak, T., Fleischer, I., Gellert, R., Bernhardt, B., Bonnes, U., Cohen, B.A., Evlanov, E.N., Foh, J., Gütlich, P., Kankeleit, E., McCoy, T., Mittlefehldt, D.W., Renz, F., Schmidt, M.E., Zubkov, B., Squyres, S.W., Arvidson, R.E., 2006. Mössbauer mineralogy of rock, soil, and dust at Meridiani Planum, Mars: Opportunity's journey across sulfate-rich outcrop, basaltic sand and dust, and hematite lag deposits. J. Geophys. Res. Planets 111, E12S15. https://doi.org/10.1029/2006JE002791

Mustard, J.F., Murchie, S.L., Pelkey, S.M., Ehlmann, B.L., Milliken, R.E., Grant, J.A., Bibring, J.-P., Poulet, F., Bishop, J., Dobrea, E.N., Roach, L., Seelos, F., Arvidson, R.E., Wiseman, S., Green, R., Hash, C., Humm, D., Malaret, E., McGovern, J.A., Seelos, K., Clancy, T., Clark, R., Marais, D.D., Izenberg, N., Knudson, A., Langevin, Y., Martin, T., McGuire, P., Morris, R., Robinson, M., Roush, T., Smith, M., Swayze, G., Taylor, H., Titus, T., Wolff, M., 2008. Hydrated silicate minerals on Mars observed by the Mars Reconnaissance Orbiter CRISM instrument. Nature 454, 305–309. https://doi.org/10.1038/nature07097

Nicklas, R.W., Puchtel, I.S., Ash, R.D., Piccoli, P.M., Hanski, E., Nisbet, E.G., Waterton, P., Pearson, D.G., Anbar, A.D., 2019. Secular mantle oxidation across the Archean-Proterozoic boundary: Evidence from V partitioning in komatiites and picrites. Geochim. Cosmochim. Acta 250, 49–75. https://doi.org/10.1016/j.gca.2019.01.037

Nie, N.X., Dauphas, N., Greenwood, R.C., 2017. Iron and oxygen isotope fractionation during iron UV photo-oxidation: Implications for early Earth and Mars. Earth Planet. Sci. Lett. 458, 179–191. https://doi.org/10.1016/j.epsl.2016.10.035

Niles, P.B., Michalski, J., 2009. Meridiani Planum sediments on Mars formed through weathering in massive ice deposits. Nat. Geosci. 2, 215–220. https://doi.org/10.1038/ngeo438

Nutman, A.P., Bennett, V.C., Friend, C.R.L., Van Kranendonk, M.J., Chivas, A.R., 2016. Rapid emergence of life shown by discovery of 3,700-million-year-old microbial structures. Nature 537, 535–538. https://doi.org/10.1038/nature19355

Olson, S.L., Ostrander, C.M., Gregory, D.D., Roy, M., Anbar, A.D., Lyons, T.W., 2019. Volcanically modulated pyrite burial and ocean–atmosphere oxidation. Earth Planet. Sci. Lett. 506, 417–427. https://doi.org/10.1016/j.epsl.2018.11.015

Ossa Ossa, F., Hofmann, A., Wille, M., Spangenberg, J.E., Bekker, A., Poulton, S.W., Eickmann, B., Schoenberg, R., 2018. Aerobic iron and manganese cycling in a redox-stratified Mesoarchean epicontinental sea. Earth Planet. Sci. Lett. 500, 28–40. https://doi.org/10.1016/j.epsl.2018.07.044

Ostrander, C.M., Nielsen, S.G., Owens, J.D., Kendall, B., Gordon, G.W., Romaniello, S.J., Anbar, A.D., 2019. Fully oxygenated water columns over continental shelves before the Great Oxidation Event. Nat. Geosci. 12, 186–191. https://doi.org/10.1038/s41561-019-0309-7

Pavlov, A. a., Kasting, J. f., 2002. Mass-Independent Fractionation of Sulfur Isotopes in Archean Sediments: Strong Evidence for an Anoxic Archean Atmosphere. Astrobiology 2, 27–41. https://doi.org/10.1089/153110702753621321

Planavsky, N.J., Asael, D., Hofmann, A., Reinhard, C.T., Lalonde, S.V., Knudsen, A., Wang, X., Ossa Ossa, F., Pecoits, E., Smith, A.J.B., Beukes, N.J., Bekker, A., Johnson, T.M., Konhauser, K.O., Lyons, T.W., Rouxel, O.J., 2014. Evidence for oxygenic photosynthesis half a billion years before the Great Oxidation Event. Nat. Geosci. 7, 283–286. https://doi.org/10.1038/ngeo2122

Planavsky, N.J., Rouxel, O.J., Bekker, A., Lalonde, S.V., Konhauser, K.O., Reinhard, C.T., Lyons, T.W., 2010. The evolution of the marine phosphate reservoir. Nature 467, 1088–1090. https://doi.org/10.1038/nature09485

Poulton, S.W., Bekker, A., Cumming, V.M., Zerkle, A.L., Canfield, D.E., Johnston, D.T., 2021. A 200-million-year delay in permanent atmospheric oxygenation. Nature 1–5. https://doi.org/10.1038/s41586-021-03393-7

Poulton, S.W., Canfield, D.E., 2011. Ferruginous Conditions: A Dominant Feature of the Ocean through Earth's History. Elements 7, 107–112. https://doi.org/10.2113/gselements.7.2.107

Ptáček, M.P., Dauphas, N., Greber, N.D., 2020. Chemical evolution of the continental crust from a data-driven inversion of terrigenous sediment compositions. Earth Planet. Sci. Lett. 539, 116090. https://doi.org/10.1016/j.epsl.2020.116090

Ramirez, R.M., Craddock, R.A., 2018. The geological and climatological case for a warmer and wetter early Mars. Nat. Geosci. 11, 230. https://doi.org/10.1038/s41561-018-0093-9

Ramirez, R.M., Kopparapu, R., Zugger, M.E., Robinson, T.D., Freedman, R., Kasting, J.F., 2014. Warming early Mars with CO2 and H2. Nat. Geosci. 7, 59–63. https://doi.org/10.1038/ngeo2000

Ramstad, R., Barabash, S., Futaana, Y., Nilsson, H., Holmström, M., 2018. Ion Escape From Mars Through Time: An Extrapolation of Atmospheric Loss Based on 10 Years of Mars Express Measurements. J. Geophys. Res. Planets 123, 3051–3060. https://doi.org/10.1029/2018JE005727

Rasmussen, B., Buick, R., 1999. Redox state of the Archean atmosphere: Evidence from detrital heavy minerals in ca. 3250–2750 Ma sandstones from the Pilbara Craton, Australia. Geology 27, 115–118. https://doi.org/10.1130/0091-7613(1999)027<0115:RSOTAA>2.3.CO;2

Rasmussen, B., Krapež, B., Muhling, J.R., Suvorova, A., 2015. Precipitation of iron silicate nanoparticles in early Precambrian oceans marks Earth's first iron age. Geology 43, 303–306. https://doi.org/10.1130/G36309.1

Reinhard, C.T., Planavsky, N.J., Gill, B.C., Ozaki, K., Robbins, L.J., Lyons, T.W., Fischer, W.W., Wang, C., Cole, D.B., Konhauser, K.O., 2017. Evolution of the global phosphorus cycle. Nature 541, 386–389. https://doi.org/10.1038/nature20772

Reinhard, C.T., Raiswell, R., Scott, C., Anbar, A.D., Lyons, T.W., 2009. A Late Archean Sulfidic Sea Stimulated by Early Oxidative Weathering of the Continents. Science 326, 713–716. https://doi.org/10.1126/science.1176711

Riding, R., Fralick, P., Liang, L., 2014. Identification of an Archean marine oxygen oasis. Precambrian Res. 251, 232–237. https://doi.org/10.1016/j.precamres.2014.06.017

Robbins, L.J., Lalonde, S.V., Planavsky, N.J., Partin, C.A., Reinhard, C.T., Kendall, B., Scott, C., Hardisty, D.S., Gill, B.C., Alessi, D.S., Dupont, C.L., Saito, M.A., Crowe, S.A., Poulton, S.W., Bekker, A., Lyons, T.W., Konhauser, K.O., 2016. Trace elements at the intersection of marine biological and geochemical evolution. Earth-Sci. Rev. 163, 323–348. https://doi.org/10.1016/j.earscirev.2016.10.013

Roscoe, S.M., 1969. Huronian rocks and uraniferous conglomerates in the Canadian shield (No. GSCAN-P--68-40). Geological Survey of Canada.

Rosing, M.T., 1999. 13C-Depleted Carbon Microparticles in >3700-Ma Sea-Floor Sedimentary Rocks from West Greenland. Science 283, 674–676. https://doi.org/10.1126/science.283.5402.674

Rye, R., Holland, H.D., 1998. Paleosols and the evolution of atmospheric oxygen; a critical review. Am. J. Sci. 298, 621–672. https://doi.org/10.2475/ajs.298.8.621

Rye, R., Kuo, P.H., Holland, H.D., 1995. Atmospheric carbon dioxide concentrations before 2.2 billion years ago. Nature 378, 603–605. https://doi.org/10.1038/378603a0

Sagan, C., Chyba, C., 1997. The Early Faint Sun Paradox: Organic Shielding of Ultraviolet-Labile Greenhouse Gases. Science 276, 1217–1221. https://doi.org/10.1126/science.276.5316.1217

Sagan, C., Mullen, G., 1972. Earth and Mars: Evolution of Atmospheres and Surface Temperatures. Science 177, 52–56. https://doi.org/10.1126/science.177.4043.52

Schaefer, M.W., 1996. Are there abiotically-precipitated iron-formations on Mars? Geochem. Soc. Spec. Publ. 5.

Scheller, E.L., Ehlmann, B.L., Hu, R., Adams, D.J., Yung, Y.L., 2021. Long-term drying of Mars by sequestration of ocean-scale volumes of water in the crust. Science. https://doi.org/10.1126/science.abc7717

Scott, C.T., Bekker, A., Reinhard, C.T., Schnetger, B., Krapež, B., Rumble, D., Lyons, T.W., 2011. Late Archean euxinic conditions before the rise of atmospheric oxygen. Geology 39, 119–122. https://doi.org/10.1130/G31571.1

Shields, G., Veizer, J., 2002. Precambrian marine carbonate isotope database: Version 1.1. Geochem. Geophys. Geosystems 3, 1 of 12–12 12. https://doi.org/10.1029/2001GC000266

Smit, M.A., Mezger, K., 2017. Earth's early O 2 cycle suppressed by primitive continents. Nat. Geosci. 10, 788–792. https://doi.org/10.1038/ngeo3030

Smith, M.L., Claire, M.W., Catling, D.C., Zahnle, K.J., 2014. The formation of sulfate, nitrate and perchlorate salts in the martian atmosphere. Icarus 231, 51–64. https://doi.org/10.1016/j.icarus.2013.11.031

Som, S.M., Catling, D.C., Harnmeijer, J.P., Polivka, P.M., Buick, R., 2012. Air density 2.7 billion years ago limited to less than twice modern levels by fossil raindrop imprints. Nature 484, 359–362. https://doi.org/10.1038/nature10890

Stucky de Quay, G., Goudge, T.A., Fassett, C.I., 2020. Precipitation and aridity constraints from paleolakes on early Mars. Geology 48, 1189–1193. https://doi.org/10.1130/G47886.1

Tabata, H., Sekine, Y., Kanzaki, Y., Sugita, S., 2021. An experimental study of photo-oxidation of Fe(II): Implications for the formation of Fe(III) (hydro)oxides on early Mars and Earth. Geochim. Cosmochim. Acta 299, 35–51. https://doi.org/10.1016/j.gca.2021.02.006

Tang, M., Chen, K., Rudnick, R.L., 2016. Archean upper crust transition from mafic to felsic marks the onset of plate tectonics. Science 351, 372–375. https://doi.org/10.1126/science.aad5513

Taylor, S.R., McLennan, S.M., 1995. The geochemical evolution of the continental crust. Rev. Geophys. 33, 241–265. https://doi.org/10.1029/95RG00262

Taylor, S.R., McLennan, S.M., 1985. The continental crust: Its composition and evolution, Blackwell Scientific Publications, Oxford.

Tosca, N.J., Guggenheim, S., Pufahl, P.K., 2016. An authigenic origin for Precambrian greenalite: Implications for iron formation and the chemistry of ancient seawater. Geol. Soc. Am. Bull. 128, 511–530. https://doi.org/10.1130/B31339.1

Tsikos, H., Matthews, A., Erel, Y., Moore, J.M., 2010. Iron isotopes constrain biogeochemical redox cycling of iron and manganese in a Palaeoproterozoic stratified basin. Earth Planet. Sci. Lett. 298, 125–134. https://doi.org/10.1016/j.epsl.2010.07.032

Veizer, J., Compston, W., 1976. 87Sr/86Sr in Precambrian carbonates as an index of crustal evolution. Geochim. Cosmochim. Acta 40, 905–914. https://doi.org/10.1016/0016-7037(76)90139-3

Voice, P.J., Kowalewski, M., Eriksson, K.A., 2011. Quantifying the Timing and Rate of Crustal Evolution: Global Compilation of Radiometrically Dated Detrital Zircon Grains. J. Geol. 119, 109–126. https://doi.org/10.1086/658295

Waldbauer, J.R., Newman, D.K., Summons, R.E., 2011. Microaerobic steroid biosynthesis and the molecular fossil record of Archean life. Proc. Natl. Acad. Sci. 108, 13409–13414. https://doi.org/10.1073/pnas.1104160108

Wang, S.-J., Rudnick, R.L., Gaschnig, R.M., Wang, H., Wasylenki, L.E., 2019. Methanogenesis sustained by sulfide weathering during the Great Oxidation Event. Nat. Geosci. 1. https://doi.org/10.1038/s41561-019-0320-z

Ward, L.M., Kirschvink, J.L., Fischer, W.W., 2016. Timescales of Oxygenation Following the Evolution of Oxygenic Photosynthesis. Orig. Life Evol. Biospheres 46, 51–65. https://doi.org/10.1007/s11084-015-9460-3

Wilde, S.A., Valley, J.W., Peck, W.H., Graham, C.M., 2001. Evidence from detrital zircons for the existence of continental crust and oceans on the Earth 4.4 Gyr ago. Nature 409, 175–178. https://doi.org/10.1038/35051550

Wordsworth, R., Knoll, A.H., Hurowitz, J., Baum, M., Ehlmann, B.L., Head, J.W., Steakley, K., 2021. A coupled model of episodic warming, oxidation and geochemical transitions on early Mars. Nat. Geosci. 14, 127–132. https://doi.org/10.1038/s41561-021-00701-8

Wordsworth, R., Pierrehumbert, R., 2013. Hydrogen-Nitrogen Greenhouse Warming in Earth's Early Atmosphere. Science 339, 64–67. https://doi.org/10.1126/science.1225759

Wordsworth, R.D., 2016. The Climate of Early Mars. Annu. Rev. Earth Planet. Sci. 44, 381–408. https://doi.org/10.1146/annurev-earth-060115-012355

Yen, A.S., Gellert, R., Schröder, C., Morris, R.V., Bell, J.F., Knudson, A.T., Clark, B.C., Ming, D.W., Crisp, J.A., Arvidson, R.E., Blaney, D., Brückner, J., Christensen, P.R., DesMarais, D.J., de Souza, P.A., Economou, T.E., Ghosh, A., Hahn, B.C., Herkenhoff, K.E., Haskin, L.A., Hurowitz, J.A., Joliff, B.L., Johnson, J.R., Klingelhöfer, G., Madsen, M.B., McLennan, S.M., McSween, H.Y., Richter, L., Rieder, R., Rodionov, D., Soderblom, L., Squyres, S.W., Tosca, N.J., Wang, A., Wyatt, M., Zipfel, J., 2005. An integrated view of the chemistry and mineralogy of martian soils. Nature 436, 49–54. https://doi.org/10.1038/nature03637

Young, G.M., Brunn, V. von, Gold, D.J.C., Minter, W.E.L., 1998. Earth's Oldest Reported Glaciation: Physical and Chemical Evidence from the Archean Mozaan Group (~2.9 Ga) of South Africa. J. Geol. 106, 523–538. https://doi.org/10.1086/516039

Yung, Y.L., Pinto, J.P., 1978. Primitive atmosphere and implications for the formation of channels on Mars. Nature 273, 730–732. https://doi.org/10.1038/273730a0

Chapter 1 – Redox Conditions of Continental Surface Weathering at 2.95 Ga

Foreword

Presently, the disappearance of sulfur isotope mass independent fractionation (S-MIF) from the geologic record somewhere around 2.43-2.32 Ga is used almost universally to define the onset of the Great Oxidation Event (GOE) (Bekker et al., 2004; Farquhar et al., 2000; Gumsley et al., 2017; Luo et al., 2016). The canonical threshold between and 'oxygenated' and 'reduced' atmosphere has thus become set at 10^{-5} × the present atmospheric level (PAL) of O_2 that photochemical models define as the upper limit for preservation of distinct, S-MIF-bearing sulfur pools (Pavlov and Kasting, 2002). However, prior to the relatively recent discovery of S-MIF, the best evidence for the timing of the GOE came from changes in the behavior of redox-sensitive elements and minerals in the geological record of rocks that interacted with Earth's surface. This includes the preservation of reduced detrital mineral grains like uraninite, siderite, and pyrite that cannot survive under an oxygenated atmosphere, in conglomerates and sandstones that saw significant transport and clearly interacted with the atmosphere prior to the GOE (Johnson et al., 2013; Rasmussen and Buick, 1999); and a major change in the behavior of Fe in paleosols; fossilized soil horizons that are most often found in the ancient geologic record when developed on volcanic substrates (reviewed in Rye and Holland, 1998).

The chemistry of paleosols was recognized early by Holland (1984) as a potential constraint on the O_2 content in the atmosphere at the time the weathering horizons formed. Specifically, paleosols formed prior to ~2.44 Ga were observed to be Fe-poor, and paleosols formed after ~2.2 Ga showed no such Fe depletion. The extent of Fe loss directly reflects the redox conditions of weathering, because Fe^{2+} is highly soluble and could easily be transported out of weathering horizons by flowing groundwater to ultimately become continental runoff. Conversely, Fe^{3+} is

highly insoluble except at very low pH, and once oxidation of Fe became prevalent under an oxygenated atmosphere, Fe would have become immobile and been retained in paleosols. Therefore, this transition seen in the paleosol record from Fe loss to Fe retention is probably the oldest constraint on the timing of Earth's first major oxygenation event (Holland, 1984; Rye and Holland, 2000, 1998).

Quite apart from the timing of the GOE, however, the mere existence of an anoxic early atmosphere was actively debated in the field of paleosol research, with Ohmoto (1996) arguing that the presence of Fe^{3+} in paleosols older and younger than the proposed GOE were evidence of persistently oxic weathering conditions and thus a persistently oxic atmosphere. In this alternative interpretation, the mobilization of Fe in paleosols older than 2.45 Ga was facilitated either by (1) late-stage hydrothermal circulation unrelated to subaerial weathering and facilitated by the deposition of fresh lava flows atop the weathering horizons or (2) reductive dissolution of Fe^{3+} oxides in sediments by organic acids produced from decaying organic matter (Ohmoto, 1996). However, this alternative interpretation of the paleosol record was rejected for several reasons. The hydrothermal mobilization hypothesis is inconsistent with geologic field relations indicating that any Fe depletion preceded later thermal events in the paleosol horizons. Meanwhile, the O_2 required to oxidize meters-deep paleosols far exceeds that required to respire any plausible thickness of organic matter formed by microbial mats on ancient weathering surfaces, so the notion that decaying organics could have caused widespread reductive dissolution of initially oxidized paleosols is not feasible from a mass-balance perspective. Furthermore, the model of Ohmoto (1996) sought to explain the presence of Fe^{3+} in pre-GOE paleosols, which could easily reflect late alteration unrelated to weathering, but failed to explain why Fe retention in paleosols became so much more prevalent after 2.2 Ga. Finally, Rye and Holland (1998) indicate five requirements for

definition as a bona fide paleosol formed by subaerial weathering, which are (1) preservation in place atop a homogeneous parent rock, exhibiting mineralogical (2), textural (3), and chemical (4) changes from the unaltered parent rock to the top of the soil that are consistent with soil-forming processes, and (5) soft-sediment deformation at the contact with overlying rocks that indicate the paleosol was indeed a soft, deformable soil horizon. The geologic sections crucial to Ohmoto (1996)'s oxygenated early atmosphere model did not satisfy the chemical criteria for immobile element behavior and thus could not be considered as paleosols suitable for atmospheric reconstruction.

Attempts to quantify atmospheric oxygen levels in the anoxic pre-GOE times led to upper limit estimates of pO_2 prior to the GOE of 5×10^{-4} atm (Rye and Holland, 1998), partial pressures higher than the constraints we now have from S-MIF records. This may in part reflect the method by which pO_2 was calculated, as the O_2 requirement for Fe^{2+} retention was tied in those early models by an estimate of atmospheric pCO_2 (Rye et al., 1995), and resulting balance of acidity for leaching vs. oxidizing power for Fe retention. As estimates for atmospheric pCO_2 become more uncertain the further back we look in Earth history, it is perhaps not surprising that this method resulted in quite different pO_2 estimates to those that come from modern data and atmospheric models (Pavlov and Kasting, 2002).

A major recent development in understanding atmospheric oxygenation is the recognition that the GOE may not have been the first time that O_2 became at least locally and transiently abundant in Earth surface environments, at levels below which the mass balance of a major element like Fe in paleosols would be able to reliably detect. Redox-sensitive trace-element accumulations in shales imply an episode of oxic weathering of sulfides on the continents by 2.5 Ga (Anbar et al., 2007), and perhaps as early as 2.8 Ga (Stüeken et al., 2012), whilst Mo and Tl isotope data point to the

formation of Mn^{4+} oxides in marine sediments, that typically require free oxygen to form, as early as 2.95 Ga (Kurzweil et al., 2016; Ossa Ossa et al., 2018; Ostrander et al., 2019; Planavsky et al., 2014a). In the Pongola Supergroup of South Africa, the same region where evidence of marine oxygenation is reported at 2.95 Ga, Crowe et al. (2013) reported Cr isotopic data for a paleosol horizon that they argued provided evidence for oxic weathering, and thus an oxygenated atmosphere, during its formation. The implications of atmospheric oxygenation at 2.95 Ga are far more severe for models of Archean atmospheric chemistry than evidence for localized 'oases' of O_2 in the marine realm at the same time. Because the atmosphere is mixed on such a rapid timescale, a 'localized' accumulation of atmospheric O_2 that persisted long enough to cause oxidative weathering of the continental crust is not possible, and thus the implication of Crowe et al. (2013)'s study was that the entire atmosphere became oxygenated for a significant period of time, ~600 million years prior to the disappearance of S-MIF. How could O_2 could overcome significant redox buffers in the atmosphere (e.g. CH_4 and H_2S) and on the continents (Fe^{2+}, S^{2-}) at 2.95 Ga without these changes becoming permanent, as they did around 2.4 Ga? Extraordinary claims require extraordinary evidence, and there are reasons to be skeptical of the isolated application of Cr isotopes in Archean paleosols, because Cr becomes more mobile when it is oxidized, and thus its isotope systematics are particularly prone to resetting by younger, more oxidized atmospheres (Albut et al., 2018).

In Chapter 1, we revisit the redox conditions of continental weathering at 2.95 Ga with a multiproxy study of a second paleosol horizon that is time-equivalent to the one studied by Crowe et al. (2013). New Cr isotope data are reported that cast doubt on earlier claims of primary oxic weathering signatures, but we focus mostly on bringing an isotopic perspective to the behavior of Fe during early weathering processes. Unlike Cr, Fe is immobile when oxidized, and therefore late

alteration that can overprint primary redox information in more sensitive proxies cannot reset primary Fe isotopic signature developed during low temperature rock-forming processes. Because Fe isotopes strongly fractionated between Fe^{2+} and Fe^{3+}, this proxy is ideally suited to 'see through' the present day redox state of Fe in paleosols to determine whether oxidation occurred during the primary weathering processes that mobilized Fe in the paleosol. By combining Fe and Cr isotopes systematics, we are able to present a more self-consistent picture of the redox conditions of subaerial weathering at 2.95 Ga.

Chapter 1 also addresses an overlooked by highly useful characteristic of paleosols; that they are the residue of chemical weathering processes that add solutes to runoff transported from the continents to the oceans. By considering paleosols as a complementary reservoir to these continentally derived solutes added to the oceans, we estimate the isotopic composition of Fe^{2+} in continental runoff, which could have been a major source of Fe^{2+} in the oceans for widespread marine chemical sedimentation (Alexander et al., 2008; Holland, 1984; Li et al., 2015). In the Pongola Supergroup, continentally derived solutes were previously shown to be an important component of shallow marine chemical sediments (Alexander et al., 2008; Delvigne et al., 2016), and our new paleosol perspective on Fe^{2+} fluxes adds to this growing dataset. Finally, as solid residues of chemical weathering, paleosols may typify the rock materials that ultimately become detrital sediment that becomes part of the clastic rock record. Shales, in particular, are becoming increasing popular proxies for the average composition of the continental crust through time, because they sample large swathes of exposed land and provide effective spatial averaging (Chen et al., 2020; Greber et al., 2017; Greber and Dauphas, 2019; Ptáček et al., 2020; Smit and Mezger, 2017; Tang et al., 2016). However, only chemical signatures that can be faithfully transferred from primary rock to shale are appropriate for reconstructing continental crustal compositions from the

latter. Therefore, in Chapter 1 we show how paleosol can be used as natural laboratories, where the resistance of different geochemical proxies in the face of intense weathering under ancient atmospheric conditions can be tested, and where the best proxies for future work can be identified.

The content of this chapter is from the accepted article for the publication:

Andy W. Heard, Sarah M. Aarons, Axel Hofmann, Xiaoqing He, Thomas Ireland, Andrey Bekker, Liping Qin, Nicolas Dauphas, "Anoxic continental surface weathering recorded by the 2.95 Ga Denny Dalton Paleosol (Pongola Supergroup, South Africa)", Geochimica et Cosmochimica Acta, Volume 295, 2021, Pages 1-23, ISSN 0016-7037, https://doi.org/10.1016/j.gca.2020.12.005

Anoxic continental surface weathering recorded by the 2.95 Ga Denny Dalton Paleosol (Pongola Supergroup, South Africa)

Abstract

Iron mobilization during continental weathering was pervasive before the Great Oxidation Event (GOE) that started at around 2.43 billion years (Ga) ago, due to the soluble nature of reduced iron. However, various geochemical proxies indicate transient oxygenation during formation in the Mesoarchean (~2.95 Ga) Pongola Supergroup, South Africa, which suggests that continental weathering could have also occurred under transiently oxic conditions before the GOE. We analyzed trace elemental and Fe, Ti, and Cr isotopic compositions of the ca. 2.95 Ga Denny Dalton paleosol in the Pongola Supergroup to better understand continental weathering and redox conditions in the ancient critical zone, and the nature of geochemical fluxes to the oceans and marine sediments. Iron isotope systematics are consistent with a model where Fe was released during intense leaching from the paleosol to concentrate in Fe-rich groundwaters in the deeper part of the soil horizon. We show for the first time that Fe isotopic fractionation during Mesoarchean continental weathering was limited, and Fe enrichments and depletions are coupled with those of divalent transition metals, Co, Ni, and particularly Zn. This suggests that Fe redox cycling was not involved in paleosol formation, and Fe^{2+} was mobilized under anoxic conditions. Chromium isotopes are also unfractionated relative to the parent igneous rock in this paleosol, which precludes removal of isotopically heavy Cr^{6+} and thus supports anoxic continental weathering. We show that previously reported Cr isotopic fractionation in another Denny Dalton paleosol profile does not follow a Cr^{6+} leaching trend, but instead scales with Cr enrichment and may reveal Cr enrichment from post-burial fluids. Thus, there is no evidence for an oxidative continental weathering in the Pongola Supergroup. Titanium isotopes are not significantly fractionated in the paleosol,

suggesting that continental weathering and erosion in the Archean did not fractionate Ti isotopes. Similarly, Ni/Co and Th/Sc ratios are reasonably conserved, which validates their use as a robust proxy for upper continental crust composition in shales, whereas La/Sc, Cr/Zn and Cr/U ratios are highly variable relative to the provenance composition, which suggests caution should be used when applying these ratios in shale studies of the ancient upper continental crust composition.

1. Introduction

Paleosols witnessed the interaction between Earth's surface and atmosphere, and Archean paleosols record Earth surface-atmosphere interaction in the critical zone from a time period when both atmospheric redox conditions and the composition of geochemical fluxes from the continents to the oceans are still uncertain. Changes in the atmospheric redox state, such as the rise of atmospheric oxygen ushered in ca. 2.43 billion years ago (Ga) (Gumsley et al., 2017), altered the behavior of redox-sensitive trace metals during weathering. A major change in continental weathering observed across the GOE is the increased retention of Fe in paleosols that accompanied the onset of oxidative continental weathering (Holland, 1984; Rye and Holland, 1998). Oxidative weathering converts ferrous iron hosted in the exposed upper continental crust into ferric iron, whereas prior to the GOE, soluble Fe^{2+} in anoxic groundwaters was effectively transported out from soils, such that pre-GOE paleosols suffered significant Fe loss (Delvigne et al., 2016; Macfarlane et al., 1994; Rye and Holland, 1998). As a result, continental Fe^{2+} fluxes to the ocean were likely higher before the GOE than now (Holland, 1984). Chemical weathering is also dependent on the primary controls of physical erosion rates such as rainfall, uplift, and global temperature (West et al., 2005), and chemical weathering rates during the Archean would be influenced by potentially smaller emerged continental area (Bindeman et al., 2018). Paleosols

rarely present a straightforward picture of Fe leaching because of chemical redistribution by downward fluid percolation and lateral groundwater migration (Delvigne et al., 2016; Macfarlane et al., 1994; Rye and Holland, 2000, 1998; Yamaguchi et al., 2007). A further complication is that even prior to the GOE, transient episodes of oxidative weathering might have occurred (Crowe et al., 2013), which might have involved Fe redox cycling.

A deeper understanding of paleosol evolution could come from applying multiple geochemical proxies. Non-traditional stable isotopic proxies (such as Si, Fe, and Cr) applied to Archean and Proterozoic paleosols have shown the potential to resolve successive stages of primary leaching and reprecipitation of silicate minerals (Delvigne et al., 2016), reveal open-system and redox-dependent behavior of Fe (Yamaguchi et al., 2007), and provide constraints on paleo-atmospheric redox conditions (*e.g.* Babechuk et al., 2017; Crowe et al., 2013; Yamaguchi et al., 2007).

Chromium isotopic analyses of a paleosol horizon (called the "Denny Dalton" paleosol), in the 2.95 Ga Pongola Supergroup, South Africa, have yielded contradictory evidence for or against oxidative weathering. A depletion in heavy Cr isotopes was initially reported by Crowe et al. (2013) in samples from the PMH-24 drill core through the paleosol as evidence for oxidative weathering and removal of mobile, isotopically heavy Cr^{6+} to the oceans. A heavy Cr isotope signature was also reported from outcrop samples of the stratigraphically overlying Ijzermyn Iron Formation and it was initially inferred that this complementary Cr isotopic signature was derived from seawater containing isotopically heavy Cr^{6+} supplied by oxidative continental weathering runoff (Crowe et al., 2013). However, subsequent work on the TSB07-26 drill core, which is located ~10 km to the southeast of PMH-24 and passes through the same Denny Dalton paleosol profile, did not replicate these results, finding Cr to be isotopically unfractionated relative to its parent rock (Colwyn et al., 2019). These new measurements questioned the veracity of early

claims of a Mesoarchean oxidative weathering linked to a rise in atmospheric O_2 (Albut et al., 2018; Colwyn et al., 2019). Iron isotope systematics present a promising complement to Cr isotopes in the study of the Pongola paleosol, because Fe is a major rock-forming element with isotopic systematics strongly affected by low-temperature aqueous redox processes at a lower redox potential than Cr, while being more resistant to metamorphic and hydrothermal overprinting (Dauphas et al., 2017). Importantly, the increasing oxygenation of the atmosphere through time favors the retention of primary Fe isotopic signatures in the rock record because when subjected to oxidative late alteration, ferric iron is fluid immobile. This contrasts with Cr, which becomes more fluid-mobile when oxidized to Cr^{6+}. Combined study of Fe and Cr isotopic systematics could thus provide a powerful tool to constrain when large-scale oxidative continental weathering first commenced.

In this study we investigate Fe isotope systematics in the 2.95 Ga Denny Dalton paleosol in the TSB07-26 drill core, which was previously studied with Si and Cr isotopic systematics (Colwyn et al., 2019; Delvigne et al., 2016), and which showed no evidence for oxidative weathering of Cr. We aim to resolve how Fe was mobilized during weathering and the role (if any) of redox processes in mobilization of Fe from the paleosol horizon. Additionally, we reexamine both new and previously published Cr isotope data from drill cores that have presented contradictory evidence for oxidative weathering in the Mesoarchean. Using both an improved understanding of redox conditions provided by Fe isotope systematics, and calculated leaching trends in Cr isotopic and concentration space, we test the need for oxygen in explaining Mesoarchean paleosol records. Finally, we examine the variability in Ti isotope composition and various elemental ratios that have been used to reconstruct upper continental crust composition from detrital sedimentary records deposited under Archean chemical weathering conditions and assess which geochemical

proxies (*e.g.* Ti isotopes, Ni/Co, La/Sc, Th/Sc, Cr/Zn, Cr/U) are most likely to retain upper continental crust composition information (Chen et al., 2020; Greber et al., 2017; McLennan, 2001; Ptáček et al., 2020; Smit and Mezger, 2017; Tang et al., 2016; Taylor and McLennan, 1985).

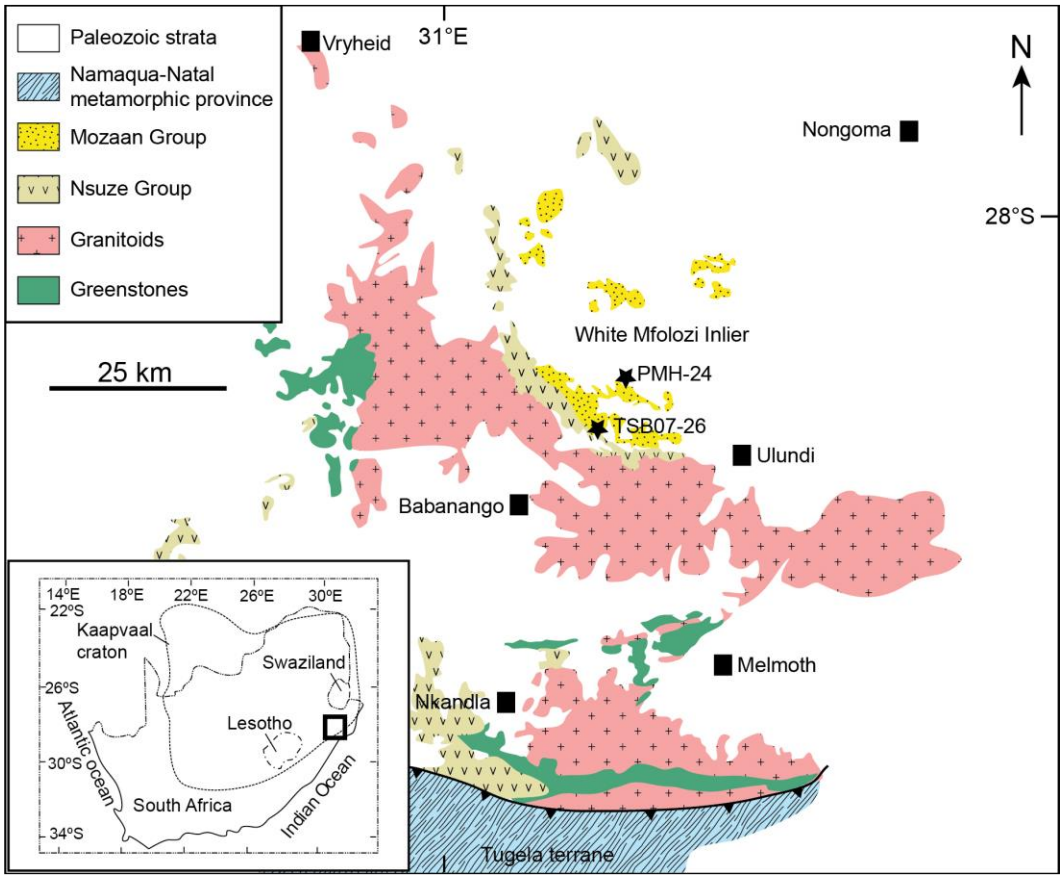

Figure 1.1. Geological map showing the distribution of the Nsuze and Mozaan groups of the Pongola Supergroup (Hofmann et al., 2019). Borehole locations of TSB07-26 (this study) and PMH-24 (Crowe et al., 2013) are shown.

2. Materials and Methods

2.1. Samples

Samples analyzed in this study come from the Denny Dalton paleosol of the Pongola Supergroup in the TSB07-26 drill core in the southeastern part of the Kaapvaal craton, South Africa (Fig. 1.1). The Pongola Supergroup is a comparatively undeformed volcano-sedimentary succession that was deposited on early Archean basement granitoids and gneisses from 2.985 Ga (Hegner et al., 1994;

Hicks and Hofmann, 2012; Mukasa et al., 2013). It outcrops in a ~250 km, roughly north-south trending linear belt that crosses the northern KwaZulu-Natal and Mpumalanga provinces, and southern Swaziland. The Pongola Supergroup is divided into the underlying Nsuze Group and the overlying Mozaan Group (Figs. 1.1,1.2). The Nsuze Group is a compositionally diverse volcanic succession dominated by basaltic andesites dated by U-Pb zircon SIMS method between 2.980 Ga at its base and 2.954 Ga at its top (Mukasa et al., 2013). The Mozaan Group is a sedimentary succession of conglomerate, shales, and locally developed iron formation (IF), deposited in a marine setting (Beukes and Cairncross, 1991).

The Denny Dalton paleosol sampled in this study comes from the White Mfolozi Inlier and occurs at the very top of the Nsuze Group (Fig. 1.2), developed on a basaltic andesite lava flow that was tilted ~10° prior to paleoweathering, so that the paleosol lies above an angular unconformity (Hicks

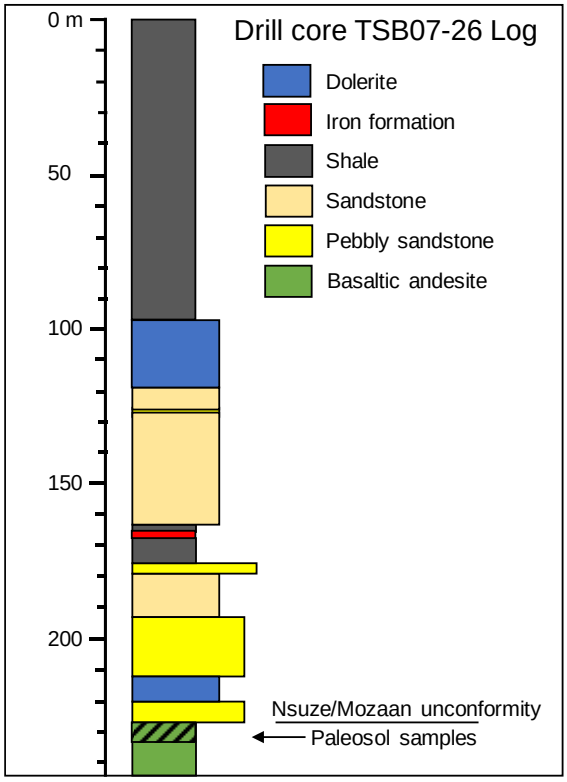

Figure 1.2. Stratigraphic log of the TSB07-26 drill core, modified from Delvigne et al. (2016). The hashed area marks the location of the paleosol at the top of the basaltic andesite unit.

and Hofmann, 2012). The basaltic andesite protolith on which the Denny Dalton paleosol was developed is an amygdaloidal lava flow with a fine-grained groundmass of amphibole, chlorite and albite, with chlorite, in addition to quartz and calcite, concentrically filling the amygdales (Nhleko, 2003). The present-day mineral assemblage of the Nsuze Group basaltic andesites corresponds to greenschist facies metamorphic conditions (Crow et al., 1989; Nhleko, 2003). Rutile is directly observed in the basaltic andesites of the White Mfolozi Inlier, and the presence of zircon and monazite in the overlying paleosols (Nhleko, 2003) indicates that these accessory minerals were also present in the protolith. Zircon grains are nevertheless small and rarely occur in the Nsuze basaltic andesites (Mukasa et al., 2013).

Sample powders are aliquots of the same samples that were analyzed for major elemental concentrations (Fig. 1.2, Table 1.1), Si isotope composition, and Ge/Si ratios by Delvigne et al. (2016), and also for Cr isotope values by Colwyn et al. (2019), who found no significant Cr isotopic variation. These samples come from the TSB07-26 drill core (Figs. 1.1,1.2), which is ~10 km southeast of the PMH-24 drill core that provided samples for an earlier Cr isotope study that inferred the oxidative mobilization of Cr under an oxygenated atmosphere (Crowe et al., 2013). Crowe et al. (2013) referred to this horizon as the Nsuze paleosol, while Delvigne et al. (2016) named it the Denny Dalton paleosol to avoid confusion with other paleosols known in the Nsuze Group; but the paleosols are stratigraphically equivalent and would have formed under the same atmospheric redox conditions. The Denny Dalton paleosol in the TSB07-26 drill core consists of a 1.9 m thick upper zone mostly composed of sericite with minor chlorite and rutile (sericite-dominated zone, SDZ), overlying a lower zone dominantly composed of chlorite with minor quartz, epidote, and rutile (chlorite-dominated zone, CDZ). The SDZ experienced metasomatism related to percolation of K (and Rb)-rich fluids during diagenesis and low-grade metamorphism

(Delvigne et al., 2016), which is a typical feature observed in many Precambrian paleosols (e.g. Macfarlane et al., 1994; Rye and Holland, 1998; Yang and Holland, 2003) . The lowermost paleosol sample (WM15) and the underlying unweathered basaltic andesite (WM16) are outcrop samples taken close to the drill core location and correspond to depths of 10 and 15 m below the top of the paleosol, respectively. Despite being taken from outcrop, the parent basaltic andesite sample (WM16) has a chemical index of alteration (CIA) in the same range as fresh unaltered andesites (Colman, 1982; Delvigne et al., 2016; Elwood Madden et al., 2020). This CIA value is also comparable to or lower than CIA values of the parent rock examined at a different location by Crowe et al. (2013). The paleosol is terminated at the top by the unconformably overlying Mozaan Group, suggesting that the very top of the paleosol profile may have been eroded away.

2.2. Analytical methods

2.2.1. Trace element analysis

Trace element analyses were conducted at Boston University. About 25 mg of sample powder was weighed into 15 mL acid-cleaned Teflon beakers. For digestion, 3 mL of concentrated HNO_3, 1 mL of concentrated HCl, and 1 mL of concentrated HF were then added to the samples, the beakers were sealed, and placed on hot plate at ~120°C for at least 24 hours. The samples were sonicated for about 30 minutes and 1 mL of hydrogen peroxide was added to oxidize any organic material that may have been present. The vessels were left loosely capped until the solutions stopped bubbling and were then re-sealed and placed on a hot plate for an additional 12-24 hours. The samples were gently evaporated to dryness, and then re-dissolved in 1 mL of concentrated HNO_3.

A small amount of H_2O_2 (0.5 to 1 mL) was added to each sample to ensure complete digestion. Samples were then diluted with MQ water and 2% HNO_3 to a final dilution factor of 5000.

All acid digestions were analyzed on a VG PlasmaQuad ExCell inductively coupled plasma mass-spectrometer (ICP-MS) at Boston University. Samples were introduced to the instrument in ~2% HNO_3, via a Meinhardt-C nebulizer with a flow rate of about 1 mL/min, and an impact-bead, Peltier cooled spray chamber. The instrument was optimized by obtaining the maximum signal intensity on a 1 ng/g solution of In, while concurrently minimizing oxide production. Oxide levels were monitored with the CeO^+/Ce^+ ratio, which was typically ~1%.

Instrumental drift was monitored and corrected for by analyzing an in-house drift solution several times during an analytical session. A blank solution, which was prepared in an identical manner to our samples, was also measured at the beginning and end of each run, and all data were blank corrected. Several geological standard reference materials were interspersed throughout an analytical run, and a calibration curve was generated by comparing the signal intensity to that of the established concentrations. The concentrations of the samples were then calculated based on these calibration curves. The method precision, estimated from the 1 r.s.d. of the mean of repeat analyses of the USGS geostandard BHVO-2, was better than 3% for the majority of elements. The accuracy of geostandard measurements, estimated from with the literature values for this material, was within 5% for a large number of elements, including many elements (V, Co, Ni, Cu, Zn, Th, and U) discussed in detail in this study. Accuracy was 5-15% for the remaining elements. The supplementary material contains the repeat analyses for BHVO-2 that were used for precision and accuracy estimates.

2.2.2. Iron isotopic analysis

Analytical procedures for iron purification and isotopic measurements followed standard procedures used in the Origins Laboratory at the University of Chicago (Dauphas et al., 2009)**.** Between 2.5 and 50 mg of powdered rock samples, calculated from published Fe concentration data to give a few 100 µg of Fe for analysis, were digested in acid-cleaned Savillex Teflon beakers using a HF + HNO_3 + $HClO_4$ mixture, followed by digestion in a HCl + HNO_3 + $HClO_4$ mixture. After full digestion and dissolution, samples were evaporated and redissolved in 0.5 ml of 6 M HCl for Fe purification. Iron was purified through a column chemistry procedure routinely used in the Origins Laboratory (Dauphas et al., 2004; 2009). After two identical purifications, samples were dried down and redissolved in 5 ml 0.3 M HNO_3 for mass spectrometry.

Iron isotopic compositions were measured on a Neptune multi-collector inductively coupled plasma mass spectrometer (MC-ICP-MS) at the University of Chicago in medium-resolution mode. Sample solutions containing 1 ppm Fe in 0.3 M HNO_3 were introduced using a quartz cyclonic spray chamber, which gave a signal of ~7 V. The isotopes $^{54}Fe^+$, $^{56}Fe^+$, $^{57}Fe^+$, and $^{58}Fe^+$ were measured simultaneously along with $^{53}Cr^+$ and $^{60}Ni^+$ for correction of $^{54}Cr^+$ and $^{58}Ni^+$ interferences on $^{54}Fe^+$ and $^{58}Fe^+$ respectively. The ^{53}Cr and ^{60}Ni interferences were corrected for using the exponential law. Flat-topped Fe peak shoulders were measured to overcome molecular interference from argide ions ($^{40}Ar^{14}N^+$, $^{40}Ar^{16}O^+$, $^{40}Ar^{16}O^1H^+$, and $^{40}Ar^{18}O^+$). Standard-sample bracketing was used to correct Fe isotopic ratio measurements for instrumental mass fractionation. Sample and standard ^{56}Fe concentrations were matched to within 5 % before analysis. Iron isotopic ratios of samples are reported in $\delta^{56}Fe$ notation, which is the per mil deviation (see Teng et al., 2017 for a discussion of δ notations in non-traditional stable isotope systematics) of the $^{56}Fe/^{54}Fe$ ratio of the sample relative to the average isotopic ratio of the IRMM-524 standard that has an

identical isotopic composition to IRMM-014 and is very close in its isotope composition to the bulk silicate Earth value(Craddock and Dauphas, 2011):

$$\delta^{56}Fe\ (‰) = [(^{56}Fe/^{54}Fe)_{sample} / (^{56}Fe/^{54}Fe)_{IRMM\text{-}014} - 1] \times 1000$$

Here and elsewhere unless otherwise stated, uncertainties are given at the 95 % confidence interval (Dauphas et al., 2009). The IF-G and BHVO-2 geostandards were processed through the same digestion and purification protocol as the paleosol samples and were analyzed along with the paleosol samples in each measurement sequence. The Fe isotopic composition for these geostandards was within error of their recommended values (Craddock and Dauphas, 2011).

2.2.3. Titanium isotopic analysis

Samples were prepared for Ti isotopic analysis following routine procedures used at the Origins Lab at the University of Chicago (Greber et al., 2017; Millet et al., 2016; Millet and Dauphas, 2014). Samples were homogenized via flux fusion using a lithium metaborate flux in a 1:6 sample to flux ratio. This step also enables complete Ti digestion in acid. Aliquots of flux fusion sample pellets, containing at least 20 μg of Ti were then digested in HNO_3, and the ^{47}Ti-^{49}Ti double spike solution was added according to known Ti concentrations to give the optimal sample-spike mixing ratio for precise determination of Ti isotope composition, to correct for any potential mass dependent fractionation during column chemistry, and instrumental mass bias during mass spectrometry (Millet and Dauphas, 2014). The dissolved samples were purified using a column chemistry procedure that followed the method of Zhang et al. (2011).

The Ti isotope composition of each sample was analyzed on the Neptune MC-ICP-MS in medium-resolution mode at the University of Chicago. The samples were introduced in a 0.3 M HNO_3 and

0.005 M HF mixture using a Cetac Aridus 1 desolvating nebulizer. Standard-sample bracketing was used, with ^{48}Ti concentrations matched within ±10 % for the sample and standard, with typical ^{48}Ti beam intensities of 20V. Following a measurement block of five samples, a Ti-free solution of 0.3 M HNO_3 and 0.005 M HF was measured to re-determine and correct for the on-peak baseline. The Ti isotope composition of each sample is reported in δ^{49}Ti notation, which is the per mil deviation of the ^{49}Ti/^{47}Ti ratio of the sample relative to the Origins Laboratory Ti reference material (OL-Ti), whose composition is close to that of chondrites and the bulk silicate Earth (Millet et al., 2016):

$$\delta^{49}\text{Ti}\ (‰) = [(^{49}\text{Ti}/^{47}\text{Ti})_{\text{sample}} / (^{49}\text{Ti}/^{47}\text{Ti})_{\text{OL-Ti}} - 1] \times 1000.$$

The uncertainty on each measurement encompasses the measurement session and the long-term external reproducibility and was evaluated according to Dauphas et al. (2009). The δ^{49}Ti isotope composition of each sample was calculated by double-spike data reduction using a Mathematica script (Millet and Dauphas, 2014). The BHVO-2 geostandard was processed through flux fusion, digestion, and Ti purification and was analyzed along with the unknown samples, giving a Ti isotopic composition within error of the recommended value.

2.2.4. Chromium isotopic analysis

About 50 mg sample powder was digested in a Microwave Digestion System (WX-8000) with 3 ml HNO_3 and 1 ml HF. The samples were heated at 220°C until complete digestion. Chromium concentrations were measured on a Perkin Elmer Elan DRCII ICP-MS at University of Science and Technology of China (USTC). Prior to Cr purification using column chromatography, sample solutions containing ~1 μg Cr were mixed with ^{50}Cr-^{54}Cr double-spike solution and dried on a hot

plate. Samples were re-dissolved in 0.2 ml 6 N HCl and heated for 3 hours at 120-130°C. Chromium was purified using a two-step cation exchange chromatography procedure following Zhang et al. (2019). Both column chemistry protocols made use of Bio-Rad 200-400 mesh AG50-X8 resin, and the full procedural blank was typically <10 ng, whilst Cr yields were 70-90%.

Chromium isotopic compositions were measured on a Triton Plus multi-collector thermal-ionization mass spectrometer (TIMS) at USTC. Before analysis, about 1 μg of purified Cr was loaded in 3 N HNO_3 on outgassed Re filaments with silica gel, saturated boric acid, and aluminum oxide. Sample and standard measurements were conducted at ionization temperatures between 1270 and 1390°C to minimize interferences present at lower and higher ionization temperatures. Chromium isotope signals ($^{50}Cr^+$, $^{52}Cr^+$, $^{53}Cr^+$, and $^{54}Cr^+$) were collected on L3, L1, axial, and H1 Faraday cups, respectively. All four cups were connected to 10^{11} Ω amplifiers. The typical beam intensity of ^{52}Cr was between 3 and 7 V. To monitor isobaric interferences from $^{50}Ti^+$ and $^{50}V^+$ on $^{50}Cr^+$ and $^{54}Fe^+$ on $^{54}Cr^+$, intensities of $^{49}Ti^+$, $^{51}V^+$, and $^{56}Fe^+$ were measured simultaneously on L4, L2, and H2 Faraday cups, respectively. L4 and L2 were connected to 10^{12} Ω amplifiers, and H2 was connected to a 10^{11} Ω amplifier. Each analysis consisted of 200 cycles, each integrating isotope ratio measurement over 8.389 seconds. Double-spike data reduction was performed off-line to correct for mass fractionation during column chemistry and TIMS isotopic analysis.

The Cr isotope ratios are expressed as the per mil variation relative to National Institute of Standards and Technology (NIST) Standard Reference Material (SRM) 979:

$$\delta^{53}Cr\ (‰) = [(^{53}Cr/^{52}Cr)_{sample} / (^{53}Cr/^{52}Cr)_{NIST\ 979} - 1] \times 1000,$$

relative to which the bulk silicate Earth value lies at -0.124 ± 0.101 ‰ (Schoenberg et al., 2008). Each analytical session began with measurements of the spiked internal Cr isotope standard SCP

(Science, ON, Canada) and NIST SRM 3112a, and SCP was analyzed between every five to six samples, which were each measured once or twice. The uncertainty reported here is the largest among 2 standard error (2SE) of a single sample measurement, 2 standard deviations (2SD) of repeat sample measurement, and the long-term reproducibility for the standard solution (SCP and NIST SRM 3112a; 0.03 ‰).

3. Results

3.1. Elemental compositions

Trace element compositions are presented along with major element composition data from Delvigne et al. (2016) in Table 1.1. Elemental concentrations in paleosols are best expressed in terms of their relative enrichments or depletions compared to the unaltered parent rock, and therefore we employ the τ notation after Brimhall and Dietrich (1987), which is a measure of the mass fraction of an element i that is lost or added to the soil horizon relative to an immobile element (in this case Ti),

$$\tau_{i,w} = \frac{[i]_w/[Ti]_w}{[i]_p/[Ti]_p} - 1$$

where the subscripts w and p refer to weathered and unaltered parent rocks, respectively. When τ is positive, it indicates that mass of element i has been added to the soil horizon at the depth at which the value has been calculated, and vice versa. Calculated τ values are reported in Table 1.2. We normalized to Ti to maintain convention with previous studies, and we demonstrate below that Ti isotopes and the τ_{Ti} value normalized to Al show that Ti was indeed immobile in this paleosol.

Table 1.1. Major element, Fe, Ti, and Cr isotopic, and trace element composition of the Denny Dalton paleosol

	WM 08	**WM 09**	**WM 10**	**WM 11**	**WM 12**	**WM 13**	**WM 14**	**WM 15**	**WM 16**
Zone	SDZ	SDZ	SDZ	INT.	CDZ	CDZ	CDZ	CDZ	BAS. AND.
Depth from paleosol top [m]	-0.2	-0.4	-0.9	-2.2	-3.4	-4.3	-5.4	-10	-15
wt%*									
SiO_2	47.8	47.8	47.9	43.5	47.6	54.1	56.8	53.6	53
Al_2O_3	37.8	37.5	37.4	27.2	17.3	15.7	16.1	18.5	17.1
Fe_2O_{3Tot}	0.8	0.9	1.1	18.3	27.2	21.8	18.2	18.7	15.8
MnO	0	0	0	0.2	0.3	0.3	0.2	0.3	0.4
MgO	0.3	0.3	0.4	3.4	5.9	6.2	6.1	5.8	6.4
CaO	0.1	0.1	0.1	0.1	0.3	0.6	0.7	0.5	4.7
Na_2O	0.4	0.3	0.4	0.1	0	0	0	0	0.5
K_2O	11	10.9	11	5.5	0.4	0.3	0.9	1.6	1.2

Table 1.1 continued									
TiO_2	2.2	2.3	2.3	1.6	1.1	0.9	0.9	1.1	1
‰									
$\delta^{56}Fe$	**0.488**	**0.509**	**0.404**	**-0.090**	**-0.023**	**-0.057**	**-0.048**	**0.053**	**0.083**
2σ (95 % C.I.)	0.030	0.030	0.084	0.084	0.084	0.032	0.032	0.032	0.030
$\delta^{49}Ti$	**0.047**	**0.067**	**0.04**	**0.076**	**0.055**	**0.039**	**0.07**	**0.075**	**0.054**
2σ (95 % C.I.)	0.027	0.028	0.045	0.013	0.016	0.023	0.026	0.029	0.023
$\delta^{53}Cr$ [(a)]	**-0.199**	**-0.252**	**-0.250**	**-0.251**	**-0.265**	**-0.268**	**-0.276**	**-0.248**	**-0.261**
2σ (95 % C.I.)	0.030	0.030	0.030	0.030	0.030	0.030	0.026	0.030	0.030
$\delta^{53}Cr$ [(b)]	**-0.240**	**-0.250**	**-0.300**	**-0.300**	**-0.290**	**-0.240**	**-0.240**	**-0.260**	**-0.310**
2σ (95 % C.I.)	0.030	0.020	0.020	0.020	0.030	0.020	0.020	0.020	0.020
ppm									
Li	3.91	3.24	2.32	29.97	55.77	65.74	61.56	59.27	60.44
Be	6.54	6.68	8.54	5.31	0.89	0.89	1.76	1.75	1.05
Sc	6.75	15.97	22.74	17.43	21.04	22.11	25.06	17.26	24.79
V	373.85	415.26	379.93	276.00	151.69	139.94	147.08	170.12	181.91

Table 1.1 continued

Cr	237.15	236.15	240.51	168.47	95.80	94.21	90.10	339.16	126.52
Co	16.23	36.78	82.13	81.25	139.50	71.03	57.83	78.59	82.24
Ni	23.10	40.24	173.20	248.56	245.31	103.68	97.39	162.34	127.83
Cu	24.96	20.20	44.35	228.86	41.81	96.96	20.88	49.62	61.44
Zn	18.53	18.95	58.35	199.84	267.74	242.76	223.28	164.05	145.28
Rb	155.43	132.64	143.37	27.52	9.58	6.31	22.13	39.86	33.61
Sr	6.00	7.88	16.16	7.01	4.39	5.11	8.99	8.91	47.86
Y	3.71	9.52	8.69	4.51	14.12	13.20	12.42	13.01	13.27
Zr	209.89	208.64	229.84	159.46	105.33	94.66	110.78	146.38	101.30
Nb	16.21	16.76	16.89	9.88	7.19	6.76	7.13	9.61	6.77
Mo	0.18	0.26	1.81	0.42	3.13	0.39	0.40	7.17	0.20
Sn	5.10	4.27	4.10	2.45	0.90	0.98	1.20	1.07	0.83
Cs	2.62	2.91	4.22	2.49	0.31	0.23	0.76	1.00	0.92
Ba	238.60	307.39	507.97	178.90	41.91	27.99	103.84	173.24	177.83
La	9.53	42.41	9.13	4.57	5.72	12.78	24.44	14.35	15.14

Table 1.1 continued

Ce	19.47	75.34	20.10	10.58	12.28	25.82	47.44	30.56	32.58
Pr	2.22	11.56	2.46	1.36	1.59	3.35	5.84	3.50	3.85
Nd	9.05	49.00	10.14	5.91	6.91	14.19	24.27	14.65	16.21
Sm	1.80	10.88	2.44	1.40	1.96	3.45	4.67	3.27	3.71
Eu	0.47	2.57	0.69	0.36	0.53	0.91	1.19	1.01	1.07
Tb	0.16	0.55	0.29	0.15	0.38	0.44	0.44	0.40	0.43
Gd	1.28	5.83	1.92	1.09	2.32	3.16	3.29	2.91	3.10
Dy	0.76	2.32	1.79	0.88	2.52	2.53	2.37	2.25	2.41
Ho	0.14	0.41	0.35	0.19	0.52	0.50	0.47	0.48	0.48
Er	0.43	1.25	1.04	0.61	1.58	1.51	1.44	1.60	1.51
Yb	0.45	1.26	1.08	0.79	1.74	1.67	1.64	1.88	1.67
Lu	0.07	0.18	0.15	0.12	0.28	0.26	0.26	0.30	0.26
Hf	7.03	6.72	7.61	5.09	3.43	3.05	3.49	4.58	3.23
Ta	0.95	0.99	0.99	0.59	0.43	0.40	0.43	0.51	0.41
Pb	2.40	3.03	6.01	2.76	2.83	9.76	25.55	1.43	2.06

Table 1.1 continued

Th	1.29	4.17	3.28	0.95	2.10	2.10	2.42	2.10	2.37
U	2.02	1.97	1.72	1.02	0.68	0.76	0.78	0.52	0.60

*Data from Delvigne et al. (2016).

[(a)]Indicates data from this study; [(b)]Indicates data from Colwyn et al. (2019).

Table 1.2. Paleosol enrichment/depletion (τ_i) indices for the Denny Dalton paleosol, calculated relative to immobile TiO_2

	WM 08	**WM 09**	**WM 10**	**WM 11**	**WM 12**	**WM 13**	**WM 14**	**WM 15**	**WM 16**
Zone	SDZ	SDZ	SDZ	INT.	CDZ	CDZ	CDZ	CDZ	BAS. AND.
Depth from paleosol top [m]	-0.2	-0.4	-0.9	-2.2	-3.4	-4.3	-5.4	-10	-15
SiO_2	-0.59	-0.61	-0.61	-0.49	-0.18	0.13	0.19	-0.08	0
Al_2O_3	0.00	-0.05	-0.05	-0.01	-0.08	0.02	0.05	-0.02	0
Fe_2O_{3Tot}	-0.98	-0.98	-0.97	-0.28	0.57	0.53	0.28	0.08	0

Table 1.2 continued

MnO	-1.00	-1.00	-1.00	-0.69	-0.32	-0.17	-0.44	-0.32	0
MgO	-0.98	-0.98	-0.97	-0.67	-0.16	0.08	0.06	-0.18	0
CaO	-0.99	-0.99	-0.99	-0.99	-0.94	-0.86	-0.83	-0.90	0
Na_2O	-0.64	-0.74	-0.65	-0.88	-1.00	-1.00	-1.00	-1.00	0
K_2O	3.17	2.95	2.99	1.86	-0.70	-0.72	-0.17	0.21	0
TiO_2*	0.00	0.05	0.05	0.01	0.09	-0.02	-0.04	0.02	0
Li	-0.97	-0.98	-0.98	-0.69	-0.16	0.21	0.13	-0.11	0
Be	1.83	1.76	2.53	2.16	-0.23	-0.06	0.86	0.51	0
Sc	-0.88	-0.72	-0.60	-0.56	-0.23	-0.01	0.12	-0.37	0
V	-0.07	-0.01	-0.09	-0.05	-0.24	-0.15	-0.10	-0.15	0
Cr	-0.15	-0.19	-0.17	-0.17	-0.31	-0.17	-0.21	1.44	0
Co	-0.91	-0.81	-0.57	-0.38	0.54	-0.04	-0.22	-0.13	0
Ni	-0.92	-0.86	-0.41	0.22	0.74	-0.10	-0.15	0.15	0
Cu	-0.82	-0.86	-0.69	1.33	-0.38	0.75	-0.62	-0.27	0
Zn	-0.94	-0.94	-0.83	-0.14	0.68	0.86	0.71	0.03	0

Table 1.2 continued

Rb	1.10	0.72	0.85	-0.49	-0.74	-0.79	-0.27	0.08	0
Sr	-0.94	-0.93	-0.85	-0.91	-0.92	-0.88	-0.79	-0.83	0
Y	-0.87	-0.69	-0.72	-0.79	-0.03	0.11	0.04	-0.11	0
Zr	-0.06	-0.10	-0.01	-0.02	-0.05	0.04	0.22	0.31	0
Nb	0.09	0.08	0.08	-0.09	-0.03	0.11	0.17	0.29	0
Mo	-0.59	-0.44	2.97	0.31	13.37	1.22	1.27	31.96	0
Sn	1.79	1.24	1.15	0.85	-0.01	0.32	0.61	0.18	0
Cs	0.30	0.38	1.00	0.69	-0.70	-0.72	-0.08	-0.01	0
Ba	-0.39	-0.25	0.24	-0.37	-0.79	-0.83	-0.35	-0.11	0
La	-0.71	0.22	-0.74	-0.81	-0.66	-0.06	0.79	-0.14	0
Ce	-0.73	0.01	-0.73	-0.80	-0.66	-0.12	0.62	-0.15	0
Pr	-0.74	0.31	-0.72	-0.78	-0.62	-0.03	0.69	-0.17	0
Nd	-0.75	0.31	-0.73	-0.77	-0.61	-0.03	0.66	-0.18	0
Sm	-0.78	0.28	-0.71	-0.76	-0.52	0.03	0.40	-0.20	0
Eu	-0.80	0.05	-0.72	-0.79	-0.55	-0.06	0.24	-0.14	0

Table 2.2 continued

Tb	-0.83	-0.45	-0.71	-0.78	-0.19	0.14	0.13	-0.16	0
Gd	-0.81	-0.18	-0.73	-0.78	-0.32	0.13	0.18	-0.15	0
Dy	-0.86	-0.58	-0.68	-0.77	-0.05	0.17	0.10	-0.15	0
Ho	-0.87	-0.63	-0.68	-0.75	-0.02	0.16	0.09	-0.10	0
Er	-0.87	-0.64	-0.70	-0.75	-0.05	0.11	0.06	-0.04	0
Yb	-0.88	-0.67	-0.72	-0.71	-0.05	0.11	0.09	0.02	0
Lu	-0.88	-0.70	-0.75	-0.71	-0.05	0.11	0.09	0.03	0
Hf	-0.01	-0.10	0.02	-0.02	-0.04	0.05	0.20	0.29	0
Ta	0.04	0.03	0.04	-0.11	-0.05	0.09	0.14	0.11	0
Pb	-0.47	-0.36	0.27	-0.16	0.25	4.27	12.80	-0.37	0
Th	-0.75	-0.24	-0.40	-0.75	-0.19	-0.02	0.13	-0.20	0
U	0.54	0.44	0.26	0.07	0.03	0.42	0.46	-0.21	0

*****Indicates normalization to immobile Al_2O_3.

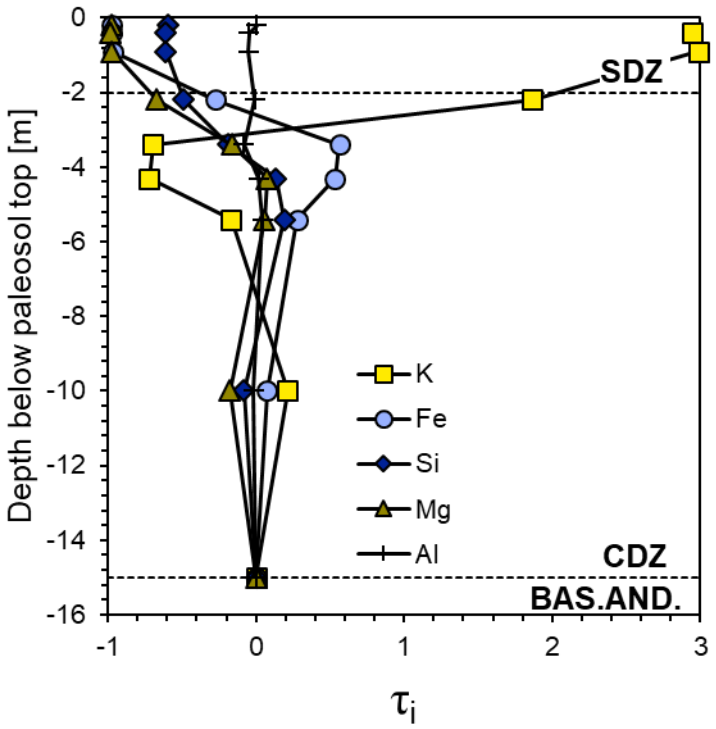

Figure 1.3. Enrichment/depletion index (τ_i) of major elements: K, Fe, Si, Mg, and Al, relative to immobile Ti, in the Denny Dalton paleosol, from Delvigne et al. (2016). Dashed lines delineate boundaries among the sericite-dominated zone (SDZ), chlorite-dominated zone (CDZ), and parent basaltic andesite (BAS.AND.).

As reported previously by Delvigne et al. (2016), the paleosol is strongly depleted in Mg, Ca, Mn, and Fe ($\tau < -0.98$), and, to a lesser extent, Ge ($\tau < -0.77$), Na ($\tau < -0.64$), and Si ($\tau < -0.61$) in the upper SDZ (Fig. 1.3, Table 1.2). These data were taken to indicate intense chemical weathering and desilication in the upper part of the paleosol, whereas moderate enrichments of Fe and Ge ($\tau < 0.63$) in the underlying CDZ were taken as evidence for the downward migration of Fe- and Ge-rich groundwaters and subsequent reprecipitation of these elements (Delvigne et al., 2016). This explanation for Fe is consistent with conventional interpretation of Fe mobility in Precambrian paleosols (Macfarlane et al., 1994; Ohmoto, 1996; Rye and Holland, 2000, 1998). The full suite of trace element data generated in this study is summarized below.

3.1.1. Fluid-immobile elements

Fluid-immobile elements are those that are retained within primary or secondary minerals resistant to weathering. Zircon is the main mineral host for zirconium (Zr) and hafnium (Hf), and small, rare zircons are found both in the Nsuze Group basaltic andesites (Mukasa et al., 2013) and in the Denny Dalton paleosol (Nhleko, 2003). Niobium (Nb) and tantalum (Ta) are retained in insoluble Ti-oxide phases, most likely rutile (TiO_2), which is present throughout the Denny Dalton paleosol and in its protolith (Delvigne et al., 2016; Nhleko, 2003). The τ values for these elements in the Denny Dalton paleosol show small deviations from zero that tend to closely follow one another (Table 1.2). The small correlated variations likely reflect nugget effect due to the concentration of these elements controlled by a few resistant minerals (Macfarlane et al., 1994) and the relatively small mass of homogenized powder studied (2.5-50 mg), and where minor decoupling of elemental concentrations (Ta in one sample in the CDZ), this variation is close to the level of analytical uncertainties. Thorium, which is also thought to be immobile and would be concentrated in zircon and monazite that are both observed in the Denny Dalton paleosol (Nhleko, 2003), is variably depleted (by up to 75%) in the upper SDZ and in the intermediate horizon (Table 1.2). These variations could easily reflect the range of protolith composition rather than an impact of weathering, because Th concentration in the Nsuze Group basaltic andesites is low and shows large relative variation that can encompass all the values reported here (*e.g.*, Crow et al., 1989).

3.1.2. Divalent transition metals

Transition metals that are divalent under Earth-surface conditions (Co^{2+}, Ni^{2+}, Zn^{2+}) express similar geochemical behavior to Fe^{2+}. All these elements are strongly depleted in the upper SDZ

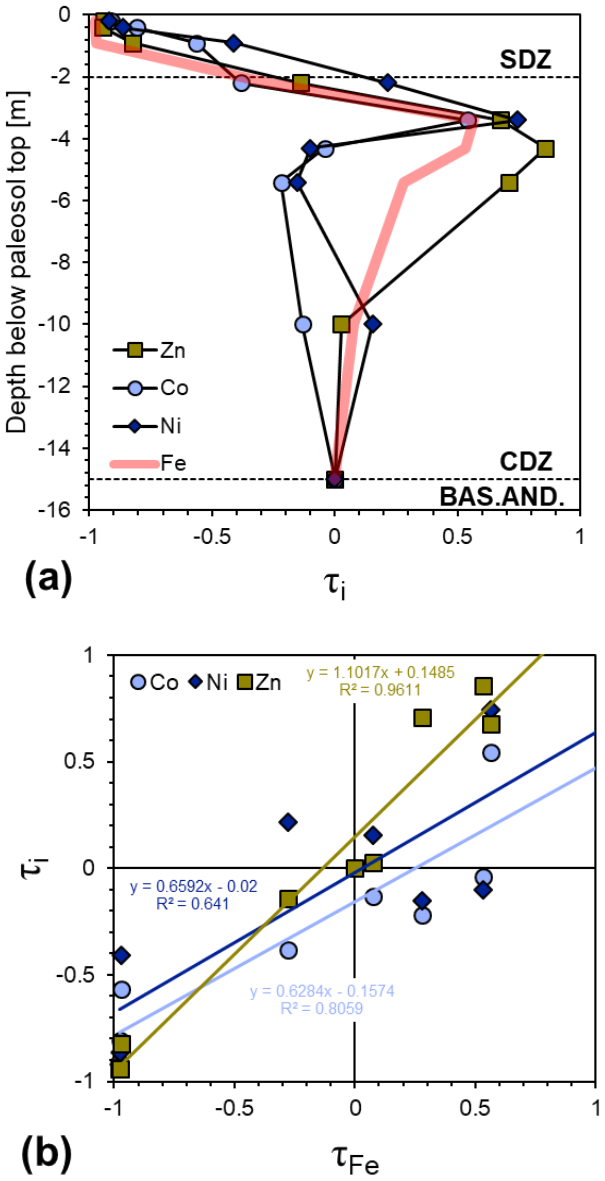

Figure 1.4. (a) Enrichment/depletion index (τ_i) of divalent transition metals: Zn, Co, and Ni, relative to Ti, in the Denny Dalton paleosol, with enrichment/depletion index of Fe for comparison. (b) Correlation of enrichment/depletion index (τ_i) for Zn, Co, and Ni with Fe enrichment/depletion index (τ_{Fe}) in the Denny Dalton paleosol. Positive correlation with slope close to 1 for τ_{Zn} vs. τ_{Fe}, in particular, suggests that little redox-dependent decoupling of Fe from Zn took place during chemical weathering.

and the intermediate zone and range from slightly depleted to strongly enriched with depth in the lower CDZ (Fig. 1.4a). These profiles are qualitatively similar to that of Fe, and positive correlations are observed between τ_{Fe} and each of τ_{Co}, τ_{Ni}, and, particularly, τ_{Zn} (Fig. 1.4b).

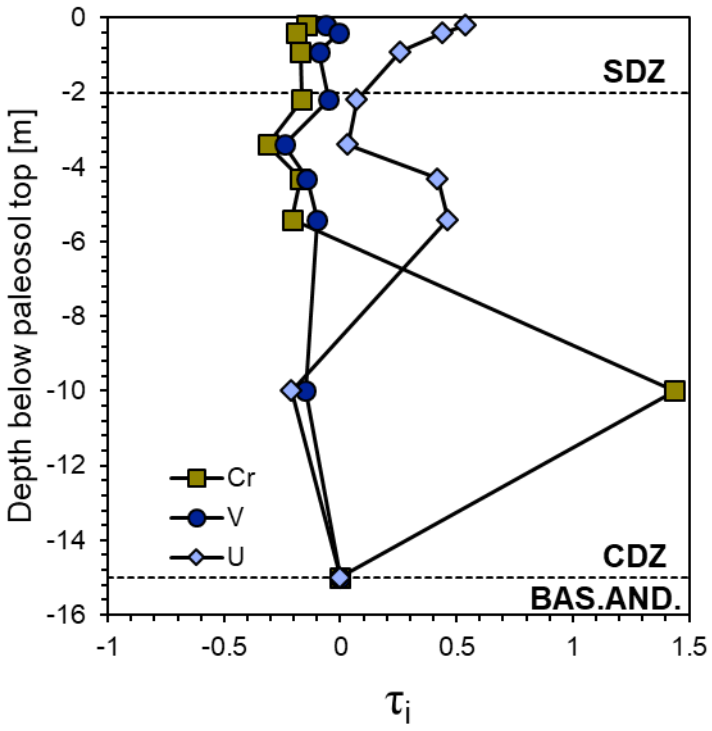

Figure 1.5. Enrichment/depletion index (τ_i) of redox-sensitive elements: Cr, V, and U, relative to Ti, in the Denny Dalton paleosol. Redox-sensitive element Mo was is not plotted due to its large variations compared to the displayed scale. Values for τ_{Mo} are in Table 1.2. Uranium variations are similar in magnitude to the dispersion in U concentrations for the parental basaltic andesite material and therefore do not necessarily represent a weathering signal.

3.1.3. Redox-sensitive trace metals

The elements V, Cr, Mo, and U require high-redox potential species, such as O_2 or Mn^{4+}, to be converted from the reduced forms in which they occur in primary igneous minerals to their fluid-mobile oxidized forms. Vanadium and Cr are both moderately depleted in the weathered paleosol (τ_V = -0.01 to -0.24; τ_{Cr} = -0.15 to -0.31), except for the lowermost sample, which is strongly enriched in Cr (τ_{Cr} = +1.44) (Fig. 1.5). Vanadium is consistently less depleted than Cr, and for both elements the upper SDZ is slightly less depleted than the lower CDZ. Chromium concentration in relation to its isotopic composition is described below. Molybdenum shows highly variable behavior in the paleosol, exhibiting both depletions (τ_{Mo} = -0.59) and strong enrichment

(τ_{Mo} = +2.97) in individual samples from the upper SDZ, and very inconsistent, but large enrichments (τ_{Mo} = +1.22 to +31.96) in the lower CDZ (Table 1.2). Uranium is slightly depleted (τ_U = -0.21) in the lowermost paleosol sample, and moderately enriched throughout the rest of the paleosol (τ_U = +0.03 to +0.54), being on average slightly more enriched in the upper CDZ than in the lower SDZ (Fig. 1.5). However, as with Th variations described above, low U concentrations and large relative variability in the Nsuze Group basaltic andesites could account for all this variation (*e.g.*, Crow et al., 1989).

3.1.4. Rare Earth elements

The rare earth element (REE) concentrations are significantly depleted in the SDZ, while in the CDZ the light REEs (LREE; La to Eu, excluding Ce) show considerable variability whereas the heavy REE (HREE; Tb to Lu) have concentrations indistinguishable from those in the protolith (Fig. 1.6). The τ value for Ce is similar to the τ value calculated for LREE excluding Ce. Therefore, Ce behaved similarly to its neighbors during weathering, suggesting that Ce was not oxidized to its more insoluble Ce^{4+} valence state. Marked enrichments and depletions in the LREE in individual paleosol samples suggest significant mobilization, including release and redistribution compared to HREE, consistent with observations on modern REE behavior in weathering profiles (Su et al., 2017). Likewise, the strong leaching of HREE from the SDZ and their retention in the CDZ are consistent with observations that HREE are mobile in modern soils in a decreasing fashion with increasing depth (Su et al., 2017). The mobilization of the REEs, which are considered to be fluid-immobile in many circumstances, resulting in REE depletions and enrichments in the paleosol, can likely be attributed to the protolith lava being originally composed of a glassy

groundmass, from which REE are easily mobilized and reincorporated into clay minerals (Price et al., 1991).

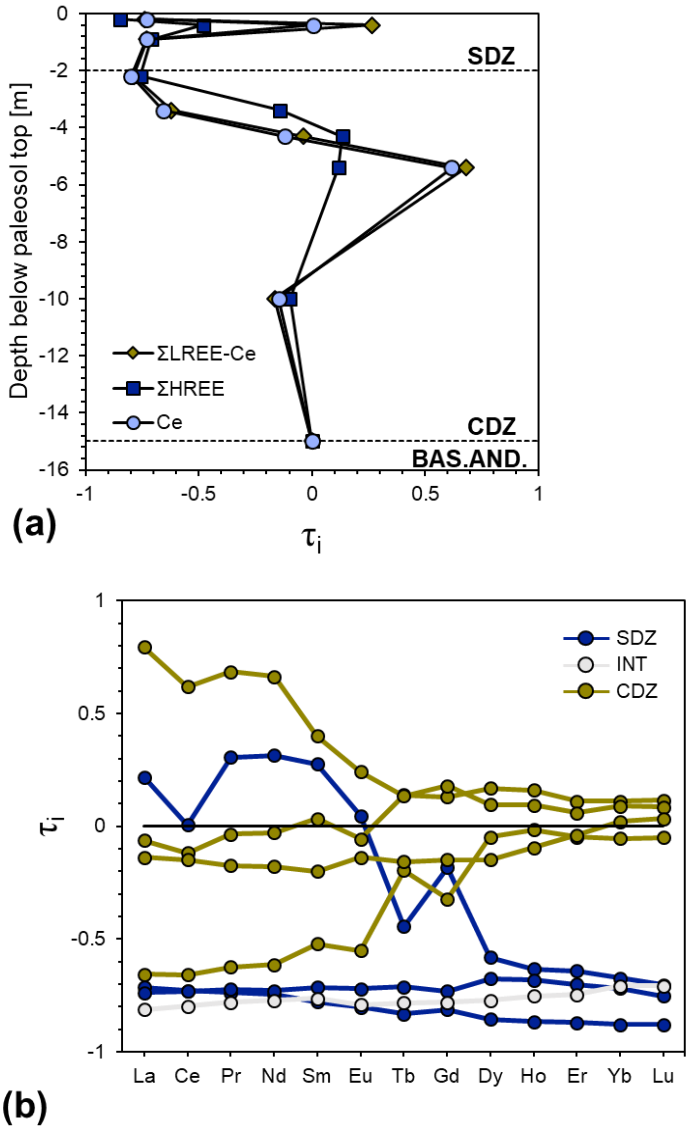

Figure 1.6. Enrichment/depletion indices (τ_i) of REE relative to Ti, in the Denny Dalton paleosol. (a) Depth profile of τ values for: total light Rare Earth Elements (La-Eu) excluding Ce (ΣLREE-Ce), total Heavy Rare Earth Elements (Tb-Lu, ΣHREE), and Ce. Note that τ_{Ce} closely tracks $\tau_{\Sigma LREE-Ce}$, suggesting that no Ce oxidation and fractionation from the other trivalent LREE took place. (b) REE spider diagrams for individual paleosol samples, expressed in τ notation relative to the parent basaltic andesite (horizontal black line). The SDZ, intermediate level, and CDZ, are shown in blue, grey, and green, respectively. The SDZ and intermediate sample are considerably more depleted in all REE than the CDZ. LREE display greater variability than HREE, particularly in the CDZ, where HREE are not significantly altered relative to the protolith.

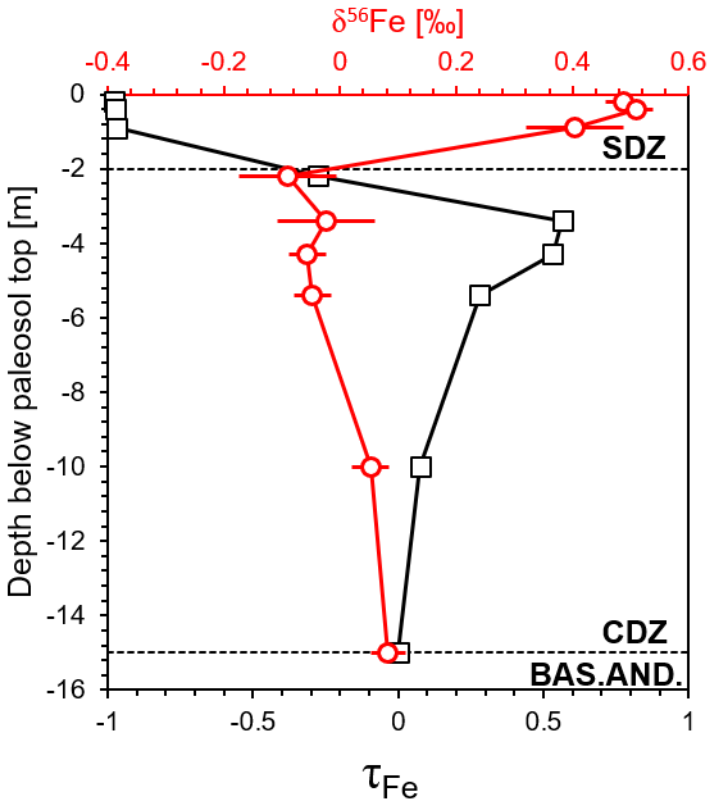

Figure 1.7. Enrichment/depletion index (τ_{Fe}, open black squares and black line), and Fe isotopic composition (δ^{56}Fe relative to IRMM-014, open red circles and red line), in the Denny Dalton paleosol.

3.2. Fe isotopic compositions

Iron isotopic compositions in the paleosol are positive in the upper SDZ, with δ^{56}Fe values of +0.400 to +0.509 ‰, and are slightly negative to slightly positive in the underlying CDZ, with δ^{56}Fe values of -0.056 to +0.053 ‰, all of which are lower than that for the parent basaltic andesite with δ^{56}Fe = +0.083 ‰ (Table 1.1, Fig. 1.7). The intermediate zone between the SDZ and CDZ has the most negative δ^{56}Fe value = -0.090 ‰ (Fig. 1.7). δ^{56}Fe values trend negatively with τ_{Fe}, although the data point from the intermediate zone falls distinctly off this trend (Fig. 1.8).

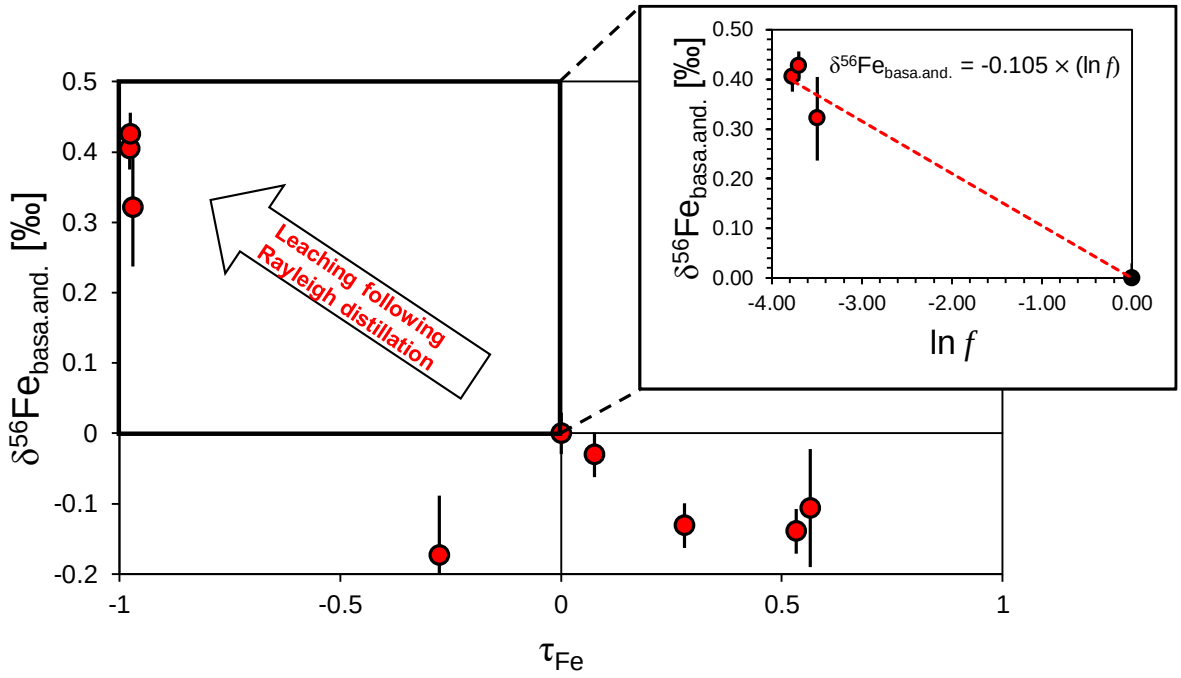

Figure 1.8. Cross-plot of Fe isotopic composition and Fe enrichment/depletion index for the Denny Dalton paleosol. $\delta^{56}Fe_{bas.and.}$ values are $\delta^{56}Fe$ values relative to the parent basaltic andesite material. There is a generally negative relationship between $\delta^{56}Fe_{bas.and.}$ and τ_{Fe}. Inset: cross-plot of $\delta^{56}Fe_{bas.and.}$ *vs.* the natural logarithm of the Fe fraction remaining (*f*) (where $f = \tau_{Fe} + 1$) in the leached SDZ and the basaltic andesite parent rock. Assuming a Rayleigh distillation process to first order, the slope of this line is used to estimate the Fe isotope fractionation between leached Fe and residue, with a negative slope indicating preferential removal of isotopically light Fe to the fluid phase. Forcing the intercept through the origin does not affect the value of the slope.

3.3. Ti isotopic compositions

Titanium isotopic compositions in the paleosol span a narrow range of $\delta^{49}Ti$ values of +0.039 to +0.076 ‰ (Table 1.1, Fig. 1.9). Only the values defining the extremes of this range are not within error of one another at the 95% confidence interval. All individual $\delta^{49}Ti$ values and the average $\delta^{49}Ti$ composition (+0.059 ± 0.010 ‰, n=8) for the paleosol are within error of the parent basaltic andesite that has $\delta^{49}Ti$ = +0.054 ‰. To assess the mobility of Ti, Al was used as the normalizing immobile element. Values of τ_{Ti} do not vary much from zero, with the largest deviation being +0.09 (Fig. 1.9). A recent study suggested that fractionation of Al/Ti ratios in paleosols is been

linked to the presence of organic acids produced by a terrestrial biosphere (Beaty and Planavsky, 2020), but we see no evidence for substantial Al/Ti fractionation in the dataset presented here. The minor variation in Ti isotopic composition of paleosol does not follow any discernible relationship with depth or the small variations in τ_{Ti} (Fig. 1.9).

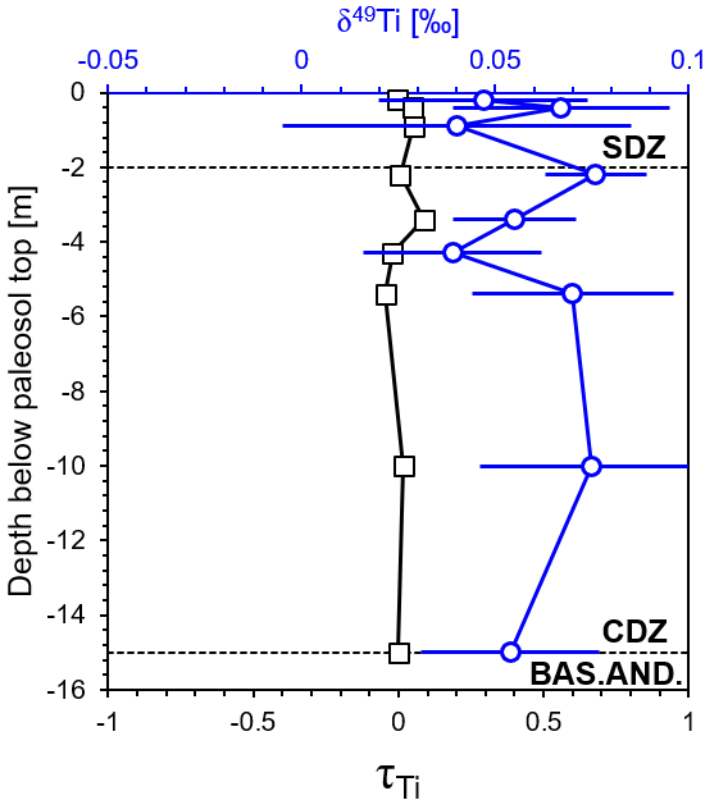

Figure 1.9. Enrichment/depletion index (τ_{Ti}, open black squares and black line), and Ti isotopic composition (δ^{49}Ti relative to OL-Ti, open blue circles and blue line), in the Denny Dalton paleosol. The enrichment/depletion index for Ti is calculated relative to immobile Al.

3.3. Cr isotopic compositions

Chromium isotopic compositions show very limited variability in the paleosol, with δ^{53}Cr values in the range of -0.276 to -0.199 ‰ (Table 1.1, Fig. 1.10). This limited δ^{53}Cr variation includes compositions that are both slightly heavier and lighter than the parent basaltic andesite value of

$\delta^{53}Cr$ = -0.261 ‰, which is slightly lighter than the average igneous composition (Schoenberg et al., 2008). The $\delta^{53}Cr$ values measured here show no systematic variation with depth or τ_{Cr}. All values that we report here are in good agreement with previously published Cr isotope data from Colwyn et al. (2019) that are from the same drill core (Table 1.1, Fig. 1.10). This limited range of isotope ratios contrasts with significant Cr isotopic depletion reported by Crowe et al. (2013) for the Denny Dalton paleosol 10 km away in the PMH-24 drill core. This is despite the fact that the paleosols in both locations come from the same stratigraphic horizon and are developed on the same basaltic andesite substrate, and each feature an upper SDZ and lower CDZ, and comparable chemical compositions. The paleosol studied here exhibits similar or even greater extent of leaching for major elements (Table 1.2) and, specifically, Cr (Fig. 1.12).

4. Discussion

4.1. Constraints on the conditions of Fe mobilization

Strong Fe depletion in the upper SDZ and moderate enrichment in the lower CDZ indicate that Fe was mobilized by groundwaters near the paleoweathering surface. Subsequently, a combination of this Fe-rich fluid percolating downwards, and potential lateral Fe-rich groundwater flow in the CDZ, enabled precipitation of secondary Fe-bearing minerals, resulting in relative Fe enrichment in the lower part of the paleosol (Delvigne et al., 2016; Macfarlane et al., 1994; Rye and Holland, 1998).

Two lines of evidence indicate that groundwaters had light Fe isotopic compositions relative to the parent rock. Positive $\delta^{56}Fe$ values in the strongly Fe-depleted upper SDZ, and negative $\delta^{56}Fe$ ratios in the Fe-enriched lower CDZ, are most parsimoniously explained through the leaching of

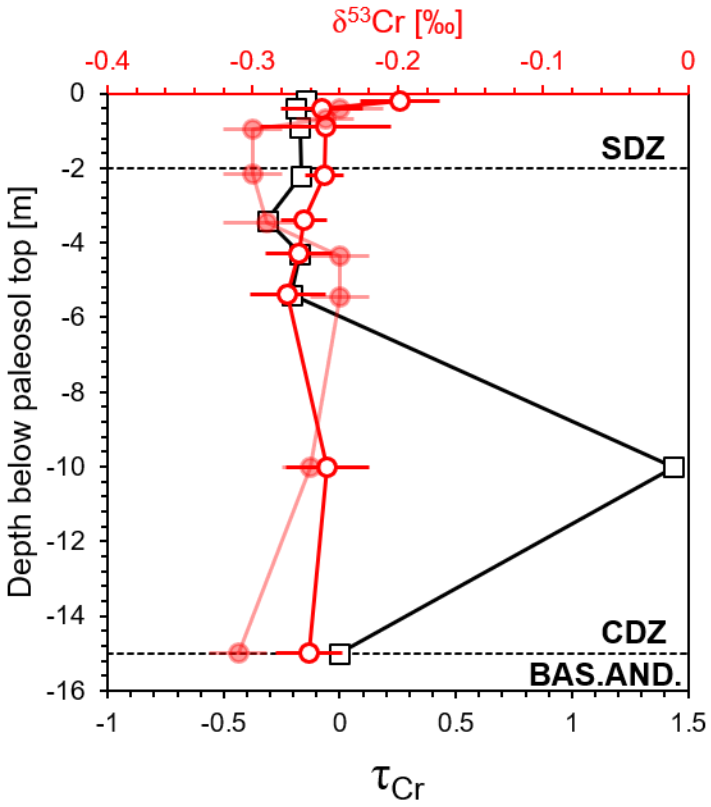

Figure 1.10. Enrichment/depletion index (τ_{Cr}, open black squares and black line), Cr isotopic composition measured in this study (δ^{53}Cr relative to NIST SRM 979, open red circles and red line), and Cr isotopic composition measured by Colwyn et al. (2019) (filled shaded red circles and line) in the Denny Dalton paleosol.

isotopically light Fe to groundwaters in the upper levels of the paleosol, and addition of isotopically light Fe to the lower soil horizon. This process would explain the negative relationship between δ^{56}Fe and τ_{Fe} observed in Figure 1.8.

The sample from the intermediate level between the SDZ and CDZ plots off of the trend in Figure 1.8; it is depleted in Fe relative to the parent rock and yet has the most negative δ^{56}Fe composition for the entire paleosol profile. These observations are most likely explained by the intermediate level sample having seen addition of isotopically light Fe to a substrate already depleted in Fe by leaching. This is the opposite of the expected sequence of Fe cycling in paleosol formed in contact with the anoxic atmosphere, wherein the weathering front is expected to migrate downwards over

time so that lower levels initially enriched in Fe by downward percolating fluids could later experience leaching as the SDZ horizon progressively approached them (Fig. 1.11a). A 'normal' sequence of enrichment followed by leaching cannot explain the intermediate datapoint because the isotope mass-balance for enrichment followed by leaching is not favorable for producing the $\delta^{56}Fe$ and τ_{Fe} values of that sample. In order for the reversed sequence to have impacted intermediate levels of the paleosol, we suggest that this part of the paleosol was close to the depth of the water table shortly before burial of the weathering horizon. Moderate fluctuations in the level of the water table could have enabled both iron leaching (when the water table was lower) and iron enrichment by absorption from groundwater (when the water table was higher) to occur and allowed for enrichment in an isotopically light Fe to be superimposed on an iron-leached substrate (Fig. 1.11b). This scenario is specifically applicable to the sample from the intermediate level between the SDZ and CDZ because the Fe isotope mass balance at that depth resulted in the singular combination of negative $\delta^{56}Fe$ value and negative τ_{Fe} value. However, overlying material now comprising the SDZ could also have experienced a similar combination of processes, though the removal of isotopically light Fe with fluids clearly overprinted its isotopic signature. Because the location of the Fe-concentration maximum in the CDZ is several meters above the base of the paleosol (Fig. 1.2), we infer that the enrichment of Fe in the CDZ by groundwater must have depended not only on the supply of Fe from groundwaters, but also on pore space available within the altered basaltic andesite for fluids to percolate. The almost constant TiO_2 concentration within the CDZ and the parent rock (Table 1.1) suggests that there was little volume lost due to compaction within the CDZ, and therefore the advance of the weathering front from the top of the paleosol downwards would result in a more pore space available for the incorporation of Fe from groundwaters higher up within the CDZ.

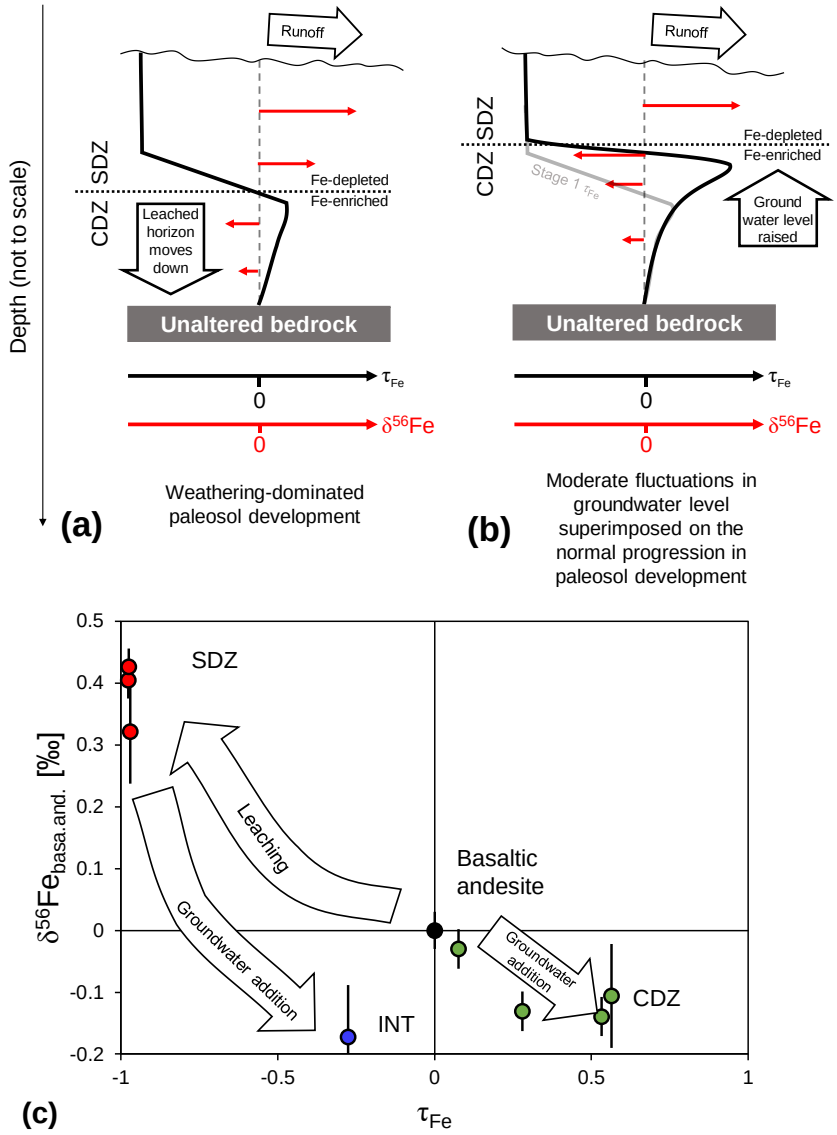

Figure 1.11. Conceptual model of chemical weathering and groundwater addition of Fe to explain $\delta^{56}Fe_{bas.and.}$ and τ_{Fe} variations in the Denny Dalton paleosol. (a) Schematics of the normal progression of weathering-dominated paleosol development. Chemical weathering preferentially depletes the upper soil horizon in isotopically light ferrous iron, removing it both with runoff and to deeper levels of the paleosol. (b) Transient rises in the groundwater level enables addition of isotopically light ferrous iron to higher levels of the paleosol, including to parts of the upper leached horizon where pore space should have been volumetrically more pervasive. Enrichment in Fe and depletion in $\delta^{56}Fe_{bas.and.}$ in the CDZ could be developed both during normal progression of the paleosol and during transient rises in the groundwater level driven by either higher rates of precipitation or lower temperature. (c) Trajectories of leaching and groundwater Fe addition in $\delta^{56}Fe_{bas.and.}$ *vs.* τ_{Fe} space.

The heavily leached upper SDZ can be used to estimate the Fe isotopic fractionation associated with leaching. Modern-day analogues for Archean weathering are limited, because Fe behavior

and isotopic systematics in Phanerozoic soils are strongly affected by both the oxygenated nature of the atmosphere, and by organic complexation and uptake of Fe by plants (Fantle and DePaolo, 2004). However, a reasonable analogue for weathering under a potentially anoxic Mesoarchean atmosphere could be highly acidic weathering, such as iron leaching from basaltic parent rock by acid sulfate fluids in Hawaii (Nie et al., 2020), because low pH conditions suppress Fe^{2+} oxidation and enable iron to be leached as Fe^{2+} even under the modern atmosphere (Singer and Stumm, 1970). Nie et al. (2020) showed that the $\delta^{56}Fe$ composition of residual solid material following intense leaching of basalt evolves in a manner that is well described by a Rayleigh distillation process expressed as:

$$\delta^{56}Fe_{res} = \delta^{56}Fe_{initial} + 1000 \times (\alpha - 1) \ln f$$

where the subscripts "res" and "initial" refer to the evolving composition of the solid residue and the initial composition of the parent material, respectively, α is the isotopic fractionation factor between Fe in the solid and Fe^{2+} released to solution, f is the fraction of ^{54}Fe remaining in the residual solid relative to the original amount. Rayleigh fractionation has also been shown to accurately model isotopic fractionation during leaching of other transition metals from a tens-of-meters-thick saprolite in India (Little et al., 2019), and therefore constitutes a reasonable approximation of the weathering process. The use of a simple Rayleigh distillation for the leaching process is a first-order approach to understanding the isotopic expression of Fe weathering in the Archean, because co-existing fluid and solid samples are not available to directly calibrate fractionation factors and uncertainties in the primary paleosol mineralogy and the isotopic fractionation factors relevant to these mineral phases prevent any more complex isotope-enabled

mechanistic model of the leaching process being meaningfully applied. The value of *f* in a leached sample is determined by comparison to immobile Ti in the weathered and unweathered material:

$$f = \frac{(\mathrm{Fe/Ti})_{\mathrm{res}}}{(\mathrm{Fe/Ti})_{\mathrm{initial}}}$$

Subtracting 1 from *f* recovers the value τ_{Fe} as defined above (Brimhall and Dietrich, 1987). The relationship between $\delta^{56}Fe_{res} - \delta^{56}Fe_{initial}$ and ln *f* is a straight line with a slope ($1000 \times (\alpha-1)$) equal to the isotopic fractionation (in per mil) between residue and leached iron. Nie et al. (2020) found in their study that Fe^{2+} leaching was associated with an isotopic fractionation of $1000 \times (\alpha-1) = -0.245$ ‰. Therefore, isotopically light Fe was removed to the fluid phase during leaching, which then drove $\delta^{56}Fe_{res}$ to more positive values with more intense leaching.

Plotting $\delta^{56}Fe_{bas.and.}$ (subscript $_{bas.and.}$ indicates $\delta^{56}Fe$ values relative to the basaltic andesite parent rock; $\delta^{56}Fe_{bas.and.} = \delta^{56}Fe - 0.083$ ‰, where 0.083 ‰ is the $\delta^{56}Fe$ value of the parent rock) against ln *f* for the strongly leached upper SDZ of the Denny Dalton paleosol gives a slope ($1000 \times (\alpha-1)$) of -0.105, suggesting that dissolved Fe liberated during Mesoarchean weathering had a $\delta^{56}Fe$ value of -0.105 ‰ relative to the parent rock (Fig. 1.8, inset). A source of uncertainty in the model is that all SDZ samples are extremely leached residues, and do not span a continuous range of *f* values. However, to first order, our findings agree with those of Nie et al. (2020) in indicating that a leached Fe^{2+} component is slightly depleted in heavy Fe isotopes relative to the parent rock. For comparison, the largest possible fractionation during leaching allowed by the paleosol data would be -0.4 ‰, which would be inferred from mass balance for the case when leaching of the SDZ had followed a closed-system batch equilibrium. However, we consider it unlikely that leaching at Earth's surface with flowing groundwaters is well represented by a batch equilibration process because Fe is continuously removed in solution and unable to re-equilibrate with the leached solid.

Therefore, we use the batch calculation only to infer the most isotopically light fluid composition possible.

The isotopic composition of Fe delivered to the underlying CDZ by groundwater can be estimated using the sample from the intermediate horizon separating the SDZ and CDZ. When considering Fe added to deeper parts of the paleosol by groundwater, we assume that the intermediate depth sample WM11 isotopically resembles an upper SDZ-like soil with an added groundwater Fe component (that could be at least partially derived from leaching of the SDZ). Using the simple mass balance calculation:

$$\delta^{56}Fe_{WM11}(1+\tau_{Fe,\,WM11}) = \delta^{56}Fe_{SDZ}(1+\tau_{Fe,\,SDZ}) + \delta^{56}Fe_{\,groundwater}(\tau_{Fe,\,WM11}-\tau_{Fe,\,SDZ}),$$

we find that the groundwater Fe had an isotopic composition of $\delta^{56}Fe_{bas.and.} \approx -0.19 \pm 0.09$ ‰. In calculating this value for the groundwater Fe isotopic composition, we made the simplification of using a single Fe isotopic composition that accounts for the net effect of the Fe composition in fluids and the precipitation of Fe from these fluids during secondary mineral formation. The isotopic composition of this component would equal the fluid composition if precipitation from groundwater was either quantitative or not associated with any fractionation. Ferrous clay minerals are expected to dominate the secondary mineral assemblage (Delvigne et al., 2016; Rye and Holland, 1998, 2000), but additionally, adsorption of Fe^{2+} could have fixed groundwater Fe in the CDZ of the paleosol with a small fractionation that would depend on the solid phase to which Fe(II) was adsorbed (*e.g.* Crosby et al., 2007). Both the original mineral assemblage and the Fe isotopic fractionation during the formation of Fe-bearing clay minerals are unknown, so we cannot determine if there was any Fe isotopic offset between the Fe added to the CDZ and the initial groundwater, however we expect this offset to be small. Our calculation suggests that continental

weathering-derived fluids at this location and at this time period had Fe isotopic compositions that spanned a narrow range with δ^{56}Fe values (relative to IRMM-014) between +0.08 ‰ (corresponding to almost quantitative leaching of basaltic andesite) and -0.32 ‰ (most negative fluid composition produced by a batch leaching process). The fluid component inferred from calculations based on the intermediate depth sample falls within this range at -0.11 ‰. This narrow range of δ^{56}Fe values should approximately correspond to the Fe isotopic composition of the continental Fe flux delivered to the oceans at this time. This result is similar to proposed marine hydrothermal inputs to the Archean oceans and agrees well with the commonly used assumption that the continental Fe flux is isotopically similar to the average upper continental crust composition (e.g. Beard et al., 2003; Dauphas et al., 2017; Rouxel et al., 2005). However, more direct constraints on the Fe isotope composition of Mesoarchean continental weathering flux was still needed, because previously proposed oxidative cycling of Fe during weathering at this locality (Crowe et al., 2013; Delvigne et al., 2016) could have imparted strong isotopic fractionations to runoff. Characterizing the continental Fe source is also important in light of the proposed contribution of continental solutes to chemical sediments in the Pongola Supergroup (Alexander et al., 2008), which have been investigated using Fe isotopes under the assumption that the initial Fe source was similar in iron isotopic composition to marine hydrothermal inputs (Ossa Ossa et al., 2018; Planavsky et al., 2014a; Smith et al., 2017).

4.2. Limited role for Fe redox cycling in Mesoarchean continental weathering

We showed above that Fe mobilization occurred with Fe isotopic fractionations that were comparatively small by the standards of low-temperature processes. Although the full range of

$\delta^{56}Fe$ values in the paleosol spans approximately 0.6 ‰, samples associated with severe (98%) levels of Fe depletion define most of this range, and their $\delta^{56}Fe$ values can be explained by progressive leaching associated with an instantaneous fractionation of just -0.105 ‰ (Fig. 1.8). Groundwater-derived Fe components with isotopic compositions fractionated by only -0.2 ‰ relative to the parent rock can also explain Fe enrichment and its isotopic composition in the intermediate depth sample and lower CDZ of the paleosol.

The small fractionations required to generate $\delta^{56}Fe$ variations observed in the Denny Dalton paleosol are difficult to explain if large, redox-controlled Fe isotope fractionations occurred. Based on both experiment and theory, the redox-controlled reactions are expected to enrich ferric iron phases in ^{56}Fe by >1 ‰ (Brantley et al., 2004, 2001; Dauphas et al., 2017; Johnson et al., 2002; Skulan et al., 2002) and partial Fe oxidation would have caused large $\delta^{56}Fe$ variations in the CDZ for which we see no evidence. Limited Fe isotope data for Precambrian paleosols are available for comparison, but the study of Yamaguchi et al. (2007) notably found heavy Fe isotopic values in the most Fe-rich parts of the Paleoproterozoic Hekpoort paleosol. The Hekpoort paleosol was developed during the GOE (Bekker et al., 2004; Gumsley et al., 2017), when redox cycling of Fe during weathering was already pervasive and could drive large fractionations between reduced and oxidized iron phases. Yamaguchi et al. (2007) reported paleosol $\delta^{56}Fe$ values > +0.5 ‰ relative to parent rocks in samples with >20 wt % Fe_2O_3 and $\delta^{56}Fe$ > +1 ‰ in iron-depleted samples. While we found a maximum $\delta^{56}Fe_{bas.and.}$ value of +0.4 ‰, this value corresponds to 98% Fe depletion, and can be fully explained by intense leaching with a small fractionation factor. By contrast, the strong isotopic enrichments reported in the most Fe-rich samples of Yamaguchi et al. (2007) must, by mass balance, require the addition of a large quantity of phase with a heavy Fe isotope composition, inferred in that study to have been an Fe-(oxyhydr)oxide. Therefore, the most

straightforward interpretation for the differing relationship of Fe isotopic values and Fe concentrations between the Denny Dalton paleosol and the Hekpoort paleosol is that in the former, redox cycling of Fe did not operate and exclusively ferrous iron was mobilized under anoxic weathering conditions; whereas in the latter, redox cycling of Fe during weathering did occur in an atmosphere that had become relatively oxygenated.

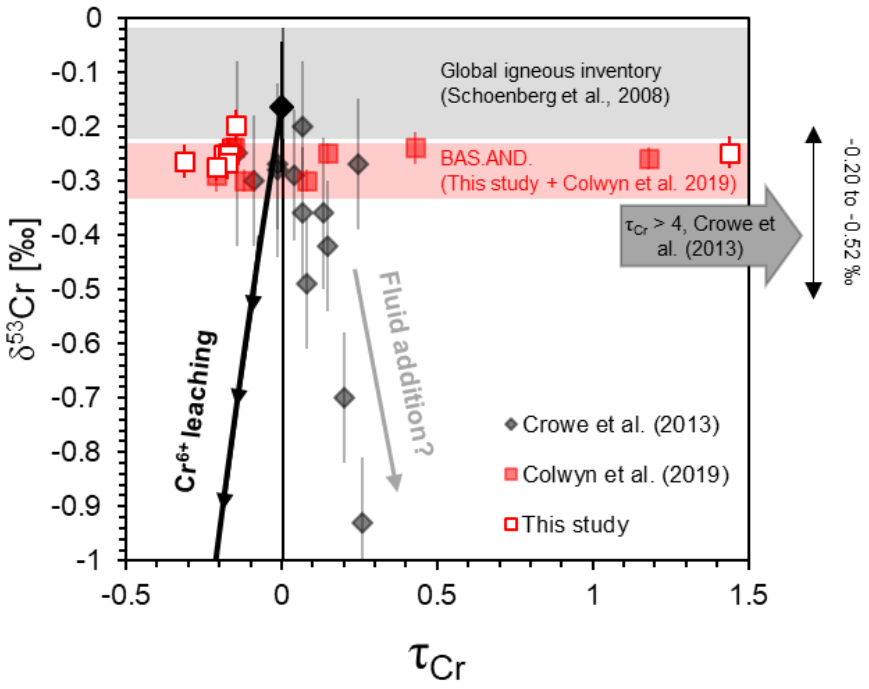

Figure 1.12. Relationship between $\delta^{53}Cr$ and τ_{Cr} in the Denny Dalton paleosols from Crowe et al. (2013), Colwyn et al. (2019), and this study. The grey- and red-shaded regions represent the range of values for the global igneous inventory (Schoenberg et al., 2008) and the range of measured values for the parent basaltic andesite rock of the Denny Dalton paleosol in the TSB07-26 drill core samples (Colwyn et al., 2019; this study), respectively. Strongly Cr-enriched samples ($\tau_{Cr} > 4$) analyzed by Crowe et al. (2013) are not shown but have $\delta^{53}Cr$ values ranging from -0.2 ‰ to -0.52 ‰. The black line indicates the expected trajectory for oxidative leaching of isotopically heavy oxidized Cr (using the 3.5 ‰ fractionation factor determined by Ellis et al. (2002) and Zink et al. (2010)) from a starting composition of the basaltic andesite rock from Crowe et al. (2013) (black diamond), with arrows indicating the direction of increased leaching. Samples with highly negative $\delta^{53}Cr$ values reported by Crowe et al. (2013) follow a different trend, suggesting addition of isotopically light Cr rather than removal of oxidized Cr. Samples from the drill core TSB07-26 (Colwyn et al., 2019; this study) have basaltic andesite rock-like $\delta^{53}Cr$ values regardless of τ_{Cr} values and thus do not support Cr oxidation.

The positive co-variation of Fe concentrations with Co, Ni, and Zn in the paleosol profile supports the notion that Fe was not oxidized (Fig. 1.4), because all of the latter transition metals are divalent at Earth's surface conditions and have similar behavior to Fe^{2+} in aqueous environments, including paleosols (De Kock et al., 2019; Macfarlane et al., 1994). In contrast, ferric iron is highly insoluble and has a markedly different geochemical behavior. Notably, ferrous iron and Zn have very similar solubility in seawater and it has recently been demonstrated that the decoupling of marine Zn/Fe ratios, driven by removal of insoluble ferric iron, is a promising paleoredox proxy (Liu et al., 2016). As such, the lack of Zn/Fe decoupling in the Denny Dalton paleosol (Fig. 1.4) precludes any significant role for Fe oxidation during weathering. This agrees with our Fe isotope measurements and calculations.

4.3. Redox conditions during Mesoarchean continental weathering

Oxidative mobilization of redox-sensitive elements V, Cr, Mo, and U requires high redox potential oxidants (such as O_2, either directly or indirectly via MnO_2). We only observe limited leaching of Cr and V during paleoweathering at this site (Fig. 1.4), which argues against the oxidative mobilization of these elements. The Mo enrichment in the paleosol must require addition from post-burial fluids because it cannot be explained by Mo contribution from the moderately leached uppermost levels of the paleosol since it violates mass balance. The extreme variability in Mo concentration thus cannot be meaningfully interpreted in the context of paleoweathering. In the case of U enrichment in some paleosol samples, we note that the unconformity between the paleosol and the basal conglomerate of the overlying Mozaan Group contains detrital uraninite (Hicks and Hofmann, 2012) and U remobilization by post-burial fluid flow along this

unconformity could have supplied U to the Denny Dalton paleosol. This would explain why this enrichment is the strongest at the very top of the paleosol (Fig. 1.4) and indicate that U in this profile also does not offer any useable paleoweathering information. However, it should also be noted that all U variations are at the scale where they could reflect natural variability in already low U concentrations in parental basaltic andesite material rather than any particular alteration signal (Crow et al., 1989).

Crowe et al. (2013) presented negative $\delta^{53}Cr$ values (Fig. 1.12) in the same paleosol as evidence for the oxidation of Cr and preferential mobilization of isotopically heavy oxidized Cr during weathering. In their study, the mobilization of oxidized Cr was used to constrain minimum atmospheric oxygen to 3×10^{-4} present atmospheric levels (PAL), or ~30 × the level estimated for the Archean from the record of mass-independent fractionation of sulfur isotopes (S-MIF) (Pavlov and Kasting, 2002). Notably, the basis for Crowe et al. (2013)'s calculation of the atmospheric oxygen level was that oxidized Cr is efficiently reduced and immobilized by ferrous iron, and atmospheric oxygen level was thus calculated based on dissolved groundwater oxygen concentration sufficient to oxidize all reactive ferrous iron at a given reaction rate during Mesoarchean weathering.

Chromium isotopic data for the TSB07-26 drill core paleosol profile (independent measurements reported here and in Colwyn et al., 2019) show no evidence for oxidative weathering, in contrast to the findings of Crowe et al. (2013) (Figs. 1.10, 1.12). The moderate leaching of Cr throughout the paleosol profile and its enrichment at 10 m depth (in the lowest CDZ sample) can be adequately explained by a moderate degree of anoxic Cr liberation from the easily dissolved matrix material of the parent basaltic andesite and its subsequent redistribution. Furthermore, our Fe isotopic and elemental data do not support a major role for ferrous iron oxidation during paleosol development

(Figs. 1.7, 1.8, 1.11). Fe oxidation occurs at a lower redox potential than that required for oxidation of Cr, and therefore it seems highly unlikely that weathering conditions during formation of this paleosol were oxidizing enough to produce mobile oxidized Cr. The question then becomes whether apparent differences in redox behavior between the paleosol studied here and by Colwyn et al. (2019) and the one studied by Crowe et al. (2013) reflect true spatiotemporal heterogeneity in surface redox conditions or post-depositional alteration.

One mechanism that was suggested to cause spatial variability in surface oxygenation is the operation of oxygenic photosynthesizers restricted to terrestrial microbial mats that generated localized oxygen oases in disequilibrium with the anoxic Archean atmosphere (Lalonde and Konhauser, 2015). Recent compilations of S and Mo sedimentary records have also been used to argue that oxidative weathering operated in terrestrial settings before the rise of atmospheric O_2 (Stüeken et al., 2012), although the Mo isotopic record suggests that the onset of oxidative weathering may instead have closely tracked the GOE itself (Greaney et al., 2020). Regardless, while surficial microbial oxidation processes are mechanistically feasible for explaining global surface geochemical fluxes (Stüeken et al., 2012) or redox-sensitive element signatures in accumulated aqueous sediments (Lalonde and Konhauser, 2015), the action of a microbial mat ecosystem should by definition be restricted to thin surface layers, which makes them an ineffective means of pervasively oxidizing tens of meters thick intervals of igneous rock substrate as would be required to explain the Cr isotopic data (Crowe et al., 2013). A pervasive Mesoarchean oxidative continental weathering signal would require a global spike in atmospheric oxygen (to ~3×10^{-4} PAL; Crowe et al., 2013) in order to extend to groundwaters. However, we have established that Fe and Cr isotopic variations in the paleosol studied here are fully consistent with anoxic weathering conditions (cf. Colwyn et al., 2019) that would require a local reduction mechanism if

the atmosphere as a whole had been more oxygenated at this time. Furthermore, any transient atmospheric oxygenation event would need to have been remarkably short-lived, in order to explain the persistence of sulfur isotope mass independent fractionation (S-MIF) signals in the overlying Mozaan Group (Farquhar et al., 2007). Indeed although the magnitude of S-MIF variation is small in the Mesoarchean (Ohmoto et al., 2006; Ono et al., 2006), such a diminished range could reflect different atmospheric compositions independent of pO_2 (Halevy et al., 2010).

It is therefore worth exploring whether Cr isotopic difference between these two paleosol profiles could reflect a late (even modern) overprint of the primary geochemical record. In an analogous manner, the fidelity of the Cr isotopic record of the Pongola Supergroup has recently been reevaluated with new analyses of samples from the Ijzermyn Iron Formation (Albut et al., 2018). In the same study that reported evidence for oxidative weathering of isotopically heavy Cr from the Denny Dalton paleosol, the stratigraphically overlying Ijzermyn Iron Formation was shown to be a possible complimentary reservoir for isotopically heavy Cr removed to the oceans (Crowe et al., 2013). Those signatures were only observed in outcrop samples of the Ijzermyn Iron Formation, whereas Albut et al. (2018) analyzed drill core samples of the Ijzermyn Iron Formation and found no deviation in $\delta^{53}Cr$ values from the igneous inventory value of -0.124 ± 0.101 ‰ (Schoenberg et al., 2008). Analysis of new outcrop samples produced positive $\delta^{53}Cr$ values, along with unusual enrichments in U, W, Tl, As, and MREEs that were absent in correlative drill core samples (Albut et al., 2018). Furthermore, outcrop samples of the Ijzermyn Iron Formation analyzed by Planavsky et al. (2014b) showed no fractionated $\delta^{53}Cr$ signature, indicating variability even among outcrop samples. The restriction of fractionated Cr isotopic signatures to outcrop samples, along with the co-enrichment in other trace elements indicating post-burial fluid flow, led Albut et al. (2018) to conclude that iron formation samples analyzed by Crowe et al. (2013)

were altered by recent oxidative weathering processes and there was no primary enrichment in ^{53}Cr.

Unlike the Ijzermyn Iron Formation samples, the fractionated $\delta^{53}Cr$ values reported from the Denny Dalton paleosol by Crowe et al. (2013) come from drill core samples, such that a direct analogy that dismisses fractionated $\delta^{53}Cr$ values as a recent alteration product is unwarranted. Rather than relying on analogy, below we directly show that fractionated $\delta^{53}Cr$ values and high Cr concentrations in the Denny Dalton paleosol are unlikely to be a signature of oxidative continental weathering in the Archean.

The paleosol studied by Crowe et al. (2013) shows only limited evidence for Cr depletion for a soil horizon supposedly affected by oxidative leaching of Cr. While the paleosol was reported to

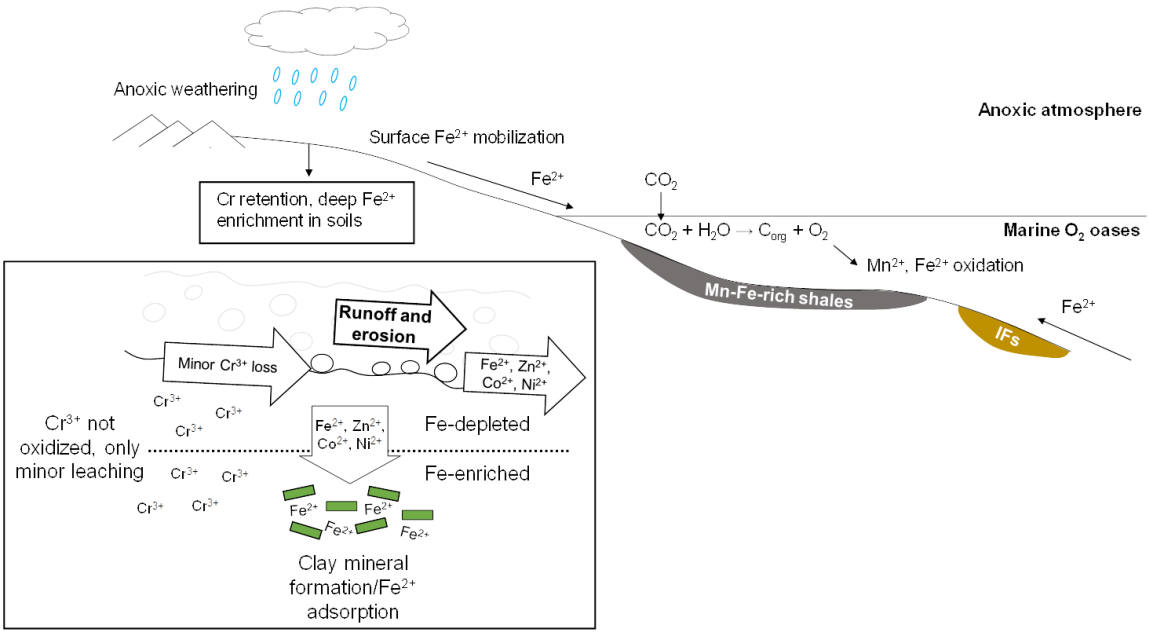

Figure 1.13. Mesoarchean Fe cycling under an anoxic atmosphere. Anoxic weathering mobilized ferrous iron in solution, which percolated with meteoric waters down to deeper groundwater levels in the paleosol. There, ferrous iron either co-precipitates with or adsorbs to clay minerals, while some amount was transported in continental runoff to the oceans, providing an additional source of Fe to fine-grained sediments and iron formations. Under anoxic conditions, Cr is largely retained in soils in reduced Cr form. Oxygen oases restricted to the marine realm drove extensive Fe and some Mn oxidation.

be depleted in ^{53}Cr and cations, when normalized to immobile Ti, only 4 of 23 paleosol samples show Cr depletion with the lowest τ_{Cr} value being -0.144 (Fig. 1.12). By comparison, all but one sample (with τ_{Cr} = 1.44) in our study shows moderate Cr depletion (τ_{Cr} = -0.15 to -0.31) (Table 1.1, Figs. 1.9, 1.11). The majority of the paleosol samples studied by Crowe et al. (2013) are actually Cr-enriched (Fig. 1.12), some to startling degrees (τ_{Cr} = +0.04 to +5.78), which was attributed to a later stage of reduced fluid flow in part of the paleosol. If only samples without extreme Cr enrichment are considered, one would expect that following oxidative weathering, the samples showing more advanced degrees of Cr removal should have more negative $\delta^{53}Cr$ signatures. We modeled oxidative Cr removal with a Rayleigh distillation assuming an isotopic fractionation of 3.5 ‰ between oxidized and reduced Cr species (Ellis et al., 2002; Zink et al., 2010) and show in Figure 1.11 that moderate amount of Cr leaching (~20 % removal of oxidized Cr) can indeed generate the full range of $\delta^{53}Cr$ values reported by Crowe et al. (2013). However, this model predicts that more Cr-leached samples would exhibit more negative $\delta^{53}Cr$ values, whereas the data of Crowe et al. (2013) show the opposite trend with negative $\delta^{53}Cr$ values being observed exclusively in samples with τ_{Cr} >0 (Fig. 1.12) (Colwyn et al., 2019). A relatively strong co-variation between negative $\delta^{53}Cr$ values and Cr enrichments in that dataset suggests the addition of isotopically light Cr rather than loss of isotopically heavy Cr (Fig. 1.12). All samples that show net Cr loss have $\delta^{53}Cr$ values within error of the unaltered igneous rock and agree with the findings of Colwyn et al. (2019) and this study (Fig. 1.12). Those samples that show real Cr depletion could have arisen from leaching of small amounts of reduced Cr hosted in easily broken-down matrix material of the parent basaltic andesite. While we cannot definitively fingerprint the sequence of events that led to large negative $\delta^{53}Cr$ fractionations in some samples of the Denny Dalton paleosol, they follow an opposite trend to that expected for oxidative leaching of Cr during

continental weathering, and their τ_{Cr} values >0 require at least one episode of Cr addition that would have likely overprinted any primary weathering signature.

Since no oxidative weathering signature is convincingly established for the Denny Dalton paleosol, there is no need to appeal to spatiotemporal redox variability during the Mesoarchean and continental weathering conditions are therefore more likely to have been uniformly anoxic, consistent with the combined Fe and Cr isotopic, and trace element, compositions of the paleosol studied here (Colwyn et al., 2019; our study). This argument is also consistent with persistent non-zero S-MIF signatures throughout the Mesoarchean (Farquhar et al., 2007) and supports the notion that locally developed shallow-marine oxygenation (for which geochemical evidence is robust; e.g., Albut et al., 2019; Eickmann et al., 2018; Ossa Ossa et al., 2018; Planavsky et al., 2014a) remained restricted to the shallow-marine realm (Fig. 1.13).

4.4. Implications of elemental fractionation during Archean continental weathering for sedimentary proxies of upper continental crust composition

Fine-grained detrital sediments have been employed to constrain the chemical composition of the upper continental crust through time because they arguably provide spatiotemporally averaged samples of emerged continental crust in their provenance (e.g. Chen et al., 2020; Greber et al., 2017; Greber and Dauphas, 2019; McLennan, 2001; Ptáček et al., 2020; Smit and Mezger, 2017; Tang et al., 2016; Taylor and McLennan, 1985). A critical component in reconstructing crustal composition from shale records is the selection of chemical and isotopic systems that retain provenance geochemical signatures throughout physical and chemical weathering processes (e.g., Greber et al., 2017; Greber and Dauphas, 2019; Ptáček et al., 2020). Paleosols represent solid

residues of chemical weathering on Earth's early continents, much like the detrital material that makes its way to the shale record, and therefore paleosol trace element systematics can be used to validate the use of specific chemical and isotopic ratios in the reconstruction of the chemical composition of the upper continental crust through time. While a single paleosol profile is just a snapshot in time and space, strong fractionation from the initial igneous composition in any paleosol should caution against using these elemental ratios in reconstructing crustal composition. In this manner, paleosols can be used as a complementary method for screening elemental and isotopic ratios for their use in inferring upper continental crust composition. The Denny Dalton paleosol is geochemically similar to nearby detrital sediments like the Mozaan shale that overlies the paleosol in the TSB07-26 drill core. The paleosol and the shale have very similar CIA values, as previously reported by (Delvigne et al., 2016), supporting the notion that the paleosol is a reasonable proxy for the solid residue of chemical weathering that eventually makes its way into detrital sediments.

Chemical ratios that have been used to reconstruct continental crust composition include Ni/Co (Greber et al., 2017; Ptáček et al., 2020; Tang et al., 2016), Cr/Zn (Tang et al., 2016), Cr/U (Smit and Mezger, 2017), La/Sc (McLennan, 2001; Taylor and McLennan, 1985), and Th/Sc (McLennan, 2001; Taylor and McLennan, 1985). To assess how these ratios are affected by paleo-weathering processes, we examined the alteration of these ratios (normalized to the protolith composition) through the paleosol depth section, and calculated the ratios of the column-integrated contents of these elements in the whole paleosol section (Fig. 1.14, Table 1.3). This approach allowed us to examine both the alteration of ratios at an individual sample level within the paleosol (Fig. 1.14a), and also whether the entire weathering profile was substantially altered from the underlying parent rock value (Fig. 1.14b).

Table 1.3. Variations in elemental ratios applied to shale studies, for the Denny Dalton paleosol

	WM 08	**WM 09**	**WM 10**	**WM 11**	**WM 12**	**WM 13**	**WM 14**	**WM 15**	**WM 16**	**Column-integrated**
Zone	SDZ	SDZ	SDZ	INT.	CDZ	CDZ	CDZ	CDZ	BAS. AND.	
Depth from paleosol top [m]	-0.2	-0.4	-0.9	-2.2	-3.4	-4.3	-5.4	-10	-15	
$[Ni/Co]_{bas.and.}$	0.92	0.70	1.36	1.97	1.13	0.94	1.08	1.33	1.00	1.20
$[La/Sc]_{bas.and.}$	2.31	4.35	0.66	0.43	0.45	0.95	160	1.36	1.00	1.21
$[Th/Sc]_{bas.and.}$	2.00	2.73	1.51	0.57	1.04	0.99	1.01	1.27	1.00	1.09
$[Cr/Zn]_{bas.and}$.	14.70	14.31	4.73	0.97	0.41	0.45	0.46	2.37	1.00	1.25
$[Cr/U]_{bas.and.}$	0.55	0.56	0.66	0.78	0.67	0.58	0.54	3.09	1.00	1.17

bas.and. Indicates normalization to the ratio in basaltic andesite parent rock.

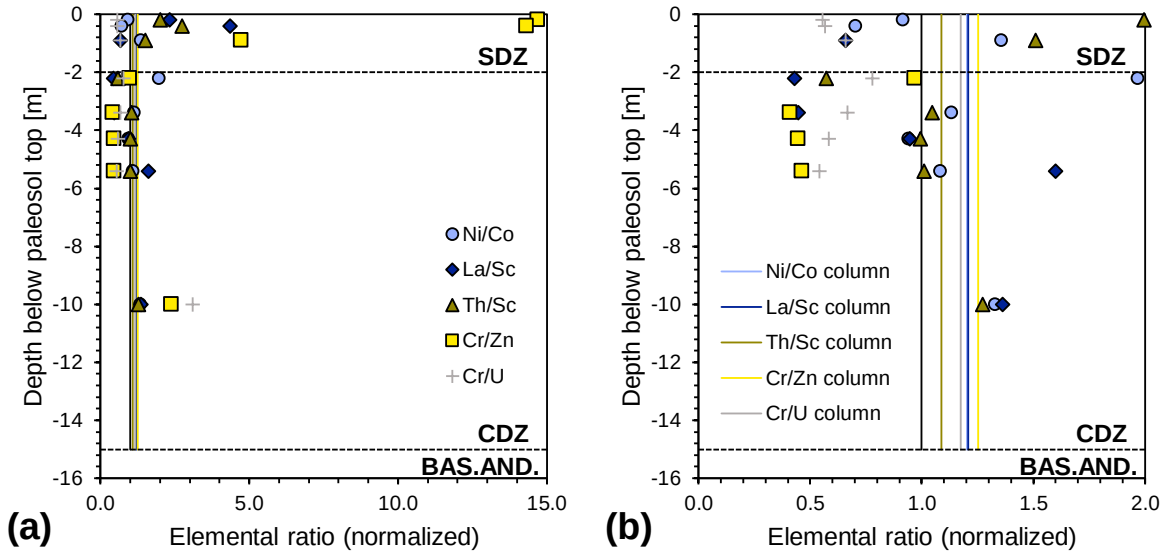

Figure 1.14. Variations in elemental ratios Ni/Co, La/Sc, Th/Sc, Cr/Zn, Cr/U used in for shale reconstructions of upper continental crust compositions, in the Denny Dalton paleosol (normalized to ratio in the basaltic andesite protolith). (a) Variations in individual samples are quite large for most elemental ratios, particularly in the upper, heavily weathered SDZ. (b) Vertical lines show ratios of column-integrated abundances of the elements considered. Column-integrated ratios are all within 25% of the protolith value, suggesting if the entire column was eroded away to become detrital sediments, a reasonable estimate of the crustal provenance could be obtained from those sediments. However, the considerable variability in the SDZ which is more likely to have been eroded means that these elemental ratios should still be used only with caution.

As Figure 1.14b shows, the ratios of the depth-integrated elemental concentrations were quite similar to the parent rock for all of the elements pairs we considered, with the largest offset between paleosol and parent rock values being 25%, for Cr/U (Table 1.3). The Th/Sc ratio paleosol-integrated value is the most similar to the underlying basaltic andesite, with a difference of 9% (Table 1.3), which may be due to the fact that Th are Sc are the two immobile elements among the element pairs considered. These data suggest that if the entire weathered horizon was eroded and transported to shallow marine environments to form shales, all of the considered elemental ratios (Ni/Co, La/Sc, Th/Sc, Cr/Zn, Cr/U) measured in shales might give an accurate representation of the initial elemental ratios of upper continental crust rocks they were sourced from. However, it is also worth considering the degree of elemental ratio variability at different depths in the paleosol,

as material in the upper SDZ is closer to the surface, and would therefore be more likely to be transported to form detrital sediment records (e.g. shales) if the entire weathered horizon was not eroded.

Individual paleosol samples show considerably more scattered elemental ratios, particularly in the heavily leached SDZ (Fig 14a). Of the ratios we consider, Ni/Co ratios for individual paleosol samples are mostly within 50% of the underlying basaltic andesite value (Table 1.3), which is comparable to the level of variation seen within single geologic formations for Ni/Co ratios of individual shale samples used in continental crust reconstructions (Ptáček et al., 2020). Nickel and Co are mobile during weathering, but their very similar behavior during weathering appears to alleviate this potential pitfall in the use of Ni/Co ratio measurements in shales. The Th/Sc ratio of individual paleosol samples varies by a factor of 5, covering a range above and below the protolith value (Table 1.3). However, almost all this range is expressed in the highly weathered upper part of the paleosol where the content of both elements was lower, which is why the mass-balanced Th/Sc ratio of the entire paleoweathering profile is still so similar to the protolith value (Table 1.3, Fig. 1.14b). The remaining elemental pairs, La/Sc, Cr/Zn, and Cr/U show a lot more variability throughout the paleosol profile, such that the small difference between column-integrated ratios and the protolith are somewhat surprising. Cr/Zn ratios span well over an order of magnitude in the profile (Table 1.3, Fig. 1.14a). This relative mobility of Zn and immobility of Cr during Archean weathering has been documented previously (Macfarlane et al., 1994). The markedly different mobilities exhibited by these elements during weathering suggest that sediments derived from this paleosol and deposited in marine shales would not reliably represent the Cr/Zn ratio in the provenance. Since both Cr and U are mobile under oxic conditions, this ratio in both shales and paleosols is highly susceptible to post-depositional alteration under recent oxidized weathering

conditions and their behavior through time would have changed significantly with evolving atmospheric oxygen level. As a result, the upper continental crust Cr/U signature is likely to be variably overprinted in shale record by precipitation of authigenic mineral phases and redox processing.

The Ti isotopic system has also been used to reconstruct upper continental crust composition because δ^{49}Ti value is strongly fractionated during magmatic differentiation (Deng et al., 2019; Greber et al., 2017; Millet et al., 2016), and its fluid immobility should suppress any major deviation from primary igneous signature during chemical weathering (Greber et al., 2017). The retention of > 90 % of Ti and the small Ti isotopic range observed within the Denny Dalton paleosol confirm that Ti was immobile despite intense chemical weathering of the parent rock (Fig. 1.9). Small variations in δ^{49}Ti values in the profile could reflect *in situ* Ti redistribution by settling of insoluble, dense Fe-Ti oxide grains within the soil profile (Schroeder and Shiflet, 2000) or local dissolution of Ti from primary minerals and the basaltic andesite silicate matrix and reprecipitation as rutile and anatase (Alló, 2004; Grey and Reid, 1975; Morad and Aldahan, 1982). Alternatively, Ti isotope range of such a small magnitude could reflect primary variations within basaltic andesitic lava flows, perhaps due to small-scale differences in mineralogy (e.g., Fe-Ti oxide abundance, distribution of cumulate minerals). To our knowledge, whole-rock variations in δ^{49}Ti values at the lava flow-scale have not been investigated. However, δ^{49}Ti composition of samples from the Kīlauea Iki lava lake suggests that magmatic differentiation and specifically the onset of Fe-Ti oxide crystallization are the primary drivers of Ti isotopic fractionation in igneous rocks (Johnson et al., 2019). It is therefore reasonable that individual lava flows could show some Ti isotopic heterogeneity, reflecting their modal mineralogy and the amount of Fe-Ti oxide enrichment and subsequent removal they experienced prior to eruption. Regardless, Ti isotopic

composition appears to have been minimally affected by intense Archean weathering and the column-integrated δ^{49}Ti value of the paleosol is within error of the parent rock, which argues against the removal of any significantly fractionated Ti phase. This strengthens the case that Ti isotopic composition of weathered material, which eventually finds its way to the fine-grained detrital sedimentary rock record, can faithfully record the Ti isotopic composition of the rocks they are sourced from.

δ^{49}Ti, and Ni/Co and Th/Sc ratios showed the most conservative behavior during the intense chemical weathering that formed the paleosol. With the data available from this small sample size, Ti isotopes in particular appear to robustly withstand the 'paleo-weathering test' provided by this snapshot of Archean weathering processes, and are expected to faithfully transfer their upper continental crust values to the shale record (Greber et al., 2017). How Ti isotopes may relate to the bulk chemical composition of the upper continental crust is debated elsewhere (Aarons et al., 2020; Deng et al., 2019; Greber et al., 2017; Hoare et al., 2020), but revisiting paleosol records through time to validate the chemical proxies used to reconstruct the upper continental crust composition is a promising avenue for further studies to explore.

5. Conclusions

We analyzed Fe isotope ratios and trace elements in the Denny Dalton paleosol of the Mesoarchean Pongola Supergroup to better understand how Fe was mobilized during Archean weathering processes and to assess the role of oxidative processes in soil formation ~2.95 billion years ago. The formation of the Denny Dalton paleosol involved strong chemical leaching in the upper part of the paleosol and an Fe addition through downward percolation of meteoric waters and/or lateral

flow of groundwaters. In addition, Fe was episodically added to shallow levels of the paleosol when increase in precipitation rate or decreases in surface temperature led to a higher groundwater level. Consistently small Fe isotopic fractionations during chemical weathering and similar behavior of Fe and divalent transition metals (Co, Ni, and, particularly, Zn) suggests that Fe mobilization was largely anoxic, and since Fe redox cycling was not involved, weathering must have occurred under an essentially anoxic atmosphere. Iron isotope evidence for anoxic weathering is consistent with unfractionated Cr isotopes in the same paleosol, but contrasts with previous Cr isotopic evidence for oxidative leaching of Cr from the same Denny Dalton paleosol horizon sampled from a different drill core nearby. We showed that the latter Cr isotopic fractionations in the Denny Dalton paleosol cannot be explained through oxidative weathering because they correlate with Cr enrichment rather than depletion. There is, therefore, no convincing Cr isotopic evidence for oxidative weathering in the Mesoarchean terrestrial record. More robust evidence for marine oxygenation at this time should therefore reflect ocean oxygen oases that did not strongly and persistently impact the atmospheric composition. We showed that Ti isotopic systematics were not compromised by strong chemical weathering that formed the Denny Dalton paleosol. This provides a first validation for the robustness of this proxy as a record that can 'see through' weathering processes, to relate the shale record to the Ti isotopic composition of the upper continental crust. We also showed that several widely used trace element ratios were fractionated by paleoweathering and should be used only with caution. Further isotopic and trace element studies of paleosols could shed more light on the currently under-constrained nature of continental geochemical fluxes to the Archean oceans.

Acknowledgements

We thank Brian Kendall for editorial handling of the manuscript, and two anonymous reviewers for providing insightful reviews that improved the quality of the paper. Work at the University of Chicago was funded by NASA grants 80NSSC17K0744 to ND and AWH (Habitable Worlds), 359NNX17AE86G to ND (LARS), NNX17AE87G and 80NSSC20K0821 to ND (Emerging Worlds), 80NSSC20K1409 to ND (Habitable Worlds), and NSF grant EAR-2001098 to ND (CSEDI). AWH was supported by an Eckhardt Scholarship from the University of Chicago. A.H. thanks Acclaim Exploration NL, J. Hancox, and N. Hicks for access to drill core samples and acknowledges support by the National Research Foundation of South Africa. A.B. acknowledges support by the University of Johannesburg in the form of Distinguished Visiting Professorship.

Competing financial interests: The authors declare that they have no competing financial interest.

References

Aarons, S.M., Reimink, J.R., Greber, N.D., Heard, A.W., Zhang, Z., Dauphas, N., 2020. Titanium isotopes constrain a magmatic transition at the Hadean-Archean boundary in the Acasta Gneiss Complex. Sci. Adv. 6. https://doi.org/10.1126/sciadv.abc9959

Albut, G., Babechuk, M.G., Kleinhanns, I.C., Benger, M., Beukes, N.J., Steinhilber, B., Smith, A.J.B., Kruger, S.J., Schoenberg, R., 2018. Modern rather than Mesoarchaean oxidative weathering responsible for the heavy stable Cr isotopic signatures of the 2.95 Ga old Ijzermijn iron formation (South Africa). Geochim. Cosmochim. Acta 228, 157–189. https://doi.org/10.1016/j.gca.2018.02.034

Albut, G., Kamber, B.S., Brüske, A., Beukes, N.J., Smith, A.J.B., Schoenberg, R., 2019. Modern weathering in outcrop samples versus ancient paleoredox information in drill core samples from a Mesoarchaean marine oxygen oasis in Pongola Supergroup, South Africa. Geochim. Cosmochim. Acta 265, 330–353. https://doi.org/10.1016/j.gca.2019.09.001

Alexander, B.W., Bau, M., Andersson, P., Dulski, P., 2008. Continentally-derived solutes in shallow Archean seawater: Rare earth element and Nd isotope evidence in iron formation from the 2.9Ga Pongola Supergroup, South Africa. Geochim. Cosmochim. Acta 72, 378–394. https://doi.org/10.1016/j.gca.2007.10.028

Alló, W., 2004. Authigenic Ti-Bearing Crystals in a Precambrian Clay from Buenos Aires Province, Argentina. Clays Clay Miner. 52, 304–310. https://doi.org/10.1346/CCMN.2004.0520305

Anbar, A.D., Duan, Y., Lyons, T.W., Arnold, G.L., Kendall, B., Creaser, R.A., Kaufman, A.J., Gordon, G.W., Scott, C., Garvin, J., Buick, R., 2007. A Whiff of Oxygen Before the Great Oxidation Event? Science 317, 1903–1906. https://doi.org/10.1126/science.1140325

Babechuk, M.G., Kleinhanns, I.C., Schoenberg, R., 2017. Chromium geochemistry of the ca. 1.85 Ga Flin Flon paleosol. Geobiology 15, 30–50. https://doi.org/10.1111/gbi.12203

Beard, B.L., Johnson, C.M., Damm, K.L.V., Poulson, R.L., 2003. Iron isotope constraints on Fe cycling and mass balance in oxygenated Earth oceans. Geology 31, 629–632. https://doi.org/10.1130/0091-7613(2003)031<0629:IICOFC>2.0.CO;2

Beaty, B.J., Planavsky, N.J., 2020. A 3 b.y. record of a biotic influence on terrestrial weathering. Geology. https://doi.org/10.1130/G47986.1

Bekker, A., Holland, H.D., Wang, P.-L., Rumble Iii, D., Stein, H.J., Hannah, J.L., Coetzee, L.L., Beukes, N.J., 2004. Dating the rise of atmospheric oxygen. Nature 427, 117–120. https://doi.org/10.1038/nature02260

Beukes, N.J., Cairncross, B., 1991. A lithostratigraphic-sedimentological reference profile for the Late Archaean Mozaan Group, Pongola Sequence: Application to sequence stratigraphy and correlation with the Witwatersrand Supergroup. South Afr. J. Geol. 94, 44–69.

Bindeman, I.N., Zakharov, D.O., Palandri, J., Greber, N.D., Dauphas, N., Retallack, G.J., Hofmann, A., Lackey, J.S., Bekker, A., 2018. Rapid emergence of subaerial landmasses and onset of a modern hydrologic cycle 2.5 billion years ago. Nature 557, 545. https://doi.org/10.1038/s41586-018-0131-1

Brantley, S.L., Liermann, L., Bullen, T.D., 2001. Fractionation of Fe isotopes by soil microbes and organic acids. Geology 29, 535–538. https://doi.org/10.1130/0091-7613(2001)029<0535:FOFIBS>2.0.CO;2

Brantley, S.L., Liermann, L.J., Guynn, R.L., Anbar, A., Icopini, G.A., Barling, J., 2004. Fe isotopic fractionation during mineral dissolution with and without bacteria1 1Associate editor: J. B. Fein. Geochim. Cosmochim. Acta, A Special Issue on Microbial Geochemistry 68, 3189–3204. https://doi.org/10.1016/j.gca.2004.01.023

Brimhall, G.H., Dietrich, W.E., 1987. Constitutive mass balance relations between chemical composition, volume, density, porosity, and strain in metasomatic hydrochemical systems: Results

on weathering and pedogenesis. Geochim. Cosmochim. Acta 51, 567–587. https://doi.org/10.1016/0016-7037(87)90070-6

Chen, K., Rudnick, R.L., Wang, Z., Tang, M., Gaschnig, R.M., Zou, Z., He, T., Hu, Z., Liu, Y., 2020. How mafic was the Archean upper continental crust? Insights from Cu and Ag in ancient glacial diamictites. Geochim. Cosmochim. Acta, The continents: Origin, evolution and interactions with other reservoirs 278, 16–29. https://doi.org/10.1016/j.gca.2019.08.002

Colman, S.M., 1982. Chemical weathering of basalts and andesites; evidence from weathering rinds (Geological Survey Professional Paper No. 1246), Professional Paper. U.S. G.P.O.,. https://doi.org/10.3133/pp1246

Colwyn, D.A., Sheldon, N.D., Maynard, J.B., Gaines, R., Hofmann, A., Wang, X., Gueguen, B., Asael, D., Reinhard, C.T., Planavsky, N.J., 2019. A paleosol record of the evolution of Cr redox cycling and evidence for an increase in atmospheric oxygen during the Neoproterozoic. Geobiology 17, 579–593. https://doi.org/10.1111/gbi.12360

Craddock, P.R., Dauphas, N., 2011. Iron Isotopic Compositions of Geological Reference Materials and Chondrites. Geostand. Geoanalytical Res. 35, 101–123. https://doi.org/10.1111/j.1751-908X.2010.00085.x

Crosby, Roden Eric E., Johnson Clark M., Beard Brian L., 2007. The mechanisms of iron isotope fractionation produced during dissimilatory Fe(III) reduction by Shewanella putrefaciens and Geobacter sulfurreducens. Geobiology 5, 169–189. https://doi.org/10.1111/j.1472-4669.2007.00103.x

Crow, C., Condie, K.C., Hunter, D.R., Wilson, A.H., 1989. Geochemistry of volcanic rocks from the Nsuze Group, South Africa: arc-like volcanics in a 3.0 Ga-old intracratonic rift. J. Afr. Earth Sci. Middle East 9, 589–597. https://doi.org/10.1016/0899-5362(89)90043-2

Crowe, S.A., Døssing, L.N., Beukes, N.J., Bau, M., Kruger, S.J., Frei, R., Canfield, D.E., 2013. Atmospheric oxygenation three billion years ago. Nature 501, 535. https://doi.org/10.1038/nature12426

Dauphas, N., Janney, P.E., Mendybaev, R.A., Wadhwa, M., Richter, F.M., Davis, A.M., van Zuilen, M., Hines, R., Foley, C.N., 2004. Chromatographic Separation and Multicollection-ICPMS Analysis of Iron. Investigating Mass-Dependent and -Independent Isotope Effects. Anal. Chem. 76, 5855–5863. https://doi.org/10.1021/ac0497095

Dauphas, N., John, S.G., Rouxel, O., 2017. Iron Isotope Systematics. Rev. Mineral. Geochem. 82, 415–510. https://doi.org/10.1515/9783110545630-012

Dauphas, N., Pourmand, A., Teng, F.-Z., 2009. Routine isotopic analysis of iron by HR-MC-ICPMS: How precise and how accurate? Chem. Geol., Advances in experimental and theoretical isotope geochemistry 267, 175–184. https://doi.org/10.1016/j.chemgeo.2008.12.011

De Kock, M.O., Monareng, B.F., Blignaut, L., Smith, A.J.B., Beukes, N.J., 2019. Geochemistry of Paleoproterozoic saprolite developed in diabase intruding the Hotazel Formation in the Avontuur deposit of the Kalahari Manganese Field, South Africa. South Afr. J. Geol. https://doi.org/10.25131/sajg.123.0001

Delvigne, C., Opfergelt, S., Cardinal, D., Hofmann, A., André, L., 2016. Desilication in Archean weathering processes traced by silicon isotopes and Ge/Si ratios. Chem. Geol. 420, 139–147. https://doi.org/10.1016/j.chemgeo.2015.11.007

Deng, Z., Chaussidon, M., Savage, P., Robert, F., Pik, R., Moynier, F., 2019. Titanium isotopes as a tracer for the plume or island arc affinity of felsic rocks. Proc. Natl. Acad. Sci. 116, 1132–1135. https://doi.org/10.1073/pnas.1809164116

Eickmann, B., Hofmann, A., Wille, M., Bui, T.H., Wing, B.A., Schoenberg, R., 2018. Isotopic evidence for oxygenated Mesoarchaean shallow oceans. Nat. Geosci. 11, 133. https://doi.org/10.1038/s41561-017-0036-x

Ellis, A.S., Johnson, T.M., Bullen, T.D., 2002. Chromium Isotopes and the Fate of Hexavalent Chromium in the Environment. Science 295, 2060–2062. https://doi.org/10.1126/science.1068368

Elwood Madden, M.E., Webb, N.D.S., Demirel-Floyd, C., Baker, C.G., Joo, Y.J., 2020. Interpreting CIA values on mars: examining the effects of proximal transport mechanisms on chemical index of alteration values observed in fluvial sediments. LPSC LI 1276.

Farquhar, J., Bao, H., Thiemens, M., 2000. Atmospheric Influence of Earth's Earliest Sulfur Cycle. Science 289, 756–758. https://doi.org/10.1126/science.289.5480.756

Farquhar, J., Peters, M., Johnston, D.T., Strauss, H., Masterson, A., Wiechert, U., Kaufman, A.J., 2007. Isotopic evidence for Mesoarchaean anoxia and changing atmospheric sulphur chemistry. Nature 449, 706–709. https://doi.org/10.1038/nature06202

Greaney, A.T., Rudnick, R.L., Romaniello, S.J., Johnson, A.C., Gaschnig, R.M., Anbar, A.D., 2020. Molybdenum isotope fractionation in glacial diamictites tracks the onset of oxidative weathering of the continental crust. Earth Planet. Sci. Lett. 534, 116083. https://doi.org/10.1016/j.epsl.2020.116083

Greber, N.D., Dauphas, N., 2019. The chemistry of fine-grained terrigenous sediments reveals a chemically evolved Paleoarchean emerged crust. Geochim. Cosmochim. Acta 255, 247–264. https://doi.org/10.1016/j.gca.2019.04.012

Greber, N.D., Dauphas, N., Bekker, A., Ptáček, M.P., Bindeman, I.N., Hofmann, A., 2017. Titanium isotopic evidence for felsic crust and plate tectonics 3.5 billion years ago. Science 357, 1271–1274. https://doi.org/10.1126/science.aan8086

Grey, I.E., Reid, A.F., 1975. The structure of pseudorutile and its role in the natural alteration of ilmenite. Am. Mineral. 60, 898–906.

Gumsley, A.P., Chamberlain, K.R., Bleeker, W., Söderlund, U., Kock, M.O. de, Larsson, E.R., Bekker, A., 2017. Timing and tempo of the Great Oxidation Event. Proc. Natl. Acad. Sci. 114, 1811–1816. https://doi.org/10.1073/pnas.1608824114

Halevy, I., Johnston, D.T., Schrag, D.P., 2010. Explaining the Structure of the Archean Mass-Independent Sulfur Isotope Record. Science 329, 204–207. https://doi.org/10.1126/science.1190298

Hegner, E., Kröner, A., Hunt, P., 1994. A precise U-Pb zircon age for the Archaean Pongola Supergroup volcanics in Swaziland. J. Afr. Earth Sci. 18, 339–341. https://doi.org/10.1016/0899-5362(94)90072-8

Hicks, N., Hofmann, A., 2012. Stratigraphy And Provenance Of The Auriferous-Uraniferous, Fluvial To Shallow-Marine Sinqeni Formation, Mozaan Group, Northern Kwazulu-Natal, South Africa. South Afr. J. Geol. 115, 327–344. https://doi.org/10.2113/gssajg.115.3.327

Hoare, L., Klaver, M., Saji, N.S., Gillies, J., Parkinson, I.J., Lissenberg, C.J., Millet, M.-A., 2020. Melt chemistry and redox conditions control titanium isotope fractionation during magmatic differentiation. Geochim. Cosmochim. Acta 282, 38–54. https://doi.org/10.1016/j.gca.2020.05.015

Holland, H.D., 1984. The Chemical Evolution of the Atmosphere and Oceans. Princeton University Press.

Johnson, A.C., Aarons, S.M., Dauphas, N., Nie, N.X., Zeng, H., Helz, R.T., Romaniello, S.J., Anbar, A.D., 2019. Titanium isotopic fractionation in Kilauea Iki lava lake driven by oxide crystallization. Geochim. Cosmochim. Acta 264, 180–190. https://doi.org/10.1016/j.gca.2019.08.022

Johnson, C.M., Skulan, J.L., Beard, B.L., Sun, H., Nealson, K.H., Braterman, P.S., 2002. Isotopic fractionation between Fe(III) and Fe(II) in aqueous solutions. Earth Planet. Sci. Lett. 195, 141–153. https://doi.org/10.1016/S0012-821X(01)00581-7

Johnson, J.E., Webb, S.M., Thomas, K., Ono, S., Kirschvink, J.L., Fischer, W.W., 2013. Manganese-oxidizing photosynthesis before the rise of cyanobacteria. Proc. Natl. Acad. Sci. 110, 11238–11243. https://doi.org/10.1073/pnas.1305530110

Kurzweil, F., Wille, M., Gantert, N., Beukes, N.J., Schoenberg, R., 2016. Manganese oxide shuttling in pre-GOE oceans – evidence from molybdenum and iron isotopes. Earth Planet. Sci. Lett. 452, 69–78. https://doi.org/10.1016/j.epsl.2016.07.013

Lalonde, S.V., Konhauser, K.O., 2015. Benthic perspective on Earth's oldest evidence for oxygenic photosynthesis. Proc. Natl. Acad. Sci. 112, 995–1000. https://doi.org/10.1073/pnas.1415718112

Li, W., Beard, B.L., Johnson, C.M., 2015. Biologically recycled continental iron is a major component in banded iron formations. Proc. Natl. Acad. Sci. U. S. A. 112, 8193–8198. https://doi.org/10.1073/pnas.1505515112

Little, S.H., Munson, S., Prytulak, J., Coles, B.J., Hammond, S.J., Widdowson, M., 2019. Cu and Zn isotope fractionation during extreme chemical weathering. Geochim. Cosmochim. Acta 263, 85–107. https://doi.org/10.1016/j.gca.2019.07.057

Liu, X.-M., Kah, L.C., Knoll, A.H., Cui, H., Kaufman, A.J., Shahar, A., Hazen, R.M., 2016. Tracing Earth's O2 evolution using Zn/Fe ratios in marine carbonates. Geochem. Perspect. Lett. 2, 24–34. https://doi.org/10.7185/geochemlet.1603

Luo, G., Ono, S., Beukes, N.J., Wang, D.T., Xie, S., Summons, R.E., 2016. Rapid oxygenation of Earth's atmosphere 2.33 billion years ago. Sci. Adv. 2, e1600134. https://doi.org/10.1126/sciadv.1600134

Macfarlane, A.W., Danielson, A., Holland, H.D., 1994. Geology and major and trace element chemistry of late Archean weathering profiles in the Fortescue Group, Western Australia: implications for atmospheric PO2. Precambrian Res. 65, 297–317. https://doi.org/10.1016/0301-9268(94)90110-4

McLennan, S.M., 2001. Relationships between the trace element composition of sedimentary rocks and upper continental crust. Geochem. Geophys. Geosystems 2. https://doi.org/10.1029/2000GC000109

Millet, M.-A., Dauphas, N., 2014. Ultra-precise titanium stable isotope measurements by double-spike high resolution MC-ICP-MS. J. Anal. At. Spectrom. 29, 1444–1458. https://doi.org/10.1039/C4JA00096J

Millet, M.-A., Dauphas, N., Greber, N.D., Burton, K.W., Dale, C.W., Debret, B., Macpherson, C.G., Nowell, G.M., Williams, H.M., 2016. Titanium stable isotope investigation of magmatic processes on the Earth and Moon. Earth Planet. Sci. Lett. 449, 197–205. https://doi.org/10.1016/j.epsl.2016.05.039

Morad, S., Aldahan, A.A., 1982. Authigenesis of titanium minerals in two Proterozoic sedimentary rocks from southern and central Sweden. J. Sediment. Res. 52, 1295–1305. https://doi.org/10.1306/212F8120-2B24-11D7-8648000102C1865D

Mukasa, S.B., Wilson, A.H., Young, K.R., 2013. Geochronological constraints on the magmatic and tectonic development of the Pongola Supergroup (Central Region), South Africa. Precambrian Res. 224, 268–286. https://doi.org/10.1016/j.precamres.2012.09.015

Nhleko, N., 2003. The Pongola Supergroup in Swaziland. University of Johannesburg, Johannesburg.

Nie, N.X., Dauphas, N., Villalon, K.L., Liu, N., Heard, A.W., Morris, R.V., Mertzman, S.A., 2020. Iron isotopic and chemical tracing of basalt alteration and hematite spherule formation in Hawaii:

A prospective study for Mars. Earth Planet. Sci. Lett. 544, 116385. https://doi.org/10.1016/j.epsl.2020.116385

Ohmoto, H., 1996. Evidence in pre–2.2 Ga paleosols for the early evolution of atmospheric oxygen and terrestrial biota. Geology 24, 1135–1138. https://doi.org/10.1130/0091-7613(1996)024<1135:EIPGPF>2.3.CO;2

Ohmoto, H., Watanabe, Y., Ikemi, H., Poulson, S.R., Taylor, B.E., 2006. Sulphur isotope evidence for an oxic Archaean atmosphere. Nature 442, 908–911. https://doi.org/10.1038/nature05044

Ono, S., Beukes, N.J., Rumble, D., Fogel, M.L., 2006. Early evolution of atmospheric oxygen from multiple-sulfur and carbon isotope records of the 2.9 Ga Mozaan Group of the Pongola Supergroup, Southern Africa. South Afr. J. Geol. 109, 97–108. https://doi.org/10.2113/gssajg.109.1-2.97

Ossa Ossa, F., Hofmann, A., Wille, M., Spangenberg, J.E., Bekker, A., Poulton, S.W., Eickmann, B., Schoenberg, R., 2018. Aerobic iron and manganese cycling in a redox-stratified Mesoarchean epicontinental sea. Earth Planet. Sci. Lett. 500, 28–40. https://doi.org/10.1016/j.epsl.2018.07.044

Ostrander, C.M., Nielsen, S.G., Owens, J.D., Kendall, B., Gordon, G.W., Romaniello, S.J., Anbar, A.D., 2019. Fully oxygenated water columns over continental shelves before the Great Oxidation Event. Nat. Geosci. 12, 186–191. https://doi.org/10.1038/s41561-019-0309-7

Pavlov, A. a., Kasting, J. f., 2002. Mass-Independent Fractionation of Sulfur Isotopes in Archean Sediments: Strong Evidence for an Anoxic Archean Atmosphere. Astrobiology 2, 27–41. https://doi.org/10.1089/153110702753621321

Planavsky, N.J., Asael, D., Hofmann, A., Reinhard, C.T., Lalonde, S.V., Knudsen, A., Wang, X., Ossa Ossa, F., Pecoits, E., Smith, A.J.B., Beukes, N.J., Bekker, A., Johnson, T.M., Konhauser, K.O., Lyons, T.W., Rouxel, O.J., 2014a. Evidence for oxygenic photosynthesis half a billion years before the Great Oxidation Event. Nat. Geosci. 7, 283–286. https://doi.org/10.1038/ngeo2122

Planavsky, N.J., Reinhard, C.T., Wang, X., Thomson, D., McGoldrick, P., Rainbird, R.H., Johnson, T., Fischer, W.W., Lyons, T.W., 2014b. Low Mid-Proterozoic atmospheric oxygen levels and the delayed rise of animals. Science 346, 635–638. https://doi.org/10.1126/science.1258410

Price, R.C., Gray, C.M., Wilson, R.E., Frey, F.A., Taylor, S.R., 1991. The effects of weathering on rare-earth element, Y and Ba abundances in Tertiary basalts from southeastern Australia. Chem. Geol. 93, 245–265. https://doi.org/10.1016/0009-2541(91)90117-A

Ptáček, M.P., Dauphas, N., Greber, N.D., 2020. Chemical evolution of the continental crust from a data-driven inversion of terrigenous sediment compositions. Earth Planet. Sci. Lett. 539, 116090. https://doi.org/10.1016/j.epsl.2020.116090

Rasmussen, B., Buick, R., 1999. Redox state of the Archean atmosphere: Evidence from detrital heavy minerals in ca. 3250–2750 Ma sandstones from the Pilbara Craton, Australia. Geology 27, 115–118. https://doi.org/10.1130/0091-7613(1999)027<0115:RSOTAA>2.3.CO;2

Rouxel, O.J., Bekker, A., Edwards, K.J., 2005. Iron Isotope Constraints on the Archean and Paleoproterozoic Ocean Redox State. Science 307, 1088–1091. https://doi.org/10.1126/science.1105692

Rye, R., Holland, H.D., 2000. Geology and geochemistry of Paleosols developed on the Hekpoort Basalt, Pretoria Group, South Africa. Am. J. Sci. 300, 85–141. https://doi.org/10.2475/ajs.300.2.85

Rye, R., Holland, H.D., 1998. Paleosols and the evolution of atmospheric oxygen; a critical review. Am. J. Sci. 298, 621–672. https://doi.org/10.2475/ajs.298.8.621

Rye, R., Kuo, P.H., Holland, H.D., 1995. Atmospheric carbon dioxide concentrations before 2.2 billion years ago. Nature 378, 603–605. https://doi.org/10.1038/378603a0

Schoenberg, R., Zink, S., Staubwasser, M., von Blanckenburg, F., 2008. The stable Cr isotope inventory of solid Earth reservoirs determined by double spike MC-ICP-MS. Chem. Geol. 249, 294–306. https://doi.org/10.1016/j.chemgeo.2008.01.009

Schroeder, P.A., Shiflet, J., 2000. Ti-Bearing Phases In The Huber Formation, An East Georgia Kaolin Deposit. Clays Clay Miner. 48, 151–158.

Singer, P.C., Stumm, W., 1970. Acidic Mine Drainage: The Rate-Determining Step. Science 167, 1121–1123. https://doi.org/10.1126/science.167.3921.1121

Skulan, J.L., Beard, B.L., Johnson, C.M., 2002. Kinetic and equilibrium Fe isotope fractionation between aqueous Fe(III) and hematite. Geochim. Cosmochim. Acta 66, 2995–3015. https://doi.org/10.1016/S0016-7037(02)00902-X

Smit, M.A., Mezger, K., 2017. Earth's early O_2 cycle suppressed by primitive continents. Nat. Geosci. 10, 788–792. https://doi.org/10.1038/ngeo3030

Smith, A.J.B., Beukes, N.J., Gutzmer, J., Czaja, A.D., Johnson, C.M., Nhleko, N., 2017. Oncoidal granular iron formation in the Mesoarchaean Pongola Supergroup, southern Africa: Textural and geochemical evidence for biological activity during iron deposition. Geobiology 15, 731–749. https://doi.org/10.1111/gbi.12248

Stüeken, E.E., Catling, D.C., Buick, R., 2012. Contributions to late Archaean sulphur cycling by life on land. Nat. Geosci. 5, 722–725. https://doi.org/10.1038/ngeo1585

Su, N., Yang, S., Guo, Y., Yue, W., Wang, X., Yin, P., Huang, X., 2017. Revisit of rare earth element fractionation during chemical weathering and river sediment transport. Geochem. Geophys. Geosystems 18, 935–955. https://doi.org/10.1002/2016GC006659

Tang, M., Chen, K., Rudnick, R.L., 2016. Archean upper crust transition from mafic to felsic marks the onset of plate tectonics. Science 351, 372–375. https://doi.org/10.1126/science.aad5513

Taylor, S.R., McLennan, S.M., 1985. The continental crust: Its composition and evolution.

Teng, F.-Z., Dauphas, N., Watkins, J.M., 2017. Non-Traditional Stable Isotopes: Retrospective and Prospective. Rev. Mineral. Geochem. 82, 1–26. https://doi.org/10.2138/rmg.2017.82.1

West, A.J., Galy, A., Bickle, M., 2005. Tectonic and climatic controls on silicate weathering. Earth Planet. Sci. Lett. 235, 211–228. https://doi.org/10.1016/j.epsl.2005.03.020

Yamaguchi, K.E., Johnson, C.M., Beard, B.L., Beukes, N.J., Gutzmer, J., Ohmoto, H., 2007. Isotopic evidence for iron mobilization during Paleoproterozoic lateritization of the Hekpoort paleosol profile from Gaborone, Botswana. Earth Planet. Sci. Lett. 256, 577–587. https://doi.org/10.1016/j.epsl.2007.02.010

Yang, W., Holland, H.D., 2003. The Hekpoort paleosol profile in Strata 1 at Gaborone, Botswana: Soil formation during the Great Oxidation Event. Am. J. Sci. 303, 187–220. https://doi.org/10.2475/ajs.303.3.187

Zhang, J., Dauphas, N., Davis, A.M., Pourmand, A., 2011. A new method for MC-ICPMS measurement of titanium isotopic composition: Identification of correlated isotope anomalies in meteorites. J. Anal. At. Spectrom. 26, 2197–2205. https://doi.org/10.1039/C1JA10181A

Zhang, Q., Liu, J., Zhang, Y., Yu, H., Qin, L., Shen, J., 2019. Factors affecting chromium isotope measurements using the double-spike method. Rapid Commun. Mass Spectrom. 33, 1390–1400. https://doi.org/10.1002/rcm.8483

Zink, S., Schoenberg, R., Staubwasser, M., 2010. Isotopic fractionation and reaction kinetics between Cr(III) and Cr(VI) in aqueous media. Geochim. Cosmochim. Acta 74, 5729–5745. https://doi.org/10.1016/j.gca.2010.07.015

Chapter 2 – Long Term Evolution of the Marine Sedimentary Iron Isotope Record

Foreword

For most of Earth history preceding the Great Oxidation Event (GOE), the oceans appear to have been dominantly ferruginous (anoxic and Fe^{2+}-rich), rather than euxinic (anoxic and H_2S-rich) (Poulton and Canfield, 2011). The most obvious and spectacular evidence for the ferruginous nature of the oceans prior to the GOE comes from the widespread deposition of iron formations (IFs), in the period between 3.8-2.4 Ga, essentially the entire pre-GOE history of the Earth for which we have a sedimentary record (Bekker et al., 2010; Konhauser et al., 2017). Iron formations are Fe and Si-rich chemical sedimentary rocks thought to have formed through the precipitation of Fe minerals and amorphous silica in the open oceans. The basic requirement for widespread chemical precipitation of these elements is that large mobile pools of these elements were available, which necessitates ferruginous ocean redox conditions, and high dissolved silica levels thought to reflect the stabilization of concentrations at amorphous silica saturation prior to the evolution of siliceous biomineralization.

High Fe^{2+} concentrations have two main proposed sources: continental runoff from anoxic weathering (Holland, 1984), a process we investigated in Chapter 1; and submarine hydrothermal vents, which are sites on the seafloor where seawater that has become hot and metal-rich through interaction with the young underlying oceanic crust emerges into the ocean, exporting Fe and other metals great distances into the open oceans (Derry and Jacobsen, 1990; Isley, 1995; Jacobsen and Pimentel-Klose, 1988; Kump and Seyfried, 2005). The hydrothermal flux of Fe^{2+} to the oceans was likely particularly strong prior to the GOE because the early crust was hotter than it is today (Isley, 1995), and because lower marine sulfate conditions would have limited the local removal of Fe in ‘black smoker’ sulfide chimneys (Kump and Seyfried, 2005).

The IFs formed prior to the GOE are mostly banded iron formations (BIFs), named for their compositional banding at a range of scales, all the way down to sub-millimeter alternations of silica and hematite/magnetite that might reveal annual depositional cycles (Bekker et al., 2010; Garrels, 1987; Konhauser et al., 2017; Trendall, 1973). The finely laminated nature of BIFs suggests they formed by the slow settling of chemical precipitates in deep ocean basins. Granular iron formations (GIFs), composed of granules formed accumulations of chemical precipitates rolling around in energetic, shallow waters, also exist in the geologic record but only become globally widespread only after the GOE, from around 1.88 Ga onwards (Bekker et al., 2010; Konhauser et al., 2017; Rasmussen et al., 2012).

Regardless of their sedimentary texture, the common requirements of all IFs are ferruginous ocean conditions, and a precipitation mechanism. Precipitating Fe^{2+} it either requires supersaturation with respect to Fe^{2+} minerals, or oxidation to Fe^{3+}, which is highly insoluble and rapidly precipitates as Fe^{3+} oxyhydroxides like ferrihydrite. Iron formations are classified into oxide-, carbonate-, and silicate-facies, where the dominant mineralogies are magnetite and hematite, Fe-rich carbonates, and the silicates greenalite ($(Fe^{2+},Fe^{3+})_{2-3}Si_2O_5(OH)_4$) and stilpnomelane ($K(Fe^{2+},Mg,Fe^{3+})_8(Si,Al)_{12}(O,OH)_{27}\cdot n(H_2O)$), respectively. These facies provide some clues as to the variety of precipitation mechanisms for Fe in the pre-GOE oceans, but IFs today are almost entirely composed of low-grade metamorphic mineral assemblages, and primary mineralogies may have been extensively altered by early diagenesis even prior to thermal processes (Bekker et al., 2010; Klein, 2005; Konhauser et al., 2017).

Sequence stratigraphic work from major pre-GOE IF-depositing basins indicates that deep-water IF deposition gave way to shallow water deposition of Fe-poor carbonate platforms (Eroglu et al., 2018; Klein and Beukes, 1989; Sumner, 1997), which suggests that the precipitation mechanism

for IFs became effective at removing Fe^{2+} from solution in shallower waters. This assumed spatial dependence of Fe deposition in IFs is consistent with the canonical model for IF deposition – that precipitation was driven by oxidation and precipitation of insoluble Fe^{3+}-oxyhydroxides, by one of several proposed near-surface sources of oxidants (Fig. 2.1.) (Bekker et al., 2010; Trendall and Morris, 2000). The most commonly-cited oxidants are O_2 from early-evolved cyanobacteria (Cloud, 1973), direct microbial oxidation by anoxygenic photoferrotrophs (phytoplankton that fix CO_2 by taking electrons from Fe^{2+}, creating Fe^{3+} as a by-product) (Kappler et al., 2005; Konhauser et al., 2002; Schad et al., 2019), or UV photons (Braterman et al., 1983; Cairns-Smith, 1978; François, 1986; Nie et al., 2017), which would have been abundant at Earth's surface before there was an ozone layer and which can oxidize Fe^{2+} during a fraction of absorption events (a process discussed in detail in the context of Mars in Chapter 7).

The Fe^{2+} oxidation model for IFs neatly explains why, and where, insoluble precipitates would form in largely reducing early oceans, and the bulk geochemistry of IFs lends support to it. The Fe in IFs has an average redox state of 2.4 (Klein, 2005), so almost half of the Fe current residing in IFs is oxidized. Given the huge quantities of Fe contained within regionally extensive IFs, it has been shown that post-depositional oxidation of a purely Fe^{2+} original IF is not mechanically feasible (Robbins et al., 2019). However, assuming a Fe^{3+}-dominated primary mineralogy for IFs (although co-precipitation of primary ferrous or mixed valence phases is also plausible; *e.g.* Johnson et al., 2018; Rasmussen et al., 2015; Tosca et al., 2016), much of the Fe^{2+} in IFs is explainable through diagenetic (Konhauser et al., 2005) or metasomatic (Köhler et al., 2013) reaction of ferric iron with organic carbon, which is now absent in IFs but may have lent isotopically light C to the carbonate phase in IFs (Craddock and Dauphas, 2011; Heimann et al., 2010).

Some of the most robust evidence for an oxidative mechanism for IF deposition comes from Fe isotopes (Dauphas et al., 2017; Johnson et al., 2020, 2008). Pre-GOE IFs were observed early on to feature large variation in $\delta^{56}Fe$ (the per mil deviation of the $^{56}Fe/^{54}Fe$ ratio relative to that in the standard material IRMM-014), and the presence of highly positive $\delta^{56}Fe$ values in even the oldest IFs on Earth, from Isua, Greenland (Dauphas et al., 2004), and Nuvvuagittuq, Canada (Dauphas et al., 2007a, 2007b), were taken as strong evidence for the existence of Fe^{2+}-oxidizing mechanisms in the oceans since the sedimentary record began. The reasoning for this interpretation is that Fe isotope ratios are generally fractionated most strongly by processes involving a change in the redox state of Fe (Dauphas et al., 2017). There is a large equilibrium isotope fractionation effect between Fe^{2+} and Fe^{3+} that enriches the ferric phase the heavier Fe isotopes. During the net reaction of aqueous Fe^{2+} oxidation and Fe^{3+} precipitation into a ferric oxyhydroxide phase that is exported to sediments, all of the proposed oxidation pathways for IFs have been shown experimentally to impart a $\geq$ 1‰ increase in $\delta^{56}Fe$ to the precipitate, relative to the instantaneous composition of the Fe^{2+} solution from which it is being precipitated (Balci et al., 2006; Bullen et al., 2001; Croal et al., 2004; Nie et al., 2017; Swanner et al., 2017). As long as oxidation does not go to completion and the bulk isotopic composition of the initial Fe^{2+} is quantitatively transferred to the Fe^{3+} phase, positive $\delta^{56}Fe$ associated with partial oxidation will be recorded in the precipitate phase. Therefore, the presence of $\delta^{56}Fe$ values up to and exceeding +1 ‰ in Pre-GOE IFs is parsimoniously explained if they were formed by the partial oxidation of marine Fe^{2+} with a $\delta^{56}Fe$ close to 0 ‰. In Chapter 1 we showed that this assumption of a near-zero value for initial marine $\delta^{56}Fe$ holds up fairly well in the case of continental Fe^{2+} sources. Observations of hydrothermal vent fluids near the modern seafloor indicate that if anything, the Fe^{2+} added to the oceans is isotopically light relative to the bulk earth values of ~ 0 ‰ (Beard et al., 2003; Rouxel et al., 2008, 2004; Severmann

et al., 2004), which only supports the need for a large positive fractionation to explain the highly positive values in many Pre-GOE IFs.

The range of $\delta^{56}Fe$ in IFs is huge, extending to > +2 ‰, some of the heaviest values observed in terrestrial geochemistry, to < -2.5 %, some of the most negative values (Fig. 2.2.) (Czaja et al., 2018; Dauphas et al., 2017; Konhauser et al., 2017). In the context of partial oxidation that could have produced isotopically heavy early IF precipitates, these negative values are also explainable in a straightforward manner, as reflecting the progressive evolution of the Fe^{2+} pool in a given parcel of water (be that an upwelling system, a depositional basin, or even the global oceans) (Planavsky et al., 2012; Rouxel et al., 2005; Tsikos et al., 2010). As partial oxidation consistently fractionates precipitates to heavy values relative to dissolved Fe^{2+}, irreversible removal of the ferric precipitates from this system should drive the Fe^{2+} to increasingly negative $\delta^{56}Fe$ values in order to maintain overall isotopic mass balance. Subsequent Fe^{3+} precipitates will continue to form isotopically heavy relative to the instantaneous Fe^{2+} pool but will track the evolution of this pool to lighter values while maintaining this offset. This type of isotopic evolution is referred to as Rayleigh distillation. Evolution of the Fe^{2+} $\delta^{56}Fe$ pool by Rayleigh distillation has been proposed as an explanation for strongly negative $\delta^{56}Fe$ values in IFs suggested to have formed in atypically oxygenated shallow marine conditions, both at 2.95 Ga in the Pongola Supergroup (Ossa Ossa et al., 2018; Planavsky et al., 2014), and most strikingly at 2.43 Ga in the Hotazel Formation of South Africa (Thibon et al., 2019; Tsikos et al., 2010), right at the onset of the canonical GOE. Both of these low $\delta^{56}Fe$ IFs have atypically high Mn/Fe contents, thought to reflect the combination of two processes; extensive depletion of Fe^{2+} relative to Mn^{2+} in the oceans due to high degrees of partial Fe^{2+} oxidation; and the incorporation of some Mn^{4+}, which also forms insoluble oxyhydroxide precipitates but strictly requires O_2 as the oxidant and so will remain reduced for far longer in

many environments where Fe can precipitate. Thus, the occurrence of the lowest $\delta^{56}Fe$ values in IFs from these types of environments makes sense in the context of the partial oxidation model. The relationship between the extent of Fe^{2+} oxidation and the $\delta^{56}Fe$ of IFs provides a powerful, if somewhat qualitative, proxy for the redox state of the pre-GOE oceans and the relative size of the oxidized sink for marine Fe through time (Czaja et al., 2018), and this relationship forms one half of the story told in Chapter 2 below.

Iron formations are the archetypal example of chemical sedimentation in ancient ferruginous oceans. In the same way, the hallmark of chemical sedimentation in sulfidic or euxinic environments is pyrite (FeS_2), which is typically found in its greatest abundance in black shales; fine-grained, organic-rich clastic sediments formed by slow accumulation in deep waters. At a global scale, ferrous iron, and not sulfide, dominated the pre-GOE oceans (Poulton and Canfield, 2011). This is because marine sedimentary sulfide is predominantly sourced from microbial sulfate reduction (MSR), which couples organic carbon and sulfate as a form of respiration when more energetically appetizing oxidants like O_2, nitrate, Mn^{4+}, and Fe^{3+} are unavailable, and the early marine sulfate pool appears to have been too small to allow abundant MSR and accumulation of sulfide (Canfield, 2004; Crowe et al., 2014; Farquhar et al., 2013; Fike et al., 2015; Johnston, 2011). A major reason for the reduced size of the early sulfate pool is that the primary source of sulfate to the oceans today is oxidative weathering of magmatic sulfide minerals on the continents. With no oxidative weathering under a low-O_2 atmosphere, exemplified by the abundance of detrital pyrite in the Archean geologic record (Rasmussen and Buick, 1999), the only source of sulfur to the oceans was slow outgassing of volcanic SO_2 and H_2S that passed through an exotic atmospheric photochemical cycle and entered the oceans carrying a S-MIF signature (Farquhar et al., 2000). Due to the globally sulfide-limited nature of the pre-GOE oceans and the ready

availability of Fe^{2+}, only highly organically productive sections of the continental margin where sulfide could be produced saw significant localized accumulation of pyrite in black shales (Kendall et al., 2010; Olson et al., 2019; Reinhard et al., 2009; Scott et al., 2011). These shales, with notable examples in the Archean being the 2.65 Ga Jeerinah Formation and the 2.53 Ga Mt McRae Shale, both found in Australia but with stratigraphic equivalents in South Africa, are characterized as 'euxinic', using an Fe-speciation redox proxy calibrated to modern environments (Raiswell et al., 2018); because their reactive Fe pool is dominated by pyrite. Accumulation of sufficient sulfide to pyritize all reactive Fe in a sediment is very achievable in modern high-productivity areas because the modern marine sulfate concentration (28 mM) is so high. However, in the high Fe^{2+}, low-sulfate pre-GOE oceans, Fe-S interactions likely looked quite different.

The potential for highly unusual Fe-S cycling in the pre-GOE oceans gained evidence from Fe isotope systematics when Rouxel et al. (2005) reported the first major $\delta^{56}Fe$ record for pyrites through Earth history, and showed that pyrites formed prior to the GOE carried the most negative bulk $\delta^{56}Fe$ values of any terrestrial materials known at the time, and to our knowledge, even to date, with $\delta^{56}Fe$ values as low as -3.5 ‰ in the Jeerinah (Australia) and time equivalent Lokommona (South Africa) formations (Fig. 2.2.). At the time these pyrite data were reported, little was known about the Fe isotopic systematics of pyrite formation, and the interpretation of these pyrite $\delta^{56}Fe$ values was that the pyrites had formed from an extremely isotopically depleted Fe^{2+} pool that had experienced up to 90 % removal of isotopically heavy Fe^{3+}-oxyhydroxide precipitates (Planavsky et al., 2012; Rouxel et al., 2005). This interpretative framework essentially required that pyrite-forming environments prior the GOE lay shoreward of IF depositional systems, and they sourced their iron from non-steady state upwellings of Fe^{2+} rich waters that passed through environments of major oxyhydroxide precipitation prior to reaching organically-

productive, sulfide-forming environments (Fig. 2.1.) (Bekker et al., 2010). This model made sense from a sequence stratigraphic framework, because Neoarchean sulfidic black shales are found shoreward relative to IFs. However, this model alone cannot satisfactorily explain how the negative $\delta^{56}Fe$ signatures of pyrites became less extreme in the runup to the GOE, when the extent of Fe^{2+} oxidation and removal to IFs was increasing (Czaja et al., 2018), or why these signals disappear entirely after the GOE.

An alternative explanation for the highly negative $\delta^{56}Fe$ in pre-GOE pyrites that also relates to redox cycling of Fe was the proposal that the Fe^{2+} source for these pyrites was generated by dissimilatory Fe^{3+} reduction (DIR), the process by which Fe^{3+} is used as an oxidant for organic matter during microbial respiration. Partial DIR produces initially isotopically light Fe^{2+} because of the equilibrium fractionation between Fe^{2+} and Fe^{3+} (Beard et al., 1999; Crosby et al., 2007) and it was suggested that either basin-scale shuttling of partial DIR products from Fe^{3+}-depositing settings to sulfidic settings (Severmann et al., 2008), or similar processes happening at a smaller scale in porewaters within the sediment column (Archer and Vance, 2006), could have produced the negative $\delta^{56}Fe$ seen in pre-GOE pyrites. The two major drawbacks of this model are that (1) it can only produce small amounts of isotopically light Fe^{2+}, because as DIR goes to completion, the Fe^{2+} pool will take on the isotopic composition of the initial Fe^{3+}, and (2) there is no obvious reason for partial DIR to have been uniquely prevalent in prior to the GOE in such as way as to reproduce the pyrite $\delta^{56}Fe$ record (Rouxel et al., 2006).

Fully understanding the pyrite $\delta^{56}Fe$ record requires understanding the pyrite-forming process itself and is now clear that pyrite precipitation both in the laboratory, and in nature, is associated with its own strong Fe isotopic effects (Guilbaud et al., 2011; Rolison et al., 2018). From an isotopic equilibrium perspective, FeS_2 is a strange mineral because despite containing Fe in the

reduced Fe^{2+} redox state, it is associated with an large positive isotopic fractionation, due to the fact that Fe has a small coordination number and forms very strong bonds in the pyrite structure (Polyakov et al., 2007). However, in geochemically relevant scenarios, pyrite formation results in a large negative isotopic fraction of at least -2.2 ‰ for $\delta^{56}Fe$ (Guilbaud et al., 2011; Rolison et al., 2018), because the kinetic isotope effect associated with the rapid growth of pyrite once nucleation dominates over any equilibrium effect, and kinetic isotope effects always enrich products in lighter isotopes (in this case ^{54}Fe). In the inverse case to partial Fe oxidation, partial pyrite formation with respect to the Fe^{2+} pool should produce the isotopically lightest pyrites, as and pyritization becomes quantitative the $\delta^{56}Fe$ of pyrite will evolve towards the initial value, or even become positive, depending on if close system evolution or Rayleigh distillation is taking place (Mansor and Fantle, 2019; Rolison et al., 2018). The progression of this isotopic evolution comes down to the relative availabilities of Fe^{2+} and sulfide, and thus, we might expect pyritization in the low sulfate, ferruginous pre-GOE oceans to have favored the preservation of large negative fractionations associated with partial pyritization of the Fe^{2+} pool. Therefore, understanding the evolution of pyrite $\delta^{56}Fe$ prior to the GOE requires a full accounting of the effects of both marine Fe^{2+} oxidation, and the availability of sulfide where the pyrite eventually formed.

Chapter 2, below, is the first of two chapters in this thesis that seeks to better constrain the evolution through time of the oxic and sulfidic pools Fe in the ferruginous pre-GOE ocean, and their impacts on global Fe isotope records, particularly that of pyrite. One way to tackle this problem, and the approach taken in this chapter, is compare how independent proxies for marine Fe oxidation, the size of the marine sulfur pool, correlate with changes in the Fe isotope record of pyrite. As discussed above, the $\delta^{56}Fe$ record of IFs is intimately tied to Fe^{2+} oxidation processes, regardless of the mechanism(s) for Fe^{2+} oxidation that dominated at any time in the Archean and

early Paleoproterozoic Eons. We also employ the mass dependent sulfur isotope ($\delta^{34}S$) record, as an independent proxy for marine sulfur availability through these time periods (Canfield, 2004; Fike et al., 2015). $\delta^{34}S$ systematics are dominated by the fractionations associated with microbial sulfate reduction (MSR), because sulfur-reducing bacteria qualitatively show greater preference for reducing the light isotopes of sulfur when there is more sulfate available for them to reduce. The observations made below in Chapter 2 produce testable hypotheses for the size of sedimentary Fe sinks through pre-GOE time, and we pick up these hypotheses again in Chapter 3.

The content of this chapter is the accepted article for the publication:

Andy W. Heard, Nicolas Dauphas, "Constraints on the coevolution of oxic and sulfidic ocean iron sinks from Archean–Paleoproterozoic iron isotope records", Geology, 2020, 48 (4), Pages 358–362, https://doi.org/10.1130/G46951.1

Use of the accepted article falls within fair use as defined by The Geological Society of America Publications.

This chapter is associated with a supplementary data file "Chapter 2 Supplementary Data File – Compiled Fe and S Isotope Records". These data files are also published in the EarthChem library. URL: https://doi.org/10.1594/IEDA/111446

Constraints on the coevolution of oxic and sulfidic ocean iron sinks from Archean-Paleoproterozoic iron isotope records

Abstract

The drivers of Fe isotope variations of Archean-Paleoproterozoic pyrite have been debated since discovery of $\delta^{56}Fe$ values (‰ shifts in $^{56}Fe/^{54}Fe$ ratios vs. IRMM-014) as low as -3.5‰ in pyrites predating the Great Oxygenation Event (GOE). These values were taken as evidence that extensive removal of high $\delta^{56}Fe$ Fe^{3+} oxides during partial oxidation of upwelled Fe^{2+}-rich waters occurred in the early oceans. However, low pyrite $\delta^{56}Fe$ can also reflect kinetic isotopic shifts during pyrite formation. Compiled $\delta^{56}Fe$ records of oxic (iron formation; IF) and sulfidic (pyrite) sinks of Fe negatively covary before the GOE, contrary to expectations that Fe^{2+} oxidation would drive the $\delta^{56}Fe$ values of these sinks on parallel trends as oxidation progressed. Positive covariation of pyrite $\delta^{56}Fe$ with the dispersion of sedimentary sulfide $\delta^{34}S$ fractionations through time suggests that S availability during pyritization at least partially drove trends in negative $\delta^{56}Fe$ fractionations before the GOE. The $\delta^{56}Fe$ records of pyrite and IF suggest that oxic and sulfidic Fe sinks grew in concert before and during the GOE.

Introduction

Iron from hydrothermal and continental sources was the dominant ocean redox element before the GOE at ~2330 Ma (Holland, 1984; Luo et al., 2016). Major pre-GOE oxic Fe sinks are chemical sediments like IF (Konhauser et al., 2017) that formed through Fe^{2+} oxidation by O_2, UV photons, or photoferrotrophy (Fig. 2.1) (Braterman et al., 1983; Cloud, 1973; Kappler et al., 2005). The main long-term Fe sulfide sink is pyrite (FeS_2), which forms in environments where H_2S is present; often due to microbial SO_4^{2-} reduction (MSR) (Fig. 2.1). Before the GOE, the Fe sulfide sink may have been limited, as [SO_4^{2-}] was presumably <1 % of modern levels (Crowe et al., 2014; Habicht et al., 2002); but elemental or organic S sources may have been important at this time (Fakhraee and Katsev, 2019; Farquhar et al., 2013).

Iron isotopic systematics of IF (Fig. 2.2a) and pyrite (Fig. 2.2b) have been used to explain changes in Fe cycling across the GOE (Dauphas et al., 2016; Rouxel et al., 2005). A schematic of relevant processes is shown in Figure 2.1. Pre-GOE pyrite has highly variable $\delta^{56}Fe$ values as low as ~-3.5‰, while post-GOE pyrites have less variable $\delta^{56}Fe$ (Rouxel et al., 2005); Fig. 2.2b). One interpretation is that pre-GOE pyrites record oceanic Fe^{2+} that saw progressive removal of high $\delta^{56}Fe$ Fe^{3+} oxides during partial oxidation of upwelled water masses, leaving behind low-$\delta^{56}Fe$ dissolved Fe^{2+} (Fig. 2.1; Rouxel et al., 2005). Rouxel et al. (2005) interpreted the disappearance of low-$\delta^{56}Fe$ pyrite after the GOE to reflect a shift to an ocean redox state that did not allow this oxidative distillation. It was also suggested that microbial dissimilatory Fe^{3+} reduction (DIR), which releases low-$\delta^{56}Fe$ Fe^{2+} during partial dissolution of Fe^{3+} oxides, supplied low-$\delta^{56}Fe$ Fe^{2+} to pyrites via a benthic Fe^{2+} shuttle (Fig. 2.1: Severmann et al., 2008). Kinetic isotope effects (KIE) during pyrite precipitation (from FeS_{aq}) also enrich pyrite in light Fe isotopes (Guilbaud et al., 2011), contrary to equilibrium expectations (Polyakov et al., 2007), so pyrite may also record

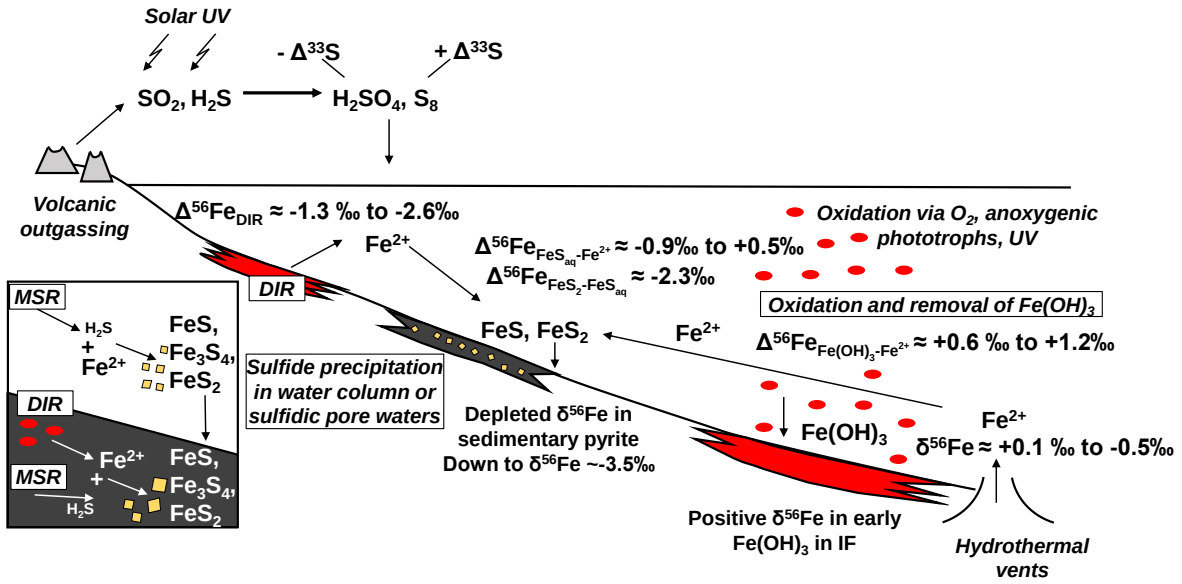

Figure 2.1. Schematic of proposed Archean-Paleoproterozoic Fe cycling and associated isotopic effects. Fe^{2+} is supplied via hydrothermal vent fluids with $\delta^{56}Fe \approx$ -0.5 to +0.1‰ (Beard et al., 2003; Rouxel et al., 2005). Upwelled Fe^{2+} undergoes partial oxidation and removal of high-$\delta^{56}Fe$ ($\Delta^{56}Fe \approx$ +0.6 to 1.2‰; Balci et al., 2006; Nie et al., 2017; Welch et al., 2003) Fe^{3+} oxyhydroxides ($Fe(OH)_3$), driving Fe^{2+} sources for pyrite and $Fe(OH)_3$ to lower $\delta^{56}Fe$ (Planavsky et al., 2012; Rouxel et al., 2005). Microbial DIR releases low-$\delta^{56}Fe$ ($\Delta^{56}Fe \approx$ -1.3 to -2.6‰) Fe^{2+} to solution, and could provide low $\delta^{56}Fe$ Fe^{2+} to pyrite via a benthic Fe shuttle (Severmann et al., 2008). Pyrite precipitates via FeS or greigite (Fe_3S_4) precursors forming from Fe^{2+} (Rickard and Luther, 2007), in the water column or in porewaters, depending on where Fe^{2+} (the ocean reservoir or DIR in sediments) and H_2S (MSR in the water column or porewaters) sources are localized (inset). Maximum net fractionation during pyrite precipitation from Fe^{2+} via FeS_{aq} is ~-3.1‰ in $\delta^{56}Fe$ (Guilbaud et al., 2011).

isotopic fractionation during S- limited pyritization before the GOE (Rolison et al., 2018). Interpretations of the pre-GOE pyrite $\delta^{56}Fe$ record and their implications for the Fe cycle have thus become the subject of much debate.

The modern interpretation of the GOE is as a protracted transition, not a sudden event at ~2330 Ma (Lyons et al., 2014). Examining the structure through time of published $\delta^{56}Fe$ values of pyrite and oxic sediments leading to the GOE could help with interpretations. The two endmember hypotheses for $\delta^{56}Fe$ in pre-GOE pyrites (they are time capsules for ocean Fe redox evolution; Rouxel et al., 2005; they preserve KIE associated with S-limited pyrite formation; Guilbaud et al., 2011; Rolison et al., 2018) make predictions for how trends in the pyrite $\delta^{56}Fe$ record would covary

with records of oxic Fe sinks, or the S cycle, respectively. In this study we assess the covariations of two sedimentary $\delta^{56}Fe$ records ($\delta^{56}Fe_{py}$, $\delta^{56}Fe_{IF}$) with each other and with $\delta^{34}S$ records, to test these hypotheses. We show that reevaluating published data helps constrain how the sedimentary Fe sinks may have evolved across the GOE.

Data Compilations

We compiled published $\delta^{56}Fe$ data for Archean and Paleoproterozoic bulk sedimentary pyrites and IF to understand their variations with time (Fig. 2.2a, b; Appendix). We use sedimentary sulfide $\delta^{34}S$ records to assess whether changes in $\delta^{56}Fe_{py}$ covary with changes in the S cycle through time. We compiled published sedimentary sulfide $\delta^{34}S$ data using earlier compilations (Johnston, 2011; Stüeken et al., 2012), and recent publications (Fig. 2.2c; SI). The dispersion of $\delta^{34}S$ fractionations expressed in sedimentary sulfides (here defined $\Sigma\delta^{34}S$) has been used as a proxy for marine [SO_4^{2-}] over time. The rationale is that the S isotopic fractionation associated with MSR is influenced by [SO_4^{2-}], such that an ocean more replete with [SO_4^{2-}] can express larger variations in $\delta^{34}S$ (Crowe et al., 2014; Habicht et al., 2002).

Results

$\delta^{56}Fe_{IF}$, $\delta^{56}Fe_{py}$, and $\delta^{34}S$ data are shown in Figure 2.2. We consider trends in average values for $\delta^{56}Fe_{IF}$, $\delta^{56}Fe_{py}$, $\Sigma\delta^{34}S$ values within 100 Ma time bins.

$\delta^{56}Fe_{IF}$ has high positive values through the Eoarchean and Paleoarchean, takes negative values in the Mesoarchean, and returns to the high positive values in the early Neoarchean. After this, $\delta^{56}Fe_{IF}$ decreases to very negative values by the GOE. After a long gap in the geological record, IFs return with positive $\delta^{56}Fe_{IF}$ values in the late Paleoproterozoic. Late Paleoarchean $\delta^{56}Fe_{py}$ values are

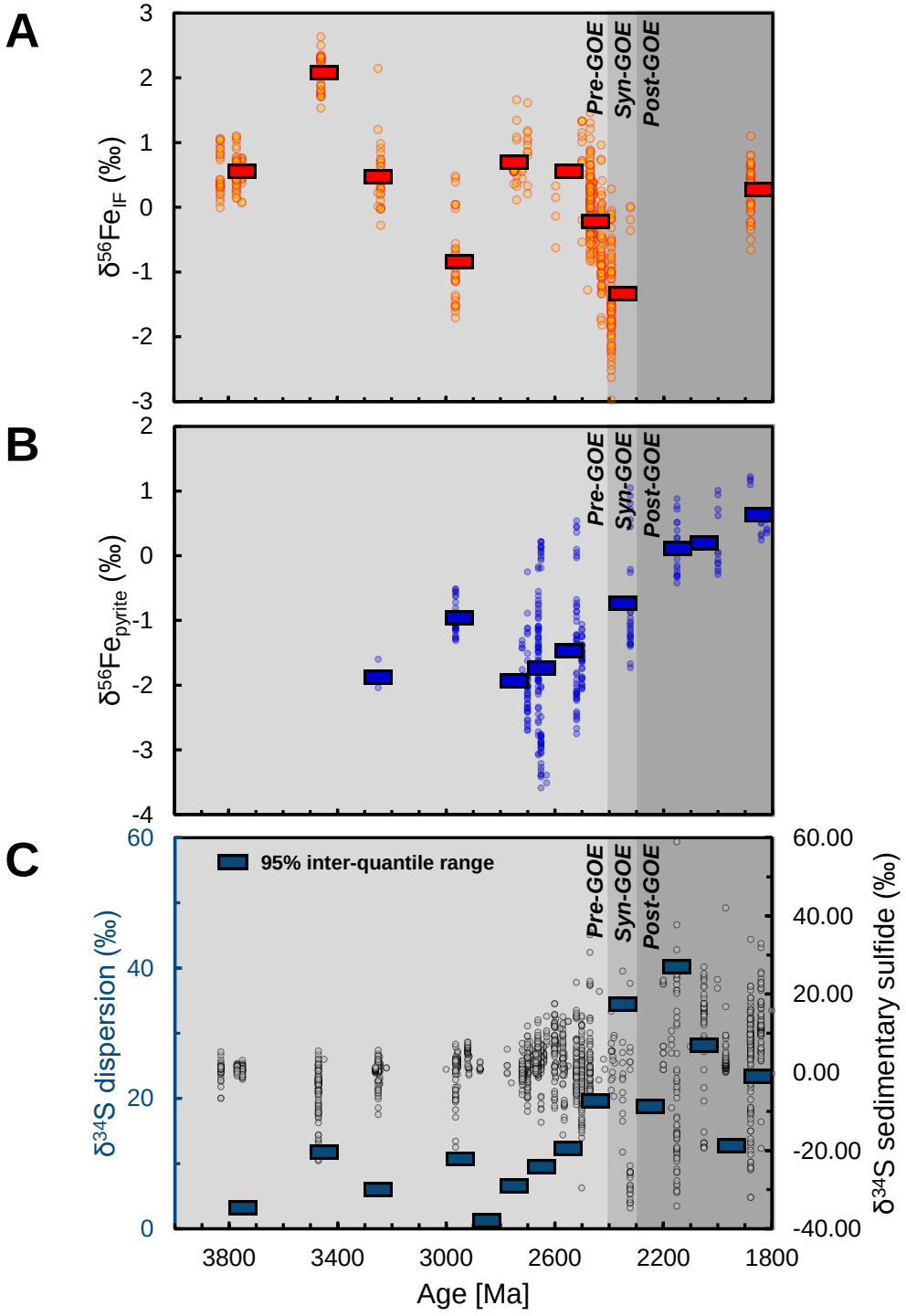

Figure 2.2. Archean-Paleoproterozoic sedimentary $\delta^{56}Fe$ and $\delta^{34}S$ records. We define Pre-GOE, Syn-GOE, and Post-GOE timeframes as >2.4 Ga, 2.4-2.3 Ga, and <2.3 Ga, respectively (Gumsley et al., 2017; Luo et al., 2016). a) $\delta^{56}Fe_{IF}$, and b) $\delta^{56}Fe_{py}$: Individual datapoints as small circles; and time bin averages as boxes. c) Sedimentary sulfide $\delta^{34}S$: Individual datapoints as open circles, values on right-hand (black) axis; dispersion of $\delta^{34}S$ fractionations ($\Sigma\delta^{34}S$, 95% inter-quantile range) as boxes, values on left-hand (dark blue) axis.

strongly negative, become less negative in the Mesoarchean, and return to strongly negative values in the early Neoarchean. From the Neoarchean through the GOE and the late Paleoproterozoic, $\delta^{56}Fe_{py}$ values increase, becoming positive by the late Paleoproterozoic. $\Sigma\delta^{34}S$ is low through the Eoarchean to Mesoarchean, but there are positive excursions around 3450 Ma and 2950 Ma due to strongly fractionated sulfides in the Dresser Formation and Mozaan Group respectively. The Dresser excursion is discussed by Johnston (2011) as potentially recording an important microbial ecosystem, and both the Dresser and Mozaan excursions may be local signals (SI). From the early Neoarchean through the GOE, $\Sigma\delta^{34}S$ increases, after which $\Sigma\delta^{34}S$ remains high relative to early Archean levels but fluctuates between the highest values in the record and values similar to the latest Archean.

For time binned data, we see a negative correlation pre- and syn-GOE, for $\delta^{56}Fe_{py}$ *vs.* $\delta^{56}Fe_{IF}$ (Fig. 2.3a), and a positive correlation for $\delta^{56}Fe_{py}$ *vs.* $\Sigma\delta^{34}S$ (Fig. 2.3b) through the full $\delta^{56}Fe_{py}$ record.

Discussion

With compiled databases spanning ~2000 Ma of Earth history, we consider whether sample bias could drive trends seen in $\delta^{56}Fe$ records. We cannot definitively rule out such biases, but we argue in the Appendix that the required biases are unlikely and do not disqualify interpretations of these $\delta^{56}Fe$ records as primary signatures, as has been done in previous studies. We assume that $\delta^{56}Fe$ records were not obliterated by metamorphism or hydrothermal circulations (SI).

How $\delta^{56}Fe_{py}$ covaries with other data can be compared to expectations of different hypotheses for the $\delta^{56}Fe$ record. First, we develop expectations for the trends through time for endmember hypotheses. Hypothesis (h_1) is the model of Rouxel et al. (2005); where progressive removal of high $\delta^{56}Fe$ Fe^{3+} oxides left low-$\delta^{56}Fe$ ocean Fe^{2+}, recorded in $\delta^{56}Fe_{py}$. Because IF and pyrite both

precipitated from water masses impacted by Fe^{3+} removal; the prediction for (*h1*) is that $\delta^{56}Fe_{py}$ and $\delta^{56}Fe_{IF}$ should evolve along parallel trends through time, offset by the fractionation between Fe^{3+} oxides and dissolved Fe^{2+} . To get the lowest $\delta^{56}Fe_{py}$ purely via high-$\delta^{56}Fe$ oxide removal, ~90 % of Fe^{2+} must be oxidized (Rouxel et al., 2005), at which point the bulk Fe^{3+} reservoir would be close to input values. Therefore, $\delta^{56}Fe$ of pyrite and IF should both be near their lowest values at the same time, at the greatest extent of Fe oxidation. We do not observe a positive correlation between $\delta^{56}Fe_{py}$ and $\delta^{56}Fe_{IF}$ before the GOE (Figs 2.2, 2.3a), and in fact any correlation we see is negative, which disagrees with (*h1*). Hence, we argue that pre-GOE $\delta^{56}Fe_{py}$ evolution cannot be attributed entirely to partial Fe^{2+} oxidation. Such processes may still drive much of the variability in $\delta^{56}Fe_{py}$ (Figs 2.2, 2.4), and the lowest $\delta^{56}Fe_{py}$ values likely require isotopically light Fe^{2+} sources (Rouxel et al., 2005).

The role of DIR in driving $\delta^{56}Fe$ through time is not simple, but it can be considered as a sub-scenario for (*h1*) as it involves a balance between high-$\delta^{56}Fe$ Fe^{3+} oxides and low-$\delta^{56}Fe$ Fe^{2+}. A DIR shuttle requires deposition of Fe^{3+} oxides on the continental shelf, and subsequent DIR and transport of Fe^{2+} to sulfidic sediments. Severmann et al. (2008) argue that more Fe^{3+} oxide deposition on shelves would provide more reactants for partial DIR, supporting larger benthic fluxes of low $\delta^{56}Fe$ Fe^{2+}. In that case, more negative $\delta^{56}Fe_{py}$ would correlate with evidence for greater Fe^{2+} oxidation, such as lower $\delta^{56}Fe_{IF}$. This picture is complicated if IF themselves were also supplied with Fe^{2+} by the DIR shuttle (Li et al., 2015). Larger benthic Fe^{2+} flux could also keep Fe/S ratios in sulfidic sediments high to promote KIE during pyritization, driving $\delta^{56}Fe_{py}$ lower still. When Fe^{3+} oxide formation on shelves was lower or DIR was more quantitative, the flux of Fe^{2+} would decrease in magnitude or take on $\delta^{56}Fe$ values closer to the initial Fe^{3+}, supporting higher $\delta^{56}Fe_{py}$. Increased organic C deposition on shelves could be one factor driving

more quantitative DIR, but it is unclear whether this, or increased Fe^{3+} oxide deposition, would be the dominant effect on $\delta^{56}Fe$ in benthic shuttle Fe^{2+}. We consider it more likely that a DIR shuttle would drive a positive correlation of $\delta^{56}Fe_{py}$ *vs.* $\delta^{56}Fe_{IF}$, but there are enough complications that we cannot rule out DIR entirely along with (*h*$_1$).

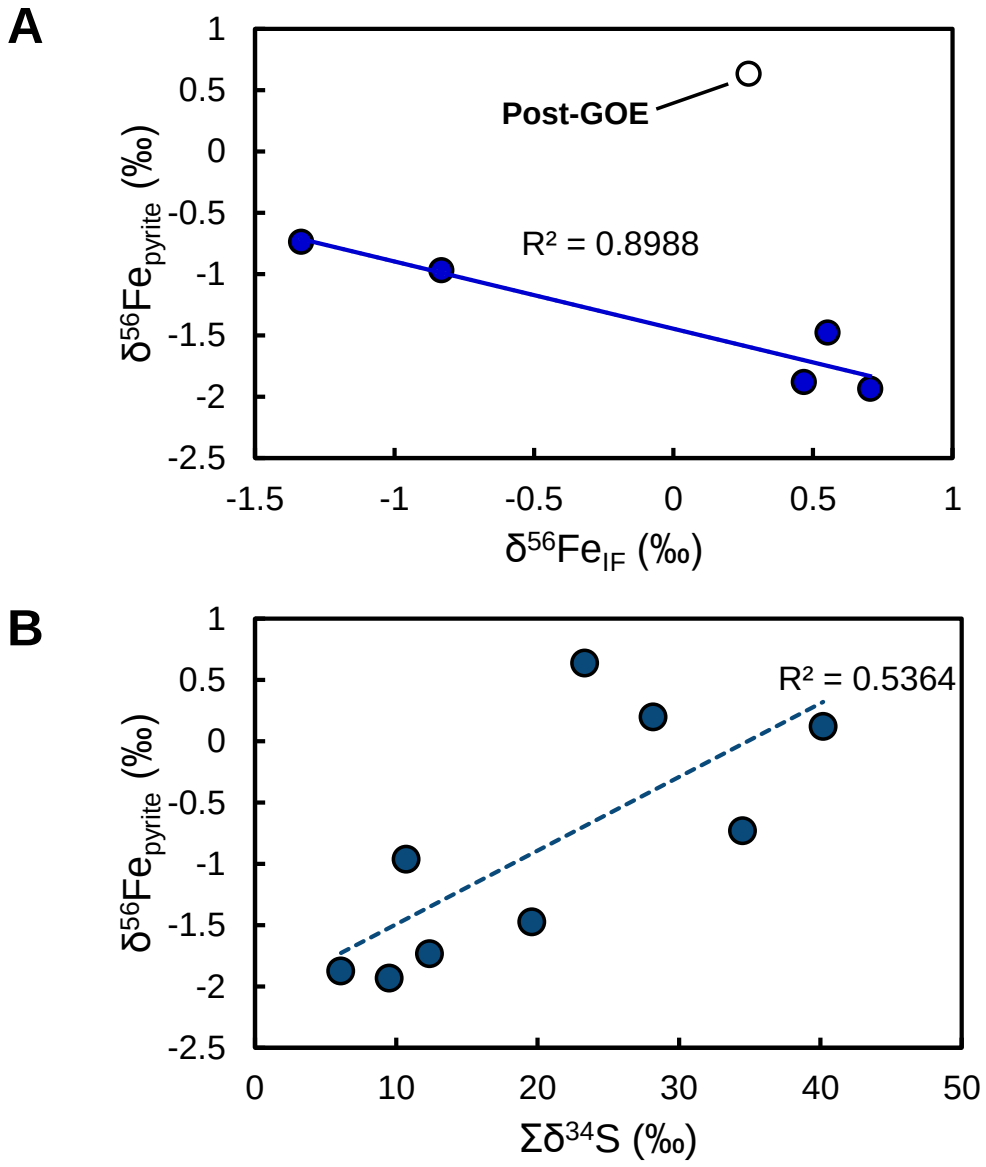

Figure 2.3. Covariation of $\delta^{56}Fe_{py}$ a) *vs.* $\delta^{56}Fe_{IF}$ for pre- and syn-GOE time bins. Negative correlation with p=0.014. Unfilled post-GOE datapoint not included in correlation. b) *vs.* $\Sigma\delta^{34}S$ for all shared time bins. Positive correlation with p=0.025.

In hypothesis (h_2), low pre-GOE $\delta^{56}Fe_{py}$ values are assumed to record partial pyritization with a large KIE (Guilbaud et al., 2011; Rolison et al., 2018). Assuming that pyrite formation in the low SO_4^{2-} pre-GOE oceans was S-limited, we expect a positive correlation of $\delta^{56}Fe_{py}$ *vs.* $\Sigma\delta^{34}S$. When dissolved Fe^{2+} in the oceans, or early diagenetic pore waters in communication with the oceans, dominated over SO_4^{2-} available for reduction to H_2S, the fraction of Fe pyritized would be small and a large KIE would be expressed in $\delta^{56}Fe_{py}$. Estimates for Archean $[Fe^{2+}]$~50-100 µM (Holland, 1984), and $[SO_4^{2-}]$~2.5 µM (Crowe et al. 2014) would indeed result in S-limited pyritization. As $[SO_4^{2-}]$ increased, more Fe in organic-rich environments would go into pyrite, and mass balance requires that $\delta^{56}Fe_{py}$ would take less negative values; while larger fractionations during MSR became possible (Crowe et al., 2014; Habicht et al., 2002). The positive correlation between $\delta^{56}Fe_{py}$ *vs.* $\Sigma\delta^{34}S$ therefore supports (h_2).

In further support of (h_2), several formations have probability distributions of $\delta^{56}Fe_{py}$ that are weighted to negative values with positive tails (Fig. 2.4), consistent with Rayleigh distillation with a negative fractionation factor like the KIE of pyritization. Rayleigh-like $\delta^{56}Fe$ behavior was previously observed *in situ* in the core to rim profile of a 2700 Ma diagenetic pyrite nodule (Marin-Carbonne et al., 2014). Not all pre-GOE formations (Fig. 2.4) have these $\delta^{56}Fe_{py}$ distributions, implying that the extra imprint of redox processes affected the $\delta^{56}Fe$ of the Fe^{2+} pool during their deposition.

We argue that the covariations between trends in Fe and S isotope records allow us to weigh the importance of two endmember hypotheses for the evolution of Fe cycling that were previously made (Rouxel et al., 2005; Guilbaud et al., 2011; Rolison et al., 2018). Declining $\delta^{56}Fe_{IF}$ values suggest increased partial oxidation of Fe^{2+} in the oceans approaching the GOE (Czaja et al., 2018), but this effect is not mirrored in the $\delta^{56}Fe_{py}$ record. This suggests that the transition away from

S-limited conditions in productive, pyrite-forming waters, was the main control on $\delta^{56}Fe_{py}$ in this time period. With increases in [SO_4^{2-}] (reduced to H_2S in organic-rich environments favoring MSR) that accompanied the GOE (Reinhard et al., 2009), KIEs during pyritization were no longer imparted to sedimentary pyrite (Rolison et al. 2018). Even aside from isotopic fractionations during pyritization, expansion of pyrite-forming ocean areas may have captured upwelled Fe^{2+} at greater depths, cutting short partial oxidation and generation of low $\delta^{56}Fe$ Fe^{2+} (Fig. 2.1). Thus, if Fe redox cycling was the sole driver of pre-GOE $\delta^{56}Fe_{py}$, the positive covariation of $\delta^{56}Fe_{py}$ *vs.* $\Sigma\delta^{34}S$ would still suggest sulfidic Fe sinks grew during Earth's oxygenation. In the scenario where KIE during pyritization did occur (supported by Fig. 2.4), a growing spatial extent of sulfidic environments can help explain why we see no signals of increasing oxidation of Fe^{2+} sources to pyrite before the GOE.

We are not the first to argue for increased S availability as the driver of increasing $\delta^{56}Fe_{py}$ across the GOE, but we have built on the work of Rolison et al. (2018) by illustrating this transition with compiled Archean-Paleoproterozoic data, and by testing the viability of this hypothesis against alternative hypotheses. Correlations in trends through time not only identify a link between the S cycle and $\delta^{56}Fe_{py}$, but also provide evidence against Fe redox being the sole driver of $\delta^{56}Fe_{py}$ before the GOE.

The positive $\delta^{56}Fe_{py}$ *vs.* $\Sigma\delta^{34}S$ relationship holds until the ~1900 Ma, when $\Sigma\delta^{34}S$ slightly declines. Positive $\delta^{56}Fe_{py}$ values at this time are perplexing, and may indicate sulfidation of high $\delta^{56}Fe$ oxides, or distillation of Fe^{2+} by extensive partial sulfide removal elsewhere. These alternatives are difficult to assess with the sparse data available. The post-GOE $\delta^{56}Fe_{IF}$ record only features ~1880 Ma granular IF (GIF) from the Animikie basin. Positive $\delta^{56}Fe_{IF}$ values suggest low degrees of partial Fe^{2+} oxidation (Planavsky et al., 2012, 2009). Whether this reflects global redox or a

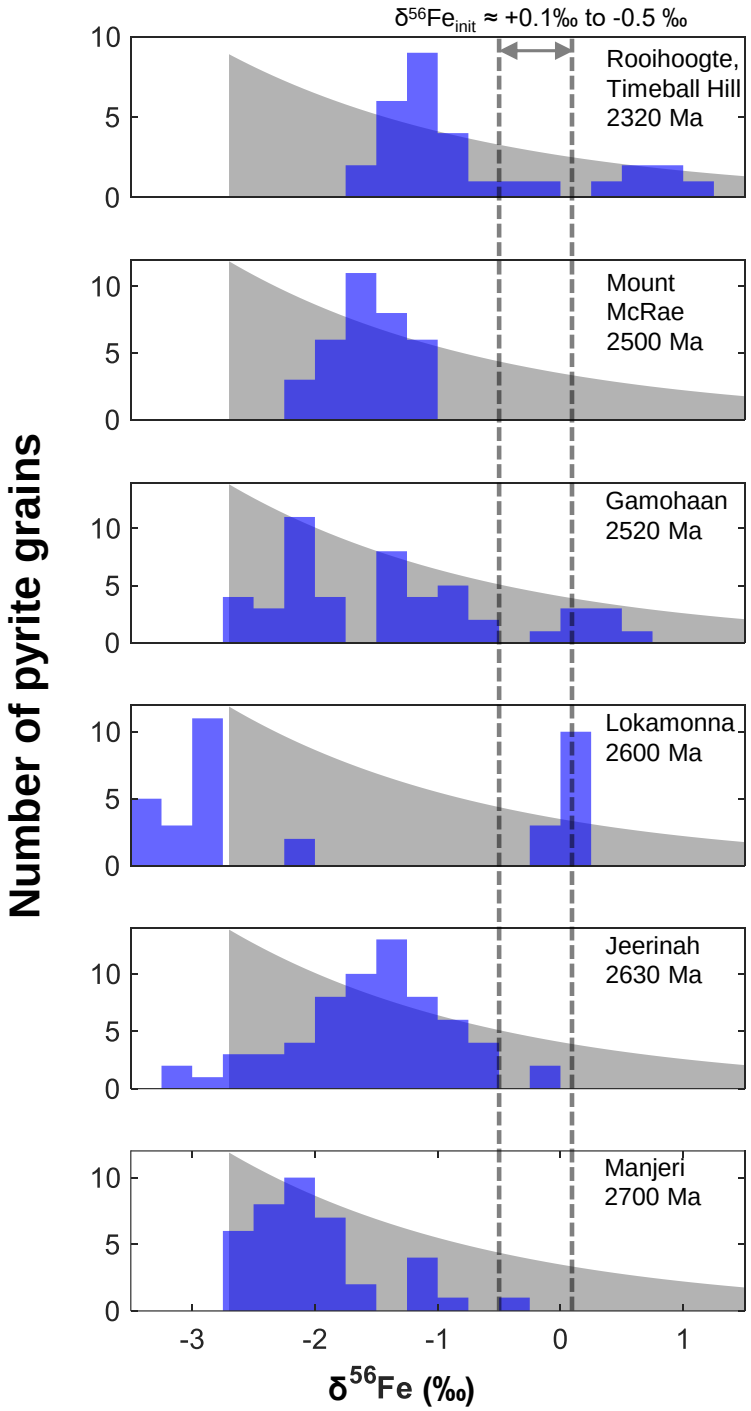

Figure 2.4. Probability distributions of $\delta^{56}Fe_{py}$ of well-sampled pre- or syn-GOE formations (blue), compared to Rayleigh distillation from pyrite precipitation (grey), with initial $\delta^{56}Fe_{init}$=-0.5‰ (Beard et al., 2003) and instantaneous fraction $\Delta^{56}Fe_{FeS2\text{-}FeSaq}$=-2.2‰ for KIE in pyrite precipitation from FeS (Guilbaud et al., 2011). The probability distribution f for the $\delta^{56}Fe$ values of precipitates of a Rayleigh distillation is given by $f(\delta^{56}Fe)=\frac{1}{|\Delta^{56}Fe_{FeS2\text{-}FeSaq}|}\exp\left[\frac{\delta^{56}Fe_{inst}-\delta^{56}Fe_{init}}{\Delta^{56}Fe_{FeS2\text{-}FeSaq}-1}\right]$ where "inst" refers to the instantaneous product.

lithological control in GIF should be the focus of future work. A return to partial Fe^{2+} oxidation $\delta^{56}Fe_{IF}$ signals unaccompanied by a negative shift in $\delta^{56}Fe_{py}$ values supports our argument that irreversible increases in [SO_4^{2-}] across the GOE played an important role in the loss of such negative $\delta^{56}Fe_{py}$ values. However, positive $\delta^{56}Fe_{IF}$ and $\delta^{56}Fe_{py}$ values at this time indicate a mass balance problem that requires a missing low-$\delta^{56}Fe$ reservoir, which suggests new avenues of inquiry for future $\delta^{56}Fe$ studies.

Conclusions

Trends in $\delta^{56}Fe_{py}$ and $\delta^{56}Fe_{IF}$ (Fig. 2.2a, b) values over the Archean-Paleoproterozoic suggest that the oxic and sulfidic ocean sinks for Fe grew in concert before the GOE. Positive correlation of $\delta^{56}Fe_{py}$ *vs.* $\Sigma\delta^{34}S$ suggests that there was a significant increase in drawdown of Fe to sulfide sinks before and during the GOE. While many complexities remain in the ancient Fe isotope record, our use of multiple geochemical datasets has allowed us to weigh the significance of different hypotheses for $\delta^{56}Fe_{py}$, helping to explain how Fe sinks may have evolved during the GOE.

Acknowledgements

We thank Sarah Aarons, Sam Holo, Andrey Bekker, Olivier Rouxel, Romain Guilbaud, and Ian Butler for discussions. We appreciated constructive reviews from Johanna Marin Carbonne, Chadlin Ostrander, and an anonymous reviewer. This work was funded by NASA Habitable Worlds Grant 80NSSC17K0744 to N. Dauphas and A. W. Heard.

Data Availability

The compiled datasets used in this study are published in the EarthChem library. URL: https://doi.org/10.1594/IEDA/111446

Appendix

This supplementary text provides:

i.) Additional discussion of the question of sample bias in $\delta^{56}Fe$ records.

ii.) Lists of references used in compiling $\delta^{56}Fe$ and $\delta^{34}S$ records for the Archean-Paleoproterozoic.

The compiled datasets used in this study are published in the EarthChem library. URL: https://doi.org/10.1594/IEDA/111446

Fidelity of the Ancient Fe Isotope Record

The Archean-Paleoproterozoic $\delta^{56}Fe$ record is notably sparse when compared to traditional stable isotope proxies, including the $\delta^{34}S$ data we have compiled. However, interpretations of the $\delta^{56}Fe$ record have in the past extrapolated the findings of relatively localized sampling in time and space, in order to develop models with broad implications for the marine Fe cycle and its relevance to the evolution of Earth surface redox conditions (*e.g.* Rouxel et al., 2005; Planavsky et al., 2012; Rolison et al., 2018; Czaja et al., 2018). Such interpretations all require that the existing $\delta^{56}Fe$ records of IF and pyrite provide a representative sampling of these sediment types. In our study, sample bias concerns are arguably greater because of how they might would affect subtler trends in the $\delta^{56}Fe$ record. Therefore, we identify three main ways in which sample bias could affect our interpretations of $\delta^{56}Fe$ records, and suggest mitigating factors in each case.

Heterogeneous sampling in time and space

The first type of sampling bias we consider is that of inhomogeneous sampling of the IF and pyrite $\delta^{56}Fe$ records in time and space. The patchy nature of both records, often with long gaps containing little to no data throughout the 2000 Ma time span we consider, makes it clear that rocks of all ages have not been sampled equally. This is unavoidable because rocks of Archean age are preserved on few cratons, and in the case of IFs, because their geological occurrence is thought to be sporadic and linked to periods of high hydrothermal Fe^{2+} supply driven by the occurrence of oceanic large igneous provinces (Bekker et al., 2010; Isley and Abbott, 1999; Konhauser et al., 2017). Care must be taken not to over-extrapolate interpretations to include spans of Earth history where no data is available. In order to address this possible bias, we choose not to interpolate $\delta^{56}Fe$ records across unsampled time periods, and base our interpretations of possible covariations between $\delta^{56}Fe_{py}$, $\delta^{56}Fe_{IF}$ and sulfur records by binning by age and only comparing time bins which contain data. In addition to time binning, we note that that $\delta^{56}Fe$ data for both IF and pyrites of a given age, in addition to more extensively sample S records, often include samples from the same sedimentary basins or successions. In particular, late Neoarchean and early Paleoproterozoic sedimentary records are very well sampled in the West Australian Hamersley and South African Transvaal Supergroups. This is where $\delta^{56}Fe$ records are the most complete, and therefore we are confident that the compilations we present capture the time period around the GOE as it affected marine Fe cycling in these locations. Whilst the possibility exists that the Hamersley and Transvaal sub-basins are not representative of late Neoarchean to early Paleoprotoerozic geochemistry, such a concern is equally applicable to the numerous interpretations of global biogeochemical change that have been formulated principally making use of samples from these very well sampled regions.

Similarly, sampling is sparse in the Meso- and Paleo-Archean. $\delta^{56}Fe$ records, where they exist, are available for IF and pyrites from closely associated formations, and therefore the covariations we present may still be descriptive of the shared evolution of Fe, S, and O_2 cycling at these times and locations (Busigny et al., 2017; Eickmann et al., 2018; Ossa Ossa et al., 2018; Planavsky et al., 2014). For example, around 2950 Ma, elevated $\delta^{56}Fe_{py}$, negative $\delta^{56}Fe_{IF}$, and a large range in $\delta^{34}S$ are all consistent with a proposed Mesoarchean environment with increased S availability in addition to multiple lines of evidence for free O_2, including Cr and Mo isotopic data (Crowe et al., 2013; Eickmann et al., 2018; Ossa Ossa et al., 2018; Planavsky et al., 2014). The fact that this record is restricted to the Pongola Supergroup of South Africa means we cannot make broader interpretations about the global ocean redox state or the entirety of the Mesoarchean. However, these highly localized data still provide meaningful information about the interaction of the Pre-GOE Fe, S, and O_2 cycles. We suggest that they can serve as a case study for how $\delta^{56}Fe$ records might be expected to change in the transition from an anoxic, low S environment to one more replete in O_2 and S, as is thought to have occurred on a global scale during the GOE. We cannot rule out that the Pongola Supergroup represents a biased sampling of Mesoarchean global biogeochemistry, capturing a localized environment in which oxidants and sulfur accumulated in quantities well in excess of the global average for the Mesoarchean. This should be testable in the future through extensive geochemical studies of other Mesoarchean sedimentary successions of similar age, including $\delta^{56}Fe$ studies.

Preservation bias in the rock record

The second form of sample bias we consider is whether the types of rocks preserved at Earth's surface may have changed over time, such that trends in $\delta^{56}Fe$ records could reflect changes in

post-depositional alteration of rocks or preferential destruction of certain lithofacies. For example, could the general trend of decreasing $\delta^{56}Fe_{IF}$ from the Eoarchean through to the GOE, noted previously by Czaja et al. (2018), reflect geological processes that led to the preferential loss of low $\delta^{56}Fe$ IF over time, such that only high $\delta^{56}Fe_{IF}$ values are preserved in the earliest portion of the rock record? This question is particularly pertinent for the IF record, because there is an observed change in the dominant style of IF deposited in through the earlier Archean versus the latest Neoarchean and Paleoprotoerozic, with older, more volcanically-influenced and laterally restricted Algoma style IF giving way to basin-scale Superior style IF deposition that occurred on more stable passive continental margins (Bekker et al., 2010; Konhauser et al., 2017). Algoma style IFs typically display positive, and less variable, $\delta^{56}Fe$ values, whereas Superior style IF show more larger ranges of $\delta^{56}Fe$, with negative values being common (Czaja et al., 2018; Dauphas et al., 2017). Gradual removal of ferric oxyhydroxide precipitates with positive $\delta^{56}Fe$ from the ocean is though to leave the residual dissolved Fe^{2+} with complementary negative $\delta^{56}Fe$ values (Planavsky et al., 2012; Rouxel et al., 2005). Therefore, the $\delta^{56}Fe$ range seen in Superior style IF could be explained by their deposition further from hydrothermal Fe sources than Algoma style IF, with the former precipitating from an Fe^{2+} reservoir that had greater opportunity to be depleted by partial oxidation during upwelling.

In light of this distinction in $\delta^{56}Fe$ systematics of different styles of IF, a preservation bias favoring one style of IF over another could theoretically lead to spurious trends in the observed $\delta^{56}Fe_{IF}$ record. The preservation bias required to reproduce our observed $\delta^{56}Fe_{IF}$ record must comprise of two factors: i.) Preferential destruction of younger Algoma style IF with almost entirely positive $\delta^{56}Fe$ in the late Neoarchean to early Paleoproterozoic, and ii.) Preferential destruction of low $\delta^{56}Fe$ Superior style IF in the Eoarchean through to the early Neoarchean. Such a preservation bias would

imply that Superior style IF were deposited throughout the Archean but only preserved later in Earth history. We consider i.) to be plausible, because volcanically associated Algoma style IF were not deposited on stable craton margins and therefore their destruction by tectonic processes would appear to be likely relative to the that of Superior style IF. In addition, early high mantle potential temperatures may have enabled formation of hotter, more buoyant Eoarchean oceanic crust that was not so easily destroyed by subduction, aiding the survival of early Algoma style IF. However, we do not consider it geologically plausible that expansive Superior style IF could have been entirely eradicated from the first 1000 Ma of the geological record, in order to create the dearth of lower-δ^{56}Fe IF seen in the early Archean, because this would require preferential preservation of oceanic crustal material relative to stable passive margin sedimentary sequences, a phenomenon which is not known otherwise in the geological record.

Theoretically, we could contrive various scenarios that explain each trend in the $\delta^{56}Fe_{IF}$ and $\delta^{56}Fe_{py}$ records entirely via preservation biases in an unchanging ocean geochemical regime. However, we would argue that these scenarios generally require non-uniformitarian geological processes. By contrast, we consider the interpretations we can make for δ^{56}Fe records by taking them at face value do not present such internal inconsistencies. Our preferred interpretation of these data can and should be subject to debate and testing by greater sampling of gaps in the geological record. However, we believe that sampling biases are not so severe as to completely disqualify meaningful interpretation of the δ^{56}Fe record as it relates to the interaction of the Fe, S and O_2 cycles.

Hydrothermal or metamorphic overprinting of δ^{56}Fe records

The third way in which sample biases could affect our interpretation of the δ^{56}Fe record is if it were dominated by hydrothermal or metamorphic overprinting as opposed to primary sedimentary

signatures. For the sake of discussion, we consider early diagenetic processes such as microbial dissimilatory Fe^{3+} reduction (DIR) to be 'primary' processes inasmuch as they occur in unconsolidated sedimentary piles still in diffusive exchange with the marine water column, and are biogeochemical rather than metamorphic processes. A forgiving aspect of $\delta^{56}Fe$ systematics is that they are generally resistant to metamorphic overprinting, as Fe is quite immobile during metamorphism (Dauphas et al., 2017). This is epitomized by the preservation of chemical sedimentary $\delta^{56}Fe$ signatures in ~3800 Ma IF from the Isua and Nuvvuagituq supracrustal belts, which have experienced metamorphism up to amphibolite facies (Czaja et al., 2013; Dauphas et al., 2007a, 2007b, 2004). Despite this, $\delta^{56}Fe$ in these rocks clearly distinguishes them from banded gneisses with igneous protoliths. The high Fe contents of IF mean that large quantities of Fe must be lost or gained in order to significantly alter their $\delta^{56}Fe$ values. Metamorphic recrystallization can redistribute Fe isotopes among constituent minerals, but high temperature equilibrium fractionations occurring in these reactions are small relative to the ‰-scale low temperature primary fractionations recorded in the bulk composition of these rocks (Dauphas et al., 2017). In addition, late-altering metamorphic fluids are expected to have formed in equilibrium with a more oxidizing atmosphere than the one under which ancient IF formed, such that metamorphic fluids are unlikely to reduce IF-hosted iron, which would be required for large scale Fe loss from IF because Fe^{3+} is fluid immobile.

Some ancient pyrites may also have been influenced by post-depositional hydrothermal and/or metamorphic processes. At first glance, pyrite has a high Fe content and is highly insoluble, which might suggest that metamorphic alteration to $\delta^{56}Fe_{py}$ is unlikely. However, we do not omit the possibility that pyrite can form as a secondary phase during hydrothermal and metamorphic processes. Textural studies suggests that some pyrites in the well-studied Mt McRae shale were

dissolved and reprecipitated in coarse-grained nodules and laminae, with internally homogenized $\delta^{34}S$ (Kakegawa et al., 1998). Furthermore, O isotope thermometry of pyrite-rimming quartz grains in this formation suggest homogenization at 100-240 °C, which supports a role for hydrothermal alteration in this pyrite reprecipitation (Haruna et al., 2003). However, this dissolution-reprecipitation of pyrite appears to have occurred in a closed system (Kakegawa et al., 1998). In many cases, Archean-Paleoprotoerozic pyrites have internal crystalline structure indicative of secondary grain growth, but the deformation of primary shale laminae around such pyrite grains argue for a primary sedimentary origin and subsequent closed system recrystallization (Rouxel et al., 2005). Again, in such cases a large quantity of new Fe, or significant loss of primary Fe, would be required to significantly overprint primary sedimentary $\delta^{56}Fe_{py}$ signatures. While hydrothermally-influenced dissolution-reprecipitation played an important role in homogenization and textural evolution of these ancient pyrites, it is unlikely to have affected their bulk $\delta^{56}Fe$ composition, particularly given the high temperatures at which these reactions occurred. Crucially, to produce the trends through time seen in $\delta^{56}Fe_{py}$ records, hydrothermal/metamorphic alteration of pyrites would need to be both pervasive, and undergo a systematic change in its effect on $\delta^{56}Fe$ through time. Whilst this is a difficult proposition to entirely rule out, it appeals to non-uniformitarian processes and therefore we consider it unlikely as a driver of global $\delta^{56}Fe$ trends through time. More fundamentally, our data compilation relies on good analytical practice on the part of workers generating geochemical data, both for $\delta^{56}Fe$ and $\delta^{34}S$ records. Such good practice should include screening for hydrothermally or metamorphically altered samples on the basis of mineralogical and trace elemental systematics, as is demonstrated through Mn/Fe systematics by Busigny et al. (2017).

References

Archer, C., Vance, D., 2006. Coupled Fe and S isotope evidence for Archean microbial Fe(III) and sulfate reduction. Geology 34, 153–156. https://doi.org/10.1130/G22067.1

Balci, N., Bullen, T.D., Witte-Lien, K., Shanks, W.C., Motelica, M., Mandernack, K.W., 2006. Iron isotope fractionation during microbially stimulated Fe(II) oxidation and Fe(III) precipitation. Geochim. Cosmochim. Acta 70, 622–639. https://doi.org/10.1016/j.gca.2005.09.025

Beard, B.L., Johnson, C.M., Cox, L., Sun, H., Nealson, K.H., Aguilar, C., 1999. Iron Isotope Biosignatures. Science 285, 1889–1892. https://doi.org/10.1126/science.285.5435.1889

Beard, B.L., Johnson, C.M., Damm, K.L.V., Poulson, R.L., 2003. Iron isotope constraints on Fe cycling and mass balance in oxygenated Earth oceans. Geology 31, 629–632. https://doi.org/10.1130/0091-7613(2003)031<0629:IICOFC>2.0.CO;2

Bekker, A., Slack, J.F., Planavsky, N., Krapež, B., Hofmann, A., Konhauser, K.O., Rouxel, O.J., 2010. Iron Formation: The Sedimentary Product of a Complex Interplay among Mantle, Tectonic, Oceanic, and Biospheric Processes. Econ. Geol. 105, 467–508. https://doi.org/10.2113/gsecongeo.105.3.467

Braterman, P.S., Cairns-Smith, A.G., Sloper, R.W., 1983. Photo-oxidation of hydrated Fe2+—significance for banded iron formations. Nature 303, 163–164. https://doi.org/10.1038/303163a0

Bullen, T.D., White, A.F., Childs, C.W., Vivit, D.V., Schulz, M.S., 2001. Demonstration of significant abiotic iron isotope fractionation in nature. Geology 29, 699–702. https://doi.org/10.1130/0091-7613(2001)029<0699:DOSAII>2.0.CO;2

Busigny, V., Marin-Carbonne, J., Muller, E., Cartigny, P., Rollion-Bard, C., Assayag, N., Philippot, P., 2017. Iron and sulfur isotope constraints on redox conditions associated with the 3.2Ga barite deposits of the Mapepe Formation (Barberton Greenstone Belt, South Africa). Geochim. Cosmochim. Acta 210, 247–266. https://doi.org/10.1016/j.gca.2017.05.002

Cairns-Smith, A.G., 1978. Precambrian solution photochemistry, inverse segregation, and banded iron formations. Nature 276, 807–808. https://doi.org/10.1038/276807a0

Canfield, D.E., 2004. The evolution of the Earth surface sulfur reservoir. Am. J. Sci. 304, 839–861. https://doi.org/10.2475/ajs.304.10.839

Cloud, P., 1973. Paleoecological Significance of the Banded Iron-Formation. Econ. Geol. 68, 1135–1143. https://doi.org/10.2113/gsecongeo.68.7.1135

Craddock, P.R., Dauphas, N., 2011. Iron and carbon isotope evidence for microbial iron respiration throughout the Archean. Earth Planet. Sci. Lett. 303, 121–132. https://doi.org/10.1016/j.epsl.2010.12.045

Croal, L.R., Johnson, C.M., Beard, B.L., Newman, D.K., 2004. Iron isotope fractionation by Fe(II)-oxidizing photoautotrophic bacteria 1. Geochim. Cosmochim. Acta 68, 1227–1242. https://doi.org/10.1016/j.gca.2003.09.011

Crosby, Roden Eric E., Johnson Clark M., Beard Brian L., 2007. The mechanisms of iron isotope fractionation produced during dissimilatory Fe(III) reduction by Shewanella putrefaciens and Geobacter sulfurreducens. Geobiology 5, 169–189. https://doi.org/10.1111/j.1472-4669.2007.00103.x

Crowe, S.A., Døssing, L.N., Beukes, N.J., Bau, M., Kruger, S.J., Frei, R., Canfield, D.E., 2013. Atmospheric oxygenation three billion years ago. Nature 501, 535. https://doi.org/10.1038/nature12426

Crowe, S.A., Paris, G., Katsev, S., Jones, C., Kim, S.-T., Zerkle, A.L., Nomosatryo, S., Fowle, D.A., Adkins, J.F., Sessions, A.L., Farquhar, J., Canfield, D.E., 2014. Sulfate was a trace constituent of Archean seawater. Science 346, 735–739. https://doi.org/10.1126/science.1258966

Czaja, A.D., Johnson, C.M., Beard, B.L., Roden, E.E., Li, W., Moorbath, S., 2013. Biological Fe oxidation controlled deposition of banded iron formation in the ca. 3770Ma Isua Supracrustal Belt (West Greenland). Earth Planet. Sci. Lett. 363, 192–203. https://doi.org/10.1016/j.epsl.2012.12.025

Czaja, A.D., Van Kranendonk, M.J., Beard, B.L., Johnson, C.M., 2018. A multistage origin for Neoarchean layered hematite-magnetite iron formation from the Weld Range, Yilgarn Craton, Western Australia. Chem. Geol. 488, 125–137. https://doi.org/10.1016/j.chemgeo.2018.04.019

Dauphas, N., Cates, N.L., Mojzsis, S.J., Busigny, V., 2007a. Identification of chemical sedimentary protoliths using iron isotopes in the > 3750 Ma Nuvvuagittuq supracrustal belt, Canada. Earth Planet. Sci. Lett. 254, 358–376. https://doi.org/10.1016/j.epsl.2006.11.042

Dauphas, N., John, S.G., Rouxel, O., 2017. Iron Isotope Systematics. Rev. Mineral. Geochem. 82, 415–510. https://doi.org/10.1515/9783110545630-012

Dauphas, N., van Zuilen, M., Busigny, V., Lepland, A., Wadhwa, M., Janney, P.E., 2007b. Iron isotope, major and trace element characterization of early Archean supracrustal rocks from SW Greenland: Protolith identification and metamorphic overprint. Geochim. Cosmochim. Acta 71, 4745–4770. https://doi.org/10.1016/j.gca.2007.07.019

Dauphas, N., Zuilen, M. van, Wadhwa, M., Davis, A.M., Marty, B., Janney, P.E., 2004. Clues from Fe Isotope Variations on the Origin of Early Archean BIFs from Greenland. Science 306, 2077–2080. https://doi.org/10.1126/science.1104639

Derry, L.A., Jacobsen, S.B., 1990. The chemical evolution of Precambrian seawater: Evidence from REEs in banded iron formations. Geochim. Cosmochim. Acta 54, 2965–2977. https://doi.org/10.1016/0016-7037(90)90114-Z

Eickmann, B., Hofmann, A., Wille, M., Bui, T.H., Wing, B.A., Schoenberg, R., 2018. Isotopic evidence for oxygenated Mesoarchaean shallow oceans. Nat. Geosci. 11, 133. https://doi.org/10.1038/s41561-017-0036-x

Eroglu, S., Schoenberg, R., Pascarelli, S., Beukes, N.J., Kleinhanns, I.C., Swanner, E.D., 2018. Open ocean vs. continentally-derived iron cycles along the Neoarchean Campbellrand-Malmani Carbonate platform, South Africa. Am. J. Sci. 318, 367–408. https://doi.org/10.2475/04.2018.01

Fakhraee, M., Katsev, S., 2019. Organic sulfur was integral to the Archean sulfur cycle. Nat. Commun. 10, 1–8. https://doi.org/10.1038/s41467-019-12396-y

Farquhar, J., Cliff, J., Zerkle, A.L., Kamyshny, A., Poulton, S.W., Claire, M., Adams, D., Harms, B., 2013. Pathways for Neoarchean pyrite formation constrained by mass-independent sulfur isotopes. Proc. Natl. Acad. Sci. 110, 17638–17643. https://doi.org/10.1073/pnas.1218851110

Farquhar, J., Savarino, J., Jackson, T.L., Thiemens, M.H., 2000. Evidence of atmospheric sulphur in the martian regolith from sulphur isotopes in meteorites. Nature 404, 50–52. https://doi.org/10.1038/35003517

Fike, D.A., Bradley, A.S., Rose, C.V., 2015. Rethinking the Ancient Sulfur Cycle. Annu. Rev. Earth Planet. Sci. 43, 593–622. https://doi.org/10.1146/annurev-earth-060313-054802
François, L.M., 1986. Extensive deposition of banded iron formations was possible without photosynthesis. Nature 320, 352–354. https://doi.org/10.1038/320352a0

Garrels, R.M., 1987. A model for the deposition of the microbanded Precambrian iron formations. Am. J. Sci. 287, 81–106. https://doi.org/10.2475/ajs.287.2.81

Guilbaud, R., Butler, I.B., Ellam, R.M., 2011. Abiotic Pyrite Formation Produces a Large Fe Isotope Fractionation. Science 332, 1548–1551. https://doi.org/10.1126/science.1202924

Habicht, K.S., Gade, M., Thamdrup, B., Berg, P., Canfield, D.E., 2002. Calibration of Sulfate Levels in the Archean Ocean. Science 298, 2372–2374. https://doi.org/10.1126/science.1078265

Haruna, M., Hanamuro, T., Uyeda, K., Fujimaki, H., Ohmoto, H., 2003. Chemical, Isotopic, and Fluid Inclusion Evidence for the Hydrothermal Alteration of the Footwall Rocks of the BIF-Hosted Iron Ore Deposits in the Hamersley District, Western Australia. Resour. Geol. 53, 75–88. https://doi.org/10.1111/j.1751-3928.2003.tb00160.x

Heimann, A., Johnson, C.M., Beard, B.L., Valley, J.W., Roden, E.E., Spicuzza, M.J., Beukes, N.J., 2010. Fe, C, and O isotope compositions of banded iron formation carbonates demonstrate a major role for dissimilatory iron reduction in ~2.5 Ga marine environments. Earth Planet. Sci. Lett. 294, 8–18. https://doi.org/10.1016/j.epsl.2010.02.015

Holland, H.D., 1984. The Chemical Evolution of the Atmosphere and Oceans. Princeton University Press.

Isley, A.E., 1995. Hydrothermal Plumes and the Delivery of Iron to Banded Iron Formation. J. Geol. 103, 169–185.

Isley, A.E., Abbott, D.H., 1999. Plume-related mafic volcanism and the deposition of banded iron formation. J. Geophys. Res. Solid Earth 104, 15461–15477. https://doi.org/10.1029/1999JB900066

Jacobsen, S.B., Pimentel-Klose, M.R., 1988. Nd isotopic variations in Precambrian banded iron formations. Geophys. Res. Lett. 15, 393–396. https://doi.org/10.1029/GL015i004p00393

Johnson, C., Beard, B., Weyer, S., 2020. The Ancient Earth, in: Johnson, C., Beard, B., Weyer, S. (Eds.), Iron Geochemistry: An Isotopic Perspective, Advances in Isotope Geochemistry. Springer International Publishing, Cham, pp. 215–360. https://doi.org/10.1007/978-3-030-33828-2_6

Johnson, C.M., Beard, B.L., Roden, E.E., 2008. The Iron Isotope Fingerprints of Redox and Biogeochemical Cycling in Modern and Ancient Earth. Annu. Rev. Earth Planet. Sci. 36, 457–493. https://doi.org/10.1146/annurev.earth.36.031207.124139

Johnson, J.E., Muhling, J.R., Cosmidis, J., Rasmussen, B., Templeton, A.S., 2018. Low-Fe(III) Greenalite Was a Primary Mineral From Neoarchean Oceans. Geophys. Res. Lett. 45, 3182–3192. https://doi.org/10.1002/2017GL076311

Johnston, D.T., 2011. Multiple sulfur isotopes and the evolution of Earth's surface sulfur cycle. Earth-Sci. Rev. 106, 161–183. https://doi.org/10.1016/j.earscirev.2011.02.003

Kakegawa, T., Kawai, H., Ohmoto, H., 1998. Origins of pyrites in the ∼2.5 Ga Mt. McRae Shale, the Hamersley District, Western Australia. Geochim. Cosmochim. Acta 62, 3205–3220. https://doi.org/10.1016/S0016-7037(98)00229-4

Kappler, A., Pasquero, C., Konhauser, K.O., Newman, D.K., 2005. Deposition of banded iron formations by anoxygenic phototrophic Fe(II)-oxidizing bacteria. Geology 33, 865–868. https://doi.org/10.1130/G21658.1

Kendall, B., Reinhard, C.T., Lyons, T.W., Kaufman, A.J., Poulton, S.W., Anbar, A.D., 2010. Pervasive oxygenation along late Archaean ocean margins. Nat. Geosci. 3, 647–652. https://doi.org/10.1038/ngeo942

Klein, C., 2005. Some Precambrian banded iron-formations (BIFs) from around the world: Their age, geologic setting, mineralogy, metamorphism, geochemistry, and origins. Am. Mineral. 90, 1473–1499. https://doi.org/10.2138/am.2005.1871

Klein, C., Beukes, N.J., 1989. Geochemistry and sedimentology of a facies transition from limestone to iron-formation deposition in the early Proterozoic Transvaal Supergroup, South Africa. Econ. Geol. 84, 1733–1774. https://doi.org/10.2113/gsecongeo.84.7.1733

Köhler, I., Konhauser, K.O., Papineau, D., Bekker, A., Kappler, A., 2013. Biological carbon precursor to diagenetic siderite with spherical structures in iron formations. Nat. Commun. 4, 1741. https://doi.org/10.1038/ncomms2770

Konhauser, K.O., Hamade, T., Raiswell, R., Morris, R.C., Ferris, F.G., Southam, G., Canfield, D.E., 2002. Could bacteria have formed the Precambrian banded iron formations? Geology 30, 1079–1082. https://doi.org/10.1130/0091-7613(2002)030<1079:CBHFTP>2.0.CO;2

Konhauser, K.O., Newman, D.K., Kappler, A., 2005. The potential significance of microbial Fe(III) reduction during deposition of Precambrian banded iron formations. Geobiology 3, 167–177. https://doi.org/10.1111/j.1472-4669.2005.00055.x

Konhauser, K.O., Planavsky, N.J., Hardisty, D.S., Robbins, L.J., Warchola, T.J., Haugaard, R., Lalonde, S.V., Partin, C.A., Oonk, P.B.H., Tsikos, H., Lyons, T.W., Bekker, A., Johnson, C.M., 2017. Iron formations: A global record of Neoarchaean to Palaeoproterozoic environmental history. Earth-Sci. Rev. 172, 140–177. https://doi.org/10.1016/j.earscirev.2017.06.012

Kump, L.R., Seyfried, W.E., 2005. Hydrothermal Fe fluxes during the Precambrian: Effect of low oceanic sulfate concentrations and low hydrostatic pressure on the composition of black smokers. Earth Planet. Sci. Lett. 235, 654–662. https://doi.org/10.1016/j.epsl.2005.04.040

Li, W., Beard, B.L., Johnson, C.M., 2015. Biologically recycled continental iron is a major component in banded iron formations. Proc. Natl. Acad. Sci. U. S. A. 112, 8193–8198. https://doi.org/10.1073/pnas.1505515112

Luo, G., Ono, S., Beukes, N.J., Wang, D.T., Xie, S., Summons, R.E., 2016. Rapid oxygenation of Earth's atmosphere 2.33 billion years ago. Sci. Adv. 2, e1600134. https://doi.org/10.1126/sciadv.1600134

Lyons, T.W., Reinhard, C.T., Planavsky, N.J., 2014. The rise of oxygen in Earth's early ocean and atmosphere. Nature 506, 307–315. https://doi.org/10.1038/nature13068

Mansor, M., Fantle, M.S., 2019. A novel framework for interpreting pyrite-based Fe isotope records of the past. Geochim. Cosmochim. Acta 253, 39–62. https://doi.org/10.1016/j.gca.2019.03.017

Marin-Carbonne, J., Rollion-Bard, C., Bekker, A., Rouxel, O., Agangi, A., Cavalazzi, B., Wohlgemuth-Ueberwasser, C.C., Hofmann, A., McKeegan, K.D., 2014. Coupled Fe and S isotope variations in pyrite nodules from Archean shale. Earth Planet. Sci. Lett. 392, 67–79. https://doi.org/10.1016/j.epsl.2014.02.009

Nie, N.X., Dauphas, N., Greenwood, R.C., 2017. Iron and oxygen isotope fractionation during iron UV photo-oxidation: Implications for early Earth and Mars. Earth Planet. Sci. Lett. 458, 179–191. https://doi.org/10.1016/j.epsl.2016.10.035

Olson, S.L., Ostrander, C.M., Gregory, D.D., Roy, M., Anbar, A.D., Lyons, T.W., 2019. Volcanically modulated pyrite burial and ocean–atmosphere oxidation. Earth Planet. Sci. Lett. 506, 417–427. https://doi.org/10.1016/j.epsl.2018.11.015

Ossa Ossa, F., Hofmann, A., Wille, M., Spangenberg, J.E., Bekker, A., Poulton, S.W., Eickmann, B., Schoenberg, R., 2018. Aerobic iron and manganese cycling in a redox-stratified Mesoarchean epicontinental sea. Earth Planet. Sci. Lett. 500, 28–40. https://doi.org/10.1016/j.epsl.2018.07.044

Planavsky, N., Rouxel, O., Bekker, A., Shapiro, R., Fralick, P., Knudsen, A., 2009. Iron-oxidizing microbial ecosystems thrived in late Paleoproterozoic redox-stratified oceans. Earth Planet. Sci. Lett. 286, 230–242. https://doi.org/10.1016/j.epsl.2009.06.033

Planavsky, N., Rouxel, O.J., Bekker, A., Hofmann, A., Little, C.T.S., Lyons, T.W., 2012. Iron isotope composition of some Archean and Proterozoic iron formations. Geochim. Cosmochim. Acta 80, 158–169. https://doi.org/10.1016/j.gca.2011.12.001

Planavsky, N.J., Asael, D., Hofmann, A., Reinhard, C.T., Lalonde, S.V., Knudsen, A., Wang, X., Ossa Ossa, F., Pecoits, E., Smith, A.J.B., Beukes, N.J., Bekker, A., Johnson, T.M., Konhauser, K.O., Lyons, T.W., Rouxel, O.J., 2014. Evidence for oxygenic photosynthesis half a billion years before the Great Oxidation Event. Nat. Geosci. 7, 283–286. https://doi.org/10.1038/ngeo2122

Polyakov, V.B., Clayton, R.N., Horita, J., Mineev, S.D., 2007. Equilibrium iron isotope fractionation factors of minerals: Reevaluation from the data of nuclear inelastic resonant X-ray scattering and Mössbauer spectroscopy. Geochim. Cosmochim. Acta 71, 3833–3846. https://doi.org/10.1016/j.gca.2007.05.019

Poulton, S.W., Canfield, D.E., 2011. Ferruginous Conditions: A Dominant Feature of the Ocean through Earth's History. Elements 7, 107–112. https://doi.org/10.2113/gselements.7.2.107

Raiswell, R., Hardisty, D.S., Lyons, T.W., Canfield, D.E., Owens, J.D., Planavsky, N.J., Poulton, S.W., Reinhard, C.T., 2018. The iron paleoredox proxies: A guide to the pitfalls, problems and proper practice. Am. J. Sci. 318, 491–526. https://doi.org/10.2475/05.2018.03

Rasmussen, B., Buick, R., 1999. Redox state of the Archean atmosphere: Evidence from detrital heavy minerals in ca. 3250–2750 Ma sandstones from the Pilbara Craton, Australia. Geology 27, 115–118. https://doi.org/10.1130/0091-7613(1999)027<0115:RSOTAA>2.3.CO;2

Rasmussen, B., Fletcher, I.R., Bekker, A., Muhling, J.R., Gregory, C.J., Thorne, A.M., 2012. Deposition of 1.88-billion-year-old iron formations as a consequence of rapid crustal growth. Nature 484, 498–501. https://doi.org/10.1038/nature11021

Rasmussen, B., Krapež, B., Muhling, J.R., Suvorova, A., 2015. Precipitation of iron silicate nanoparticles in early Precambrian oceans marks Earth's first iron age. Geology 43, 303–306. https://doi.org/10.1130/G36309.1

Reinhard, C.T., Raiswell, R., Scott, C., Anbar, A.D., Lyons, T.W., 2009. A Late Archean Sulfidic Sea Stimulated by Early Oxidative Weathering of the Continents. Science 326, 713–716. https://doi.org/10.1126/science.1176711

Robbins, L.J., Funk, S.P., Flynn, S.L., Warchola, T.J., Li, Z., Lalonde, S.V., Rostron, B.J., Smith, A.J.B., Beukes, N.J., Kock, M.O. de, Heaman, L.M., Alessi, D.S., Konhauser, K.O., 2019. Hydrogeological constraints on the formation of Palaeoproterozoic banded iron formations. Nat. Geosci. 1. https://doi.org/10.1038/s41561-019-0372-0

Rolison, J.M., Stirling, C.H., Middag, R., Gault-Ringold, M., George, E., Rijkenberg, M.J.A., 2018. Iron isotope fractionation during pyrite formation in a sulfidic Precambrian ocean analogue. Earth Planet. Sci. Lett. 488, 1–13. https://doi.org/10.1016/j.epsl.2018.02.006

Rouxel, O., Fouquet, Y., Ludden, J.N., 2004. Subsurface processes at the lucky strike hydrothermal field, Mid-Atlantic ridge: evidence from sulfur, selenium, and iron isotopes 1 1Associate editor: S. Sheppard. Geochim. Cosmochim. Acta 68, 2295–2311. https://doi.org/10.1016/j.gca.2003.11.029

Rouxel, O., Shanks, W.C., Bach, W., Edwards, K.J., 2008. Integrated Fe- and S-isotope study of seafloor hydrothermal vents at East Pacific Rise 9–10°N. Chem. Geol. 252, 214–227. https://doi.org/10.1016/j.chemgeo.2008.03.009

Rouxel, O.J., Bekker, A., Edwards, K.J., 2006. Response to Comment on "Iron Isotope Constraints on the Archean and Paleoproterozoic Ocean Redox State." Science 311, 177–177. https://doi.org/10.1126/science.1118420

Rouxel, O.J., Bekker, A., Edwards, K.J., 2005. Iron Isotope Constraints on the Archean and Paleoproterozoic Ocean Redox State. Science 307, 1088–1091. https://doi.org/10.1126/science.1105692

Schad, M., Halama, M., Bishop, B., Konhauser, K.O., Kappler, A., 2019. Temperature fluctuations in the Archean ocean as trigger for varve-like deposition of iron and silica minerals in banded iron formations. Geochim. Cosmochim. Acta 265, 386–412. https://doi.org/10.1016/j.gca.2019.08.031

Scott, C.T., Bekker, A., Reinhard, C.T., Schnetger, B., Krapež, B., Rumble, D., Lyons, T.W., 2011. Late Archean euxinic conditions before the rise of atmospheric oxygen. Geology 39, 119–122. https://doi.org/10.1130/G31571.1

Severmann, S., Johnson, C.M., Beard, B.L., German, C.R., Edmonds, H.N., Chiba, H., Green, D.R.H., 2004. The effect of plume processes on the Fe isotope composition of hydrothermally derived Fe in the deep ocean as inferred from the Rainbow vent site, Mid-Atlantic Ridge, 36°14′N. Earth Planet. Sci. Lett. 225, 63–76. https://doi.org/10.1016/j.epsl.2004.06.001

Severmann, S., Lyons, T.W., Anbar, A., McManus, J., Gordon, G., 2008. Modern iron isotope perspective on the benthic iron shuttle and the redox evolution of ancient oceans. Geology 36, 487–490. https://doi.org/10.1130/G24670A.1

Stüeken, E.E., Catling, D.C., Buick, R., 2012. Contributions to late Archaean sulphur cycling by life on land. Nat. Geosci. 5, 722–725. https://doi.org/10.1038/ngeo1585

Sumner, D.Y., 1997. Carbonate precipitation and oxygen stratification in late Archean seawater as deduced from facies and stratigraphy of the Gamohaan and Frisco formations, Transvaal Supergroup, South Africa. Am. J. Sci. 297, 455–487. https://doi.org/10.2475/ajs.297.5.455

Swanner, E.D., Bayer, T., Wu, W., Hao, L., Obst, M., Sundman, A., Byrne, J.M., Michel, F.M., Kleinhanns, I.C., Kappler, A., Schoenberg, R., 2017. Iron Isotope Fractionation during Fe(II) Oxidation Mediated by the Oxygen-Producing Marine Cyanobacterium Synechococcus PCC 7002. Environ. Sci. Technol. https://doi.org/10.1021/acs.est.6b05833

Thibon, F., Blichert-Toft, J., Tsikos, H., Foden, J., Albalat, E., Albarede, F., 2019. Dynamics of oceanic iron prior to the Great Oxygenation Event. Earth Planet. Sci. Lett. 506, 360–370. https://doi.org/10.1016/j.epsl.2018.11.016

Tosca, N.J., Guggenheim, S., Pufahl, P.K., 2016. An authigenic origin for Precambrian greenalite: Implications for iron formation and the chemistry of ancient seawater. Geol. Soc. Am. Bull. 128, 511–530. https://doi.org/10.1130/B31339.1

Trendall, A.F., 1973. Varve Cycles in the Weeli Wolli Formation of the Precambrian Hamersley Group, Western Australia. Econ. Geol. 68, 1089–1097. https://doi.org/10.2113/gsecongeo.68.7.1089

Trendall, A.F., Morris, R.C., 2000. Iron-Formation: Facts and Problems. Elsevier.
Tsikos, H., Matthews, A., Erel, Y., Moore, J.M., 2010. Iron isotopes constrain biogeochemical redox cycling of iron and manganese in a Palaeoproterozoic stratified basin. Earth Planet. Sci. Lett. 298, 125–134. https://doi.org/10.1016/j.epsl.2010.07.032

Data Compilation References

IF δ^{56}Fe record

Busigny, V., Marin-Carbonne, J., Muller, E., Cartigny, P., Rollion-Bard, C., Assayag, N., and Philippot, P., 2017, Iron and sulfur isotope constraints on redox conditions associated with the 3.2Ga barite deposits of the Mapepe Formation (Barberton Greenstone Belt, South Africa): Geochimica et Cosmochimica Acta, v. 210, p. 247–266, doi:10.1016/j.gca.2017.05.002.

Czaja, A.D., Johnson, C.M., Beard, B.L., Roden, E.E., Li, W., and Moorbath, S., 2013, Biological Fe oxidation controlled deposition of banded iron formation in the ca. 3770Ma Isua Supracrustal Belt (West Greenland): Earth and Planetary Science Letters, v. 363, p. 192–203, doi:10.1016/j.epsl.2012.12.025.

Czaja, A.D., Van Kranendonk, M.J., Beard, B.L., and Johnson, C.M., 2018, A multistage origin for Neoarchean layered hematite-magnetite iron formation from the Weld Range, Yilgarn Craton, Western Australia: Chemical Geology, v. 488, p. 125–137, doi:10.1016/j.chemgeo.2018.04.019.

Dauphas, N., Cates, N.L., Mojzsis, S.J., and Busigny, V., 2007a, Identification of chemical sedimentary protoliths using iron isotopes in the > 3750 Ma Nuvvuagittuq supracrustal belt, Canada: Earth and Planetary Science Letters, v. 254, p. 358–376, doi:10.1016/j.epsl.2006.11.042.

Dauphas, N., van Zuilen, M., Busigny, V., Lepland, A., Wadhwa, M., and Janney, P.E., 2007b, Iron isotope, major and trace element characterization of early Archean supracrustal rocks from SW Greenland: Protolith identification and metamorphic overprint: Geochimica et Cosmochimica Acta, v. 71, p. 4745–4770, doi:10.1016/j.gca.2007.07.019.

Dauphas, N., Zuilen, M. van, Wadhwa, M., Davis, A.M., Marty, B., and Janney, P.E., 2004, Clues from Fe Isotope Variations on the Origin of Early Archean BIFs from Greenland: Science, v. 306, p. 2077–2080, doi:10.1126/science.1104639.

Haugaard, R., Pecoits, E., Lalonde, S., Rouxel, O., and Konhauser, K., 2016, The Joffre banded iron formation, Hamersley Group, Western Australia: Assessing the palaeoenvironment through detailed petrology and chemostratigraphy: Precambrian Research, v. 273, p. 12–37, doi:10.1016/j.precamres.2015.10.024.

Heimann, A., Johnson, C.M., Beard, B.L., Valley, J.W., Roden, E.E., Spicuzza, M.J., and Beukes, N.J., 2010, Fe, C, and O isotope compositions of banded iron formation carbonates demonstrate a major role for dissimilatory iron reduction in ~2.5 Ga marine environments: Earth and Planetary Science Letters, v. 294, p. 8–18, doi:10.1016/j.epsl.2010.02.015.

Kurzweil, F., Wille, M., Gantert, N., Beukes, N.J., and Schoenberg, R., 2016, Manganese oxide shuttling in pre-GOE oceans – evidence from molybdenum and iron isotopes: Earth and Planetary Science Letters, v. 452, p. 69–78, doi:10.1016/j.epsl.2016.07.013.

Li, W., Beard, B.L., and Johnson, C.M., 2015, Biologically recycled continental iron is a major component in banded iron formations: Proceedings of the National Academy of Sciences of the United States of America, v. 112, p. 8193–8198, doi:10.1073/pnas.1505515112.

Li, W., Czaja, A.D., Van Kranendonk, M.J., Beard, B.L., Roden, E.E., and Johnson, C.M., 2013, An anoxic, Fe(II)-rich, U-poor ocean 3.46 billion years ago: Geochimica et Cosmochimica Acta, v. 120, p. 65–79, doi:10.1016/j.gca.2013.06.033.

Planavsky, N.J. et al., 2014, Evidence for oxygenic photosynthesis half a billion years before the Great Oxidation Event: Nature Geoscience, v. 7, p. 283–286, doi:10.1038/ngeo2122.

Planavsky, N., Rouxel, O.J., Bekker, A., Hofmann, A., Little, C.T.S., and Lyons, T.W., 2012, Iron isotope composition of some Archean and Proterozoic iron formations: Geochimica et Cosmochimica Acta, v. 80, p. 158–169, doi:10.1016/j.gca.2011.12.001.

Planavsky, N., Rouxel, O., Bekker, A., Shapiro, R., Fralick, P., and Knudsen, A., 2009, Iron-oxidizing microbial ecosystems thrived in late Paleoproterozoic redox-stratified oceans: Earth and Planetary Science Letters, v. 286, p. 230–242, doi:10.1016/j.epsl.2009.06.033.

Rouxel, O.J., Bekker, A., and Edwards, K.J., 2005, Iron Isotope Constraints on the Archean and Paleoproterozoic Ocean Redox State: Science, v. 307, p. 1088–1091, doi:10.1126/science.1105692.

Satkoski, A.M., Beukes, N.J., Li, W., Beard, B.L., and Johnson, C.M., 2015, A redox-stratified ocean 3.2 billion years ago: Earth and Planetary Science Letters, v. 430, p. 43–53, doi:10.1016/j.epsl.2015.08.007.

Smith, A.J.B., Beukes, N.J., Gutzmer, J., Czaja, A.D., Johnson, C.M., and Nhleko, N., 2017, Oncoidal granular iron formation in the Mesoarchaean Pongola Supergroup, southern Africa: Textural and geochemical evidence for biological activity during iron deposition: Geobiology, v. 15, p. 731–749, doi:10.1111/gbi.12248.

Teixeira, N.L., Caxito, F.A., Rosière, C.A., Pecoits, E., Vieira, L., Frei, R., Sial, A.N., and Poitrasson, F., 2017, Trace elements and isotope geochemistry (C, O, Fe, Cr) of the Cauê iron formation, Quadrilátero Ferrífero, Brazil: Evidence for widespread microbial dissimilatory iron reduction at the Archean/Paleoproterozoic transition: Precambrian Research, v. 298, p. 39–55, doi:10.1016/j.precamres.2017.05.009.

Thibon, F., Blichert-Toft, J., Tsikos, H., Foden, J., Albalat, E., and Albarede, F., 2019, Dynamics of oceanic iron prior to the Great Oxygenation Event: Earth and Planetary Science Letters, v. 506, p. 360–370, doi:10.1016/j.epsl.2018.11.016.

Tsikos, H., Matthews, A., Erel, Y., and Moore, J.M., 2010, Iron isotopes constrain biogeochemical redox cycling of iron and manganese in a Palaeoproterozoic stratified basin: Earth and Planetary Science Letters, v. 298, p. 125–134, doi:10.1016/j.epsl.2010.07.032.

Yamaguchi, K.E., Johnson, C.M., Beard, B.L., and Ohmoto, H., 2005, Biogeochemical cycling of iron in the Archean–Paleoproterozoic Earth: Constraints from iron isotope variations in sedimentary rocks from the Kaapvaal and Pilbara Cratons: Chemical Geology, v. 218, p. 135–169, doi:10.1016/j.chemgeo.2005.01.020.

Pyrite $\delta^{56}Fe$ record

Archer, C., and Vance, D., 2006, Coupled Fe and S isotope evidence for Archean microbial Fe(III) and sulfate reduction: Geology, v. 34, p. 153–156, doi:10.1130/G22067.1.

Busigny, V., Marin-Carbonne, J., Muller, E., Cartigny, P., Rollion-Bard, C., Assayag, N., and Philippot, P., 2017, Iron and sulfur isotope constraints on redox conditions associated with the 3.2Ga barite deposits of the Mapepe Formation (Barberton Greenstone Belt, South Africa): Geochimica et Cosmochimica Acta, v. 210, p. 247–266, doi:10.1016/j.gca.2017.05.002.

Eickmann, B., Hofmann, A., Wille, M., Bui, T.H., Wing, B.A., and Schoenberg, R., 2018, Isotopic evidence for oxygenated Mesoarchaean shallow oceans: Nature Geoscience, v. 11, p. 133, doi:10.1038/s41561-017-0036-x.

Hofmann, A., Bekker, A., Rouxel, O., Rumble, D., and Master, S., 2009, Multiple sulphur and iron isotope composition of detrital pyrite in Archaean sedimentary rocks: A new tool for provenance analysis: Earth and Planetary Science Letters, v. 286, p. 436–445, doi:10.1016/j.epsl.2009.07.008.

Rouxel, O.J., Bekker, A., and Edwards, K.J., 2005, Iron Isotope Constraints on the Archean and Paleoproterozoic Ocean Redox State: Science, v. 307, p. 1088–1091, doi:10.1126/science.1105692.

Sedimentary sulfide $\delta^{34}S$ record

Bekker, A., Holland, H.D., Wang, P.-L., Rumble Iii, D., Stein, H.J., Hannah, J.L., Coetzee, L.L., and Beukes, N.J., 2004, Dating the rise of atmospheric oxygen: Nature, v. 427, p. 117–120, doi:10.1038/nature02260.

Busigny, V., Marin-Carbonne, J., Muller, E., Cartigny, P., Rollion-Bard, C., Assayag, N., and Philippot, P., 2017, Iron and sulfur isotope constraints on redox conditions associated with the 3.2 Ga barite deposits of the Mapepe Formation (Barberton Greenstone Belt, South Africa): Geochimica et Cosmochimica Acta, v. 210, p. 247–266, doi:10.1016/j.gca.2017.05.002.

Cameron, E.M., and Garrels, R.M., 1980, Geochemical compositions of some Precambrian shales from the Canadian Shield: Chemical Geology, v. 28, p. 181–197, doi:10.1016/0009-2541(80)90046-7.

Carrigan, W.J., and Cameron, E.M., 1991, Petrological and stable isotope studies of carbonate and sulfide minerals from the Gunflint Formation, Ontario: evidence for the origin of early Proterozoic iron-formation: Precambrian Research, v. 52, p. 347–380, doi:10.1016/0301-9268(91)90088-R.

Cates, N.L., and Mojzsis, S.J., 2006, Chemical and isotopic evidence for widespread Eoarchean metasedimentary enclaves in southern West Greenland: Geochimica et Cosmochimica Acta, v. 70, p. 4229–4257, doi:10.1016/j.gca.2006.05.014.

Eickmann, B., Hofmann, A., Wille, M., Bui, T.H., Wing, B.A., and Schoenberg, R., 2018, Isotopic evidence for oxygenated Mesoarchaean shallow oceans: Nature Geoscience, v. 11, p. 133, doi:10.1038/s41561-017-0036-x.

Farquhar, J., Bao, H., and Thiemens, M., 2000, Atmospheric Influence of Earth's Earliest Sulfur Cycle: Science, v. 289, p. 756–758, doi:10.1126/science.289.5480.756.

Farquhar, J., Peters, M., Johnston, D.T., Strauss, H., Masterson, A., Wiechert, U., and Kaufman, A.J., 2007, Isotopic evidence for Mesoarchaean anoxia and changing atmospheric sulphur chemistry: Nature, v. 449, p. 706–709, doi:10.1038/nature06202.

Guo, Q. et al., 2009, Reconstructing Earth's surface oxidation across the Archean-Proterozoic transition: Geology, v. 37, p. 399–402, doi:10.1130/G25423A.1.

Hofmann, A., Bekker, A., Rouxel, O., Rumble, D., and Master, S., 2009, Multiple sulphur and iron isotope composition of detrital pyrite in Archaean sedimentary rocks: A new tool for provenance analysis: Earth and Planetary Science Letters, v. 286, p. 436–445, doi:10.1016/j.epsl.2009.07.008.

Hou, K., Li, Y., and Wan, D., 2007, Constraints on the Archean atmospheric oxygen and sulfur cycle from mass-independent sulfur records from Anshan-Benxi BIFs, Liaoning Province, China: Science in China Series D: Earth Sciences, v. 50, p. 1471–1478, doi:10.1007/s11430-007-0106-9.

Jamieson, J.W., Wing, B.A., Hannington, M.D., and Farquhar, J., 2006, Evaluating Isotopic Equilibrium Among Sulfide Mineral Pairs in Archean Ore Deposits: Case Study From The Kidd Creek Vms Deposit, Ontario, Canada: Economic Geology, v. 101, p. 1055–1061, doi:10.2113/gsecongeo.101.5.1055.

Johnston, D.T., Poulton, S.W., Fralick, P.W., Wing, B.A., Canfield, D.E., and Farquhar, J., 2006, Evolution of the oceanic sulfur cycle at the end of the Paleoproterozoic: Geochimica et Cosmochimica Acta, v. 70, p. 5723–5739, doi:10.1016/j.gca.2006.08.001.

Kamber, B.S., and Whitehouse, M.J., 2007, Micro-scale sulphur isotope evidence for sulphur cycling in the late Archean shallow ocean: Geobiology, v. 5, p. 5–17, doi:10.1111/j.1472-4669.2006.00091.x.

Kaufman, A.J., Johnston, D.T., Farquhar, J., Masterson, A.L., Lyons, T.W., Bates, S., Anbar, A.D., Arnold, G.L., Garvin, J., and Buick, R., 2007, Late Archean Biospheric Oxygenation and Atmospheric Evolution: Science, v. 317, p. 1900–1903, doi:10.1126/science.1138700.

Marin-Carbonne, J., Rollion-Bard, C., Bekker, A., Rouxel, O., Agangi, A., Cavalazzi, B., Wohlgemuth-Ueberwasser, C.C., Hofmann, A., and McKeegan, K.D., 2014, Coupled Fe and S isotope variations in pyrite nodules from Archean shale: Earth and Planetary Science Letters, v. 392, p. 67–79, doi:10.1016/j.epsl.2014.02.009.

Melezhik, V.A., Grinenko, L.N., and Fallick, A.E., 1998, 2000-Ma sulphide concretions from the `Productive' Formation of the Pechenga Greenstone Belt, NW Russia: genetic history based on morphological and isotopic evidence: Chemical Geology, v. 148, p. 61–94, doi:10.1016/S0009-2541(98)00021-7.

Mojzsis, S.J., Coath, C.D., Greenwood, J.P., McKeegan, K.D., and Harrison, T.M., 2003, Mass-independent isotope effects in Archean (2.5 to 3.8 Ga) sedimentary sulfides determined by ion microprobe analysis: Geochimica et Cosmochimica Acta, v. 67, p. 1635–1658, doi:10.1016/S0016-7037(03)00059-0.

Ohmoto, H., Watanabe, Y., Ikemi, H., Poulson, S.R., and Taylor, B.E., 2006, Sulphur isotope evidence for an oxic Archaean atmosphere: Nature, v. 442, p. 908–911, doi:10.1038/nature05044.

Ono, S., Beukes, N.J., and Rumble, D., 2009a, Origin of two distinct multiple-sulfur isotope compositions of pyrite in the 2.5Ga Klein Naute Formation, Griqualand West Basin, South Africa: Precambrian Research, v. 169, p. 48–57, doi:10.1016/j.precamres.2008.10.012.

Ono, S., Beukes, N.J., Rumble, D., and Fogel, M.L., 2006, Early evolution of atmospheric oxygen from multiple-sulfur and carbon isotope records of the 2.9 Ga Mozaan Group of the Pongola Supergroup, Southern Africa: South African Journal of Geology, v. 109, p. 97–108, doi:10.2113/gssajg.109.1-2.97.

Ono, S., Eigenbrode, J.L., Pavlov, A.A., Kharecha, P., Rumble, D., Kasting, J.F., and Freeman, K.H., 2003, New insights into Archean sulfur cycle from mass-independent sulfur isotope records from the Hamersley Basin, Australia: Earth and Planetary Science Letters, v. 213, p. 15–30, doi:10.1016/S0012-821X(03)00295-4.

Ono, S., Kaufman, A.J., Farquhar, J., Sumner, D.Y., and Beukes, N.J., 2009b, Lithofacies control on multiple-sulfur isotope records and Neoarchean sulfur cycles: Precambrian Research, v. 169, p. 58–67, doi:10.1016/j.precamres.2008.10.013.

Ossa Ossa, F., Eickmann, B., Hofmann, A., Planavsky, N.J., Asael, D., Pambo, F., and Bekker, A., 2018, Two-step deoxygenation at the end of the Paleoproterozoic Lomagundi Event: Earth and Planetary Science Letters, v. 486, p. 70–83, doi:10.1016/j.epsl.2018.01.009.

Papineau, D., Mojzsis, S.J., and Schmitt, A.K., 2007, Multiple sulfur isotopes from Paleoproterozoic Huronian interglacial sediments and the rise of atmospheric oxygen: Earth and Planetary Science Letters, v. 255, p. 188–212, doi:10.1016/j.epsl.2006.12.015.

Partridge, M.A., Golding, S.D., Baublys, K.A., and Young, E., 2008, Pyrite paragenesis and multiple sulfur isotope distribution in late Archean and early Paleoproterozoic Hamersley Basin sediments: Earth and Planetary Science Letters, v. 272, p. 41–49, doi:10.1016/j.epsl.2008.03.051.

Philippot, P., Zuilen, M.V., Lepot, K., Thomazo, C., Farquhar, J., and Kranendonk, M.J.V., 2007, Early Archaean Microorganisms Preferred Elemental Sulfur, Not Sulfate: Science, v. 317, p. 1534–1537, doi:10.1126/science.1145861.

Poulton, S.W., Fralick, P.W., and Canfield, D.E., 2004, The transition to a sulphidic ocean ~ 1.84 billion years ago: Nature, v. 431, p. 173–177, doi:10.1038/nature02912.

Scott, C.T., Bekker, A., Reinhard, C.T., Schnetger, B., Krapež, B., Rumble, D., and Lyons, T.W., 2011, Late Archean euxinic conditions before the rise of atmospheric oxygen: Geology, v. 39, p. 119–122, doi:10.1130/G31571.1.

Scott, C., Wing, B.A., Bekker, A., Planavsky, N.J., Medvedev, P., Bates, S.M., Yun, M., and Lyons, T.W., 2014, Pyrite multiple-sulfur isotope evidence for rapid expansion and contraction of the early Paleoproterozoic seawater sulfate reservoir: Earth and Planetary Science Letters, v. 389, p. 95–104, doi:10.1016/j.epsl.2013.12.010.

Shen, Y., Farquhar, J., Masterson, A., Kaufman, A.J., and Buick, R., 2009, Evaluating the role of microbial sulfate reduction in the early Archean using quadruple isotope systematics: Earth and Planetary Science Letters, v. 279, p. 383–391, doi:10.1016/j.epsl.2009.01.018.

Strauss, H., and Moore, T., 1992, Abundances and Isotopic Compositions of Carbon and Sulfur Species in Whole Rock and Kerogen Samples: In J. Schopf and C. Klein (Eds.), The Proterozoic Biosphere: A Multidisciplinary Study (pp. 709-798). Cambridge: Cambridge University Press. doi:10.1017/CBO9780511601064.019

Strauss, H., 2002, The Isotopic Composition of Precambrian Sulphides – Seawater Chemistry and Biological Evolution: In W. Altermann and P. L. Corcoran (Eds.), Precambrian Sedimentary Environments: A Modern Approach to Ancient Depositional Systems (pp. 67-105). International Association of Sedimentologists. doi:10.1002/9781444304312

Strauss, H., and Beukes, N.J., 1996, Carbon and sulfur isotopic compositions of organic carbon and pyrite in sediments from the Transvaal Supergroup, South Africa: Precambrian Research, v. 79, p. 57–71, doi:10.1016/0301-9268(95)00088-7.

Thomazo, C., Ader, M., Farquhar, J., and Philippot, P., 2009, Methanotrophs regulated atmospheric sulfur isotope anomalies during the Mesoarchean (Tumbiana Formation, Western Australia): Earth and Planetary Science Letters, v. 279, p. 65–75, doi:10.1016/j.epsl.2008.12.036.

Ueno, Y., Ono, S., Rumble, D., and Maruyama, S., 2008, Quadruple sulfur isotope analysis of ca. 3.5Ga Dresser Formation: New evidence for microbial sulfate reduction in the early Archean: Geochimica et Cosmochimica Acta, v. 72, p. 5675–5691, doi:10.1016/j.gca.2008.08.026.

Watanabe, Y., Naraoka, H., Wronkiewicz, D.J., Condie, K.C., and Ohmoto, H., 1997, Carbon, nitrogen, and sulfur geochemistry of Archean and Proterozoic shales from the Kaapvaal Craton, South Africa: Geochimica et Cosmochimica Acta, v. 61, p. 3441–3459, doi:10.1016/S0016-7037(97)00164-6.

Whitehouse, M.J., Kamber, B.S., Fedo, C.M., and Lepland, A., 2005, Integrated Pb- and S-isotope investigation of sulphide minerals from the early Archaean of southwest Greenland: Chemical Geology, v. 222, p. 112–131, doi:10.1016/j.chemgeo.2005.06.004.

Yamaguchi (2002) PhD thesis, 485 pages, Pennsylvania State University

Zerkle, A.L., Claire, M.W., Domagal-Goldman, S.D., Farquhar, J., and Poulton, S.W., 2012, A bistable organic-rich atmosphere on the Neoarchaean Earth: Nature Geoscience, v. 5, p. 359–363, doi:10.1038/ngeo1425.

Zhelezinskaia, I., Kaufman, A.J., Farquhar, J., and Cliff, J., 2014, Large sulfur isotope fractionations associated with Neoarchean microbial sulfate reduction: Science, v. 346, p. 742–744, doi:10.1126/science.1256211.

Chapter 3 – Re-evaluating the Early Pyrite Iron Isotope Record Using a Novel Triple Iron Isotope Proxy

Foreword

In Chapter 2, the apparent coevolution of different sedimentary isotopic records was used to make a qualitative reinterpretation of the Fe isotope record of pyrite before the GOE. We suggested that the $\delta^{56}Fe$ of IFs and pyrite, which were on average strongly positive and strongly negative, respectively, prior to the GOE, converged towards similar values in the runup to the oxygenation of the atmosphere (Fig. 3.1.). The explanation we propose for this convergence is that the degree of partial Fe oxidation, and the degree of pyritization, in the respective formation environments of oxic and sulfidic/euxinic sedimentary sinks, increased prior to the GOE. This suggests that oxidation of the shallow oceans with respect to Fe, and sulfur availability, increased coincidentally, from the early Neoarchean (about 2.7 Ga) through to the GOE (2.43-2.32 Ga). Our reinterpretation of the pre-GOE Fe isotope record motivates us to ask some new questions. First: what is the implication of these changing Fe sinks for the redox balance of Earth's surface; and what role did the marine Fe cycle play in stalling the rise of atmospheric O_2? Second, if the size of oxic and sulfidic sinks for Fe was a major factor for the rise of atmospheric O_2, how can we quantify the changing size of these sinks in the pre-GOE oceans?

The relative size of the oxic and sulfidic sinks Fe in the oceans is crucial for understanding how the Fe cycle affected the rise of atmospheric O_2 because these two sinks potentially have opposite effects on the redox balance of Earth's surface. Ferrous iron is typically considered as one of the major buffers on rising O_2 levels, because it is the most abundant reductant available at Earth's surface, and the oxidation of Fe^{2+} to Fe^{3+} draws O_2 down from the atmosphere and locks this oxidizing power into geologically long-lived ferric iron mineral deposits (Catling et al., 2001;

Holland, 1984; Ward et al., 2016). The ferruginous global oceans certainly would have provided a readily available reductant for free O_2, particularly considering that the earliest oxygenated environments were produced in marine settings by cyanobacteria (Planavsky et al., 2014), placing them very close to the large and mobile Fe^{2+} pool. Conversely, it is possible for the sulfidic sink for Fe to be a net source of oxidation for the Earth's surface (Gaillard et al., 2011; Lyons and Gill, 2010; Olson et al., 2019); but this net source behavior is subject to a number of caveats and strictly speaking concerns the redox chemistry of S, not Fe^{2+}. Ferrous iron is necessary for the permanent sequestration of reducing power in sediments as Fe sulfides, but it is a redox change in S, not Fe, that can subsequently oxidize Earth's surface.

Sedimentary pyrite is generated from the reaction of Fe^{2+} with H_2S, where H_2S is generated via microbial sulfate reduction (MSR) in the presence of organic matter. Organic matter is ultimately sourced from photosynthetic primary production, so the net effect of MSR and pyrite burial is to transfer electrons from the initial electron donor involved in photosynthesis to sulfur, and then to bury this sulfur. However, the sulfate (S^{6+}) pool in the ocean comes from the oxidation of more reduced initial S sources to Earth's surface, and whether the entire pyrite burial process becomes oxidizing depends on the initial redox state of this primary sulfur. The sedimentary sulfide sink can be net source of oxidation for Earth surface environments only if the ultimate source of S is volcanic outgassing, and not the weathering of magmatic sulfide minerals on the continents (Olson et al., 2019). This is because S gases emitted from volcanoes, a combination of H_2S (S^{2-}) and SO_2 (S^{4+}), can have an average redox state that is more oxidizing than that of pyrite (S^{-}), while, magmatic sulfides, comprised of pyrite and other more reduced monosulfide minerals (S^{2-}), always have an average redox state equal to or more reducing than the eventual pyrite sink. The pre-GOE S isotope record provides strong evidence for a major volcanic component to early surface sulfur

supplies. The persistent presence of a sulfur isotope mass independent fractionation (S-MIF) signature in Archean and early Paleoproterozoic rocks, including many of the euxinic black shales that our low $\delta^{56}Fe$ pyrites come from, indicates that sulfur was being cycled through atmospheric photochemical cycles, and this is only possible if sulfur was added to the atmosphere in volcanic gases (Farquhar et al., 2000; Halevy et al., 2010; Johnston, 2011). Additionally, we showed in Chapter 2 that sulfur availability was generally low in the pre-GOE oceans, and this is most easily explained by the lack of a major continental oxidative weathering flux, an assumption that is consistent with anoxic atmospheric conditions.

A large number of assumptions, many of which are detailed below in the main text of Chapter 3, go into understanding the exact relationship between the composition of volcanic sulfur degassing and the effectiveness of pyrite burial as a net oxidant for early surface environment. Important factors to consider that are debated extensively in the literature are whether the H_2S/SO_2 of volcanic emissions shifted towards more oxidizing values in the runup the GOE (Brounce et al., 2017; Gaillard et al., 2011; Holland, 2002; Kump and Barley, 2007), and whether an increase in the absolute flux of sufficiently oxidizing volcanic S gases drove an uptick in sedimentary pyrite burial at a global scale (Olson et al., 2019; Scott et al., 2011). Both of these proposed mechanisms can been intriguingly linked to increased continental emergence following a major global tectonic event around 2.5 Ga (Bindeman et al., 2018; Flament et al., 2008) and were discussed in the Introduction section of this thesis.

In Chapter 3, we focus on the overlooked aspect of the pyrite-modulated oxygenation model, which is that Fe, and not just S, participated in the inorganic redox balance of the early atmosphere-ocean system. We propose that the specific role of the Fe cycle in surface oxidation can be simplified to the question: could Fe^{2+} oxidation in the oceans consume more O_2 than could be

exported by pyrite burial under the most favorable of conditions? To answer this first-order question, we must pivot from looking at qualitative trends in $\delta^{56}Fe$ records through time to pulling most quantitative information that we possibly can from a small number of carefully selected samples, in order to better quantify the relative sizes of the oxic and sulfidic Fe sinks through time. Highly fractionated pre-GOE pyrites (Rouxel et al., 2005), which sampled the marine Fe^{2+} reservoir but also participated in the sulfide burial process, are the key samples we use to address this quantitative problem. The barrier to understanding why pre-GOE pyrites are so isotopically light has always been that multiple processes, which can be broadly categorized into: (i) formation from a strongly fractionated Fe^{2+} pool that produced during Fe redox cycling, either through extensive partial oxidation (Planavsky et al., 2012; Rouxel et al., 2005), or partial dissimilatory Fe^{3+} reduction (DIR) (Archer and Vance, 2006; Severmann et al., 2008; Yamaguchi and Ohmoto, 2006); (ii) or partial pyritization from in a sulfide-limited regime (Guilbaud et al., 2011; Mansor and Fantle, 2019; Rolison et al., 2018); can plausibly produce $\delta^{56}Fe$ values < -3.0 ‰ in pyrite that are indistinguishable from each other. The conundrum this presents is akin to trying to solve equation with multiple unknowns (the processes listed above), while only having one variable ($\delta^{56}Fe$).

One way of introducing a second variable into this system is to measure a second isotope ratio of Fe. Iron has four isotopes: ^{54}Fe, ^{56}Fe, ^{57}Fe, and ^{58}Fe. Iron-58 has limited use for stable isotope geochemistry purposes because it its low relative abundance (0.2919 % of natural Fe) means that measuring it precisely is extremely challenging (Dauphas et al., 2017). This still leaves the opportunity to measure two isotope ratios, $\delta^{56}Fe$ and $\delta^{57}Fe$, doubling the number of variables we can apply to the pre-GOE pyrite formation question. At first glance, measuring two isotope ratios of the same element may not seem to add an extra independent variable for interpreting

fractionation processes, because the principles of stable isotope geochemistry hinge on fractionation processes being mass dependent. To first order, any mass dependent process must fractionate isotope ratios in proportion to the mass difference between the normalizing isotope and the isotope of interest. Therefore, mass dependence dictates that changes in $\delta^{56}Fe$ (the $^{56}Fe/^{54}Fe$ ratio) should be ~2/3 × the change in $\delta^{57}Fe$ (the $^{57}Fe/^{54}Fe$ ratio) for the same process. Plotting $\delta^{56}Fe$ *vs.* $\delta^{57}Fe$ for any mass dependently fractionated materials therefore is always expected to result in a linear array called a mass fractionation line (MFL) with a slope of ~2/3. However, in detail, the mass dependence of isotope fractionation processes is not strictly linear with mass, and different classes of fractionation processes can be associated with subtly different slopes for their MFLs (Dauphas and Schauble, 2016; Young et al., 2002), as shown in detail in Chapter 3. The differences in these slopes are so subtle that they are not considered in standard Fe isotope studies and resolving them required development of new higher precision 'triple Fe isotope' measurements (McCoy-West et al., 2018; Nie et al., 2017). For the processes invoked in producing extremely negative $\delta^{56}Fe$ in pre-GOE pyrites, the two classes of fractionation processes turn out to be broadly separable into: equilibrium isotope fractionation processes associated with redox processes, where Fe^{2+} and Fe^{3+} rapidly isotopically equilibrate with one another; and kinetic fractionation processes associated with the unidirectional precipitation of pyrite.

In Chapter 3, extensive work was undertaken to determine the slopes of the MFLs associated with processes invoked in the production of pre-GOE light isotope signatures (Fig. 3.1.). Once these endmember MFLs are calibrated, we apply the triple Fe isotope technique to the most isotopically depleted pyrites from the pre-GOE sedimentary record, and we show that their position in triple Fe isotope space relative to the endmember MFLs can be used to quantify, for the first time, the relative contributions to their isotopic composition from pyrite forming processes (that reflect the

availability of S relative to Fe); and redox processing of Fe^{2+} in the oceans (Figs. 3.2, 3.3). While undoubtedly still in the very early stages of understanding the full utility of this new isotopic proxy, in Chapter 3 we provide the most quantitative estimates to date for the relative sizes of the oxic and sulfidic sinks for Fe on productive continental shelves in the runup to the GOE, and explore the implications of these results for the role of Fe in the early oxygenation of Earth's atmosphere.

The content of this chapter is the accepted article for the publication:

Andy W. Heard1, Nicolas Dauphas, Romain Guilbaud, Olivier J. Rouxel, Ian B. Butler, Nicole X. Nie, Andrey Bekker, "Triple iron isotope constraints on the role of ocean iron sinks in early atmospheric oxygenation", Science, 2020, Vol. 370, Issue 6515, Pages. 446-449, https://doi.org/10.1126/science.aaz8821

Triple Iron Isotope Constraints on the Role of Ocean Iron Sinks in Early Atmospheric Oxygenation

Abstract

The role that iron played in the oxygenation of Earth's surface is equivocal. Iron could have consumed O_2 when Fe^{3+}-oxyhydroxides formed in the oceans, or promoted atmospheric oxidation via pyrite burial. Through high-precision Fe isotopic measurements of Archean-Paleoproterozoic sediments and laboratory grown pyrites, we show that the triple-Fe-isotopic composition of Neoarchean-Paleoproterozoic pyrites requires both extensive marine iron oxidation and sulfide-limited pyritization. Using an isotopic fractionation model informed by these data, we constrain the relative sizes of sedimentary Fe^{3+}-oxyhydroxide and pyrite sinks for Neoarchean marine iron. We show that pyrite burial could have resulted in O_2 export exceeding local Fe^{2+} oxidation sinks, thus contributing to early episodes of transient oxygenation of Archean surface environments.

Main Text

Irreversible changes to oxic and euxinic sedimentary iron sinks during the Archean and Paleoproterozoic were intimately linked with the oxygenation of Earth's atmosphere during the Great Oxygenation Event (GOE) beginning *ca*. 2.43 Ga (Gumsley et al., 2017; Holland, 1984). Early oxygenation coincided with enhanced sedimentary burial of iron sulfide (pyrite) driven by the greater availability of sulfate (Reinhard et al., 2009; Scott et al., 2011; Stüeken et al., 2012). Through the pyrite iron sink, enhanced volcanic SO_2 fluxes in the Neoarchean could have indirectly induced the release of oxygen via the microbial reduction of volcanically-derived sulfate and the sequestration of sulfide in sedimentary pyrite (Gaillard et al., 2011; Kump and Barley, 2007; Olson et al., 2019). Meanwhile, iron could have acted as a net sink of oxygen produced during oxygenic photosynthesis, if Fe^{2+} dissolved in the oceans was not sequestered in sediments as pyrite, but rather as Fe^{3+}-oxyhydroxides. It is presently unknown if the balance of iron oxyhydroxide and pyrite sinks in certain marine sediments resulted in the net production or removal of oxygen in the period leading to the GOE.

Sedimentary Fe isotopic records show large shifts across the GOE (Planavsky et al., 2012; Rouxel et al., 2005) (Fig. 3.1A), and reflect evolution of the Fe, S, and O cycles through the Archean and Paleoproterozoic (Heard and Dauphas, 2020). Pre-GOE pyrites can have $^{56}Fe/^{54}Fe$ ratios shifted by up to -3.5‰ relative to most terrestrial rocks, a degree of fractionation rarely seen in the post-GOE rock record (Rouxel et al., 2005). The interpretation of these pyrite Fe isotopic compositions is not straightforward, because they could be controlled by (*i*) the size of oxidizing iron sinks that removed isotopically heavy Fe^{3+}-oxyhydroxides, leaving an isotopically light dissolved Fe^{2+} pool from which pyrite formed (Planavsky et al., 2012; Rouxel et al., 2005); (*ii*) microbial dissimilatory Fe^{3+} reduction (DIR) that preferentially releases an isotopically light Fe^{2+} pool (Archer and Vance,

2006; Beard et al., 1999); and (*iii*) a kinetic isotope effect (KIE) accompanying partial pyrite precipitation, which produces isotopically light pyrite (Guilbaud et al., 2011; Rolison et al., 2018). The relative importance of these processes remains debated (Archer and Vance, 2006; Beard et al., 1999; Dauphas et al., 2017; Guilbaud et al., 2011; Heard and Dauphas, 2020; Marin-Carbonne et al., 2014; Marin-Carbonne et al., 2020; Planavsky et al., 2012; Rolison et al., 2018; Rouxel et al., 2005), and this uncertainty has hindered quantitative interpretation of the ancient iron cycle, exemplified by the fact that Fe isotope records have not yet constrained the degree to which Fe removal on highly productive continental margins was a net sink or source for early O_2 (Olson et al., 2019).

Here, we report triple-Fe-isotopic ratio measurements that allow us to remove ambiguities in interpretations of the pre-GOE iron cycle. This approach relies on our discovery that the main isotopic fractionation processes implicated in the formation of pre-GOE pyrites follow distinct isotopic mass fractionation laws (MFLs), which describe how different isotopic ratios of the same element covary (Dauphas and Schauble, 2016; Young et al., 2002). To resolve MFLs, measurement of Fe isotopic ratios must be at higher precision than is typically reported in analysis of ancient sediments. This approach has been used in igneous geochemistry to show that Fe isotopic variations in magmatic olivine followed a kinetic MFL for diffusive transport (McCoy-West et al., 2018), and in aqueous UV photo-oxidation experiments to investigate pathways to the deposition of iron formations (IF) (Nie et al., 2017). Measurements of this type, to a comparable or higher precision, are used more frequently in cosmochemistry to resolve nucleosynthetic anomalies in meteorite samples (Dauphas et al., 2008, p. 60; Schiller et al., 2020; Tang et al., 2009; Tang and Dauphas, 2012). For a given MFL, the ratio of $^{56}Fe/^{54}Fe$ to that of $^{57}Fe/^{54}Fe$ defines the slope

$\theta^{56/57} = \Delta\delta'^{56}Fe/\Delta\delta'^{57}Fe,$ (Eq. 1)

where $\Delta\delta'^{x}Fe$ is a change in $\delta'^{x}Fe$; where $\delta'^{x}Fe$ (‰) = 1000 $\ln[(^{x}Fe/^{54}Fe)_{sample}/(^{x}Fe/^{54}Fe)_{IRMM\text{-}014}]$; imparted by physical, chemical, or biological processes. The $\Delta\delta'^{x}Fe$ for natural samples is taken as the difference from the bulk silicate Earth, which is approximated by IRMM-014 (Dauphas et al., 2008; Dauphas and Schauble, 2016; Nie et al., 2017; Tang et al., 2009). As discussed below, we also ran pyrite synthesis experiments and there the $\Delta\delta'^{x}Fe$ value is taken as the difference from the starting material for each experiment. Isotopic trends following an array of MFLs are by definition mass-dependent. Apparent departures ($\epsilon'^{56}Fe$) from an arbitrary reference MFL (Dauphas et al., 2008; Dauphas and Schauble, 2016), which we choose here to be the high-temperature equilibrium limit law with $\theta^{56/57}$=(1/53.939-1/55.935)/(1/53.939-1/56.935)=0.678, are defined as,

$\epsilon'^{56}Fe = (\Delta\delta'^{56}Fe - 0.678 \times \Delta\delta'^{57}Fe) \times 10.$ (Eq. 2)

In $\epsilon'^{56}Fe$ *vs.* $\Delta\delta'^{57}Fe$ space, MFLs form straight lines whose slopes can be related to $\theta^{56/57}$ through,

$\epsilon'^{56}Fe = 10 \times (\theta^{56/57} - 0.678) \times \Delta\delta'^{57}Fe.$ (Eq. 3)

In order to establish the values of $\theta^{56/57}$ corresponding to two end-member hypotheses that have been put forward to explain the $\delta'^{56}Fe$ pyrite record (Guilbaud et al., 2011; Planavsky et al., 2012; Rouxel et al., 2005), we measured:

(*i*) A suite of IF samples that show a large range in $\delta'^{56}Fe$ values, including low $\delta'^{56}Fe$ values that most likely reflect precipitation from an iron pool that had experienced extensive iron oxidation (Tsikos et al., 2010) (Table 3.1). These samples are well-suited to characterize the MFL expected if sedimentary pyrite formed from a distilled pool of Fe^{2+} enriched in light Fe isotopes (low $\delta'^{56}Fe$) by precipitation of heavy (high $\delta'^{56}Fe$) Fe^{3+}-oxyhydroxides.

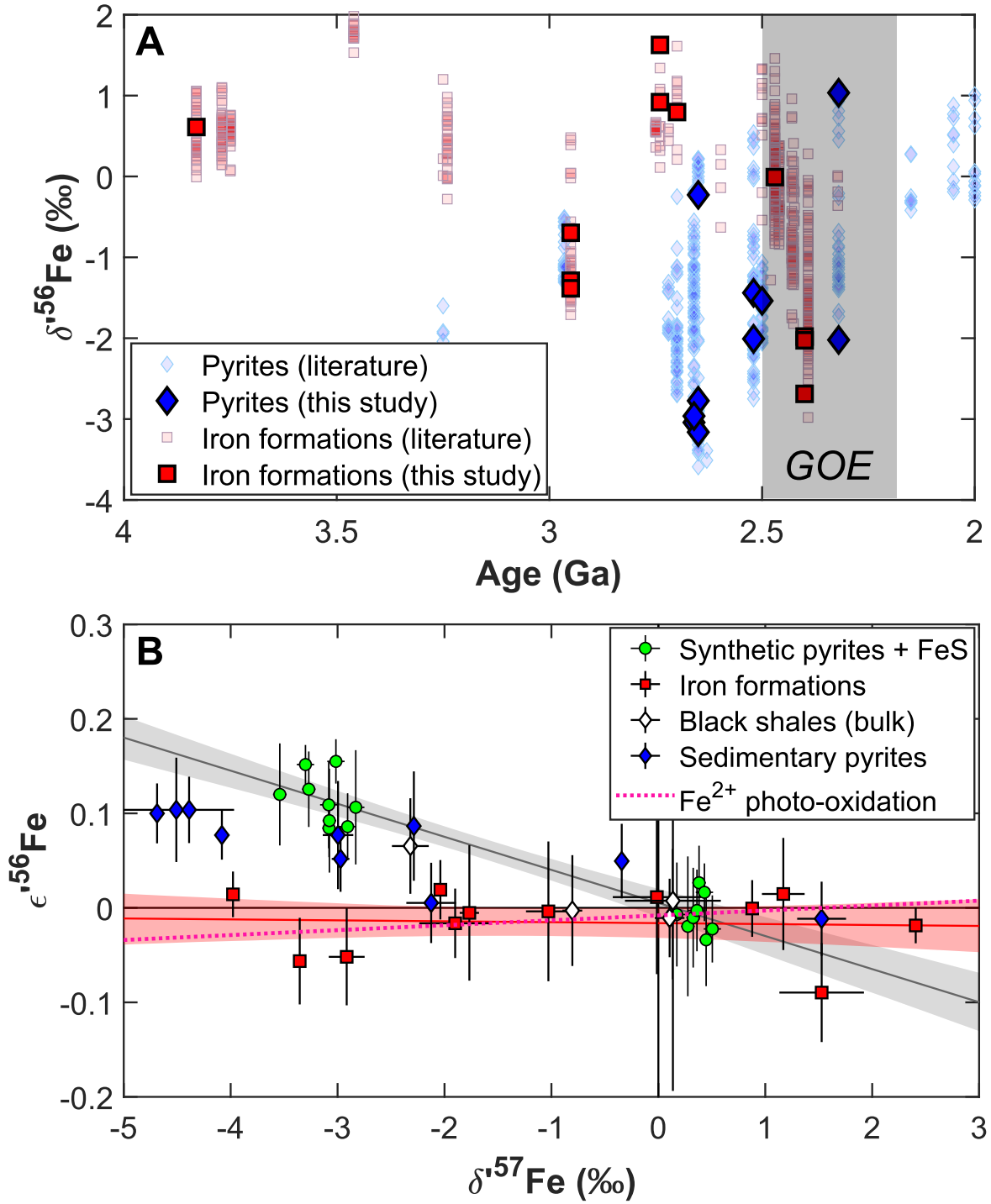

Figure 3.1. Iron isotope systematics of (*i*) pre-GOE sediments and natural pyrites, and (*ii*) synthetic pyrites and FeS produced in laboratory experiments (Tables 3.1 and 3.2). A. δ'^{56}Fe (relative to IRMM-014) values of IFs and pyrites analyzed in this study, plotted against their age (published IF and pyrite data compiled in (Heard and Dauphas, 2020) are also plotted for reference). B. Triple-Fe-isotopic systematics for IFs, pyrites, and black shales in ϵ'^{56}Fe *vs.* $\Delta\delta'^{57}$Fe space. $\Delta\delta'^{57}$Fe values are reported as differences from IRMM-014 and the starting material of experiments, for the natural samples and the synthetic pyrites, respectively…

Figure 3.1. continued Error bars and envelopes are 95% confidence intervals. The slopes of end-member MFLs associated with iron-redox processes (red line and red envelope) and kinetic isotope effects (black line and grey envelope) during pyritization are constrained through analysis of isotopically light Mn-rich IFs and laboratory pyrite precipitated via the H_2S pathway (Guilbaud et al., 2011; Rickard and Luther, 2007) (Appendix), respectively. The slope of the IF MFL agrees well with the theoretical high-temperature equilibrium limit law (defined by the horizontal axis, (Dauphas and Schauble, 2016)), and an experimentally determined MFL for Fe^{2+} oxidation (via UV photo-oxidation (Nie et al., 2017)), implying control by Fe^{2+}-Fe^{3+} equilibrium. Synthetic pyrite and FeS define a kinetic MFL for sulfide precipitation. Pre-GOE pyrites fall in an intermediate space between redox-equilibrium and kinetic endmembers.

(*ii*) Experimental products of pyrite synthesis via the FeS-H_2S pathway (Fig. 3.5, Table 3.2), which produced pyrite that is isotopically lighter by as much as -2.4‰ in δ'^{56}Fe relative to the initial FeS pool (Fig. 3.5) (Appendix). In these experiments, we precipitated pyrite in anoxic conditions from an FeS precursor (Appendix) following previously established protocols (Guilbaud et al., 2011; Rickard, 1997). The experiment yielded a pyrite precipitate and a residual FeS phase that were separated using a calibrated sequential extraction (Guilbaud et al., 2011), enabling us to measure the isotopic fractionation between the reactant and product (Fig. 3.5). This fractionation represents a unidirectional KIE associated with pyrite precipitation, because once formed pyrite is highly insoluble and does not readily exchange with iron in solution. These pyrite samples represent a cumulative product reservoir rather than an instantaneous precipitate, but any deviations from an intrinsic Fe isotope MFL caused by cumulative effects are unresolvable within analytical uncertainties (Appendix). Therefore, these experimental run products are well suited to characterize the MFL expected if sedimentary pyrite formation imparted a KIE on Fe isotopes.

The IFs, which were formed in the oceans after varying degrees of partial Fe^{2+} oxidation, define a slope of $\theta^{56/57}_{ox}$=0.6779±0.0006 for the oxidizing iron sink (here and elsewhere, the error bars are 95% confidence intervals), which agrees with iron photo-oxidation experiments (Nie et al., 2017) and is consistent with the view that equilibrium isotope exchange dominates during Fe^{2+} oxidation (Dauphas and Schauble, 2016; Nie et al., 2017). The pyrite-precipitation experiments involving a

KIE gave $\theta^{56/57}_{KIE}$=0.6743±0.0005. Triple-Fe-isotopic slopes for the two end-member scenarios are measurably distinct (Fig 3.1B). Thus, we can use these slopes to address what caused Fe isotopic variations in pre-GOE sedimentary pyrites.

We analyzed a suite of pre-GOE Neoarchean-Paleoproterozoic (2.66-2.32 Ga) pyrites with depleted δ'^{56}Fe values (as low as -3.1‰) and four black shales from the same formations (Fig 3.1A, Table 3.1). The pyrites and shales fall in an intermediate space on the triple-Fe-isotopic diagram between the endmember MFLs for Fe oxidation and pyrite precipitation (Fig 3.1B). We do not interpret this data array as following a single MFL, because the pyrite and shale samples come from several distinct formations and each sample requires contributions from more than one fractionation process (with distinct MFLs). More likely, pre-GOE pyrite and shale δ'^{56}Fe values record a two-step process; partial marine Fe^{2+} oxidation during upwelling of Fe^{2+}-rich deep waters (Rouxel et al., 2005), and subsequent kinetic fractionation during partial, sulfide-limited pyrite formation from the remaining Fe^{2+} reservoir (Guilbaud et al., 2011; Rolison et al., 2018; Rouxel et al., 2006). In this model, Fe-oxyhydroxide and pyrite sinks sequestered iron upwelling from deep oceans lacking a discrete redoxcline that allowed progressive partial Fe^{2+} oxidation, towards black shale depositional settings (Fig 3.2A, 3.9) (Bekker et al., 2010; Planavsky et al., 2012). The loss of such depleted $\delta'^{56}Fe_{py}$ values after the GOE, which incidentally would prevent us resolving of MFLs for younger samples, indicates that prevailing conditions of sulfide-limitation, and progressive partial Fe oxidation, were diminished following biogeochemical overturn taking place from 2.32 Ga (Heard and Dauphas, 2020).

The pyrite samples that we analyzed are nodular, deforming sedimentary laminations around them, and must have formed in the sediment during early diagenesis. They most likely inherited their Fe isotopic compositions from pyrite precipitated in porewater near the sediment-seawater interface,

but in some cases dissolution-reprecipitation has eradicated their primary textural features and caused recrystallization into massive forms. *In situ* work on Archean pyrites suggests that these secondary texture-altering processes do not eradicate primary sedimentary Fe isotopic signatures (Marin-Carbonne et al., 2020). A major source of iron to porewaters would have been downward diffusion of overlying Fe^{2+}-rich seawater into the sediments (Rouxel et al., 2005). The crux of the debate is whether pyrite simply inherited the Fe isotopic composition of seawater, which was by far the largest exchangeable Fe reservoir, or whether some kinetic isotopic fractionation was expressed, if pyritization was incomplete due to limited sulfide supply. The new triple-Fe-isotopic measurements reported here indicate that the latter case was true for the low $\delta'^{56}Fe$ pre-GOE pyrites we studied.

For any isotopically light pyrite sample, we can estimate contributions to the $\delta'^{56}Fe$ value from prior oxidation of the Fe^{2+} pool, and the KIE during pyritization. To do so, we first calculate contributions of Fe-oxidation to $\delta'^{56}Fe$ values of the water mass ($\delta'^{56}Fe_w$) from which pyrite formed, from intercepts of the kinetic pyritization MFL passing through individual datapoints with the oxidation MFL (Fig 3.2B). We then determine the Fe isotopic fractionation imparted by pyritization by taking the difference in $\delta'^{56}Fe$ values between those of pyrite and $\delta'^{56}Fe_w$ (Figs. 3.2B, 3.7).

Our approach assumes that partial iron oxidation and pyritization were the main drivers of $\delta'^{56}Fe$ variations in sedimentary pyrite. It is however conceivable that some porewater or marine Fe^{2+} was sourced from DIR (Archer and Vance, 2006; Beard et al., 1999; Severmann et al., 2008), a microbial metabolism that seems to have been active since at least 3.2 Ga (Marin-Carbonne et al., 2020). This represents a source of uncertainty in our model. Experiments to date suggest that the isotopic fractionation during DIR reflects equilibration of Fe^{2+} and Fe^{3+} after the reduction step

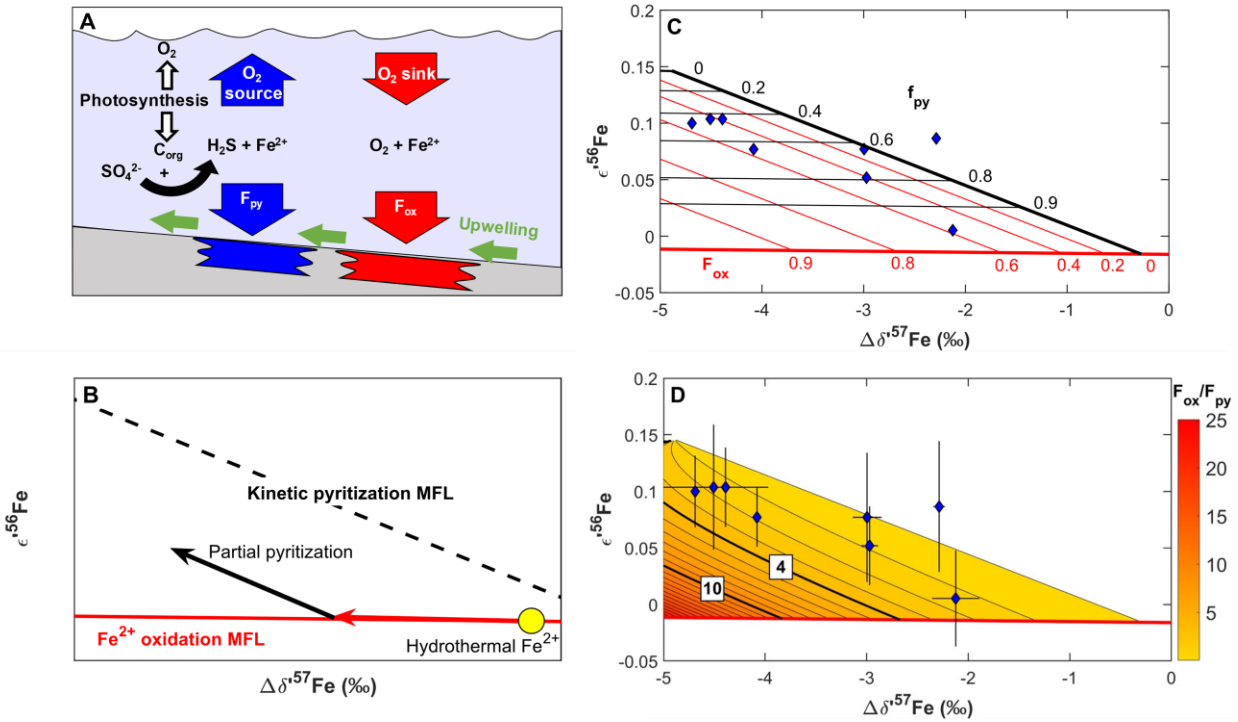

Figure 3.2. Interpretation of triple-Fe-isotope compositions of isotopically light pyrites. A. Schematic representation of the Fe sinks (F_{ox} and F_{py}), and their inferred links to O_2 cycling in the pre-GOE oceans. B. Triple Fe isotopic interpretation of the two-step process involved in pyrite formation. Iron with starting composition resembling hydrothermal fluids (yellow circle; $\Delta\delta'^{57}Fe$=-0.3‰ relative to IRMM-014 with $\epsilon'^{56}Fe$ on the empirical MFL defined by IFs) is oxidized, driving residual Fe^{2+} to lighter $\delta'^{57}Fe$ compositions along the Fe^{2+} oxidation MFL. Partial pyrite precipitation from this residual Fe^{2+} subsequently causes fractionation along the kinetic pyritization MFL. The approach is detailed in Figure 3.7 with mathematical derivations provided in the Appendix. C. Pyrite data and contours for F_{ox} and f_{py} in triple-Fe-isotopic space. Both Fe^{2+} oxidation and pyritization are modeled using Rayleigh distillations. Iron isotopic fractionation during iron oxidation is assumed to reflect the composition of residual dissolved Fe^{2+} experiencing fractional removal of Fe^{3+}-oxyhydroxide upon upwelling into oxidizing near surface waters. Iron isotopic fractionation during pyritization is assumed to reflect the composition of the cumulative product, as we analyzed relatively large pyrite nodules. The fraction of total upwelled Fe deposited as pyrite is calculated as $F_{py} = f_{py} \times (1 - F_{ox})$. D. Pyrite data and contours of F_{ox}/F_{py} (relative size of oxyhydroxide and pyrite sedimentary Fe sinks). Bold contours at 4 and 10 indicate thresholds for net O_2 source *vs.* sink behavior for volcanic H_2S/SO_2 inputs ratios of 1 (Gaillard et al., 2011) and 0 (Olson et al., 2019), respectively. In B.-D., $\Delta\delta'^{57}Fe$ values are reported as differences from IRMM-014.

(Crosby. et al., 2007), and therefore we expect that it would fall into the same class of redox equilibrium processes that define the Fe^{2+} oxidation MFL. The observed departure of natural pyrite from this MFL therefore implies that regardless of the potential role of DIR, a KIE during pyritization is also required to explain pre-GOE $\delta'^{56}Fe_{py}$ values.

The fraction of Fe^{3+}-oxyhydroxide removed to give the $\delta'^{56}Fe_w$ value on the intercept (F_{ox}=Fe in oxyhydroxide sink/total Fe sink), and the fraction of pyrite removed from that remaining Fe^{2+} pool (f_{py}=Fe in pyrite/Fe remaining after Fe removal to the oxyhydroxide sink), were calculated under Rayleigh fractionation conditions (Figs. 3.2, 3.7; Table 3.3). The setting that we envision is progressive Fe^{2+} oxidation as Fe^{2+}-rich deep-waters are upwelled towards more oxidizing photic zone conditions (Planavsky et al., 2012; Rouxel et al., 2005) (Fig. 3.9). We also explored a 1-D dispersion-reaction steady-state model for water-column Fe^{2+} oxidation, and find that our conclusions using Rayleigh distillation are robust (Czaja et al., 2012). We treated pyrite as a cumulative product of pyritization. The fractional pyrite sink, F_{py}, for iron in the whole depositional system is $F_{py}=f_{py} \times (1–F_{ox})$. In Fig 3.2D, we plot contours of constant F_{ox}/F_{py}, showing that $\epsilon'^{56}Fe$ measurements are diagnostic of the relative size of the oxide and pyrite iron sinks.

To fully propagate the effect of uncertainties in sample measurements and $\theta^{56/57}$ values for the end-member processes on uncertainties in F_{ox}, f_{py}, and F_{py}, we used a Monte-Carlo simulation (Fig 3.3). Estimates for F_{py} span 10 to 80 % of the upwelled iron pool (within 95 % confidence interval) for the low $\delta'^{56}Fe$ pyrites that we studied. With initial pre-GOE deep-water [Fe^{2+}] concentration ~50 µM (Holland, 1984), the pyrite sink could have removed 5 to 40 µM of dissolved iron. This requires ~10 to 80 µM of seawater-dissolved sulfate to be microbially reduced to sulfide, ~350 to 1,400 times less than the modern seawater sulfate concentration of 28 mM, but within recent estimates for Archean seawater sulfate based on S isotope modelling (Jamieson et al., 2013; Crowe

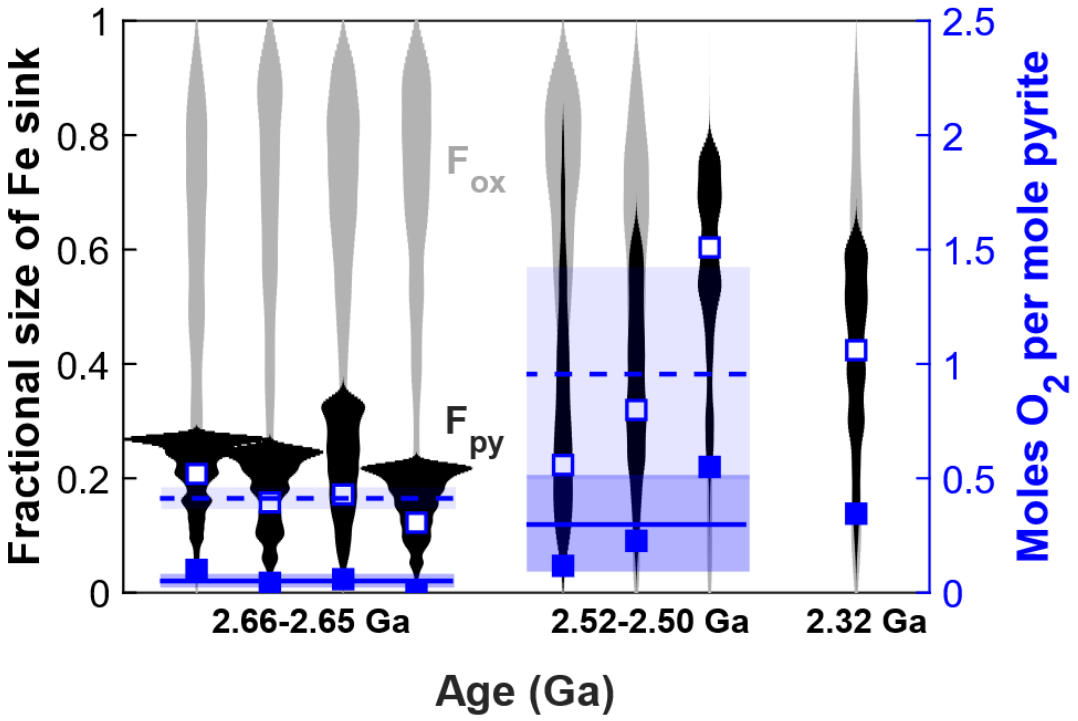

Figure 3.3. F_{ox} and F_{py}, and molar O_2 yield estimates from a Monte Carlo error propagation. Violin plots for probability densities of fractional size of Fe sink (grey: F_{ox}, black: F_{py}) determined from propagation of errors on the $\epsilon'^{56}Fe$ and $\Delta\delta'^{57}Fe$ values for each measured pyrite and the errors on the slopes of the MFLs. Blue filled and open squares: estimated molar O_2 yields per mole of pyrite buried for individual samples using H_2S/SO_2 input ratios of 1 (Gaillard et al., 2011) and 0 (Olson et al., 2019), respectively. Blue solid and dashed lines and shaded areas: mean molar O_2 yields for H_2S/SO_2 input ratios of 1 (Gaillard et al., 2011) and 0 (Olson et al., 2019), respectively, and 95% confidence intervals for pyrites in two age bins.

et al., 2014). For the ~2.65 Ga Jeerinah and Lokammona formations, we infer that as little as 10% of iron upwelled onto the shelf was deposited as pyrite (Figs. 3.2C, 3.3, 3.8).

When volcanic SO_2 is the primary sulfur source, burial of reduced sulfur in pyrite represents a net oxidation of Earth's surface (Gaillard et al., 2011; Kump and Barley, 2007; Olson et al., 2019) (Fig 3.2A). For example, the reaction $2SO_2 + H_2O + Fe^{2+} \rightarrow FeS_2 + 2H^+ + 2.5O_2$; describing the net effect of SO_2 photolysis and hydrolysis, cyanobacterial photosynthesis, microbial sulfate reduction, and pyrite precipitation; indicates that pyrite burial can indirectly drive net O_2 export to the atmosphere-ocean system (Olson et al., 2019). The reaction provides a maximum estimate for O_2 export during pyrite burial because: (*i*) a more reduced original sulfur source would weaken

the net oxidative effect of pyrite burial, and (*ii*) other types of primary productivity, such as anoxygenic photoferrotrophy, which oxidizes Fe^{2+} directly, could have contributed organic matter for sulfate reduction, but only cyanobacterial activity would have produced O_2. A more realistic estimate for the volcanic H_2S/SO_2 emission ratio at ~1 (Gaillard et al., 2011) would result in a net 1 mole O_2 yield per mole of pyrite buried.

To oxygenate the atmosphere via pyrite burial, the produced O_2 would also need to overcome O_2 buffers in the ocean, primarily the upwelled Fe^{2+} flux (Fig 3.2A). Oxygen-driven Fe^{2+} oxidation consumes 0.25 moles of O_2 per mole of Fe^{3+} buried, so net O_2 sources and sinks will be balanced when F_{ox}/F_{py} is 4 and 10 for volcanic H_2S/SO_2 emission ratios of 1 (*7*) and 0 (*8*), respectively. Depending on F_{ox}/F_{py} ratios, iron deposition on productive continental margins could have been a net source or sink for O_2 in the atmosphere-ocean system. Triple-Fe-isotopic systematics are diagnostic of F_{ox}/F_{py} ratios (Fig 3.2D). Pre-GOE pyrite data all fall above the F_{ox}/F_{py}=4 contour, and the F_{ox}/F_{py}=10 contour is outside of the error bar on pyrite $\epsilon'^{56}Fe$ values. We can therefore rule out net O_2 sink-like behavior for the case where SO_2 dominated Neoarchean volcanic emissions. Even with a conservative volcanic H_2S/SO_2 ratio of 1 (Gaillard et al., 2011), our data support a net O_2 source in Neoarchean pyrite-forming environments, particularly after 2.52 Ga (Figs. 3.2D, 3.3). The inference that the oxic sink did not overwhelm local oxygen sources associated with pyrite deposition also holds if F_{ox} is calculated using a 1-D dispersion-reaction model (Appendix) (Czaja et al., 2012). Average results from Monte Carlo simulations imply that even in the cases where we find the smallest F_{py} and largest F_{ox}, in ~2.65 Ga Jeerinah and Lokamonna formation pyrites, some O_2 could have been exported to the atmosphere-ocean system during pyrite burial after exhausting local Fe^{2+} oxidation sinks. We focused on the lowest $\delta'^{56}Fe$ pyrites because these give us the most leverage to characterize MFLs. Pre-GOE pyrites, while displaying much more negative $\delta'^{56}Fe$

values (average of about -2 ‰) than post-GOE pyrites (Fig 3.1A), span a range of values. The more typical pyrites could have formed from a seawater reservoir that did not experience such protracted Fe^{2+} oxidation (Planavsky et al., 2012; Rouxel et al., 2005) or may reflect higher degrees of pyritization. The amount of oxygen produced in such settings (moles of O_2 generated per mole of pyrite buried) would have been higher than the values calculated here for the isotopically lightest pyrites. The conclusion that iron oxide burial did not locally buffer O_2 generated by pyrite burial in the Neoarchean is therefore robust.

The triple-Fe-isotopic proxy provides new insights into the iron cycle in Earth's early oceans. Before the GOE, large and probably fluctuating hydrothermal and riverine iron fluxes to the oceans (Bekker et al., 2010) were removed to two sedimentary sinks (Figs. 3.2A, 3.8). The major sink was Fe^{3+}-oxyhydroxides that were deposited from upwelling water masses in the oceans that lacked a discrete redoxcline and allowed protracted partial iron oxidation (Planavsky et al., 2012; Rouxel et al., 2005). The second iron sink was on highly productive continental margins, where deposition of pyrite-rich sediments was generally sulfide-limited due to a small marine sulfate pool. Small relative changes in iron removal to these oxyhydroxide and sulfide sinks potentially led to perturbations in the net O_2 supply to the atmosphere-ocean system that fueled shallow-marine oxygen oases (Olson et al., 2013; Ostrander et al., 2019) and helped prime the Earth system for 'whiffs' of atmospheric O_2 in the runup to the GOE (Anbar et al., 2007).

Acknowledgments: Discussions with Stephanie Olson Jake Waldbauer, Sarah Aarons, and Sam Holo were appreciated. Nigel Brauser and Anne Davis are thanked for comments on the clarity of the manuscript. We thank Angelo Olinto, James Passolano, Dan DeYoung, James Eason, Michael Grosse, Fred Ciesla, Kimberly Mormann, Jolene Hanchar, Sarah Lippert, Ronald Klain, Victor

Gavin, Steven Bandyk, Alfredo Peralta, Chris Kielch, Thomas Indelli, Timo Hopp, and Mike Andrews and the UJAMAA Construction team for renovating our laboratory infrastructure and supporting its operation. This work was funded by NASA grants 80NSSC17K0744 to ND and AWH (Habitable Worlds), 359NNX17AE86G to ND (LARS), NNX17AE87G and 80NSSC20K0821 to ND (Emerging Worlds), and NSF grant EAR-2001098 to ND (CSEDI). AWH was supported by an Eckhardt Scholarship from the University of Chicago. Participation by AB was supported by NSERC Discovery and Acceleration grants.

Author contributions: AWH, ND, and NXN initiated the study. OJR and AB provided samples. AWH, RG, and IBB performed the pyrite synthesis experiments. AWH and NXN measured iron isotopic compositions. AWH and ND performed modeling. All authors contributed to interpretation of results. AWH, ND, and AB wrote the first draft of the manuscript, which was subsequently edited with input from all authors.

Competing financial interests: The authors declare that they have no competing financial interests.

Data availability: All original data are reported in Tables in the Supplementary Online Materials. Literature iron isotope data presented in Figure 3.1A are compiled in the EarthChem library at https://doi.org/10.1594/IEDA/111446

Appendix

Materials and Methods

Pyrite synthesis experiments

To constrain the triple-Fe-isotopic expression of pyrite precipitation, we performed new laboratory pyrite precipitation experiments in an anoxic environment. Pyrite was synthesized at the University of Edinburgh, via the FeS-H_2S pathway following the methodology of Guilbaud et al. (2011) (Guilbaud et al., 2011) and references therein, which produces pyrite precipitates from an FeS_m (mackinawite) reactant. We provide a brief overview here, and the detailed protocol is described below. First, we produced a solid FeS_m precursor by combining equimolar solutions of Fe^{2+} and sulfide. This solid reactant was filtered and freeze dried and then sealed into reaction vessels in a pH buffer solution. The sealed reaction vessels were then attached to a gas-mixing manifold and injected with a controlled volume of H_2S, which was generated by reacting sodium sulfide with sulfuric acid. The vessels were resealed, and the pyrite precipitation reaction was allowed to proceed for a few hours to a few days, after which pyrite and residual FeS were separated using a calibrated chemical extraction technique (Guilbaud et al., 2011). We measured the triple-Fe-isotopic fractionation between FeS and pyrite, which has been shown previously to be the reaction where a large kinetic isotope effect is imparted to pyrite (Guilbaud et al., 2011).

All reagents were of analytical grade, and solutions were prepared using 18 MΩ/cm deionized water and sparged for 30 min with O_2-free grade N_2 before use. Solutions were prepared and solid FeS_m was synthesized in N_2-filled recirculating Saffron alpha anoxic chamber under O_2-free conditions. FeS_m was precipitated by mixing 100 mL of 0.6 M iron (Fe^{2+}) solution prepared with Mohr's salt [$(NH_4)_2Fe(SO_4)_2 \cdot 6H_2O$; Sigma Aldrich] with 100 mL of 0.6 M sulfide solution made with $Na_2S \cdot 9H_2O$ (Sigma Aldrich). This reaction produced a black precipitate. The precipitate was

filtered using a Buchner filter with Whatman™ No 1 filter paper, resuspended in sparged water and the filtration was repeated three times. The freshly precipitated FeS_m was freeze-dried overnight on a Mini-Lyotrap (LTE) freeze-dryer then transferred back to the anoxic chamber and stored under O_2-free conditions until use. The low-metal complexing MOPS (3-(N-morpholino)propanesulfonic acid, pKa = 7.31, Fisher) buffer was made by dissolution of its sodium salt in sparged water, buffered to pH 6 by NaOH titration. Redox buffer Ti^{3+} citrate, required for poising the Eh during sample recovery, was prepared by adding 5 mL 15% $TiCl_3$ to 50 mL 0.2 M Na citrate and buffered to pH 7 with Na_2CO_3. The solutions were stored in the glove box under O_2-free conditions until use.

The pyrite precipitation experiments were prepared in the glove box. Approximately 300 mg of the freeze-dried FeS_m was weighed into serum bottles, 10 mL of 0.05 M MOPS buffer solution was added, and the bottles were sealed with rubber stoppers and aluminum crimper seals. The sealed bottles were attached to a gas transfer manifold via a hypodermic needle inserted through the rubber stopper, and the manifold and reaction bottle were flushed with O_2-free grade N_2 and pumped down to -14 PSI (-97 kPa) three times. A sealed serum bottle containing 800 mg solid $Na_2S{\cdot}9H_2O$ was attached to the manifold via a hypodermic needle and flushed and pumped three times. A syringe was used to inject 2 mL of sparged, 50 vol% H_2SO_4 into the $Na_2S{\cdot}9H_2O$-containing bottle to generate H_2S. After H_2S transfer into the FeS_m-containing serum bottle, N_2 was added until pressure in the serum bottle was at only slight under-pressure relative to atmospheric pressure (~ -2.5 PSI or ~ -17 kPa). The needle holes in the serum bottle septa were covered with silicone sealant and the bottles were transferred to an oven at 40°C to allow the pyrite precipitation reaction to take place. After different, pre-determined reaction durations (between ~5

and 120 hours), the serum bottle reaction vessels were removed from the oven and frozen to stop the reaction.

Once frozen, the serum bottles were unsealed under flushing N_2 and excess H_2S in the headspace was removed. The bottles were then re-stoppered, the stoppers pierced with a hypodermic needle under flushing N_2, and the bottles left in the freeze-dryer for a day. The freeze-dried serum bottles were transferred to the anoxic chamber, and 2 mL sparged water and a few drops of the Ti^{3+} citrate were added to poise the Eh at low negative values to prevent FeS_m oxidation and ensure full dissolution of FeS_m following a previously established preferential dissolution protocol (Guilbaud et al., 2011; Rickard et al., 2006) . The serum bottles were resealed and moved to a fume hood for preferential dissolution. In the fume hood, 20 mL of sparged 1.2 M HCl was injected into the serum bottle via hypodermic syringe to fully dissolve only FeS_m and MOPS salt. Remaining solids, essentially pyrite, were separated by filtering on a 0.45 µm Millipore filter, and rinsing with sparged water. The FeS_m in HCl solutions were adjusted to 50 mL by addition of water and a 10 mL (20%) cut was dried down in clean Savillex Teflon beakers for transport and isotopic analysis. Pyrite was dissolved with drops of concentrated HNO_3, solutions were adjusted to 50 mL by addition of water and a 10 mL (20%) cut was dried down in clean Savillex Teflon beakers for transport and isotopic analysis. A 20 mL cut was taken for pyrite samples SB5 Py and SB6 Py, which were produced over short (4.66 hours) duration experiments and for which low pyrite iron yields were anticipated. In the Origins Laboratory at the University of Chicago, samples were dissolved in Aqua Regia with drops of 11 M $HClO_4$ at 140°C, and dried down twice, then treated three times with 2 mL of H_2O_2 to remove organic carbon salts left in the FeS_m solutions by MOPS. The solutions were then re-dissolved in 5 mL 6 M HCl for iron purification. A small aliquot of each solution was dried down and redissolved in 0.3 M HNO_3 to check for iron concentration of

these solutions using MC-ICP-MS and determine the correct amount of volume of each sample solution to be passed through iron purification.

Analytical methods

Analytical procedures for iron purification and isotopic measurements followed standard procedures used at the Origins Laboratory of The University of Chicago (Craddock and Dauphas, 2011; Dauphas et al., 2009; Nie et al., 2017; Tang et al., 2009; Tang and Dauphas, 2012). Samples were prepared from powders of black shale and IF materials, and hand-picked pyrite grains. Sample masses ranged between 12-22, 2-6, and 13-84 mg for black shale, IF, and pyrite grains, respectively. Samples were digested in clean Savillex Teflon beakers. First, 1 ml of 28 M HF + 0.5 ml of 15 M HNO_3 + a few drops of 11 M $HClO_4$ was added, and closed beakers were heated at 130ºC. Samples were evaporated to dryness and re-dissolved in Aqua Regia (0.75 ml of 11 M HCl + 0.25 ml of 15 M HNO_3) and a few drops of 11 M $HClO_4$, before heating and evaporation was repeated. The Aqua Regia + $HClO_4$ step was repeated 3 times to release all iron to solution. Samples were evaporated to dryness and 0.5 ml of 6 M HCl or 10 M HCl was added, depending on the purification procedure to be used. Larger volumes of the same acid were used for digestion of pyrite grains, which contained greater masses of Fe. Iron purification made use of both the standard 'short column' procedure, which is now routinely used in the Origins Laboratory (Craddock and Dauphas, 2011; Dauphas et al., 2009), and a 'long column' procedure designed to more effectively eliminate Cu from the matrix (Tang et al., 2009; Tang and Dauphas, 2012), which was a potential concern for sulfide samples.

Short-column iron purification: Disposable Bio-Rad Poly-Prep polyethylene columns were filled with 1 ml of AG1-X8 200-400 mesh Cl-form anion exchange resin. The resin was pre-conditioned with 10 ml of MilliQ H_2O, 5 ml of 1 M HNO_3, 10 ml of MilliQ H_2O, 9 ml of 0.4 M HCl, 5 ml of

MilliQ H_2O, and 2 ml of 6 N HCl. Samples were loaded onto columns in 0.25 ml of 6 M HCl. Matrix and interfering elements were eliminated by passing 8 ml of 6 M HCl through the column. Iron was eluted with 9 ml of 0.4 M HCl and recovered in clean Teflon beakers. Samples were evaporated to dryness and re-dissolved in 0.25 ml of 6 M HCl, before repeating the column procedure a second time with new resin. All experimentally synthesized pyrite and FeS_m samples were also purified using this procedure.

Long-column iron purification: This alternative iron purification procedure was used to eliminate Cu as a potentially significant matrix element associated with natural sulfide phases. Reusable 30 ml Savillex Teflon columns with a 0.64 cm ID cut to 10.5 cm length were loaded with 3 ml of AG1-X8 anion exchange resin. The resin was preconditioned with 10 ml of MilliQ H_2O, 10 ml of 0.4 M HCl, 5 ml of MilliQ H_2O, 10 ml of 0.4 M HCl, and 4 ml of 10 M HCl. Samples were loaded onto columns in 0.25 ml of 10 M HCl. Matrix and interfering elements were eliminated by passing 4.5 ml of 10 M HCl, and 30 ml of 4 M HCl, the latter to eliminate Cu. Iron was eluted with 9 ml of 0.4 M HCl and recovered in clean Teflon beakers. Samples were evaporated to dryness and re-dissolved in 0.25 ml of 10 M HCl before repeating the column procedure with new resin.

Iron isotopic compositions were measured on a Neptune MC-ICPMS at the University of Chicago. Analyses were made of the extent of isotopic fractionation (δ' values), and the departure from a reference mass-dependent fractionation law (ϵ'). The Fe isotopes at masses 54, 56, 57, and 58 were measured simultaneously along with ^{53}Cr and ^{60}Ni for correction of ^{54}Cr and ^{58}Ni interferences on ^{54}Fe and ^{58}Fe, respectively. The ^{53}Cr and ^{60}Ni interferences were corrected for using the exponential law. All the Fe isotopes have molecular interferences with argide ions ($^{40}Ar^{14}N^+$, $^{40}Ar^{16}O^+$, $^{40}Ar^{16}O^1H^+$, and $^{40}Ar^{18}O^+$), which present a significant hindrance to obtaining the requisite precision to resolve mass-dependent fractionation laws. Therefore, measurements were

made on the flat-topped peak shoulder in high-resolution mode using a standard Neptune entrance slit. A few analyses were done at ultra-high resolution using a Thermo Element 2 slit. Results were consistent with those obtained using the standard HR method, but offered no improvement in precision while requiring higher iron concentrations to obtain the same signal. Nickel or aluminum sampler and H skimmer cones were used. Standard-sample bracketing was used to correct isotopic ratio measurements for instrumental mass fractionation, and Fe isotopic ratios of samples are reported relative to the average isotopic ratios of the bracketing standard solutions of IRMM-524, which has an identical Fe isotopic composition to IRMM-014. The exponential law was initially used to calculate ϵ values by fixing $^{57}Fe/^{54}Fe_{std}$ to 0.362549, the value of IRMM-014. The δ and ϵ values of samples are given by:

$$\delta = \left[\left({}^{i}Fe/{}^{54}Fe \right)_{sample} / \left({}^{i}Fe/{}^{54}Fe \right)_{std} - 1 \right] \times 10^{3}, \qquad \text{(Eq. 4)}$$

$$\epsilon = \left[\left({}^{i}Fe/{}^{54}Fe \right)^{*}_{sample} / \left({}^{i}Fe/{}^{54}Fe \right)^{*}_{std} - 1 \right] \times 10^{4}, \qquad \text{(Eq. 5)}$$

and the logarithmic forms, δ' and ϵ', are given by:

$$\delta' = \ln \left[\left({}^{i}Fe/{}^{54}Fe \right)_{sample} / \left({}^{i}Fe/{}^{54}Fe \right)_{std} \right] \times 10^{3}, \qquad \text{(Eq. 6)}$$

$$\epsilon' = \ln \left[\left({}^{i}Fe/{}^{54}Fe \right)^{*}_{sample} / \left({}^{i}Fe/{}^{54}Fe \right)^{*}_{std} \right] \times 10^{4}, \qquad \text{(Eq. 7)}$$

where i = 56, 57, or 58 and the * indicates that ratios were corrected for mass fractionation by internal normalization to a fixed reference $^{57}Fe/^{54}Fe$ ratio using the exponential law with $\theta^{56/57} = \ln\left(m_{i_{Fe}}/m_{54_{Fe}}\right) / \ln\left(m_{56_{Fe}}/m_{54_{Fe}}\right) = 0.672$, using the following equation,

$$\ln\left({}^{i}Fe/{}^{54}Fe \right)^{*}_{sample,\ corrected} = \ln\left({}^{i}Fe/{}^{54}Fe \right)_{sample,\ measured} - \ln \frac{\left({}^{57}Fe/{}^{54}Fe \right)_{sample,\ measured}}{\left({}^{57}Fe/{}^{54}Fe \right)_{fixed\ reference}} \frac{\ln\left(m_{i_{Fe}}/m_{54_{Fe}} \right)}{\ln\left(m_{57_{Fe}}/m_{54_{Fe}} \right)}. \qquad \text{(Eq. 8)}$$

Bracketing standards were also internally normalized using the same exponential law. The bracketing standards were solutions of IRMM-524, which has the same isotopic composition as IRMM-014.

Subsequent to measurements, data were renormalized to the high-temperature equilibrium limit law running through IRMM-014 with $\theta^{56/57} = 0.678$, for display on Figs. 3.1B, 3.2B-D, consistent with the common convention used with other isotopic systems (*e.g.* Bindeman et al., 2018; Farquhar et al., 2003; McCoy-West et al., 2018). The renormalization of ϵ'^{56} values was done using

$$\epsilon'_{\text{high-T eq}} = \epsilon'_{\text{exp}} - 10 \times (0.678 - 0.672) \times \Delta\delta'^{57}\text{Fe}. \qquad \text{(Eq. 9)}$$

Both the data normalized to the exponential law and to the high-temperature equilibrium limit law are presented in Tables 3.1 and 3.2, and a version of Figure 3.1B using normalization to the exponential law is shown on Figure 3.4.

Samples and standards were measured in 0.3 M HNO_3 and introduced into the plasma torch using a Cetac Aridus II or ESI Apex Omega desolvating nebulizer system with no auxiliary N_2 flow. On-peak zero was determined at the start of each measurement sequence by analyzing a clean aliquot of the same HNO_3 in which samples were measured. Sample and standard concentrations between 5 and 30 ppm were used in different measurement sessions depending on sensitivity and the mass-resolution slit being used, but most analyses made use of 10-12 ppm iron in sample and standard solutions. Measurements were made with the use of bracketing standards matched to sample concentrations within ± 5 %. Measurements of ^{56}Fe were made on a 10^{10} Ω amplifier resistor because signal intensities were generally higher than 50 V, and 10^{11} Ω amplifier resistors were used for measurement of ^{54}Cr, ^{54}Fe, ^{57}Fe, ^{58}Fe, and ^{60}Ni.

For experimentally synthesized samples, the Fe isotopic fractionation (δ'^{56}Fe) was also determined by standard Fe isotopic analytical methods. A quartz cyclonic spray chamber was used to introduce

Table 3.1. Triple-Fe-isotope data for Pre-GOE sediments, normalized to exponential (exp) and high-T equilibrium limit (eq) laws

Sample	Type	$\delta'^{56}Fe$	95% C.I.	$\delta'^{57}Fe$	95% C.I.	$\epsilon'^{56}Fe_{exp}$	$\epsilon'^{56}Fe_{eq}$	95% C.I.	n
EBA-1 1057.5 Py	pyrite	1.034	0.153	1.527	0.229	0.080	-0.012	0.039	42
EBA 2/30 Py	pyrite	-2.023	0.095	-2.996	0.143	-0.103	0.077	0.057	12
DO29 14.95 Py	pyrite	-1.539	0.037	-2.286	0.057	-0.051	0.087	0.058	34
WB-98 520.8 Py	pyrite	-2.010	0.056	-2.972	0.083	-0.127	0.052	0.035	33
WB-98 519.68 Py	pyrite	-1.440	0.156	-2.125	0.232	-0.122	0.005	0.042	27
SF-1 599.88 Py	pyrite	-3.166	0.018	-4.688	0.025	-0.181	0.100	0.032	53
SF-1 623.6 Py	pyrite	-2.762	0.020	-4.082	0.028	-0.168	0.077	0.026	76
SF-1 642.8 Py	pyrite	-0.228	0.024	-0.343	0.035	0.029	0.049	0.039	55
FVG-1 752.8 A Py	pyrite	-3.046	0.367	-4.508	0.540	-0.167	0.104	0.055	21
FVG-1 752.8 B Py	pyrite	-2.967	0.020	-4.389	0.030	-0.160	0.104	0.035	55
EBA-1 1057.5 BS	black shale	0.072	0.091	0.105	0.139	-0.004	-0.011	0.042	46
FVG-1 765.8 BS	black shale	-0.546	0.064	-0.804	0.093	-0.051	0.065	0.059	12
FVG-1 774 BS	black shale	-1.577	0.123	-2.319	0.172	-0.074	0.008	0.051	29
FVG-1 827.8 BS	black shale	0.093	0.284	0.136	0.448	0.016	-0.003	0.201	10

Table 3.1 continued

REX 167.5	IF	-1.981	0.115	-2.915	0.168	-0.227	-0.052	0.051	12
REX 187.5	IF	-2.692	0.008	-3.978	0.011	-0.224	0.014	0.024	109
Hotazel #41	IF	-2.286	0.021	-3.354	0.032	-0.258	-0.056	0.046	39
RM5	IF	-0.008	0.276	-0.014	0.412	0.011	0.011	0.082	12
WIT-18-740A	IF	-1.199	0.067	-1.767	0.090	-0.111	-0.005	0.072	10
ZO4-31	IF	0.796	0.132	1.169	0.200	0.085	0.015	0.059	26
JD-C165A	IF	1.624	0.019	2.407	0.028	0.126	-0.019	0.019	184
JD-65-296-1	IF	1.030	0.265	1.527	0.396	0.002	-0.090	0.052	23
PO5-1	IF	-1.384	0.028	-2.039	0.039	-0.103	0.019	0.031	55
PO5-6	IF	-0.696	0.142	-1.028	0.210	-0.065	-0.004	0.074	26
PO5-7	IF	-1.290	0.224	-1.900	0.336	-0.130	-0.016	0.037	12
IF-G	IF	0.611	0.012	0.878	0.019	0.052	-0.001	0.030	24

All isotope ratios are reported normalized to IRMM-524, which has an isotopic composition identical to IRMM-014 (Craddock and Dauphas, 2011). The value of n refers to the total number of standard-sample brackets analyzed. $\delta'^{57}Fe$ and $\epsilon'^{56}Fe$ were determined from the same analyses. δ' values for natural samples are discussed as Δδ' values (differences from IRMM-014) in the text.

Table 3.2. Triple-Fe-isotopic data for pyritization experiments, normalized to exponential (exp) and high-T equilibrium (eq) laws

Sample	$\delta'^{56}Fe$	$\Delta\delta'^{56}Fe$	95% C.I.	$\delta'^{57}Fe$	$\Delta\delta'^{57}Fe$	95% C.I.	n(δ′)	$\epsilon'^{56}Fe_{exp}$ IRMM-524	$\epsilon'^{56}Fe_{eq}$ IRMM-524	$\epsilon'^{56}Fe_{exp}$	$\epsilon'^{56}Fe_{eq}$	95% C.I.	n(ϵ′)
SB1-4 FeS	0.262		0.045	0.371		0.064	5	0.031	0.009			0.020	40
SB5-10 FeS	0.236		0.041	0.414		0.081	5	0.027	0.002			0.014	76
SB1 FeS	0.505	0.243	0.045	0.752	0.381	0.064	5	0.080	0.035	0.049	0.027	0.039	21
SB1 Py	-1.939	-2.201	0.045	-2.897	-3.269	0.064	5	-0.039	0.134	-0.070	0.126	0.040	26
SB2 FeS	0.421	0.159	0.045	0.647	0.276	0.064	5	0.028	-0.011	-0.003	-0.020	0.074	10
SB2 Py	-2.320	-2.582	0.045	-3.168	-3.540	0.064	5	-0.061	0.129	-0.092	0.120	0.054	9
SB3 FeS	0.494	0.232	0.045	0.697	0.326	0.064	5	0.040	-0.002	0.009	-0.010	0.053	20
SB3 Py	-1.810	-2.072	0.045	-2.708	-3.080	0.064	5	-0.069	0.093	-0.100	0.084	0.031	17
SB4 FeS	0.564	0.302	0.045	0.818	0.447	0.064	5	0.024	-0.025	-0.007	-0.034	0.049	9
SB4 Py	-1.816	-2.078	0.045	-2.705	-3.077	0.064	5	-0.061	0.101	-0.092	0.092	0.055	10
SB5 FeS	0.353	0.117	0.041	0.547	0.133	0.081	5	0.028	-0.005	0.001	-0.007	0.069	9
SB5 Py	-1.915	-2.151	0.041	-2.885	-3.300	0.081	5	-0.019	0.153	-0.046	0.152	0.021	27
SB6 FeS	0.412	0.176	0.041	0.587	0.173	0.081	5	0.030	-0.005	0.003	-0.007	0.055	9

Table 3.2 continued

SB6 Py	-1.777	-2.013	0.041	-2.668	-3.083	0.081	5	-0.049	0.111	-0.076	0.109	0.046	9
SB8 FeS	0.551	0.315	0.041	0.775	0.361	0.081	5	0.046	-0.001	0.019	-0.003	0.043	20
SB8 Py	-1.755	-1.991	0.041	-2.600	-3.016	0.081	5	0.001	0.157	-0.026	0.155	0.023	28
SB9 FeS	0.563	0.327	0.041	0.845	0.431	0.081	5	0.069	0.018	0.042	0.016	0.031	27
SB9 Py	-1.636	-1.873	0.041	-2.415	-2.830	0.081	5	-0.037	0.108	-0.063	0.106	0.060	20
SB10 FeS	0.620	0.384	0.041	0.919	0.505	0.081	5	0.035	-0.020	0.008	-0.022	0.036	29
SB10 Py	-1.693	-1.930	0.041	-2.491	-2.906	0.081	5	-0.062	0.088	-0.088	0.086	0.035	28

δ' and $\epsilon'^{56}Fe_{IRMM\text{-}524}$ values are reported normalized to IRMM-524, which has an isotopic composition identical to IRMM-014 (Craddock and Dauphas, 2011). $\Delta\delta'$ values are the differences between FeS and pyrite samples and the starting material for the experiments. $\epsilon'^{56}Fe$ is defined in the text based on differences from the starting material, so $\epsilon'^{56}Fe$ values given here and displayed in the figures reflect differences between the $\epsilon'^{56}Fe_{IRMM\text{-}524}$ values of the experimental products (FeS: residual FeS, and Py: pyrite precipitate) and the $\epsilon'^{56}Fe_{IRMM\text{-}524}$ values of the respective initial batches of starting FeS (used for samples SB1-4, and SB5-10). The values of $n(\delta')$ and $n(\epsilon')$ refer to the total number of standard-sample brackets analyzed for δ' and ϵ' measurements, respectively. δ' and ϵ' measurements were made separately using different analytical methods, detailed in the text. Starting material for samples SB1-4 and SB5-10 were analyzed 40 and 76 times, respectively.

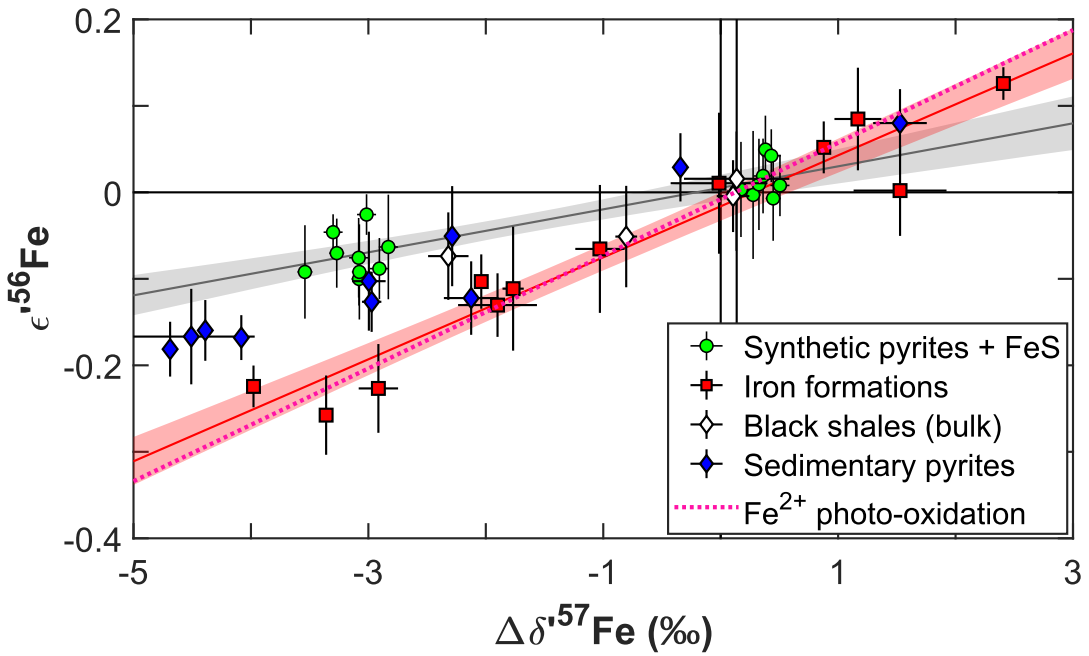

Figure 3.4. Triple-Fe-isotopic systematics for IFs, pyrites, black shales, and laboratory grown pyrite and FeS, in ϵ'^{56}Fe *vs.* $\Delta\delta'^{57}$Fe space, normalized to the exponential law (Tables 3.1, 3.2; Fig. 3.1A of the main text shows the same figure normalized to the high-T equilibrium MFL). $\Delta\delta'^{57}$Fe values are reported as differences from IRMM-014 and the starting material of experiments, for the natural samples and the synthetic pyrites, respectively. Error bars and envelopes are 95% confidence intervals. The slopes of end-member MFLs associated with iron-redox processes (red line and red envelope) and KIEs (black line and grey envelope) during pyritization are constrained through analysis of IFs and laboratory pyrite precipitates via the H_2S pathway (Guilbaud et al., 2011; Rickard and Luther, 2007), respectively. The slope of the IF MFL agrees well with the theoretical high temperature equilibrium limit law (defined by the horizontal axis, (Dauphas and Schauble, 2016)), and an experimentally determined MFL for Fe^{2+} oxidation (via UV photo-oxidation (Nie et al., 2017)), implying control by Fe^{2+}-Fe^{3+} equilibrium. Synthetic pyrite and FeS define a kinetic MFL for sulfide precipitation. Pre-GOE pyrites fall in an intermediate space between redox-equilibrium and kinetic endmembers.

1 ppm solutions into the Neptune operating in medium-resolution mode, resulting in a signal of ~7 V. Isotopic compositions were determined by standard-sample bracketing. All Fe isotopic analyses of experimentally synthesized samples (both triple isotopic and conventional) were bracketed and normalized to IRMM-524 during analysis. The average fractionation factor we determined for the pyrite precipitation reaction was $\alpha^{56}_{\text{FeS-pyrite}}$ = 1.0023 ± 0.0003 (95% C.I.) (Fig. 3.5), consistent with the results of Guilbaud et al. (2011) who obtained a value of 1.0022 ± 0.0007 (Guilbaud et

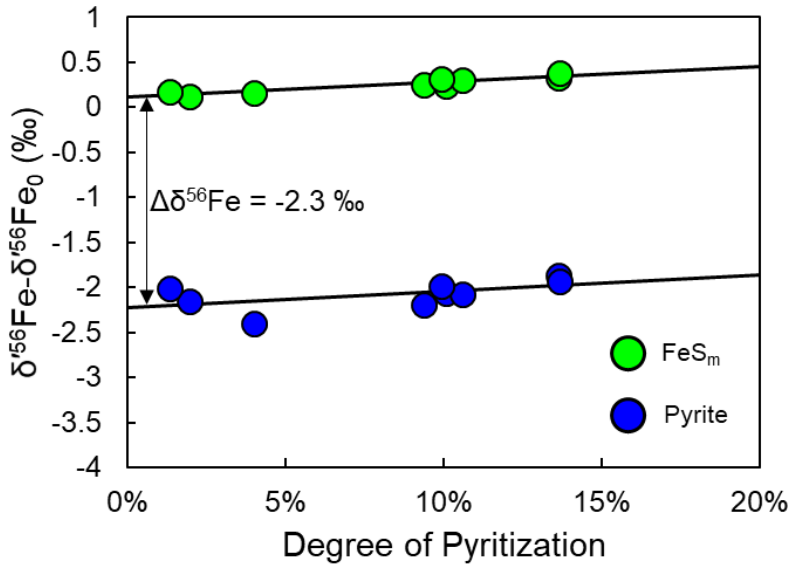

Figure 3.5. Iron isotopic fractionation between FeS_m and pyrite during abiotic precipitation of pyrite. The average Fe-isotopic fractionation between FeS_m and pyrite, a shift in $\delta'^{56}Fe$ of -2.3 ‰, is determined both through taking the average difference between the two phases in individual experiments, and through the difference between linear fit lines of $\delta^{56}Fe$ *vs*. degree of pyritization.

al., 2011). This fractionation factor was determined by calculating the average difference between the FeS_m and pyrite splits from each serum bottle experiment. The degree of pyritization (the fraction of the total Fe in the pyrite pool) was calculated from the total iron masses in each split indicated by concentration measurements and known dilution factors. The low degree of pyritization values (maximum ~14 %) obtained in our experiments were not conducive to fitting the data to a Rayleigh distillation trend, however the difference between linear trends plotted through $\delta'^{56}Fe$ *vs*. degree of pyritization for the FeS_m and pyrite data also gave an average fractionation factor of $\alpha^{56}_{FeS\text{-}pyrite} = 1.0023$ (Fig. 3.5).

We saw no systematic difference between short- and long-column purification techniques in triple-Fe-isotopic data for IF sample JD-C165A, and pyrite sample SF-1 599.8 Py, which were each processed multiple times using either column procedure to check the reproducibility of our measurements in the absence of geostandard materials that have been analyzed to this level of precision (Fig. 3.6). In all cases, the individual analyses for the pyrite sample had $\epsilon'^{56}Fe$ values

that were significantly more positive than the value anticipated for IF with the same $\Delta\delta'^{57}$Fe value (Fig. 3.6). In addition, as a check for possible matrix effects in the preparation of IF and pyrite samples, we performed a matrix test with IRMM-524 standard iron solution. Briefly, aliquots of an IF sample (REX 187.5) and a pyrite sample (SF-1 623.6 Py) were passed through the short-column purification procedure and the eluted matrix from each was collected. These matrix cuts were further purified by passing them through this column chemistry procedure again. The matrix

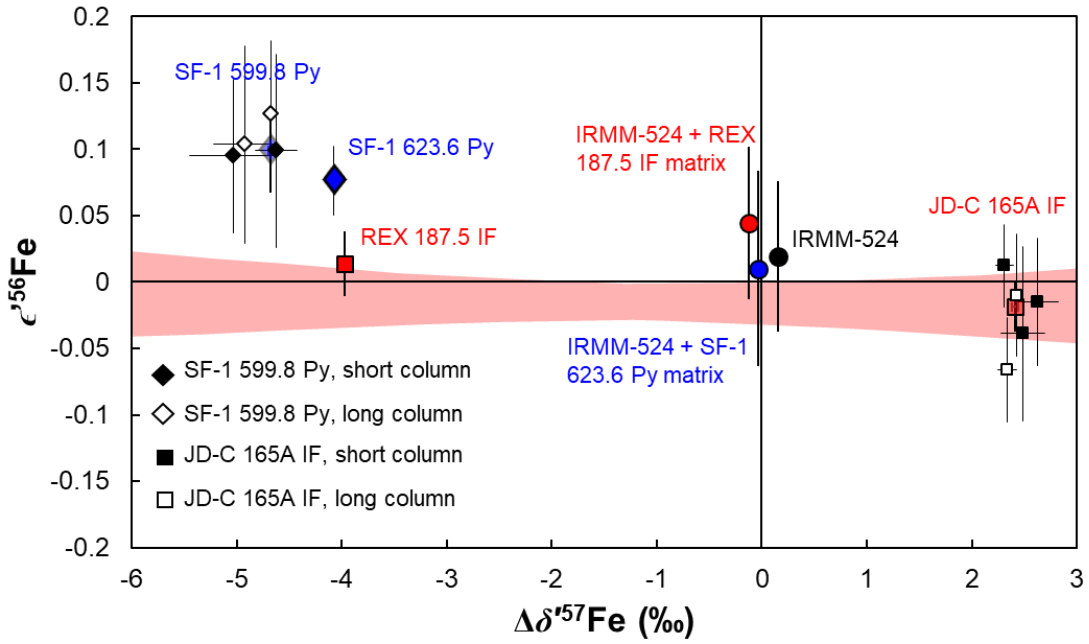

Figure 3.6. Tests performed on triple-Fe-isotopic analyses. Replicate aliquots of IF sample JD-C 165A and pyrite sample SF-1 599.8, purified using short-column (black-filled symbols) and long-column (open symbols) chromatography procedures were analyzed, with the average values for each sample shown with the pale-colored symbols in the background. Despite some analytical scatter, we see no significant or systematic effect of using one purification procedure over another, and all replicate pyrite analyses were distinct from the triple-Fe-isotopic composition one would expect for a sample that was fractionated solely by the redox processes driving the IF MFL (error enveloped of the IF MFL is shaded in red). Matrix mixing tests were performed with IRMM-524 and matrix from IF sample REX 187.5 (bold, red square) and pyrite sample SF-1 623.6 Py (bold, blue diamond). These revealed no resolvable matrix effect on ϵ'^{56}Fe analysis, with the pure IRMM-524 solution (black circle), IF matrix and IRMM-524 solution (red circle), and pyrite matrix and IRMM-524 solution (blue circle) all having ϵ'^{56}Fe values which are within error of one another and zero. Note that if matrix effects drove the difference between pyrite and IF triple-Fe-isotope variations, the IRMM-524 sample doped with pyrite matrix would have significantly more positive ϵ'^{56}Fe values than the IF-doped standard, which is not the case. $\Delta\delta'^{57}$Fe values are differences from to IRMM-014.

cuts were mixed with a solution of IRMM-524 containing the same amount of iron as originally present in the sample aliquots, and the iron was purified with two passes on short columns in the same manner as other samples. The $\epsilon'^{56}Fe$ values of both matrix-adjusted solutions and a pure solution of IRMM-524 were all within error of zero and all identical within error (Fig. 3.6), suggesting that sample matrix did not systematically affect our $\epsilon'^{56}Fe$ analyses.

Modeling methods - Calculation of oxic and sulfidic sink sizes

Triple-Fe-isotopic systematics allows the isotopic composition of any low-$\delta'^{57}Fe$ pyrite to be broken into contributions from KIE during pyrite precipitation and the isotopic fractionation resulting from the removal of isotopically heavy Fe^{3+} oxyhydroxides. Because MFLs are straight lines in $\epsilon'^{56}Fe$ *vs.* $\Delta\delta'^{57}Fe$ space, the contributions of the two fractionating processes can be determined by solving for the intersection of two straight line equations (shown schematically in Fig. 3.7), or as shown below, by solving a pair of simultaneous equations.

For each individual pyrite, the two unknowns are the $\epsilon'^{56}Fe$ value and the $\Delta\delta'^{57}Fe$ of the Fe^{2+} pool from which pyrite formed ($\delta'^{56}Fe_w$ in the main text). We denote these two unknowns $\epsilon'^{56}Fe_w$ and $\Delta\delta'^{57}Fe_w$. In the context of the two-stage model described here and in the main text, we have the two following constraints: (1) the parcel of seawater that experienced iron oxide removal must be on the empirical MFL defined by iron formation, and (2) the line that ties a pyrite sample to the seawater parcel from which is formed must define a slope identical to the MFL for pyritization. The two equations relating $\epsilon'^{56}Fe_w$ and $\Delta\delta'^{57}Fe_w$ are:

$$\epsilon'^{56}Fe_w = a_{ox}\Delta\delta'^{57}Fe_w + b_{ox}, \qquad \text{(Eq. 10)}$$

$$\frac{\epsilon'^{56}Fe_{py} - \epsilon'^{56}Fe_w}{\Delta\delta'^{57}Fe_{py} - \Delta\delta'^{57}Fe_w} = a_{KIE}, \qquad \text{(Eq. 11)}$$

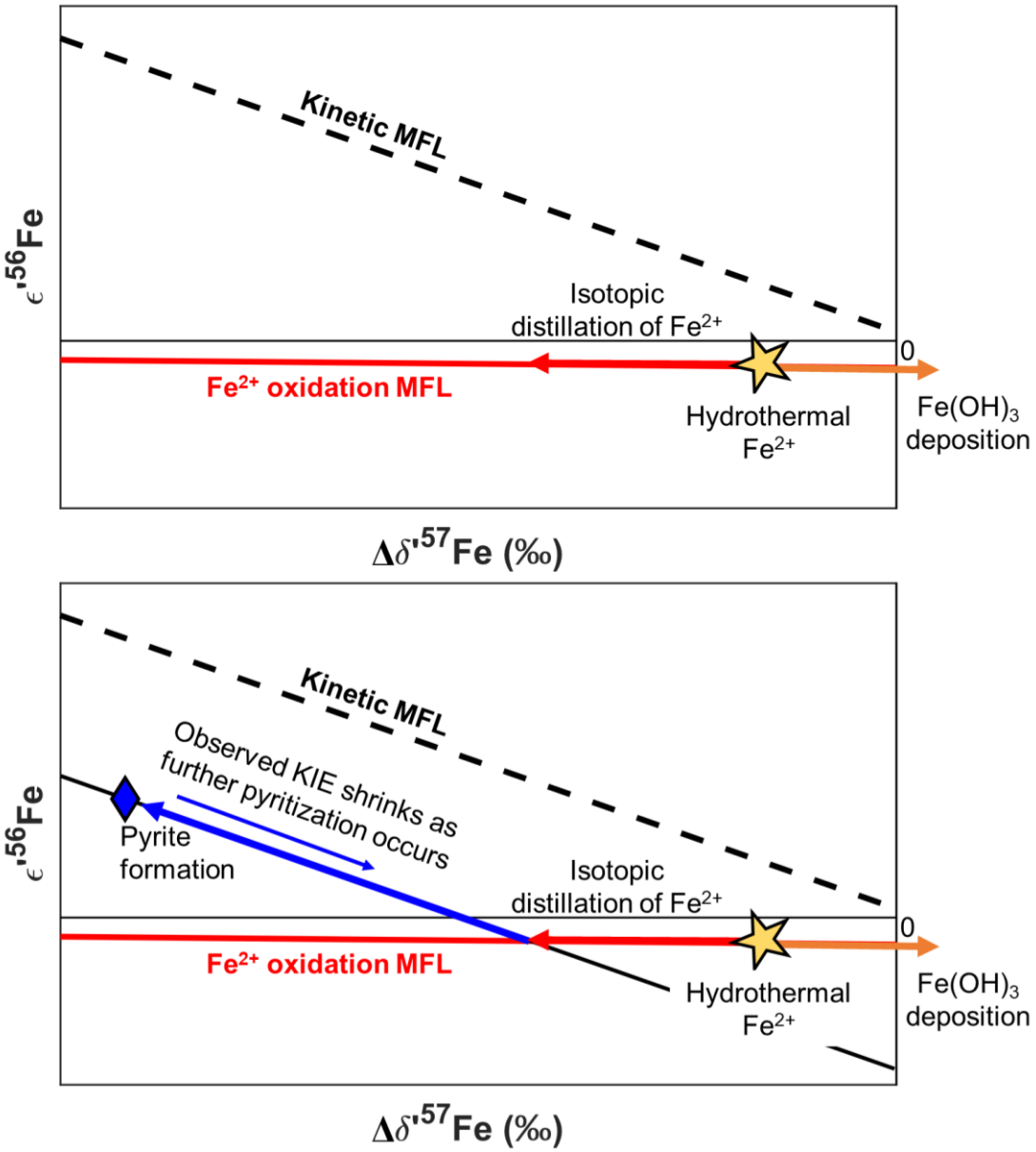

Figure 3.7. Conceptual illustration of the two-step process (Fe^{2+} isotopic distillation by partial oxidation and subsequent partial pyritization) that we propose for generating triple-Fe-isotopic composition of isotopically depleted pre-GOE pyrites, and the procedure for determining Fe-isotopic contributions of pyritization and initial isotopic composition of the pyrite-forming water mass to the Fe-isotopic composition of pyrite. The $\Delta\delta'^{57}Fe$ value at where a trajectory for KIE during pyrite precipitation (with slope a_{KIE}) intercepts the oxidative IF MFL ($\Delta\delta'^{57}Fe_w$) is determined by simultaneous solving of two linear equations. The difference between $\Delta\delta'^{57}Fe_w$ and $\Delta\delta'^{57}Fe_{py}$ gives the expression of the KIE during pyritization, which is used to determine the degree of pyritization (f_{py}) of the pre-pyritization water mass, assuming that the pyrite is a cumulative product of all precipitated pyrite. $\Delta\delta'^{57}Fe_w$ is assumed to be the $\Delta\delta'^{57}Fe$ value of the pre-pyritization water mass, and its isotopic composition reflects the degree of isotopically heavy Fe^{3+}-oxyhydroxide removal (F_{ox}) that took place prior to the formation of pyrite. $\Delta\delta'^{57}Fe$ values are differences from IRMM-014.

where a_{ox}, b_{ox}, and a_{KIE} are the known empirical values from our measurements of endmember MFLs, and $\Delta\delta'^{57}Fe$ are taken as fractionations relative to IRMM-014. These two equations can be solved for the two unknowns and we have,

$$\Delta\delta'^{57}Fe_w = \frac{(\epsilon'^{56}Fe_{py} - a_{KIE}\Delta\delta'^{57}Fe_{py} - b_{ox})}{(a_{ox} - a_{KIE})}, \quad \text{(Eq. 12)}$$

$$\epsilon'^{56}Fe_w = a_{ox}\frac{(\epsilon'^{56}Fe_{py} - a_{KIE}\Delta\delta'^{57}Fe_{py} - b_{ox})}{(a_{ox} - a_{KIE})} + b_{ox}. \quad \text{(Eq. 13)}$$

Note that $\Delta\delta'^{57}Fe_w \sim 1.5\times \Delta\delta'^{56}Fe_w$ where $\delta'^{56}Fe_w$ values are discussed in the main text. The extent of Fe^{2+} oxidation (F_{ox}) to give a certain $\Delta\delta'^{57}Fe_w$ was calculated using a Rayleigh distillation model:

$$\Delta\delta'^{57}Fe_w = \Delta\delta'^{57}Fe_i + 1000(\alpha - 1)\ln(1 - F_{ox}), \quad \text{(Eq. 14)}$$

where α is the fractionation factor during Fe^{2+} oxidation and precipitation that gives a fractionation $1000\times(\alpha^{56}-1) = 1‰$ $[(\alpha^{57}-1) \sim 1.5\times(\alpha^{56}-1)]$ during Fe^{3+} oxyhydroxide removal (Dauphas et al., 2017), the subscript $_i$ denotes the starting $\Delta\delta'^{57}Fe$ value for a hydrothermal Fe^{2+} source of

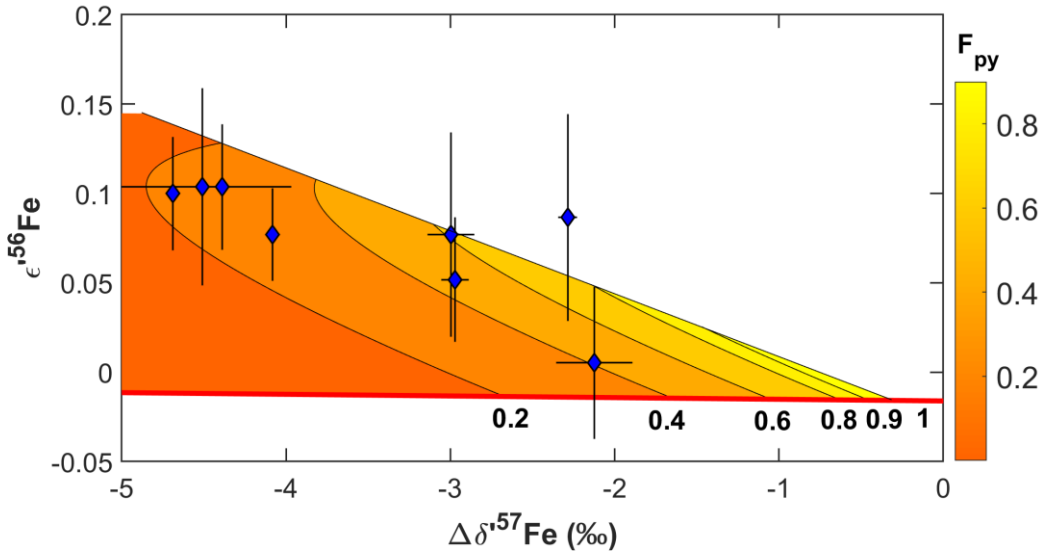

Figure 3.8. Fractional pyrite sink for upwelled Fe (F_{py}) from triple-Fe-isotopic data. F_{py} values are calculated as $F_{py} = f_{py} \times (1 - F_{ox})$. Corresponding f_{py} and F_{ox} contours are plotted in Figure 3.2C of the main text. $\Delta\delta'^{57}Fe$ values are differences from IRMM-014.

approximately -0.3 ‰ (Beard et al., 2003), assumed to be on the empirical MFL defined by iron formations.

The fraction of pyrite precipitated (f_{py} in the main text) was also determined with a Rayleigh distillation model (shown in Figure 3.8). In this case, the measured fractionation was taken to reflect the cumulative product of pyrite precipitation from a dissolved Fe^{2+} reservoir with initial $\Delta\delta'^{57}Fe$ value of $\Delta\delta'^{57}Fe_w$. This contrasts with how one might consider *in situ* measurements of individual nodule layers, because those better approximate instantaneous precipitate compositions during the growth of pyrite grains (Marin-Carbonne et al., 2014; Marin-Carbonne et al., 2020). The magnitude of the KIE that was expressed in the product was calculated as the difference between the product and initial reactant:

$$\Delta\delta'^{57}Fe_{py} - \Delta\delta'^{57}Fe_w = \frac{(f_{py} - 1) \times 1000(\alpha^{57} - 1)\ln(1 - f_{py})}{f_{py}}, \qquad \text{(Eq. 15)}$$

where we assumed the maximum fractionation for pyrite precipitation (via FeS_m) from Fe^{2+} of $1000\times(\alpha^{56}-1) = -3.1‰$ $[(\alpha^{57}-1) \sim 1.5\times(\alpha^{56}-1)]$ suggested by ref. (Guilbaud et al., 2011). The value of f_{py} was determined by solving this transcendental equation numerically. The fractional size of the sulfidic sink, F_{py}, witnessed by each pyrite, was calculated as,

$$F_{py}=f_{py}\times (1 - F_{ox}). \qquad \text{(Eq. 16)}$$

An uncertainty not considered in calculating f_{py} is the effect of isotopic exchange between freshly precipitated pyrite and ambient Fe^{2+}. A recent experimental study (Mansor and Fantle, 2019) provided some evidence that the growing surface of freshly precipitated microscopic pyrite grains may undergo isotopic equilibration with the ambient Fe^{2+} pool. Because the anticipated equilibrium fractionation factor for pyrite formation is large and positive (Polyakov et al., 2007), such a process could partially offset large kinetic isotope effects enriching pyrite in light Fe isotopes, resulting in a smaller net fractionation between pyrite and Fe^{2+} at a given F_{py}. In practice,

however, isotopic re-equilibration of pyrite has been observed only at elevated temperatures (80°C), and where the surface area to volume ratio of microscopic pyrites allows this surface exchange effect to exert a significant control on the bulk Fe isotopic composition. This process should become diminishingly important at lower temperatures, as observed in experiments (Guilbaud et al., 2011) and nature (Rolison et al., 2018), and as pyrite grains grow larger than 10 μm, and certainly as they reach macroscopic sizes like the diagenetic nodules studied here. While the required kinetic data on pyrite growth and isotopic exchange rates are not currently available to model this process accurately at appropriate low-temperature marine conditions, it is unlikely that isotopic re-equilibration of pyrite was a major control on the bulk Fe isotopic composition of diagenetic pyrites.

In practice, all the parameters $\epsilon'^{56}Fe_{py}$, $\Delta\delta'^{57}Fe_{py}$, a_{ox}, b_{ox}, and a_{KIE} have analytical uncertainties associated with them. The effects of these errors on estimates of fractional iron sinks were propagated using a Monte Carlo method implemented in MATLAB. For each pyrite and IF datapoint, an array of simulated datapoints was generated by randomly sampling 1000 times from a normal distribution defined by the reported 95 % C.I. of the measured $\epsilon'^{56}Fe$ and $\delta'^{57}Fe$ values (Table 3.1). From the 1000 sets of randomly generated IF datapoints, 1000 MFLs were generated by linear regression to encompass the anticipated range of seawater Fe^{2+} evolutions in $\epsilon'^{56}Fe$ *vs.* $\Delta\delta'^{57}Fe$ space that could be driven by Fe^{3+} oxyhydroxide precipitation. An array of 1000 values for the kinetic slope was generated by randomly sampling 1000 times from a normal distribution defined by the 95 % C.I. of the experimentally determined slope. We then solved the 1000 resulting simultaneous equations 1000 times for the randomly generated datasets using the approach described above. Certain output values from the random resampling had to be rejected, as they did not allow for solving for F_{ox} and f_{py} values using the Rayleigh distillation equations. These cases

Table 3.3. Estimated fractional size of iron sinks and shelf sedimentary Fe/S ratios for isotopically light pyrites

Sample	Age bin (Ga)	F_{ox}	f_{py}	F_{py}	Moles O_2 yield (per mole FeS_2)	Age-bin average O_2 yield
EBA 2/30	2.32	$0.47^{+0.45}_{-0.42}$	$0.69^{+0.31}_{-0.51}$	$0.43^{+0.18}_{-0.32}$	0.35 (1.06)	0.35 (1.06)
DO29 14.95	2.50-2.52	$0.33^{+0.56}_{-0.25}$	$0.57^{+0.41}_{-0.51}$	$0.58^{+0.19}_{-0.35}$	0.55 (1.51)	0.30 ± 0.21 (0.96 ± 0.47)
WB-98 520.8	2.50-2.52	$0.59^{+0.18}_{-0.54}$	$0.84^{+0.16}_{-0.51}$	$0.36^{+0.26}_{-0.26}$	0.23 (0.80)	0.30 ± 0.21 (0.966 ± 0.47)
WB-98 519.68	2.50-2.52	$0.71^{+0.19}_{-0.59}$	$0.99^{+0.01}_{-0.27}$	$0.29^{+0.44}_{-0.23}$	0.12 (0.56)	0.30 ± 0.21 (0.96 ± 0.47)
SF-1 599.88	2.65-2.66	$0.70^{+0.23}_{-0.60}$	$0.65^{+0.35}_{-0.58}$	$0.18^{+0.04}_{-0.13}$	0.003 (0.31)	0.05 ± 0.02 (0.41 ± 0.05)
SF-1 623.6	2.65-2.66	$0.70^{+0.24}_{-0.60}$	$0.75^{+0.25}_{-0.59}$	$0.23^{+0.10}_{-0.17}$	0.06 (0.42)	0.05 ± 0.02 (0.41 ± 0.05)
FVG-1 752.8 A	2.65-2.66	$0.67^{+0.28}_{-0.59}$	$0.63^{+0.37}_{-0.58}$	$0.21^{+0.04}_{-0.16}$	0.04 (0.39)	0.05 ± 0.02 (0.41 ± 0.05)
FVG-1 752.8 B	2.65-2.66	$0.62^{+0.31}_{-0.55}$	$0.58^{+0.40}_{-0.52}$	$0.24^{+0.03}_{-0.17}$	0.10 (0.51)	0.05 ± 0.02 (0.41 ± 0.05)

For F_{ox}, f_{py}, and F_{py} values, central estimates are 50% percentiles, and uncertainties are 95 % C.I. from Monte Carlo simulations. For O_2 yields, central estimates are calculated from central estimates for F_{ox} and $F_{py\ values}$. The first number assumes volcanic H_2S/SO_2 input ratio of 1 (Gaillard et al., 2011), second number (in parentheses) assumes volcanic H_2S/SO_2 input ratio of 0 (Olson et al., 2019). Error bars for Age-bin averages are the 95 % C.I. of the average values.

were where: (*i*) the required fractionation during pyritization ($\Delta\delta'^{57}Fe_{py}$ - $\Delta\delta'^{57}Fe_{w}$) was larger in magnitude than the maximum instantaneous fractionation for pyrite precipitation from Fe^{2+} (via FeS_m) with $1000\times(\alpha^{56}-1) = -3.1‰$ [$(\alpha^{57}-1) \sim 1.5\times(\alpha^{56}-1)$] (Guilbaud et al., 2011)); (*ii*) the randomly generated data placed a pyrite datapoint below the IF line in $\epsilon'^{56}Fe$ *vs.* $\Delta\delta'^{57}Fe$ space, thus requiring a positive $\Delta\delta'^{57}Fe$ offset of the pyrite from the IF line; and (*iii*) where the randomly generated data required an intercept between the IF and KIE lines at a $\Delta\delta'^{57}Fe_{w}$ value more positive than the assumed hydrothermal Fe^{2+} source $\Delta\delta'^{57}Fe$ value of approximately -0.3‰ (Beard et al., 2003). The probability distributions for F_{ox} and F_{py} from the Monte Carlo simulation are shown in Fig 3.3 and Table 3.3, and we also used central estimates of F_{ox} and F_{py} from the Monte Carlo simulations to calculate the O_2 yields given in Fig 3.3 and Table 3.3. Monte Carlo simulation estimates of f_{py} and F_{ox} for each pyrite sample span a large range, but these variations are strongly correlated. This is because a more negative estimate for the isotopic composition of seawater $\Delta\delta'^{57}Fe_{w}$ (which implies a larger F_{ox}), gives a smaller estimate for the fractionation during precipitation of pyrite from the oceanic iron pool (which implies a larger f_{py}). These two effects have an opposite impact on the estimate of F_{py}, therefore, F_{py} estimates vary less than F_{ox} and f_{py}.

As an alternative to a Rayleigh distillation describing upward large scale advection of Fe^{2+}-rich deep waters (*e.g.* Trendall and Morris, 2000; Konhauser et al., 2002; Kappler et al., 2005; Klein, 2005) (Fig. 3.9), we also explored the possibility that the isotopic evolution of the Fe^{2+} reservoir during removal of Fe^{3+} oxyhydroxides to the oxic Fe sink was controlled by steady-state eddy diffusion of Fe^{2+} from deep waters, and O_2 from the photic zone, following the model of Czaja *et al.* (2012) (Czaja et al., 2012). We developed a model to replicate its salient features, using a finite difference approach. In the model, a photic zone with a fixed O_2 level overlies a basin that contains anoxic, Fe^{2+}-rich water at depth. Dissolved O_2 is transported downward, and Fe^{2+} upward, by eddy

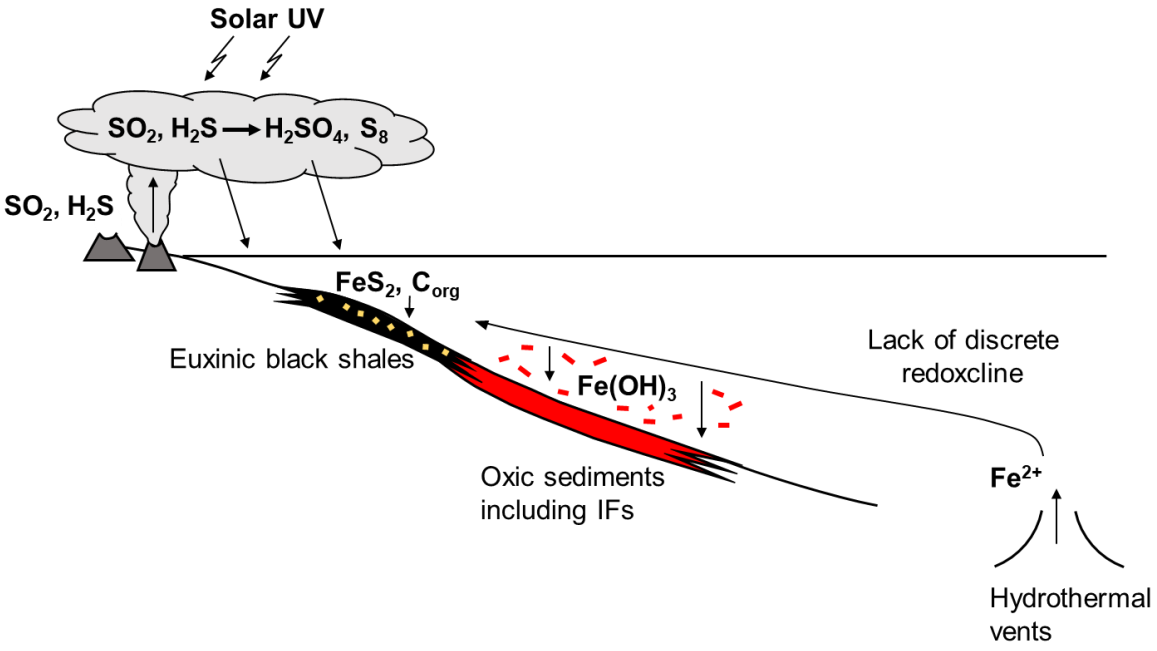

Figure 3.9. Basin cross-section illustrating marine iron cycle before the GOE informed by triple-Fe-isotopic systematics (Bekker et al., 2010; Planavsky et al., 2012; Rouxel et al., 2005)**.** Dissolved Fe^{2+} in deep-ocean waters fed by hydrothermal vents was upwelled onto continental margins. Oxidation of Fe^{2+} across a spatially diffuse redoxcline led to deposition of Fe^{3+}-oxyhydroxide-rich sediments including IFs. In sedimentary environments with high organic carbon burial, the remaining dissolved Fe^{2+} was incorporated into pyrite, with pyritization before the GOE being limited by sulfur availability controlled by volcanic outgassing.

diffusion, and $Fe(OH)_3$ precipitates where these species meet, following second-order reaction kinetics with temperature and salinity-dependent rates calculated after ref. (Millero et al., 1987). Precipitation rates peak in a narrow reaction zone, around which both dissolved species' concentrations decrease to near zero levels. Precipitated $Fe(OH)_3$ is removed from the column with a first-order rate constant of 0.79 day^{-1}. The Fe^{2+} oxidation reaction (which consumes Fe^{2+} and O_2) follows a second-order kinetic rate law that is dependent on temperature, salinity, and pH. This parameter space was explored extensively by ref. (Czaja et al., 2012) and we simply followed their preferred input parameters in order to replicate their model. In the model, the equilibrium fractionation for Fe^{2+}-Fe^{3+} isotopic exchange was implemented by treating ^{56}Fe and ^{54}Fe as separate species and scaling the reaction rate constants according to the relevant fractionation

factor. No fractionation factor was applied to the eddy diffusion process. In the model, the majority of Fe oxidation takes place within the narrow reaction zone, and it is there that significant Fe isotopic fractionations are developed in the Fe^{2+} reservoir in a steady-state distillation process.

A list of input parameters for different model runs is provided in Table 3.4. For simplicity, in contrast to (Czaja et al., 2012), we employed a fixed concentration rather than a fixed production rate boundary condition for O_2. The fixed concentration we chose matches the steady-state O_2 level at the base of the photic zone in ref. (Czaja et al., 2012)'s model. Our results (Fig. 3.10) replicate theirs, so this simplification of the boundary condition does not affect the model output.

It can be shown with a simple scaling argument that the steady state reaction zone develops at the location where eddy diffusive transport of O_2 downwards, and Fe^{2+} upwards, lead to concentrations of O_2 and Fe^{2+} in a 1:4 ratio, the stoichiometry required for complete titration of dissolved Fe^{2+} by O_2-mediated oxidation. Consider a water column with 5 levels: Level 1 – ocean surface; Level 2, photic zone base; Level 3 – top of reaction zone; Level 4 – base of reaction zone; and Level 5 – base of model basin (Fig. 3.10). The diffusive fluxes, J_{O2} and $J_{Fe2+,}$ are given approximately by,

$$J_{O2} = D[O_2]_2/z_{2\text{-}3}, \qquad \text{(Eq. 17)}$$

$$J_{Fe2+} = D[Fe^{2+}]_5/z_{5\text{-}4}, \qquad \text{(Eq. 18)}$$

where D is the eddy diffusivity (0.1 cm^2s^{-1}), and $z_{i\text{-}j}$ is the depth difference between level i and level j, and the subscripts on the concentrations indicate concentrations at the fixed boundary conditions for O_2 at the top of of the model, and Fe^{2+} at the base of the model. In the reaction zone, Fe^{2+} is quantitatively oxidized by O_2, in a 4:1 stoichiometry, which gives the approximation $J_{O2} \approx ¼\ J_{Fe2+}$ at this depth. Rearranging for $z_{5\text{-}4}$ gives:

Table 3.4. Fe-O_2 dispersion-reaction steady-state model parameters		
Parameter		**Value**
Water column depth (m)		500
Eddy diffusion coefficient (cm^2 s^{-1})		0.1
[O_2] (µmol L^{-1})	Upper (within photic zone)	50
	Lower	No-flux
[Fe^{2+}] (µmol L^{-1})	Upper	No-flux
	Lower	100
Photic zone depth range (m)		0-100
Temperature (°C)		25
Salinity (ppt)		35
$Fe(OH)_3$ settling rate constant (day^{-1})		0.79
Simulation time (yrs)		2000
$\delta^{56}Fe_{Fe2+,initial}$ (‰)		0
$\alpha_{Fe(OH)3\text{-}Fe2+}$		1.001, 1.002, 1.004
Input parameters match those of Czaja *et al*. (2012) (Czaja et al., 2012), except the fixed photic-zone [O_2], which matches the value reached at the base of the photic zone in Czaja *et al*. (Czaja et al., 2012), for the equivalent model run (run 1 in that study).		

$z_{5\text{-}4} \approx (z_{2\text{-}3}[Fe^{2+}]_5)/(4[O_2]_2)$. (Eq. 19)

Recognizing that $z_{5\text{-}2} = z_{5\text{-}4} + z_{2\text{-}3}$ for the case where the reaction zone is ultimately thin, and substituting appropriately gives:

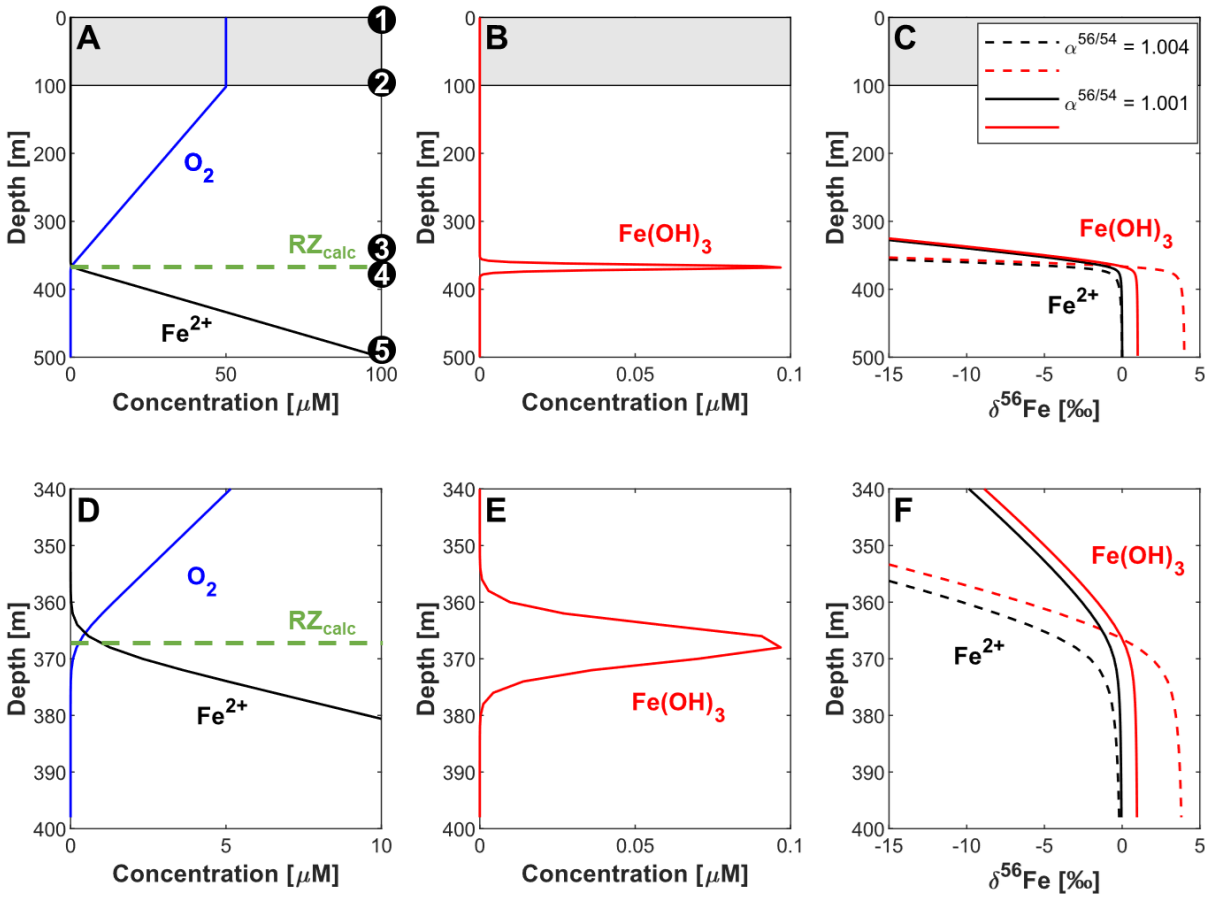

Figure 3.10. Depth profiles of outputs from 1-D dispersion-reaction model for Fe^{2+} oxidation (Czaja et al., 2012). Input parameters are given in Table 3.4. A. Depth profiles of O_2 (blue) and Fe^{2+} (black). The green dashed line indicates the position of the reaction zone calculated using a simple scaling argument, and agrees well with the depth in the model output where concentrations O_2 and Fe^{2+} go to zero as $Fe(OH)_3$ concentrations peak. Black circles indicate the layer numbers referred to in Equations 17-20. B. Depth profile of $Fe(OH)_3$. C. Iron isotopic composition of Fe^{2+} (black) and $Fe(OH)_3$ (red) using two different fractionation factors. D-F. As A-C, zoomed on the depth region surrounding the reaction zone.

$$z_{5\text{-}4} \approx z_{5\text{-}2}/(1+(4[O_2]_2/[Fe^{2+}]_5)), \qquad \text{(Eq. 20)}$$

and thus, the depth of the reaction zone can be calculated. This depth level is plotted in Figure 3.10 and agrees well with the depth level in the numerical model where the peak in $Fe(OH)_3$ is located. This comparison and the fact that we can reproduce the profiles calculated by Czaja et al. (2012) validates our numerical code.

In the dispersion reaction model, the calculation of F_{ox} is less straightforward than in the Rayleigh distillation because there is no provision for Fe removal as pyrite. In the context of an upward Fe^{2+} supply, F_{ox} at a given depth was calculated by integrating the steady-state Fe^{2+} oxidation rate from the bottom of the model upward to that depth, and dividing this value by the Fe^{2+} oxidation rate integrated over the entire water column.

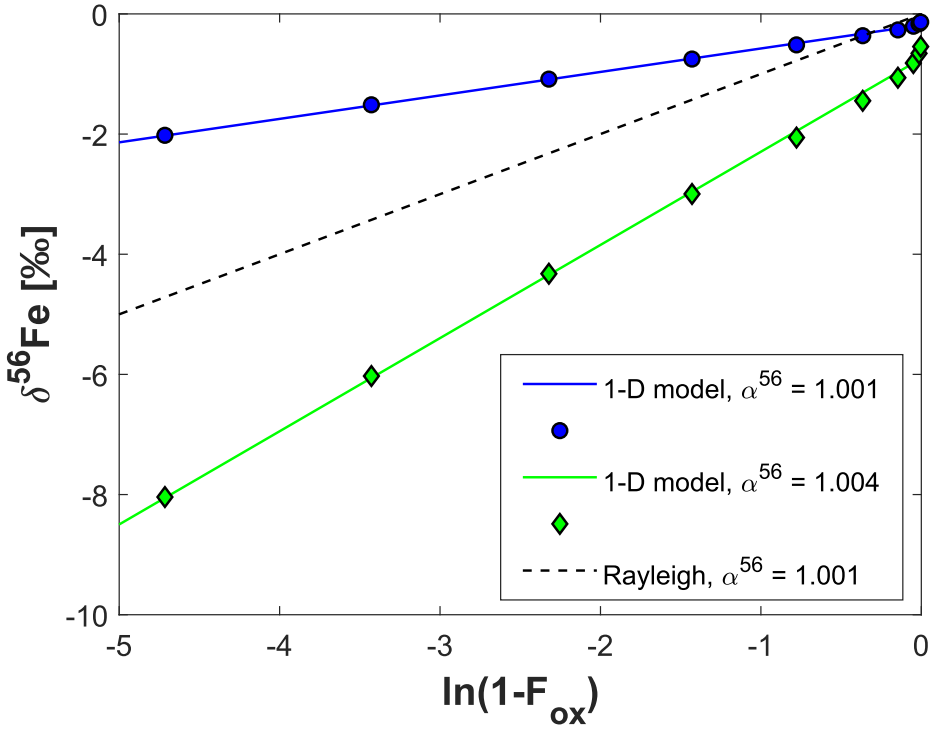

Figure 3.11 Evolution of the Fe isotopic composition of Fe^{2+} within the reaction zone of 1-D dispersion-reaction models with different fractionation factors for $Fe(OH)_3$ removal, as a function of F_{ox} (calculated as the $Fe(OH)_3$ formation rate integrated from the base of the model to variable depths, normalized by the total integrated $Fe(OH)_3$ precipitation in the model water column). All arrays show linear relationships between $\delta^{56}Fe$ and $\ln(1-F_{ox})$, in the same manner as a Rayleigh distillation model (dashed black line), but the slopes of these linear relationships are ~0.4 times the slope expected for a Rayleigh distillation model with the same fractionation factor, α^{56}. Small isotopic depletions at negligible values of F_{ox} likely reflect eddy diffusive effects.

We plotted $\delta^{56}Fe_{Fe2+}$ *vs.* $\ln(1-F_{ox})$ from this model in Fig. 3.11, for different values of the fractionation factor between Fe^{2+} and $Fe(OH)_3$. A feature of these model runs is that a small, but significant negative isotopic fractionation is imparted to $\delta^{56}Fe_{Fe2+}$ before it reaches the reaction

zone, whilst F_{ox} is still very close to zero. This fractionation can be understood as resulting from diffusion. The Fe^{2+} input at the base of the model region has a fixed $^{56}Fe/^{54}Fe$, but due to preferential removal of ^{56}Fe in the reaction zone, the ratio of concentration gradients is fractionated relative to the input $^{56}Fe/^{54}Fe$ ratio, with a relatively steeper concentration gradient for ^{56}Fe. As a result, ^{56}Fe diffuses slightly faster into the reaction zone, leaving the column underlying the reaction zone with a slightly lower $^{56}Fe/^{54}Fe$. This is expressed in the slightly negative $\delta^{56}Fe_{Fe2+}$ already established at the base of the reaction zone before Fe^{2+} oxidation begins to dominate the isotopic evolution.

Once within the reaction zone, $\delta^{56}Fe_{Fe2+}$ evolves linearly versus $\ln(1-F_{ox})$, becoming increasingly negative as F_{ox} increases, so this evolution is functionally very similar to a Rayleigh distillation. However, for a given input isotopic fractionation factor α^{56} between Fe^{2+} and $Fe(OH)_3$, the slope of $\delta^{56}Fe_{Fe2+}$ vs. $\ln(1-F_{ox})$ is ~$0.39 \times (\alpha^{56} - 1)\times 1000$, while an upwelling modelled using a Rayleigh distillation would yield a correlation of slope $(\alpha^{56} - 1)\times 1000$. As such, reaching a given negative value of $\delta^{56}Fe_{Fe2+}$ would require a larger F_{ox} at the same value of α^{56}, or vice versa, in the dispersion-reaction model versus a Rayleigh distillation. This effect is partially offset, particularly at lower F_{ox} values, by the initial depletion in $\delta^{56}Fe_{Fe2+}$ caused by eddy diffusion in the underlying water column.

F_{ox} and F_{ox}/F_{py} were recalculated using the evolution described by model outputs in order to compare to results from the model using Rayleigh distillation (Fig. 3.12). Dispersion-reaction modeling conducted with an input value for α^{56} of 1.001 as used in our Rayleigh model, or 1.004 as used in ref. (Czaja et al., 2012). Using $\alpha^{56} = 1.001$ in the dispersion-reaction model gives higher F_{ox} values than in our Rayleigh distillation modeling. All pyrite triple Fe isotope compositions still lie at $F_{ox}/Fe_{py}<10$ (allowing positive O_2 fluxes in certain scenarios) but the error bars would also

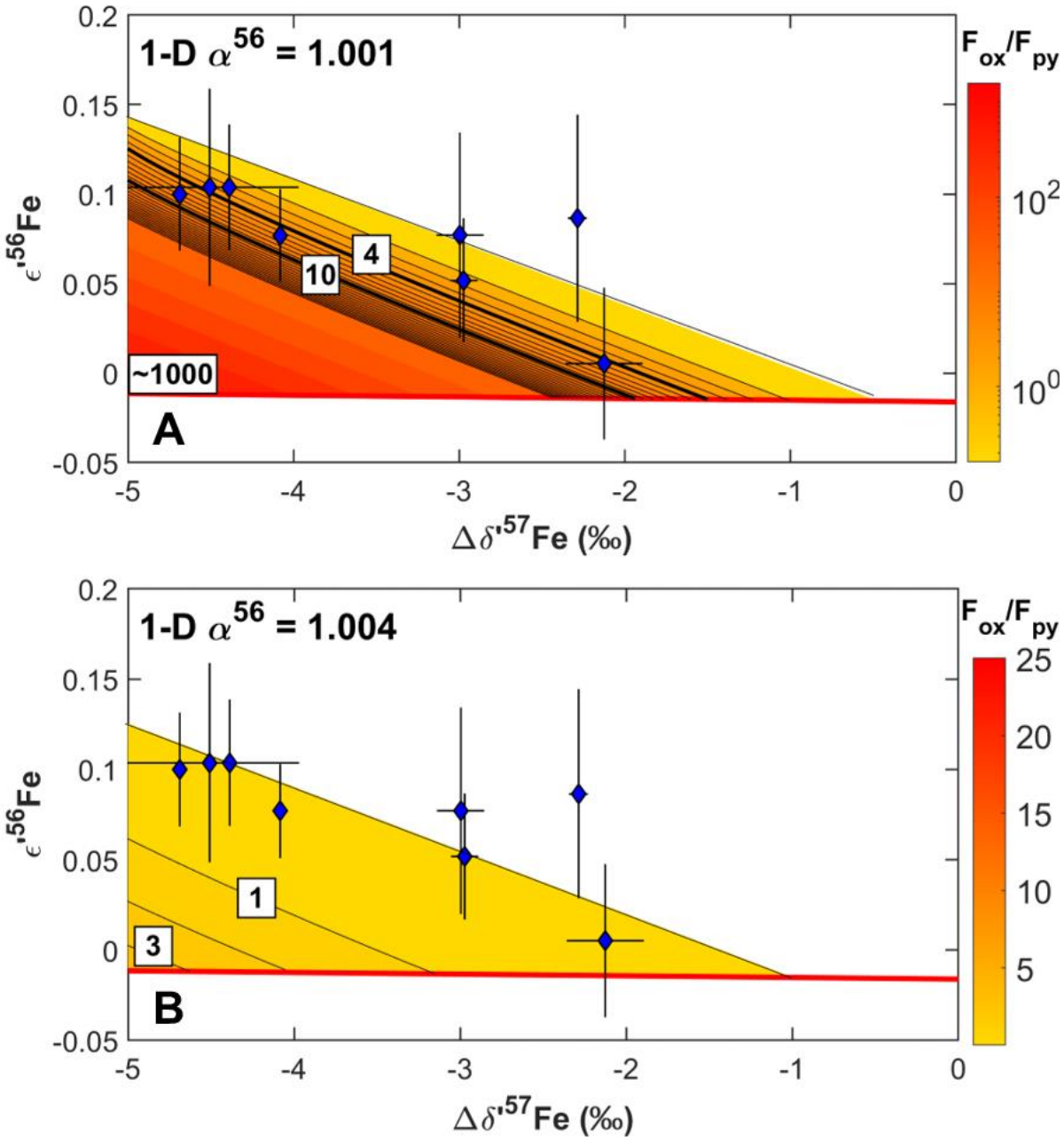

Figure 3.12. Pyrite triple-Fe-isotope data and contours of F_{ox}/F_{py} (relative sizes of oxyhydroxide and pyrite sedimentary Fe sinks) calculated using a 1-D dispersion-reaction model for isotopic fractionation during Fe^{2+} oxidation (Czaja et al., 2012). Bold contours at 4 and 10 indicate thresholds for net O_2 source *vs*. sink behavior for volcanic H_2S/SO_2 inputs ratios of 1 (Gaillard et al., 2011) and 0 (Olson et al., 2019), respectively. A. Model using $\alpha^{56} = 1.001$ for Fe^{2+} oxidation. B. Model using $\alpha^{56} = 1.004$ for Fe^{2+} oxidation (following the approach of ref. (Czaja et al., 2012)). Contours in A are spaced in logarithmic scale. Pyrite triple-Fe-isotopic compositions are consistent with net O_2 sources not being overwhelmed by Fe^{3+} oxyhydroxide formation. $\Delta\delta'^{57}Fe$ values are differences from IRMM-014.

allow marginal cases with higher F_{ox}/Fe_{py} (Fig. 3.12). However, the same model would require $[Fe^{2+}]$ to be depleted by partial oxidation by a factor of several hundreds in order to explain the lowest recorded $\delta^{56}Fe_{IF}$ values, and it is unclear whether such extreme Fe^{2+} depletions would still allow the deposition of Fe-rich chemical sediments at all. This suggests that the use of such a small α^{56} value might not appropriate in the context of this model, and why the larger fractionation factor was employed in previous iterations of the model (Czaja et al., 2012). That larger fractionation factor yields low F_{ox}/F_{py} consistent with pyrite burial being a net oxygen source (Fig. 3.12).

Sample Materials

Geological setting and age constraints for shale-hosted pyrite are given by Rouxel et al. (2005) (Rouxel et al., 2005). Ages and stratigraphic positions for all samples used in this study are provided in Table 3.5. References to age constraints for pyrite and shale samples, and most IF samples, are provided in refs. (Planavsky et al., 2012; Rouxel et al., 2006, 2005). Ages for the Hotazel Formation and Isua Supracrustal Belt IFs are from ref. (Gumsley et al., 2017) and ref. (Moorbath et al., 1973), respectively, and the geologic setting and Fe isotopic systematics of these IF have been discussed in the literature elsewhere (Dauphas et al., 2004; Thibon et al., 2019; Tsikos et al., 2010).

Pyrite grains from organic-rich shales as well as a few whole-rock organic-rich shale and IF samples were selected for this study. Pyrite grains and whole-rock shale samples were selected from a set of drill core samples previously studied for Fe isotopic variations by refs. (Rouxel et al., 2006, 2005). New pyrite grains were picked at the University of Hawaii. The nature of these grains was described in detail by ref.(*6*). Pyrite in organic-rich shales that were subsampled in our study occur as nodules ~ 1 mm to 1 cm in diameter, with C-rich inclusions in variable amounts. The

Table 3.5. Geological units and age for Archean-Paleoproterozoic pyrite, black shales, and IFs

Sample	Geological unit	Age (Ga)	Type	Refs.
EBA-1 1057.5 Py	Timeball Hill Fm	2.32	pyrite	(Rouxel et al., 2005)
EBA 2/30 Py	Timeball Hill Fm	2.32	pyrite	(Rouxel et al., 2005)
DO29 14.95 Py	Mount McRae Shale	2.50	pyrite	(Rouxel et al., 2005)
WB-98 520.8 Py	Gamohaan Fm	2.52	pyrite	(Rouxel et al., 2005)
WB-98 519.68 Py	Gamohaan Fm	2.52	pyrite	(Rouxel et al., 2005)
SF-1 599.88 Py	Lokammona Fm	2.65	pyrite	(Rouxel et al., 2005)
SF-1 623.6 Py	Lokammona Fm	2.65	pyrite	(Rouxel et al., 2005)
SF-1 642.8 Py	Lokammona Fm	2.65	pyrite	(Rouxel et al., 2005)
FVG-1 752.8 A Py	Jeerinah Fm	2.66	pyrite	(Rouxel et al., 2005)
FVG-1 752.8 B Py	Jeerinah Fm	2.66	pyrite	(Rouxel et al., 2005)
EBA-1 1057.5 BS	Timeball Hill Fm	2.32	black shale	(Rouxel et al., 2006, 2005)
FVG-1 765.8 BS	Jeerinah Fm	2.66	black shale	(Rouxel et al., 2006, 2005)
FVG-1 774 BS	Jeerinah Fm	2.66	black shale	(Rouxel et al., 2006, 2005)
FVG-1 827.8 BS	Jeerinah Fm	2.66	black shale	(Rouxel et al., 2006, 2005)
REX 167.5	Hotazel Fm	2.43	IF	(Gumsley et al., 2017; Thibon et al., 2019; Tsikos et al., 2010)

Table 3.5 continued				
REX 187.5	Hotazel Fm	2.43	IF	(Gumsley et al., 2017; Thibon et al., 2019; Tsikos et al., 2010)
Hotazel #41	Hotazel Fm	2.43	IF	(Gumsley et al., 2017; Thibon et al., 2019; Tsikos et al., 2010)
RM5	Brockman IF	2.47	IF	(Planavsky et al., 2012)
WIT-18-740A	Westerburg area IF	2.48	IF	(Planavsky et al., 2012)
ZO4-31	Manjeri IF	2.70	IF	(Planavsky et al., 2012)
JD-C165A	Mary River IF	2.74	IF	(Planavsky et al., 2012)
JD-65-296-1	Mary River IF	2.74	IF	(Planavsky et al., 2012)
PO5-1	Mozaan Gp	2.95	IF	(Planavsky et al., 2012)
PO5-6	Mozaan Gp	2.95	IF	(Planavsky et al., 2012)
PO5-7	Mozaan Gp	2.95	IF	(Planavsky et al., 2012)
IF-G	Isua Supracrustal Belt	3.83	IF	(Dauphas et al., 2004; Moorbath et al., 1973)

nodular pyrite either had no internal texture, or was composed of concentrically laminated, fine-grained pyrite or bladed pyrite crystals. Euhedral pyrite crystals commonly overgrew the outer part of the nodules. Shale laminae typically bend around pyrite nodules, which supports interpretation of their origin as being formed early on during diagenesis. Pyrite nodules often display complex features such as multiple-growth bands or composite nodules formed by coalescence of several

nodules. Dissolution and reprecipitation of early diagenetic sulfide crystals and nodules could have happened in some samples and likely resulted in formation of massive, pre-compactional pyrite, often characterized by euhedral grains free of C-rich inclusions.

Localized dissolution-reprecipitation is unlikely to have affected Fe-isotopic compositions of pyrites. In the large sets of samples analyzed per formation by ref. (Rouxel et al., 2005), strongly negative δ^{56}Fe values were a consistent feature, and no relationship between Fe isotopic composition and the nature of individual pyrite grains was reported, which supports the notion that these are primary sedimentary signatures and not the results of later alteration of the host rocks. The fidelity of the pyrite Fe isotope record as an archive of primary sedimentary signatures was recently discussed by ref. (Heard and Dauphas, 2020). In brief, the resistance of this system to metamorphic overprinting due to the high abundance of Fe, low solubility of pyrite, and small size of Fe isotopic fractionations at metamorphic temperatures all make it unlikely that primary sedimentary Fe isotopic signatures have been compromised by secondary processes that may nonetheless have affected the texture of pyrite grains. It was recently demonstrated through *in situ* work that Archean pyrites that experienced late fluid circulation, which led to partial recrystallization and alteration of S isotopic systematics, did not modify the Fe isotopic composition (Marin-Carbonne et al., 2020), in line with our expectations outlined above.

Background on mass fractionation laws for Fe isotopes

Instantaneous fractionations

Numerous reaction pathways have been proposed to create the >5‰ δ^{56}Fe range in Archean IFs, shales, and pyrites. The extent of Fe isotopic fractionation is insufficient to discriminate between different scenarios for sedimentary iron cycling in the Archean oceans, because several

fractionation processes can generate a large and indistinguishable range in delta values. Considering two isotopic ratios can resolve this ambiguity for sedimentary pyrite, because different processes impart isotopic fractionations that follow different slopes in $\delta^{56}Fe$ *vs.* $\delta^{57}Fe$ space corresponding to mass fractionation laws (MFL). Mass-dependent fractionation is described with a power law:

$$\alpha^{56}{}_{A/B} = \alpha^{57}{}_{A/B}{}^{\theta^{56/57}}, \qquad \text{(Eq. 21)}$$

where $\alpha^{x}{}_{A/B}$ are fractionation factors for isotope x between reservoirs A and B, and $^{56/57}\theta$ is the mass dependent exponent or slope in triple Fe isotope space (Dauphas and Schauble, 2016). Natural processes imparting different slopes of MFLs in three-isotope diagrams have been identified for O (Angert et al., 2003; Cao and Liu, 2011; Levin et al., 2014; Young et al., 2014), Mg (Davis et al., 2015; Young et al., 2002), S (Farquhar et al., 2003; Johnston et al., 2008; Ono et al., 2006), Ca (Zhang et al., 2014), Ti (Zhang et al., 2014), and Fe (McCoy-West et al., 2018; Nie et al., 2017), but this has yet to be investigated for Fe isotopes in sedimentary rocks with enough precision to resolve distinct slopes. The slope $\theta^{56/57}$ for the triple-Fe-isotopic diagram is given by:

$$\theta^{56/57} = \frac{\Delta\delta'^{56}Fe}{\Delta\delta'^{57}Fe} = \frac{\ln\left[\left(\frac{^{56}Fe}{^{54}Fe}\right)_{sample} \Big/ \left(\frac{^{56}Fe}{^{54}Fe}\right)_{std}\right] - \ln\left[\left(\frac{^{56}Fe}{^{54}Fe}\right)_{initial} \Big/ \left(\frac{^{56}Fe}{^{54}Fe}\right)_{std}\right]}{\ln\left[\left(\frac{^{57}Fe}{^{54}Fe}\right)_{sample} \Big/ \left(\frac{^{57}Fe}{^{54}Fe}\right)_{std}\right] - \ln\left[\left(\frac{^{57}Fe}{^{54}Fe}\right)_{initial} \Big/ \left(\frac{^{57}Fe}{^{54}Fe}\right)_{std}\right]}, \qquad \text{(Eq. 22)}$$

where δ' is related to the standard δ notation by:

$$\delta' = 1000 \times \ln[(\delta/1000)+1]. \qquad \text{(Eq. 23)}$$

Slopes vary only subtly between MFLs and therefore it is convenient for the purpose of visualization to express one isotopic ratio in terms of its deviation from an arbitrary reference law in parts per 10,000 by using ϵ' notation (Dauphas and Schauble, 2016; Nie et al., 2017) where:

$$\epsilon'^{56}Fe = \left(\Delta\delta'^{56}Fe - \theta_r{}^{56/57} \times \Delta\delta'^{57}Fe\right) \times 10. \qquad \text{(Eq. 24)}$$

In $\epsilon'^{56}Fe$ *vs.* $\Delta\delta'^{57}Fe$ diagram, MFLs are straight lines, and when the high-temperature equilibrium limit law with $\theta_r^{56/57} = 0.678$ is used as the reference law, $\epsilon'^{56}Fe$ values are 0 if fractionation follows the high-temperature equilibrium limit law. Other MFLs will then have positive or negative slopes if $\theta^{56/57}$ is larger or smaller than 0.678, respectively.

These laws describe mass-dependent fractionation in a single-step process. This approach is an oversimplification in cases where isotopes have been fractionated via several geochemical pathways, or via Rayleigh distillation. These complications are well-documented in the more mature field of triple O and S isotopes (Angert et al., 2003; Farquhar et al., 2003; Johnston et al., 2008; Ono et al., 2006; Young et al., 2014) but we show here that these concerns are of diminished importance in application to low-temperature Fe isotope systematics. This is because Rayleigh distillation produces trends in $\epsilon'^{56}Fe$ *vs.* $\Delta\delta'^{57}Fe$ space that are practically indistinguishable from instantaneous MFLs over the natural range of Fe isotopic variations.

Rayleigh distillation

Reactant reservoir

In the case of Rayleigh distillation, closed-system evolution of a reactant reservoir (A) during formation of a product (B) results in an observed slope in three-isotope space for A that is distinct from the intrinsic slope of the instantaneous fractionation process (Fig. 3.13A) (Ono et al., 2006; Tang and Dauphas, 2012). In this study, the evolution of the reactant reservoir corresponds to the generation of an isotopically light Fe^{2+} pool through the removal of an isotopically heavy Fe^{3+}-oxyhydroxide product. The evolution of the reactant, written in δ' notation, is,

$$\delta'^{x}Fe_A=(\alpha^{x}-1)\times\ln\left({}^{54}f_A\right)\times1000+\delta'^{x}Fe_{A,i}, \qquad \text{(Eq. 25)}$$

where $\delta'^{x}Fe_{A,i}$ is the initial isotopic composition of the reactant, $\delta'^{x}Fe_{A}$ is the isotopic composition of the reactant when a fraction f_A of the reactant A remains, and α^x is the isotopic fractionation factor for isotope x in the reaction of A to form product B.

In three-isotope space, the isotopic composition of the reactant will evolve with an effective slope, $\theta^{56/57}_{eff}$,

$$\theta^{56/57}_{eff} = \frac{\delta'^{56}Fe_A - \delta'^{56}Fe_{A,i}}{\delta'^{57}Fe_A - \delta'^{57}Fe_{A,i}} = \frac{(\alpha^{56}-1)\times\ln\left({}^{54}f_A\right)}{(\alpha^{57}-1)\times\ln\left({}^{54}f_A\right)} = \frac{\alpha^{57\theta^{56/57}_{inst}}-1}{\alpha^{57}-1}, \qquad \text{(Eq. 26)}$$

where $\theta^{56/57}_{inst}$ is the intrinsic slope for the instantaneous reaction.

Distinction between θ_{inst} and θ_{eff} is significant in the O and S isotope systems, where fractionations and relative isotopic mass differences are large. In the case of Fe isotopes, specifically Rayleigh distillation of aqueous Fe^{2+} driven by oxidation and removal of Fe^{3+} minerals, the relevant values for $\theta^{56/57}_{inst}$ and α^{57} are 0.678 and on the order of 1.0015, respectively. Using these values results in $\theta^{56/57}_{eff} \approx 0.6778$, which is smaller than the intrinsic slope by only 0.0002 and not resolvable from the intrinsic slope for any naturally occurring range of fractionations (Fig. 3.13A). A slightly different relation between the effective and intrinsic slopes for UV photo-oxidation, with α^{56} = 1.0012, previously gave the same result that the effective slope for the evolving reactant reservoir was smaller than the instantaneous slope by just 0.0002, and thus the two slopes were indistinguishable within current measurement uncertainties (Nie et al., 2017). These calculations imply that theoretical, single-step MFLs are an appropriate approximation for the evolution in triple-Fe-isotopic space of an Fe^{2+} reservoir affected by oxidation and removal of Fe^{3+} products following a Rayleigh distillation.

Cumulative product reservoir

The cumulative product reservoir during Rayleigh distillation, which is how we treat the pyrite precipitation along the kinetic MFL, also follows a trend in triple-Fe-isotope space that is distinct from the instantaneous MFL, however in this case the evolution is not linear. The evolution of the cumulative product B is:

$$\delta'^{x}Fe_B = \left({}^{54}f_B - 1\right) \times \ln\left[\frac{\left(1-{}^{54}f_B\right)}{{}^{54}f_B}\right] \times (\alpha^{x}\text{-}1) \times 1000 + \delta'^{x}Fe_{A,i}, \qquad \text{(Eq. 27)}$$

where $\delta'^{x}Fe_B$ is the isotopic composition of the cumulative product when a fraction f_B (= 1- f_A) of the reactant has been consumed.

Nie *et al*. (Nie et al., 2017) showed that as the cumulative product reservoir grows and the reactant pool is consumed, the deviation of the cumulative product $\epsilon'^{56}Fe$ value, $\epsilon'^{56}Fe_{cumulative}$, relative to value $\epsilon'^{56}Fe_{inst}$ that is expected to fall on the instantaneous MFL at a given $\delta'^{57}Fe$ value is:

$$\epsilon'^{56}Fe_{cumulative} - \epsilon'^{56}Fe_{inst} = 10{,}000 \left[\left(\theta^{\,56/57}{}_{inst} - 1\right) \times \ln\left(1-{}^{54}f_A\right) + \ln\left(1-{}^{54}f_A{}^{\alpha^{56}}\right) - \theta^{\,56/57}{}_{inst} \times \ln\left(1- {}^{54}f_A{}^{\left(\alpha^{56\,1/\theta\,56/57}{}_{inst}\right)}\right)\right]. \qquad \text{(Eq. 28)}$$

Here, the relevant values for $\theta^{56/57}{}_{inst}$ and α^{56} are 0.6743 (derived from our triple-Fe-isotope measurements) and 0.9969 (the largest proposed Fe isotopic fractionation during pyrite precipitation from Fe^{2+} via FeS_m (Guilbaud et al., 2011), respectively. Inserting these values into S25 gives a non-linear trend shown in Fig. 3.13B, where the maximum deviation of the cumulative product reservoir from the instantaneous MFL is less than 0.01 $\epsilon'^{56}Fe$ units, and thus well within typical analytical errors of 0.05 (95 % C.I.). These calculations imply that theoretical, single-step

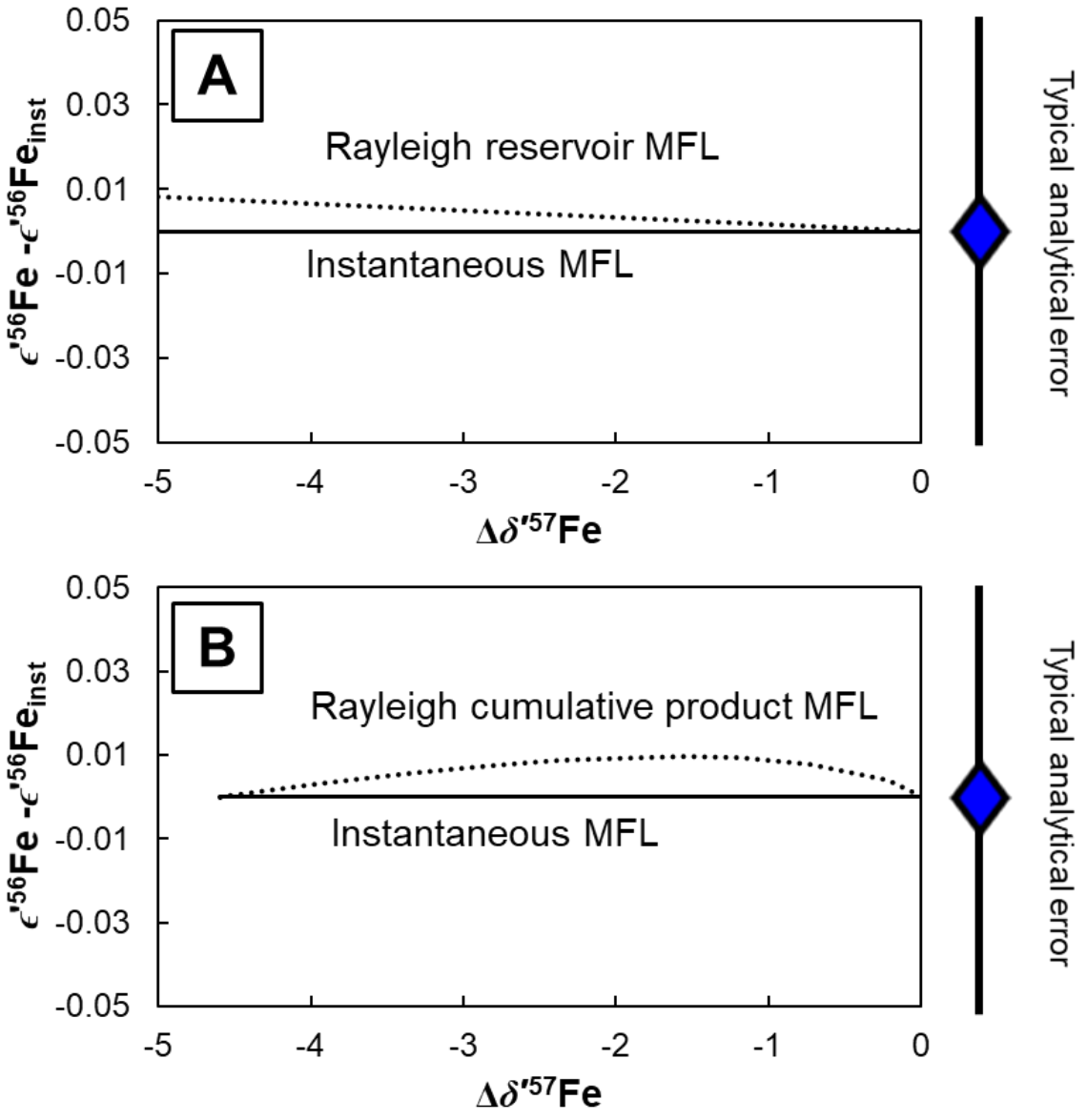

Figure 3.13. Rayleigh distillation effects in triple-Fe-isotopic space. A. Comparison of the effective MFL for Rayleigh distillation (dotted line) with the instantaneous MFL for the fractionation between reactant and product (solid line). The differing slopes result in a $\theta^{56/57}$ difference of just 0.0002, well within achievable analytical error for natural ranges of fractionation. B. Comparison of the effective mass fractionation array (dotted line) with the instantaneous MFL for the product precipitation (solid line), for the case of pyrite precipitation from solution as a cumulative Rayleigh distillation product with the maximum instantaneous fractionation $1000 \times (\alpha^{56}-1)$ of -3.1 ‰ suggested by ref. (Guilbaud et al., 2011). The maximum deviation is less than 0.01 ϵ'^{56}Fe units, well within analytical error. Both reactant and product reservoir trends are identical to the instantaneous MFL for the process driving Fe isotopic fractionation over the naturally observed range of values within analytical error for ϵ'^{56}Fe value, which is typically on the order of ±0.05 (95 % C.I.).

MFLs are an appropriate approximation for the evolution in triple-Fe-isotopic space of cumulative product reservoir pyrite following a Rayleigh distillation.

Iron isotope MFLs

Mass-dependent triple-Fe-isotopic systematics have been explored in few publications to date, and only once previously in the context of low-temperature aqueous geochemistry. Nie *et al.* (Nie et al., 2017) determined $\theta^{56/57} = 0.6785 \pm 0.0009$ associated with UV photo-oxidation of dissolved Fe^{2+} in anoxic solutions at near-neutral pH. A high precision measurement of the ca. 3.83 Ga IF-G geostandard from an IF in Isua, Greenland has $\epsilon'^{56}Fe$ and $\Delta\delta'^{57}Fe$ values consistent with isotopically heavy ferric precipitates from those experiments (Nie et al., 2017) and both are within error of the high-temperature limit equilibrium law with $\theta^{56/57} = 0.678$. However, the magnitude of isotopic enrichment in IF-G and isotopically heavy IF oxyhydroxides in general provide insufficient leverage in three-isotope space to distinguish different MFLs at the available precision for $\epsilon'^{56}Fe$. Whether different iron oxidation pathways for IF deposition do have distinct MFLs has not yet been tested experimentally. However, the fact that the high-temperature equilibrium law, the MFL for photo-oxidation, and our observed MFL defined by IFs including the Hotazel Mn-rich IF samples that were most likely fractionated by direct O_2 oxidation (Tsikos et al., 2010), are all within error of one another, suggests that fractionations of Fe isotopes driven by Fe^{2+}-Fe^{2+} equilibration may follow the equilibrium MFL regardless of the oxidation process involved (Welch et al., 2003). The empirical constraints provided by new natural samples measurements here, and the experiments of Nie et al. (2017), agree with the previously documented phenomenon that the high-temperature equilibrium limit law is broadly applicable in equilibrium isotope exchange processes including some of those that occur at low temperatures (Dauphas and Schauble, 2016).

The same may be true for Fe isotopic fractionation during iron reduction processes like DIR, as it has been shown that this process introduces fractionation during Fe^{2+}-Fe^{3+} equilibration following the reduction step (Crosby et al., 2007). It will be important for future studies to constrain the value of $\theta^{56/57}$ for the remaining proposed oxidation pathway for IF, anoxygenic photoferrotrophy (Kappler et al., 2005; Konhauser et al., 2017). However our results to date suggest it is unlikely that triple-Fe-isotopic systematics will be able to identify the oxidation pathway for IF due to the tendency of Fe^{2+} and Fe^{3+} to rapidly isotopically equilibrate (Welch et al., 2003).

Precipitation of pyrite is a kinetically controlled process associated with a large kinetic isotope effect that enriches early precipitates in the light isotopes of Fe (Guilbaud et al., 2011; Rolison et al., 2018). The $\theta^{56/57}$ for kinetic processes can take a range of values depending on the specific reaction process taking place, but is in general expected to be smaller than the high-temperature equilibrium limit law $\theta^{56/57}$ value (Dauphas and Schauble, 2016; Young et al., 2002). The value of $\theta^{56/57}$ relevant to pyrite precipitation did not have an empirical constraint prior to our study. Our pyrite precipitation experiments resulted in maximum degree of pyritization of ~14% (Fig. 3.5). By mass balance most iron was always left in the FeS_m pool and large fractionations from the starting composition of the experiment were observed in the pyrite pool, which provides leverage to determine the slope of the instantaneous MFL associated with pyrite precipitation. Our triple-Fe-isotopic analysis is consistent with a single kinetic MFL, with a slope $\theta^{56/57}_{KIE} = 0.6743 \pm 0.0005$. This is a much shallower slope than that of the equilibrium limit law associated with redox equilibrium (Dauphas and Schauble, 2016; Young et al., 2002).

References

Anbar, A.D., Duan, Y., Lyons, T.W., Arnold, G.L., Kendall, B., Creaser, R.A., Kaufman, A.J., Gordon, G.W., Scott, C., Garvin, J., Buick, R., 2007. A Whiff of Oxygen Before the Great Oxidation Event? Science 317, 1903–1906. https://doi.org/10.1126/science.1140325

Angert, A., Rachmilevitch, S., Barkan, E., Luz, B., 2003. Effects of photorespiration, the cytochrome pathway, and the alternative pathway on the triple isotopic composition of atmospheric O2. Glob. Biogeochem. Cycles 17, 1030. https://doi.org/10.1029/2002GB001933

Archer, C., Vance, D., 2006. Coupled Fe and S isotope evidence for Archean microbial Fe(III) and sulfate reduction. Geology 34, 153–156. https://doi.org/10.1130/G22067.1

Beard, B.L., Johnson, C.M., Cox, L., Sun, H., Nealson, K.H., Aguilar, C., 1999. Iron Isotope Biosignatures. Science 285, 1889–1892. https://doi.org/10.1126/science.285.5435.1889

Beard, B.L., Johnson, C.M., Damm, K.L.V., Poulson, R.L., 2003. Iron isotope constraints on Fe cycling and mass balance in oxygenated Earth oceans. Geology 31, 629–632. https://doi.org/10.1130/0091-7613(2003)031<0629:IICOFC>2.0.CO;2

Bekker, A., Slack, J.F., Planavsky, N., Krapež, B., Hofmann, A., Konhauser, K.O., Rouxel, O.J., 2010. Iron Formation: The Sedimentary Product of a Complex Interplay among Mantle, Tectonic, Oceanic, and Biospheric Processes. Econ. Geol. 105, 467–508. https://doi.org/10.2113/gsecongeo.105.3.467

Bindeman, I.N., Zakharov, D.O., Palandri, J., Greber, N.D., Dauphas, N., Retallack, G.J., Hofmann, A., Lackey, J.S., Bekker, A., 2018. Rapid emergence of subaerial landmasses and onset of a modern hydrologic cycle 2.5 billion years ago. Nature 557, 545. https://doi.org/10.1038/s41586-018-0131-1

Brounce, M., Stolper, E., Eiler, J., 2017. Redox variations in Mauna Kea lavas, the oxygen fugacity of the Hawaiian plume, and the role of volcanic gases in Earth's oxygenation. Proc. Natl. Acad. Sci. 114, 8997–9002. https://doi.org/10.1073/pnas.1619527114

Cao, X., Liu, Y., 2011. Equilibrium mass-dependent fractionation relationships for triple oxygen isotopes. Geochim. Cosmochim. Acta 75, 7435–7445. https://doi.org/10.1016/j.gca.2011.09.048

Catling, D.C., Zahnle, K.J., McKay, C.P., 2001. Biogenic Methane, Hydrogen Escape, and the Irreversible Oxidation of Early Earth. Science 293, 839–843. https://doi.org/10.1126/science.1061976

Craddock, P.R., Dauphas, N., 2011. Iron Isotopic Compositions of Geological Reference Materials and Chondrites. Geostand. Geoanalytical Res. 35, 101–123. https://doi.org/10.1111/j.1751-908X.2010.00085.x

Crosby, Roden Eric E., Johnson Clark M., Beard Brian L., 2007. The mechanisms of iron isotope fractionation produced during dissimilatory Fe(III) reduction by Shewanella putrefaciens and Geobacter sulfurreducens. Geobiology 5, 169–189. https://doi.org/10.1111/j.1472-4669.2007.00103.x

Crowe, S.A., Paris, G., Katsev, S., Jones, C., Kim, S.-T., Zerkle, A.L., Nomosatryo, S., Fowle, D.A., Adkins, J.F., Sessions, A.L., Farquhar, J., Canfield, D.E., 2014. Sulfate was a trace constituent of Archean seawater. Science 346, 735–739. https://doi.org/10.1126/science.1258966

Czaja, A.D., Johnson, C.M., Roden, E.E., Beard, B.L., Voegelin, A.R., Nägler, T.F., Beukes, N.J., Wille, M., 2012. Evidence for free oxygen in the Neoarchean ocean based on coupled iron–molybdenum isotope fractionation. Geochim. Cosmochim. Acta 86, 118–137. https://doi.org/10.1016/j.gca.2012.03.007

Dauphas, N., Cook, D.L., Sacarabany, A., Fröhlich, C., Davis, A.M., Wadhwa, M., Pourmand, A., Rauscher, T., Gallino, R., 2008. Iron 60 Evidence for Early Injection and Efficient Mixing of Stellar Debris in the Protosolar Nebula. Astrophys. J. 686, 560–569. https://doi.org/10.1086/589959

Dauphas, N., John, S.G., Rouxel, O., 2017. Iron Isotope Systematics. Rev. Mineral. Geochem. 82, 415–510. https://doi.org/10.1515/9783110545630-012

Dauphas, N., Pourmand, A., Teng, F.-Z., 2009. Routine isotopic analysis of iron by HR-MC-ICPMS: How precise and how accurate? Chem. Geol., Advances in experimental and theoretical isotope geochemistry 267, 175–184. https://doi.org/10.1016/j.chemgeo.2008.12.011

Dauphas, N., Schauble, E.A., 2016. Mass Fractionation Laws, Mass-Independent Effects, and Isotopic Anomalies. Annu. Rev. Earth Planet. Sci. 44, 709–783. https://doi.org/10.1146/annurev-earth-060115-012157

Dauphas, N., Zuilen, M. van, Wadhwa, M., Davis, A.M., Marty, B., Janney, P.E., 2004. Clues from Fe Isotope Variations on the Origin of Early Archean BIFs from Greenland. Science 306, 2077–2080. https://doi.org/10.1126/science.1104639

Davis, A.M., Richter, F.M., Mendybaev, R.A., Janney, P.E., Wadhwa, M., McKeegan, K.D., 2015. Isotopic mass fractionation laws for magnesium and their effects on 26Al–26Mg systematics in solar system materials. Geochim. Cosmochim. Acta 158, 245–261. https://doi.org/10.1016/j.gca.2015.01.034

Farquhar, J., Bao, H., Thiemens, M., 2000. Atmospheric Influence of Earth's Earliest Sulfur Cycle. Science 289, 756–758. https://doi.org/10.1126/science.289.5480.756

Farquhar, J., Johnston, D.T., Wing, B.A., Habicht, K.S., Canfield, D.E., Airieau, S., Thiemens, M.H., 2003. Multiple sulphur isotopic interpretations of biosynthetic pathways: implications for biological signatures in the sulphur isotope record. Geobiology 1, 27–36. https://doi.org/10.1046/j.1472-4669.2003.00007.x

Flament, N., Coltice, N., Rey, P.F., 2008. A case for late-Archaean continental emergence from thermal evolution models and hypsometry. Earth Planet. Sci. Lett. 275, 326–336. https://doi.org/10.1016/j.epsl.2008.08.029

Gaillard, F., Scaillet, B., Arndt, N.T., 2011. Atmospheric oxygenation caused by a change in volcanic degassing pressure. Nature 478, 229–232. https://doi.org/10.1038/nature10460

Guilbaud, R., Butler, I.B., Ellam, R.M., 2011. Abiotic Pyrite Formation Produces a Large Fe Isotope Fractionation. Science 332, 1548–1551. https://doi.org/10.1126/science.1202924

Gumsley, A.P., Chamberlain, K.R., Bleeker, W., Söderlund, U., Kock, M.O. de, Larsson, E.R., Bekker, A., 2017. Timing and tempo of the Great Oxidation Event. Proc. Natl. Acad. Sci. 114, 1811–1816. https://doi.org/10.1073/pnas.1608824114

Halevy, I., Johnston, D.T., Schrag, D.P., 2010. Explaining the Structure of the Archean Mass-Independent Sulfur Isotope Record. Science 329, 204–207. https://doi.org/10.1126/science.1190298

Heard, A.W., Dauphas, N., 2020. Constraints on the coevolution of oxic and sulfidic ocean iron sinks from Archean–Paleoproterozoic iron isotope records. Geology 48, 358–362. https://doi.org/10.1130/G46951.1

Holland, H.D., 2002. Volcanic gases, black smokers, and the great oxidation event. Geochim. Cosmochim. Acta 66, 3811–3826. https://doi.org/10.1016/S0016-7037(02)00950-X

Holland, H.D., 1984. The Chemical Evolution of the Atmosphere and Oceans. Princeton University Press.

Jamieson, J.W., Wing, B.A., Farquhar, J., Hannington, M.D., 2013. Neoarchaean seawater sulphate concentrations from sulphur isotopes in massive sulphide ore. Nat. Geosci. 6, 61–64. https://doi.org/10.1038/ngeo1647

Johnston, D.T., 2011. Multiple sulfur isotopes and the evolution of Earth's surface sulfur cycle. Earth-Sci. Rev. 106, 161–183. https://doi.org/10.1016/j.earscirev.2011.02.003

Johnston, D.T., Farquhar, J., Habicht, K.S., Canfield, D.E., 2008. Sulphur isotopes and the search for life: strategies for identifying sulphur metabolisms in the rock record and beyond. Geobiology 6, 425–435. https://doi.org/10.1111/j.1472-4669.2008.00171.x

Kappler, A., Pasquero, C., Konhauser, K.O., Newman, D.K., 2005. Deposition of banded iron formations by anoxygenic phototrophic Fe(II)-oxidizing bacteria. Geology 33, 865–868. https://doi.org/10.1130/G21658.1

Klein, C., 2005. Some Precambrian banded iron-formations (BIFs) from around the world: Their age, geologic setting, mineralogy, metamorphism, geochemistry, and origins. Am. Mineral. 90, 1473–1499. https://doi.org/10.2138/am.2005.1871

Konhauser, K.O., Hamade, T., Raiswell, R., Morris, R.C., Ferris, F.G., Southam, G., Canfield, D.E., 2002. Could bacteria have formed the Precambrian banded iron formations? Geology 30, 1079–1082. https://doi.org/10.1130/0091-7613(2002)030<1079:CBHFTP>2.0.CO;2

Konhauser, K.O., Planavsky, N.J., Hardisty, D.S., Robbins, L.J., Warchola, T.J., Haugaard, R., Lalonde, S.V., Partin, C.A., Oonk, P.B.H., Tsikos, H., Lyons, T.W., Bekker, A., Johnson, C.M., 2017. Iron formations: A global record of Neoarchaean to Palaeoproterozoic environmental history. Earth-Sci. Rev. 172, 140–177. https://doi.org/10.1016/j.earscirev.2017.06.012

Kump, L.R., Barley, M.E., 2007. Increased subaerial volcanism and the rise of atmospheric oxygen 2.5 billion years ago. Nature 448, 1033–1036. https://doi.org/10.1038/nature06058

Levin, N.E., Raub, T.D., Dauphas, N., Eiler, J.M., 2014. Triple oxygen isotope variations in sedimentary rocks. Geochim. Cosmochim. Acta 139, 173–189. https://doi.org/10.1016/j.gca.2014.04.034

Lyons, T.W., Gill, B.C., 2010. Ancient Sulfur Cycling and Oxygenation of the Early Biosphere. Elements 6, 93–99. https://doi.org/10.2113/gselements.6.2.93

Mansor, M., Fantle, M.S., 2019. A novel framework for interpreting pyrite-based Fe isotope records of the past. Geochim. Cosmochim. Acta 253, 39–62. https://doi.org/10.1016/j.gca.2019.03.017

Marin-Carbonne, J., Busigny, V., Miot, J., Rollion-Bard, C., Muller, E., Drabon, N., Jacob, D., Pont, S., Robyr, M., Bontognali, T.R.R., François, C., Reynaud, S., Zuilen, M.V., Philippot, P., 2020. In Situ Fe and S isotope analyses in pyrite from the 3.2 Ga Mendon Formation (Barberton Greenstone Belt, South Africa): Evidence for early microbial iron reduction. Geobiology n/a. https://doi.org/10.1111/gbi.12385

Marin-Carbonne, J., Rollion-Bard, C., Bekker, A., Rouxel, O., Agangi, A., Cavalazzi, B., Wohlgemuth-Ueberwasser, C.C., Hofmann, A., McKeegan, K.D., 2014. Coupled Fe and S isotope variations in pyrite nodules from Archean shale. Earth Planet. Sci. Lett. 392, 67–79. https://doi.org/10.1016/j.epsl.2014.02.009

McCoy-West, A.J., Fitton, J.G., Pons, M.-L., Inglis, E.C., Williams, H.M., 2018. The Fe and Zn isotope composition of deep mantle source regions: Insights from Baffin Island picrites. Geochim. Cosmochim. Acta 238, 542–562. https://doi.org/10.1016/j.gca.2018.07.021

Millero, F.J., Sotolongo, S., Izaguirre, M., 1987. The oxidation kinetics of Fe(II) in seawater. Geochim. Cosmochim. Acta 51, 793–801. https://doi.org/10.1016/0016-7037(87)90093-7

Moorbath, S., O'nions, R.K., Pankhurst, R.J., 1973. Early Archaean Age for the Isua Iron Formation, West Greenland. Nature 245, 138. https://doi.org/10.1038/245138a0

Nie, N.X., Dauphas, N., Greenwood, R.C., 2017. Iron and oxygen isotope fractionation during iron UV photo-oxidation: Implications for early Earth and Mars. Earth Planet. Sci. Lett. 458, 179–191. https://doi.org/10.1016/j.epsl.2016.10.035

Olson, S.L., Kump, L.R., Kasting, J.F., 2013. Quantifying the areal extent and dissolved oxygen concentrations of Archean oxygen oases. Chem. Geol., Special Issue dedicated to H.D. Holland: Evolution of the atmosphere and ocean through time 362, 35–43. https://doi.org/10.1016/j.chemgeo.2013.08.012

Olson, S.L., Ostrander, C.M., Gregory, D.D., Roy, M., Anbar, A.D., Lyons, T.W., 2019. Volcanically modulated pyrite burial and ocean–atmosphere oxidation. Earth Planet. Sci. Lett. 506, 417–427. https://doi.org/10.1016/j.epsl.2018.11.015

Ono, S., Wing, B., Johnston, D., Farquhar, J., Rumble, D., 2006. Mass-dependent fractionation of quadruple stable sulfur isotope system as a new tracer of sulfur biogeochemical cycles. Geochim. Cosmochim. Acta 70, 2238–2252. https://doi.org/10.1016/j.gca.2006.01.022

Ostrander, C.M., Nielsen, S.G., Owens, J.D., Kendall, B., Gordon, G.W., Romaniello, S.J., Anbar, A.D., 2019. Fully oxygenated water columns over continental shelves before the Great Oxidation Event. Nat. Geosci. 12, 186–191. https://doi.org/10.1038/s41561-019-0309-7

Planavsky, N., Rouxel, O.J., Bekker, A., Hofmann, A., Little, C.T.S., Lyons, T.W., 2012. Iron isotope composition of some Archean and Proterozoic iron formations. Geochim. Cosmochim. Acta 80, 158–169. https://doi.org/10.1016/j.gca.2011.12.001

Planavsky, N.J., Asael, D., Hofmann, A., Reinhard, C.T., Lalonde, S.V., Knudsen, A., Wang, X., Ossa Ossa, F., Pecoits, E., Smith, A.J.B., Beukes, N.J., Bekker, A., Johnson, T.M., Konhauser, K.O., Lyons, T.W., Rouxel, O.J., 2014. Evidence for oxygenic photosynthesis half a billion years before the Great Oxidation Event. Nat. Geosci. 7, 283–286. https://doi.org/10.1038/ngeo2122

Polyakov, V.B., Clayton, R.N., Horita, J., Mineev, S.D., 2007. Equilibrium iron isotope fractionation factors of minerals: Reevaluation from the data of nuclear inelastic resonant X-ray scattering and Mössbauer spectroscopy. Geochim. Cosmochim. Acta 71, 3833–3846. https://doi.org/10.1016/j.gca.2007.05.019

Reinhard, C.T., Raiswell, R., Scott, C., Anbar, A.D., Lyons, T.W., 2009. A Late Archean Sulfidic Sea Stimulated by Early Oxidative Weathering of the Continents. Science 326, 713–716. https://doi.org/10.1126/science.1176711

Rickard, D., 1997. Kinetics of pyrite formation by the H2S oxidation of iron (II) monosulfide in aqueous solutions between 25 and 125°C: The rate equation. Geochim. Cosmochim. Acta 61, 115–134. https://doi.org/10.1016/S0016-7037(96)00321-3

Rickard, D., Griffith, A., Oldroyd, A., Butler, I.B., Lopez-Capel, E., Manning, D.A.C., Apperley, D.C., 2006. The composition of nanoparticulate mackinawite, tetragonal iron(II) monosulfide. Chem. Geol. 235, 286–298. https://doi.org/10.1016/j.chemgeo.2006.07.004

Rolison, J.M., Stirling, C.H., Middag, R., Gault-Ringold, M., George, E., Rijkenberg, M.J.A., 2018. Iron isotope fractionation during pyrite formation in a sulfidic Precambrian ocean analogue. Earth Planet. Sci. Lett. 488, 1–13. https://doi.org/10.1016/j.epsl.2018.02.006

Rouxel, O.J., Bekker, A., Edwards, K.J., 2006. Response to Comment on "Iron Isotope Constraints on the Archean and Paleoproterozoic Ocean Redox State." Science 311, 177–177. https://doi.org/10.1126/science.1118420

Rouxel, O.J., Bekker, A., Edwards, K.J., 2005. Iron Isotope Constraints on the Archean and Paleoproterozoic Ocean Redox State. Science 307, 1088–1091. https://doi.org/10.1126/science.1105692

Schiller, M., Bizzarro, M., Siebert, J., 2020. Iron isotope evidence for very rapid accretion and differentiation of the proto-Earth. Sci. Adv. 6, eaay7604. https://doi.org/10.1126/sciadv.aay7604

Scott, C.T., Bekker, A., Reinhard, C.T., Schnetger, B., Krapež, B., Rumble, D., Lyons, T.W., 2011. Late Archean euxinic conditions before the rise of atmospheric oxygen. Geology 39, 119–122. https://doi.org/10.1130/G31571.1

Severmann, S., Lyons, T.W., Anbar, A., McManus, J., Gordon, G., 2008. Modern iron isotope perspective on the benthic iron shuttle and the redox evolution of ancient oceans. Geology 36, 487–490. https://doi.org/10.1130/G24670A.1

Stüeken, E.E., Catling, D.C., Buick, R., 2012. Contributions to late Archaean sulphur cycling by life on land. Nat. Geosci. 5, 722–725. https://doi.org/10.1038/ngeo1585

Tang, H., Dauphas, N., 2012. Abundance, distribution, and origin of 60Fe in the solar protoplanetary disk. Earth Planet. Sci. Lett. 359–360, 248–263. https://doi.org/10.1016/j.epsl.2012.10.011

Tang, H., Dauphas, N., Craddock, P.R., 2009. High Precision Iron Isotopic Analyzes Of Meteorites And Terrestrial Rocks: 60fe Distribution And Mass Fractionation Laws. LPS XXXX 40, 1903.

Thibon, F., Blichert-Toft, J., Tsikos, H., Foden, J., Albalat, E., Albarede, F., 2019. Dynamics of oceanic iron prior to the Great Oxygenation Event. Earth Planet. Sci. Lett. 506, 360–370. https://doi.org/10.1016/j.epsl.2018.11.016

Trendall, A.F., Morris, R.C., 2000. Iron-Formation: Facts and Problems. Elsevier.

Tsikos, H., Matthews, A., Erel, Y., Moore, J.M., 2010. Iron isotopes constrain biogeochemical redox cycling of iron and manganese in a Palaeoproterozoic stratified basin. Earth Planet. Sci. Lett. 298, 125–134. https://doi.org/10.1016/j.epsl.2010.07.032

Ward, L.M., Kirschvink, J.L., Fischer, W.W., 2016. Timescales of Oxygenation Following the Evolution of Oxygenic Photosynthesis. Orig. Life Evol. Biospheres 46, 51–65. https://doi.org/10.1007/s11084-015-9460-3

Welch, S.A., Beard, B.L., Johnson, C.M., Braterman, P.S., 2003. Kinetic and equilibrium Fe isotope fractionation between aqueous Fe(II) and Fe(III). Geochim. Cosmochim. Acta 67, 4231–4250. https://doi.org/10.1016/S0016-7037(03)00266-7

Yamaguchi, K.E., Ohmoto, H., 2006. Comment on "Iron Isotope Constraints on the Archean and Paleoproterozoic Ocean Redox State." Science 311, 177–177. https://doi.org/10.1126/science.1118221

Young, E.D., Galy, A., Nagahara, H., 2002. Kinetic and equilibrium mass-dependent isotope fractionation laws in nature and their geochemical and cosmochemical significance. Geochim. Cosmochim. Acta 66, 1095–1104. https://doi.org/10.1016/S0016-7037(01)00832-8

Young, E.D., Yeung, L.Y., Kohl, I.E., 2014. On the Δ17O budget of atmospheric O2. Geochim. Cosmochim. Acta 135, 102–125. https://doi.org/10.1016/j.gca.2014.03.026
Zhang, J., Huang, S., Davis, A.M., Dauphas, N., Hashimoto, A., Jacobsen, S.B., 2014. Calcium and titanium isotopic fractionations during evaporation. Geochim. Cosmochim. Acta 140, 365–380. https://doi.org/10.1016/j.gca.2014.05.022

Chapter 4: Rapid iron oxidation at the microbial epicenter of an oxygen oasis predating the rise of atmospheric oxygen.

Foreword

The first major oxygenation of Earth's atmosphere in the Great Oxidation Event (GOE) took place ~2.43 billion years (Ga) ago (Bekker et al., 2004; Gumsley et al., 2017; Luo et al., 2016), when O_2 produced by cyanobacteria accumulated to $>>10^{-5}$ × present atmospheric levels (PAL = 0.21 atm) (Pavlov and Kasting, 2002). The accumulation of atmospheric oxygen on Earth should have had two basic preconditions: (i) oxygenic photosynthesis was being performed by cyanobacteria, and (ii) an imbalance in Earth's surface oxidants and reductants that led to all major reductants for O_2 being overwhelmed. Surface redox buffers were saturated over geologic timescales by a range of processes including irreversible H_2 escape to space (Catling et al., 2001), oxidative weathering of the continents, changing volcanic gas fluxes (Gaillard et al., 2011; Kadoya et al., 2020; Kump and Barley, 2007), and greater extents of shallow marine Fe^{2+} oxidation and removal (Czaja et al., 2018).

Thus far in this thesis, we have focused mostly in (ii); the evolution of geological redox sinks, implicitly assuming that oxygenic photosynthesis was already operating on Earth. In Chapter 1, we showed that the atmosphere remained anoxic at 2.95 Ga, allowing the efficient mobilization of Fe^{2+} from the continents; despite contemporaneous evidence for free O_2 in the marine realm at this time. And in Chapters 2 and 3, we showed how the oxic and sulfidic sinks for marine Fe co-evolved in the runup to the GOE, and explored the implications of a growing sulfidic sink, in particular, for the next oxidation of the Neoarchean Earth surface. A few details of the geological record prior to the GOE, such as Mo and Tl isotopic evidence for Mn oxidation in marine O_2 'oases' at as early as 2.95 Ga (Kurzweil et al., 2016; Ossa Ossa et al., 2018; Ostrander et al., 2019; Planavsky et al.,

2014a), and coincident whiffs of atmospheric O_2 around 2.52 Ga (Anbar et al., 2007), lead us to assuming O_2 was already available as an oxidant long prior to the GOE.

More skeptical viewpoints exist that argue for a late evolution of cyanobacteria and a rapid, overwhelming oxygenation of the atmosphere immediately following this biogeochemical revolution (Fischer et al., 2016; Johnson et al., 2013; Ward et al., 2016). In particular, many of the geochemical arguments for pre-GOE oxygenic photosynthesis rely on indirect trace isotopic evidence for substantial Mn^{2+} oxidation and Mn oxide burial (Kurzweil et al., 2016; Ossa Ossa et al., 2018; Ostrander et al., 2019; Planavsky et al., 2014a), a process though to strictly require O_2 to occur in natural environments. In the alternative 'O_2-skeptical' viewpoint, Mn oxide burial could have been facilitated by newly described anoxygenic Mn^{2+}-oxidizing photosynthetic bacteria (Daye et al., 2019; Johnson et al., 2013). In one iteration of this alternative model, the evolution of Mn-oxidizing photosynthesis was a critical step in the process of the assembling the water-oxidizing complex involved in oxygenic photosynthesis that shortly preceded the rise of cyanobacteria and the GOE (Fischer et al., 2016; Johnson et al., 2013). However, this version of the model struggles to explain Mn oxidation signatures in the 2.95 Ga Pongola Supergroup, half a billion years before the GOE (Ossa Ossa et al., 2018; Planavsky et al., 2014a), and has not become well-accepted. We must also bear in mind that the Mn-oxidation debate frames the timing for the evolution of oxygenic photosynthesis in terms of accumulations of 'geochemically interesting' levels of O_2, which in the case of driving appreciable marine Mn^{2+} oxidation, lie in the 0.1-10 μM range (Clement et al., 2009). However, lipid biomarkers indicate that steroid synthesis was also taking place in the surface oceans prior to the GOE, and steroid biosynthesis has itself been shown to be a microaerobic process, albeit one that requires mere nanomolar concentrations of dissolved O_2 (Waldbauer et al., 2011). This blurs the lines between the inorganic geochemical arguments for

and against early oxygenic photosynthesis, because it could be true both that anoxygenic photosynthesis was important in pre-GOE Mn oxide burial, and that cyanobacteria and oxygenic photosynthesis evolved hundreds of millions of years prior to the GOE.

Regardless, recent changes in understanding the (bio)geochemical pathways to Mn oxidation prior to the GOE serves as a good motivation to revisit precondition (i) for the rise of atmospheric oxygen: the emergence of oxygenic photosynthesis as a geochemically significant process. In addition to geochemical and biomarker evidence for pre-GOE oxygenic photosynthesis, there is a rich sedimentological record for early photosynthetic life, including potentially cyanobacterial life, in the form of stromatolites. Stromatolites are sedimentary rock features that are thought to be the fossilized remnants of accumulations of layers of microbial mats. They are formed in very few places on the modern Earth, because during their active formation, stromatolites are little more than mounds of vulnerable and nutritious organic material that grazing organisms can eat. The most notable modern-day examples of actively growing stromatolites are found in Shark Bay, Australia, and they survive because the waters in Shark Bay are hypersaline, and uninhabitable for the kinds of life that would typically feed on stromatolites. Stromatolites, much like modern microbial accumulations, can take on a wide range of shapes that reflect the physical environment they form in, but all of them are characterized by containing layers, or laminations, of sequential microbial mat growth (Bosak et al., 2013). When these individual microbial mat surfaces become lithified, either by chemical precipitation of minerals like carbonates, oxides, and silica, or by the physical trapping of sedimentary grains, they can become preserved in the rock record as sedimentary rocks with laminations that have a rich variety of 3-dimensional structures. Given that all life for the first ~4 billion years of Earth history was purely microbial, stromatolites are the main feature of the Precambrian ‘fossil’ record, and putative stromatolites have been reported in

rocks as old as 3.7 Ga, in Isua, Greenland (Nutman et al., 2016). The biogenicity of the 3.7 Ga Isua 'stromatolites' is highly controversial because they occur in heavily metamorphosed rocks and could plausibly be rock deformation features rather than primary sedimentary structures (Allwood et al., 2018; Zawaski et al., 2020), but more widely accepted stromatolites are still found as early as ~3.5-3.43 Ga (Allwood et al., 2007, 2006; Djokic et al., 2017).

Stromatolites that are studied with the most interest, particularly in the pre-GOE record, those that show morphological evidence of phototaxis, which is upward growth towards a light source. Phototaxis implies that the stromatolites were continually growing above the surface of accumulating sediment, and this morphology is commonly taken as evidence that the microbial mats within these stromatolites were composed of photosynthetic organisms. Examples of this morphology are stromatolites that have conical or columnar shapes (Bosak et al., 2013). The stromatolites in Shark Bay, for instance, appear as steep-sided mounds that stand proud of the seafloor. Conical stromatolites can be found in the fossil record from 3.4 Ga onward (Allwood et al., 2007), providing strong evidence that photosynthesis, if not oxygenic photosynthesis, had evolved by this time. Additionally, morphological observations of conical stromatolites as old as 2.7 Ga have been made that suggest that their inhabitants might have been performing oxygenic photosynthesis. Bosak et al. (2009) investigated the central axis of Precambrian conical stromatolites and observed that from 2.7 Ga onward, contorted laminae filled with carbonate cement, suggesting the initial presence of voids, can be found. They argued that these apparent axial void spaces were caused by the formation of gas bubbles between stromatolitic laminae during active growth and compared these structures to the voids found in modern-day conical microbial structures from Yellowstone National Park. Bosak et al. (2009) suggested that the most likely biogenic gas being produced in these conical stromatolites was O_2, generated during

oxygenic photosynthesis, because the other possible biogenic gases (H_2, CH_4, CO_2, CO, H_2S, N_2O, or N_2) would not be generated at apex of the stromatolites, instead tending to eradicate primary laminations and form irregular structures.

Many pre-GOE stromatolites, including those in which possible O_2 bubble formation (Bosak et al., 2009) has been observed, are developed on shallow water carbonate platforms, and are composed dominantly of limestone, dolomite, or chert. Many redox-sensitive trace isotope systems are also reliably preservable in limestones over billion-year timescales. Due to the lack of suitability and/or interest for targeting such samples in the trace metal isotope studies used to infer ancient ocean redox conditions, the morphological and geochemical lines of evidence for early oxygenic photosynthesis are spatially separated, with a possible O_2 production being indicated by shallow water stromatolite morphologies, and possible O_2 consumption being indicated with evidence for Mn oxide burial in oxygen oases sampled further offshore (Olson et al., 2013; Ossa Ossa et al., 2018; Ostrander et al., 2019; Planavsky et al., 2014a). The models for these oases all assume a diffuse O_2 distribution in the shallow water column but have yet to identify specific sources for this O_2. A true 'smoking gun' sample for early cyanobacteria would be one that provides both morphological evidence for photosynthetic life, and geochemical evidence for the local consumption of oxygen, such as evidence for extensive local oxidation of a redox-sensitive metals. One reason such samples might be rare in the pre-GOE rock record is that Archean and early Paleoprotoerozic ocean basins appear to have had a well-established vertical redox structure, where the deep basins were ferruginous, and shallow shelf environments were generally Fe-poor, lending themselves to the deposition of limestones and dolomites that cannot precipitate in the presence of elevated [Fe^{2+}] (*e.g.* Eroglu et al., 2018; Klein and Beukes, 1989; Riding et al., 2014; Sumner, 1997). As Fe^{2+} upwelled from deep basins, Fe^{2+} would be progressively removed by

partial oxidation or hydrous silicate precipitation to form deep water iron formations (IFs) (Bekker et al., 2010; Eroglu et al., 2018; Planavsky et al., 2012; Rouxel et al., 2005), with little Fe^{2+} remaining once upwelled waters reached the shelf. This model is supported by Fe isotope and Mn/Fe data from IFs that show a negative log-linear correlation consistent with Rayleigh distillation of Fe by partial oxidation, and the passive enrichment of Mn/Fe because oxidation mechanisms were insufficient to effectively oxidize Mn^{2+} (Hiebert et al., 2018; Thibon et al., 2019; Tsikos et al., 2010). This basin structure and geochemical interpretation works with any of the proposed oxidation mechanisms for IFs (O_2, anoxygenic photosynthesis, and UV photooxidation), so the redox structure and geochemical characteristics of Neoarchean basins does not provide definitive evidence of oxygenic photosynthesis. It does, however, explain why the shallow carbonate platforms where putative oxygenic photosynthesis was taking place remained Fe-poor despite the ferruginous nature of anoxic deep waters.

Here in Chapter 4, we report an occurrence of Fe-rich columnar stromatolites from the ~2.45 Ga Griquatown Iron Formation, South Africa. The Griquatown IF is a rare pre-GOE example of a shallow-water granular iron formation (GIF), formed within the high-energy peritidal zone, in contrast to deep water banded iron formations (BIFs) (Beukes, 1984; Beukes and Klein, 1990). It overlies a deep-water BIF, the Kuruman Formation, and the stratigraphic context of these deposits is that they formed in a basin where shallow water limestone/dolostone carbonate platform was previously established at its margins around 2.5 Ga (Klein and Beukes, 1989; Sumner, 1997). The Kuruman and Griquatown IFs, along with the correlative Brockman IF in the Hamersley province of Western Australia, and numerous other IFs of similar age formed on multiple continents, together mark the most voluminous episode of IF deposition anywhere in the geological record, accounting for up to 70 % of Precambrian Fe mineral resources (Bekker et al., 2010). Massive IF

deposition at this time in Earth history has been ascribed to enhanced submarine volcanism and hydrothermal Fe^{2+} supply to the oceans accompanying a global mantle plume breakout event (e.g. (Heaman, 1997). The occurrence of the Griquatown GIF at this time could thus reflect elevated Fe^{2+} levels in upwelling deep waters overwhelming the normal deep-water removal mechanisms that drove BIF deposition, allowing the encroachment of Fe^{2+}-rich waters into shallower shelf environments.

Therefore, the stromatolites we report on in Chapter 4 are snapshot of the interaction between shallow water photosynthetic microbial communities and Fe^{2+} rich seawater. In such an environment, Fe is likely to be have been an active participate in redox reactions taking place as a result of biological activity but can also serve as a witness as to the nature of this redox cycling in the geologic record. In Chapter 4 we explore what the elemental composition and Fe isotope systematics of this shallow water stromatolite-forming environment can tell us about microbial activity in the shallow oceans, at a snapshot in time shortly before the GOE. In fact, in the drill core that provided these samples, just a few meters further up, the GIF sequence is terminated by the deposition of a glacial diamictite, the Makganyene Formation, which was deposited during the first Snowball Earth glaciation of the Paleoproterozoic and has been linked to the collapse of a methane greenhouse atmosphere following the rise of atmospheric O_2 (Evans et al., 1997; Gumsley et al., 2017; Kirschvink et al., 2000). The closeness of our stromatolites to the GOE means that they are not well-suited to addressing the question of how early on in Earth history that oxygenic photosynthesis emerged (Fischer et al., 2016). However, if they provide geochemical evidence for oxygenic photosynthesis, then they might be among the best samples described to date, for characterizing the microbial O_2 factories that provided the fuel for the GOE to occur.

Abstract

By the time Earth's surface became permanently oxygenated for the first time 2.43 billion years ago, shallow water oases of molecular oxygen (O_2) amid the broadly anoxic and iron-rich global oceans may have existed transiently for hundreds of millions of years. However, despite rich geochemical evidence for the presence of elevated ambient O_2 in the Archean upper ocean, the point of origin for O_2 has never been geochemically fingerprinted. We report geochemical and iron isotopic data from a horizon of iron-rich stromatolites in the Paleoproterozoic Griquatown Iron Formation in South Africa that formed on the margins of an anoxic ferruginous basin. Bulk and micro-sampled iron isotope data indicate that the stromatolites quantitatively oxidized iron from solution, which is most parsimoniously explained by the stromatolites being inhabited by cyanobacteria producing O_2-enriched microenvironments. Modest enrichments of Mn and Ce also suggest a local onset of oxidation most easily facilitated by excess cyanobacterial O_2 at similar levels to Neoarchean oxygen oases. This unique snapshot of the simultaneous production and consumption of cyanobacterial O_2 before the Great Oxidation Event provides direct evidence of the seafloor microbial communities that were a source of O_2 to oxygen oases. The iron rich nature of these stromatolites, which is uncommon prior to the GOE, indicates that upwelling iron in the early Paleoproterzoic overwhelmed established iron removal mechanisms that had maintained iron-poor conditions in shallow tidal zone waters during much of the Neoarchean.

Introduction

The first permanent oxygenation of Earth's atmosphere (the Great Oxidation Event or GOE) started ~2.43 billion years (Ga) ago (Bekker et al., 2004; Gumsley et al., 2017), when O_2 produced by cyanobacteria oscillated around the 10^{-5} x present atmospheric level (PAL = 0.21 atm) threshold

for production and preservation of mass-independent fractionation of sulfur (Lyons et al., 2014; Pavlov and Kasting, 2002). The accumulation of atmospheric oxygen on Earth required oxygenic photosynthesis begin via the evolution of cyanobacteria, and for surface reductants in exposed rocks, the oceans, and the atmosphere to be outbalanced by sources of oxidation. In the oceans, dissolved ferrous iron (Fe^{2+}) was the dominant source of this reducing power, attested to by widespread Neoarchean-Paleoproterozoic iron formations (IFs) show that the deep oceans were Fe^{2+}-rich and anoxic until the GOE (Bekker et al., 2010). The specific primary mineralogy for IFs remain debated, but Fe isotopic data suggest that dissolved Fe^{2+} was generally removed from the oceans by gradual partial oxidation during upwelling on continental margins (Johnson et al., 2020; Planavsky et al., 2012; Thibon et al., 2019). Meanwhile, shallow water limestones with low Fe contents were deposited on the margins of multiple cratons from at least the Neoarchean onwards (*e.g.* Klein and Beukes, 1989; Riding et al., 2014; Sumner, 1997). High levels of Fe^{2+} suppress $CaCO_3$ precipitation, so the occurrence of compositionally pure limestones in some shallow water Neoarchean settings implies a strong relative Fe^{2+} depletion in the shallowest waters compared to ferruginous depths. Iron isotopic ratios in pure carbonates from the Neoarchean Campbellrand-Malmani carbonate platform of South Africa support this model, featuring strongly negative $\delta^{56}Fe$ values ($\delta^{56}Fe$ is the per mil deviation in the $^{56}Fe/^{54}Fe$ ratio of a sample relative to IRMM-014, a standard with an isotopic composition similar to the bulk Earth) consistent with intensive removal of upwelled basinal iron via partial oxidation (Eroglu et al., 2018). Combined, the complementary records of deeper water IFs and platformal carbonates imply that the Archean oceans had significant redox structure, with more oxidizing conditions prevailing near the ocean surface even while the atmosphere remained O_2-poor; although this redox structure alone does not constrain the oxidative removal mechanism for Fe, of which oxidation by microbially produced O_2 (Cloud,

1973) is only explanation among many that also include oxidation by anoxygenic photosynthesis, chemolithoautotrophy, and abiotically by UV photons (Bekker et al., 2010; Cairns-Smith, 1978; Kappler et al., 2005; Konhauser et al., 2002).

However, new discoveries based on trace element and isotopic studies of Archean sediments in the past 15 years indicate that despite the oceans and atmosphere being generally anoxic prior to the GOE, local accumulations of O_2 at in the shallow oceans, and perhaps even transient accumulations ('whiffs') of O_2 in the atmosphere, took place as early as 2.95 Ga (*e.g.* Anbar et al., 2007; Kendall et al., 2010; Kurzweil et al., 2016; Ossa Ossa et al., 2018; Ostrander et al., 2019; Planavsky et al., 2014). Much of the geochemical evidence for O_2-rich environments before the GOE predominantly comes from isotopic tracers of manganese (Mn) oxide burial in shallow marine sediments (Kurzweil et al., 2016; Ossa Ossa et al., 2018; Ostrander et al., 2019; Planavsky et al., 2014a), because Mn^{2+} oxidation requires high potential oxidants of which abundant O_2 is the most plausible for open ocean. In all such cases these geochemical tracers point to elevated ambient O_2 at or near the site of deposition, while providing no constraint on the location or nature of the environments where O_2 was being produced. One possibility is that O_2 was produced on the shallow seafloor in stromatolites hosting early cyanobacteria, with textural evidence for accumulation of biogenic gas, potentially photosynthetic O_2, being found in the axes of conical stromatolites as old as 2.7 Ga (Bosak et al., 2009; Wilmeth et al., 2019). However, pre-GOE stromatolites to date are found shallow water carbonates not rich in redox-sensitive elements, and geochemical confirmation of O_2 production is currently lacking. A site of active microbial O_2 production before the GOE that geochemically interacted with an abundant supply of a redox-sensitive element would represent the best opportunity to identify a smoking gun locality for pre-GOE oxygenic photosynthesis. We report the discovery of Fe-rich stromatolites from the early

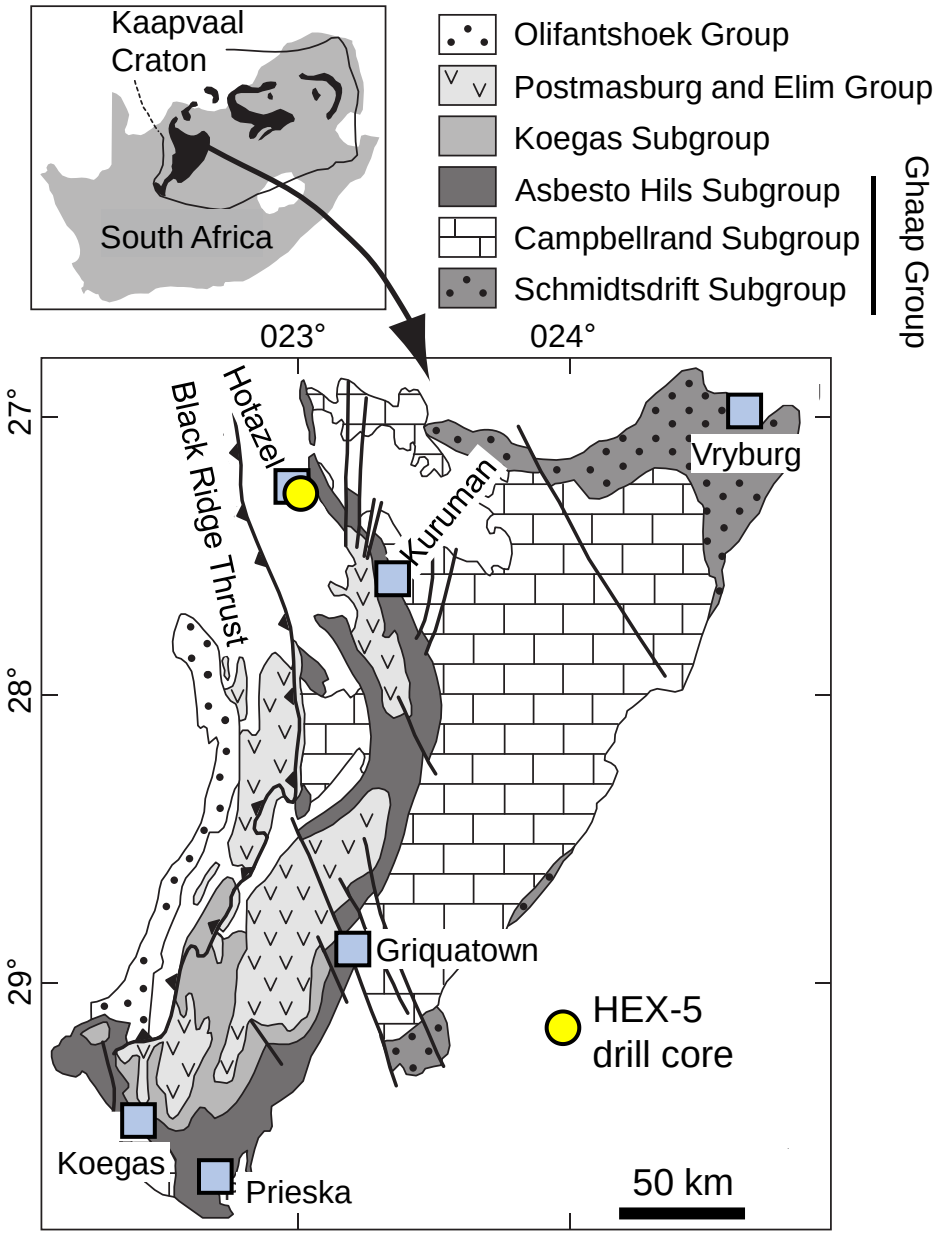

Figure 4.1. Simplified geological map of the Kaapvaal Craton, South Africa, adapted from Oonk et al. (2017) with permission of Elsevier. The HEX-5 drill core that provided the stromatolites is marked by a yellow circle.

Paleoproterozoic Griquatown IF, that constitute the shallowest depositional facies in a sequence of Fe-rich sedimentation before the GOE spanning several million years (Beukes, 1984). These stromatolites should capture the interaction between upwelling ferruginous waters and a

near-surface microbial ecology, and thus provide an unrivaled opportunity to investigate biological redox cycling, and potential geochemically fingerprint a site of active pre-GOE O_2 production.

Geological Background

The Kuruman and Griquatown iron formations are a continuous succession of IF that together comprise the Asbestos Hills Subgroup within the Transvaal Supergroup of southern Africa (Fig 4.1). The HEX-5 drill core sampled in this study (Fig. 4.2A) comes from the northern part of the Griqualand West Basin, near Hotazel in the Western Cape of South Africa (Oonk et al., 2018, 2017). The IF deposits in this region conformably overly the thick Campbellrand-Malmani carbonate platform that is comprised of stromatolitic limestones and dolostones, and the transition to deposition of the Kuruman Iron Formation at 2.4846 $\pm$ 0.0003 Ga (Lantink et al., 2019) corresponds to an initiation of the foreland basin (Bekker et al., 2020) and a deepening of the depositional basin, presumably below an Fe^{2+} chemocline, that enabled the precipitation of authigenic Fe from Fe^{2+}-rich anoxic waters (Klein and Beukes, 1989). The Kuruman-Griquatown succession in the region is a shallowing-upward sequence beginning in a deep-water, low-energy basinal setting and grading into shallower, storm dominated deposits (Beukes, 1984; Beukes and Gutzmer, 2008; Beukes and Klein, 1990). The basal Kuruman Formation is a microbanded magnetite-chert IF deposited in a deep-water, lower-energy environment, and grades upward into rhythmically banded, carbonate-silicate IF. The Griquatown Iron Formation, dated to between 2.464 and 2.431 Ga (Lantink et al., 2019; Trendall et al., 1990), begins with a massive carbonate-silicate lutite and shallows upward into a true granular IF, consisting of compositionally and texturally diverse granules of Fe-rich carbonate and authigenic silicates, along with chert nodules that might be storm-reworked hardgrounds (Beukes, 1984; Beukes and Klein, 1990). The Fe-rich

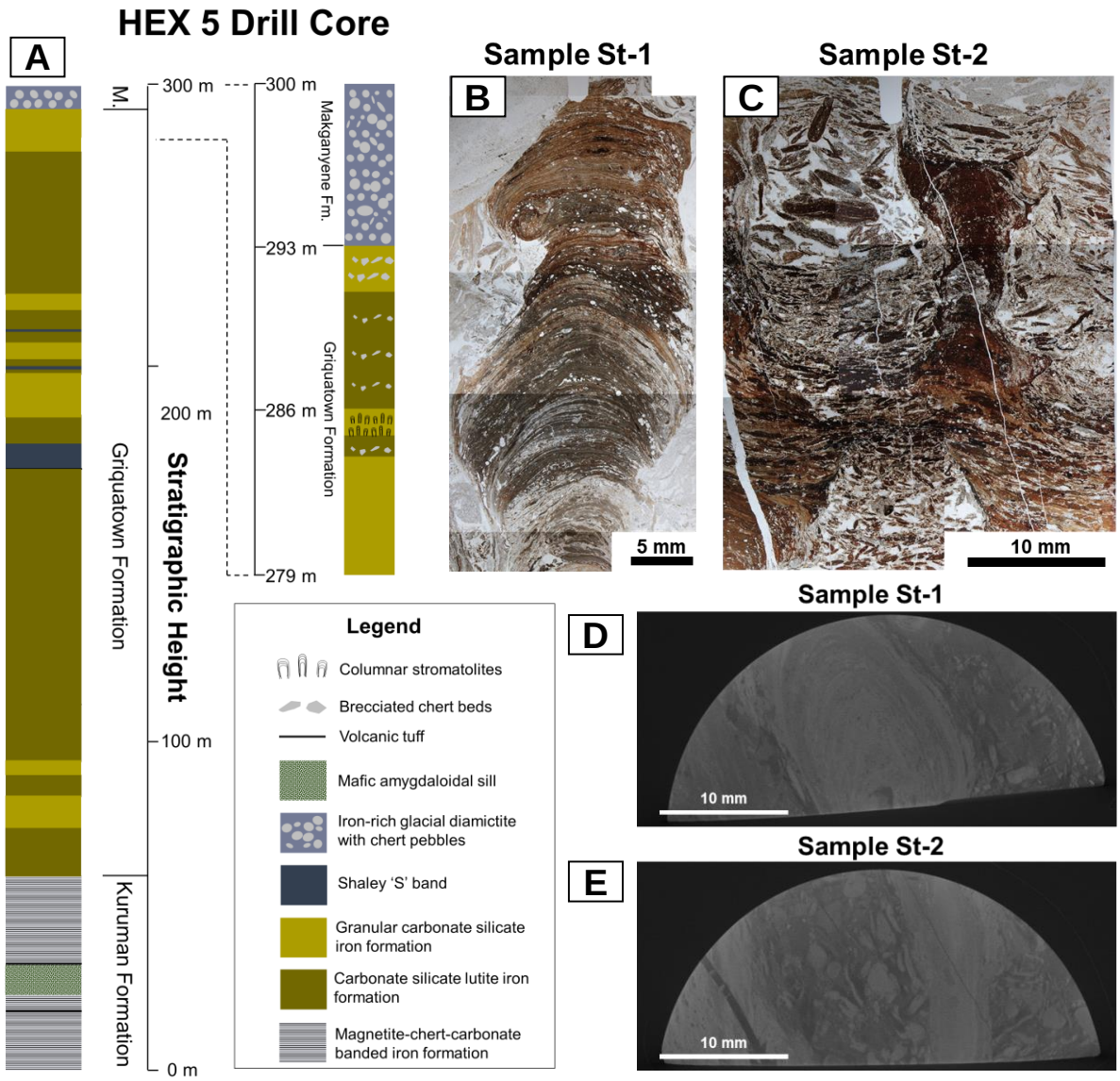

Figure 4.2. Geology of Griquatown Formation stromatolites. A: Stratigraphy of the HEX-5 drill core, in the upper Kuruman and the Griquatown Iron Formations. Stromatolites occur near the top of the dominantly granular Griquatown IF, and the sequence is terminated by the Makganyene Formation diamictite. B-C: Reflected light optical thin section images of stromatolitic beds in the upper Griquatown Formation. The stromatolitic columns are ~1 cm in diameter with intercolumnar distance also ~1 cm. Coarse fragments in the transparent carbonate matrix are reworked stromatolitic material. D-E: X-ray microtomographic sections; top-down view of half drill core sections from which thin sections in B and C were made. The tomographic sections reveal that the iron-rich stromatolites (bright areas) are elongate columns, suggesting their growth in water flowing parallel to their lateral elongation axis (vertical in the image).

carbonate and silicate-dominated composition of the granules and their deposition as part of a continuous succession with deeper-water IFs contrast with the hematitic, oolitic, granular IFs of

the late Paleoproterozoic (Bekker et al., 2010).

The stromatolitic horizon at the top of the Griquatown Formation in the HEX-5 drill core contains larger clasts than the underlying granular IF and was likely deposited in the shallowest depositional facies seen in the entire formation. The stratigraphic variations seen throughout the succession is representative of lateral facies migration related to shallowing, and thus this stromatolitic environment could have been long lived. Indeed, stromatolites are also present in the underlying Gamohaan Formation at the top of the Campbellrand-Malmani carbonate platform (Sumner, 1997). The Griquatown IF is terminated in this area by the Makganyene Diamictite, dated to 2.426 $\pm$ 0.032 Ga (Gumsley et al., 2017). The Makganyene Formation has been linked with Earth's first earl Paleoproterozoic global glaciation and may reflect the onset of atmospheric oxygenation that destroyed an ancient methane greenhouse atmosphere and initiated a snowball Earth event (Evans et al., 1997; Gumsley et al., 2017; Kirschvink et al., 2000). The Koegas Group of shallow-marine, carbonate and siliciclastic sediments, and Mn-rich IF, found in other localities is entirely absent from the succession in this area (Oonk et al., 2018) and the contact between the Griquatown IF and the Makganyene Diamictite appears to be conformable in this drill core. Therefore, either the Koegas Group represents a locally developed, siliciclastic-influenced time equivalent to the upper Griquatown IF, or the unconformable nature of the lower diamictite contact is not apparent in the drill-core.

Samples

Stromatolites were sampled from a 1 m section of the HEX-5 drill core (Fig. 4.2A) at the top of the Griquatown IF, ~7 m below a gradual contact with the Makganyene Formation. The stromatolites are Fe-rich, reddish brown ~1 cm-diameter columns within a buff colored carbonate

matrix that contains coarse (1-5 mm), elongate granules of Fe-rich stromatolitic material (Figs. 4.2B-C). The stromatolites have steep sides and elongate top down cross sections (Figs. 4.2D-E; Supplementary Video File) suggesting at least episodic strong water flow and scour conditions, so lithification must have been rapid to preserve such small features (Bosak et al., 2013). The apparent cm-scale spacing between stromatolitic columns is consistent with photosynthetic growth that depleted local nutrients by diffusion on diurnal timescales (Petroff et al., 2010). Indeed, the overall morphology, size, and spacing of the stromatolites visible in the drill core section seem to closely resemble 1 cm-scale, elongate columnar stromatolites observed in laminar flow environments (Reynolds number, Re ~1,000) at modern day hot springs in Yellowstone National Park (Bosak et al., 2013; Petroff et al., 2010), which are assembled by cyanobacteria and rapidly lithify by oxidizing Fe (Pierson et al., 1999; Pierson and Parenteau, 2000; Trouwborst et al., 2007). Stronger flows caused roll-ups and rip-ups of stromatolite laminae and redeposition of coarse stromatolite granules between the columns. Conditions seem to have been at least episodically quiescent, however, as indicated by the growth of intercolumnar bridges formed in low water energy conditions (Bosak et al., 2013). As the depositional environment requires relatively low Re flows but features periods of both relative quiescence and stronger scour, we suggest the stromatolites were deposited below fair-weather wave base (> 5 m), but considerably above storm wave base (< 40 m) because the underlying and deeper-water granular facies of the Griquatown IF are also storm-influenced (Beukes and Klein, 1990).

Analytical methods

Rock chips taken from half drill core sections were ground in an agate mortar to generate bulk rock powders. Aliquots of were taken for major element, trace element, and iron isotopic analysis.

Table 4.1. Bulk Fe isotopic and major element concentrations of Griquatown Stromatolites

Sample	δ56Fe	δ57Fe	δ56Fe	δ57Fe	P_2O5	SiO_2	MnO	Fe_2O_3	MgO	Al_2O_3	TiO_2	CaO	Na_2O	K_2O	CO_2
	‰ relative to IRMM-524		95 % C.I.		wt %										
Hex 1-2 a	-1.55	-2.29	0.03	0.06	0.04	4.72	2.32	21.58	2.72	0.87	0.03	33.14	0.05	0.05	34.47
Hex 1-2 b	-1.55	-2.26	0.03	0.06	0.11	2.18	2.94	31.65	3.81	0.80	0.04	24.67	0.16	0.09	33.54
Hex 1-4 a	-1.55	-2.27	0.03	0.05	0.03	3.77	2.01	16.76	2.42	0.96	0.03	36.28	0.04	0.03	37.66
Hex 1-4 b	-1.53	-2.26	0.03	0.05	0.05	5.24	2.25	22.64	2.65	0.97	0.03	30.32	0.08	0.10	35.67
Hex 1-4 c	-1.53	-2.24	0.03	0.06	0.09	4.33	2.83	34.25	3.37	0.83	0.04	20.29	0.10	0.15	33.73
Hex 2-2	-1.52	-2.22	0.03	0.04	0.09	13.86	2.98	46.02	4.45	1.46	0.08	5.42	0.32	0.61	24.72
Hex 2-3 a	-1.50	-2.21	0.03	0.06	0.09	14.41	2.76	44.31	4.17	1.60	0.07	11.94	0.28	0.57	19.81
Hex 2-3 b	-1.49	-2.18	0.03	0.04	0.10	13.39	2.55	40.38	3.91	1.55	0.07	11.49	0.25	0.56	25.74
Hex 2-3 c	-1.45	-2.15	0.03	0.06	0.08	10.02	1.80	24.53	2.50	1.56	0.04	30.25	0.18	0.37	28.68
Hex 2-5 a	-1.52	-2.23	0.03	0.05	0.09	10.54	2.68	39.00	4.35	1.32	0.25	15.48	0.24	0.43	25.63
Hex 2-5 b	-1.49	-2.18	0.03	0.04	0.10	10.31	2.28	32.55	3.58	1.46	0.10	19.60	0.22	0.44	29.36
Hex 2-6 a	-1.51	-2.24	0.03	0.04	0.06	7.24	2.01	21.50	2.78	1.10	0.04	28.91	0.10	0.17	36.09

Table 4.1. continued															
Hex 2-6 b	-1.50	-2.24	0.03	0.05	0.06	10.22	2.71	37.06	3.85	1.26	0.05	17.34	0.21	0.36	26.88
Hex 3-2	-1.53	-2.26	0.03	0.06	0.05	4.41	2.06	18.14	2.71	1.01	0.03	34.28	0.06	0.07	37.18
Hex 3-3	-1.53	-2.25	0.03	0.06	0.05	4.92	2.10	22.39	2.63	1.11	0.04	31.64	0.12	0.15	34.86
Hex 3-5 a	-1.51	-2.21	0.03	0.04	0.07	5.75	2.16	20.45	3.04	0.99	0.03	32.40	0.07	0.07	34.96
Hex 3-5 b	-1.53	-2.26	0.03	0.05	0.07	5.31	2.34	24.51	3.01	0.96	0.03	30.14	0.43	0.09	33.11
CO_2 calculated as 'loss acid on digestion' by taking the difference of summed oxide contents from 100 %															

Table 4.2. Rare earth element compositions of bulk Griquatown stromatolite samples, normalized to post Archean Australian shale																
	La	**Ce**	**Pr**	**Nd**	**Sm**	**Eu**	**Gd**	**Tb**	**Dy**	**Ho**	**Er**	**Yb**	**Lu**			
PAAS [ppm]	38	80	8.9	32	5.6	1.1	4.7	0.77	4.4	1	2.9	2.8	0.43			
	Shale-normalized													**La/La***	**Ce/Ce***	**Nd/Nd***
Hex 1-2 a	0.22	0.18	0.20	0.25	0.35	0.47	0.63	0.68	0.86	0.95	1.04	1.07	1.10	1.63	1.11	0.94
Hex 1-2 b	0.33	0.27	0.29	0.36	0.47	0.61	0.76	0.73	0.85	0.91	0.97	1.04	1.16	1.73	1.15	0.97
Hex 1-4 a	0.24	0.19	0.20	0.24	0.31	0.43	0.54	0.57	0.71	0.81	0.91	1.01	1.08	1.69	1.11	0.97

Table 4.2. continued

Hex 1-4 b	0.25	0.21	0.23	0.28	0.38	0.50	0.67	0.72	0.90	1.00	1.10	1.14	1.15	1.65	1.11	0.95
Hex 1-4 c	0.26	0.21	0.23	0.29	0.38	0.49	0.61	0.59	0.69	0.74	0.81	0.91	1.03	1.67	1.12	0.96
Hex 2-2	0.20	0.17	0.19	0.23	0.32	0.38	0.51	0.53	0.64	0.69	0.77	0.96	1.05	1.54	1.10	0.93
Hex 2-3 a	0.42	0.37	0.38	0.43	0.47	0.53	0.66	0.67	0.80	0.87	0.97	1.15	1.24	1.34	1.08	1.00
Hex 2-3 b	0.40	0.36	0.37	0.42	0.47	0.53	0.66	0.67	0.80	0.88	0.98	1.16	1.27	1.40	1.11	1.00
Hex 2-3 c	0.79	0.70	0.69	0.75	0.73	0.83	0.96	0.92	1.08	1.17	1.30	1.42	1.56	1.35	1.10	1.06
Hex 2-5 a	0.29	0.27	0.29	0.34	0.47	0.60	0.81	0.90	1.16	1.30	1.49	1.74	1.86	1.44	1.10	0.93
Hex 2-5 b	0.30	0.28	0.32	0.39	0.54	0.72	0.88	0.93	1.15	1.27	1.42	1.60	1.72	1.43	1.09	0.95
Hex 2-6 a	0.58	0.51	0.52	0.59	0.61	0.71	0.84	0.82	0.98	1.06	1.17	1.30	1.42	1.44	1.11	1.04
Hex 2-6 b	0.28	0.24	0.26	0.32	0.43	0.53	0.66	0.68	0.83	0.89	0.98	1.14	1.23	1.61	1.12	0.96
Hex 3-2	0.26	0.21	0.22	0.26	0.32	0.44	0.55	0.56	0.69	0.77	0.85	0.92	1.00	1.74	1.14	0.98
Hex 3-3	0.33	0.26	0.28	0.33	0.39	0.50	0.60	0.59	0.71	0.77	0.86	0.96	1.05	1.67	1.12	1.01
Hex 3-5 a	0.29	0.23	0.25	0.30	0.38	0.50	0.62	0.60	0.72	0.78	0.85	0.90	0.99	1.72	1.13	0.98
Hex 3-5 b	0.30	0.24	0.26	0.31	0.40	0.53	0.65	0.65	0.77	0.84	0.93	1.01	1.09	1.71	1.13	0.98

PAAS composition from Taylor and McLennan (1985). Calculation of La/La*, Ce/Ce*, and Nd/Nd* is detailed in the text.

Major element analysis

Major element analyses were carried out at Boston University following the methods outlined in (Dunlea et al., 2015). Approximately 400 mg of lithium metaborate flux powder was weighed into an 8 mL high-purity graphite crucible. To achieve the ideal flux to sample ratio of 4:1, 100 mg of sample powder was added to the crucible and carefully mixed with the flux. The crucible was then placed in a preheated muffle furnace at 1050 °C for 11 minutes. During heating, a fusion melt bead formed at the bottom of the crucible. This bead was carefully swirled around the crucible bowl to collect any stray melt droplets, and then poured directly into a 60 mL HDPE bottle containing 50 g of 5% nitric acid (HNO_3). To ensure full dissolution of the fusion melt bead, the bottle was then shaken vigorously for 2-3 minutes, followed by sonication for at least 15 minutes. This initial dilution step results in a sample dilution factor of about 500. A second dilution step was employed in order to obtain the proper range of concentrations for analysis. Approximately 5 g of the first fusion solution was extracted and passed through a 0.45 μm PVDF filter to remove any residual graphite. An appropriate amount of 5% HNO_3 (~35 g) was then added to reach a final dilution factor of 4000. The amount of total dissolved solids, which includes the $LiBO_2$ flux, represents about 0.2% of the final solution.

All flux fusion digestions were analyzed on a Jobin-Yvon Ultima-C ICP-OES at Boston University. Samples were introduced to the instrument in 5% HNO_3, via a Meinhardt-C nebulizer with a flow rate of about 1 mL/min, and a concentric spray chamber. Instrumental drift was monitored and corrected for by analyzing an in-house drift solution several times during an analytical session. The Ultima-C routinely achieves better than 3 to 4 % drift over a period of 10 to 12 hours, the length of a typical analytical session. A blank solution, which was prepared in an identical manner to our samples, was also measured at the beginning and end of each run, and all

data presented is blank corrected. For all major elements, the blank correction was inconsequential, as the blank was several orders of magnitude below the sample. Several standard reference materials were interspersed throughout the analytical run, and a calibration curve was generated by comparing the signal intensity to that of the established concentrations. These calibration curves typically had r^2 value of 0.99 or better and were used to calculate the concentration in the samples.

Trace element analysis

Trace element analyses were carried out at Boston University. About 25 mg of rock powder digested in 3 mL of concentrated HNO_3, 1 mL of concentrated HCl, and 1 mL of concentrated HF, in sealed, acid-cleaned Teflon beakers placed on hot plate at a sub-boiling temperature for at least 24 hours. Samples were then sonicated for about 30 minutes and 1 mL of H_2O_2 was added to oxidize any organic material that may have been present. Beakers were left loosely capped until the reaction stopped, and were then re-sealed and placed on a hot plate for 12-24 hours. The samples were gently evaporated to dryness and re-dissolved in 1 mL of concentrated HNO_3. A small amount of H_2O_2 (0.5 to 1 mL) was added to each sample to ensure complete digestion. Prior to analysis samples were diluted with MQ water and 2% HNO_3 to a final dilution factor of 5000. Trace element concentrations were measured on a VG PlasmaQuad ExCell inductively coupled plasma mass-spectrometer (ICP-MS) at Boston University. Samples in ~2% HNO_3 were introduced to the instrument via a Meinhardt-C nebulizer with a ~1 mL/min flow rate with an impact-bead, Peltier cooled spray chamber. Optimization was performed by obtaining a maximum signal intensity on a 1 ng/g indium solution, while concurrently minimizing oxide production. Oxide levels were monitored by measuring the CeO^+/Ce^+ ratio and were typically ~1%.

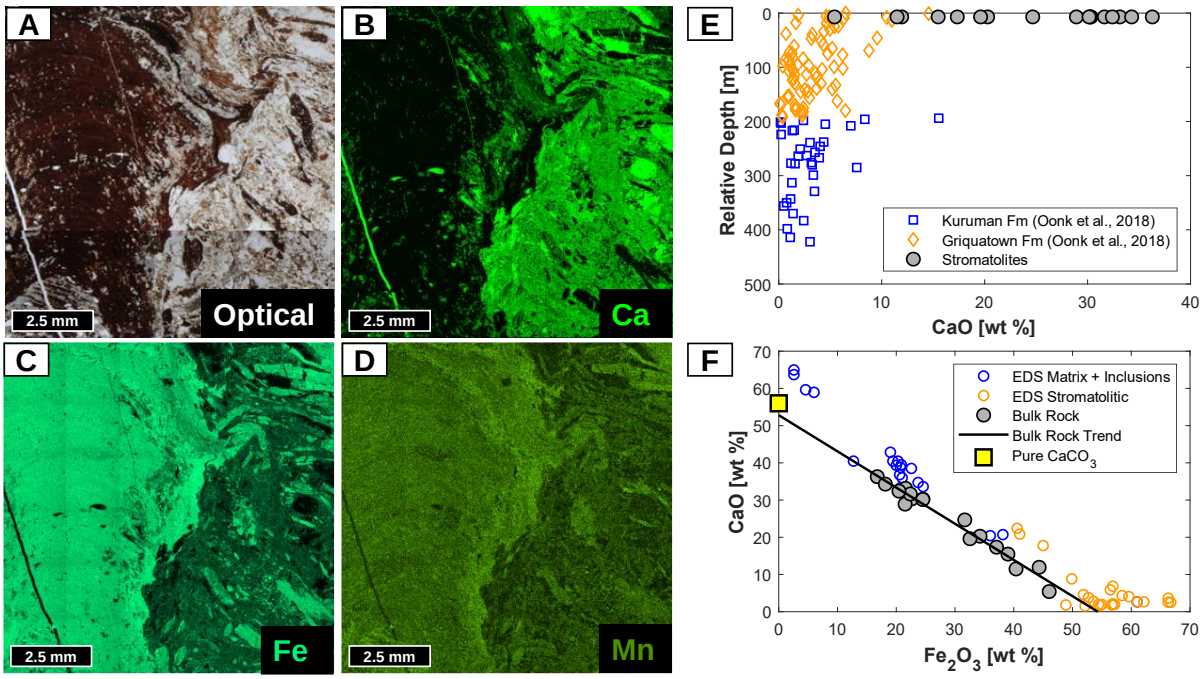

Figure 4.3. Major element chemistry of stromatolites. A: Reflected light optical image of part of the thin section of St-2 shown in Fig. 4.2C. B-D: EDS chemical maps of the corresponding sample area on a polished thick section, showing B: Ca, C: Fe, and D: Mn contents. The stromatolitic column material (left of image) and reworked fragments in the matrix are Fe- and Mn-rich and Ca-poor. The carbonate matrix material (right of image) is Ca-rich and Fe- and Mn-poor. E: CaO contents through the Kuruman and Griquatown Iron Formations as a function of stratigraphic height, showing the stromatolites are more CaO-rich than the underlying IF with composite stratigraphic section data from (Oonk et al., 2018). F: CaO *vs.* Fe_2O_3 in stromatolites. Bulk rock samples and EDS spot analysis data suggest mixing between an Fe-rich, Ca-poor stromatolitic composition and a nearly pure $CaCO_3$ matrix component.

An in-house drift solution was analyzed several times during an analytical session to monitor and correct for instrumental drift. A blank solution prepared identically to samples was measured at the beginning and end of each run, and all data were blank corrected. Several geologic standard reference materials were interspersed throughout an analytical run and calibration curves were produced by comparing the measured signal intensity to that of the established concentrations. Concentrations of the samples were then calculated using the calibration curves. The method precision, estimated from the 1 r.s.d of the mean of repeat analyses of two bulk stromatolite samples, was better than 5% for most elements, and for the REEs, which were used to calculate

cerium anomalies, the 1 r.s.d was typically ~2%, and in all cases lower than 4%. The accuracy of measurements was assessed by comparison of measurements of the geostandard BHVO-2 with literature values. The accuracy measured in this way was better than 10 % for most elements, and within less than 5 % for REEs used to calculate cerium anomalies.

Iron isotopic analysis

Iron purification and isotopic measurements followed standard procedures established at the University of Chicago (Craddock and Dauphas, 2011; Dauphas et al., 2009, 2004). Approximately 3-9 mg of powder from each stromatolite rock chip were digested overnight in acid-cleaned Savillex Teflon beakers in HF + HNO_3 + $HClO_4$ on a hot plate at 130°C, evaporated to dryness, and redigested twice in a HCl + HNO_3 + $HClO_4$ mixture. After full dissolution, samples were again dried down, and redissolved in 0.5 ml of 6 M HCl for Fe purification. Iron was purified by two identical passes through a routine column chmeistry procedure used in the Origins Laboratory and described elsewhere. purification samples were dried down and taken up in in 5 ml 0.3 M HNO_3 for mass spectrometry.

Iron isotopic compositions were measured in medium resolution mode on a Neptune multi-collector inductively coupled plasma mass spectrometer (MC-ICP-MS) at the University of Chicago. A quartz cyclonic spray chamber was used to introduce sample solutions containing 1 ppm Fe in 0.3 M HNO_3, which gave a signal of ~7 V. Intensities on $^{54}Fe^+$, $^{56}Fe^+$, $^{57}Fe^+$, and $^{58}Fe^+$ were measured simultaneously, in addition to $^{53}Cr^+$ and $^{60}Ni^+$. The ^{53}Cr and ^{60}Ni signals were used to correct for $^{54}Cr^+$ and $^{58}Ni^+$ interferences on $^{54}Fe^+$ and $^{58}Fe^+$ respectively, using the exponential law. Iron was measured on flat topped peak shoulders to the side of molecular interference peaks resulting from argide ions ($^{40}Ar^{14}N^+$, $^{40}Ar^{16}O^+$, $^{40}Ar^{16}O^1H^+$, and $^{40}Ar^{18}O^+$). Standard-sample bracketing was used to correct Fe isotopic ratio measurements for instrumental mass fractionation.

Sample and standard solutions were prepared using the same batch of 0.3 M HNO_3 and, standard and sample intensities on ^{56}Fe were matched to better than 5% prior to analysis. Sample iron isotope ratios are reported in $\delta^{56}Fe$ notation, the per mil deviation of the $^{56}Fe/^{54}Fe$ ratio of the sample relative to the IRMM-524 standard, which has an identical isotopic composition to IRMM-014 such that:

$$\delta^{56}Fe\ (‰) = [(^{56}Fe\ /^{54}Fe)_{sample}\ /\ (^{56}Fe\ /^{54}Fe)_{IRMM\text{-}014} - 1] \times 1000 \qquad \text{(Eq. 1)}$$

Here and elsewhere unless otherwise stated, uncertainties are given at the 95% confidence interval (Dauphas et al., 2009). The IF-G and AGV-2 geostandards were processed through the same digestion and purification protocol as the stromatolite samples and at least one geostandard was analyzed during each sample measurement sequence, always giving $\delta^{56}Fe$ values within error of the recommended values (Craddock and Dauphas, 2011).

Microscale iron isotope analysis

Small scale samples targeting stromatolitic laminations, and fragments and carbonate in the surrounding matrix for Fe isotope analyses, were obtained using a micromill (MicroMill, New Wave Instruments) fitted with a tungsten carbide bit (Brasseler, scriber H1621.11). Sample slurries were generated by milling over polished thick sections to which droplets of MilliQ water were added and transferred to Teflon beakers with a clean pipette. The slurries were then dried down on a hot plate, and subsequently digested, purified with column chemistry procedures, and analyzed for Fe isotopic compositions via MC-ICP-MS in the same manner as bulk rock chip powders as described above. The IF-G and BHVO-2 geostandards were processed through the same digestion and purification protocol as the stromatolite samples and at least one geostandard was analyzed during each sample measurement sequence, always giving $\delta^{56}Fe$ values within error of the recommended values (Craddock and Dauphas, 2011).

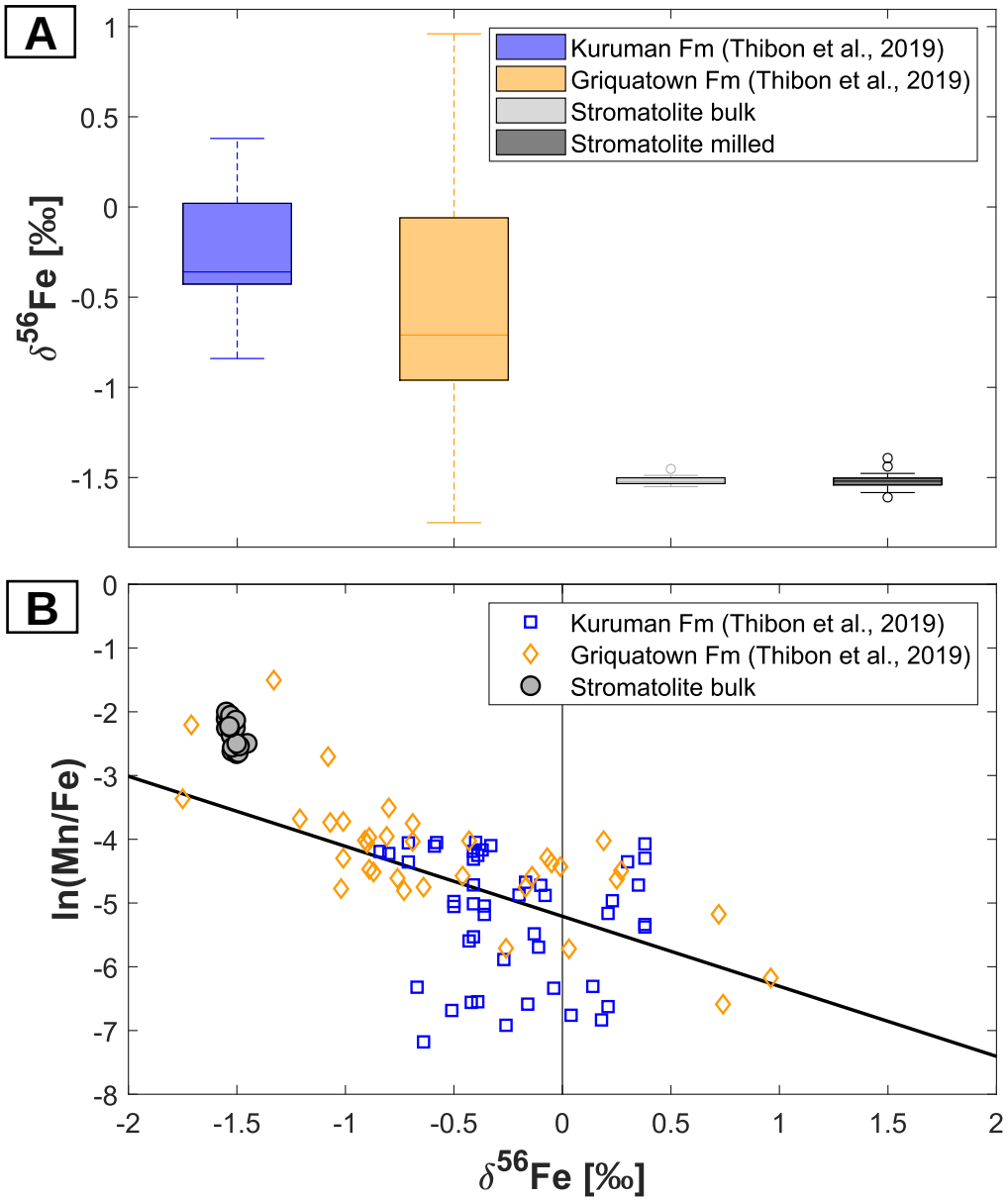

Figure 4.4. Iron isotope systematics of Griquatown Formation stromatolites. A: Box plots of δ^{56}Fe values in the Kuruman and Griquatown Iron Formations, and bulk and micromilled samples from the stromatolitic horizons. Boxes show the interquartile range, with the line within the box showing the median value. Whiskers show the most extreme outlying datapoint within 1.5 times the interquartile range. Outliers beyond the whisker length are represented by open circles. The bulk and milled stromatolites show an extremely restricted range of δ^{56}Fe values and have identical mean values. B: ln(Mn/Fe) *vs.* δ^{56}Fe in the Kuruman and Griquatown Iron Formations (Thibon et al., 2019) and bulk stromatolitic materials. The heavy black line is a linear regression through the literature data, which captures the passive enrichment of Mn/Fe by removal of isotopically heavy iron. Mn/Mn* is calculated from comparing the Mn/Fe of the stromatolite samples to the Mn/Fe at the corresponding δ^{56}Fe value on the regression.

Results

Major elements

EDS mapping of a selected section revealed a bimodal compositional distribution where stromatolitic columns and fragments are Fe- and Mn-rich and Ca-poor, and light colored intercolumnar and stromatolitic void-filling cements are Fe- and Mn-poor and Ca-rich (Table 4.1, Figs. 4.3A-D). The composition of bulk sample powders is dominated by Fe, Ca, Si, with substantial Mn, Mg, and Al. The CO_2 content in carbonate matrix component, which is evident in thin section, was calculated for bulk-rock powders from the loss of mass on digestion (Table 4.1). Carbonate content is higher in samples with higher Ca and lower Fe, Mn and Mg, indicating that bulk-rock samples include a relatively pure $CaCO_3$ component that dominates the carbonate composition. These samples include the most Ca-rich materials from the Kuruman and Griquatown IFs, with CaO up to 35 wt %, twice as high as any value measured elsewhere in the succession (Fig. 4.3E) (Oonk et al., 2018). A negative trendline of CaO *vs.* Fe_2O_3 extrapolates to ~53 wt % CaO at Fe_2O_3 = 0, similar to 56 wt % CaO in $CaCO_3$ (Fig. 4.3F). Bulk rock compositions thus reflect two-component mixing of Fe- and Mn-rich, Ca-poor stromatolitic material, and an Fe-poor, chemically pure $CaCO_3$ cement. Higher SiO_2 and Al_2O_3 contents are both associated with Fe-rich stromatolitic columns, which likely reflects the trapping of small amounts of detrital material by the growing microbial mats, and additionally in the case of SiO_2, silicification, incorporation of authigenic Fe silicates and adsorption of amorphous silica to ferric oxyhydroxide precipitates.

Rare Earth Elements

Concentrations of Rare Earth Elements (REEs) in bulk stromatolite samples are 0.18-1.74 times the concentrations of these elements in average Post-Archean Australian Shale (Table 4.2) (Taylor and McLennan, 1985). The PAAS-normalized (subscript SN; Taylor and McLennan, 1985) REE

compositions of the stromatolites have a depletion in light REEs and enrichment in heavy REEs (Table 4.2), consistent with similar trends shown by the Kuruman and Griquatown IFs and the contemporaneous Brockman IF in Western Australia (Oonk et al., 2018), along with numerous other Archean and Paleoproterozoic IFs (Konhauser et al., 2017; Planavsky et al., 2010). All samples have large positive La anomalies, La/La^*_{SN}, defined as

$$La/La^*_{SN} = [La]_{SN}/\left([Pr]_{SN}^{3}/[Nd]_{SN}^{2}\right), \quad \text{(Eq. 2)}$$

where we use the geometric assumption for behavior of nearest non anomalous neighbor REEs (Lawrence et al., 2006; McLennan, 1989), which is consistent with other analyses of Paleoproterozoic IFs (Oonk et al., 2018; Planavsky et al., 2010). We use the Ce anomaly, Ce/Ce^*_{SN}:

$$Ce/Ce^*_{SN} = [Ce]_{SN}/\left([Pr]_{SN}^{2}/[Nd]_{SN}\right), \quad \text{(Eq. 3)}$$

which gives a ratio of the measured Ce concentration relative to the expected Ce concentration for a smooth trend in behavior of neighboring REEs while avoiding normalization to anomalous La (Lawrence et al., 2006). Samples consistently feature small positive Ce anomalies (Ce/Ce^*_{SN} = 1.08-1.15) that are distinct from values centered around one and slightly below it in the underlying Kuruman and Griquatown IFs respectively (Fig. 4.6A) (Oonk et al., 2018). Analytical errors in either Pr or Nd can result in uncertainty in Ce/Ce^*_{SN}, which can be checked for by calculating the Nd anomaly:

$$Nd/Nd^*_{SN} = [Nd]_{SN}/\sqrt{\left([Pr]_{SN} \times [Sm]_{SN}\right)}, \quad \text{(Eq. 4)}$$

which should be close to 1.0 if Nd and Pr behave conservatively and do not have large uncertainties (Bellefroid et al., 2018). In all stromatolite samples Nd/Nd^*_{SN} is within 0.07 or less of 1.0, and there is no correlation between Ce/Ce^*_{SN} and Nd/Nd^*_{SN}, suggesting that the small measured Ce anomalies are real. The stromatolite samples have no discernible Eu anomaly, indicating that any

high-temperature hydrothermal influences in the depositional setting at this time were highly attenuated.

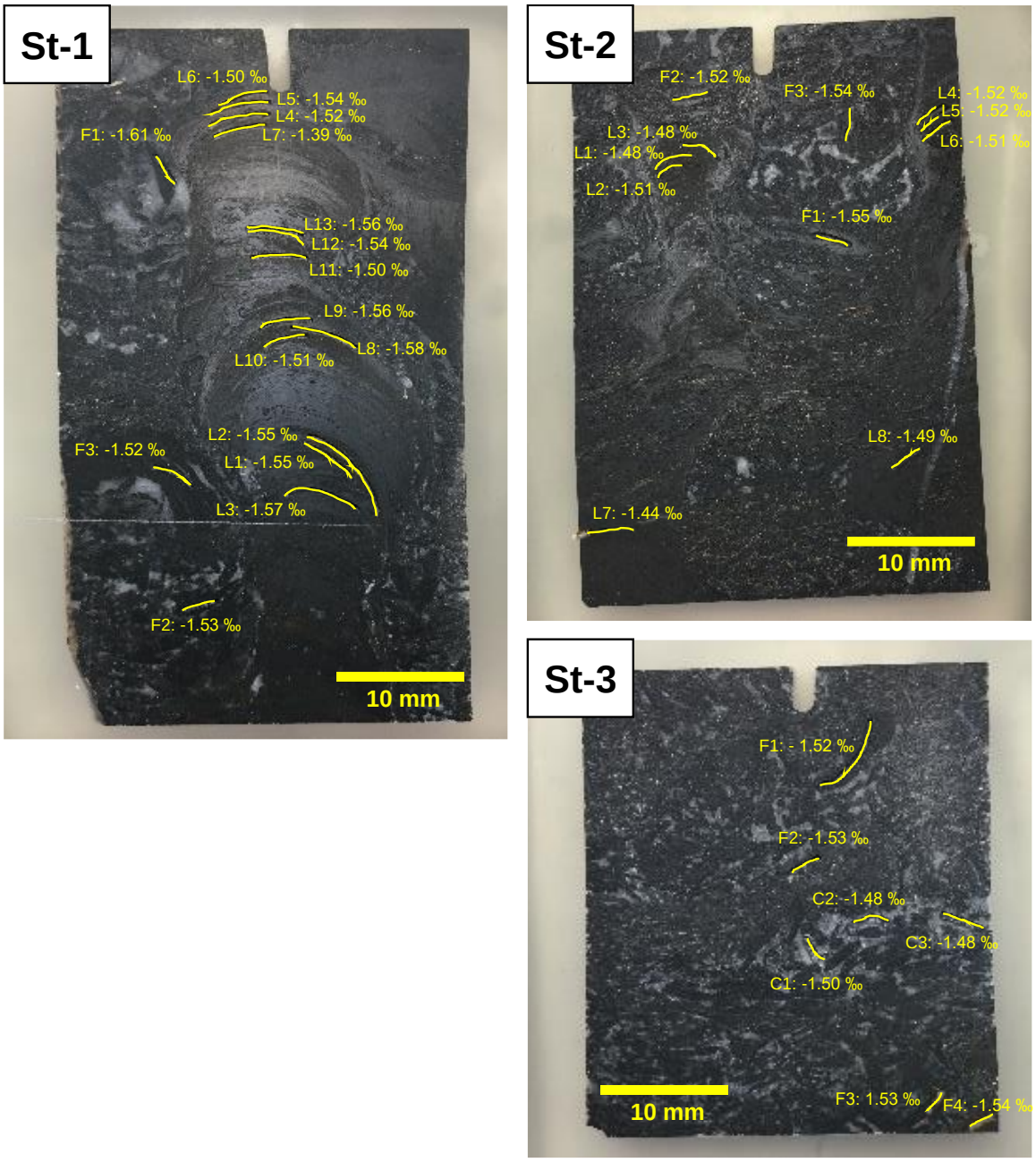

Figure 4.5. δ^{56}Fe (‰) values of micromilled stromatolite samples, thick sections St-1, St-2, and St-3. L = Lamination, C = Cement, F = Fragment. St-1 and St-2 feature *in situ* stromatolitic columns whilst St-3 is dominated by redeposited fragments and cement that comprise the intercolumnar matrix in the other samples. δ^{56}Fe values of micromilled samples have a very small range and are particularly similar in most cases for samples from adjacent stromatolitic laminations.

Iron isotope and Mn/Fe systematics

Bulk rock sample Fe isotope ratios span a narrow range between -1.45‰ and -1.55‰ with an average value of -1.52‰, placing them among the most isotopically light values for pre-GOE IFs in the Griqualand West basin (Table 4.1, Fig. 4.4A) (Thibon et al., 2019). The stromatolites define a near-vertical trend of Mn/Fe *vs*. δ^{56}Fe, with elevated Mn/Fe compared to the log-linear array defined by the underlying Griquatown IF (Fig. 4.4B). Small scale micromilled samples have a δ^{56}Fe range of -1.39 to -1.61‰ (Fig. 4.5), with an average value of -1.52‰, identical to the bulk-rock samples (Fig. 4.4A). With one exception (δ^{56}Fe = -1.39‰), sets of adjacent micromilled laminations from a given region of a stromatolite have identical δ^{56}Fe values. The lightest δ^{56}Fe value of -1.61‰ was observed in a redeposited granule (Fig. 4.5) but otherwise, fragments and carbonate matrix material sample both have δ^{56}Fe values identical to those for the stromatolitic columns.

Discussion

Rapid oxidation of upwelled iron in stromatolite environment

The δ^{56}Fe values of the Griquatown stromatolites are strongly negative and very uniform (total range of ~0.1‰ at a bulk scale and ~0.2‰ at a microscale). Such negative values likely reflect the result of progressive partial removal of isotopically heavy Fe^{3+} phases from the dissolved Fe^{2+} inventory of an upwelling water mass (Planavsky et al., 2012; Rouxel et al., 2005; Tsikos et al., 2010). This interpretation is supported by the negative correlation between Mn/Fe ratios and δ^{56}Fe in the underlying Griquatown IF, which is as expected for a distillation that preferentially removed isotopically heavy Fe relative to Mn (Nie et al., 2020; Planavsky et al., 2014; Thibon et al., 2019; Tsikos et al., 2010). The stromatolites have δ^{56}Fe values among the most negative reported from

the Griquatown IF, which is consistent with their formation at shallow depths at the distal part of an upwelling system from which iron continuously precipitated via partial Fe^{2+} oxidation. Their degree of isotopic homogeneity sets these stromatolites apart from similarly Fe isotopically depleted, high Mn/Fe IFs from before the GOE, like the well-studied the Sinqeni Formation in the 2.95 Ga Pongola Supergroup, which has $\delta^{56}Fe$ as low as -1.71‰ but features variations of several tenths of a per mil over the space of a few cm, a similar spatial scale to that sampled within individual stromatolitic sections investigated here. Therefore, stromatolites from the Griquatwon Formation show the strongest evidence for quantitative Fe^{2+} oxidation of any pre-GOE sediments we are aware of.

The low variability of stromatolite $\delta^{56}Fe$ values is not consistent with formation by partial oxidation, because Fe^{2+} oxidation by photoferrotrophy and microaerophilic chemolithoautotrophy, sorption to cyanobacterial cells, and slow abiotic Fe^{2+} oxidation, all tend to produce Fe^{3+} oxyhydroxide precipitates that are isotopically heavy relative to the dissolved Fe^{2+} pool (Balci et al., 2006; Bullen et al., 2001; Croal et al., 2004; Mulholland et al., 2015; Nie et al., 2017). Therefore, slow partial oxidation by any these means produces precipitates with $\delta^{56}Fe$ values that vary considerably based on the instantaneous degree of Fe^{2+} oxidation. The small range in $\delta^{56}Fe$ measured in the stromatolites suggests that Fe^{2+} oxidation was rapid enough to quantitatively precipitate any Fe^{2+} that met the stromatolites. Specifically, the identical $\delta^{56}Fe$ values of adjacent laminations within a single stromatolitic column suggest that for extended periods of stromatolite growth, no change in Fe isotopic fractionation during Fe^{2+} oxidation took place. This is straightforward to explain via quantitative precipitation from an Fe^{2+} that did not isotopically evolve on short timescales, but very difficult to explain via partial oxidation where both the extent of fractionation during oxidation and the isotopic composition of the Fe^{2+} pool would need to either

remain constant, or perfectly compensate changes in one another; both of which are unlikely because partial oxidation should drive isotopic evolution in the residual Fe^{2+} pool and subsequent precipitates to more negative $\delta^{56}Fe$ values.

If essentially all upwelled Fe was removed from solution in the stromatolitic environment this would also have enabled the precipitation of Ca carbonate (Klein and Beukes, 1989; Riding et al., 2014; Sumner, 1997), such as the very compositionally pure intercolumnar cement observed in EDS mapping and inferred from the mixing pattern in the bulk-rock samples. The precipitation of low-Fe calcium carbonate requires $[Fe^{2+}]$ to be at or below low micromolar levels where siderite (Fe carbonate) precipitation is unfavored (Riding et al., 2014; Sumner, 1997), and thus its in these samples might imply that oxidation of all remaining Fe in the stromatolites created such conditions at this locality, both during intervals where all upwelled Fe had been oxidized out of solution, and shoreward of the Fe-depositing environment. Indeed, various Archean and early Paleoproterozoic successions including underlying deposits in the Transvaal Supergroup that formed the Campbellrand-Malmani carbonate platform, feature low-Fe limestones and dolostones in shallow water (Klein and Beukes, 1989; Sumner, 1997).

Rapid near-quantitative oxidation of high initial $[Fe^{2+}]$ within microbial mats should be uniquely associated with cyanobacteria (Planavsky et al., 2009). Extensive study of cyanobacteria in high (>100 μM) $[Fe^{2+}]$ environments has revealed their ability to quantitatively oxidize Fe^{2+} within thin (~1 mm) microbial mats (Trouwborst et al., 2007). Rapid oxidation of Fe^{2+} in modern cyanobacterial mats regardless of ambient O_2 levels, is a result of oxygenic photosynthesis creating localized O_2 concentrations of 10s-100s of μM (Pierson et al., 1999; Pierson and Parenteau, 2000; Trouwborst et al., 2007). Even in mats where anoxygenic phototrophs were identified, Fe^{2+} oxidation was shown in experiments to be tied dominantly to cyanobacteria and can draw down

100 μM [Fe^{2+}] in minutes, and the minimum reported Fe^{2+} oxidation rate for a cyanobacterial mat in daylight was 1.6 μMs^{-1} at initial [Fe^{2+}] of ~100 μM (Trouwborst et al., 2007). We are not aware of similar Fe^{2+} oxidation rate data for pure photoferrotrophic microbial mats, but all existing data for planktonic photoferrotroph cultures in suspension indicate Fe^{2+} oxidation rates on the order of a few 100 μM per day, or up to 0.003 μM s^{-1} (Hegler et al., 2008; Kappler et al., 2005; Schad et al., 2019), 2-3 orders of magnitude lower than rates observed in cyanobacterial mats, despite the photoferrotrophs typically being cultured in millimolar [Fe^{2+}], as opposed to tens to hundreds of micromolar [Fe^{2+}] in cyanobacterial experiment. The timescales of days taken by photoferrotrophic culture experiments to reach complete Fe^{2+} oxidation is inconsistent with the Fe isotopic signatures of quantitative Fe^{2+} oxidation.

Conceptually, quantitative oxidation signatures in Fe^{2+} isotopic compositions of stromatolites require that Fe oxidation rates significantly outstrip local diffusive replenishment of Fe^{2+} to the stromatolite surface. The diffusive flux J_{Fe} of Fe^{2+} to the stromatolite surface (assuming rapid Fe^{2+} oxidation and drawdown to zero) is

$$J_{Fe} \sim \frac{D_{Fe}[Fe^{2+}]}{d}, \qquad \text{(Eq. 5)}$$

where D_{Fe} is the diffusivity of Fe^{2+} and d is a characteristic length scale over which a solute utilized in the growing stromatolite is depleted during daylight hours (Petroff et al., 2010). In still water d is on the order of the spacing λ between columns (Petroff et al., 2010), which in this case is ~1 cm. In flowing water, far-field diffusive gradients are destroyed by eddy advection, and d is the distance at which viscous forces balance inertia, given by $\lambda Re^{-1/2}$ (Petroff et al., 2010). The cm-scale diameter and morphology of the stromatolites suggests growth occurred in a water flow environment with a maximum possible value for Re of 2300, giving $d \approx 0.02$ cm. Taking $D_{Fe} = 6 \times 10^{-6}$ cm^2 s^{-1} (Boudreau, 1997) and a canonical [Fe^{2+}] ≈ 50 μM (Holland, 1984) results in J_{Fe}

estimates from 0.0003-0.014 μM cm s^{-1} for the range of values of *d* discussed above. Rates of Fe^{2+} oxidation at [Fe^{2+}] ~50 μM measured within cyanobacterial mats are 1.6-6.4 μM s^{-1} over the ~0.05 cm observed depth of active [Fe^{2+}] oxidation defined by light penetration (Trouwborst et al., 2007), or 0.08-0.32 μM cm s^{-1}. This is much larger than the calculated J_{Fe} and thus satisfies conditions to record quantitative Fe^{2+} oxidation. By comparison, Fe^{2+} oxidation rates $\leq$ 0.003 μM s^{-1} for photoferrotrophy equate to 0.00015 μM cm s^{-1} in a 0.05 cm-thick active layer, lower than the whole range of calculated J_{Fe}. This suggests that photoferrotrophic Fe^{2+} oxidation is unlikely to result in Fe isotopic signature of quantitative oxidation, confirming the framework wherein quantitative oxidation is best explained with an rapid O_2-driven process in a cyanobacterial stromatolites (Planavsky et al., 2009). Cyanobacterial mats by no means guarantee quantitative oxidation, as demonstrated by study of modern hot spring assemblages in the Kamchatka Peninsula, and the local chemical and flow conditions all play important roles in determining what isotopic signature is exported to the geological record (Mulholland et al., 2015), but rapid oxidation of [Fe^{2+}] in O_2-rich microenvironments produced by cyanobacterial mats creates the most favorable conditions for quantitative and thus non-fractionating Fe deposition in stromatolites.

Manganese and cerium enrichments imply elevated ambient O_2

Quantitative Fe^{2+} oxidation in Griquatown Formation stromatolites suggests that free O_2 exceeding that required to locally oxidize Fe^{2+} could accumulate in this shallow marine setting. As this is not an oxidant-limited process, Fe systematics cannot constrain [O_2]. Manganese and cerium are both only converted to insoluble oxidized phases at high redox potential, so their modest enrichment in the stromatolites, implying their localized partial oxidation, might shed more light on shallow water redox conditions at the top of the Griquatown formation. We define an enrichment index

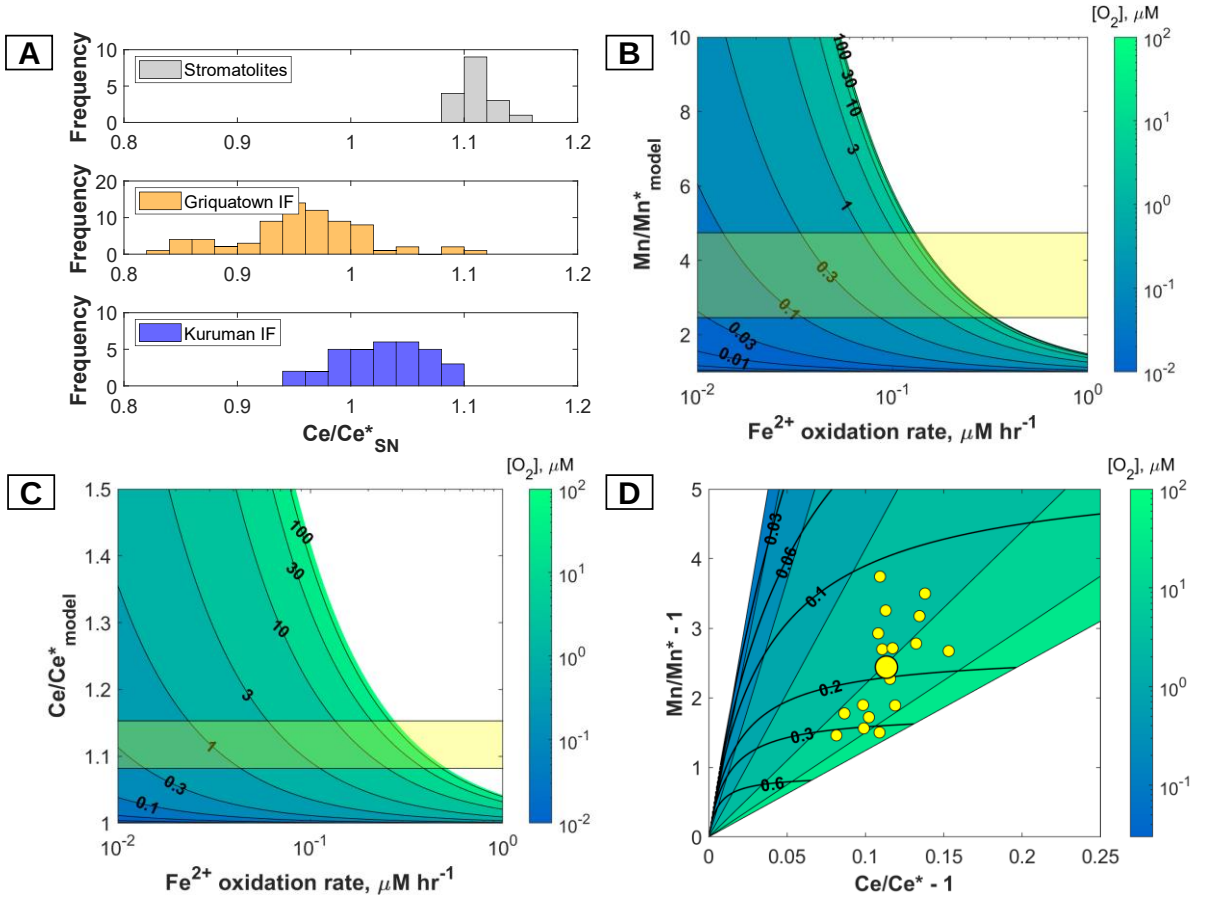

Figure 4.6. Interpreting Mn and Ce enrichments in Griquatown Formation stromatolites. A: Ce anomalies in Griquatown Formation stromatolites, and the underlying Kuruman and Griquatown Iron Formations (recalculated from the data of Oonk et al., 2018 using Eq. 3). Assuming that stromatolites precipitated Ce from a non-anomalous seawater source gives conservative estimates of the degree of local Ce enrichment as the underlying Griquatown IF has slightly negative average Ce/Ce^*_{SN}. B-C: Modeled oxidative Mn (B) and Ce (C) enrichments as a function of Fe oxidation rate and dissolved O_2 (contoured). The height of the yellow box spans the range of measured values of Mn/Mn*, and Ce/Ce^*_{SN} in Griquatown stromatolites. D: Cross plot of Mn/Mn* and Ce/Ce* in stromatolite samples (small circles) and the oxidative enrichment model. Heavy black contours show Fe oxidation rates in μM hr^{-1}, and the color scale tracks dissolved O_2. The large circle gives the mean of stromatolite data. The mean O_2 estimate of ~10.5 μM agrees with previous estimates for Pre-GOE oxygen oases (Olson et al., 2013; Riding et al., 2014). See text for details of all model calculations.

Mn/Mn*, as the ratio of the Mn/Fe ratio in the sample ($(Mn/Fe)_{sample}$) relative to $(Mn/Fe)_{IF}$, to the 'background' Mn/Fe ratio for precipitated along with IF precursor minerals:

$$Mn/Mn^* = \frac{(Mn/Fe)_{sample}}{(Mn/Fe)_{IF}}. \qquad \text{(Eq. 6)}$$

In this definition, Mn/Mn* > 1 can be developed by the deposition of an oxidized Mn phase. Little is known about Mn^{2+} adsorption onto IF precursor materials from experiments, and where such experiments have been conducted, the relevant data required to extrapolate results from laboratory conditions to the ancient ocean conditions is not available. However, we can infer the rate of adsorption of Mn^{2+} to IF precursor minerals in the Griquatown formation directly from the geochemical systematics of the underlying IF (Nie et al., 2020). There is a well-established negative correlation between the $\delta^{56}Fe$ of Archean and Paleoproterozoic IFs and the logarithm of (Mn/Fe) that can be seen both in compiled records (Hiebert et al., 2018), and exclusively from the Kuruman and Griquatown formations that underlie the stromatolites analyzed here (Fig. 4.4B) (Nie et al., 2020; Thibon et al., 2019). If Fe was removed by any process that enriched the precipitate in heavy Fe isotopes and this removal was not associated with back-reaction (reasonable for sinking insoluble phases), a linear ln(1/Fe) *vs.* $\delta^{56}Fe$ relationship is expected, and therefore the observed linear ln(Mn/Fe) *vs.* $\delta^{56}Fe$ could mostly reflect passive Mn enrichment relative to Fe in seawater and a constant relationship between dissolved Mn/Fe and Mn/Fe imparted to IF precipitates (Fig. 4.4B). Therefore, to estimate $(Mn/Fe)_{IF}$, the Mn/Fe ratio in IF precipitates not associated with Mn oxidation, we take the Mn/Fe ratio on the ln(Mn/Fe) *vs.* $\delta^{56}Fe$ trendline fitted through Kuruman-Griquatown formation data at the average $\delta^{56}Fe$ value of the stromatolites (-1.52‰), making the assumption that the vertical displacement above this line reflects additional Mn precipitation as oxides. This value, ≈0.029, is used for $(Mn/Fe)_{IF}$ in our modeling. We also make use of the Ce anomaly (Eq. 3). Experimental REE partitioning studies suggest that non-oxidative Ce^{3+} adsorption onto Fe oxyhydroxides follows a smooth pattern with neighboring REEs, giving $Ce/Ce^*_{SN} \approx 1$, while the additional incorporation of locally oxidized and insoluble Ce^{4+} should result in $Ce/Ce^*_{SN} > 1$ (Koeppenkastrop and De Carlo, 1992; Quinn et al., 2004).

All stromatolitic samples exhibit moderate enrichments in both Mn (Mn/Mn* = 2.5-4.7) and Ce (Ce/Ce^*_{SN} = 1.08-1.15) (Fig. 4.6). These enrichments positively covary, consistent with a common enrichment process such incorporation of additional oxidized Mn^{4+} and Ce^{4+} phases, which are less soluble than Mn^{2+}, Ce^{3+} and the neighboring trivalent REEs. Widespread oxidation depletes waters in Ce relative to neighboring REEs, resulting in Ce/Ce^*_{SN} values < 1 that are often inherited by chemical precipitates. Therefore, $Ce/Ce^*_{SN} > 1$ suggests that a local onset of oxidation of Ce overwrote any depleted reservoir effects that could be inherited from seawater (Fig. 4.6A). Moderate enrichments in Ce in shallow Fe^{3+}-oxide-rich facies have also been documented in IFs from the Paleoproterozoic and Neoproterozoic and attributed to local scavenging of oxidized Ce (O'Connell et al., 2020; Planavsky et al., 2009).

Mn^{2+} and Ce^{3+} oxidation require high-potential oxidants, generally assumed to be free O_2, which would be readily available if as Fe isotope systematics suggest, the stromatolites contained cyanobacteria doing oxygenic photosynthesis. So, Mn and Ce enrichments in Griquatown stromatolites could be used to estimate ambient O_2 levels in the stromatolite depositional environment. We modeled Mn and Ce deposition as composed of two phases: adsorbed pool that scales with Fe oxyhydroxide deposition, and an oxidized pool, the latter of which is sensitive to dissolved O_2. Modeled Mn/Mn* and Ce/Ce* values are given by the ratio of total deposition of each element to their respective adsorbed fluxes such that:

$$Mn/Mn^*_{model} = \frac{\left(F_{Mn_{ox}} + F_{Mn_{ads}}\right)}{F_{Mn_{ads}}} = \frac{F_{Mn_{ox}}}{F_{Mn_{ads}}} + 1, \quad (7)$$

and

$$Ce/Ce^*_{model} = \frac{\left(f_{Ce_{ox}/Ce_{dissolved}} + f_{Ce_{ads}/Ce_{dissolved}}\right)}{f_{Ce_{ads}/Ce_{dissolved}}} = \frac{f_{Ce_{ox}/Ce_{dissolved}}}{f_{Ce_{ads}/Ce_{dissolved}}} + 1. \quad (8)$$

where F is the deposition rate in μM hr^{-1}, and f is a specific deposition rate in hr^{-1}, which is used to compare to specific Ce^{3+} oxidation rate data (Moffett, 1994). We assume a local onset of Mn^{2+} and Ce^{3+} oxidation and therefore assume that no significant reservoir depletion effects (Mn/Mn* or Ce/Ce* < 1) are established in the water column. This should give a robust lower bound on Mn^{2+} and Ce^{3+} oxidation rates because greater degrees of local oxidation would be required to create local Mn and Ce enrichments if the marine pool was already depleted in these elements. In order to make comparisons to geochemical data, the model by necessity considers both the adsorbed and oxidized fluxes of Mn and Ce as constant, time-averaged rates. However, Fe^{2+} oxidation in the stromatolites was likely rapid and quantitative, and also localized to the growing stromatolite surface, so the adsorbed flux associated with Fe deposition was probably similarly punctuated, and is considered as a constant flux here purely for the purposes of comparison. In the case of the oxidized flux, data from growing stromatolitic mats in Fe-rich waters suggest that Mn is not oxidized within cyanobacterial mats, and given the similar oxidation behaviors of Mn and Ce, it is likely that Ce is not oxidized in these mats either. As such, we expect Mn and Ce to follow steady oxidation rates tied to the ambient O_2 levels prevailing in the stromatolitic environment rather than the punctuated by episodes of Fe^{2+} influx and oxidation.

The deposition rates for adsorbed Mn^{2+} and Ce^{3+} are:

$$F_{Mn_{ads}} = (Mn/Fe)_{IF} \times F_{Fe}, \quad \text{(Eq. 9)}$$

and

$$f_{Ce_{ads}/Ce_{dissolved}} = A_{Ce} \times F_{Fe}. \quad \text{(Eq. 10)}$$

where the sorption coefficient A_{Ce} describes the dependent of the adsorbed [Ce^{3+}] as a function of dissolved [Ce^{3+}] and concentration of ferric oxyhydroxide precipitates. Experimental studies of Ce adsorption onto amorphous Fe^{3+} oxyhydroxide in seawater give values of A_{Ce} = 7.6 μM^{-1} at pH

7.8 (Koeppenkastrop and De Carlo, 1992), and 0.083 μM^{-1} at pH 6.12 (Quinn et al., 2004). From this approximate logarithmic dependence on pH, we estimate a value of $A_{Ce} = 0.65\ \mu M^{-1}$ at pH 7.0, which is a best-estimate for the oceans at around 2.4 Ga (Halevy and Bachan, 2017).

Mn^{2+} and specific Ce^{3+} oxidation reactions are thought be microbially mediated and can be shown to follow Michaelis-Menten kinetics (or pseudo Michaelis-Menten kinetics for specific rates) in the forms (Clement et al., 2009; Moffett, 1994):

$$F_{Mn_{ox}} = \frac{(V_{Mn} \times [O_2])}{(K_{M,Mn} + [O_2])}, \quad \text{(Eq. 11)}$$

and

$$f_{Ce_{ox}/Ce_{dissolved}} = \frac{(V_{f,Ce} \times [O_2])}{(K_{M,Ce} + [O_2])}, \quad \text{(Eq. 12)}$$

where V is a maximum oxidation rate, V_f is a maximum specific oxidation rate, K_M is a saturation coefficient, and $[O_2]$ is the dissolved O_2 concentration. Clement et al., (2009) indicate a range of coupled values from $V = 0.014\ \mu M\ hr^{-1}$, $K_{M,\,Mn} = 0.87\ \mu M$; to $V = 0.0036\ \mu M\ hr^{-1}$, $K_{M,\,Mn} = 10.5\ \mu M$ from a detailed study of Mn^{2+} oxidation in the Black Sea, and we use the first pair of values to give the fastest Mn^{2+} oxidation rates at the lowest $[O_2]$, thus making any $[O_2]$ estimates conservative. Kinetic data for Ce oxidation is only available as specific oxidation rates (Moffett, 1994), reported at 100 %, 5 %, and 'zero' % of the modern atmospheric O_2 concentration. We fit values of $V_{f,\,Ce} = 0.0285\ hr^{-1}$, $K_{M,\,Ce} = 11.31\ \mu M$, assuming Henry's law solubility for O_2 in seawater at 25°C for those experiments. These estimated values broadly agree with the range of values for Mn oxidation with the higher value of $K_{M,\,Ce}$ being consistent with the standard electrode potential for Ce^{3+} oxidation to Ce^{4+} (+1.61 V) being higher than that for Mn^{2+} oxidation to Mn^{4+} (+1.224 V). We assume all oxidized Mn and Ce is deposited immediately, due to insolubility and/or high affinity for scavenging onto oxide particles. Specific Ce oxidation rates (oxidation rate as a fraction of the dissolved [Ce]) are used in order to utilize the limited available kinetic data

(Moffett, 1994). The scaling of Mn/Mn* and Ce/Ce* as a function of F_{Fe} is shown in Figures 4.6B-C, where contours of $[O_2]$ can be mapped onto this space.

The equations for Mn/Mn^*_{model} and Ce/Ce^*_{model} can be combined to eliminate the unknown Fe deposition flux F_{Fe} and solve for dissolved $[O_2]$. In order to solve for $[O_2]$ directly, we recognize that Equations 7 and 8 for oxidative Mn and Ce enrichment can be expressed in the form:

$$Mn/Mn^*_{model} - 1 = \frac{a}{F_{Fe}}, \quad \text{(Eq. 13)}$$

and

$$Ce/Ce^*_{model} - 1 = \frac{b}{F_{Fe}}, \quad \text{(Eq. 14)}$$

respectively, where a and b are

$$a = \frac{F_{Mn_{ox}}}{(Mn/Fe)_{IF}}, \quad \text{(Eq. 15)}$$

and

$$b = \frac{f_{Ce_{ox}/Ce_{dissolved}}}{A_{Ce}}, \quad \text{(Eq. 16)}$$

Taking the ratio of Equations 13 and 14 eliminates F_{Fe}:

$$\frac{Mn/Mn^*_{model} - 1}{Ce/Ce^*_{model} - 1} = \frac{a}{b} = \theta, \quad \text{(Eq. 17)}$$

where we have defined the ratio θ for convenience. Expanding the expressions for a and b and rearranging for dissolved $[O_2]$ gives:

$$[O_2] = \frac{V_{Mn} \times K_{M,Ce} \times A_{Ce} - \theta \times V_{f,Ce} \times K_{M,Mn} \times (Mn/Fe)_{IF}}{\theta \times V_{f,Ce} \times (Mn/Fe)_{IF} - V_{Mn} \times A_{Ce}}. \quad \text{(Eq. 18)}$$

θ, the only undefined variable in the equation, is constrained from the ratio of measured values of (Mn/Mn*-1) and $(Ce/Ce^*_{SN}-1)$ in the stromatolites. Either Mn/Mn* or Ce/Ce* can be used to calculate F_{Fe} at any given $[O_2]$, by rearranging Equations 13 or 14, *e.g.*:

$$F_{Fe} = \frac{V_{Mn} \times [O_2]}{(Mn/Fe)_{IF} \times (K_{M,Mn} + [O_2]) \times (Mn/Mn^* - 1)} \quad \text{(Eq. 19)}$$

Contours of both environmental parameters in (Mn/Mn* - 1) *vs.* (Ce/Ce* - 1) space can be shown simultaneously. All Griquatown stromatolite data falls within the model space and solving the equations for stromatolite data gives estimates of [O_2] from 4-48 μM, with a value of ~10.5 μM for the average of these data. These values overlap both with quasi-3D modeling of Archean oxygen oases that estimated an [O_2] range of 1-10 μM range (Olson et al., 2013). The corresponding time-averaged Fe deposition rates F_{Fe} range from 0.11-0.32 μM hr^{-1} with the average data giving ~0.24 μM hr^{-1}. These Fe oxidation rates are orders of magnitude slower than measured rates in modern cyanobacterial mats of 1.6-6.4 μM s^{-1} (Trouwborst et al., 2007) but as alluded to above, the physical meaning of F_{Fe} in this context is unclear, because it is a time- and space-averaged deposition rate required for interpreting the geochemical record, whereas Fe was rapidly precipitated in the localized microenvironment of the active layer in the stromatolite.

A site of active oxygen production and utilization before the GOE

Previous studies identified trace element and isotopic evidence for Mn oxide burial in the pre-GOE oceans (Kurzweil et al., 2016; Ossa Ossa et al., 2018; Ostrander et al., 2019; Planavsky et al., 2014a) that implied redox cycling driven by elevated ambient O_2 in the oceans. Textural evidence for bubble creation in carbonate-hosted stromatolites (Bosak et al., 2009; Wilmeth et al., 2019) implicated stromatolitic sites in pre-GOE O_2 production, but lacked redox-sensitive geochemical confirmation. We are unaware of any other samples where geochemical data confirms both the production and utilization of O_2 at a specific site (Fig. 4.7). The data reported here therefore represent a unique smoking gun for microbial O_2 production in the shallow oceans before the first resolvable oxygenation of the atmosphere.

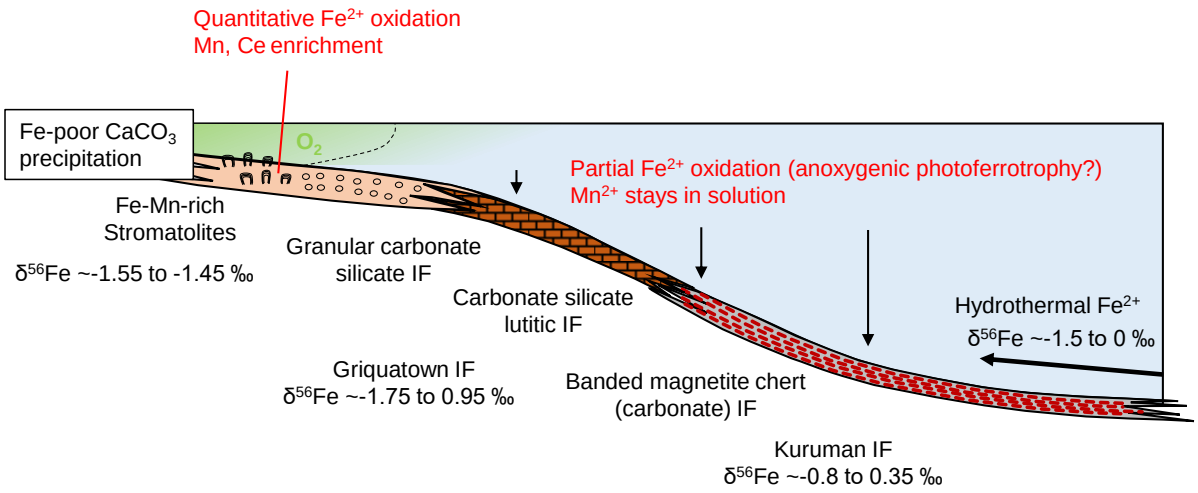

Figure 4.7. Schematic illustration of proposed formation environment of Griquatown Formation stromatolites. Iron isotope systematics and sedimentological features suggest the stromatolites formed in shallow waters as the terminal sink for Fe^{2+} in upwelled waters from deep anoxic basin that deposited the underlying IFs. Progressive partial oxidation of Fe^{2+} to form the Kuruman and Griquatown IFs preferentially removed isotopically heavy Fe^{3+}, causing Fe^{2+} in solution to become increasingly isotopically light heading shoreward. Quantitative removal of remaining Fe^{2+} by the stromatolites would have enabled precipitation of Fe-poor $CaCO3_3$ as intercolumnar and void-filling cement, and local accumulations of O_2 around the stromatolites contributed to partial oxidation of Mn and Ce.

Given that much of the evidence for oxygen oases is significantly older than the Griquatown IF stromatolites, it is surprising that there are not more examples of quantitative Fe oxidation in shallow waters from the Archean, and that shallow water granular iron formations and Fe-rich stromatolites are comparatively rare in this time period (Bekker et al., 2010). One possible explanation is that throughout the Archean eon, the mechanisms that precipitated deep marine-sourced Fe^{2+} as it upwelled, whether by progressive partial oxidation, precipitation of hydrated silicates, or a combination of these, was comparatively efficient, restricting the large-scale deposition of IFs to deep basins and as typical banded iron formations. Waters upwelled onto the continental shelf were generally Fe-depleted, with Fe isotopic compositions reflecting extensive partial removal processes (Eroglu et al., 2018; Heard et al., 2020; Planavsky et al., 2012; Rouxel et al., 2005). This ocean redox structure, established even without an oxygenated atmosphere, enabled the deposition of shallow-water limestone- and dolostone-dominated carbonate platforms

(Klein and Beukes, 1989; Riding et al., 2014; Sumner, 1997). In certain time periods and locations, this ocean redox structure also allowed the accumulation of some ambient O_2 that expanded into areas of Fe and Mn availability and caused the deposition of Mn oxides and their associated trace element isotopic signatures (Kurzweil et al., 2016; Ossa Ossa et al., 2018; Ostrander et al., 2019; Planavsky et al., 2014a). However, wholesale interaction of Fe-rich waters and the microbial oxygen factories inhabiting the tidal zone never took place.

What changed around the time of deposition of the Kuruman-Griquatown succession was a global increase in the deposition of IFs, with as much as 70 % of Precambrian Fe mineral resources being laid down in the interval 2.60-2.40 Ga (Bekker et al., 2010). This time period saw the deposition of the massive Kuruman-Griquaton and Brockman IFs in the Transvaal and Hamersley (SW Australia) Provinces, respectively, along with the broadly time-equivalent deposition of IFs on reactivated continental margins in the Quadrilátero Ferrífero region in Brazil, Krivoy Rog area in Ukraine, and Kursk Magnetic Anomaly region in Russia. This period of deposition is closely associated in age with enhanced volcanism accompanying a global mantle plume breakout event (*e.g.* Heaman, 1997) and a genetic link between the two events, with unprecedented IF deposition accompanying enhanced global hydrothermal Fe^{2+} fluxes to the oceans, is likely (Bekker et al., 2010). With a ramp-up in the supply of Fe^{2+} to the deep oceans in the late-Neoarchean to early Paleoproterozoic, previously efficient Fe^{2+} removal pathways could have been overwhelmed, allowing delivery of Fe^{2+} to the tidal zone, resulting in some of the earliest granular iron formations (GIFs) and crucially, and encroachment of ferruginous waters on environments hosting cyanobacterial O_2 production (Fig. 4.7). Here, the O_2-rich microenvironment of the stromatolites acted as the terminal sink for Fe^{2+} that reached such shallow waters, and isotopic signatures of quantitative Fe^{2+} oxidation preserved evidence of the nature of these environments. Whenever

upwelled Fe^{2+} made its way to the tidal zone, it was likely rapidly consumed, causing a return to Fe-poor conditions under which Ca-rich carbonate precipitated could prevail, producing the intercolumnar and void-filling cement observed surrounding the Fe-rich stromatolites (Figs 4.2, 4.3). During Fe-poor intervals, ambient O_2 levels could have increased in shallow waters, producing the transient oases that allowed areal precipitation of Mn oxides (Fig. 4.7).

The model we invoke has clear parallels with models for global granular IF deposition in the late Paleoproterozoic, where widespread hematite GIFs or 'ironstones', were deposition in multiple continents at 1.88 Ga following upwelling of Fe^{2+} onto shallow marine shelves, in an event that has also been linked to globally enhanced mafic volcanism and submarine hydrothermal Fe^{2+} fluxes (Rasmussen et al., 2012). The main difference between these depositional episodes is the dominant carbonate-silicate mineralogy of the Griquatown IF compared to a dominantly hematitic mineralogy of the 1.88 Ga deposits (Bekker et al., 2010). This contrast may indicate that Fe^{2+} oxidation in the tidal zone was widespread at 1.88 Ga, whereas prior to the GOE, Fe^{2+} oxidation in the tidal zone was outpaced by carbonate and silicate precipitation except in the immediate vicinity of O_2-producing stromatolites. We briefly suggest two possible factors. First, the presence of an appreciable atmospheric O_2 reservoir at 1.88 Ga, even at only 1 % of PAL (Planavsky et al., 2014b), could perhaps the tidal zone buffered at a non-zero O_2 concentration where microaerophilic chemolithoautotrophs could effectively oxidize Fe^{2+} (Planavsky et al., 2009), whereas prior to the GOE atmospheric pO_2 was $< 10^{-5}$ PAL (Pavlov and Kasting, 2002). Second, the tidal zone during Griquatown IF deposition was likely supersaturated with respect to Fe carbonate (Sumner, 1997), and potentially the Fe^{2+} silicate greenalite (Rasmussen et al., 2019; Tosca et al., 2016), when upwelling of Fe^{2+} occurred. The contrast in the precipitation mechanisms of GIFs before and after the GOE poses important questions for future studies that will have

bearing on understanding redox dynamics in the tidal zone and the O_2 levels of the atmosphere they directly interacted with.

Conclusions

The redox structure of the pre-oxygenation oceans, with Fe-rich deep waters, and Fe-poor and potentially locally or transiently oxygenated shallow waters, has become widely accepted, but the source of O_2 for more recently recognized 'oxygen oases' has never been geochemically fingerprinted. We reported the discovery of Fe-rich stromatolites from the shallowest facies of an extensive succession of iron formation that ranges from deep basinal to shallow storm-influenced shelf environments. These stromatolites have extremely homogeneous Fe isotopic signatures at bulk and lamination scale (Figs 4.4, 4.5), constituting the strongest evidence of quantitative Fe^{2+} oxidation in any pre-GOE IFs and most parsimoniously explained by oxidation by O_2-rich microenvironments produced by cyanobacterial inhabitants for the stromatolites. Modest enrichments in Mn and Ce in the bulk stromatolite material similarly suggest that ambient O_2 levels in the shallow water setting were elevated to micromolar conditions, consistent with previous models for oxygen oases (Fig. 4.6). These samples represent, to our knowledge, the first discovery of O_2 production and utilization at a single site prior to the GOE, and therefore provide a smoking gun for the microbial O_2 factories that fueled Archean and early Paleoproterozoic oxygen oases (Fig. 4.7). The rare preservation of this environment in such Fe-rich chemical sediments suggests that the ocean conditions that drove widespread global IF deposition from 2.6-2.4 Ga overwhelmed deep basin removal pathways for Fe^{2+} and delivered it to the tidal zone where O_2 producing communities were already established. The nature of shallow marine Fe cycling immediately prior to the GOE bears similarities to the widespread deposition of GIFs at 1.88 Ga, and future work to

compare and contrast these depositional modes should shed more light on the evolution of redox cycling in the shallowest regions of the ancient oceans.

Acknowledgements

Conversations with Nic Beukes, Mark Van Zuilen, and Dylan Wilmeth were appreciated. We thank April Isch in the University of Chicago Paleo-CT lab for providing X-Ray tomography images.

References

Allwood, A.C., Rosing, M.T., Flannery, D.T., Hurowitz, J.A., Heirwegh, C.M., 2018. Reassessing evidence of life in 3,700-million-year-old rocks of Greenland. Nature 1. https://doi.org/10.1038/s41586-018-0610-4

Allwood, A.C., Walter, M.R., Burch, I.W., Kamber, B.S., 2007. 3.43 billion-year-old stromatolite reef from the Pilbara Craton of Western Australia: Ecosystem-scale insights to early life on Earth. Precambrian Res., Earliest Evidence of Life on Earth 158, 198–227. https://doi.org/10.1016/j.precamres.2007.04.013

Allwood, A.C., Walter, M.R., Kamber, B.S., Marshall, C.P., Burch, I.W., 2006. Stromatolite reef from the Early Archaean era of Australia. Nature 441, 714–718. https://doi.org/10.1038/nature04764

Anbar, A.D., Duan, Y., Lyons, T.W., Arnold, G.L., Kendall, B., Creaser, R.A., Kaufman, A.J., Gordon, G.W., Scott, C., Garvin, J., Buick, R., 2007. A Whiff of Oxygen Before the Great Oxidation Event? Science 317, 1903–1906. https://doi.org/10.1126/science.1140325

Balci, N., Bullen, T.D., Witte-Lien, K., Shanks, W.C., Motelica, M., Mandernack, K.W., 2006. Iron isotope fractionation during microbially stimulated Fe(II) oxidation and Fe(III) precipitation. Geochim. Cosmochim. Acta 70, 622–639. https://doi.org/10.1016/j.gca.2005.09.025

Bekker, A., Holland, H.D., Wang, P.-L., Rumble Iii, D., Stein, H.J., Hannah, J.L., Coetzee, L.L., Beukes, N.J., 2004. Dating the rise of atmospheric oxygen. Nature 427, 117–120. https://doi.org/10.1038/nature02260

Bekker, A., Krapež, B., Karhu, J.A., 2020. Correlation of the stratigraphic cover of the Pilbara and Kaapvaal cratons recording the lead up to Paleoproterozoic Icehouse and the GOE. Earth-Sci. Rev. 211, 103389. https://doi.org/10.1016/j.earscirev.2020.103389

Bekker, A., Slack, J.F., Planavsky, N., Krapež, B., Hofmann, A., Konhauser, K.O., Rouxel, O.J., 2010. Iron Formation: The Sedimentary Product of a Complex Interplay among Mantle, Tectonic, Oceanic, and Biospheric Processes. Econ. Geol. 105, 467–508. https://doi.org/10.2113/gsecongeo.105.3.467

Bellefroid, E.J., Hood, A. v S., Hoffman, P.F., Thomas, M.D., Reinhard, C.T., Planavsky, N.J., 2018. Constraints on Paleoproterozoic atmospheric oxygen levels. Proc. Natl. Acad. Sci. 115, 8104–8109. https://doi.org/10.1073/pnas.1806216115

Beukes, N.J., 1984. Sedimentology of the Kuruman and Griquatown Iron-formations, Transvaal Supergroup, Griqualand West, South Africa. Precambrian Res. 24, 47–84. https://doi.org/10.1016/0301-9268(84)90069-X

Beukes, N.J., Gutzmer, J., 2008. Origin and Paleoenvironmental Significance of Major Iron Formations at the Archean-Paleoproterozoic Boundary. https://doi.org/10.5382/Rev.15.01

Beukes, N.J., Klein, C., 1990. Geochemistry and sedimentology of a facies transition — from microbanded to granular iron-formation — in the early Proterozoic Transvaal Supergroup, South Africa. Precambrian Res. 47, 99–139. https://doi.org/10.1016/0301-9268(90)90033-M

Bosak, T., Knoll, A.H., Petroff, A.P., 2013. The Meaning of Stromatolites. Annu. Rev. Earth Planet. Sci. 41, 21–44. https://doi.org/10.1146/annurev-earth-042711-105327

Bosak, T., Liang, B., Sim, M.S., Petroff, A.P., 2009. Morphological record of oxygenic photosynthesis in conical stromatolites. Proc. Natl. Acad. Sci. 106, 10939–10943. https://doi.org/10.1073/pnas.0900885106

Boudreau, B., 1997. Diagenetic models and their implementation: modelling transport and reactions in aquatic sediments. Springer, Berlin.

Bullen, T.D., White, A.F., Childs, C.W., Vivit, D.V., Schulz, M.S., 2001. Demonstration of significant abiotic iron isotope fractionation in nature. Geology 29, 699–702. https://doi.org/10.1130/0091-7613(2001)029<0699:DOSAII>2.0.CO;2

Cairns-Smith, A.G., 1978. Precambrian solution photochemistry, inverse segregation, and banded iron formations. Nature 276, 807–808. https://doi.org/10.1038/276807a0

Catling, D.C., Zahnle, K.J., McKay, C.P., 2001. Biogenic Methane, Hydrogen Escape, and the Irreversible Oxidation of Early Earth. Science 293, 839–843. https://doi.org/10.1126/science.1061976

Clement, B.G., Luther, G.W., Tebo, B.M., 2009. Rapid, oxygen-dependent microbial Mn(II) oxidation kinetics at sub-micromolar oxygen concentrations in the Black Sea suboxic zone. Geochim. Cosmochim. Acta 73, 1878–1889. https://doi.org/10.1016/j.gca.2008.12.023

Cloud, P., 1973. Paleoecological Significance of the Banded Iron-Formation. Econ. Geol. 68, 1135–1143. https://doi.org/10.2113/gsecongeo.68.7.1135

Craddock, P.R., Dauphas, N., 2011. Iron Isotopic Compositions of Geological Reference Materials and Chondrites. Geostand. Geoanalytical Res. 35, 101–123. https://doi.org/10.1111/j.1751-908X.2010.00085.x

Croal, L.R., Johnson, C.M., Beard, B.L., Newman, D.K., 2004. Iron isotope fractionation by Fe(II)-oxidizing photoautotrophic bacteria 1. Geochim. Cosmochim. Acta 68, 1227–1242. https://doi.org/10.1016/j.gca.2003.09.011

Czaja, A.D., Van Kranendonk, M.J., Beard, B.L., Johnson, C.M., 2018. A multistage origin for Neoarchean layered hematite-magnetite iron formation from the Weld Range, Yilgarn Craton, Western Australia. Chem. Geol. 488, 125–137. https://doi.org/10.1016/j.chemgeo.2018.04.019

Dauphas, N., Janney, P.E., Mendybaev, R.A., Wadhwa, M., Richter, F.M., Davis, A.M., van Zuilen, M., Hines, R., Foley, C.N., 2004. Chromatographic Separation and Multicollection-ICPMS Analysis of Iron. Investigating Mass-Dependent and -Independent Isotope Effects. Anal. Chem. 76, 5855–5863. https://doi.org/10.1021/ac0497095

Dauphas, N., Pourmand, A., Teng, F.-Z., 2009. Routine isotopic analysis of iron by HR-MC-ICPMS: How precise and how accurate? Chem. Geol., Advances in experimental and theoretical isotope geochemistry 267, 175–184. https://doi.org/10.1016/j.chemgeo.2008.12.011

Daye, M., Klepac-Ceraj, V., Pajusalu, M., Rowland, S., Farrell-Sherman, A., Beukes, N., Tamura, N., Fournier, G., Bosak, T., 2019. Light-driven anaerobic microbial oxidation of manganese. Nature 576, 311–314. https://doi.org/10.1038/s41586-019-1804-0

Djokic, T., Van Kranendonk, M.J., Campbell, K.A., Walter, M.R., Ward, C.R., 2017. Earliest signs of life on land preserved in ca. 3.5 Ga hot spring deposits. Nat. Commun. 8, 15263. https://doi.org/10.1038/ncomms15263

Dunlea, A.G., Murray, R.W., Sauvage, J., Spivack, A.J., Harris, R.N., D'Hondt, S., 2015. Dust, volcanic ash, and the evolution of the South Pacific Gyre through the Cenozoic. Paleoceanography 30, 1078–1099. https://doi.org/10.1002/2015PA002829

Eroglu, S., Schoenberg, R., Pascarelli, S., Beukes, N.J., Kleinhanns, I.C., Swanner, E.D., 2018. Open ocean vs. continentally-derived iron cycles along the Neoarchean Campbellrand-Malmani Carbonate platform, South Africa. Am. J. Sci. 318, 367–408. https://doi.org/10.2475/04.2018.01

Evans, D.A., Beukes, N.J., Kirschvink, J.L., 1997. Low-latitude glaciation in the Palaeoproterozoic era. Nature 386, 262–266. https://doi.org/10.1038/386262a0

Fischer, W.W., Hemp, J., Johnson, J.E., 2016. Evolution of Oxygenic Photosynthesis. Annu. Rev. Earth Planet. Sci. 44, 647–683. https://doi.org/10.1146/annurev-earth-060313-054810

Gaillard, F., Scaillet, B., Arndt, N.T., 2011. Atmospheric oxygenation caused by a change in volcanic degassing pressure. Nature 478, 229–232. https://doi.org/10.1038/nature10460

Gumsley, A.P., Chamberlain, K.R., Bleeker, W., Söderlund, U., Kock, M.O. de, Larsson, E.R., Bekker, A., 2017. Timing and tempo of the Great Oxidation Event. Proc. Natl. Acad. Sci. 114, 1811–1816. https://doi.org/10.1073/pnas.1608824114

Halevy, I., Bachan, A., 2017. The geologic history of seawater pH. Science 355, 1069–1071. https://doi.org/10.1126/science.aal4151

Heaman, L.M., 1997. Global mafic magmatism at 2.45 Ga: Remnants of an ancient large igneous province? Geology 25, 299–302. https://doi.org/10.1130/0091-7613(1997)025<0299:GMMAGR>2.3.CO;2

Heard, A.W., Dauphas, N., Guilbaud, R., Rouxel, O.J., Butler, I.B., Nie, N.X., Bekker, A., 2020. Triple iron isotope constraints on the role of ocean iron sinks in early atmospheric oxygenation. Science 370, 446–449. https://doi.org/10.1126/science.aaz8821

Hegler, F., Posth, N.R., Jiang, J., Kappler, A., 2008. Physiology of phototrophic iron(II)-oxidizing bacteria: implications for modern and ancient environments. FEMS Microbiol. Ecol. 66, 250–260. https://doi.org/10.1111/j.1574-6941.2008.00592.x

Hiebert, R.S., Bekker, A., Houlé, M.G., Rouxel, O.J., 2018. Depositional setting of the Late Archean Fe oxide- and sulfide-bearing chert and graphitic argillite in the Shaw Dome, Abitibi

greenstone belt, Canada. Precambrian Res. 311, 98–116. https://doi.org/10.1016/j.precamres.2018.04.004

Holland, H.D., 1984. The Chemical Evolution of the Atmosphere and Oceans. Princeton University Press.

Johnson, C., Beard, B., Weyer, S., 2020. The Ancient Earth, in: Johnson, C., Beard, B., Weyer, S. (Eds.), Iron Geochemistry: An Isotopic Perspective, Advances in Isotope Geochemistry. Springer International Publishing, Cham, pp. 215–360. https://doi.org/10.1007/978-3-030-33828-2_6

Johnson, J.E., Webb, S.M., Thomas, K., Ono, S., Kirschvink, J.L., Fischer, W.W., 2013. Manganese-oxidizing photosynthesis before the rise of cyanobacteria. Proc. Natl. Acad. Sci. 110, 11238–11243. https://doi.org/10.1073/pnas.1305530110

Kadoya, S., Catling, D.C., Nicklas, R.W., Puchtel, I.S., Anbar, A.D., 2020. Mantle data imply a decline of oxidizable volcanic gases could have triggered the Great Oxidation. Nat. Commun. 11, 2774. https://doi.org/10.1038/s41467-020-16493-1

Kappler, A., Pasquero, C., Konhauser, K.O., Newman, D.K., 2005. Deposition of banded iron formations by anoxygenic phototrophic Fe(II)-oxidizing bacteria. Geology 33, 865–868. https://doi.org/10.1130/G21658.1

Kendall, B., Reinhard, C.T., Lyons, T.W., Kaufman, A.J., Poulton, S.W., Anbar, A.D., 2010. Pervasive oxygenation along late Archaean ocean margins. Nat. Geosci. 3, 647–652. https://doi.org/10.1038/ngeo942

Kirschvink, J.L., Gaidos, E.J., Bertani, L.E., Beukes, N.J., Gutzmer, J., Maepa, L.N., Steinberger, R.E., 2000. Paleoproterozoic snowball Earth: Extreme climatic and geochemical global change and its biological consequences. Proc. Natl. Acad. Sci. 97, 1400–1405. https://doi.org/10.1073/pnas.97.4.1400

Klein, C., Beukes, N.J., 1989. Geochemistry and sedimentology of a facies transition from limestone to iron-formation deposition in the early Proterozoic Transvaal Supergroup, South Africa. Econ. Geol. 84, 1733–1774. https://doi.org/10.2113/gsecongeo.84.7.1733

Koeppenkastrop, D., De Carlo, E.H., 1992. Sorption of rare-earth elements from seawater onto synthetic mineral particles: An experimental approach. Chem. Geol. 95, 251–263. https://doi.org/10.1016/0009-2541(92)90015-W

Konhauser, K.O., Hamade, T., Raiswell, R., Morris, R.C., Ferris, F.G., Southam, G., Canfield, D.E., 2002. Could bacteria have formed the Precambrian banded iron formations? Geology 30, 1079–1082. https://doi.org/10.1130/0091-7613(2002)030<1079:CBHFTP>2.0.CO;2

Konhauser, K.O., Planavsky, N.J., Hardisty, D.S., Robbins, L.J., Warchola, T.J., Haugaard, R., Lalonde, S.V., Partin, C.A., Oonk, P.B.H., Tsikos, H., Lyons, T.W., Bekker, A., Johnson, C.M., 2017. Iron formations: A global record of Neoarchaean to Palaeoproterozoic environmental history. Earth-Sci. Rev. 172, 140–177. https://doi.org/10.1016/j.earscirev.2017.06.012

Kump, L.R., Barley, M.E., 2007. Increased subaerial volcanism and the rise of atmospheric oxygen 2.5 billion years ago. Nature 448, 1033–1036. https://doi.org/10.1038/nature06058

Kurzweil, F., Wille, M., Gantert, N., Beukes, N.J., Schoenberg, R., 2016. Manganese oxide shuttling in pre-GOE oceans – evidence from molybdenum and iron isotopes. Earth Planet. Sci. Lett. 452, 69–78. https://doi.org/10.1016/j.epsl.2016.07.013

Lantink, M.L., Davies, J.H.F.L., Mason, P.R.D., Schaltegger, U., Hilgen, F.J., 2019. Climate control on banded iron formations linked to orbital eccentricity. Nat. Geosci. 12, 369–374. https://doi.org/10.1038/s41561-019-0332-8

Lawrence, M.G., Greig, A., Collerson, K.D., Kamber, B.S., 2006. Rare Earth Element and Yttrium Variability in South East Queensland Waterways. Aquat. Geochem. 12, 39–72. https://doi.org/10.1007/s10498-005-4471-8

Luo, G., Ono, S., Beukes, N.J., Wang, D.T., Xie, S., Summons, R.E., 2016. Rapid oxygenation of Earth's atmosphere 2.33 billion years ago. Sci. Adv. 2, e1600134. https://doi.org/10.1126/sciadv.1600134

Lyons, T.W., Reinhard, C.T., Planavsky, N.J., 2014. The rise of oxygen in Earth's early ocean and atmosphere. Nature 506, 307–315. https://doi.org/10.1038/nature13068

McLennan, S.M., 1989. Rare earth elements in sedimentary rocks; influence of provenance and sedimentary processes. Rev. Mineral. Geochem. 21, 169–200.

Moffett, J.W., 1994. The relationship between cerium and manganese oxidation in the marine environment. Limnol. Oceanogr. 39, 1309–1318. https://doi.org/10.4319/lo.1994.39.6.1309

Mulholland, D.S., Poitrasson, F., Shirokova, L.S., González, A.G., Pokrovsky, O.S., Boaventura, G.R., Vieira, L.C., 2015. Iron isotope fractionation during Fe(II) and Fe(III) adsorption on cyanobacteria. Chem. Geol. 400, 24–33. https://doi.org/10.1016/j.chemgeo.2015.01.017

Nie, N.X., Dauphas, N., Greenwood, R.C., 2017. Iron and oxygen isotope fractionation during iron UV photo-oxidation: Implications for early Earth and Mars. Earth Planet. Sci. Lett. 458, 179–191. https://doi.org/10.1016/j.epsl.2016.10.035

Nie, N.X., Dauphas, N., Villalon, K.L., Liu, N., Heard, A.W., Morris, R.V., Mertzman, S.A., 2020. Iron isotopic and chemical tracing of basalt alteration and hematite spherule formation in Hawaii: A prospective study for Mars. Earth Planet. Sci. Lett. 544, 116385. https://doi.org/10.1016/j.epsl.2020.116385

Nutman, A.P., Bennett, V.C., Friend, C.R.L., Van Kranendonk, M.J., Chivas, A.R., 2016. Rapid emergence of life shown by discovery of 3,700-million-year-old microbial structures. Nature 537, 535–538. https://doi.org/10.1038/nature19355

O'Connell, B., Wallace, M.W., Hood, A. v. S., Lechte, M.A., Planavsky, N.J., 2020. Iron-rich carbonate tidal deposits, Angepena Formation, South Australia: A redox-stratified Cryogenian basin. Precambrian Res. 342, 105668. https://doi.org/10.1016/j.precamres.2020.105668

Olson, S.L., Kump, L.R., Kasting, J.F., 2013. Quantifying the areal extent and dissolved oxygen concentrations of Archean oxygen oases. Chem. Geol., Special Issue dedicated to H.D. Holland: Evolution of the atmosphere and ocean through time 362, 35–43. https://doi.org/10.1016/j.chemgeo.2013.08.012

Oonk, P.B.H., Mason, P.R.D., Tsikos, H., Bau, M., 2018. Fraction-specific rare earth elements enable the reconstruction of primary seawater signatures from iron formations. Geochim. Cosmochim. Acta 238, 102–122. https://doi.org/10.1016/j.gca.2018.07.005

Oonk, P.B.H., Tsikos, H., Mason, P.R.D., Henkel, S., Staubwasser, M., Fryer, L., Poulton, S.W., Williams, H.M., 2017. Fraction-specific controls on the trace element distribution in iron formations: Implications for trace metal stable isotope proxies. Chem. Geol. 474, 17–32. https://doi.org/10.1016/j.chemgeo.2017.10.018

Ossa Ossa, F., Hofmann, A., Wille, M., Spangenberg, J.E., Bekker, A., Poulton, S.W., Eickmann, B., Schoenberg, R., 2018. Aerobic iron and manganese cycling in a redox-stratified Mesoarchean epicontinental sea. Earth Planet. Sci. Lett. 500, 28–40. https://doi.org/10.1016/j.epsl.2018.07.044

Ostrander, C.M., Nielsen, S.G., Owens, J.D., Kendall, B., Gordon, G.W., Romaniello, S.J., Anbar, A.D., 2019. Fully oxygenated water columns over continental shelves before the Great Oxidation Event. Nat. Geosci. 12, 186–191. https://doi.org/10.1038/s41561-019-0309-7

Pavlov, A. a., Kasting, J. f., 2002. Mass-Independent Fractionation of Sulfur Isotopes in Archean Sediments: Strong Evidence for an Anoxic Archean Atmosphere. Astrobiology 2, 27–41. https://doi.org/10.1089/153110702753621321

Petroff, A.P., Sim, M.S., Maslov, A., Krupenin, M., Rothman, D.H., Bosak, T., 2010. Biophysical basis for the geometry of conical stromatolites. Proc. Natl. Acad. Sci. 107, 9956–9961. https://doi.org/10.1073/pnas.1001973107

Pierson, B.K., Parenteau, M.N., 2000. Phototrophs in high iron microbial mats: microstructure of mats in iron-depositing hot springs. FEMS Microbiol. Ecol. 32, 181–196. https://doi.org/10.1111/j.1574-6941.2000.tb00711.x

Pierson, B.K., Parenteau, M.N., Griffin, B.M., 1999. Phototrophs in High-Iron-Concentration Microbial Mats: Physiological Ecology of Phototrophs in an Iron-Depositing Hot Spring. Appl. Environ. Microbiol. 65, 5474–5483. https://doi.org/10.1128/AEM.65.12.5474-5483.1999

Planavsky, N., Bekker, A., Rouxel, O.J., Kamber, B., Hofmann, A., Knudsen, A., Lyons, T.W., 2010. Rare Earth Element and yttrium compositions of Archean and Paleoproterozoic Fe formations revisited: New perspectives on the significance and mechanisms of deposition. Geochim. Cosmochim. Acta 74, 6387–6405. https://doi.org/10.1016/j.gca.2010.07.021

Planavsky, N., Rouxel, O., Bekker, A., Shapiro, R., Fralick, P., Knudsen, A., 2009. Iron-oxidizing microbial ecosystems thrived in late Paleoproterozoic redox-stratified oceans. Earth Planet. Sci. Lett. 286, 230–242. https://doi.org/10.1016/j.epsl.2009.06.033

Planavsky, N., Rouxel, O.J., Bekker, A., Hofmann, A., Little, C.T.S., Lyons, T.W., 2012. Iron isotope composition of some Archean and Proterozoic iron formations. Geochim. Cosmochim. Acta 80, 158–169. https://doi.org/10.1016/j.gca.2011.12.001

Planavsky, N.J., Asael, D., Hofmann, A., Reinhard, C.T., Lalonde, S.V., Knudsen, A., Wang, X., Ossa Ossa, F., Pecoits, E., Smith, A.J.B., Beukes, N.J., Bekker, A., Johnson, T.M., Konhauser, K.O., Lyons, T.W., Rouxel, O.J., 2014a. Evidence for oxygenic photosynthesis half a billion years before the Great Oxidation Event. Nat. Geosci. 7, 283–286. https://doi.org/10.1038/ngeo2122

Planavsky, N.J., Reinhard, C.T., Wang, X., Thomson, D., McGoldrick, P., Rainbird, R.H., Johnson, T., Fischer, W.W., Lyons, T.W., 2014b. Low Mid-Proterozoic atmospheric oxygen levels and the delayed rise of animals. Science 346, 635–638. https://doi.org/10.1126/science.1258410

Quinn, K.A., Byrne, R.H., Schijf, J., 2004. Comparative Scavenging of Yttrium and the Rare Earth Elements in Seawater: Competitive Influences of Solution and Surface Chemistry. Aquat. Geochem. 10, 59–80. https://doi.org/10.1023/B:AQUA.0000038959.03886.60

Rasmussen, B., Fletcher, I.R., Bekker, A., Muhling, J.R., Gregory, C.J., Thorne, A.M., 2012. Deposition of 1.88-billion-year-old iron formations as a consequence of rapid crustal growth. Nature 484, 498–501. https://doi.org/10.1038/nature11021

Rasmussen, B., Muhling, J.R., Tosca, N.J., Tsikos, H., 2019. Evidence for anoxic shallow oceans at 2.45 Ga: Implications for the rise of oxygenic photosynthesis. Geology. https://doi.org/10.1130/G46162.1

Riding, R., Fralick, P., Liang, L., 2014. Identification of an Archean marine oxygen oasis. Precambrian Res. 251, 232–237. https://doi.org/10.1016/j.precamres.2014.06.017

Rouxel, O.J., Bekker, A., Edwards, K.J., 2005. Iron Isotope Constraints on the Archean and Paleoproterozoic Ocean Redox State. Science 307, 1088–1091. https://doi.org/10.1126/science.1105692

Schad, M., Halama, M., Bishop, B., Konhauser, K.O., Kappler, A., 2019. Temperature fluctuations in the Archean ocean as trigger for varve-like deposition of iron and silica minerals in banded iron formations. Geochim. Cosmochim. Acta 265, 386–412. https://doi.org/10.1016/j.gca.2019.08.031

Sumner, D.Y., 1997. Carbonate precipitation and oxygen stratification in late Archean seawater as deduced from facies and stratigraphy of the Gamohaan and Frisco formations, Transvaal Supergroup, South Africa. Am. J. Sci. 297, 455–487. https://doi.org/10.2475/ajs.297.5.455

Taylor, S.R., McLennan, S.M., 1985. The continental crust: Its composition and evolution.
Thibon, F., Blichert-Toft, J., Tsikos, H., Foden, J., Albalat, E., Albarede, F., 2019. Dynamics of oceanic iron prior to the Great Oxygenation Event. Earth Planet. Sci. Lett. 506, 360–370. https://doi.org/10.1016/j.epsl.2018.11.016

Tosca, N.J., Guggenheim, S., Pufahl, P.K., 2016. An authigenic origin for Precambrian greenalite: Implications for iron formation and the chemistry of ancient seawater. Geol. Soc. Am. Bull. 128, 511–530. https://doi.org/10.1130/B31339.1

Trendall, A.F., Nelson, D.R., Thorne, A.M., Compston, W., Williams, I.S., Armstrong, R.A., 1990. Precise zircon U-Pb chronological comparison of the volcano-sedimentary sequences of the Kaapvaal and Pilbara Cratons between about 3.1 and 2.4 Ga. Third Int. Archaean Symp. Perth 1990.

Trouwborst, R.E., Johnston, A., Koch, G., Luther, G.W., Pierson, B.K., 2007. Biogeochemistry of Fe(II) oxidation in a photosynthetic microbial mat: Implications for Precambrian Fe(II) oxidation. Geochim. Cosmochim. Acta 71, 4629–4643. https://doi.org/10.1016/j.gca.2007.07.018

Tsikos, H., Matthews, A., Erel, Y., Moore, J.M., 2010. Iron isotopes constrain biogeochemical redox cycling of iron and manganese in a Palaeoproterozoic stratified basin. Earth Planet. Sci. Lett. 298, 125–134. https://doi.org/10.1016/j.epsl.2010.07.032

Waldbauer, J.R., Newman, D.K., Summons, R.E., 2011. Microaerobic steroid biosynthesis and the molecular fossil record of Archean life. Proc. Natl. Acad. Sci. 108, 13409–13414. https://doi.org/10.1073/pnas.1104160108

Ward, L.M., Kirschvink, J.L., Fischer, W.W., 2016. Timescales of Oxygenation Following the Evolution of Oxygenic Photosynthesis. Orig. Life Evol. Biospheres 46, 51–65. https://doi.org/10.1007/s11084-015-9460-3

Wilmeth, D.T., Corsetti, F.A., Beukes, N.J., Awramik, S.M., Petryshyn, V., Spear, J.R., Celestian, A.J., 2019. Neoarchean (2.7 Ga) lacustrine stromatolite deposits in the Hartbeesfontein Basin, Ventersdorp Supergroup, South Africa: Implications for oxygen oases. Precambrian Res. 320, 291–302. https://doi.org/10.1016/j.precamres.2018.11.009

Zawaski, M.J., Kelly, N.M., Orlandini, O.F., Nichols, C.I.O., Allwood, A.C., Mojzsis, S.J., 2020. Reappraisal of purported ca. 3.7 Ga stromatolites from the Isua Supracrustal Belt (West Greenland) from detailed chemical and structural analysis. Earth Planet. Sci. Lett. 545, 116409. https://doi.org/10.1016/j.epsl.2020.116409

Chapter 5 – Computational and Spectroscopic Constraints on the Equilibrium Iron Isotope Behaviors of Greenalite and Ferrihydrite: Implications for Precambrian Iron Formations

Foreword

Iron formations (IFs) are an important piece in the puzzle of understanding early Earth's ocean and atmospheric chemistry (Bekker et al., 2010; Konhauser et al., 2017). To briefly recap, IFs are chemically precipitated sediments rich in iron (Fe) and silicon (Si) that typically feature banding or lamination at a variety of scales. The widespread deposition of IFs before the Great Oxidation Event (GOE) indicates that the global oceans had high dissolved Fe concentrations. This requires that the oceans were anoxic, because Fe^{2+} is highly soluble, but Fe^{3+} rapidly precipitates out of solution at near-neutral pH. High Fe^{2+} levels in anoxic pre-GOE oceans was supported by Fe^{2+}-rich continental runoff from anoxically-weathered continents (Holland, 1973), and fluids from seafloor hydrothermal vents (Bekker et al., 2010; Isley, 1995; Konhauser et al., 2017). The dominance of the hydrothermal Fe^{2+} supply to the early oceans is supported by the rare earth element patterns and Nd isotopic compositions of IFs (Derry and Jacobsen, 1990; Jacobsen and Pimentel-Klose, 1988), as well as coincidence peaks in the geological record in IF deposition and the occurrence of submarine large igneous provinces that would have been potent sources of hydrothermal fluid (Bekker et al., 2010; Isley and Abbott, 1999). Against the backdrop of anoxic and ferruginous (Fe^{2+}-rich, O_2- and H_2S-poor) pre-GOE oceans, the canonical interpretation of IFs is that Fe^{2+} from deep waters was oxidized upon upwelling into more oxidizing shallow water settings, leading to the precipitation and burial of hydrous ferric oxides.

The mechanism for Fe^{2+} oxidation in the oceans remains a major open question for the canonical IF model. Oxidation by O_2, produced by early cyanobacteria, was initially proposed by Cloud (1973), but subsequently, alternative pathways were put forward that did not require oxygen, and

were thus more easily reconciled with an anoxic early atmosphere. These anaerobic pathways to Fe^{2+} oxidation are anoxygenic photosynthetic Fe^{2+} oxidation wherein Fe^{2+}, rather than water, is used as an electron donor for biological CO_2 fixation (Kappler et al., 2005; Konhauser et al., 2002); and UV photooxidation, an abiotic process that could have been effective under an early, UV-active Sun, on an early Earth without a protective ozone layer (Anbar and Holland, 1992; Braterman et al., 1983; Cairns-Smith, 1978; François, 1986; Nie et al., 2017; Tabata et al., 2021). In geochemical terms, the products of these different oxidation reactions are indistinguishable. Once Fe is oxidized, Fe^{3+} precipitates as a hydrous ferric oxide, and this primary mineral phase would be dehydrated, recrystallized, and diagenetically altered, in the process of becoming an IF. A distinct lack of organic carbon in IFs could be used to argue against a direct biological origin of IFs (Dodd et al., 2019); but decoupling of Fe^{3+} oxides and organic matter, or destruction of organic matter during diagenesis and metamorphic alteration of the rock (Craddock and Dauphas, 2011a; Heimann et al., 2010; Köhler et al., 2013; Konhauser et al., 2005; Walker, 1984), are plausible explanations for the loss of organic material. The Fe isotopic compositions of Fe^{3+} oxides formed by the different oxidation mechanisms are all indistinguishable and can satisfactorily explain the Fe isotope record of pre-GOE IFs (Bullen et al., 2001; Croal et al., 2004; Nie et al., 2017). While possible oxidation mechanisms for IFs remain debated, the general redox structure they prescribe for the oceans are moreorless the same: a shallow upper ocean layer that was oxidizing with respect to Fe^{2+}, overlying ferruginous deep ocean basins (Bekker et al., 2010; Planavsky et al., 2012). This is consistent with the sequence stratigraphy of Archean continental margins, which typically feature Fe-poor carbonate platforms in shallow waters shoreward of IF-depositing deeper water settings (Klein and Beukes, 1989; Sumner, 1997).

Our previous discussion of IFs in Chapters 2 to 4 has mostly accepted the canonical model at face value, because it underpins many assumptions about the general redox structure and chemistry of ocean basins prior to the GOE, and it is still the accepted interpretation of these deposits for the large majority of Precambrian researchers. However, here in Chapter 5, we turn our attention to an alternative hypothesis for the deposition of IFs that has been developed within the last decade. This alternative hypothesis, which has been championed in large part by Rasmussen and coworkers, is that the primary precipitates for IFs were comprised entirely of ferrous Fe silicates, specifically, the serpentine group mineral greenalite ($Fe_3Si_2O_5(OH)_4$) (Johnson et al., 2018; Rasmussen et al., 2014a, 2014b, 2015, 2017, 2019, 2021; Tosca et al., 2016, 2019). The basis of this alternative hypothesis is an ever-growing catalogue of painstaking petrographic observations of IFs; using imaging techniques that range down to the nanometer scale; which reveal tiny greenalite crystals to be the most primary mineral phase present in the IF, based on textural relations (reviewed in detail by Rasmussen et al., 2021). In the greenalite model for IFs, the abundant ferric Fe oxides hematite and magnetite were both formed by late oxidation of a primary greenalite mineralogy, long after both IF deposition and the oxygenation of the atmosphere (Rasmussen et al., 2014a, 2014b; Rasmussen and Muhling, 2018). The implication of Rasmussen's alternative model for IF deposition is that oxidants for Fe^{2+} were absent from the ocean right up until the GOE, and the deposition of greenalite was controlled entirely by the pH-dependent saturation of precursor phases from solution (Rasmussen et al., 2019; Tosca et al., 2016, 2019).

The greenalite hypothesis being correct would motivate a severe overhaul of our understanding of pre-GOE ocean redox dynamics, early microbial metabolisms, and past concentrations of nutrients in the ocean, the latter of which are of typically estimated by assuming that elemental partitioning onto ferric oxide precipitates can link IF chemistry to ocean chemistry (Bjerrum and Canfield,

2002; Jones et al., 2015; Konhauser et al., 2009; Planavsky et al., 2010; Robbins et al., 2016). Therefore, inertia alone presents a formidable barrier to this hypothesis becoming widely accepted. Aside from this, many aspects of IF geochemistry are well-explained by the canonical model, including i) heavy Fe isotopic compositions of IFs consistent with the incorporation of isotopically heavy Fe^{3+} oxides (Dauphas et al., 2017; Heard and Dauphas, 2020, and references therein); ii) the ^{13}C-depleted composition of Fe-rich carbonate minerals in IFs that can be well explained by their formation from remineralized organic matter oxidized by Fe^{3+} in the sediment column (Craddock and Dauphas, 2011a; Heimann et al., 2010); and iii) the average redox state of 2.4+ for Fe in IFs (Klein, 2005); which is difficult to explain via post-depositional oxidation at the scale of major sedimentary basins (Robbins et al., 2019). Furthermore, observations of greenalite, while numerous and indicative of early precipitation, are for the most part restricted to chert nodules and enclaves within IFs (Rasmussen et al., 2021 and references therein). Chert, comprised of microcrystalline silica, has a high preservation potential, which means that it is often the best substrate in which to preserve delicate primary mineralogical and biological information in rocks that go through extensive diagenetic and metamorphic reworking. However, in the case of IFs, cherty regions are also Fe-poor regions; they define pale-colored bands in a typical banded iron formation (BIF), whereas most Fe is found in dark, oxide-rich bands (see Fig. 5.1A). Therefore, while petrography confirms greenalite as one of the primary mineral precipitates in IFs (Rasmussen et al., 2015, 2017), it offers no direct quantitative information on the original redox state of most of the mass of Fe that was precipitated from the oceans.

To better constrain the origin of IFs, we need a way to reconcile qualitative petrographic observations of greenalite with quantitative bulk geochemical data that favor a ferric oxide precursor. This means devising a geochemical test for primary greenalite as the major IF precursor.

As the work in this thesis has shown so far, there are reasons to expect that Fe isotopes can provide a test for the greenalite hypothesis, and because Fe isotopes are resistant to secondary overprinting, and Fe becomes less mobile when oxidized, we would not expect late oxidative alteration of primary greenalite in IFs to overprint a primary Fe isotopic signature (Heard and Dauphas, 2020). Greenalite precipitation (in the case of pure $Fe^{2+}{}_3Si_2O_5(OH)_4$) from dissolved Fe^{2+} does not involve a change in the Fe redox state. With a few exceptions, notably pyrite precipitation as we explored in Chapters 2 and 3, non-redox reactions relevant to marine geochemistry are not generally associated with large Fe isotopic fractionations, so we might expect that a pure greenalite precursor could not produce the >5 ‰ variation in $^{56}Fe/^{54}Fe$ ratios seen in pre-GOE IFs (Dauphas et al., 2017). However, this is purely an informed speculation, because no experiments to date have constrained the Fe isotopic systematics of greenalite.

Therefore, here in Chapter 5, we take the first steps towards defining the equilibrium Fe isotopic systematics of greenalite relative to ferric oxyhydroxides, by using spectroscopic techniques pioneered at the University of Chicago (Blanchard et al., 2015; Dauphas et al., 2012, 2014, 2018), and *ab initio* calculations. As describe in detail below, further experimental work will be needed to build on the preliminary data we present here. Equilibrium fractionation is the baseline assumption we make when considering the isotopic effects of geochemical processes, but kinetic isotope effects, as seen in Chapters 2 and 3, can exert such strong effects in natural systems that they can even reverse the direction of fractionations relative to equilibrium; and these can only be calibrated empirically with careful experiments. Despite the fact that much more work on this problem that remains to be done, the equilibrium data presented here should give us cause for a little caution in the assumptions we make about the isotopic behavior of under-explored geochemical processes when discussing the ancient geochemical record.

Abstract

Before the rise of atmospheric oxygen in the Great Oxidation Event (GOE) around 2.4-2.3 billion years ago, the oceans were rich in ferrous iron (Fe^{2+}). One of the hallmarks of the geological record from this time is the widespread deposition of iron formations, marine chemical sediments rich in Fe and silica (Si). The global deposition of Fe-rich chemical sediments before the GOE indicates that Fe was mobile in the global oceans; owing due to reducing conditions that stabilized soluble Fe^{2+}; but also that environmental conditions existed that allowed for the precipitation of authigenic Fe minerals, which eventually became IFs. The canonical model for the deposition of IFs is that they formed by the oxidation of upwelled Fe^{2+} in near-surface waters, and the precipitation of insoluble Fe^{3+} oxides. Oxidation could have been driven by cyanobacterial O_2, direct anoxygenic photosynthetic oxidation, or UV photons, so two of the three models for IF deposition directly implicate early microbial life. This model for IF deposition has informed a more general picture of Archean ocean redox structure and forms the basis of reconstructed nutrient concentrations for the ancient oceans. However, recent micro- and nano-scale petrographic studies indicate that the most primary Fe-bearing mineral that exists in well-preserved IFs is a ferrous iron silicate, greenalite, and that much of the ferric Fe now found in IFs is a secondary alteration product. These observations have motivated the development of an alternative model for IF deposition, where precipitation took place in a fully anoxic ocean and was determined by pH-dependent mineral saturation, not spatial redox variations. In this study, we aim to test this alternative model by constraining the equilibrium Fe isotopic fractionation of greenalite relative to ferrihydrite, a hydrous ferric oxide representative of the precipitates invoked in the canonical model for IF deposition. Iron isotopes are fractionated most strongly by the equilibrium isotope exchange between $Fe^{2+}$and Fe^{3+}, and the dominance of isotopically heavy compositions, along with a large

(>5 ‰) overall variation in the $^{56}Fe/^{54}Fe$ ratio of pre-GOE IFs, has long been taken as evidence for redox reactions during their deposition. Meanwhile, it has been assumed that ferrous greenalite would be associated with minimal Fe isotopic fractionation during its precipitation. However, using *ab initio* calculations and nuclear resonant inelastic X-ray scattering (NRIXS) spectroscopy, we show that the equilibrium fractionation between ferrihydrite and pure ferrous greenalite is ≤ 1 ‰ for $^{56}Fe/^{54}Fe$. Anchoring this fractionation to the 1-3 ‰ Fe isotopic fractionation between hydrous ferric oxides and Fe^{2+} that have been determined in aqueous geochemistry experiments, we find that ferrous greenalite could be enriched by 0-2 ‰ in $^{56}Fe/^{54}Fe$ during equilibrium precipitation from aqueous Fe^{2+}. At the high end of this range, ferrous greenalite precipitation could explain the Fe isotopic composition of most pre-GOE IFs, but some amount of Fe oxidation would still be required to form the isotopically heaviest IFs on record. Our results define the baseline equilibrium fractionation behavior for greenalite, but we emphasize that aqueous geochemistry experiments that capture the true net fractionation during greenalite precipitation, which may include kinetic isotope effects, if required to further assess the degree to which the greenalite model for IF deposition is consistent with the Fe isotopic record.

Introduction

Until approximately 2.43 billion years ago (Ga), Earth's atmosphere was devoid of free oxygen (O_2) (Gumsley et al., 2017). This is evidenced by the preservation of O_2-sensitive detrital mineral grains in conglomerates and shallow marine sediments (Rasmussen and Buick, 1999; Roscoe, 1969), a lack of iron (Fe) oxidation in ancient weathering profiles (paleosols) (Rye and Holland, 1998), and the preservation of exotic mass-independent fractionations of sulfur isotopes (MIF-S) that are indicators of an S cycle affected by UV photochemistry in an ozone-free atmosphere (Farquhar et al., 2000; Farquhar and Wing, 2003; Johnston, 2011; Pavlov and Kasting, 2002). Prior to the first atmospheric oxygenation (termed the Great Oxidation Event or GOE), and for substantial periods of time after it, the oceans were also largely anoxic (Poulton and Canfield, 2011), and had high concentrations of dissolved Fe^{2+} and silica ($SiO_{2(aq)}$), the former of which was likely source predominantly from seafloor hydrothermal vents (Isley, 1995). The widespread deposition iron formations (IFs), distinctive chemical sediments rich in Fe and Si, is a hallmark of pre-GOE sedimentation thought be to be linked to the formation of authigenic precipitates in the global oceans (Fig. 5.1) (Bekker et al., 2010; Holland, 1973; Konhauser et al., 2017). Most IFs preceding the GOE are banded iron formations (BIFs), characterized by compositional banding at a variety of scales ranges from sub-mm rhythmic microbands of alternating Fe-rich and silica-rich material, to meter-scale macrobands defining facies transitions during major accumulations over millions of years (Fig. 5.1) (Trendall and Morris, 2000). The mineralogy of IFs is diverse, and can be broadly categorized into oxide-facies, carbonate-facies, and silicate-facies, where the mineralogy is dominated by magnetite and hematite, Fe-rich carbonates, and silicates greenalite ($(Fe^{2+},Fe^{3+})_{2-3}Si_2O_5(OH)_4$) and stilpnomelane ($K(Fe^{2+},Mg,Fe^{3+})_8(Si,Al)_{12}(O,OH)_{27}\cdot n(H_2O)$), respectively.

Both the mineralogy and the chemistry of IFs has been used extensively to understand ancient ocean chemistry through time, but it is widely recognized that the present-day mineralogy of IFs is almost entirely secondary in nature, a result of prolonged early and late diagenesis, metamorphism, and fluid interaction over their billion year histories in the rock record (Bekker et al., 2010; Konhauser et al., 2017). However, by far the most common interpretation is that the primary precipitate that formed IFs was a ferric oxyhydroxide, formed through the oxidation of Fe^{2+} and rapid precipitation of due to the insolubility of Fe^{3+} in seawater conditions (Fig. 5.2A) (Cloud, 1973). Subsequent dehydration of an $Fe(OH)_{3(s)}$ would eventually produce hematite, which is found in microcrystalline form in some chert enclaves within IFs and was thus considered to be the earliest-formed IF mineral (Ayres, 1972; Beukes and Gutzmer, 2008; Beukes and Klein, 1990). The formation of Fe^{3+} oxyhydroxide-amorphous silica gels during sinking was also proposed as a means of transporting SiO_2 to the sediment column to form the chert component of IFs (Fischer and Knoll, 2009). The Fe^{3+}-oxyhydroxide model for IFs is appealing from a solubility standpoint (Cloud, 1973) and its major implication is that there must have been an oxidant for Fe^{2+} in the pre-GOE oceans (Bekker et al., 2010; Konhauser et al., 2017). Possible oxidants include O_2 (produced by cyanobacteria required to have already evolved) (Cloud, 1973), UV photons (Anbar and Holland, 1992; Braterman et al., 1983; Cairns-Smith, 1978; François, 1986; Nie et al., 2017), and direct oxidation by anoxygenic photosynthesis (Kappler et al., 2005; Konhauser et al., 2007, 2002), all of which would need to operate in the photic zone and thus restrict Fe precipitation to shallower waters supplied with Fe^{2+} upwelled from depth (Fig 5.2A).

While IFs contain appreciable Fe^{3+} they are by no means dominated by it, with the average redox state of Fe being ~2.4 (Klein, 2005). This is evident both at the bulk scale, where IFs contain a variety of ferric and ferrous minerals, and in mixed-valence Fe minerals like magnetite. In the

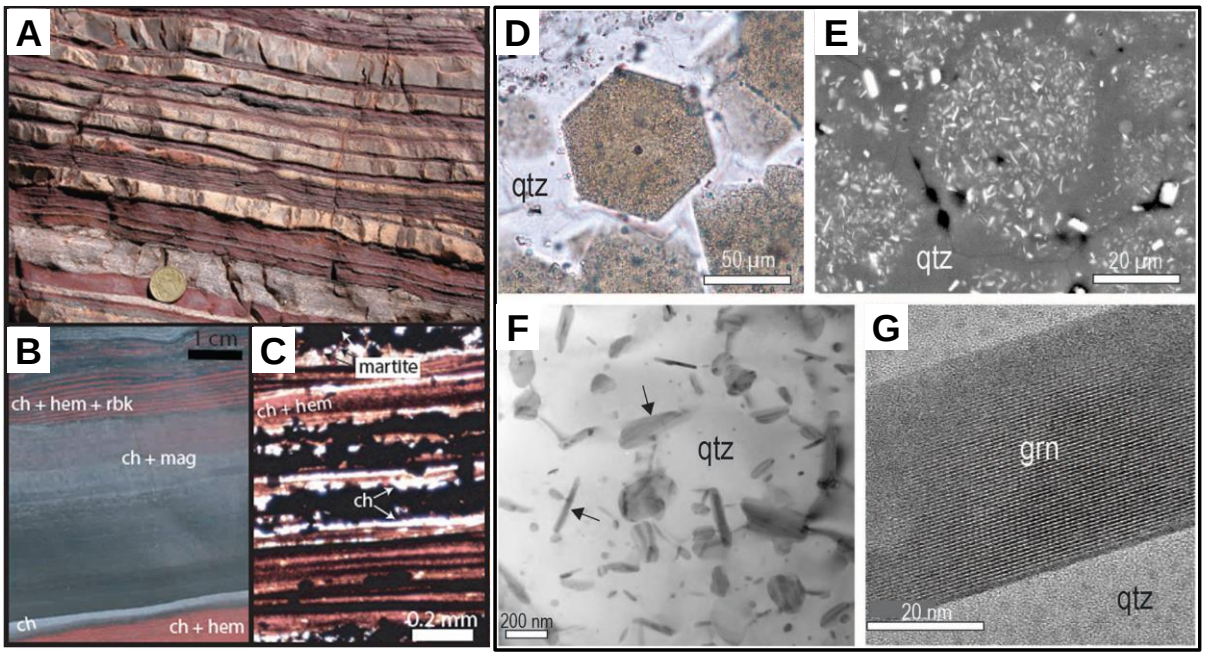

Figure 5.1. Images of pre-GOE iron formations (IFs) at various scales. **A-C:** The Joffre Member of the 2.46 Ga Brockman IF, in the Hamersley basin, Australia, reproduced from Konhauser et al. (2017) with permission of Elsevier, showing Fe-oxide rich mineralogy **A.** Centimeter scale banding, **B.** Micro- and mesobanding, with chert, hematite, and riebeckite, microbanded layers and thicker chert and magnetite layers. **C.** Photomicrograph showing thin chert-hematite microbands, and coarser magnetite microbands (thick black layers). **D-G:** Examples of greenalite in IFs, reproduced from Rasmussen et al. (2021) with permission of Elsevier. **D.** Photomicrograph of greenalite-rich hexagonal chert pod surrounded by Fe-poor chert, from the 2.48 Ga Klein Naute Formation, Griqualand Wesr Basin South Africa. **E.** Backscattered electron image; **F.** Bright-field transmission electron microscope (TEM) image; and **G.** High-resolution TEM image of greenalite nano particles, from the 2.56 Ga Bee Gorge Member, Witenoom Formation, Hamersley basin, Australia.

Fe^{3+}-oxyhydroxide model, much of the Fe^{2+} content in IFs is attributable to early or late diagenetic reduction of Fe^{3+} during the oxidation of organic matter, either through microbial dissimilatory Fe reduction (DIR), or metasomatic reactions during burial heating (Craddock and Dauphas, 2011a; Heimann et al., 2010; Köhler et al., 2013; Konhauser et al., 2005; Walker, 1984). The Fe^{2+} produced in these reactions may have reacted with remaining Fe^{3+} oxyhydroxide to form magnetite, or precipitated Fe carbonate (siderite) or ferrous silicates as early diagenetic phases.

Assumptions related to the Fe^{2+} oxidation model for IFs underpin most models for the chemistry of the oceans prior to the GOE. First and foremost, the model prescribes an oceanic redox structure

characterized by reducing deep marine basins enriched in Fe^{2+} sourced from hydrothermal vents, and near-surface conditions that were sufficiently oxidizing to precipitate Fe^{3+} primary mineral phases. Of the proposed Fe^{2+} oxidation mechanisms for IF deposition, anoxygenic photosynthesis and oxidation by O_2 implicate microbial life (in the case of O_2, indirectly via cyanobacterial photosynthesis) in global scale cycling of the most important redox element in the early oceans, while UV photooxidation alone can proceed purely abiotically, and its efficacy in silica-rich early oceans has been questioned (Konhauser et al., 2007). Meanwhile, life is also implicated in the subsequent reduction of fresh Fe^{3+} oxyhydroxides, via DIR. So, despite having a dearth of organic matter at present (Dodd et al., 2019; Rasmussen et al., 2021), redox models for IFs support a rich microbial cycle with primary production and respiration being linked in some way to marine Fe (Konhauser et al., 2005; Walker, 1984). The oldest sedimentary rocks on Earth are 3.8 billion-year-old IFs located Southwest Greenland (Moorbath et al., 1973), and the connection between life and IFs is one of the lines of evidence to push the origin of life back far enough to pre-date the geologic record. Beyond IFs themselves, the redox structure in the oceans implied by oxidative IF deposition has informed models for the development of early carbonate platforms at the margins of ferruginous basins (Klein and Beukes, 1989; Riding et al., 2014; Sumner, 1997).

The Fe^{3+}-oxyhydroxide precipitation model is also a cornerstone assumption in attempts to constrain the concentrations of some key nutrient elements in the Precambrian oceans from the geochemical archive of IFs (Robbins et al., 2016). This approach consists of calibrating a partition coefficient for an element of interest by allowing it to adsorb from solutions of known concentration onto an Fe^{3+}-oxyhydroxide like ferrihydrite. This partitioning behavior is then used to relate abundances of the elements of interest relative to Fe in IFs, to the concentration of that element in seawater at the time the IFs precipitated. In this manner, it is possible to reconstruct the

concentration of nutrient elements in the global oceans through time, at least during periods where IFs are available to be sampled. This approach has been used to determine phosphorous (P) (Bjerrum and Canfield, 2002; Jones et al., 2015; Planavsky et al., 2010) and nickel (Ni) (Konhauser et al., 2015, 2009) concentrations throughout the Precambrian. Phosphorous is the main biolimiting nutrient over geological timescales, and IF-based reconstructions of the marine P reservoir through time have drawn an intimate link between nutrient-limited photosynthetic primary production and O_2 levels through geologic time (Bjerrum and Canfield, 2002; Jones et al., 2015; Planavsky et al., 2010). Meanwhile, Ni is an important co-factor in an enzyme required for microbial methanogenesis. An IF-based reconstruction of a declining oceanic Ni reservoir in the runup to the GOE was the basis for a 'Nickel Famine' hypothesis for waning atmospheric methane levels prior to atmospheric oxygenation (Konhauser et al., 2015, 2009; Wang et al., 2019). A decline in methanogenesis can potentially be linked to both the rise of O_2 and the collapse of a greenhouse atmosphere, which plunged Earth into its first global glaciation during the GOE (Bekker and Kaufman, 2007; Kopp et al., 2005).

Recently, the model of Fe^{3+}-oxyhydroxide precursors for Precambrian IFs has been challenged by an alternative hypothesis in which the precursor mineralogy for IFs was entirely composed of nominally Fe^{2+}-dominated hydrous silicates, such as the ferrous endmember of greenalite ($Fe_3Si_2O_5(OH)_4$), with the ferric iron component of IFs reflecting late metamorphic overprinting (Johnson et al., 2018; Rasmussen et al., 2021; Tosca et al., 2019). This new model for IF precursors is based mostly on a growing number of nanoscale observations of IFs from the ~2.5 Ga Hamersley Basin of Western Australia and the Transvaal Basin of South Africa that seem to suggest Fe silicates, not oxide phases like hematite, are the most primary mineral in IFs (Rasmussen et al., 2014, 2015, 2019). Nanoscale imaging techniques and elemental mapping in those studies

specifically targeted early diagenetic chert bands and nodules within IFs, because silicification effectively preserves delicate microstructures early on in diagenesis (Fig. 5.1D-G). These chert nodules and layers contained abundant nanometer scale (10 nm × 200-1000 nm) plates of greenalite, and where hematite is also preserved in these early-silicified regions, it occurs as a replacement for greenalite or Fe carbonate (Rasmussen et al., 2014, 2016). This provides strong evidence that greenalite was the earliest-formed Fe-bearing mineral phase that was preserved in sediments during deposition of chert-rich regions of IFs. A hardline interpretation of this primary greenalite mineralogy implies that the oceans were fully anoxic during IF deposition, with ferrous greenalite being the dominant mode of primary Fe precipitation because highly insoluble Fe^{3+} phases were unable to form (Fig. 5.2B) (Rasmussen et al., 2019, 2021). A more nuanced picture comes from analysis of the redox state of Fe in greenalite in IFs. Johnson et al. (2018) used XANES analyses techniques to determine the Fe^{3+}/total Fe ratio in individual greenalite grains characterized from the best-preserved 2.5 Ga IF samples. They observed small, variable, but non-negligible quantities of Fe^{3+}, that comprised 10-20 % of the Fe in greenalite nanoparticles. These data confirmed that the earliest-formed identifiable minerals in these IFs were dominantly reduced, but if the Fe^{3+} in these minerals reflects primary incorporation of an oxidized Fe pool formed in the ancient water column, then the hypothesis that the pre-GOE oceans were devoid of oxidants for Fe^{2+} (Rasmussen et al., 2021) would be weakened somewhat.

Even without an extreme endmember model of purely ferrous greenalite precipitation from the ancient oceans, if the precursor material for IFs prior to the GOE was dominantly ferrous in nature then many assumptions about Precambrian ocean chemistry would need to be revised. If the bulk of IF precursor material were greenalite, rather than an Fe^{3+}-oxyhydroxide, then all constraints on

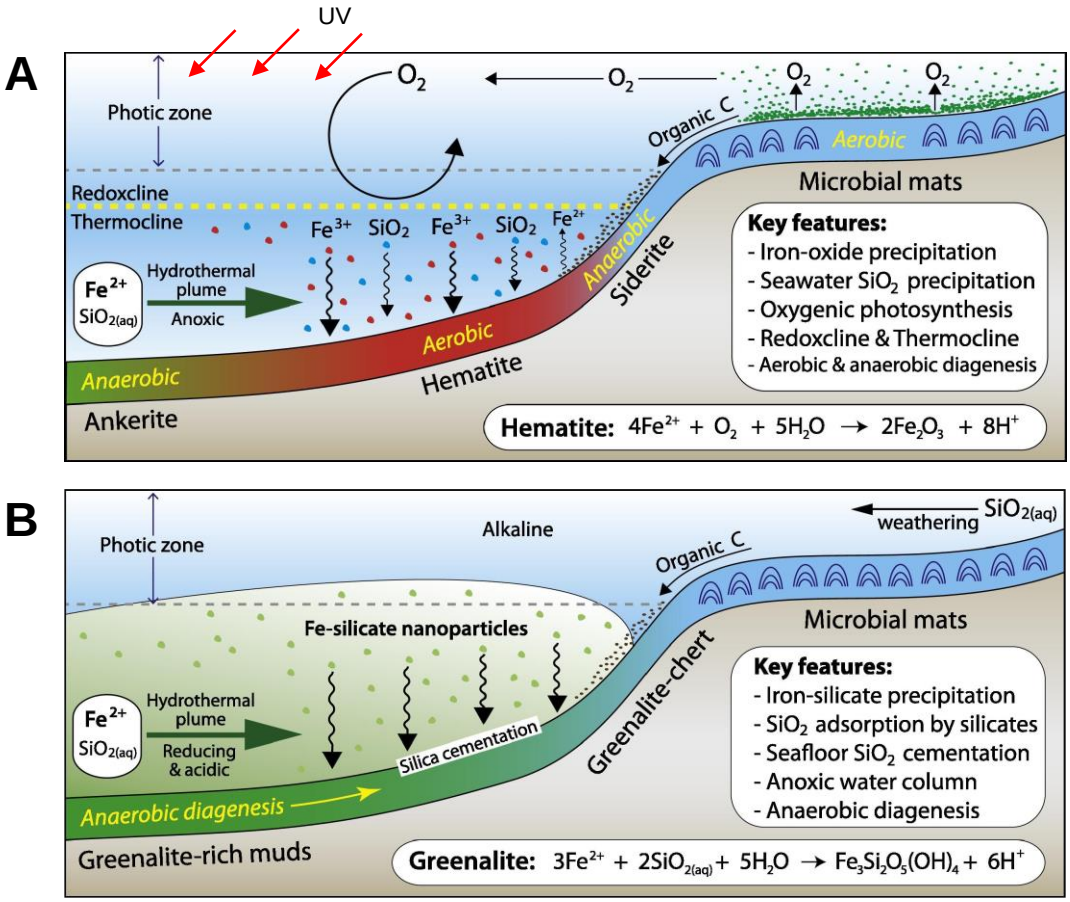

Figure 5.2. Schematic illustration of opposing models for the deposition of iron formations (IFs), adapted from Rasmussen et al. (2017) with permission from Elsevier. **A.** The canonical model of IF deposition, wherein Fe^{2+} in anoxic deep waters was oxidized during upwelling into a shallow photic zone, with oxidation facilitated by cyanobacterial O_2, anoxygenic photosynthesis, and/or UV radiation. **B.** The alternative ferrous silicate model, wherein all primary Fe deposition in IFs took place in anoxic conditions and deppsited greenalite, which was oxidized only long after deposition.

[P] and [Ni] in the early oceans, which are based on ferrihydrite absorption experiments (Bjerrum and Canfield, 2002; Jones et al., 2015; Konhauser et al., 2009; Planavsky et al., 2010), would be invalidated and new models based on incorporation of these element into Fe^{2+} silicate precipitates would be necessary. In the endmember case of purely ferrous greenalite precipitation, which would assume some post-depositional oxidation of even the most pristine greenalite, a major overhaul of models for the redox structure of the oceans prior to the GOE would be required. In the revised alternative model, no near-surface oxidants would be present (or at least able to interact with Fe^{2+}),

and the location and rate of ocean Fe^{2+} removal and IF deposition would depend entirely on the degree of greenalite saturation in seawater, which increases with higher [Fe^{2+}], [$SiO_{2\,(aq)}$] and pH (Rasmussen et al., 2021; Tosca et al., 2016, 2019). In the models of Rasmussen et al. (2021) and Tosca et al. (2016, 2019), greenalite saturation may be reached immediately upon mixing of seawater and hydrothermal fluids close to vent sites, with a nanoparticle-rich plume then transporting slowly precipitating greenalite across wide areas of depositional basins. However, greenalite saturation could potentially also be reached by evaporation, as implied by an occurrence of shallow water greenalite-rich granular iron formation (GIF) in the Paleoproterozoic Griquatown Formation of South Africa (Rasmussen et al., 2019). The lack of near-surface oxidants implied by this model is very difficult to reconcile with photosynthetic primary productivity in the pre-GOE oceans, because carbon fixation must oxidize the environment, regardless of electron donors, and it is difficult to envisage this environmental oxidizing power having no influence on Fe-bearing chemical sediments. However, it is valuable to consider the implications of the most extreme endmember because the observed Fe^{3+} contents in the most primary greenalites are so low (Johnson et al., 2018), and XANES analysis has documented incidences of Fe oxidation by the synchrotron X-Ray beam (Cottrell et al., 2018).

Developing a diagnostic tool that can distinguish between different precursor phases for IFs would be valuable for confirming or ruling out either of endmember models for primary IF deposition. Iron isotope geochemistry can potentially provide such a diagnostic tool, because: Fe isotopes are strongly fractionated at low temperature by redox processes; they are resistant to resetting by metamorphism and can thus preserve primary sedimentary signals in ancient rocks with complex histories; and an extensive archive of Fe isotopic measurements of IFs spanning > 3 Ga of Earth history is readily available to interpret in the context of different IF precursor hypotheses (Fig. 5.3)

(Dauphas et al., 2017; Heard and Dauphas, 2020). The $^{56}Fe/^{54}Fe$ ratio (expressed as $\delta^{56}Fe$, the deviation in ‰ of the $^{56}Fe/^{54}Fe$ in a sample relative to that in the standard material IRMM-014 that has an isotopic composition similar to the bulk Earth; Craddock and Dauphas, 2011b) is expected to be significantly different for some of the proposed IF precursor phases. Fe^{3+} mineral phases are typically associated with a large equilibrium fractionation factor that enriches the ferric phase in heavy Fe isotopes relative to coexisting Fe^{2+} (Dauphas et al., 2017). The fractionation between Fe^{3+}-oxyhydroxides and Fe^{2+} has been studied extensively in experiments, and the $\delta^{56}Fe$ of solid phase can be shifted by $\geq$ +1-3 ‰ relative to the Fe^{2+} in solution, depending on whether batch equilibrium, or partial precipitation conditions prevail (Beard et al., 2010; Bullen et al., 2001; Croal et al., 2004; Nie et al., 2017; Skulan et al., 2002; Wu et al., 2011).

The strong positive $\delta^{56}Fe$ fractionation associated with partial oxidation products has been one of the most robust arguments in favor of the Fe^{3+}-oxyhydroxide model for IF deposition, almost from the inception of Fe isotope geochemistry. Iron formations were among the earliest sedimentary rocks studied with Fe isotopes, and they show a very large range in $\delta^{56}Fe$ values with a bias throughout much of geologic time towards isotopically heavy values, relative to hydrothermal Fe^{2+} (Heard and Dauphas, 2020). The entire Fe isotopic record of IFs can be explained through partial oxidation, and progressive distillation of Fe^{2+} reservoir during upwelling. The $\delta^{56}Fe$ of Fe^{2+} should evolve towards more negative values as more precipitates with positive $\delta^{56}Fe$ are removed, and thus precipitates from this Fe^{2+} source will also become progressively more isotopically light and span the range observed in IFs (Planavsky et al., 2012; Rouxel et al., 2005; Tsikos et al., 2010). This conceptual framework can identify periods in Earth history where Fe oxidation was partial and thus oxidant limited and can be used to broadly trace the redox balance of the oceans through

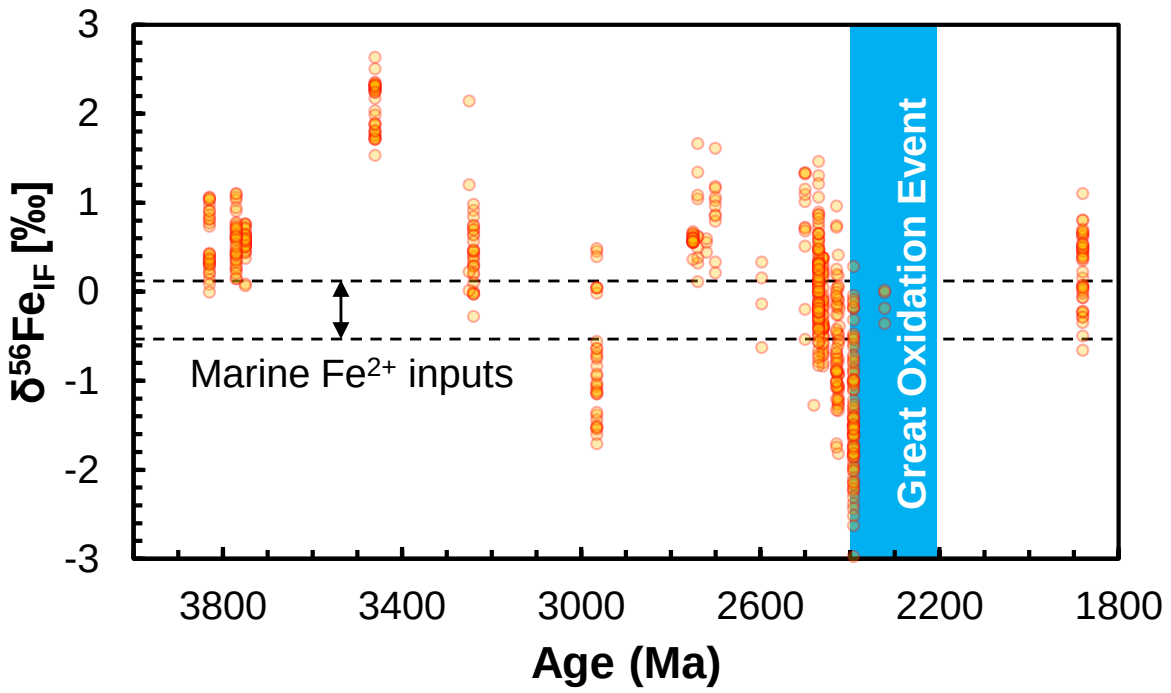

Figure 5.3. The Fe isotopic record of Archean and Paleoproterozoic iron formations (IFs), compiled by Heard and Dauphas (2020). δ^{56}Fe is the per mil ‰ deviation in the ^{56}Fe/^{54}Fe ratio of samples relative to a standard material, IRMM-014 that is isotopically similar to the bulk Earth. The most striking Fe isotopic feature of IFs pre-dating the Great Oxidation Event (GOE) is the prevalence of extremely positive δ^{56}Fe values. These positive values have long been taken as evidence for partial Fe^{2+} oxidation in the Archean oceans, because oxidation induces a strong fractionation in Fe isotopes that partitions isotopically heavy Fe into Fe^{3+} relative to Fe^{2+}.

time, with isotopically light materials being associated with higher degrees of oxidation (Czaja et al., 2018; Heard and Dauphas, 2020). Isotopic signatures of DIR, the metabolism that uses ferric iron as an oxidant for respiration, have also been identified in IF through coupled analysis of C isotope ratios in carbonates (Craddock and Dauphas, 2011a; Heimann et al., 2010), reinforcing the isotopic argument for active redox cycling in the pre-GOE oceans and sediment column.

By contrast, Fe^{2+} precipitates are often non-fractionated or weakly fractionated to slightly lighter δ^{56}Fe values relative to dissolved Fe^{2+}, because the strong equilibrium partitioning between Fe^{2+} and Fe^{3+} does not feature in these non-redox precipitation reactions (*e.g.* Wiesli et al., 2004).

However, the equilibrium fractionation associated with greenalite precipitation has not yet been determined. Theoretically, one might predict that greenalite and associated ferrous silicate precursors should be associated with minimal Fe isotopic fractionation, because many ferrous silicate minerals all very similar Fe isotopic behavior that indicates they should be ^{56}Fe-depleted relative to Fe^{3+} phases (Dauphas et al., 2017). In this case, we could take the Fe isotopic record of IFs as strong positive proof for the Fe^{3+}-oxyhydroxide model. However, equilibrium Fe isotope fractionation is not only a function of Fe redox state, but of the overall strength of chemical bonds to Fe. For example, pyrite, an Fe^{2+} mineral, is associated with a strongly positive equilibrium fractionation relative to even most Fe^{3+} minerals (Polyakov et al., 2007; Syverson et al., 2013), although this equilibrium fractionation is rarely expressed in nature (Mansor and Fantle, 2019). Therefore, it is insufficient to simply assume any specific equilibrium Fe isotopic behavior for greenalite without confirmation by experimental means, because of the major implications this fractionation behavior has for understanding Precambrian ocean chemistry.

The objective of this work is to characterize the equilibrium Fe isotope fractionation between greenalite with different Fe redox states, and a representative Fe^{3+} oxyhydroxide, ferrihydrite. The relative fractionation behavior of these two phases should indicate whether greenalite can impart the requisite positive isotopic fractionation to IFs to explain an Fe isotope record that is so effectively described by partial oxidation and ferrihydrite (or equivalent hydrous ferric oxide) precipitation. We use a combined experimental and computational approach that has proven to be powerful in determining the equilibrium Fe isotopic behavior of other Fe-bearing minerals with relevance to low temperature geochemistry, such as goethite and jarosite (Blanchard et al., 2015; Dauphas et al., 2012).

Methods

General approach

Our objective is to determine the reduced partition function ratios (also called β factors) for the materials of interest. These can be combined for two different materials a and b, to determine the isotopic fractionation factor, $\alpha_{a\text{-}b}$, between them, where

$$1000\, ln\, \alpha_{a-b} = 1000\, ln\, \beta_b - 1000\, ln\, \beta_b, \qquad \text{(Eq. 1)}$$

gives the isotopic fractionation between the two phases in per mil (‰), for the isotopic ratio of interest that β factors were calculated for. In our combined approach, we use *ab initio* density functional theory (DFT) computations of mineral structures, and nuclear resonant inelastic X-ray scattering (NRIXS), a synchrotron spectroscopic technique, to probe the force constant $\langle F \rangle$, that characterizes the strength of bonds holding Fe in the mineral structure, and which can be used to calculate β factors. The use of the two independent techniques together should allow us to check for consistency in the fractionation factors between ferrihydrite and greenalite that we will determine (Blanchard et al., 2015).

It is difficult to determine the fractionation between a solid phase and Fe^{2+} in solution from first principles, because aqueous solutions require a different class of *ab initio* models that cannot be reliably compared to NRIXS measurements and simulations of solids. Although this approach is taken in some studies (*e.g.* Rustad and Dixon, 2009), it should be regarded with caution and best practice is to compare β factors from a single technique (Blanchard et al., 2015). Both NRIXS and *ab initio* simulations specifically allow us to determine the equilibrium Fe isotopic fractionation behavior of the solid phases of interest. Establishing the equilibrium isotopic behavior of mineral phase is the first step in characterizing its full Fe isotopic systematics, because equilibrium fractionation is the null assumption for a chemical reaction, against which deviations attributable

to kinetic and/or reservoir effects can be assessed. The equilibrium isotopic fractionation should also prescribe the heaviest isotopic composition a precipitate may take during initial precipitation (as kinetic effects result in isotopically lighter products), making it the fractionation of interest when determining the role of greenalite in producing pre-GOE IFs with strongly positive $\delta^{56}Fe$ (Dauphas et al., 2017; Heard and Dauphas, 2020).

Sample materials

Greenalite precursors

Synthesis of greenalite precursor material was conducted at the University of Michigan after the protocol of (Hinz et al., 2020). All experiments were conducted in an Mbraun glovebox under a pure nitrogen atmosphere with < 0.1 ppm O_2 at room temperature (25 °C). Ultrapure water used for the experiments was deoxygenated by heating and then purging the solution with pure nitrogen gas, before being brought into the glovebox where the solution was stirred uncapped for 48 hours under the < 0.1 ppm O_2 atmosphere. First, 1 mM of sodium orthosilicate (Na_4SiO_4) was added from an anoxic 100 mM stock solution (stock filtered using cellulose acetate) and the experimental pH was adjusted to ~8 with 1 M hydrochloric acid, HCl. All reagents were deoxygenated by purging with nitrogen and storage in the glovebox environment prior to use. The solution was stirred for 24 hours with a magnetic stir bar at pH 8 to depolymerize any dissolved silica (Dietzel, 2000). Prior to the addition of ferrous iron to the experiment, the solution pH was adjusted to < 3 with HCl, in order to minimize any minor oxidation for taking place. Iron was introduced to the experiment as ferrous chloride ($FeCl_2$) from a 300 mM stock solution that with its Eh buffered by the addition of excess Fe^0 and HCl. An amount of the $FeCl_2$ solution was added to bring the ferrous iron concentration in the experiment to 1mM. The pH of the silica and iron solution was

subsequently brought up to the desired level of pH 8 by addition of 1 M NaOH, whereupon an off-white wispy-looking precipitate formed. The magnetic stir bar was then removed. Aluminum foil was wrapped around the experiment bottle to limit any photooxidation of Fe(II) by artificial light sources, and the reaction vessel was sealed with a rubber stopper.

Two identical experiments were set up in this way, and then treated with two separate methods to determine the optimum conditions for preservability of reduced precipitates during transport. Experiment (#1) was allowed to equilibrate/react for 40 days at room temperature (25 °C) in the anoxic glovebox. Experiment (#2) was allowed to react for 24 hours, then hydrothermally aged. The off-white precipitated material, and approximately 10 mL of solution was then transferred to a 22 mL anoxic Parr vessel with a PTFE gasket. The precipitated material and overlying solution were sealed in the Parr vessel inside the glovebox. The sealed Parr vessel was then taken out of the glovebox and transferred to an oven set at 150°C to age for 15 days.

All subsequent treatment and preparation of material from both experiments was then conducted once again inside the glovebox. Precipitated material from experiments #1 and #2 were centrifuged to concentrate the material in epitubes. The precipitated materials were then decanted onto weighing paper inside the <0.1 ppm O_2 glovebox atmosphere for 30 minutes, before being loaded into ~2” sections of kapton tube (1.46 mm, ID, 1.56 mm OD). The end of the kapton tubes were heat sealed with an impulse sealer. These sealed kapton tubes were then slid inside lengths of a slightly larger diameter kapton tube (1.8 mm ID, 1.89 mm OD), and the ends of the outer tube were heat sealed again. This double layered kapton tube preparation was designed to minimize the penetration of air into the sample and thus limit oxidation of ferrous iron in the sample during NRIXS analysis. The double layered kapton tube samples were then placed in separate mylar bags and heat sealed inside the glovebox. Once the mylar bags were sealed and considered airtight, they

were taken out of the glovebox and shipped to the Advanced Photon Source at Argonne National Laboratory for analysis.

Ferrihydrite

Ferrihydrite samples doped in Fe-57 were synthesized based on the methods of Schwertmann and Cornell (2000), with some departures necessary due to the use of ^{57}Fe metal rather than $Fe(NO_3)_3$ as a starting material. Both 2-line (1-3 nm crystallite size) and 6-line (5-6 nm crystallite size) ferrihydrite samples were synthesized and analyzed. For 2-line ferrihydrite, 85.6 mg of Fe-57 (95%, Cambridge Isotope Laboratories) was dissolved in 3 mL 15.4 M HNO_3 at 100˚ C for 3 days. The solution was allowed to cool to 25˚ C, then rapidly titrated with ~30 mL of a 1.5 M NaOH solution to pH 7.0, all while vigorously stirring. All aqueous solutions were prepared with deionized (DI) water (18 MΩ cm resistivity). The precipitate was collected by centrifuging 10 times at 10-fold dilution in DI water, followed by drying under a fume hood at 25˚ C. For 6-line ferrihydrite, 56.5 mg of Fe-57 was dissolved in 1.5 mL 11 M $HClO_4$ at 100˚C for 2 days. The solution was partially evaporated at 110˚ C and refilled with 11 M $HClO_4$. This process was repeated 5 times. The solution was evaporated completely at 110˚C. The resultant salt was dissolved in 40 mL DI water at 75˚ C for 10 minutes, then cooled to 25˚ C in an ice bath. The solution was continuously dialyzed with DI water for 10 days, then freeze dried to isolate the solid.

NRIXS analysis of greenalite precursors and ferrihydrite

NRIXS analyses were conducted at Sector 3-ID of the Advanced Photon Source (APS) synchrotron beamline at Argonne National Laboratory in Lemont, IL, USA. NRIXS is a relatively recently discovered spectroscopic technique (Seto et al., 1995; Sturhahn et al., 1995) that can be

used to probe the vibrational properties of select elements within a solid crystal structure. In the case of Fe, NRIXS is effective because the ^{57}Fe is a Mössbauer isotope that has a low-lying nuclear excited state at 14.4125 keV. The nuclear recoil associated with this nuclear transition is small relative to linewidth of the nuclear transition itself, therefore sequential de-excitation, emission, and reabsorption of the resultant photons within the crystal lattice by other ^{57}Fe nuclei is possible. This phenomenon, known as nuclear resonance, creates a finite decay timescale (141 ns for ^{57}Fe) for the emission of a gamma ray following initial absorption that is long relative to both the duration of electronic scattering of most X-rays (< 1 ps), and the duration of pulsed X-ray flashes provided by the synchrotron source (70 ps pulses, separated by 153 ns). As such, nuclear resonance allows us to use time discrimination to isolate the energy scattering spectrum caused by nuclear transitions.

The nuclear scattering spectrum allows us to probe the vibrational properties of Fe in solids. Recoilless elastic scattering produces part of the signal. The rest of the scattering signal is influenced by the material lattice holding Fe atoms in place. The inelastic scattering spectrum spans a far broader energy range (on the order of +/- 100 meV) than just at the linewidth of the nuclear transition. When the incident photon has a higher energy than the low-lying excited state of the ^{57}Fe nucleus, the excess energy can be dispersed to the solid material lattice by exciting quantized modes of vibration called phonons. This process is known as phonon creation. Conversely, X-rays with an energy slightly below that required for the nuclear transition can cause excitation because the vibration in the mineral lattice can provide the extra energy required to the nucleus. This process is known as phonon annihilation. After removing the strong central elastic peak associated with absorption by X-rays at the resonant energy level, NRIXS data allow us to probe the full vibrational spectrum of ^{57}Fe in the mineral lattice as a function of energy, called the

partial phonon density of states (pDOS), or *g*(E), where this is partial because only the vibrational properties of Fe are determined (Sturhahn et al., 1995). We can determine β factors from taking the moments of either *g*(E) or the energy scattering spectrum *S*(E) (Dauphas et al., 2012; Hu et al., 2013). In the case of *S*(E), the formula to determine β factors is:

$$1000 \ln \beta \approx 1000 \left(\frac{M}{M^*} - 1\right) \frac{1}{E_R} \left[\frac{R_3^S}{8k^2T^2} - \frac{R_5^S - 10R_2^S R_3^S}{480k^4T^4} + \frac{R_7^S + 210\left(R_2^S\right)^2 R_3^S - 35R_3^S R_4^S - 21R_2^S R_5^S}{20160k^6T^6}\right], \quad \text{(Eq. 2)}$$

where M and M^* are the masses of two isotopes of interest (*e.g.* 56 and 54), E_R is the free recoil energy (1.956 meV for ^{57}Fe), T is the temperature, k is the Boltzmann constant, and R_i^S is the ith centered moment of the scattering spectrum *S*(E) where $R_i^S = \int_{-\infty}^{+\infty} S(E)(E - E_R)^i dE$. The equation relating 1000lnβ to *S*(E) was derived separately by Dauphas et al. (2012) and Hu et al. (2013). A mathematically equivalent expression exists for using *g*(E) instead of *S*(E) to determine 1000lnβ, however *g* is itself determined from a decomposition of *S* and is less straightforward to use and assessment of errors is more complicated (Blanchard et al., 2015). The above equation for 1000lnβ fits the general expected functional form for β factors of:

$$1000 \ln \beta \approx \frac{A_1}{T^2} + \frac{A_2}{T^4} + \frac{A_3}{T^6}, \quad \text{(Eq. 3)}$$

where A_1, A_2, and A_3 can be calculated from Equation 2, above.

Alternatively, 1000lnβ can be expressed as a more compact function of the force constant $\langle F \rangle$:

$$1000 \ln \beta \approx \frac{B_1 \langle F \rangle}{T^2} + \frac{B_2 \langle F \rangle}{T^4}, \quad \text{(Eq. 4)}$$

where B_1 is 2904, B_2 is a constant that depends on the pDOS *g*, and the mean force constant $\langle F \rangle$ of bonds that hold Fe in position is given by

$$\langle F \rangle = \frac{M}{E_R \hbar^2} R_3^S, \quad \text{(Eq. 5)}$$

where $\hbar$ is the reduced Planck's constant. The equation for 1000lnβ can be reduced to just the first term at high temperatures. Additionally, Dauphas et al. (2012) showed that using a fixed value of

52000 for B_2 introduces less than 0.2 ‰ error at 22 °C, which is smaller than the overall uncertainty of the NRIXS method.

In practice, NRIXS data are collected scanning in 1 meV energy intervals around the nominal resonance energy the using a set of high-resolution monochromators. Scattered X-rays are measured with avalanche photo-diodes. Ferrihydrite and greenalite precursors material were analyzed in different sessions. For 2-line and 6-line ferryhydrite, samples powders were scanned between over the range -160 to +160 meV relative to the resonant peak. Greenalite precursor material was scanned over -107 to +139 meV relative to the resonant peak. The broad energy scan is used to monitor count rates in the tails of the distribution that are used for background corrections (Dauphas et al., 2018). Because ferrihydrite samples were prepared with ^{57}Fe enriched material they provided stronger signals, and 5 and 7 scans were made for 2-line and 6-line ferrihydrite, respectively. For greenalite precursor material, 17 and 22 scans were made for samples from Exp. #1 and Exp. #2, respectively. Additionally, the material from Exp. #2 was removed from the kapton tubes, allowed to sit under air for 1 day, repacked, and remeasured with 18 scans, to determine whether environmental oxidation of the material, for example during transport, could take place and affect the interpretation of NRIXS data. All NRIXS data were reduced in Mathematica using the SciPhon program designed for this purpose (Dauphas et al., 2018).

The redox state of Fe in experimentally synthesized greenalite precursor samples was an unknown. While greenalite is nominally ferrous with the chemical formula $Fe^{2+}{}_3Si_2O_5(OH)_4$ and was produced in anoxic (<1 ppm O_2) conditions, unintended oxidation by UV light, minor O_2 contamination, or catalytic autooxidation, during synthesis or transport, may have oxidized some Fe in the mineral structure, as is observed in natural pre-GOE IF samples. Therefore, the redox state of Fe (Fe^{2+}/Fe_{total}) was determined prior to NRIXS analysis using the forward-scattered X-ray

spectrum (van Bürck et al., 1992), where the synchrotron signal is used in place of a traditional Mössbauer source to determine the Mössbauer spectrum of the material (Synchrotron Mössbauer Spectroscopy - SMS; Alp et al., 1995).

Ab initio calculation of reduced partition function ratios

We conducted *ab initio* density functional theory (DFT) calculations to determine the force constant and reduced partition function ratios for ferrihydrite and pure Fe^{2+} and Fe^{3+} endmembers of greenalite. The ferrihydrite (Fe_5O_8H) model was built from the hexagonal structure proposed by Michel et al. (2007) where iron atoms are both tetrahedrally and octahedrally coordinated. For greenalite, we modeled the Fe^{2+} and Fe^{3+} endmembers with the monoclinic cell corresponding to the compositions $Fe_3Si_2O_5(OH)_4$ and $Fe_2Si_2O_5(OH)_4$ respectively. The Fe^{3+} endmember for greenalite is not a naturally occurring phase, and charge balance in the structure was facilitated by placing a vacancy in every third Fe site in the greenalite structure.

Structure relaxations are done with the PWscf code (Giannozzi et al., 2009; http://www.quantum-espresso.org) using the density functional theory plus Hubbard *U* method (DFT+*U*) and the generalized gradient approximation (GGA) to the exchange-correlation functional with the PBE parameterization (Perdew et al., 1996). The ionic cores are described by ultrasoft pseudopotentials from the Garrity-Bennett-Rabe-Vanderbilt (GBRV) library (Garrity et al., 2014). After energy convergence tests, the wave-functions and the charge density are expanded in plane-waves with 40 and 400 Ry cutoffs, respectively. For the electronic integration, the Brillouin zone is sampled according to the Monkhorst-Pack scheme (Monkhorst and Pack, 1976), using shifted $2 \times 2 \times 2$ *k*-point grids. Calculations are spin-polarized and magnetic moments are free to relax. The ferrihydrite magnetic ordering was set to be ferrimagnetic, with the Fe-site spins ordering with

alternating alignment in layers stacked along the c-direction in the crystallographic unit cell, following the theoretical investigation of Pinney et al. (2009). Greenalite displays antiferromagnetically ordered layers (Coey et al., 1981). However, since we use the one-layer unit cell, our model imposes a ferromagnetic structure by periodic repetition of layers with parallel magnetic alignments. The value of the Hubbard *U* for Fe sites is determined using a linear response approach in an internally consistent way (Cococcioni and de Gironcoli, 2005; Kulik et al., 2006). Details of the practical procedure can be found in Blanchard et al. (2009). The value of the Hubbard *U* is found equal to 5.7 eV for ferrihydrite, and equal to 7.2 eV and 5.2 eV for Fe^{2+} and Fe^{3+} greenalite endmembers, respectively.

Following the method described reviewed in detail by Blanchard et al. (2017), iron β-factors were calculated from their harmonic vibrational frequencies using

$$\beta(\alpha, Y) = \left[\prod_{i=1}^{3N_{at}} \prod_{\{q\}} \frac{\nu^*_{q,i}}{\nu_{q,i}} \frac{e^{-h\nu^*_{q,i}/(2kT)}}{1-e^{-h\nu^*_{q,i}/(kT)}} \frac{1-e^{-h\nu_{q,i}/(kT)}}{e^{-h\nu_{q,i}/(2kT)}}\right]^{1/(N_q N)}, \qquad \text{(Eq. 6)}$$

where $\nu_{q,i}$ are the frequencies of the phonon with wavevector q and branch index i = 1, $3N_{at}$, where N_{at} is the number of atoms in the unit cell. $\nu_{q,i}$ and $\nu^*_{q,i}$ are the vibrational frequencies in two isotopologues. *N* is the number of sites for the *Y* atom in the unit cell, *T* is the temperature, *h* is the Planck constant and *k* is the Boltzmann constant. Phonon frequencies were calculated within the harmonic approximation using the linear response theory (Baroni et al., 2001) as implemented in the PHonon code (Giannozzi et al., 2009; http://www.quantum-espresso.org). Phonon frequencies were computed on a centered 2 × 2 × 2 *q*-point grid for ferrihydrite and using one *q*-point shifted with respect to the center of the Brillouin zone for greenalite. The same calculations enable us to obtain the average force constant $\langle F \rangle$ of each iron crystallographic sites. This quantity corresponds to the harmonic restoring force constants, along the three orthogonal directions, that tend to pull

Table 5.1. Polynomial fits for $1000\ln\beta = A_1X+A_2X^2+A_3X^3$, with $X = 10^6/T^2$ (T in K), and force constants, $\langle F \rangle$, for Fe in greenalite and ferrihydrite.

	A_1	A_2	A_3	$\langle F \rangle$ (Nm^{-1})
DFT+*U*				
Fe^{2+} Greenalite	6.19×10^{-1}	-2.40×10^{-3}		214
Ferrihydrite	7.15×10^{-1}	-3.24×10^{-3}		235
Fe^{3+} Greenalite	8.49×10^{-1}	-4.73×10^{-3}		295
NRIXS				
Gr Exp. #1	$7.31\times10^{-1} \pm 4.2\times10^{-2}$	$-4.49\times10^{-3} \pm 7.0\times10^{-4}$	$5.97\times10^{-5} \pm 2.07\times10^{-5}$	256 ± 15
Gr Exp. #2	$7.16\times10^{-1} \pm 4.6\times10^{-2}$	$-4.88\times10^{-3} \pm 9.9\times10^{-4}$	$8.17\times10^{-5} \pm 3.65\times10^{-5}$	251 ± 16
Gr Exp. #2 after opening	$7.02\times10^{-1} \pm 3.6\times10^{-2}$	$-4.30\times10^{-3} \pm 6.0\times10^{-4}$	$5.76\times10^{-5} \pm 1.72\times10^{-5}$	246 ± 13
Gr Exp. #1 average	$7.07\times10^{-1} \pm 2.9\times10^{-2}$	$-4.45\times10^{-3} \pm 5.1\times10^{-4}$	$6.20\times10^{-5} \pm 1.56\times10^{-5}$	248 ± 10
Ferrihydrite 2L	$7.31\times10^{-1} \pm 3.7\times10^{-2}$	$-4.71\times10^{-3} \pm 6.9\times10^{-4}$	$6.96\times10^{-5} \pm 2.47\times10^{-5}$	256 ± 13
Ferrihydrite 6L	$7.52\times10^{-1} \pm 3.7\times10^{-2}$	$-5.56\times10^{-3} \pm 8.5\times10^{-4}$	$1.19\times10^{-5} \pm 3.81\times10^{-5}$	263 ± 13
Ferrihydrite average	$7.41\times10^{-1} \pm 2.6\times10^{-2}$	$-5.04\times10^{-3} \pm 5.4\times10^{-4}$	$8.44\times10^{-5} \pm 2.07\times10^{-5}$	260 ± 9

back the studied atom in its equilibrium position and can be calculated from the linear response method. It has been checked using the computationally less demanding DFT method (without Hubbard *U*) that considering only one shifted *q*-point leads to a relative uncertainty smaller than 3% on both the iron β-factor and its force constant.

Results

NRIXS and *ab initio* simulations produced the pDOS (Figs. 5.4-5.5) β factors (using Eq. 2) and $\langle F \rangle$ values (Figs. 5.6-5.8) for Fe in ferrihydrite and greenalite. The polynomial expressions for β are given in Table 5.1, where we display the first three terms for NRIXS, and we obtained the first two terms for *ab initio* calculations; and the temperature dependence of the β factors is shown in Figure 5.7. In the simulations, the DFT+*U* approach resulted in a relaxed structure that better fitted experimental constraints on the crystallographic dimensions for Fe^{2+} greenalite ($Fe_3Si_2O_5(OH)_4$) whilst for other minerals the DFT and DFT+U approaches gave similar levels of agreement with experiments. Therefore, we report and focus our discussion of simulations on the DFT+*U* results, whilst noting that qualitatively the DFT model results are similar and do not affect our conclusions about the relative behavior of the two greenalite models and ferrihydrite.

Greenalite

The DFT+*U* calculations result in 1000lnβ values of 6.71 ‰ and 9.02 ‰ respectively for the $^{56}Fe/^{54}Fe$ ratio at 22 °C, a temperature selected to compare with earlier studies (Blanchard et al., 2015). We also obtained $\langle F \rangle$ values of 214 Nm^{-1} for Fe^{2+} greenalite, and 295 Nm^{-1} for Fe^{3+} greenalite. We consider the $^{56}Fe/^{54}Fe$ isotopic ratio throughout, as this is the ratio most commonly reported in Fe isotopic ratio measurements of natural samples.

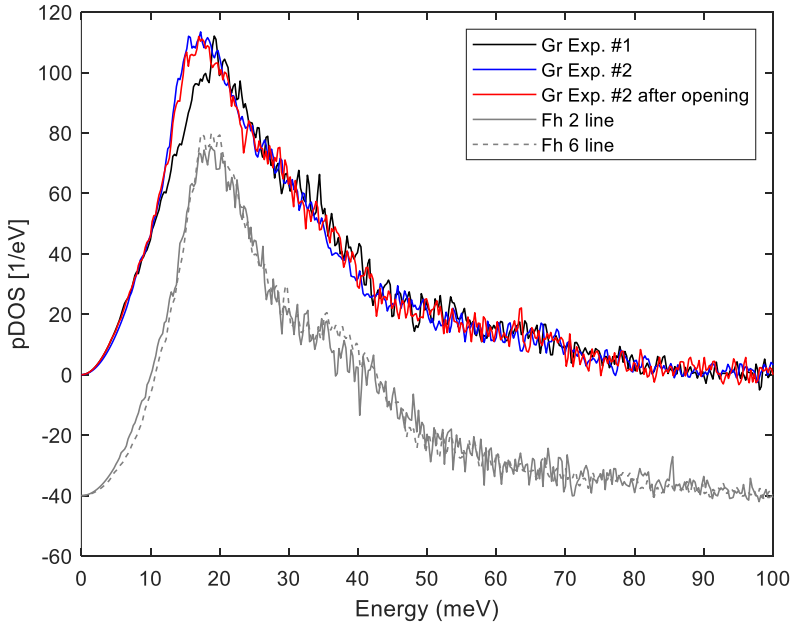

Figure 5.4. Average measured partial phonon density of states (pDOS) of iron in greenalite precursor material (Gr) and ferrihydrite (Fh), determined by NRIXS analysis. Spectra are quite featureless, possibly due to the sample material being an amorphous powder.

For the experimentally synthesized samples, the forward-scattering spectrum indicated that Exp. #1 contained 5 % Fe^{2+} and 95 % Fe^{3+}, and Exp. #2 contained 72 % Fe^{2+} and 28 % Fe^{3+}. The high degree of oxidation in Exp. #1 despite the steps taken to minimize oxidation during synthesis and preparation suggest that the wet gel produced in the experiments at ambient temperature is highly unstable if hydrothermal aging is not conducted, consistent with the previous findings of Hinz et al. (2020). Oxidation may have occurred during transportation in spite of efforts taken to seal the material in as airtight manner as possible. No significant change in Fe redox state was seen in the Exp. #2 sample exposed to air and repacked, which is also consistent with previous observations that hydrothermally aged, dark-green greenalite precursor material is resistant to oxidation for timescales on the order of months (Hinz et al., 2020). We therefore took the average of the two Exp. #2 analyses to increase the overall number of scans used and to decrease uncertainties. The 1000lnβ values calculated using *S*(E) from NRIXS (Eq. 2) analysis are 7.79 ± 0.591 ‰ and 7.53

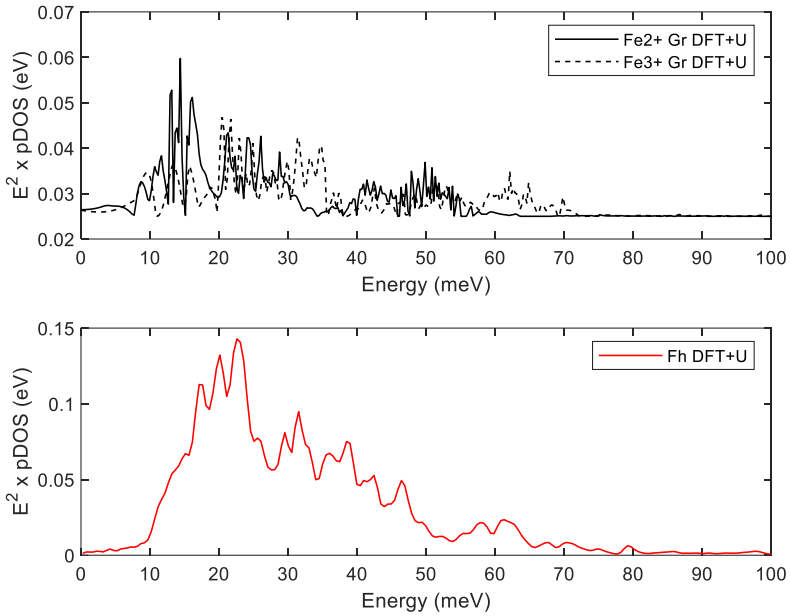

Figure 5.5. Average measured partial phonon density of states (pDOS) of iron in Fe^{2+} and Fe^{2+} greenalite (Gr) and ferrihydrite (Fh), determined by DFT+*U* simulations.

± 0.41 ‰ for Exp. #1 and Exp. #2 respectively, for the $^{56}Fe/^{54}Fe$ ratio at 22 °C. We obtained $\langle F \rangle$ values of 256 ± 15 Nm^{-1} for Exp. #1, and 248 ± 10 Nm^{-1} for Exp. #2.

Ferrihydrite

The DFT+*U* for ferrihydrite (Fe_5O_8H) gave a 1000lnβ value of 7.69 ‰ for the $^{56}Fe/^{54}Fe$ ratio at 22 °C, and a $\langle F \rangle$ value of 235 Nm^{-1}. For the NRIXS analysis of experimentally synthesized ferrihydrite, we calculated 1000lnβ = 7.79 ± 0.54 ‰ for 2-line ferrihydrite and 1000lnβ = 7.98 ± 0.58 ‰ for 6-line ferrihydrite from *S*(E). As these values are within error, we took the average to decrease uncertainty, resulting in 1000lnβ = 7.88 ± 0.39 ‰. We obtain an average $\langle F \rangle$ value of 260 ± 9 Nm^{-1}.

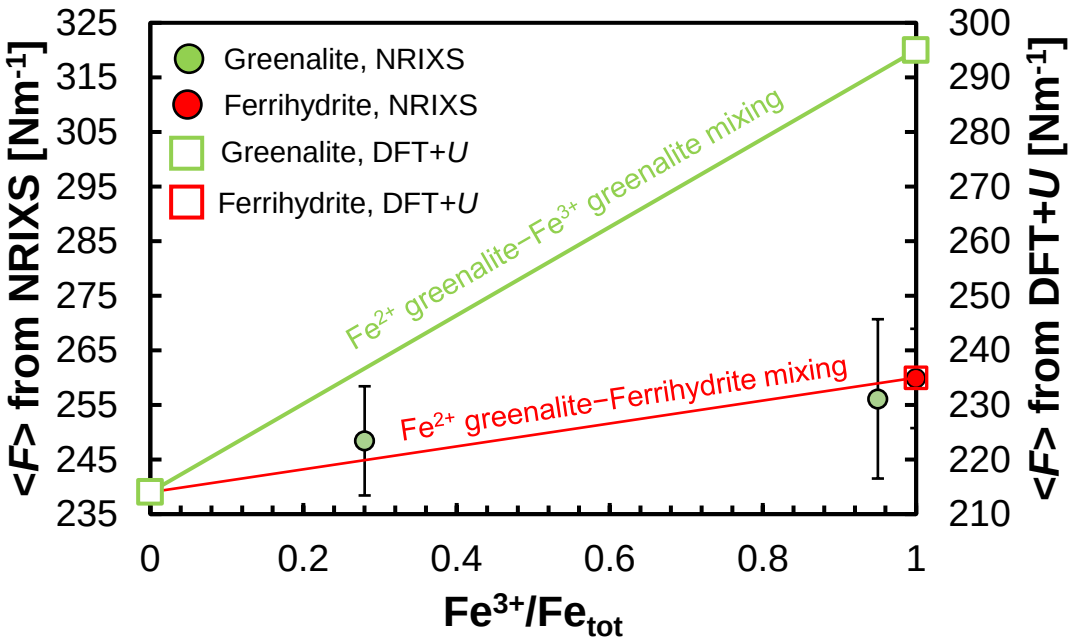

Figure 5.6. Force constant ($\langle F \rangle$) of greenalite and ferrihydrite, *vs*. Fe^{3+} content as a proportion of total Fe (Fe_{tot}). Filled circles show $\langle F \rangle$ for greenalite (green) and ferrihydrite (red) from NRIXS analyses (left-hand axis). Error bars show the 95 % confidence interval. Open squares show $\langle F \rangle$ for greenalite (green) and ferrihydrite (red) from DFT+*U* calculations (right-hand axis). The axis scales are identical, with the axis for NRIXS data shifted up by 25 Nm^{-1} so that ferrihydrite $\langle F \rangle$ values are equivalent for both methods. The solid green line shows the DFT+*U* predicted trend for mixing between Fe^{2+} and Fe^{3+} endmembers for greenalite. The red dashed line shows the DFT+*U* predicted trend for mixing between Fe^{2+} greenalite and ferrihydrite (representative for hydrous ferric oxides). Greenalite NRIXS data are consistent with the shallower trend for Fe^{2+} greenalite–ferrihydrite mixing, suggesting that the Fe^{3+} content in the greenalite samples analyzed with NRIXS reflects secondary oxidation to a hydrous ferric oxide, not structural Fe^{3+} in greenalite itself.

Discussion

*Discrepancy between DFT+*U *and NRIXS determinations of* $\langle F \rangle$

The $\langle F \rangle$ of Fe in ferrihydrite determined from DFT+*U* simulations (235Nm^{-1}) is ~25 Nm^{-1} lower than the average value we determined from moments of the NRIXS scattering spectrum *S*(E), of 260 $\pm$ 9 Nm^{-1}. In the case of greenalite, it is not straightforward to compare our mixed-valence

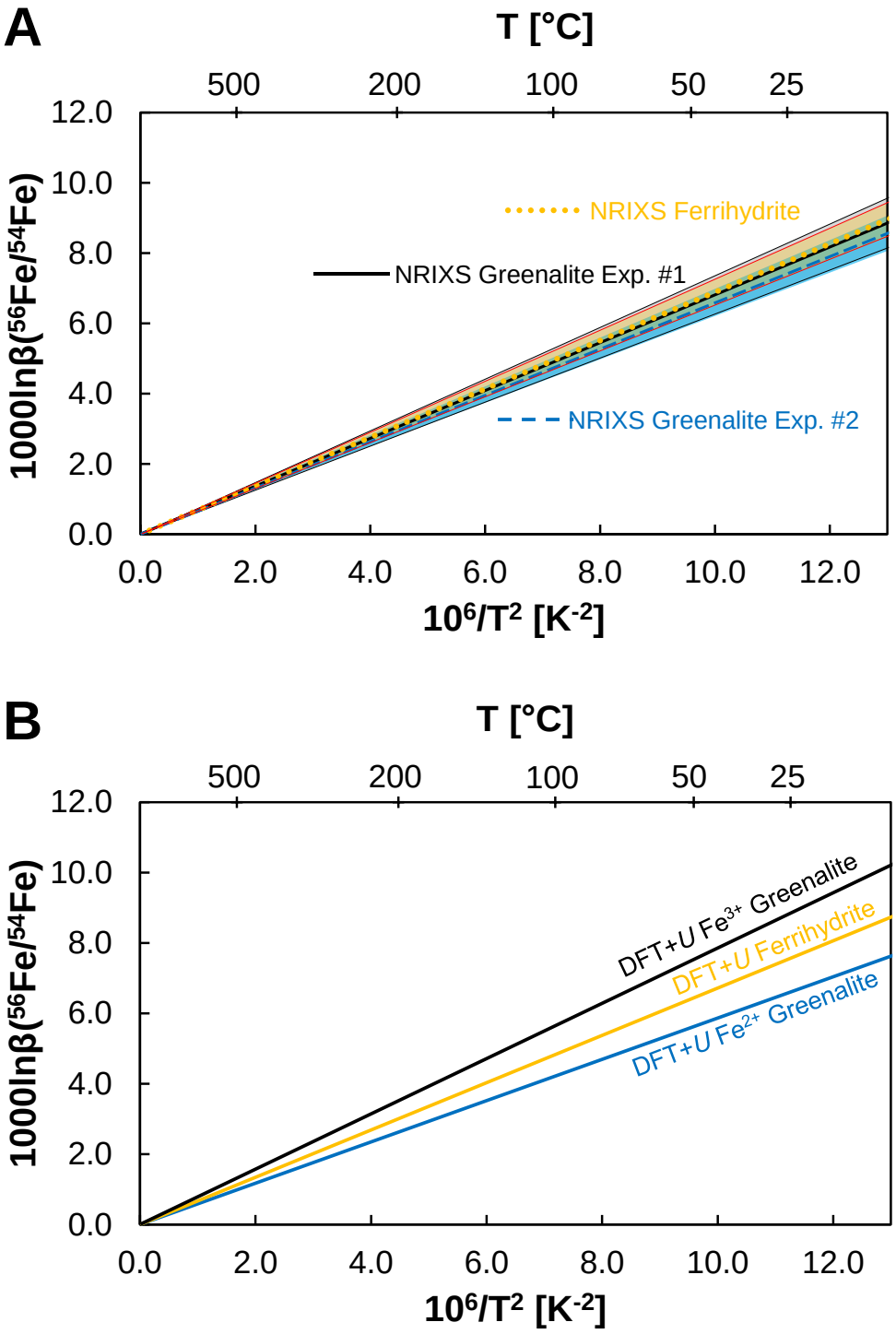

Figure 5.7. Temperature dependence of the iron β factor for greenalite and ferrihydrite, from **A.** NRIXS analysis of synthetic materials, and **B.** DFT+*U* simulations. Error envelops in **A.** are 95 % confidence intervals, and there is a large degree of overlap shows that the beta factors of ferrihydrite and the two synthetic greenalites (Exp. #1 with 95 % Fe^{3+}, Exp. #2 with 72 % Fe^{2+}).

experimentally synthesized precursor material to pure modeled endmembers, but the force constant from the mostly ferrous Exp. #2 (248 $\pm$ 10 Nm^{-1}) is ~34 Nm^{-1} higher than the DFT+*U* determined value for pure ferrous greenalite (214 Nm^{-1}). These offsets are similar to those that have been observed between DFT+*U* calculations and NRIXS determinations of $\langle F \rangle$ for several Fe minerals relevant to low temperature geochemistry (Fig. 5.8). In this combined dataset, it can be seen that NRIXS consistently results in $\langle F \rangle$ values that fall above a 1:1 line *vs.* $\langle F \rangle$ values determined from DFT+*U*. For the hydrous Fe minerals on the diagram (goethite, ferrihydrite, 72 % Fe^{2+} greenalite), the data form an array parallel to the 1:1 line that is explainable within error via a consistent ~25 Nm^{-1} positive offset in NRIXS-derived $\langle F \rangle$ values relative to those from DFT+*U* calculations (Fig. 5.8)

The case of ferrihydrite is somewhat analogous to that of goethite (FeO(OH)), which was previously studied using the same combined approach of DFT+*U* and NRIXS as described here. Both ferrihydrite and goethite are hydrous ferric oxides that show a ~20-25 Nm^{-1} offset between $\langle F \rangle$ values determined by the two methods. Meanwhile, a smaller discrepancy is seen for hematite (Fe_2O_3). Therefore, one immediate possible explanation for these discrepancies is the presence of hydrogen, because the accurate modeling of OH bonds in DFT simulations remains difficult. However, in Blanchard et al. (2015) it was emphasized that Fe-O and Fe-OH bond lengths were in good agreement between model and previous experimental constraints. Alternatively, Blanchard et al. (2015) also suggest a possible reason for this offset is that 'real' mineral material made in the laboratory, like all natural minerals, tends to contain crystal defects and vacancies that may be accommodated by non-stoichiometric protons, and the local bonding environment of Fe in a real material will vary considerably more than model expectations. Molecular-scale characterization of materials would be required to account for this level of natural variation, and this is unfeasible

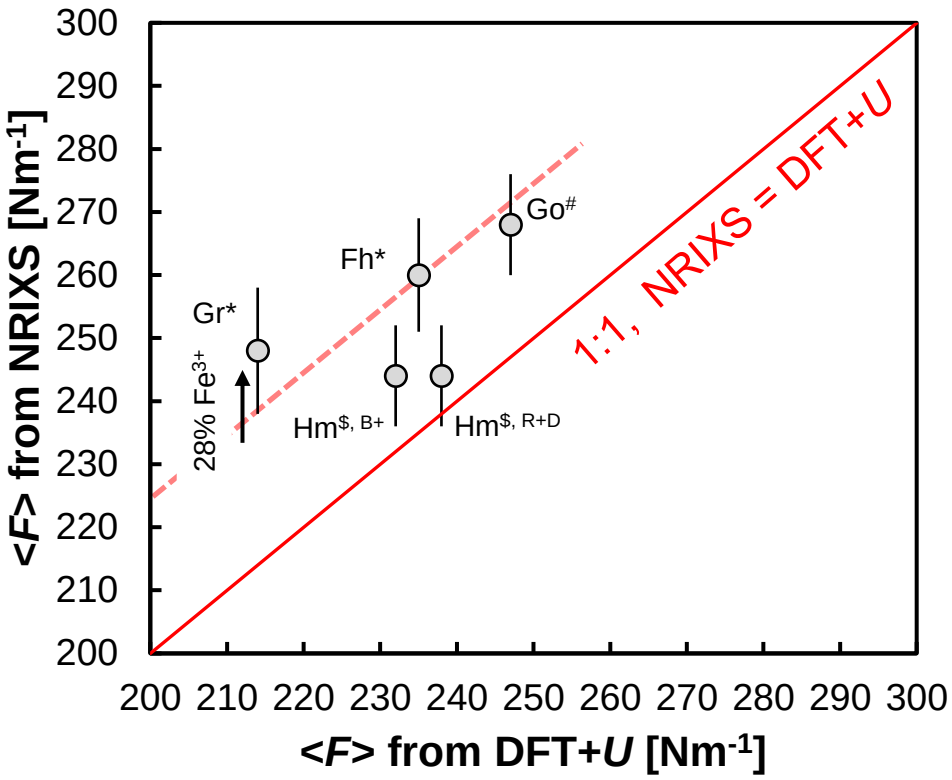

Figure 5.8. Intercomparison of force constants ⟨*F*⟩ data from NRIXS and *ab initio* DFT+*U* simulations for ferrous greenalite (Gr), ferrihydrite (Fh), goethite (Go), and hematite (Hm). The solid red line is a slope 1:1 line where data would fall if there was perfect agreement between the two techniques An offset towards higher ⟨*F*⟩ values is consistently seen in NRIXS data from hydrous minerals. A 1:1 scaling between techniques with a constant 25 Nm^{-1} offset towards higher ⟨*F*⟩ values for NRIXS would be consistent with greenalite, ferrihydrite, and goethite data (dashed pale red line). Part of the positive offset in greenalite data may reflect the 28 % oxidation of Fe in the NRIXs sample to Fe^{3+}, compared to a pure ferrous endmember modeled in the DFT+*U* calculation. Subscripts: * NRIXS and DFT+*U* data from this study; $^{\#}$ NRIXS and DFT+*U* data from Blanchard et al. (2015); $^{\$}$ NRIXS data from Dauphas et al. (2012); $^{B+}$ DFT+*U* data from Blanchard et al. (2009); $^{R+D}$ DFT data from Rustad and Dixon (2009). Error bars for NRIXS data show the 95 % confidence interval.

for bulk powder samples used in NRIXS. However, it has also been suggested that local defect-driven variations in force constants cancel one another out at the bulk scale (Blanchard 2010). It is also plausible that crystal size will play a role in increasing the apparent ⟨*F*⟩ determined with NRIXS, as fine-grained powder samples have larger surface areas and a preference for heavy

isotopic enrichment. This would suggest stronger local bonding environment, as was previously reported for surface-bound Fe in goethite *vs.* bulk goethite based on equilibration experiments (Beard et al., 2010).

All of the above-mentioned explanations for the discrepancy between NRIXS and DFT+*U* determinations of $\langle F \rangle$ relate to active areas of research that are outside the limited scope of our particular study. We note that the similar apparent offset between methods in both the ferrihydrite and greenalite material we studied suggests that similar drivers of this systematic offset may be responsible. Our approach is therefore to compare the relative differences in 1000lnβ, between ferrihydrite and greenalite and greenalite precursor material that the two independent methods indicate, rather than compare absolute values determined by the two separate methods. For example, we will not calculate an Fe isotopic fractionation between greenalite and ferrihydrite by taking the difference between a 1000lnβ value determined from DFT+*U* for one mineral, and a 1000lnβ value determined by NRIXS for the other mineral.

Equilibrium Fe isotopic fractionation between ferrihydrite and greenalite

Both DFT+*U* and NRIXS data indicate that ferrous greenalite should be isotopically depleted relative to ferrihydrite at equilibrium. From DFT+*U*, $1000\ln\alpha_{\text{Ferrihydrite-Fe(II) greenalite}} = 0.99$ ‰ at 22 °C, while for NRIXS, $1000\ln\alpha_{\text{Ferrihydrite-Exp. \#2}} = 0.35 \pm 0.71$ ‰, where Exp. #2 was the Fe(II)-dominated (72 %) greenalite precursor sample. The 1000lnα value determined from NRIXS is within error of zero at the 95 % confidence interval. However, the central value qualitatively agrees with the DFT+*U* result, in that it indicates a small (≤1 ‰) equilibrium isotopic fractionation between ferrihydrite and ferrous greenalite, favoring higher $^{56}Fe/^{54}Fe$ in ferrihydrite. Both methods therefore support first-order expectations that ferrous greenalite should be isotopically light

relative to hydrous ferric oxides. Surprisingly, the $\langle F \rangle$ values of Fe^{2+}-rich greenalite, determined with both DFT+*U* and NRIXS, are substantially higher than any other force constants determined to date for silicates containing predominantly octahedrally-coordinated Fe^{2+}, such as olivine ($\langle F \rangle$=144-197 Nm^{-1}) (Dauphas et al., 2014; Nie et al., 2021) and orthoenstatite ($\langle F \rangle$=177 Nm^{-1}) (Dauphas et al., 2012). Our $\langle F \rangle$ values of Fe^{2+}-rich greenalite are also higher than those for reduced silicate glasses with $Fe^{3+}/Fe_{tot} < 0.05$ ($\langle F \rangle$=197, 199, and 206 Nm^{-1} for reduced tholeiitic basalt, andesite, and dacite, respectively) (Dauphas et al., 2014).

Meanwhile DFT+*U* simulations indicate that a theoretical ferric endmember greenalite should be significantly isotopically heavier than ferrihydrite, with $1000\ln\alpha_{\text{Ferrihydrite-Fe(III) greenalite}} = -1.32$ ‰. This result is consistent with the only data we are aware of for Fe isotopic fractionation between ferrihydrite and clay minerals in an oxidized environment, where Fekiacova et al. (2021) used mineral mass balance to calculate a fractionation of 0.66 – 1.57 ‰ between ferrihydrite and a presumably Fe^{3+}-bearing clay mineral fraction during formation of a modern soil. The DFT+*U* result disagrees significantly with our NRIXS data, where we see very little dependence of $\langle F \rangle$ and $1000\ln\beta$, on the Fe^{2+}/Fe^{3+} ratio measured in greenalite precursor material using the forward-scattered X-ray signal (Figs. 5.6-5.7, Table 5.1). While the force constant for the 95 % Fe^{3+} Exp. #1, at 256 ± 15 Nm^{-1} is higher than the force constant for the 72 % Fe^{2+} Exp. #2, at 248 ± 10 Nm^{-1}, these values are still identical within error. Any minor difference in $\langle F \rangle$ that is possibly present in NRIXS data is certainly far smaller than the ~54 Nm^{-1} difference that would be expected if $\langle F \rangle$ scaled linearly with the proportion of Fe^{2+} and Fe^{3+} endmembers. We consider it highly unlikely that the dependence of $\langle F \rangle$ on the Fe^{2+}/Fe^{3+} ratio would be strongly non-linear over the range 72 % Fe^{2+} to 95 % Fe^{3+}.

We suggest the more likely explanation is that the high Fe^{3+} content in Exp. #1 may reflect secondary oxidation of the greenalite precursor to a ferric oxide phase rather than greenalite containing structural Fe^{3+}. The material produced in Exp. #1 was an initially an off-white gel-like precipitate at the point it was loaded into kapton tubing, suggesting that it was dominated by primary Fe^{2+} (Hinz et al., 2020). However, as noted previously, the material from Exp. #1 that was loaded into the kapton tubing was a moist gel that was briefly filtered but never hydrothermally aged. In this hydrous gel-like state, greenalite precursor precipitates are highly sensitive to oxidation by O_2 on the timescale of minutes, and if the 95 % oxidation of the sample took place prior after the precipitation experiment was ended, it is quite possible that the secondary alteration product that was formed was not a greenalite endmember with structural Fe^{3+}, but a hydrous ferric oxide, similar to ferrihydrite, or goethite, (Blanchard et al., 2015). The pDOS of all of the samples analyzed in this study lack strong features likely due to the fine-grained and amorphous nature of materials, so they are not easily distinguishable by these means. However, the similarity of $\langle F \rangle$ for Exp. #1 with that of ferrihydrite supports the interpretation that this sample was oxidatively altered, and Fe^{3+} was hosted predominantly in a secondary hydrous ferric oxide phase, rather than an Fe^{3+}-endmember greenalite-like material at the time of analysis. Qualitatively, linear mixing of Fe^{2+}-greenalite and ferrihydrite with $\langle F \rangle$ values similar to those indicated by DFT+*U* can reproduce the variations in $\langle F \rangle$ as a function of Fe^{3+} that we observed in NRIXS data for Exps. #1 and #2 (assuming a near-constant offset between DFT+*U* and NRIXS-derived $\langle F \rangle$ values; Figs. 5.6, 5.8). By contrast, mixing of Fe^{2+} and Fe^{3+} greenalite endmembers with differences in $\langle F \rangle$ consistent with DFT+*U* calculations, would produce too large an offset in $\langle F \rangle$ over the 67 % difference in Fe^{2+}/Fe_{tot} seen between Exps. #1 and #2 for this change to be unresolvable in NRIXS-derived $\langle F \rangle$ values (Fig. 5.6).

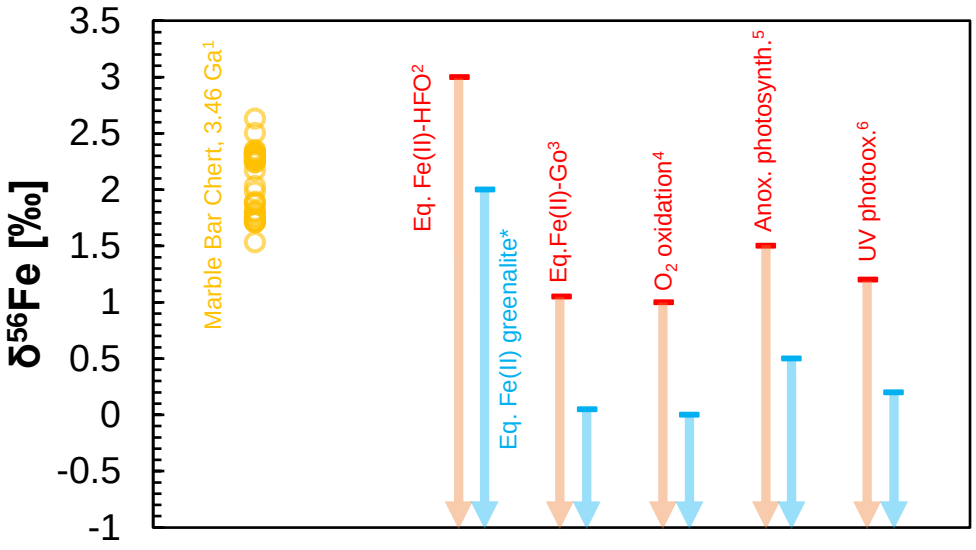

Figure 5.9. Range of allowable Fe isotopic fractionations for Fe(II) greenalite precipitation (blue marks and arrows) determined by anchoring to published fractionations between Fe(II) and hydrous ferric oxide (HFO) determined in different experimental studies (red marks and arrows). Data are compared to δ^{56}Fe from the 3.46 Ga Marble Bar Chert, which include the isotopically heaviest bulk pre-GOE IF material recorded to date. Assuming an initial Fe^{2+} source with δ^{56}Fe=0 ‰, pure Fe(II) greenalite precipitation cannot explain these data, suggesting that some amount of Fe oxidation was taking place in the oceans by 3.46 Ga. Superscripts: *This study, DFT+*U* result; [1]Li et al. (2013); [2]Wu et al. (2011); [3]Beard et al. (2010); [4]Bullen et al. (2001); [5]Croal et al. (2004); [6]Nie et al. (2017). 'Eq.' denotes equilibration experiments. The remaining fractionations associated with HFOs are from unidirectional oxidation-precipitation experiments

Iron isotopic fractionation during precipitation of greenalite

The computational methods used to calculate theretical Fe β factors for aqueous species (Rustad and Dixon, 2009; Schauble et al., 2001) result have indicated equilibrium fractionations between Fe(II) and Fe(III) that that are up to ~2 times those directly observed in Fe isotope equilibration experiments (e.g. Johnson et al., 2001, Welch et al., 2003); although more recent computations do find better agreement with empirical experiments (Rustad and Dixon, 2009). As seen when examining the fractionation factors that we calculate using NRIXS or DFT+*U* data, systematic

differences between different approaches can be comparable to inter-mineral fractionations determined using a single approach. Therefore, it is advisable to avoid using 'mixed' data to calculate fractionations for the precipitation of minerals from solution (Blanchard et al., 2015). With this in mind, when calculating the fractionation associated with the precipitation of greenalite from solution, our approach is to take the $1000\ln\alpha_{\text{Ferrihydrite-Greenalite}}$ values determined from NRIXS or DFT+*U* calculations, and anchor them to the fractionation associated with ferrihydrite (or similar hydrous ferric oxide) precipitation from Fe(II) solutions, which numerous studies have attempted to quantify (Fig. 5.9) (Beard et al., 2010; Bullen et al., 2001; Croal et al., 2004; Crosby et al., 2007; Johnson et al., 2002; Nie et al., 2017; Skulan et al., 2002; Swanner et al., 2017; Welch et al., 2003; Wu et al., 2011).

Long-timescale equilibration experiments consistently result in very similar $1000\ln\alpha_{\text{Ferrihydrite-Fe(II)}}$, $1000\ln\alpha_{\text{Hematite-Fe(II)}}$, and $1000\ln\alpha_{\text{Fe(III)-Fe(II)}}$ on the order of 3.0 – 3.2 ‰ for δ^{56}Fe (Johnson et al., 2002; Skulan et al., 2002; Wu et al., 2011). These results indicate that i) the fractionation associated with ferric (oxyhydr)oxide precipitation from ferrous iron solution is dominated by the equilibrium fractionation between Fe(II) and Fe(III) (Wu et al., 2011), and ii) the equilibrium fractionation between ferric (oxyhydr)oxides and aqueous Fe(III) is small (Skulan et al., 2002). An outlier among those experiments is the finding of a ~1 ‰ fractionation between Fe(II) and goethite (Beard et al., 2010). However, similar force constants were found for ferrihydrite and goethite in this study and that of Blanchard et al. (2015), with goethite having a slightly ~10 Nm^{-1} higher value of $\langle F \rangle$ in both DFT+*U* and NRIXS datasets. Therefore, we see no support for a large discrepancy equilibrium isotopic behavior of ferrihydrite and goethite. Surface exchange effects were a complicating factor in interpreting the equilibration experiments of Beard et al. (2010) and these might have impacted the net fractionation during goethite formation from solution while obscuring

the equilibrium value of $1000\ln\alpha_{\text{Goethite-Fe(II)}}$. Anchoring to the ~3.0 ‰ equilibrium fractionation between ferrihydrite and Fe(II) and taking our calculated fractionation between ferrihydrite and greenalite would result in $1000\ln\alpha_{\text{Fe(II) greenalite-Fe(II)}}$ = 2.0 ‰ (DFT+*U*), $1000\ln\alpha_{\text{72 \% Fe(II) greenalite-Fe(II)}}$ = 2.7 ‰ (NRIXS), and $1000\ln\alpha_{\text{Fe(III) greenalite-Fe(II)}}$ = 4.3 ‰ (DFT+*U*), at 22 °C.

Alternatively, $1000\ln\alpha_{\text{Greenalite-Fe(II)}}$ could be determined by anchoring $1000\ln\alpha_{\text{Ferrihydrite-Greenalite}}$ values to the fractionations observed during unidirectional precipitation of ferrihydrite or similar hydrous ferric oxides (HFOs) from anoxic Fe^{2+} solutions. Experiments of this type have been conducted for with all the major Fe^{2+} oxidation pathways proposed for the deposition of iron formations, resulting in values of $1000\ln\alpha_{\text{HFO-Fe(II)}}$ = 1.5 ‰ (anoxygenic photosynthesis) (Croal et al., 2004), 1.2 ‰ (UV photooxidation) (Nie et al., 2017), and 1.0 ‰ (air/O_2) (Bullen et al., 2001). Taking $1000\ln\alpha_{\text{Ferrihydrite-Fe(II) greenalite}}$ = 0.99 ‰ from DFT+*U* simulations, we could therefore plausibly infer a fractionation associated with ferrous greenalite precipitation as low as ~0.0 ‰. Such a small fractionation would support arguments against a pure ferrous greenalite precursor for IFs (Fig. 5.9). However, this method of calculating $1000\ln\alpha_{\text{Greenalite-Fe(II)}}$ assumes that a ~1 ‰ net fractionation associated with the precipitation of HFOs reflects a pure equilibrium process. Only the experimental results of (Beard et al., 2010), which found a ~1 ‰ 'equilibrium' fractionation between Fe(II) and goethite, support this line of reasoning, while the majority of experimental data discussed above do not (summarized by Wu et al., 2011). Alternatively, the smaller net fractionation observed in Fe^{2+} oxidation experiments may reflect a combination of equilibrium and kinetic effects, both during the precipitation of the ferric oxide phase (Skulan et al., 2002), and during oxidation. This would invalidate any estimates of $1000\ln\alpha_{\text{Greenalite-Fe(II)}}$ made using these experiments as an intermediate calculation step, because the kinetic isotope effects involved in Fe^{2+} oxidation and oxide precipitation are unlikely to be exactly equivalent to those involved in

the precipitation of greenalite. Recent triple Fe isotopic data indicate that the mass fractionation law (MFL) governing the covariation of $^{56}Fe/^{54}Fe$ and $^{57}Fe/^{54}Fe$ for samples formed by Fe^{2+} oxidation (Heard et al., 2020), including by photooxidation with a net fractionation of just 1.2 ‰ in $\delta^{56}Fe$ (Nie et al., 2017), is identical to the MFL for equilibrium isotope exchange. Therefore, any significant kinetic isotope effect involved in the oxidation and precipitation of Fe would be required to follow a similar MFL to the equilibrium. law This is a difficult proposition as all available data and theory indicate the kinetic MFLs should have a significantly shallower slope in $\delta^{56}Fe$ *vs*. $\delta^{57}Fe$ space (Dauphas and Schauble, 2016; Heard et al., 2020; Young et al., 2002). However, the reason for the large discrepancy in fractionation factors seen in precipitation experiments *vs*. long term equilibration experiments is still unclear.

The large variability in $1000\ln\alpha_{HFO\text{-}Fe(II)}$ observed in different experiments and the incomplete understanding to date of what drives these variations, mean that there is an equal degree of uncertainty in our estimates of $1000\ln\alpha_{Greenalite\text{-}Fe(II)}$ that are anchored to these values via $1000\ln\alpha_{Ferrihydrite\text{-}Greenalite}$, as can be seen in Figure 5.9. Equilibrium-focused constraints like β factors are an important initial baseline for determining the isotopic behavior of an unexplored mineral phase. However, a perhaps unsurprising implication of the current dataset is that direct Fe isotopic measurements of coexisting experimentally precipitated greenalite precursors gels, and Fe^{2+} in parent solutions, is required to understand the range of fractionations that would be produced by greenalite in nature. Mineral precipitation rates from saturated solutions depend on both the degree of supersaturation and the presence of nucleation sites or other mineral phases that can catalyze mineral formation or growth. More rapid precipitation of greenalite may be expected to be associated with kinetic isotope effects, which preferentially enrich reaction products in light isotopes. For example, it has been shown that small amounts of ferric iron, for which there is

evidence in Archean greenalite, can catalyze the growth of ferrous silicates in solution (Hinz et al., 2020). Therefore, the precise conditions of greenalite precipitation could potentially have a strong influence on the net fractionation (positive equilibrium effect + negative but variable kinetic effect) expressed when greenalite precipitates are removed from solution. It is worth noting that multiple other ferrous iron minerals are observed to precipitate with much lighter Fe isotopic compositions than would be prescribed by their equilibrium fractionation factors, including siderite (Polyakov and Mineev, 2000; Schauble et al., 2001; Wiesli et al., 2004), and pyrite (Guilbaud et al., 2011; Heard et al., 2020; Mansor and Fantle, 2019; Polyakov et al., 2007; Syverson et al., 2013), which most likely reflects a dominant role of kinetics in their Fe isotope geochemistry. Future studies should therefore focus on empirically determining the full range of net isotopic fractionations expressed during greenalite precipitation under a range of geochemically plausible conditions, by measuring co-sampled solids and solutions. The results presented in this study should play an important role in assessing any departure from isotopic equilibrium in these precipitation experiments.

Implications for the origins of Archean iron formations

Despite significant remaining uncertainties that we discussed above; the equilibrium β factors determined in this study can already address some endmember assumptions about the origin of pre-GOE IFs. Our major result is that the β factor for Fe^{2+}-rich greenalite at equilibrium is much closer to that of ferrihydrite than we would have predicted based on pre-existing data for (anhydrous) Fe silicates (Dauphas et al., 2014, 2017; Nie et al., 2021). Taking $1000\ln\alpha_{\text{Ferrihydrite-Fe(II)}_{\text{greenalite}}} = 0.99$ ‰ at 22°C from DFT+*U* simulations, our results indicate that unless the equilibrium fractionation between ferrihydrite and Fe^{2+} is close to the lowest values observed in precipitation

experiments (Bullen et al., 2001; Croal et al., 2004; Nie et al., 2017), ferrous greenalite precipitated at equilibrium from Fe^{2+} will have a $\delta^{56}Fe$ closer to that of ferrihydrite than to the Fe^{2+} source. Therefore, our data indicate that any blanket assumption of ferrous greenalite being isotopically similar to dissolved Fe^{2+} is incorrect and is not a valid argument against a ferrous greenalite precursor to IFs when taken in isolation.

In fact, the range of possible equilibrium fractionations between ferrous greenalite and Fe^{2+} that we would infer from our data could encompass both typical isotopically heavy Archean IFs ($\delta^{56}Fe \sim +1$ ‰), and isotopically depleted IFs ($\delta^{56}Fe < -1.5$ ‰), through instantaneous partial precipitation and Rayleigh distillation processes, respectively. However, the isotopically heaviest bulk pre-GOE IF material on record, from the 3.46 Ga Marble Bar Chert, has $\delta^{56}Fe$ values as high as +2.6 ‰ (Fig. 5.9) (Li et al., 2013). Assuming that the hydrothermal Fe^{2+} source to the Archean oceans had a zero or slightly negative $\delta^{56}Fe$ value similar to the present day (Beard et al., 2003; Severmann et al., 2004), such an extreme isotopic enrichment in the Marble Bar Chert is difficult to explain with a maximum possible $1000\ln_{Fe(II)\ greenalite\text{-}Fe(II)} \approx 2.0$ ‰ (Fig. 5.9). This problem would be exacerbated if kinetic effects decreased the fractionation relative to the equilibrium value, and/or if reservoir effects, driving later-forming precipitates to isotopically lighter values, played any role in the formation of the Marble Bar Chert. Therefore, even with the large uncertainty range allowed by our preliminary data, we can conclude that a ferrous greenalite precursor might be able to explain the majority of pre-GOE IF Fe isotopic compositions, but it cannot explain the most extreme positive $\delta^{56}Fe$ values. Some amount of partial Fe^{2+} oxidation occurring in the oceans as early as 3.46 Ga is appears to be required (Li et al., 2013). This makes it likely that oxidation processes were able to operate in the shallow oceans throughout the Archean, and the most extreme

endmember hypothesis (Rasmussen et al., 2019, 2021) that all Fe chemical sedimentation was as reduced species, can probably be ruled out.

The requirement for partial oxidation of Fe^{2+} in the genesis of at least some pre-GOE IF does not necessarily mean that a ferrihydrite primary mineralogy was required, however. Our force constant and β factor data indicate that greenalite with significant structural Fe^{3+} should form isotopically heavy, even relative to hydrous ferric oxides, and greenalite with ≥25 % Fe^{3+} should already have a force constant similar to or higher than that of ferrihydrite. Therefore, if purely equilibrium isotope fractionation was taking place in the Archean oceans, our data indicate that IFs formed from a hydrous ferric oxide precursor or a mixed valence greenalite precursor could take on indistinguishable $\delta^{56}Fe$ values if the Fe^{2+}/Fe^{3+} ratio in the primary greenalite was similar to the values (Fe^{3+}/Fe_{tot} ≈0.1-0.2) observed in well-preserved IFs using Fe XANES measurements (Johnson et al., 2018).

Mineral precipitation experiments should provide a more refined picture of Fe isotopic fractionation associated with natural greenalite formation. In particular, experiments should be conducted with solutions containing both Fe^{2+} and Mn^{2+}. By coupling $\delta^{56}Fe$ measurements with measurements of Mn/Fe in co-sampled solutions and greenalite precursor precipitates, the chemical evolution of solutions and precipitates could be compared to the well-established negative correlation seen in ln(Mn/Fe) *vs.* $\delta^{56}Fe$ plots of IFs of all ages (Hiebert et al., 2018; Planavsky et al., 2014). This negative correlation is well-explained by preferential incorporation of Fe^{3+} into IF precipitates relative Mn^{2+}, which requires higher redox potentials to be oxidized to insoluble Mn^{4+} hydroxides. Meanwhile, Fe^{2+} and Mn^{2+} have very similar geochemical behaviors, so the degree of incorporation of Mn in ferrous greenalite precursor material may provide a useful

second variable to disentangle the surprisingly similar $\delta^{56}Fe$ systematics of hydrous ferric oxides and low-Fe^{3+} greenalite.

Our data do not allow us to rule out some role for Fe^{2+} oxidation in the Archean oceans, so the most extreme iteration of the greenalite model might be ruled out. However, our finding that the Fe isotope record could be consistent with a dominant role for greenalite as an IF precursor has troubling implications for our understanding of nutrient availability in the oceans prior to the GOE (Bjerrum and Canfield, 2002; Jones et al., 2015; Konhauser et al., 2009; Robbins et al., 2016). Future experimental studies into the precipitation of greenalite precursor material should include an exploration of the adsorption and coprecipitation of P and Ni onto these phases in anoxic solutions. Having a fuller understanding of the range of dissolved [P] levels in the Archean oceans, in particular, is vital for assessing the role that nutrient limitation and global rates of photosynthetic primary productivity played in the eventual rise of atmospheric O_2 (Reinhard et al., 2017).

Implications for alteration of oceanic crust

Greenalite is the Fe endmember of the serpentine mineral group, and it is also formed during serpentinization – the hydrothermal alteration of basalt and ultramafic rocks that comprise the oceanic crust. Serpentinization of ultramafic crust at slow spreading mid oceanic ridges produces hydrogen (H_2) that provides a source of chemical energy for chemotrophic microbes (Martin et al., 2008; Sleep et al., 2011), and in the geologic past, may have aided in greenhouse warming of the Earth both by facilitating methane (CH_4) production (Kharecha et al., 2005; Konhauser et al., 2009), and directly through the effects of collision-induced absorption (Wordsworth and Pierrehumbert, 2013). Hydrogen is produced during serpentinization because Fe^{2+} in igneous minerals is oxidized by water, a process which is balanced by the reduction of the H^+ bound in the

water. The mineral phase commonly cited in this reaction is the magnetite (Evans, 2010; Frost, 1985; Frost and Beard, 2007), however more recently it has been shown that ferric iron produced during serpentinization is predominantly incorporated into Fe^{3+}-bearing serpentine group silicates like greenalite and cronstedtite ($Fe^{2+}_2Fe^{3+}(Si,Fe^{3+})O_5)(OH)_4$) (Klein et al., 2014, 2009; Seyfried et al., 2007; Tutolo et al., 2020).

The β factor of our modeled Fe^{3+} greenalite endmember at relevant temperatures of ~200 °C (Tutolo et al., 2020) is 3.7 ‰, and $1000\ln\alpha_{Fe(III)\ greenalite\text{-}Fe(II)\ greenalite} \approx 1.0$ ‰. In detail, the of Fe^{3+}-substituted greenalite formed in these reactions follows features a ferri-Tschermaks substitution where two Fe^{3+} ion replace one Fe^{2+} or Mg^{2+} atom and one Si^{4+} atom, and activity of $SiO_{2(aq)}$ plays an important role in driving the extent of this substitution (Tutolo et al., 2020). Therefore, our modeling of an Fe^{3+} greenalite endmember that is charge-balanced solely with vacancies is not a perfect analog to the Fe^{3+} greenalite formed during oceanic crustal serpentinization. However, partial substitution of Fe^{3+} into a lower coordination number environment (where it replaces Si^{4+} in the tetrahedral site) should theoretically result in an even higher value of $\langle F \rangle$ in this ferric greenalite endmember. We anticipate that the formation of ferric greenalite and similar hydrous silicate phases during serpentinization reactions could lead to heavy Fe isotopic enrichment in the altered oceanic crust, and correspondingly isotopically light fluids that exchange with the marine reservoir. This qualitatively agrees with Fe isotopic measurements of the altered oceanic crust, where a 0.5-1.3 ‰ enrichment in $\delta^{57}Fe$ in the solid altered oceanic crust relative to Fe^{2+} in alteration fluids was inferred (Rouxel et al., 2003). Those measurements were made of altered basaltic crust and the exact mineralogy of the hydrous silicate fraction may have differed from the Fe-bearing hydrous silicates formed in ultramafic serpentinization settings, so the comparison should be made with caution. However, we emphasize that the large β factor of ferric greenalite

indicated by DFT+*U* calculations suggests that clay mineral formation during hydrothermal alteration of the oceanic crust may exert a significant control on Fe isotope mass balance in oceanic crustal settings. This isotopic mass balance could be explored in appropriate geological localities in order to constrain the amount of Fe^{3+}-forming serpentinization and coincident H_2 production taking place beneath the seafloor through Earth history.

Conclusions

The primary mineralogy of iron formations (IFs) deposited prior to the Great Oxidation Event (GOE) has major bearing on how we understand the chemistry of the early oceans. The canonical assumption that hydrous ferric oxides like ferrihydrite were the main primary minerals informs a view of the Archean oceans where Fe^{2+}, anoxic deep waters encountered oxidizing conditions in the shallow oceans, possibly as a direct or indirect effect of bacterial photosynthesis. This model also underpins assumptions about nutrient availability in the early oceans, with consequences for the biological drivers of changes in ocean and atmospheric oxygenation. However, a wealth of petrographic data indicate that the most primary minerals preserved in IFs were not ferric oxides, but Fe^{2+} rich hydrous silicates that crystallized to form greenalite. Iron isotope ratios for a large collection of pre-GOE IFs provide quantitative constraints that any model for primary IF mineralogy must satisfy. Therefore, to test the two opposing models for the original mineralogy of IFs, we determined the Fe force constant ($\langle F \rangle$) and Fe isotope β factors (which determine equilibrium Fe isotopic fractionation between phases) for greenalite and ferrihydrite, using DFT+*U ab initio* calculations and NRIXS analysis of synthetic materials. We find that under equilibrium conditions, $1000\ln\alpha_{\text{Ferrihydrite-Fe(II) greenalite}} \approx 1.0$ ‰ at 22 °C for $^{56}Fe/^{54}Fe$, and $1000\ln\alpha_{\text{Ferrihydrite-Fe(III) greenalite}} \approx -1.3$ ‰. NRIXS data were partially affected by the apparent

oxidative alteration of sample materials prior to analysis, but we obtain $1000\ln\alpha_{\text{Ferrihydrite-Fe(II)}}$ $_{\text{greenalite}} \approx 0.34 \pm 0.71$ ‰ for a sample with 72 % Fe^{2+} at 22 °C, which agrees with the DFT+*U* simulation within error. By anchoring these data to experimentally determined fractionations between ferric (oxyhydr)oxides and Fe^{2+}, we find that ferrous greenalite should precipitate with an Fe isotopic composition more similar to ferrihydrite than to dissolved Fe^{2+}, unless the smallest fractionations observed between ferric oxide phases and Fe^{2+} in previous experiments are the ones that reflect isotopic equilibrium. Therefore, we suggest that if equilibrium fractionations were expressed in the ancient oceans, an Fe^{2+}-rich greenalite precursor may be consistent with the Fe isotopic record of the majority of pre-GOE IFs. However, the most positive $\delta^{56}Fe$ values in Archean IFs cannot be explained without some contribution of an Fe^{3+} phase, either a ferric oxide or some Fe^{3+} substitution into greenalite; therefore we can tentatively rule out the endmember hypothesis that zero Fe^{2+} oxidation was taking place in the pre-GOE oceans.

Precipitation experiments that can constrain the net Fe isotopic fractionation accompanying greenalite precipitation, including kinetic effects that may be dependent on precipitation rates, are likely required to determine the full natural range of Fe isotopic compositions that Fe^{2+}-rich greenalite precipitation may have imparted to IFs. Combining Fe isotope and Mn/Fe ratio measurements of precipitation experiments may offer the opportunity to resolve between the ferric oxide and greenalite models where Fe isotopes alone may not.

Lastly, the isotopic leverage provided by the large β factor of ferric greenalite indicated by our experiments, may provide a means to determine the extent of Fe^{3+} incorporation in the oceanic crust during hydrothermal alteration. Further calibrating the Fe isotopic behavior of naturally occurring ferric Fe clay minerals, and making targeted measurements of ancient altered oceanic

crust, may provide a promising area of future research for determining rates of seafloor serpentinization and H_2 production over geologic time.

Acknowledgements

This work represents the results of a collaboration that would not have been possible without many coworkers. We thank Marc Blanchard for providing *ab initio* DFT+*U* calculations, Jena Johnson, Isaac Hinz, and Mark Fornace for producing mineral samples, and Ercan Alp, Michael Hu, Jiyong Zhao and Barbabra Lavina for running NRIXS analyses. Ercan Alp is also thanked for providing Fe^{2+}/Fe^{3+} ratio information from synchrotron Mössbauer data.

References

Alp, E.E., Sturhahn, W., Toellner, T.S., 1995. Synchrotron Mossbauer spectroscopy of powder samples. Nucl. Instrum. Methods Phys. Res. Sect. B Beam Interact. Mater. At. 97, 526–529. https://doi.org/10.1016/0168-583X(94)00743-8

Anbar, A.D., Holland, H.D., 1992. The photochemistry of manganese and the origin of banded iron formations. Geochim. Cosmochim. Acta 56, 2595–2603. https://doi.org/10.1016/0016-7037(92)90346-K

Ayres, D.E., 1972. Genesis of Iron-bearing Minerals in Banded Iron Formation Mesobands in The Dales Gorge Member, Hamersley Group, Western Australia. Econ. Geol. 67, 1214–1233. https://doi.org/10.2113/gsecongeo.67.8.1214

Baroni, S., de Gironcoli, S., Dal Corso, A., Giannozzi, P., 2001. Phonons and related crystal properties from density-functional perturbation theory. Rev. Mod. Phys. 73, 515–562. https://doi.org/10.1103/RevModPhys.73.515

Beard, B.L., Handler, R.M., Scherer, M.M., Wu, L., Czaja, A.D., Heimann, A., Johnson, C.M., 2010. Iron isotope fractionation between aqueous ferrous iron and goethite. Earth Planet. Sci. Lett. 295, 241–250. https://doi.org/10.1016/j.epsl.2010.04.006

Beard, B.L., Johnson, C.M., Damm, K.L.V., Poulson, R.L., 2003. Iron isotope constraints on Fe cycling and mass balance in oxygenated Earth oceans. Geology 31, 629–632. https://doi.org/10.1130/0091-7613(2003)031<0629:IICOFC>2.0.CO;2

Bekker, A., Kaufman, A.J., 2007. Oxidative forcing of global climate change: A biogeochemical record across the oldest Paleoproterozoic ice age in North America. Earth Planet. Sci. Lett. 258, 486–499. https://doi.org/10.1016/j.epsl.2007.04.009

Bekker, A., Slack, J.F., Planavsky, N., Krapež, B., Hofmann, A., Konhauser, K.O., Rouxel, O.J., 2010. Iron Formation: The Sedimentary Product of a Complex Interplay among Mantle, Tectonic, Oceanic, and Biospheric Processes. Econ. Geol. 105, 467–508. https://doi.org/10.2113/gsecongeo.105.3.467

Beukes, N.J., Gutzmer, J., 2008. Origin and Paleoenvironmental Significance of Major Iron Formations at the Archean-Paleoproterozoic Boundary. Rev. Econ. Geol. 15. https://doi.org/10.5382/Rev.15.01

Beukes, N.J., Klein, C., 1990. Geochemistry and sedimentology of a facies transition — from microbanded to granular iron-formation — in the early Proterozoic Transvaal Supergroup, South Africa. Precambrian Res. 47, 99–139. https://doi.org/10.1016/0301-9268(90)90033-M

Bjerrum, C.J., Canfield, D.E., 2002. Ocean productivity before about 1.9 Gyr ago limited by phosphorus adsorption onto iron oxides. Nature 417, 159–162. https://doi.org/10.1038/417159a

Blanchard, M., Balan, E., Schauble, E.A., 2017. Equilibrium Fractionation of Non-traditional Isotopes: a Molecular Modeling Perspective. Rev. Mineral. Geochem. 82, 27–63. https://doi.org/10.2138/rmg.2017.82.2

Blanchard, M., Dauphas, N., Hu, M.Y., Roskosz, M., Alp, E.E., Golden, D.C., Sio, C.K., Tissot, F.L.H., Zhao, J., Gao, L., Morris, R.V., Fornace, M., Floris, A., Lazzeri, M., Balan, E., 2015. Reduced partition function ratios of iron and oxygen in goethite. Geochim. Cosmochim. Acta 151, 19–33. https://doi.org/10.1016/j.gca.2014.12.006

Blanchard, M., Poitrasson, F., Méheut, M., Lazzeri, M., Mauri, F., Balan, E., 2009. Iron isotope fractionation between pyrite (FeS2), hematite (Fe2O3) and siderite (FeCO3): A first-principles density functional theory study. Geochim. Cosmochim. Acta 73, 6565–6578. https://doi.org/10.1016/j.gca.2009.07.034

Braterman, P.S., Cairns-Smith, A.G., Sloper, R.W., 1983. Photo-oxidation of hydrated Fe2+— significance for banded iron formations. Nature 303, 163–164. https://doi.org/10.1038/303163a0
Bullen, T.D., White, A.F., Childs, C.W., Vivit, D.V., Schulz, M.S., 2001. Demonstration of significant abiotic iron isotope fractionation in nature. Geology 29, 699–702. https://doi.org/10.1130/0091-7613(2001)029<0699:DOSAII>2.0.CO;2

Cairns-Smith, A.G., 1978. Precambrian solution photochemistry, inverse segregation, and banded iron formations. Nature 276, 807–808. https://doi.org/10.1038/276807a0

Cloud, P., 1973. Paleoecological Significance of the Banded Iron-Formation. Econ. Geol. 68, 1135–1143. https://doi.org/10.2113/gsecongeo.68.7.1135

Cococcioni, M., de Gironcoli, S., 2005. Linear response approach to the calculation of the effective interaction parameters in the LDA+U method. Phys. Rev. B 71, 035105. https://doi.org/10.1103/PhysRevB.71.035105

Coey, J.M.D., Ballet, O., Moukarika, A., Soubeyroux, J.L., 1981. Magnetic properties of sheet silicates; 1:1 layer minerals. Phys. Chem. Miner. 7, 141–148. https://doi.org/10.1007/BF00308232

Cottrell, E., Lanzirotti, A., Mysen, B., Birner, S., Kelley, K.A., Botcharnikov, R., Davis, F.A., Newville, M., 2018. A Mössbauer-based XANES calibration for hydrous basalt glasses reveals radiation-induced oxidation of Fe. Am. Mineral. 103, 489–501. https://doi.org/10.2138/am-2018-6268

Craddock, P.R., Dauphas, N., 2011a. Iron and carbon isotope evidence for microbial iron respiration throughout the Archean. Earth Planet. Sci. Lett. 303, 121–132. https://doi.org/10.1016/j.epsl.2010.12.045

Craddock, P.R., Dauphas, N., 2011b. Iron Isotopic Compositions of Geological Reference Materials and Chondrites. Geostand. Geoanalytical Res. 35, 101–123. https://doi.org/10.1111/j.1751-908X.2010.00085.x

Croal, L.R., Johnson, C.M., Beard, B.L., Newman, D.K., 2004. Iron isotope fractionation by Fe(II)-oxidizing photoautotrophic bacteria 1. Geochim. Cosmochim. Acta 68, 1227–1242. https://doi.org/10.1016/j.gca.2003.09.011

Crosby, Roden Eric E., Johnson Clark M., Beard Brian L., 2007. The mechanisms of iron isotope fractionation produced during dissimilatory Fe(III) reduction by Shewanella putrefaciens and Geobacter sulfurreducens. Geobiology 5, 169–189. https://doi.org/10.1111/j.1472-4669.2007.00103.x

Czaja, A.D., Van Kranendonk, M.J., Beard, B.L., Johnson, C.M., 2018. A multistage origin for Neoarchean layered hematite-magnetite iron formation from the Weld Range, Yilgarn Craton, Western Australia. Chem. Geol. 488, 125–137. https://doi.org/10.1016/j.chemgeo.2018.04.019

Dauphas, N., Hu, M.Y., Baker, E.M., Hu, J., Tissot, F.L.H., Alp, E.E., Roskosz, M., Zhao, J., Bi, W., Liu, J., Lin, J.-F., Nie, N.X., Heard, A., 2018. SciPhon: a data analysis software for nuclear resonant inelastic X-ray scattering with applications to Fe, Kr, Sn, Eu and Dy. J. Synchrotron Radiat. 25, 1581–1599. https://doi.org/10.1107/S1600577518009487

Dauphas, N., John, S.G., Rouxel, O., 2017. Iron Isotope Systematics. Rev. Mineral. Geochem. 82, 415–510. https://doi.org/10.1515/9783110545630-012

Dauphas, N., Roskosz, M., Alp, E.E., Golden, D.C., Sio, C.K., Tissot, F.L.H., Hu, M.Y., Zhao, J., Gao, L., Morris, R.V., 2012. A general moment NRIXS approach to the determination of equilibrium Fe isotopic fractionation factors: Application to goethite and jarosite. Geochim. Cosmochim. Acta 94, 254–275. https://doi.org/10.1016/j.gca.2012.06.013

Dauphas, N., Roskosz, M., Alp, E.E., Neuville, D.R., Hu, M.Y., Sio, C.K., Tissot, F.L.H., Zhao, J., Tissandier, L., Médard, E., Cordier, C., 2014. Magma redox and structural controls on iron isotope variations in Earth's mantle and crust. Earth Planet. Sci. Lett. 398, 127–140. https://doi.org/10.1016/j.epsl.2014.04.033

Dauphas, N., Schauble, E.A., 2016. Mass Fractionation Laws, Mass-Independent Effects, and Isotopic Anomalies. Annu. Rev. Earth Planet. Sci. 44, 709–783. https://doi.org/10.1146/annurev-earth-060115-012157

Derry, L.A., Jacobsen, S.B., 1990. The chemical evolution of Precambrian seawater: Evidence from REEs in banded iron formations. Geochim. Cosmochim. Acta 54, 2965–2977. https://doi.org/10.1016/0016-7037(90)90114-Z

Dietzel, M., 2000. Dissolution of silicates and the stability of polysilicic acid. Geochim. Cosmochim. Acta 64, 3275–3281. https://doi.org/10.1016/S0016-7037(00)00426-9

Dodd, M.S., Papineau, D., Pirajno, F., Wan, Y., Karhu, J.A., 2019. Minimal biomass deposition in banded iron formations inferred from organic matter and clay relationships. Nat. Commun. 10, 1–13. https://doi.org/10.1038/s41467-019-12975-z

Evans, B.W., 2010. Lizardite versus antigorite serpentinite: Magnetite, hydrogen, and life(?). Geology 38, 879–882. https://doi.org/10.1130/G31158.1

Farquhar, J., Bao, H., Thiemens, M., 2000. Atmospheric Influence of Earth's Earliest Sulfur Cycle. Science 289, 756–758. https://doi.org/10.1126/science.289.5480.756

Farquhar, J., Wing, B.A., 2003. Multiple sulfur isotopes and the evolution of the atmosphere. Earth Planet. Sci. Lett. 213, 1–13. https://doi.org/10.1016/S0012-821X(03)00296-6

Fekiacova, Z., Montagne, D., Duvivier, A., Guihou, A., Deschamps, P., Cornu, S., 2021. Evolution of Retisol impacted by artificial drainage: What can we learn from stable Fe isotope ratios? Geoderma 384, 114771. https://doi.org/10.1016/j.geoderma.2020.114771

Fischer, W.W., Knoll, A.H., 2009. An iron shuttle for deepwater silica in Late Archean and early Paleoproterozoic iron formation. GSA Bull. 121, 222–235. https://doi.org/10.1130/B26328.1

François, L.M., 1986. Extensive deposition of banded iron formations was possible without photosynthesis. Nature 320, 352–354. https://doi.org/10.1038/320352a0

Frost, B.R., 1985. On the Stability of Sulfides, Oxides, and Native Metals in Serpentinite. J. Petrol. 26, 31–63. https://doi.org/10.1093/petrology/26.1.31

Frost, B.R., Beard, J.S., 2007. On Silica Activity and Serpentinization. J. Petrol. 48, 1351–1368. https://doi.org/10.1093/petrology/egm021

Garrity, K.F., Bennett, J.W., Rabe, K.M., Vanderbilt, D., 2014. Pseudopotentials for high-throughput DFT calculations. Comput. Mater. Sci. 81, 446–452. https://doi.org/10.1016/j.commatsci.2013.08.053

Giannozzi, P., Baroni, S., Bonini, N., Calandra, M., Car, R., Cavazzoni, C., Ceresoli, D., Chiarotti, G.L., Cococcioni, M., Dabo, I., Dal Corso, A., de Gironcoli, S., Fabris, S., Fratesi, G., Gebauer, R., Gerstmann, U., Gougoussis, C., Kokalj, A., Lazzeri, M., Martin-Samos, L., Marzari, N., Mauri, F., Mazzarello, R., Paolini, S., Pasquarello, A., Paulatto, L., Sbraccia, C., Scandolo, S., Sclauzero, G., Seitsonen, A.P., Smogunov, A., Umari, P., Wentzcovitch, R.M., 2009. QUANTUM ESPRESSO: a modular and open-source software project for quantum simulations of materials. J. Phys. Condens. Matter Inst. Phys. J. 21, 395502. https://doi.org/10.1088/0953-8984/21/39/395502

Guilbaud, R., Butler, I.B., Ellam, R.M., 2011. Abiotic Pyrite Formation Produces a Large Fe Isotope Fractionation. Science 332, 1548–1551. https://doi.org/10.1126/science.1202924

Heard, A.W., Dauphas, N., 2020. Constraints on the coevolution of oxic and sulfidic ocean iron sinks from Archean–Paleoproterozoic iron isotope records. Geology 48, 358–362. https://doi.org/10.1130/G46951.1

Heard, A.W., Dauphas, N., Guilbaud, R., Rouxel, O.J., Butler, I.B., Nie, N.X., Bekker, A., 2020. Triple iron isotope constraints on the role of ocean iron sinks in early atmospheric oxygenation. Science 370, 446–449. https://doi.org/10.1126/science.aaz8821

Heimann, A., Johnson, C.M., Beard, B.L., Valley, J.W., Roden, E.E., Spicuzza, M.J., Beukes, N.J., 2010. Fe, C, and O isotope compositions of banded iron formation carbonates demonstrate a major role for dissimilatory iron reduction in ~2.5 Ga marine environments. Earth Planet. Sci. Lett. 294, 8–18. https://doi.org/10.1016/j.epsl.2010.02.015

Hiebert, R.S., Bekker, A., Houlé, M.G., Rouxel, O.J., 2018. Depositional setting of the Late Archean Fe oxide- and sulfide-bearing chert and graphitic argillite in the Shaw Dome, Abitibi greenstone belt, Canada. Precambrian Res. 311, 98–116. https://doi.org/10.1016/j.precamres.2018.04.004

Hinz, I.L., Nims, C., Theuer, S., Templeton, A.S., Johnson, J.E., 2020. Ferric Iron Catalyzes The Formation Of Iron-Rich Silicates Under Archean Ocean-Like Conditions. Presented at the North-Central Section-54th Annual Meeting, GSA.

Holland, H.D., 1973. The Oceans; A Possible Source of Iron in Iron-Formations. Econ. Geol. 68, 1169–1172. https://doi.org/10.2113/gsecongeo.68.7.1169

Hu, M.Y., Toellner, T.S., Dauphas, N., Alp, E.E., Zhao, J., 2013. Moments in nuclear resonant inelastic x-ray scattering and their applications. Phys. Rev. B 87, 064301. https://doi.org/10.1103/PhysRevB.87.064301

Isley, A.E., 1995. Hydrothermal Plumes and the Delivery of Iron to Banded Iron Formation. J. Geol. 103, 169–185.

Isley, A.E., Abbott, D.H., 1999. Plume-related mafic volcanism and the deposition of banded iron formation. J. Geophys. Res. Solid Earth 104, 15461–15477. https://doi.org/10.1029/1999JB900066

Jacobsen, S.B., Pimentel-Klose, M.R., 1988. Nd isotopic variations in Precambrian banded iron formations. Geophys. Res. Lett. 15, 393–396. https://doi.org/10.1029/GL015i004p00393

Johnson, C.M., Skulan, J.L., Beard, B.L., Sun, H., Nealson, K.H., Braterman, P.S., 2002. Isotopic fractionation between Fe(III) and Fe(II) in aqueous solutions. Earth Planet. Sci. Lett. 195, 141–153. https://doi.org/10.1016/S0012-821X(01)00581-7

Johnson, J.E., Muhling, J.R., Cosmidis, J., Rasmussen, B., Templeton, A.S., 2018. Low-Fe(III) Greenalite Was a Primary Mineral From Neoarchean Oceans. Geophys. Res. Lett. 45, 3182–3192. https://doi.org/10.1002/2017GL076311

Johnston, D.T., 2011. Multiple sulfur isotopes and the evolution of Earth's surface sulfur cycle. Earth-Sci. Rev. 106, 161–183. https://doi.org/10.1016/j.earscirev.2011.02.003

Jones, C., Nomosatryo, S., Crowe, S.A., Bjerrum, C.J., Canfield, D.E., 2015. Iron oxides, divalent cations, silica, and the early earth phosphorus crisis. Geology 43, 135–138. https://doi.org/10.1130/G36044.1

Kappler, A., Pasquero, C., Konhauser, K.O., Newman, D.K., 2005. Deposition of banded iron formations by anoxygenic phototrophic Fe(II)-oxidizing bacteria. Geology 33, 865–868. https://doi.org/10.1130/G21658.1

Kharecha, P., Kasting, J., Siefert, J., 2005. A coupled atmosphere–ecosystem model of the early Archean Earth. Geobiology 3, 53–76. https://doi.org/10.1111/j.1472-4669.2005.00049.x

Klein, C., 2005. Some Precambrian banded iron-formations (BIFs) from around the world: Their age, geologic setting, mineralogy, metamorphism, geochemistry, and origins. Am. Mineral. 90, 1473–1499. https://doi.org/10.2138/am.2005.1871

Klein, C., Beukes, N.J., 1989. Geochemistry and sedimentology of a facies transition from limestone to iron-formation deposition in the early Proterozoic Transvaal Supergroup, South Africa. Econ. Geol. 84, 1733–1774. https://doi.org/10.2113/gsecongeo.84.7.1733

Klein, F., Bach, W., Humphris, S.E., Kahl, W.-A., Jöns, N., Moskowitz, B., Berquó, T.S., 2014. Magnetite in seafloor serpentinite—Some like it hot. Geology 42, 135–138. https://doi.org/10.1130/G35068.1

Klein, F., Bach, W., Jöns, N., McCollom, T., Moskowitz, B., Berquó, T., 2009. Iron partitioning and hydrogen generation during serpentinization of abyssal peridotites from 15°N on the Mid-Atlantic Ridge. Geochim. Cosmochim. Acta 73, 6868–6893. https://doi.org/10.1016/j.gca.2009.08.021

Köhler, I., Konhauser, K.O., Papineau, D., Bekker, A., Kappler, A., 2013. Biological carbon precursor to diagenetic siderite with spherical structures in iron formations. Nat. Commun. 4, 1741. https://doi.org/10.1038/ncomms2770

Konhauser, K.O., Amskold, L., Lalonde, S.V., Posth, N.R., Kappler, A., Anbar, A., 2007. Decoupling photochemical Fe(II) oxidation from shallow-water BIF deposition. Earth Planet. Sci. Lett. 258, 87–100. https://doi.org/10.1016/j.epsl.2007.03.026

Konhauser, K.O., Hamade, T., Raiswell, R., Morris, R.C., Ferris, F.G., Southam, G., Canfield, D.E., 2002. Could bacteria have formed the Precambrian banded iron formations? Geology 30, 1079–1082. https://doi.org/10.1130/0091-7613(2002)030<1079:CBHFTP>2.0.CO;2

Konhauser, K.O., Newman, D.K., Kappler, A., 2005. The potential significance of microbial Fe(III) reduction during deposition of Precambrian banded iron formations. Geobiology 3, 167–177. https://doi.org/10.1111/j.1472-4669.2005.00055.x

Konhauser, K.O., Pecoits, E., Lalonde, S.V., Papineau, D., Nisbet, E.G., Barley, M.E., Arndt, N.T., Zahnle, K., Kamber, B.S., 2009. Oceanic nickel depletion and a methanogen famine before the Great Oxidation Event. Nature 458, 750–753. https://doi.org/10.1038/nature07858

Konhauser, K.O., Planavsky, N.J., Hardisty, D.S., Robbins, L.J., Warchola, T.J., Haugaard, R., Lalonde, S.V., Partin, C.A., Oonk, P.B.H., Tsikos, H., Lyons, T.W., Bekker, A., Johnson, C.M., 2017. Iron formations: A global record of Neoarchaean to Palaeoproterozoic environmental history. Earth-Sci. Rev. 172, 140–177. https://doi.org/10.1016/j.earscirev.2017.06.012

Konhauser, K.O., Robbins, L.J., Pecoits, E., Peacock, C., Kappler, A., Lalonde, S.V., 2015. The Archean Nickel Famine Revisited. Astrobiology 15, 804–815. https://doi.org/10.1089/ast.2015.1301

Kopp, R.E., Kirschvink, J.L., Hilburn, I.A., Nash, C.Z., 2005. The Paleoproterozoic snowball Earth: A climate disaster triggered by the evolution of oxygenic photosynthesis. Proc. Natl. Acad. Sci. 102, 11131–11136. https://doi.org/10.1073/pnas.0504878102

Kulik, H.J., Cococcioni, M., Scherlis, D.A., Marzari, N., 2006. Density Functional Theory in Transition-Metal Chemistry: A Self-Consistent Hubbard U Approach. Phys. Rev. Lett. 97, 103001. https://doi.org/10.1103/PhysRevLett.97.103001

Li, W., Czaja, A.D., Van Kranendonk, M.J., Beard, B.L., Roden, E.E., Johnson, C.M., 2013. An anoxic, Fe(II)-rich, U-poor ocean 3.46 billion years ago. Geochim. Cosmochim. Acta 120, 65–79. https://doi.org/10.1016/j.gca.2013.06.033

Mansor, M., Fantle, M.S., 2019. A novel framework for interpreting pyrite-based Fe isotope records of the past. Geochim. Cosmochim. Acta 253, 39–62. https://doi.org/10.1016/j.gca.2019.03.017

Martin, W., Baross, J., Kelley, D., Russell, M.J., 2008. Hydrothermal vents and the origin of life. Nat. Rev. Microbiol. 6, 805–814. https://doi.org/10.1038/nrmicro1991

Michel, F.M., Ehm, L., Antao, S.M., Lee, P.L., Chupas, P.J., Liu, G., Strongin, D.R., Schoonen, M.A.A., Phillips, B.L., Parise, J.B., 2007. The structure of ferrihydrite, a nanocrystalline material. Science 316, 1726–1729. https://doi.org/10.1126/science.1142525

Monkhorst, H.J., Pack, J.D., 1976. Special points for Brillouin-zone integrations. Phys. Rev. B 13, 5188–5192. https://doi.org/10.1103/PhysRevB.13.5188

Moorbath, S., O'nions, R.K., Pankhurst, R.J., 1973. Early Archaean Age for the Isua Iron Formation, West Greenland. Nature 245, 138. https://doi.org/10.1038/245138a0

Nie, N.X., Dauphas, N., Alp, E.E., Zeng, H., Sio, C.K., Hu, J.Y., Chen, X., Aarons, S.M., Zhang, Z., Tian, H.-C., Wang, D., Prissel, K.B., Greer, J., Bi, W., Hu, M.Y., Zhao, J., Shahar, A., Roskosz, M., Teng, F.-Z., Krawczynski, M.J., Heck, P.R., Spear, F.S., 2021. Iron, magnesium, and titanium isotopic fractionations between garnet, ilmenite, fayalite, biotite, and tourmaline: results from NRIXS, ab initio, and study of mineral separates from the Moosilauke metapelite. Geochim. Cosmochim. Acta. https://doi.org/10.1016/j.gca.2021.03.014

Nie, N.X., Dauphas, N., Greenwood, R.C., 2017. Iron and oxygen isotope fractionation during iron UV photo-oxidation: Implications for early Earth and Mars. Earth Planet. Sci. Lett. 458, 179–191. https://doi.org/10.1016/j.epsl.2016.10.035

Pavlov, A. a., Kasting, J. f., 2002. Mass-Independent Fractionation of Sulfur Isotopes in Archean Sediments: Strong Evidence for an Anoxic Archean Atmosphere. Astrobiology 2, 27–41. https://doi.org/10.1089/153110702753621321

Perdew, J.P., Burke, K., Ernzerhof, M., 1996. Generalized Gradient Approximation Made Simple. Phys. Rev. Lett. 77, 3865–3868. https://doi.org/10.1103/PhysRevLett.77.3865

Pinney, N., Kubicki, J.D., Middlemiss, D.S., Grey, C.P., Morgan, D., 2009. Density Functional Theory Study of Ferrihydrite and Related Fe-Oxyhydroxides. Chem. Mater. 21, 5727–5742. https://doi.org/10.1021/cm9023875

Planavsky, N., Rouxel, O.J., Bekker, A., Hofmann, A., Little, C.T.S., Lyons, T.W., 2012. Iron isotope composition of some Archean and Proterozoic iron formations. Geochim. Cosmochim. Acta 80, 158–169. https://doi.org/10.1016/j.gca.2011.12.001

Planavsky, N.J., Asael, D., Hofmann, A., Reinhard, C.T., Lalonde, S.V., Knudsen, A., Wang, X., Ossa Ossa, F., Pecoits, E., Smith, A.J.B., Beukes, N.J., Bekker, A., Johnson, T.M., Konhauser, K.O., Lyons, T.W., Rouxel, O.J., 2014. Evidence for oxygenic photosynthesis half a billion years before the Great Oxidation Event. Nat. Geosci. 7, 283–286. https://doi.org/10.1038/ngeo2122

Planavsky, N.J., Rouxel, O.J., Bekker, A., Lalonde, S.V., Konhauser, K.O., Reinhard, C.T., Lyons, T.W., 2010. The evolution of the marine phosphate reservoir. Nature 467, 1088–1090. https://doi.org/10.1038/nature09485

Polyakov, V.B., Clayton, R.N., Horita, J., Mineev, S.D., 2007. Equilibrium iron isotope fractionation factors of minerals: Reevaluation from the data of nuclear inelastic resonant X-ray scattering and Mössbauer spectroscopy. Geochim. Cosmochim. Acta 71, 3833–3846. https://doi.org/10.1016/j.gca.2007.05.019

Polyakov, V.B., Mineev, S.D., 2000. The use of Mössbauer spectroscopy in stable isotope geochemistry. Geochim. Cosmochim. Acta 64, 849–865. https://doi.org/10.1016/S0016-7037(99)00329-4

Poulton, S.W., Canfield, D.E., 2011. Ferruginous Conditions: A Dominant Feature of the Ocean through Earth's History. Elements 7, 107–112. https://doi.org/10.2113/gselements.7.2.107

Rasmussen, B., Buick, R., 1999. Redox state of the Archean atmosphere: Evidence from detrital heavy minerals in ca. 3250–2750 Ma sandstones from the Pilbara Craton, Australia. Geology 27, 115–118. https://doi.org/10.1130/0091-7613(1999)027<0115:RSOTAA>2.3.CO;2

Rasmussen, B., Krapež, B., Meier, D.B., 2014a. Replacement origin for hematite in 2.5 Ga banded iron formation: Evidence for postdepositional oxidation of iron-bearing minerals. Geol. Soc. Am. Bull. B30944.1. https://doi.org/10.1130/B30944.1

Rasmussen, B., Krapež, B., Muhling, J.R., 2014b. Hematite replacement of iron-bearing precursor sediments in the 3.46-b.y.-old Marble Bar Chert, Pilbara craton, Australia. Geol. Soc. Am. Bull. 126, 1245–1258. https://doi.org/10.1130/B31049.1

Rasmussen, B., Krapež, B., Muhling, J.R., Suvorova, A., 2015. Precipitation of iron silicate nanoparticles in early Precambrian oceans marks Earth's first iron age. Geology 43, 303–306. https://doi.org/10.1130/G36309.1

Rasmussen, B., Muhling, J.R., 2018. Making magnetite late again: Evidence for widespread magnetite growth by thermal decomposition of siderite in Hamersley banded iron formations. Precambrian Res. 306, 64–93. https://doi.org/10.1016/j.precamres.2017.12.017

Rasmussen, B., Muhling, J.R., Krapež, B., 2021. Greenalite and its role in the genesis of early Precambrian iron formations – A review. Earth-Sci. Rev. 103613. https://doi.org/10.1016/j.earscirev.2021.103613

Rasmussen, B., Muhling, J.R., Suvorova, A., Krapež, B., 2017. Greenalite precipitation linked to the deposition of banded iron formations downslope from a late Archean carbonate platform. Precambrian Res. 290, 49–62. https://doi.org/10.1016/j.precamres.2016.12.005

Rasmussen, B., Muhling, J.R., Suvorova, A., Krapež, B., 2016. Dust to dust: Evidence for the formation of "primary" hematite dust in banded iron formations via oxidation of iron silicate nanoparticles. Precambrian Res. 284, 49–63. https://doi.org/10.1016/j.precamres.2016.07.003

Rasmussen, B., Muhling, J.R., Tosca, N.J., Tsikos, H., 2019. Evidence for anoxic shallow oceans at 2.45 Ga: Implications for the rise of oxygenic photosynthesis. Geology. https://doi.org/10.1130/G46162.1

Reinhard, C.T., Planavsky, N.J., Gill, B.C., Ozaki, K., Robbins, L.J., Lyons, T.W., Fischer, W.W., Wang, C., Cole, D.B., Konhauser, K.O., 2017. Evolution of the global phosphorus cycle. Nature 541, 386–389. https://doi.org/10.1038/nature20772

Riding, R., Fralick, P., Liang, L., 2014. Identification of an Archean marine oxygen oasis. Precambrian Res. 251, 232–237. https://doi.org/10.1016/j.precamres.2014.06.017

Robbins, L.J., Funk, S.P., Flynn, S.L., Warchola, T.J., Li, Z., Lalonde, S.V., Rostron, B.J., Smith, A.J.B., Beukes, N.J., Kock, M.O. de, Heaman, L.M., Alessi, D.S., Konhauser, K.O., 2019. Hydrogeological constraints on the formation of Palaeoproterozoic banded iron formations. Nat. Geosci. 1. https://doi.org/10.1038/s41561-019-0372-0

Robbins, L.J., Lalonde, S.V., Planavsky, N.J., Partin, C.A., Reinhard, C.T., Kendall, B., Scott, C., Hardisty, D.S., Gill, B.C., Alessi, D.S., Dupont, C.L., Saito, M.A., Crowe, S.A., Poulton, S.W., Bekker, A., Lyons, T.W., Konhauser, K.O., 2016. Trace elements at the intersection of marine biological and geochemical evolution. Earth-Sci. Rev. 163, 323–348. https://doi.org/10.1016/j.earscirev.2016.10.013

Roscoe, S.M., 1969. Huronian rocks and uraniferous conglomerates in the Canadian shield (No. GSCAN-P--68-40). Geological Survey of Canada.

Rouxel, O., Dobbek, N., Ludden, J., Fouquet, Y., 2003. Iron isotope fractionation during oceanic crust alteration. Chem. Geol. 202, 155–182. https://doi.org/10.1016/j.chemgeo.2003.08.011

Rouxel, O.J., Bekker, A., Edwards, K.J., 2005. Iron Isotope Constraints on the Archean and Paleoproterozoic Ocean Redox State. Science 307, 1088–1091. https://doi.org/10.1126/science.1105692

Rustad, J.R., Dixon, D.A., 2009. Prediction of Iron-Isotope Fractionation Between Hematite (α-Fe2O3) and Ferric and Ferrous Iron in Aqueous Solution from Density Functional Theory. J. Phys. Chem. A 113, 12249–12255. https://doi.org/10.1021/jp9065373

Rye, R., Holland, H.D., 1998. Paleosols and the evolution of atmospheric oxygen; a critical review. Am. J. Sci. 298, 621–672. https://doi.org/10.2475/ajs.298.8.621

Schauble, E.A., Rossman, G.R., Taylor, H.P., 2001. Theoretical estimates of equilibrium Fe-isotope fractionations from vibrational spectroscopy. Geochim. Cosmochim. Acta 65, 2487–2497. https://doi.org/10.1016/S0016-7037(01)00600-7

Schwertmann, U., Cornell, R.M., 2000. Ferrihydrite, in: Iron Oxides in the Laboratory. John Wiley & Sons, Ltd, pp. 103–112. https://doi.org/10.1002/9783527613229.ch08

Seto, M., Yoda, Y., Kikuta, S., Zhang, X.W., Ando, M., 1995. Observation of Nuclear Resonant Scattering Accompanied by Phonon Excitation Using Synchrotron Radiation. Phys. Rev. Lett. 74, 3828–3831. https://doi.org/10.1103/PhysRevLett.74.3828

Severmann, S., Johnson, C.M., Beard, B.L., German, C.R., Edmonds, H.N., Chiba, H., Green, D.R.H., 2004. The effect of plume processes on the Fe isotope composition of hydrothermally derived Fe in the deep ocean as inferred from the Rainbow vent site, Mid-Atlantic Ridge, 36°14′N. Earth Planet. Sci. Lett. 225, 63–76. https://doi.org/10.1016/j.epsl.2004.06.001

Seyfried, W.E., Foustoukos, D.I., Fu, Q., 2007. Redox evolution and mass transfer during serpentinization: An experimental and theoretical study at 200°C, 500bar with implications for ultramafic-hosted hydrothermal systems at Mid-Ocean Ridges. Geochim. Cosmochim. Acta 71, 3872–3886. https://doi.org/10.1016/j.gca.2007.05.015

Skulan, J.L., Beard, B.L., Johnson, C.M., 2002. Kinetic and equilibrium Fe isotope fractionation between aqueous Fe(III) and hematite. Geochim. Cosmochim. Acta 66, 2995–3015. https://doi.org/10.1016/S0016-7037(02)00902-X

Sleep, N.H., Bird, D.K., Pope, E.C., 2011. Serpentinite and the dawn of life. Philos. Trans. R. Soc. B Biol. Sci. 366, 2857–2869. https://doi.org/10.1098/rstb.2011.0129

Sturhahn, W., Toellner, T.S., Alp, E.E., Zhang, X., Ando, M., Yoda, Y., Kikuta, S., Seto, M., Kimball, C.W., Dabrowski, B., 1995. Phonon Density of States Measured by Inelastic Nuclear Resonant Scattering. Phys. Rev. Lett. 74, 3832–3835. https://doi.org/10.1103/PhysRevLett.74.3832

Sumner, D.Y., 1997. Carbonate precipitation and oxygen stratification in late Archean seawater as deduced from facies and stratigraphy of the Gamohaan and Frisco formations, Transvaal Supergroup, South Africa. Am. J. Sci. 297, 455–487. https://doi.org/10.2475/ajs.297.5.455

Swanner, E.D., Bayer, T., Wu, W., Hao, L., Obst, M., Sundman, A., Byrne, J.M., Michel, F.M., Kleinhanns, I.C., Kappler, A., Schoenberg, R., 2017. Iron Isotope Fractionation during Fe(II) Oxidation Mediated by the Oxygen-Producing Marine Cyanobacterium Synechococcus PCC 7002. Environ. Sci. Technol. https://doi.org/10.1021/acs.est.6b05833

Syverson, D.D., Borrok, D.M., Seyfried, W.E., 2013. Experimental determination of equilibrium Fe isotopic fractionation between pyrite and dissolved Fe under hydrothermal conditions. Geochim. Cosmochim. Acta 122, 170–183. https://doi.org/10.1016/j.gca.2013.08.027

Tabata, H., Sekine, Y., Kanzaki, Y., Sugita, S., 2021. An experimental study of photo-oxidation of Fe(II): Implications for the formation of Fe(III) (hydro)oxides on early Mars and Earth. Geochim. Cosmochim. Acta 299, 35–51. https://doi.org/10.1016/j.gca.2021.02.006

Tosca, N.J., Guggenheim, S., Pufahl, P.K., 2016. An authigenic origin for Precambrian greenalite: Implications for iron formation and the chemistry of ancient seawater. Geol. Soc. Am. Bull. 128, 511–530. https://doi.org/10.1130/B31339.1

Tosca, N.J., Jiang, C.Z., Rasmussen, B., Muhling, J., 2019. Products of the iron cycle on the early Earth. Free Radic. Biol. Med., Early Life on Earth and Oxidative Stress 140, 138–153. https://doi.org/10.1016/j.freeradbiomed.2019.05.005

Trendall, A.F., Morris, R.C., 2000. Iron-Formation: Facts and Problems. Elsevier.

Tsikos, H., Matthews, A., Erel, Y., Moore, J.M., 2010. Iron isotopes constrain biogeochemical redox cycling of iron and manganese in a Palaeoproterozoic stratified basin. Earth Planet. Sci. Lett. 298, 125–134. https://doi.org/10.1016/j.epsl.2010.07.032

Tutolo, B.M., Seyfried, W.E., Tosca, N.J., 2020. A seawater throttle on H2 production in Precambrian serpentinizing systems. Proc. Natl. Acad. Sci. https://doi.org/10.1073/pnas.1921042117

van Bürck, U., Siddons, D.P., Hastings, J.B., Bergmann, U., Hollatz, R., 1992. Nuclear forward scattering of synchrotron radiation. Phys. Rev. B 46, 6207–6211. https://doi.org/10.1103/PhysRevB.46.6207

Walker, J.C.G., 1984. Suboxic diagenesis in banded iron formations. Nature 309, 340–342. https://doi.org/10.1038/309340a0

Wang, S.-J., Rudnick, R.L., Gaschnig, R.M., Wang, H., Wasylenki, L.E., 2019. Methanogenesis sustained by sulfide weathering during the Great Oxidation Event. Nat. Geosci. 1. https://doi.org/10.1038/s41561-019-0320-z

Welch, S.A., Beard, B.L., Johnson, C.M., Braterman, P.S., 2003. Kinetic and equilibrium Fe isotope fractionation between aqueous Fe(II) and Fe(III). Geochim. Cosmochim. Acta 67, 4231–4250. https://doi.org/10.1016/S0016-7037(03)00266-7

Wiesli, R.A., Beard, B.L., Johnson, C.M., 2004. Experimental determination of Fe isotope fractionation between aqueous Fe(II), siderite and “green rust” in abiotic systems. Chem. Geol. 211, 343–362. https://doi.org/10.1016/j.chemgeo.2004.07.002

Wordsworth, R., Pierrehumbert, R., 2013. Hydrogen-Nitrogen Greenhouse Warming in Earth’s Early Atmosphere. Science 339, 64–67. https://doi.org/10.1126/science.1225759

Wu, L., Beard, B.L., Roden, E.E., Johnson, C.M., 2011. Stable Iron Isotope Fractionation Between Aqueous Fe(II) and Hydrous Ferric Oxide. Environ. Sci. Technol. 45, 1847–1852. https://doi.org/10.1021/es103171x

Young, E.D., Galy, A., Nagahara, H., 2002. Kinetic and equilibrium mass-dependent isotope fractionation laws in nature and their geochemical and cosmochemical significance. Geochim. Cosmochim. Acta 66, 1095–1104. https://doi.org/10.1016/S0016-7037(01)00832-8

Chapter 6 – Evolution of Volatile Sinks on Mars after 3.5 Billion Years Ago

Foreword

Here in Chapter 6, we explore how planetary surface oxidation, atmospheric escape, and Mars's transition from a planet warm enough to sustain liquid water to its frigid present-day climate state, are all interlinked processes. We specifically investigate the evolution of Martian surface volatile inventories since ~3.5 Ga. This interval of Martian history encompasses essentially the entire Hesperian (3.56 – 3.24 Ga) and Amazonian (3.0 – 0.0 Ga) epochs, and it is interesting for a few reasons. Broadly, the beginning of the Hesperian period marks a major transition in Mars surface conditions recorded by the transition in the mineralogy of aqueous alteration products (Ehlmann and Edwards, 2014; Wordsworth et al., 2021). The Noachian (>3.56 Ga) epoch is characterized by extensive clay mineral (phyllosilicate) formation, consistent with prolonged warm and wet conditions in which protracted water-rock interaction took place (Bibring et al., 2006; Cannon et al., 2017; Ehlmann et al., 2011; Ehlmann and Edwards, 2014; Mustard et al., 2008; Poulet et al., 2005; Sun and Milliken, 2015). The remotely sensed surface record, and the meteorite record both indicate that carbonate mineral formation also took place in Martian crustal rocks during the Noachian epoch (Edwards and Ehlmann, 2015; Niles et al., 2013), whilst post-Noachian carbonate mineral precipitation appears to have been negligible. Formation of carbonate minerals draws down atmospheric CO_2 and thus can be a significant factor in determining planetary climate.

The beginning of the Hesperian coincides with the end of widespread clay mineral and carbonate formation and the onset of evaporite deposition, dominated by sedimentary sulfate minerals (Bibring et al., 2006; Ehlmann and Edwards, 2014). Evaporites are chemical sediments formed when salts precipitate from solution during evaporation, concentration, and saturation of brines. The onset of a global episode in sulfate evaporite deposition is generally accepted to indicate the

transition to an increasingly arid Mars during the Hesperian, coinciding with increasing surficial oxidation, which is required to explain the oxidation of primitive S in crustal sulfides and volcanic volatiles (S^{2-} to S^{4+}) to sulfate (S^{6+}), abundant formations of ferric Fe oxides, and putative oxidation of Mn^{2+} at certain localities of ~3.5 Ga age mapped by the Curiosity and Opportunity rovers (Arvidson et al., 2016; Bibring et al., 2006; Lanza et al., 2016, 2014; Squyres et al., 2006; Wordsworth et al., 2021). We have uniquely detailed insights into the transition in Mars conditions surface at ~3.5 Ga, because this is the approximate age of paleo-lake sediments under intense investigation by the Mars Science Laboratory Curiosity rover at Gale Crater (Grotzinger, 2013). Curiosity's investigation at Gale Crater provides one of the few *in situ* datapoints of Mars surface conditions at a snapshot in time where long-lived lakes were sustainable but global environmental conditions were trending towards increased aridity.

However, despite mineralogical evidence for waning water-rock interaction across the Noachian-Hesperian boundary, the geomorphological record indicates that lakes and river channels continued to form, fed by precipitation and subsequent intense runoff, until well after 3.0 Ga and perhaps until <1 Ga (Kite et al., 2019). Intense runoff and lake formation on Mars from 3.5 Ga to present poses a major climate modeling problem (Kite, 2019). As with solving the Faint Young Sun problem for Earth during the Archean, stable liquid water on Mars at 3.5 Ga requires that there was a strong greenhouse effect provided by a thick CO_2 atmosphere (Ramirez et al., 2014; Ramirez and Kasting, 2017; Urata and Toon, 2013), in addition to smaller quantities of more potent greenhouse gases such as CH_4 and H_2 (which can effect warming by collision-induced absorption of longwave radiation) (Kite et al., 2017; Ramirez et al., 2014; Wordsworth et al., 2017; Wordsworth and Pierrehumbert, 2013). For Mars, constraints on pCO_2 at any given come down to the total available surface inventory of C, rather than the thermodynamic upper limit on carbonate

formation that applies to Earth (Rye et al., 1995), and while other greenhouse C gases like CH_4 could be required for climate solutions, CO_2 is the volumetrically dominant phase we are concerned with when total C availability is at issue. The present-day Martian exchangeable CO_2 reservoir is ~12 mbar pCO_2 equivalent (6 mbar in the current atmosphere, ~6 mbar in shallow ground ice) (Putzig et al., 2018), so in order for pCO_2 (>0.25 bar in the most optimistic climate model with strong warming from clouds; Urata and Toon, 2013) to have been capable of supporting sufficiently elevated global temperatures for stable liquid water at ≤ 3.5 Ga, this CO_2 inventory must have been lost from Mars since that date. The loss of exchangeable CO_2 is a far trickier problem to solve for post-3.5 Ga Mars, because formation of carbonate minerals in the crust, which may have drawn down on the order of 0.5 bar of CO_2, seems to have largely concluded within the Noachian epoch, making this C unavailable to the post-Noachian atmosphere (Edwards and Ehlmann, 2015; Niles et al., 2013). Alternatively, C from a > 0.25 bar pCO_2 post-3.5 Ga atmosphere might have been lost to space. Atmospheric loss from Mars comes dominantly from photochemical escape driven by high energy extreme UV (EUV) radiation from the Sun (Jakosky et al., 2018), the intensity of which decreases over time as stellar rotation slows downs (Ribas et al., 2005; Sanz-Forcada et al., 2011; Tu et al., 2015). So again, this is a loss mechanism for C from Mars's volatile reservoirs which would have been more effective in the Noachian, than in the Hesperian and Amazonian. Loss of the Martian Magnetic field at around 4.0 Ga would have exposed the Martian atmosphere to erosion by the solar wind, the resulting time-integrated C ion loss from Mars is equates to a few mbar of atmospheric pCO_2 (Barabash et al., 2007).

In Chapter 6 we attempt a to put indirect upper limits on the pCO_2 at 3.5 Ga by constraining other Martian volatile sinks processes from that time through to the present. A difficulty in understanding the loss of CO_2 from Mars's surface over time is that modern-day channels of C

escape to space from Mars are either extremely slow (Barabash et al., 2007), or not well characterized in comparison to the escape rates O and H (Cui et al., 2019; Dong et al., 2018; Lillis et al., 2017), the other main constituents of the Martian atmosphere. In the absence of good constraints on C escape from Mars over time, we make use of the independent constraints on H and O loss from Mars since 3.5 Ga, and attempt to distinguish the loss of 'water-associated' O from residual 'CO_2-associated' O, and thus estimate Martian pCO_2 at 3.5 Ga. This approach accounts for C loss by any potential loss channels not considered in the modern Martian C escape flux.

Fortunately, the last decade has brought a wealth of new data on the evolution of the Martian volatile H and O inventories, with both *in situ* from the Curiosity rover, and with measurements of globally-integrated atomic and ionic escape rates from the top of the atmosphere, measured by the Mars Atmosphere and Volatile EvolutioN (MAVEN) probe currently orbiting Mars. Our understanding of the hydrosphere benefits immeasurably from access to *in situ* H isotope ratio (D/H) from both ancient sediments that sample the 3.5 billion-year-old hydrosphere, and the modern atmosphere, on Mars (Mahaffy et al., 2015; Webster et al., 2013). Enrichment in D/H occurs due to the preferential escape of lighter H atoms to space, relative to more massive D atoms, and can be used to estimate the planetary loss rate of H, and thus quantify the drying of Mars, over time (Krasnopolsky, 2015; Kurokawa et al., 2014), with the caveat that non-fractionating shrinkage of the hydrosphere due to irreversible crustal hydration may have also occurred on a significant scale (Scheller et al., 2021).

Meanwhile, extrapolating state-of-the-art O escape rate data from MAVEN back through time by modeling the evolution of solar EUV fluxes allows us to estimate O loss from the surface volatile inventory (Jakosky et al., 2018; Lillis et al., 2017). A full accounting of Mars's volatile inventory

cannot ignore other sinks of O, notably the O that is involved in the net oxidation of the planet's surface driven by the overwhelmingly preferential escape of H (Wordsworth et al., 2021). Therefore, in Chapter 6 we also produce, to our knowledge, the most complete accounting to date of post-3.5 Ga oxidized Fe and S sinks in the Martian crust. As is described in detail below, our eventual calculated range in Hesperian pCO_2 leads us to ask new questions about our current assumptions for Martian history.

If we briefly zoom out away from Mars, and put this study in the context of what has come earlier in this thesis, we can see that the evolution of Mars's volatile inventories provides a stark and useful contrast with how some of the same processes have affected Earth's surface over the same span of time. On Earth, H escape to space, coupled with oxidation of Fe and S at the planet's surface (Catling et al., 2001), provided a useful and unidirectional drive towards saturation of surface redox buffers, setting the stage for the rise of atmospheric oxygen when a critical threshold was reached (Lyons et al., 2014). However, these same processes represent an irretrievable loss of the planetary hydrosphere, creating a trade-off in their implications for long-term planetary habitability that can play out quite differently on an already-arid world, compared to one with long-lived global oceans.

The content of this chapter is the accepted article for the publication:

Andy W. Heard, Edwin S. Kite, "A probabilistic case for a large missing carbon sink on Mars after 3.5 billion years ago", Earth and Planetary Science Letters, Volume 531, 2020, 116001, ISSN 0012-821X, https://doi.org/10.1016/j.epsl.2019.116001

A Probabilistic Case For A Large Missing Carbon Sink On Mars After 3.5 Billion Years Ago

Abstract

Mars has a thin (6 mbar) CO_2 atmosphere currently. There is strong evidence for paleolakes and rivers formed by warm climates on Mars, including after 3.5 billion years (Ga) ago, which indicates that a CO_2 atmosphere thick enough to permit a warm climate was present at these times. Since Mars no longer has a thick CO_2 atmosphere, it must have been lost. One possibility is that Martian CO_2 was lost to space. Oxygen escape rates from Mars are high enough to account for loss of a thick CO_2 atmosphere, if CO_2 was the main source of escaping O. But here, using H isotope ratios, O escape calculations, and quantification of the surface O sinks on Mars, we show for the first time that O escape from Mars after 3.5 Ga must have been predominantly associated with the loss of H_2O, not CO_2, and therefore it is unlikely that ≥250 mbar Martian CO_2 has been lost to space in the last 3.5 Ga, because such results require highly unfavored O loss scenarios. It is possible that the presence of young rivers and lakes on Mars could be reconciled with limited CO_2 loss to space if crater chronologies on Mars are sufficiently incorrect that all apparently young rivers and lakes are actually older than 3.5 Ga, or if climate solutions exist for sustained runoff on Mars with atmospheric CO_2 pressure <250 mbar. However, our preferred solution to reconcile the presence of <3.5 Gya rivers and lakes on Mars with the limited potential for CO_2 loss to space is a large, as yet undiscovered, geological C sink on Mars.

1. Introduction

Changes in Mars' carbon dioxide (CO_2) and water (H_2O) inventories are key unknowns in understanding the planet's climate evolution, and constraining these changes requires knowledge of Martian historical volatile sinks (Figure 6.1; Catling and Kasting, 2017; Jakosky and Phillips, 2001). The Late Hesperian-Amazonian (Kite et al., 2019; see Table 6.1 for a summary of Martian epoch dates) poses a particular challenge for Mars' CO_2 evolution. Post-3.5 Ga ago river channels and lakes indicate significant flowing water, and thus sufficient CO_2 to permit a climate warm enough for water to flow (e.g. Dickson et al., 2009; Grant and Wilson, 2012; Irwin III et al., 2015; Kite, 2019; Kite et al., 2019; Palucis et al., 2016); but the currently postulated $\geq$0.25 bar CO_2 atmospheres required sustained to warm climates (Haberle et al., 2017; Kite, 2019; Mansfield et al., 2018; Ramirez et al., 2014; Urata and Toon, 2013; Wordsworth, 2016), greatly exceed the current exchangeable inventory of 12 mbar (6 mbar in atmosphere + 6 mbar in ice caps; Putzig et al., 2018) CO_2. A lot of CO_2 must have been lost from Mars's atmosphere somehow.

The possible CO_2 sinks for Mars are gradual escape to space, either as CO_2, CO_2^+, or the constituent C and O atoms; or fixing of C in the Martian (sub)surface as carbonates, clathrates, or ices. After 3.5 Ga, impact erosion of the atmosphere should no longer be significant. Some of these sinks for CO_2 on late Hesperian-Amazonian Mars are demonstrably too small. Only a few mbar of CO_2 can be accounted for by 3.5 Ga-integrated CO_2^+ loss to space (Dong et al., 2018; Ramstad et al., 2018), and known post-Noachian carbonate sequestration was very limited in extent (Edwards and Ehlmann, 2015; Niles et al., 2013). However, the potential for loss of CO_2 to space as its constituent atoms is supported by significant modern-day escape of O from Mars, which has been measured by the Mars Atmosphere and Volatile EvolutioN (MAVEN) mission (Jakosky et al., 2018; Lillis et al., 2017). Furthermore, this Martian atmospheric O loss can be extrapolated to

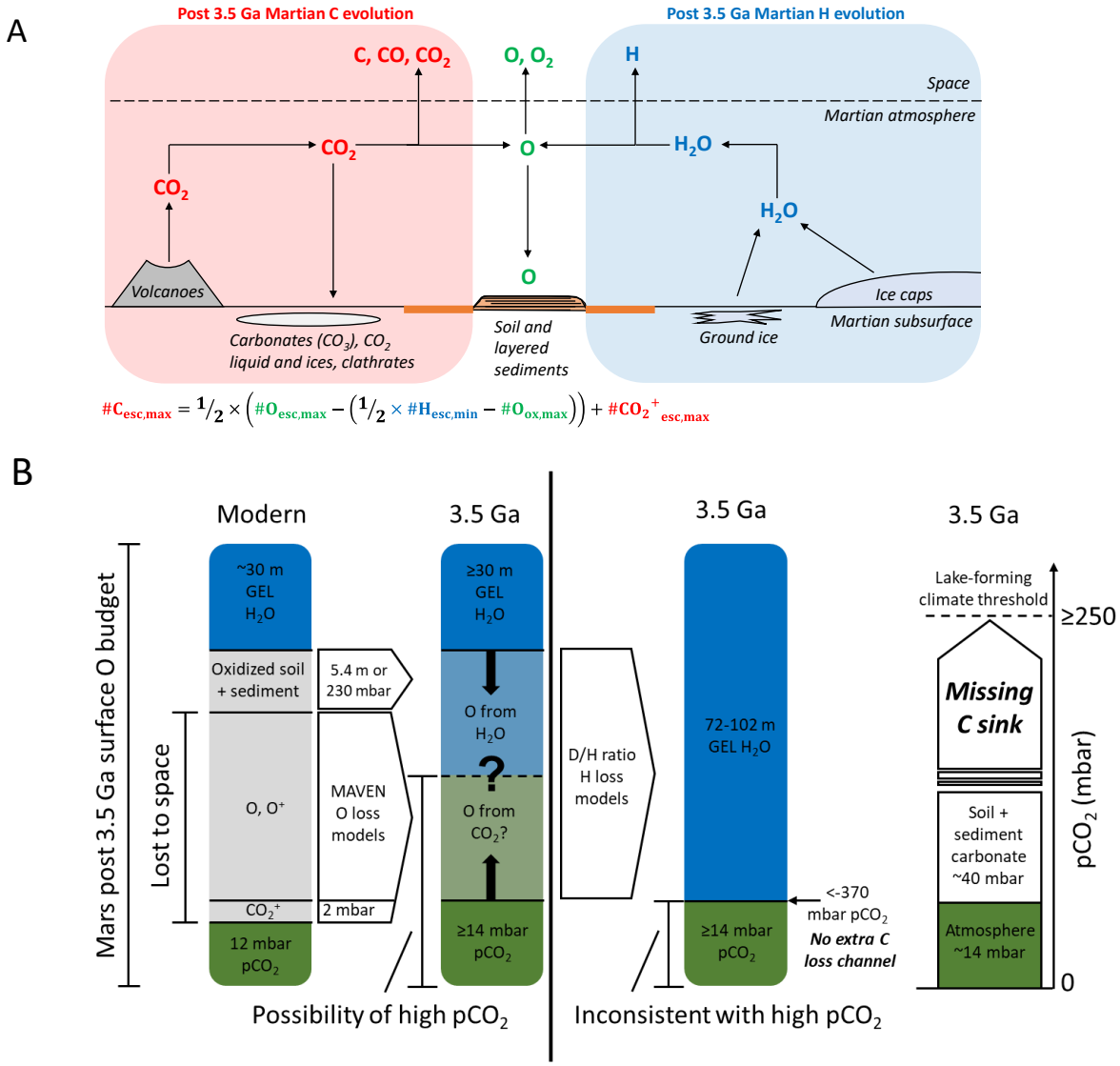

Figure 6.1 – A.) Sketch of Martian H, C, and O fluxes considered in our study. C species can also be lost to space, either as CO_2 molecules or as constituent C, O, and CO. Atmospheric CO_2 might be sequestered into (sub)surface carbonates, CO_2 liquids and ices, and clathrates. Atmospheric H_2O is sourced from polar caps and ground ice, and H and O can be lost to space. Both CO_2- and H_2O-derived O not lost to space can be sequestered in soils and layered sedimentary rocks during oxidative weathering processes, principally through interactions with reduced Fe and S species. B.) Graphical summary of the modelling approach and relative sizes of various O sinks as identified in our study. The heavy black vertical line separates the state of knowledge before this study (to the left), from the stronger constraint placed on pCO_2 by considering the D/H constraint on H_2O loss, to the right.

higher rates in the past using estimates of the Sun's evolving radiative flux and stellar wind, which provides energy for atmospheric escape to space. Since O is a very minor constituent of Mars'

atmosphere, this O must be ultimately sourced from CO_2 or H_2O. There is degeneracy to the problem of O escape in that escaping O may ultimately derive from either CO_2 or H_2O (Jakosky et al. 2018). Modern loss rate ratios for H:O are consistent with ≈2:1 and suggest that at present, most O being lost from Mars derives from H_2O (Jakosky et al., 2018). It is highly uncertain whether this coupling has held at a constant value over geological timescales, or even whether it holds on year-to-year dust storm-influenced or 11-year Solar cycle-influenced timescales (Jakosky et al., 2018). Meanwhile, the fraction of H_2O- or CO_2-derived O that went into oxidation of soil and sediments rather than escaping to space (Lammer et al., 2003) is not well constrained. These uncertainties leave the possibility that a large portion of the historical O loss flux corresponds to CO_2, which would imply a major loss-to-space channel for C or CO (ions or neutrals) was active on Mars after 3.5 Ga ago.

Table 6.1. Ages of Martian epoch boundaries

Epoch	Start of epoch (Ga)
Late Amazonian	0.274
Middle Amazonian	1.03
Early Amazonian	3.24
Late Hesperian	3.39
Early Hesperian	3.56
Late Noachian	3.85
Middle Noachian	3.96
Early Noachian	N/A

Chronology data after (Michael, 2013), making use of the 'Hartmann 2004' iteration in that study.

Complementing the new constraints on O loss from Mars that MAVEN provides, new constraints on Mars's H loss history come from recent hydrogen isotope ratio (D/H) data. The Mars Science Laboratory (MSL) mission's Curiosity Rover has provided modern and ancient (≈ 3.5 Ga) datapoints for Martian D/H in the modern atmosphere (Webster et al., 2013; Villanueva et al., 2015) and ancient hydrosphere (Mahaffy et al., 2015). The ancient D/H measurement is from a lacustrine mudstone, and therefore samples the hydrosphere at a time when lakes were present (Mahaffy et al., 2015). D/H data show that the Martian H reservoir has become isotopically heavier over time, which implies the preferential loss of isotopically lighter H to space over time, with a greater change in D/H implicating more severe loss of H (Usui 2019). These observations can be used to estimate historical H loss from Mars after 3.5 Ga ago. In this way, the rover data bypasses the uncertainty in whether or not MAVEN-era H escape is representative of H escape over 11-year and longer (geological) timescales.

Finally, better maps of Mars's post-3.5 Ga sedimentary deposits (Michalski and Niles, 2012), and better estimates of the true regolith depth on Mars (Warner et al., 2017), make it easier to quantify the sedimentary O sink.

We ask if the three independent datasets; on O escape, D/H evolution, and the soil and sedimentary reservoir; reveal C escape from Mars over the last 3.5 Ga at a sufficient rate to account for the loss of a ≥250 mbar CO_2 atmosphere. In this work we combine constraints on O and H loss from Mars to extract the O loss corresponding to CO_2 (Figure 6.1). Then, we use an error-propagation approach to determine upper limits on 3.5 Ga pCO_2 allowed by plausible O-loss and hydrosphere evolution scenarios (Figure 6.1b). Our model includes an improved accounting for post-3.5 Ga soil and sedimentary oxidative O sinks. We describe the model approach and input parameters in Section 2. We present model results in Section 3. We discuss the model results and their

implications in Section 4. Section 5 contains our conclusions. Our main results are shown in Figures 6.2, 6.3, 6.4 and 6.6.

2. Model Description

2.1. Extracting CO_2 loss from O and H constraints

The expression for the upper limit of CO_2-derived C atoms escaped from Mars to space is

$$\#\mathrm{C}_{\mathrm{esc,max}} = {}^{1}/_{2} \times \left(\#\mathrm{O}_{\mathrm{esc,max}} - \left({}^{1}/_{2} \times \#\mathrm{H}_{\mathrm{esc,min}} - \#\mathrm{O}_{\mathrm{ox,max}}\right)\right) + \#{\mathrm{CO}_2}^{+}{}_{\mathrm{esc,max}} \qquad (1)$$

where #C, #O, and #H, and $\#CO_2^+$ are the number of C, O and H atoms and CO_2^+ ions that are lost from the Martian hydrosphere-atmosphere system through escape to space, or oxidation of surficial rock reservoirs, denoted by the subscripts $_{esc}$, and $_{ox}$, respectively (Figure 6.1). The expression dictates that the maximum CO_2-derived C lost to space over a given time interval is half (due to the stoichiometry of CO_2) of the amount of O escaping over that time interval that cannot be attributed to escape of H_2O-derived O. The loss of H_2O-derived O is independently constrained by the escape of H atoms determined from D/H evolution on Mars, while accounting for the fraction of O which was sequestered in Martian soil and layered sedimentary deposits by oxidation (Figure 6.1). The expression above does not account for sequestration of CO_2 in Mars's crust but such additional sinks are also considered in our discussion. We also do not consider the additional sinks for Martian water that we consider unlikely to be strongly fractionating for H isotopes. For example, crustal hydration reactions such as clay mineral formation could constitute a major sink for Martian water (Wernicke and Jakosky, 2019), but clay mineral formation would not cause a several-times enrichment in D in the residual Martian hydrosphere (e.g. Liu and Epstein, 1984). Furthermore, clay mineral formation at the scale likely to influence the Martian planetary water budget predates the 3.5 Ga start of our model and was largely restricted to the Noachian (Ehlmann

et al., 2011; Ehlmann and Edwards, 2014). Our parameterization of H escape to space is done solely to identify the water-associated loss of O from Mars since 3.5 Ga and we do not intend this work to be a complete accounting of Martian hydrological evolution.

Our model assumes a unidirectional decline of Martian pCO_2 as a result of sink processes operating after 3.5 Ga. We do not rule out a later introduction for some of the CO_2 lost on Mars after 3.5 Ga; but including it in our model could only strengthen our upper limits on post-3.5 Ga pCO_2 on Mars. If later outgassing occurred, this CO_2 was subsequently lost from known exchangeable reservoirs on Mars, in addition to the CO_2 that was present at 3.5 Ga. Moreover, later-outgassed CO_2 was vulnerable to sink processes for a shorter duration and must still be drawn down to 12 mbar equivalent present-day exchangeable CO_2 (Putzig et al., 2018). This places a greater demand on sink processes. In the case of escape to space, we expect any loss fluxes to be attenuating towards the present.

2.2. Oxygen loss to space

Our new approach to inferring post-3.5 Ga ago pCO_2 is made timely in part by new constraints on O loss from Mars to space provided by MAVEN measurements. Loss of O to space occurs through several loss channels, separable into photochemical escape of hot O atoms following sputtering by solar wind; pickup ion loss; and dissociative recombination (Dong et al., 2018; Jakosky et al., 2018). Dissociative recombination was recently confirmed to be the dominant modern escape route for O (Jakosky et al., 2018). The approach to calculating the integrated effect of dissociative recombination over 3.5 Ga is detailed below. Our calculations of O loss to space were performed following the approach of Lillis et al. (2017) for the main dissociative recombination loss channel, and the parameterizations of Jakosky et al. (2018) for the other loss channels of pickup O^+ ion loss,

O sputtering, and ionospheric O^+ outflow. The details of these calculations are provided in the Appendix, including a discussion of the solar extreme ultraviolet (EUV) evolution that drove dissociative recombination, and a discussion of the uncertainty on various input parameters for this calculation.

2.3. CO_2 ion loss

Carbon dioxide can escape Mars directly as CO_2^+ ions. Early results from the Mars Express mission indicated a loss rate of 8 x 10^{22} CO_2^+ s^{-1} (Barabash et al., 2007). This number has subsequently been revised upward with MAVEN data to 3.6 x 10^{23} CO_2^+ s^{-1} (Dong et al., 2018; Ramstad et al., 2018). In this study, the modelled CO_2^+ loss history from Dong et al. (2018) is used as published. This loss channel is included for completeness but loss since 3.5 Ga is ≈ 2-6 mbar and therefore is not a strong control on overall results (Dong et al., 2018; Ramstad et al., 2018).

2.4. Surface oxygen sinks

Some oxygen which initially resided in the Martian hydrosphere (H_2O), or atmosphere (H_2O, CO_2), now resides in chemically weathered rocks near Mars's surface. Indeed, aqueous minerals, many of them oxidized, formed in abundance before 3.5 Ga ago (Ehlmann and Edwards, 2014). However, the present study is concerned only with oxidative alteration that occurred after 3.5 Ga ago. In this epoch, the main surficial O sinks are layered sedimentary deposits, including dust deposits lying within polar and low latitude glacial deposits; and soil. The list of deposits, their estimated mass, and the sequestered oxygen they represent, is given in the Appendix, Table 6.4.

The reactions considered are (1) the oxidation of ferrous iron (Fe^{2+}) in igneous materials to ferric iron (Fe^{3+}) in hematite, goethite, nanophase iron oxide phases etc.; and (2) oxidation of sulfur

species; primarily SO_2 and H_2S volatiles but potentially also igneous crustal sulfides and sedimentary sulfite; to sulfate (SO_3). The Fe^{2+} oxidation reaction consumes 0.5 moles of O per mole of Fe. The sulfur oxidation reactions require 1 mole and 4 moles of O per mole of S to oxidize SO_2 and H_2S, respectively. Both Fe and S may either be oxidized directly by oxygen liberated by photolysis in the atmosphere, or via UV-promoted photo-oxidation reactions that derive the oxygen in the stable reaction products from hydrolysis of water (Hurowitz et al., 2010). Large quantities of sulfur volatiles erupted to the Martian surface in the Late Hesperian, and some of the largest late-formed layered sedimentary deposits on Mars have a high sulfur content relative to the Martian crust and appear to derive their S from volcanic outgassing (Michalski and Niles, 2012). Because volcanically erupted S-volatiles are piped directly into the oxidizing surface environment, and S has greater reducing power per mole, sulfur provides a major O sink despite being a minor constituent of the bulk Martian crust relative to Fe. Surface oxygen sinks are assessed assuming a ferric iron content of typical Martian soils (Morris et al., 2006). We adopt SO_3 (sulfate in rock) content of 20 wt%, following Michalski and Niles (2012), which they assess to be a representative composition of layered sedimentary deposits, which volumetrically dominate over the global soil layer. We assume that the initial speciation of sulfur volatiles now residing in sulfate was 50% SO_2, 50% H_2S, consistent with the more reducing redox state of the Martian mantle relative to Earth's (e.g. Halevy et al., 2007). We calculate that the total soil and layered sedimentary oxidative O sink is $\approx 4.3 \times 10^{19}$ moles of O, which is equivalent to a 242 mbar pCO_2 drawdown (Table 6.2; Appendix, Table 6.4).

2.5. D/H ratio constraint on post 3.5 Ga water loss

Hydrogen isotope (D/H) ratios track Martian hydrosphere evolution independent of constraints from O loss (Jakosky, 1991; Mahaffy et al., 2015). Hydrogen is preferentially lost relative to heavier deuterium during atmospheric escape. Therefore, progressive Martian D/H enrichment over time can track loss of the Martian hydrosphere. The relative size of exchangeable (surface water and exchangeable ground ice) water reservoirs at two points in time (R_{t1}, R_{t2}) relate to the D/H ratio through time (I_{t2}, I_{t2}) through the expression

$$\frac{R_{t1}}{R_{t2}} = \left(\frac{I_{t2}}{I_{t1}}\right)^{\frac{1}{1-f}} \quad (2)$$

Where f is the fractionation factor, and t2 refers to a time after t1 (Kurokawa et al., 2014). In this study, t1 refers to 3.5 Ga, and t2 refers to present day. The values for parameters used in this model are listed in Table 6.2. Accurate assessment of Martian water loss ($R_{t2} - R_{t1}$) requires constraints on the modern water reservoir, modern and ancient D/H ratios, and a reasonable value for f, defined by the expression

$$f = \frac{\Delta[D]/[D]}{\Delta[H]/[H]} \quad (3)$$

Where [D] and [H] are the atomic abundances of D and H respectively in the hydrosphere (Kurokawa et al., 2014). A smaller value for f gives greater preferential loss of H relative to D. The net fractionation factor for H escape f is the product ($f = f_a \times f_{esc}$) of fractionation between H_2O and H_2, with $f_a = 0.41$; and the effect of different escape rates for H and D, f_{esc}. Modern Mars has f = 0.016, which gives the most strongly fractionating regime for hydrogen escape that we expect; however, this corresponds to nonthermal escape processes not thought to dominate on early Mars (Krasnopolsky et al., 1998; Kurokawa et al., 2016). On ancient Mars, a more likely lower limit on f is given by the Jeans escape-limited case, where the escape step has $f_{Jeans} \approx 0.26$, resulting in a net fractionation factor f = 0.105 (Kurokawa et al., 2016). On early Mars, enhanced UV

radiation could make thermal escape to space efficient enough that all H and D atoms escape the exobase, such that the process is non-fractionating. Here, H loss would be limited by diffusion of H from the homopause to the exobase. In this diffusion-limited regime, the diffusion step has f_{diff} ≈ 0.70-0.81, resulting in a maximum net fractionation factor f = 0.33 (Kurokawa et al., 2016). More fractionating escape (lower f) implies less water loss, and thus a smaller share of historical O loss that must be attributed to water, which may instead be attributed to CO_2 (Figure 6.1). Therefore, for estimating upper limit paleo-pCO_2, water escape is modeled here with a full range of f values extending to the most fractionating possible value of 0.016. The upper limit on f is 0.33 for diffusion-limited escape. A uniform distribution of f values is assumed between these values (Table 6.2). We adopt a uniform distribution because we think that the true average value for f is relatively large for the escaped-to-space H reservoir. This is an appropriate assumption because strong solar UV early in Martian history would favor diffusion-limited H escape, at a time when the hydrosphere was largest and thus when most H escape was occurring.

The size of the modern water reservoir on Mars, R_{t2}, is given as global equivalent layer of water (GEL) in units of meters (m); the liquid water depth if the reservoir were evenly distributed across the Martian surface. Carr and Head (2015) estimate of R_{t2} = 34 m GEL; comprised of 22 m inferred volume shared between polar ice deposits, ≥7 m of ground ice between 50-60° latitude, and <2.6 m of shallow buried ice between 30-60° latitude. The selection by Carr and Head (2015) of 34 m GEL total exceeds the strict sum to ≈ 31.5 m GEL of the above values. An overestimation of R_{t2} propagates to an overestimation of R_{t1} and thus water loss. We use R_{t2} = 31.5 ± 1.25 (1σ) m GEL to encompass the Carr and Head (2015) value, as well as lower estimates of 29 m if shallow buried ice is negligible (Table 6.2).

Table 6.2. List of input parameters for Mars 3.5 Gyr volatile evolution model described by Equation 1

Parameter	Symbol	Value	Distribution in range
Modern dissociative recombination O loss (atoms/sec)	$R_{present}$	$4.3^{+5.2}_{-2.3}$ x 10^{25} $(1\sigma)^{(1)}$	Log-normal
Solar EUV evolution exponent	β_{rot}	$1.22^{+0.96}_{-0.26}$ (10^{th}, 90^{th} percentiles)$^{(2)}$	Half normal about mean
	β_{lum}	1.24 ± 0.14 $(1\sigma)^{(3)}$	Normal
EUV flux dependence exponent	$\gamma_{2.64}$	2.64 ± 0.60 $(1\sigma)^{(1)}$	Normal
	$\gamma_{1.7}$	1.70 ± 0.39 $(1\sigma)^{(4)}$	Normal
	$\gamma_{1.0}$	1.0 ± 0.23 $(1\sigma)^{(5)}$	Normal
Martian 3.5 Ga D/H, in situ mudstone	I_{t1}	3.0 ± 0.2 x SMOW $(2\sigma)^{(6)}$	Normal
Martian modern D/H, in situ	I_{t2}	6.0 ± 1 x SMOW $(2\sigma)^{(7)}$	Normal
Martian modern D/H, global		8.0 ± 1 x SMOW $(2\sigma)^{(8*)}$	Normal
Fractionation factor	F	0.016-$0.33^{(9)}$	Uniform
Martian modern H_2O GEL (m)	R_{t2}	31.5 ± 1.25 $(2\sigma)^{(10)}$	Normal

Table 6.2. continued

Martian modern exchangeable CO_2 (mbar)	$pCO_{2(modern)}$	12[11]	N/A
Martian post 3.5 Ga soil and sediment O sink	O_{soil}	242 mbar pCO_2 equivalent/5.34 m GEL H_2O[12]	N/A
3.5 Ga total CO_2^+ loss	$\#CO_2^+{}_{esc}$	2.1 mbar pCO_2 equivalent[13]	N/A

[1]Lillis et al. (2017)

[2]Tu et al. (2015), stellar rotational modeling, uncertainties as two half-normal distributions about mean

[3]Sanz-Forcada et al. (2011), fit to X-ray luminosity observations

[4]R. J. Lillis, personal communication. Fractional error in exponent assumed same as [1]

[5]Cravens et al. (2018). Proportional error assumed same as [1]

[6]Mahaffy et al. (2015)

[7]Webster et al. (2013)

[8]Villanueva et al. (2015), error bars assumed same as [6]

[9]Kurokawa et al. (2016), uniform distribution within range assumed

[10]Carr and Head (2015), error bars assigned based on upper and lower limits described

[11]Putzig et al. (2018), accounts for seasonal CO_2 ice deposits and atmospheric reservoir

[12]Held fixed at estimated value from Appendix, Table 6.4

[13]Dong et al. (2018)

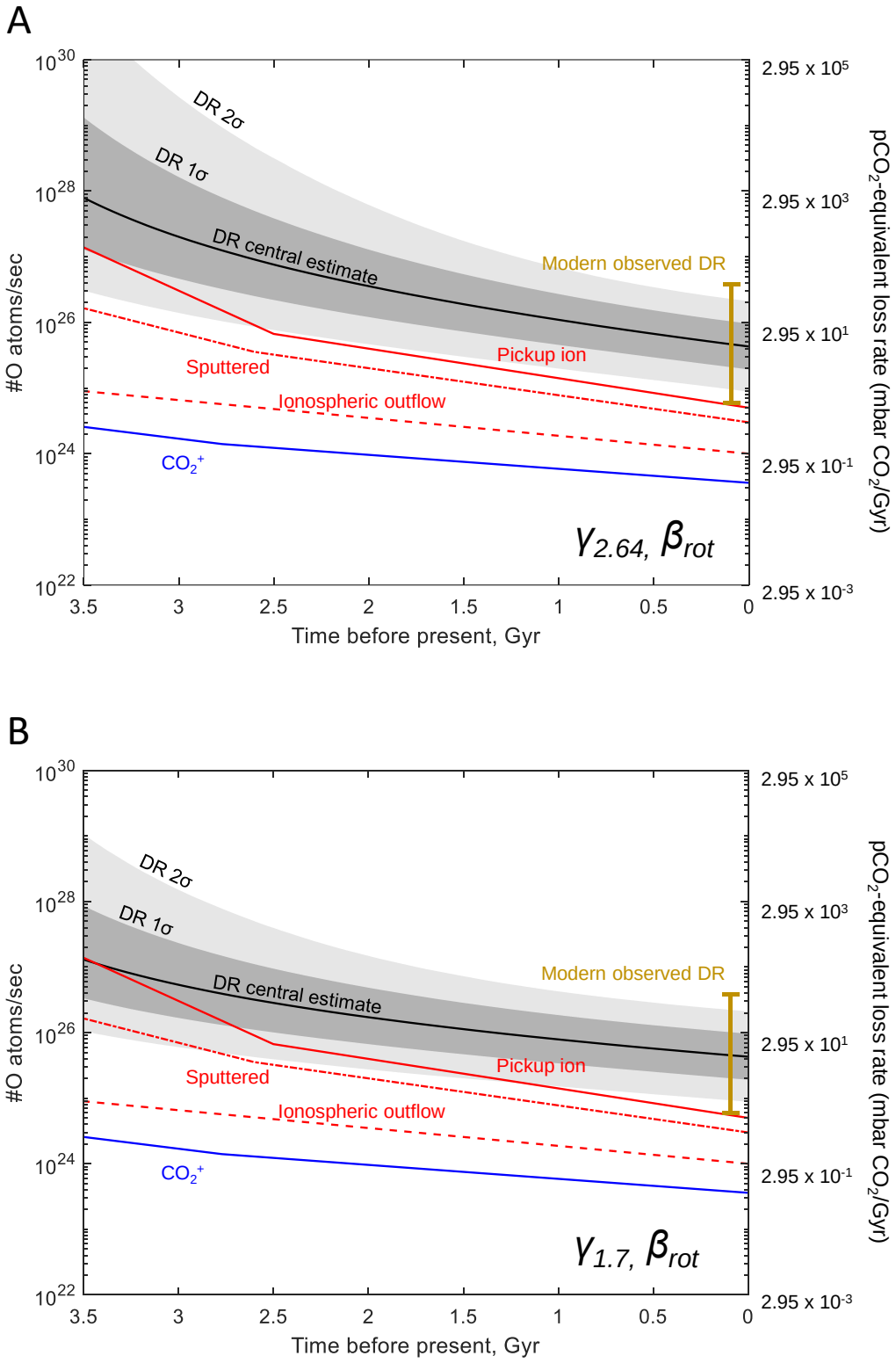

Figure 6.2. Martian oxygen loss over time

Figure 6.2. continued

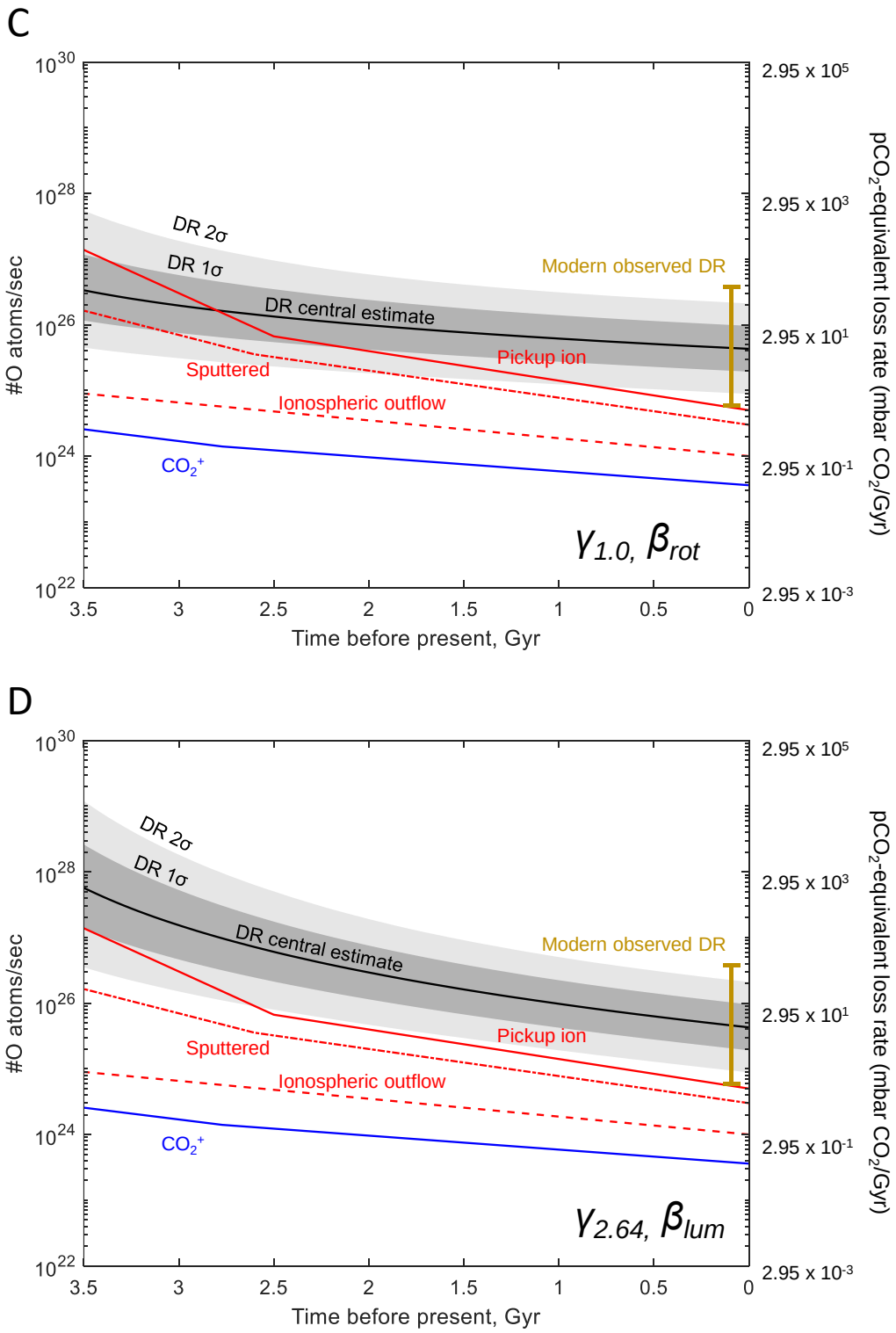

Figure 6.2. continued

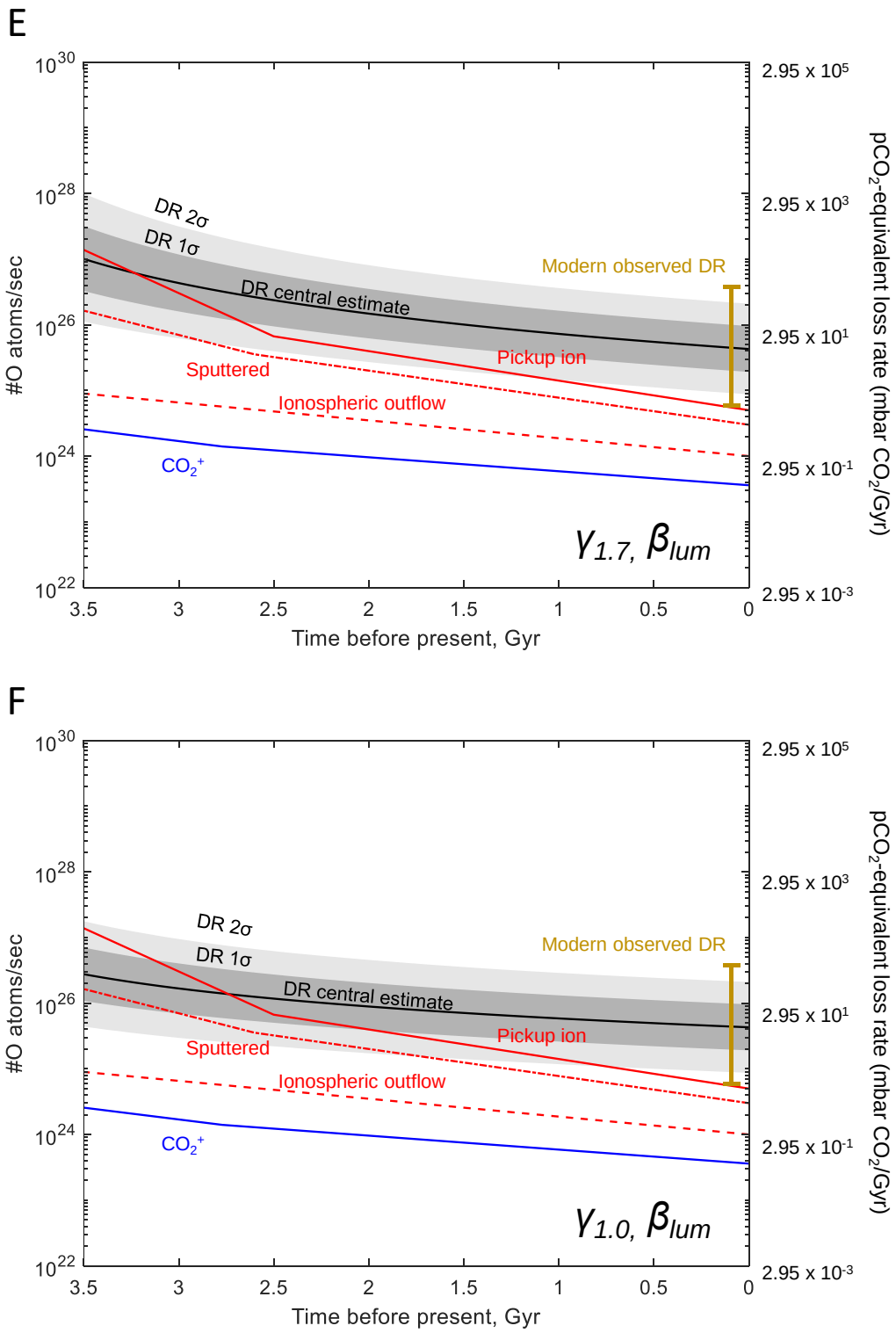

Figure 6.2 continued. Martian oxygen loss over time for different EUV flux dependence ($\gamma_{2.64}$, $\gamma_{1.7}$, $\gamma_{1.0}$) and solar EUV evolution (β_{rot}, β_{lum}) scenarios. A.) $\gamma_{2.64}$, β_{rot}; B.) $\gamma_{1.7}$, β_{rot}; C.) $\gamma_{1.0}$, β_{rot}; D.) $\gamma_{2.64}$, β_{lum}; E.) $\gamma_{1.7}$, β_{lum}; F.) $\gamma_{1.0}$, β_{lum}. Refer to Table 6.2 and Appendix Equations A1 and A2, for these parameter values and sources. The heavy black line shows the evolution of the dissociative recombination (DR) loss flux: dark and light grey shaded areas constrain the 1σ and 2σ uncertainty envelope on this flux, respectively. The red solid, dot-dashed, and dashed lines show the loss fluxes of pickup O^+ ions, sputtered O atoms, and O^+ ionospheric outflow, respectively. Functional forms follow Chassefière et al., (2013), adjusted to fit updated modern loss fluxes recorded by MAVEN (Jakosky et al., 2018). The blue solid line shows the CO_2^+ ion loss channel, modeled following Dong et al., (2018). The orange bar indicates the full range of observed hot O (dissociative recombination) loss rates inferred over Mars observational history, spanning 5 x 10^{24} – 4 x 10^{26} atoms/s. The right-hand axis shows the loss rates in pCO_2 equivalents in mbar/Gyr.

The value of I_{t1} comes from measurements of D/H in clay mineral-bound water in 3.5 Ga Yellowknife Bay mudstone (Mahaffy et al., 2015), with a value of (3.0 ± 0.2, 2σ) x SMOW, where SMOW is the D/H ratio of terrestrial Standard Mean Ocean Water (D/H_{SMOW} = 1.558 x 10^{-4}). Modern D/H ratios on Mars vary significantly depending on the measurement technique applied. A measurement of Martian atmospheric D/H at Gale Crater made with the Tunable Laser Spectrometer (TLS) onboard the Curiosity Rover gave I_{t2} = (6 ± 1, 2σ) x SMOW (Webster et al., 2013), consistent with D/H measurements of young indigenous water in Martian meteorites (Greenwood et al., 2008). However, globally averaged measurements of Mars made with spectrometers at Earth-based observatories estimate 7 x SMOW for typical Martian atmosphere, resulting in an inferred D/H ≈ 8 x SMOW for the ice reservoirs where most Martian water resides (Villanueva et al., 2015). Discrepant estimates for I_{t2} propagate to tens of m GEL differences in 3.5 Gyr water loss, or hundreds of mbar CO_2-equivalent O loss; thus these differences are important. Direct measurement of D/H in Mars ice by a polar-cap lander could remove this uncertainty (Vos et al., 2019). We run models with both I_{t2} estimates and compare the resulting effects on paleo-pCO_2 estimates (Table 6.3; Figures 6.3, 6.4,). Villanueva et al. (2015) do not

report an analytical uncertainty for their estimate, so here the range (8.0 ± 1.0, 2σ) x SMOW is applied to compare on equal terms with Webster et al. (2013).

The H loss model in Equation 2 prescribes a single Martian water reservoir that exchanges with the atmosphere rapidly relative to timescales of atmospheric loss. However, alternative H escape models exist to explain intermediate-D/H components in the bound water of SNC meteorites (e.g. Kurokawa et al., 2016). The alternative models invoke an 'unexchangeable' buried ice reservoir which cannot interact directly with the atmosphere, but does supply the exchangeable surface hydrosphere/cryosphere on Mars. Because the surface exchangeable reservoir is constantly supplied with comparatively low-D/H water throughout atmospheric escape, such models generally require greater total water loss to satisfy a given modern D/H constraint. In a similar manner, late (post 3.5 Ga) degassing of juvenile, unfractionated Martian water to the surface would act to buffer the D/H evolution of the hydrosphere (e.g. see Alsaeed and Jakosky, 2019), essentially creating the need for even greater H loss to match D/H data, in only a fraction of the time after 3.5 Ga and thus under weaker solar forcing for escape processes. Moreover, as stated above, we do not consider additional sinks of water that we expect to be unfractionating. Therefore, without ruling on the plausibility of any of these more complex models for Martian hydrospheric evolution, they are not included in this study because it would imply a significantly greater O loss fraction that must be attributed to water loss, and thus act to drive down paleo-pCO_2 estimates (Figure 6.1), only strengthening our upper limit on post-3.5 Ga pCO_2.

2.6. Integrated model

Post 3.5 Ga Martian volatile histories were modeled in a Monte Carlo simulation run in MATLAB. Input parameters and their uncertainty distributions are given in Table 6.2. Dissociative

recombination rates through time (Appendix) were calculated 10^5 times from parameters randomly generated within the uncertainty distributions of the input parameters, and total O loss rates through time for each simulation were calculated as the sum of a given dissociative recombination history and the functions for ion and sputtering loss. Total 3.5 Ga O loss was determined by discrete numerical integration with 1 Myr time steps. The results of O loss scenarios through time for different γ (solar EUV dependence of O loss, see Appendix) and β (solar EUV devolution parameter, see Appendix) ranges are shown with uncertainty distributions for dissociative recombination in Figure 6.2.

D/H evolution scenarios were also modelled in a Monte Carlo simulation, with input parameters and their uncertainty distributions given in Table 6.2. Post-3.5 Ga water loss was calculated by rearranging Equation 6 to give R_{t1}, and subtracting R_{t2} from the result. Resulting model distributions for lost water for the local MSL and global telescope-based measurement for I_{t2} are shown in Figure 6.3. Results were converted to H atom equivalents and combined with O loss results and oxidative sink estimates, in Equation 1, to generate a large number of post-3.5 Ga C (CO_2) loss histories. These output distributions were added to integrated CO_2^+ ion loss, and the modern atmospheric CO_2 reservoirs (6 mbar in atmosphere, 6 mbar in CO_2 ice; Putzig et al., 2018) to give probability distributions for 3.5 Ga Martian paleo-pCO_2.

The pCO_2 values we calculate by applying Equation 1 can take negative or positive values, because total O loss is calculated by integrating the extrapolated model O loss rate backwards in time, and the O loss model is independent of sedimentary O sink and D/H ratio H loss constraints. Negative 3.5 Ga ago pCO_2 outputs of our models should not, therefore, be taken to indicate that there was a net source of CO_2 to Mars since that time. Rather, negative 3.5 Ga ago pCO_2 estimates in our models would indicate that all sinks for O are required to balance H loss to space implied by D/H

evolution. In these cases, negligible loss of CO_2 would be allowed, such that loss to space would not account for the depletion of a thicker CO_2 atmosphere in the past.

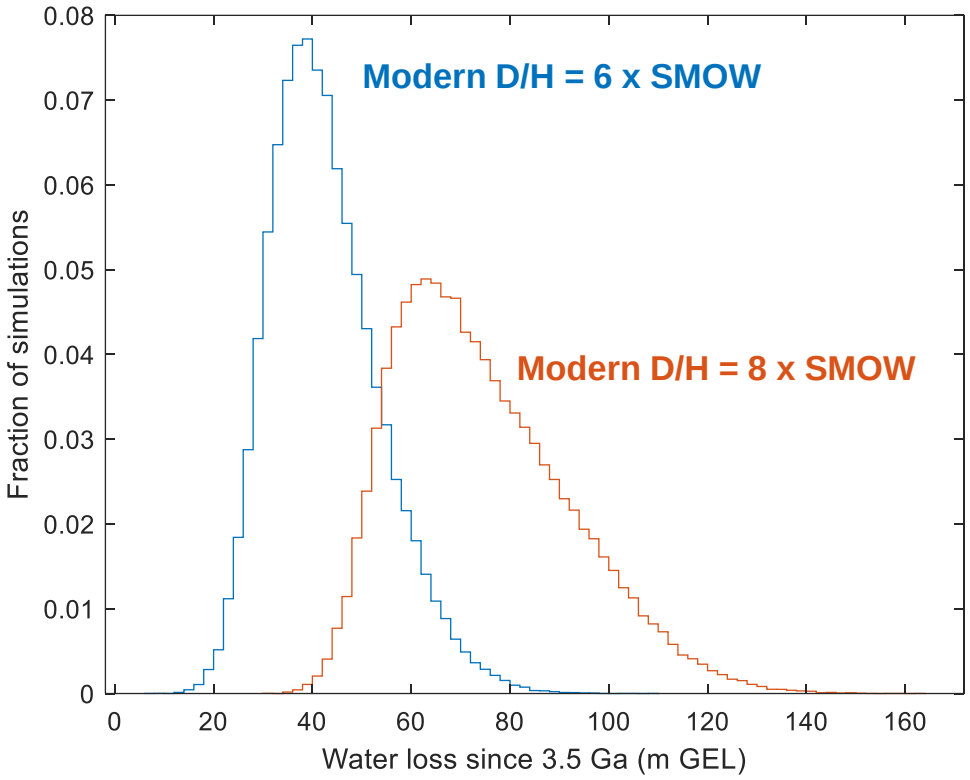

Figure 6.3. Probability distributions of water loss simulations since 3.5 Ga for Mars, in terms of meters Global Equivalent Layer of water, constrained by D/H ratios. The two scenarios use identical parameter ranges for D/H at 3.5 Ga, the size of the modern Martian water reservoir, and the fractionation factor, but with different estimates for the average modern D/H of water on Mars (Villanueva et al., 2015; Webster et al., 2013). The difference between central estimates is ≈ 30 m GEL, equating to a little over 1 bar CO_2 equivalent O.

3. Results

Water loss scenarios are shown in Figure 6.3, and range up to ≈140 m GEL. The median estimate for water loss was 41 m GEL, or 71 m GEL, depending on the modern D/H constraint, with the estimate of 8 x SMOW instead of 6 x SMOW giving an additional ≈30 m GEL average water loss.

Table 6.3. Simulated 3.5 Ga paleo-pCO_2 for different input parameters							
Modern D/H = 6.0 ± 1 x SMOW							
	3.5 Ga paleo pCO_2 (mbar)						
	Significance level: full distribution			Significance level: discarding <12 mbar pCO_2 outcomes			% >12 mbar
EUV model	0.05	0.50	0.95	0.05	0.50	0.95	
$\gamma_{2.64}$ β_{rot}	-1846	-369	83442	153	4137	363325	42.2
$\gamma_{1.7}$ β_{rot}	-2132	-1032	2501	89	1430	25169	13.5
$\gamma_{1.0}$ β_{rot}	-2281	-1254	-460	43	499	4267	1.4
$\gamma_{2.64}$ β_{lum}	-1884	-614	4835	88	1296	11153	30.6
$\gamma_{1.7}$ β_{lum}	-2181	-1134	-124	46	450	2741	3.7
$\gamma_{1.0}$ β_{lum}	-2305	-1288	-583	30	226	1300	0.03
Modern D/H = 8.0 ± 1 x SMOW							
$\gamma_{2.64}$ β_{rot}	-3714	-1639	81953	310	8088	626049	29.9
$\gamma_{1.7}$ β_{rot}	-4077	-2347	1158	153	2932	44652	7.0
$\gamma_{1.0}$ β_{rot}	-4261	-2620	-1567	65	967	7183	0.3
$\gamma_{2.64}$ β_{lum}	-3778	-1910	3458	131	1963	16165	15.0
$\gamma_{1.7}$ β_{lum}	-4142	-2487	-1289	70	683	4143	0.7
$\gamma_{1.0}$ β_{lum}	-4281	-2659	-1668	59	757	2275	0.001

Combinations of three different values for γ and two different ranges of β in dissociative recombination (Appendix) generated six post-3.5 Ga O loss scenarios (Figure 6.2), which are consistent with previous estimates (e.g. Chassefière et al., 2013; Dong et al., 2018; Lillis et al.,

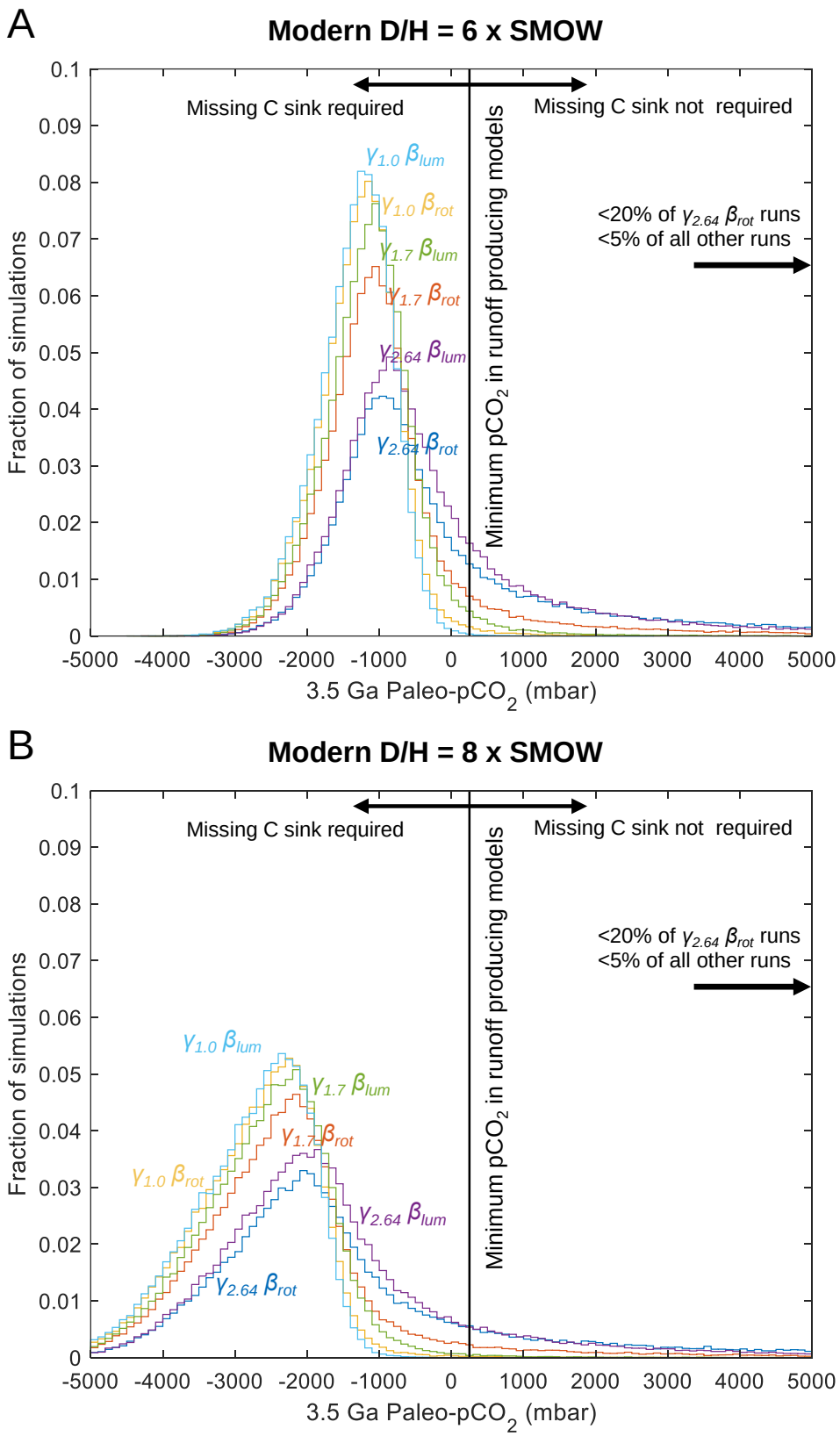

Figure 6.4. Probability distributions of 3.5 Ga paleo-pCO_2.

Figure 6.4. continued

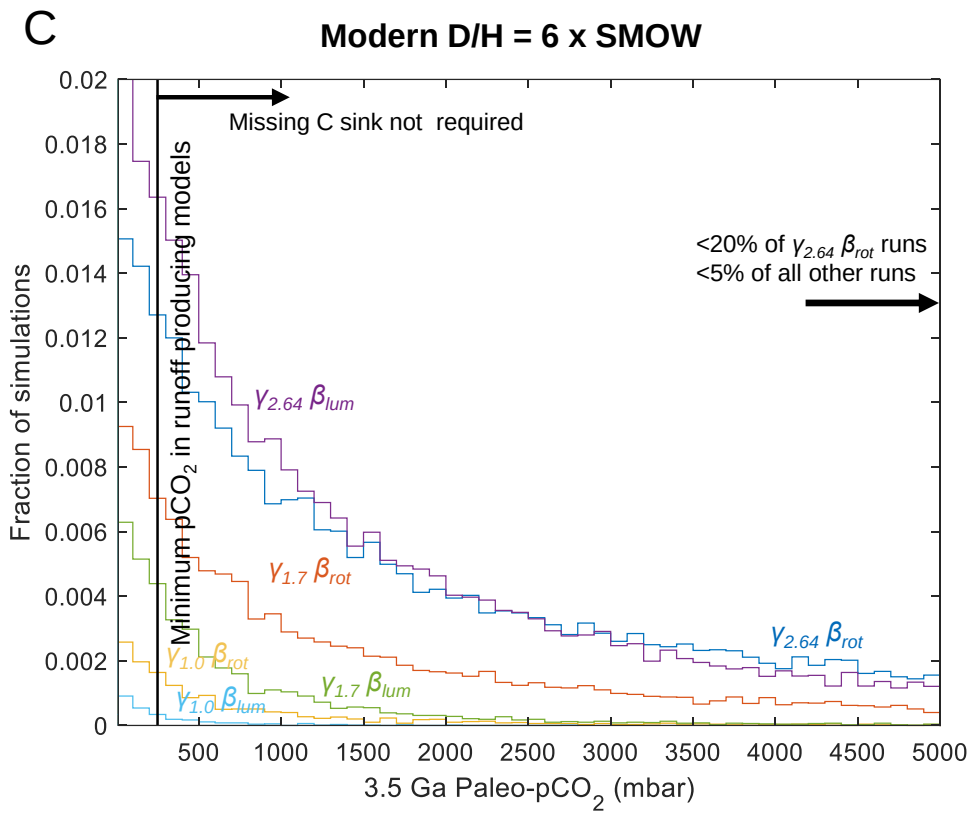

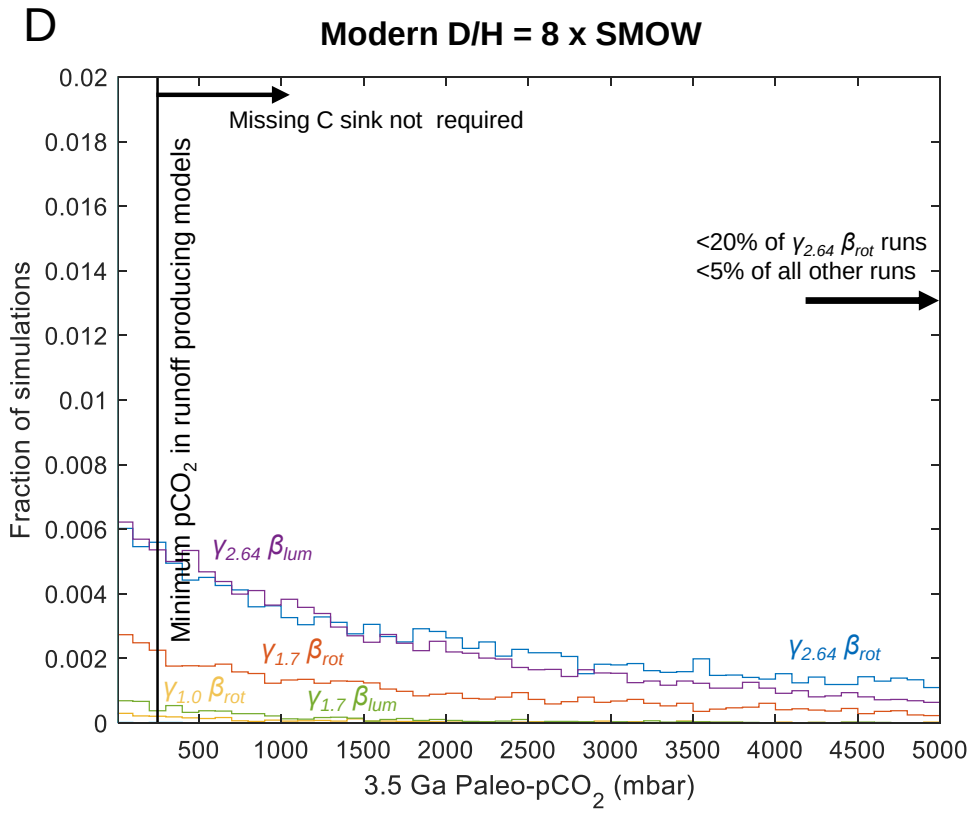

Figure 6.4 continued. Probability distributions of 3.5 Ga paleo-pCO_2, for different O loss scenarios and utilizing water loss scenarios constrained by A.) the 6 x SMOW and, B.) 8 x SMOW modern D/H ratios (Villanueva et al., 2015; Webster et al., 2013). The light black vertical line in each case shows the minimum pCO_2 of 250 mbar shown to enable 3.5 Ga runoff in climate models (Urata and Toon, 2013). C.) and D.) show the part of the probability distributions of 3.5 Ga paleo-pCO_2 with results >12 mbar (i.e., indicating net loss of CO_2 since 3.5 Ga), from A.) and B.) respectively. The percentage of simulations falling above 12 mbar for each simulation can be found in Table 6.3. The black arrow indicates model paleo-pCO_2 results greater than 5 bar. These constitute <5 % of all simulations except for the case of $\gamma_{2.64}$ combined with β_{rot}, where they constitute <20 % of all simulations.

2017). Almost two orders of magnitude variation at the 95% confidence interval in the dissociative recombination loss rate at 3.5 Ga for a given scenario, emphasizes the uncertain nature of extrapolating Martian O loss. When $\gamma = 2.64$ (Lillis et al., 2017) and β from Tu et al. (2015) were used in combination, the 95% upper limit for the 3.5 Ga O loss rate is $>10^{30}$ atoms/s, but in such high EUV scenarios the extrapolated positive relationship between EUV and O loss might break down (R.J. Lillis, personal communication).

Scenarios with all γ, β, and I_{t2} (modern D/H) input combinations generated 12 model probability distributions (Table 6.3; Figure 6.4) for 3.5 Ga paleo-pCO_2, which all have negative central estimates. The average additional water loss of ≈30 m GEL in the I_{t2} = 8 x SMOW model runs equates to a further ≈ 1.3 bar equivalent of CO_2 that cannot be allocated to the past atmospheric inventory. Dividing the models into two groups based on the modern D/H constraint used, there is still significant variation, which we describe in detail for I_{t2} = 6 x SMOW (it is similar with a constant offset in the 8 x SMOW case).

Central estimates of paleo-pCO_2 range from ≈-1290 to -370 mbar (Table 6.3, Figure 6.4). Models with $\gamma = 2.64$ give strongly positive 95% upper limits for paleo-pCO_2, from >4 to several tens of bars (Table 6.3), which all exceed the independent pCO_2 constraints from crater size distributions (Kite et al., 2014; Warren et al., 2019). For other values of γ, the only model which results in

positive paleo-pCO_2 is the one that uses Tu et al. (2015)'s β range and $\gamma = 1.7$. All other scenarios give negative paleo-pCO_2 at the 95% level between -580 and -120 mbar. These results emphasize a need for a reliable consensus on values for γ and β and their range of uncertainty (Appendix). Alternatively, we can determine what fraction of model runs give a physically acceptable result of paleo-pCO_2 >12 mbar, which is larger than the modern CO_2 reservoir size and thus is consistent with net loss of CO_2 since 3.5 Ga (Figure 6.4C, D). These values range from ≈0.001 to 42% of model runs (Table 6.3), with scenarios that favor greater O loss giving a larger proportion of positive paleo-pCO_2 results, including values exceeding independent upper limits (e.g. Kite et al., 2014).

4. Discussion

Our integrated model includes the best available constraints on Mars atmosphere/hydrosphere evolution. Our central estimates of 3.5 Ga Martian pCO_2 are negative. This is physically unrealistic. Therefore, either an important term is missing from our model, or one of our terms must take a value near the edge of its uncertainty range. Consistently negative central estimates of 3.5 Ga Martian pCO_2 can be interpreted in two general ways:

i.) Negative paleo-pCO_2 could be evidence for a missing sink of Mars' 3.5 Ga surface volatiles. This is because negative pCO_2 estimates indicate that MAVEN-derived historical O loss estimates are unable to even fully account for the central estimate for Martian water loss implied by D/H ratio evolution. This observation by itself favors more fractionating (lower f) H escape than the diffusion limited endmember case through the last 3.5 Ga of Mars history. However, negative pCO_2 estimates also indicate that it is highly unlikely that any significant C loss to space has occurred via an additional unknown channel not seen in the modern day, leaving only the few mbar

levels of C escape allowed by extrapolation of modern measurements (Cui et al., 2019; Dong et al., 2018). The required missing sink could be a CO_2 reservoir fixed at or below the Martian surface, such as voluminous deposits of CO_2 ice, liquid, or clathrates; or CO_2 adsorbed on dust or carbonates (Jakosky, 2019; Kurahashi-Nakamura and Tajika, 2006; Manning et al., 2019; Niles et al., 2013). Alternatively, an increase in the surface oxidized sink increases the upper paleo-pCO_2 limit for a given O loss to space simulation, per Equation 1. Therefore, the missing volatile sink could also be oxidized lithological unit(s) not counted within the post-3.5 Ga soil and layered sediments.

ii.) If no large missing volatile sinks exist, the accounting of O atoms in the model is complete, and therefore model runs with positive pCO_2 outputs are the only ones with physically reasonable combinations of input parameters. Posterior distributions generated from the positive values of the Monte Carlo simulations should provide the true estimate of 3.5 Ga Martian pCO_2. A 3.5 Ga pCO_2 $\geq$0.25 bar was possible, but unlikely; particularly considering that the model runs in our study which give the most positive pCO_2 results used input parameters have been revised downward with larger datasets. This interpretation also requires a major C/CO escape channel not recorded by MAVEN.

4.1. Missing volatile sinks

4.1.1. CO_2-fixing sinks

Fixing CO_2 in (sub)surface reservoirs on Mars is a direct alternative to CO_2 loss to space. The negative central estimates of Martian paleo-pCO_2 from O and H loss models could be explained by sequestration of a few bars CO_2 into post-3.5 Ga carbonate rocks. Carbonate in Martian meteorites (Niles et al., 2013, and references therein), and observations of carbonate on the Martian

surface (Boynton et al., 2009; Edwards and Ehlmann, 2015; Ehlmann and Edwards, 2014), show that these phases have formed on Mars, but their role as a globally significant post-3.5 Ga sink is uncertain. Most observed Martian carbonate occurrences suggest local alteration at low water to rock ratios (Niles et al., 2013). Edwards and Ehlmann (2015) found only minor late Noachian-early Hesperian carbonate alteration, equivalent to ≤12 mbar CO_2 drawdown, had occurred through basalt alteration in the Nilli Fossae region, suggesting post-Noachian carbonate sequestration was minor. Jakosky and Edwards (2018) estimated <50 mbar of CO_2-equivalent Martian carbonate globally. Niles et al. (2013) determined that with a generous crustal carbonate fraction of 0.5 wt% within the top 1 km of Martian crust, ≤0.25 bar of CO_2 could be sequestered in the Martian subsurface. Most of this crustal carbonate would have formed long prior to 3.5 Ga, so this CO_2 would not have been in the atmosphere when later lakes and rivers were forming. However, global post-3.5 Ga soil and layered sedimentary deposits used in our oxidative weathering balance may also have sequestered CO_2. Taking the total mass of these deposits from the Appendix, Table 6.4, and an optimistic 4 wt% of carbonate minerals (Boynton et al., 2009), present as magnesite ($MgCO_3$), we estimate a maximum ≈ 41 mbar CO_2-equivalent of carbonate that may be incorporated in the post-3.5 Ga soil and layered sedimentary reservoir. Again, whilst this upper limit value is several times the current exchangeable CO_2 inventory on Mars, it falls far short of overcoming the ≈ 1-2 bar deficit to explain both negative pCO_2 estimates in this study and additional climatic requirements. Frozen CO_2 may have been in sequestered in large volumes deep in the Martian regolith as a result of basal melting of CO_2 ice in the polar caps in earlier periods with greater geothermal heat flow (Manning et al., 2019). Indeed, a subsurface radar anomaly exists in an area of past ice-cap basal melting (Whitten et al., 2018). We do not explore this

intriguing mechanism further here; however, it could provide a substantial missing C sink in the context of our modeling.

4.1.2. Oxidation of post-Noachian lava

The oxidative sink included in the model only accounted for observed layered sedimentary deposits and soil. However, buried paleo-weathering horizons (paleosols) on post-3.5 Ga lava flows on the Tharsis Plateau, Olympus Mons, Elysium, and other young flood lavas, could also sequester O. Surface cratering ages for Tharsis (Tanaka et al., 2014), and the <1.3 Ga crystallization of Shergottite, Nakhlite and Chassignite (SNC) meteorites imply that substantial volumes of lava erupted after the Noachian, and therefore fresh lava may have been periodically exposed, weathered, and then buried by more lava during the 3.5 Ga of most recent Martian history. Kite et al. (2009) estimate a maximum of 5.7×10^{19} kg of Martian lava was erupted late, and some fraction of this lava could have been weathered since 3.5 Ga.

Lava flow paleosol development is illustrated in Figure 6.5. Downward propagation of the weathering front into Martian lava flows can be modelled as a diffusive process, with the depth L of the regolith scaling as $L \approx \sqrt{(\kappa\tau)}$, where κ is the diffusivity and τ is time. Assessment of the NASA InSight landing site found the regolith to be 3-17 m thick in a surface with 1.7 Ga cratering age (Warner et al., 2017), which results in estimates for κ in the range $5.3 \times 10^{-9} – 1.7 \times 10^{-7}$ m^2/yr. If the weathering front moves downwards as √time, lava flow oxidation is maximal for evenly time-spaced eruption of lava flows over 3.5 Gyr (Figure 6.5) to build up a 10 km characteristic thickness for parts of Tharsis. Regolith on each individual flow deepens to $L_{lava} = \sqrt{(\kappa\tau_{lava})}$ where τ_{lava} is the time between lava flows. Thinner lava flows enable the most extensive total oxidation, with altimetry estimates placing the lower bound for lava flow thickness on Tharsis at 4 m

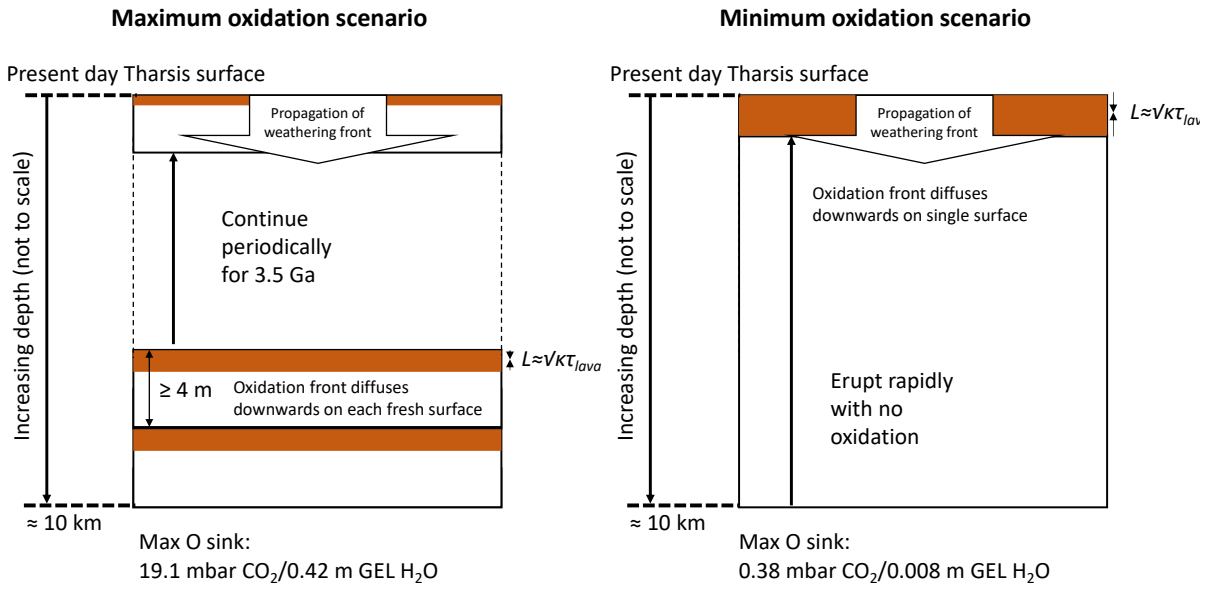

Figure 6.5. Cartoon illustrating scenarios for the formation of oxidized paleosols on lava flows within a ≈ 10 km thick column of lava flows in the Tharsis region, taken as representative for young post-Noachian lavas on Mars. Regolith develops on a fresh lava surface as a diffusive process, deepening as the square root of the exposure time. The optimum scenario for oxidation is for uniform periodic eruption of the thinnest lava flows possible (>4 m; Basilevskaya et al., 2006), and development of a regolith on top of each one. The worst-case scenario for oxidation is for geologically instantaneous eruption of the entire post-3.5 Ga Tharsis column, and oxidation at a single surface for 3.5 Gyr. Assuming oxidation of Fe to a degree consistent with typical Martian soil (Morris et al., 2006), neither scenario can sequester enough O atoms to explain a large fraction of Mars' post-3.5 Ga H_2O loss of presumed post-3.5 Ga CO_2 loss.

(Basilevskaya et al., 2006). Assuming oxidation of 39% of total Fe to Fe^{3+} within the developed regolith, as per the global soil layer (Morris et al., 2006), the maximum O sink available from young lava paleosol oxidation is ≈3.4 x 10^{18} moles of O, which equates to 0.42 m GEL water or 19.1 mbar CO_2 equivalent oxygen. The minimum oxidation scenario, instantaneous eruption of all lava and weathering at a single surface for 3.5 Gyr, sequesters ≤10^{17} moles of O, equating to 0.008 m GEL water or 0.38 mbar CO_2. Greater Fe oxidation per unit mass, or faster diffusive growth of regolith on a younger Mars, could increase this number, but not to the ≈1-2 bar CO_2 equivalent required.

4.2. Posterior distributions for positive pCO_2

Posterior distributions for paleo-pCO_2 were generated by considering only the results with pCO_2 >12 mbar at 3.5 Ga (Figure 6.4C, D). These represent scenarios with net CO_2 loss to space since 3.5 Ga. The probability distributions cut off below 12 mbar are shown in panels C and D of Figure 6.4. If large missing volatile sinks are discounted, results above 250 mbar, the lowest pCO_2 resulting in runoff that has been used in Early Mars climate models (Urata and Toon, 2013), would be expected to be consistent with lake forming climates.

The proportion of runs with paleo-pCO_2>12 mbar is 0.001 to 42 % (Table 6.3). Scenarios with identical O loss contain a smaller proportion of results with positive pCO_2 when the 8 x SMOW modern D/H constraint (Villanueva et al., 2015) is used. However, in every case, the more enriched modern D/H also gives higher upper limits on pCO2 at the 95% level in the posterior distribution. These distributions were cut off further from the central value in the original simulations, giving increased importance to their long tails (Figure 6.4D).

Model runs using $\gamma = 2.64$ (Lillis et al., 2017), result in very high upper limit positive paleo-pCO_2 estimates at the 95% level. As we have outlined above, this high value for γ is probably an overestimate of the true value. However, results of models run with modest O loss rates resulting from combinations of lower values of γ and β, still result in upper limits on paleo-pCO_2 of $\geq$1.3 bar (Table 6.3). Three error-propagation scenarios; two using 6 x SMOW and one using 8 x SMOW for the modern D/H constraint; which also made use of more conservative ranges for both β and γ, had positive pCO_2 distributions for which the posterior 95% percentiles (1.3-2.7 bar) were consistent with independent upper limits imposed by crater size distributions (Kite et al., 2014). Posterior distributions generated from combined O and H loss simulations cannot in any case, rule out the >1 bar pCO_2 atmospheres required by many lake-forming climate solutions at the 95%

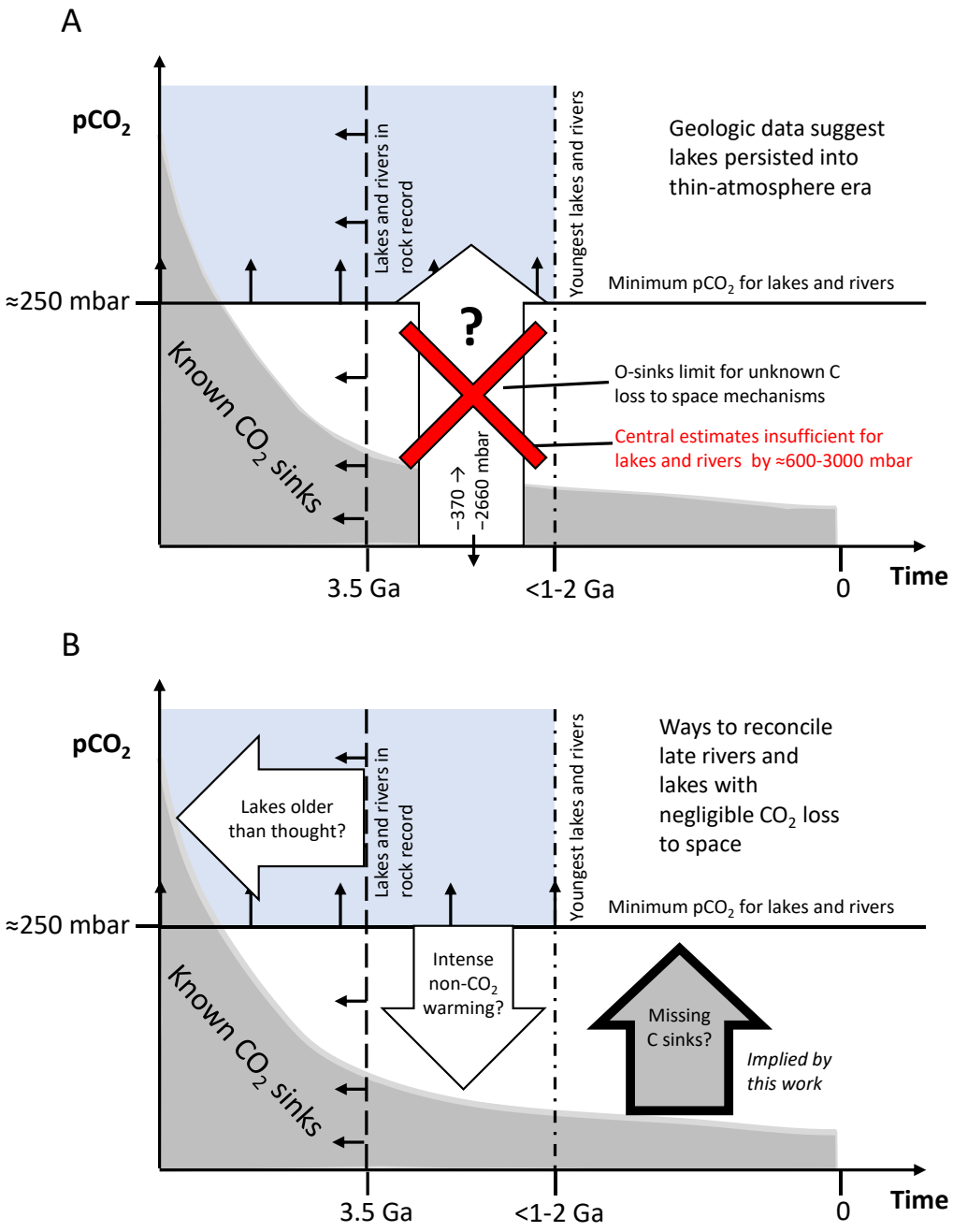

Figure 6.6. Graphical illustration of new constraints and future directions for investigation provided by this study. A. Geologic data suggest lakes persisted after almost all atmosphere was lost: Evidence for lakes and rivers up to 1-2 Ga (Dickson et al., 2009) and abundant evidence in the rock record (including lacustrine mudstones) at 3.5 Ga require higher pCO_2 (according to existing climate models), than that provided by known CO_2 sinks, or by unknown C loss mechanisms implied by O sinks. B. Possible ways to reconcile negligible CO_2 loss to space with rivers and lakes after 3.5 Ga ago are large missing C sinks; new climate models capable of producing extensive runoff at far lower pCO_2 than existing models; and revision of age data such that all evidence for lakes and rivers could predate loss of major C sinks.

confidence level. This suggests that existing climate models for Mars can be consistent with a subset of volatile evolution histories on Mars, with the caveat that these positive outcomes are unlikely results of our model overall. Results with pCO_2 >0.25 bar in all posterior distributions for 3.5 Ga pCO_2 are consistent with the minimum constraint required by the climate model of Urata and Toon (2013), suggesting that low probability outcomes of even the most pessimistic estimates of the Mars volatile budget could enable lake-forming climates under at least some climate models (Kite et al., 2017; Mansfield et al., 2018; Ramirez et al., 2014). These hypotheses are potentially testable via Curiosity measurements of $\delta^{13}C$ in the rocks of Mt. Sharp (Franz et al. 2015).

5. Conclusions

Mars no longer has the thick CO_2 atmosphere that climate models indicate would have been required to sustain lakes that formed more recently than 3.5 Ga ago. This suggests that large quantities of C have been lost from Mars's atmosphere. Combining multiple independent constraints on post-3.5 Ga evolution of Martian volatile reservoirs (Figure 6.1) has enabled us address whether this C was lost to space. Our key results are illustrated in Figure 6.6. In order to address this problem, we estimated both the ranges of Martian oxygen and hydrogen loss to space over the past 3.5 Gyr using an error propagation approach (Figures 6.2-6.4), breaking a previous degeneracy in attributing oxygen lost to space to either H_2O or CO_2. We also refined the picture of the Martian oxidative soil and layered sediment oxygen sink (Figure 6.5), finding it to be small relative to the flux of oxygen lost to space. Despite the reddening of Mars attributable to surficial oxidation of iron equating to <0.5m GEL of H_2O-equivalent oxygen, we showed that the main oxygen-consuming component in the oxidative soil and layered sedimentary budget could have been sulfur, provided that volcanic sulfur gases on Mars reflect the redox state of magma inferred

from meteorites. With our multiproxy approach we determined upper limits on 3.5 Ga Martian paleo-pCO_2 that were agnostic about loss mechanisms for carbon itself. Despite significant spread in results, a consistent feature of our models was negative (-370 to -2660 mbar) central estimates for Martian 3.5 Ga paleo-pCO_2, with the least negative results only being obtained with model parameters which do not represent the best current understanding of atmospheric oxygen escape. Our negative central pCO_2 estimates suggest either i.) a missing component of the volatile loss model, such as a large, unaccounted for volatile sink on Mars; or ii.) that post-3.5 Ga atmospheric loss processes were more vigorous than currently thought. Evidence suggests post-3.5 Ga carbonate formation was minor, and a previously unconsidered oxygen sink of Fe^{3+}-rich paleosols on Tharsis lavas can only account for a small fraction of the CO_2-equivalent oxygen needed for >250 mbar atmospheres postulated to be required by climate models. More likely, our results indicate that of C loss to space cannot account for loss of hundreds of mbar of CO_2 in the last 3.5 Ga of Martian history. The apparent lack of sufficient sinks for C lost since 3.5 Ga ago could be solved by the discovery of large, as-yet undiscovered, carbon sinks in Martian (sub)surface deposits. Our preferred solution, missing C sinks, is only one of three possible solutions to this problem (Figure 6.6). These three possible solutions are that i.) there is a missing C sink on (in) Mars's (sub)surface; ii.) climate solutions for sustained runoff on Mars with atmospheric CO_2 pressure <<250 mbar; or iii.) crater chronologies on Mars being sufficiently incorrect that all apparently young rivers and lakes date are actually older than 3.5 Ga (Figure 6.6). Each of these possibilities merits substantial dedicated investigation in future studies.

Acknowledgements

We thank Rob Lillis for insightful discussions that significantly improved the manuscript. We also thank Bruce Jakosky and an anonymous reviewer for thorough and thoughtful reviews, and Itay Halevy for editorial handling of the manuscript. A. W. Heard was supported by NASA grant NNH16ZDA001N to Nicolas Dauphas and A. W. Heard. E. S. Kite was supported by NASA grant NNX16AG55G to E. S. Kite.

Appendix

Oxygen Loss to Space

Major O loss process: Oxygen loss through dissociative recombination

Careful extrapolation of photochemical O loss through time is central to determining a reasonable spread of Martian volatile budgets back to 3.5 Ga. Table 6.2 contains a list of the parameters used in our modeling. Photochemical loss is driven by solar extreme ultraviolet (EUV, 10-92 nm) radiation. MAVEN constrained a temporal spread in dissociative recombination O loss driven primarily by EUV variation associated with the solar cycle. A number of approaches have yielded average determinations on the order of 5×10^{25} O s^{-1}, and here we apply the recommended range of Lillis et al. (2017), with a mean of 4.3×10^{25} O s^{-1}, and with upper and lower (1σ) bounds of 9.6×10^{25} O s^{-1} and 1.9×10^{25} O s^{-1} respectively, following a log-normal distribution (Table 6.2). The central value reported by Lillis et al. is in flux (R. J. Lillis, personal communication), therefore including this range should adequately encompass temporal variation in the loss rate, including short-term solar storm enhancement of the EUV flux which can enhance photochemical loss by a factor of approximately 10.

Dissociative recombination O loss flux F, is assumed to follow a power law relationship with the EUV ionization frequency I

$$F = BI^{\gamma} \qquad \text{(Eq. A1)}$$

with the power law exponent γ, where B is a fitting parameter. Published literature indicates $\gamma = 2.64 \pm 0.60$ (1σ) (Lillis et al., 2017). However, an enlarged dataset suggests the average value of γ should be revised downward to $\gamma = 1.7 \pm 0.39$ (R. J. Lillis, personal communication, where we have assumed identical proportional size of error bars to Lillis et al., 2017). A simple analytical theory suggests dissociative recombination is directly proportional to the EUV irradiance, with $\gamma = 1$ (Cravens et al., 2017). We run models with all three values and compare the results (Table 6.2, Figure 6.2).

Extrapolation of the loss flux backwards in time requires an expression for the time evolution of the ionization frequency

$$I_{past} = I_{present}\left(\frac{t_{past}}{4.5\ Gyr}\right)^{-\beta} \qquad \text{(Eq. A2)}$$

where t_{past} is the age of Mars at some point in the past in Gyr, and β is the power law exponent for the decay of solar EUV intensity over time, with the form $t^{-\beta}$, where t is the stellar age (Lillis et al., 2017). Converting flux F from (2) to planetary loss rate R through multiplying by the surface area of Mars, recasting in terms of Ga and combining Equation 1 and Equation 2 yields the expression for the past dissociative recombination flux R_{past} at a given time before present t_{Ga}

$$R_{past} = R_{present}\left(\frac{4.5}{4.5 - t_{Ga}}\right)^{\gamma\beta} \qquad \text{(Eq. A3)}$$

where here the maximum value of t_{Ga} is 3.5 (Lillis et al., 2017).

The value of β (Table 6.2) is uncertain in very young stars because stellar X-Ray and EUV radiation scale with magnetic activity inside stars, which depends on the stellar dynamo and thus

the star's rotation (Tu et al., 2015). Young stars show a range of rotational speeds but by the 1 Gyr age of the Sun when our models begin, such rotational activity converges on a narrower range because fast-spinning stars spin down faster (Mamajek and Hillenbrand, 2008). The solar EUV evolution exponent β can be determined by measurement of UV and X-ray luminosities for stars of known age (with a fitted relationship between X-ray and EUV luminosity), or through modeling the rotational evolution of stars and calculating the anticipated X-ray (and consequently, fitted EUV), luminosities (Ribas et al., 2005; Sanz-Forcada et al., 2011; Tu et al., 2015). Ribas et al. (2005) found that the EUV decay power law exponent $\beta = 1.20$ or 1.23 within a sample of 6 G stars when spectra were averaged over the wavelength ranges 10-36 and 0.1-110 nm respectively. Sanz-Forcada et al. (2011) examined 29 M to F class stars (3 M, 26 FGK) with exoplanetary systems and found $\beta = 1.24 \pm 0.15$ for EUV luminosity. Tu et al. (2015) used hundreds of observations of young stars combined with a stellar evolution model and determined a spread in early X-Ray and EUV luminosities with $\beta = 1.22$ with large and highly asymmetric uncertainty, with 10^{th} and 90^{th} percentiles of 0.96 and 2.15, respectively. While the study of Ribas et al. (2005) has a smaller sample size, the parameter β in that study is constrained by stars spanning 6.7 Gyr in age with 3 of 6 samples being older than 1 Gyr. The study of Sanz-Forcada et al. (2011) includes a fraction of stars up to 3 Gyr in age, and Tu et al. (2015) exclusively made use of stars less than 600 million years (Myr) old, and extrapolated their model through to the age of the Sun. Those latter two studies do not utilize direct observations in the EUV spectral range, but instead apply a fitted relationship between X-Ray and EUV luminosity given by Sanz-Forcada et al. (2011)

$$\log L_{EUV} = 4.8 + 0.86 \log L_X \qquad \text{(Eq. A4)}$$

where L_{EUV} and L_X are the modeled EUV and observed X-Ray luminosities respectively.

Early rotational evolution of stars leads to a spread in their X-Ray (and inferred EUV) luminosities before 500 Myr, after which these parameters converge on a more limited spread of values for a given stellar age (Tu et al., 2015). The implication of this is that Tu et al. (2015)'s confidence interval, defined as it is by young and highly rotationally variable stars, overestimates the level of uncertainty in the value of β for later stages of stellar evolution. In our work we are interested in the evolution of a >1 Gyr old star, the post-3.5 Ga Sun, and its influence on volatile evolution on Mars For this age range, β shows less spread. A larger upper limit value of β corresponds to historically higher EUV flux and thus enhanced early photochemical loss of O (Lillis et al., 2017). Determination of conservative upper limits for the total O loss will result in robust upper limits on paleo-pCO_2 per Equation 1. Sensitivity of Mars's photochemical O loss history to the EUV evolution of the Sun is assessed by using two ranges of β (Table 6.2), from Sanz-Forcada et al. (2011) and Tu et al. (2015), and comparing results.

Smaller O loss processes: Oxygen ion and sputtering loss

Other O loss channels are also significant for Martian volatile history (Figure 6.2). Following the approach of Jakosky et al. (2018), we include two additional O loss channels; O ion loss, and sputtering O loss. Previous workers such as Chassefière et al. (2013) considered the separate O ion loss channels of pickup ion loss and ionospheric outflow. However, Jakosky et al. (2018) reported a single number for O ion loss of 5×10^{24} O^+ s^{-1}. In detail, ionospheric outflow loss is smaller (by $\approx 10^2$ times) than pickup ion loss, and barely affects integrated O loss (Chassefière et al., 2013). However, the unmodified function from Chassefière et al. (2013) is included here for completeness. Pickup ion loss at present day is fixed at the modern ion loss rates determined by MAVEN. Following Jakosky et al. (2018), the evolution of the loss flux back in time is modeled following the functional form of Chassefière et al. (2013), after Lammer et al. (2003).

The functions chosen in this study for the ion and sputtering loss channels give higher loss rates at 3.5 Ga than another recent, MAVEN-led study of Dong et al. (2018). These parameters are chosen to allow the most generous upper limits on historical Martian O loss and thus paleo-pCO_2. In the work of Dong et al. (2018), total O ion loss at 3.5 Ga is 2.4 x 10^{26} O^+ s^{-1}, compared to ≈1.4 x 10^{27} O^+ s^{-1} in the parameterization of Chassefière et al. (2013). Our selection is consistent with the aim of obtaining strong upper limits on paleo-pCO2, without intending to comment on the relative accuracy of these values.

Sputtering loss is driven by the reimpacting of O^+ ions, accelerated by the electrical field of the solar wind, back into the atmosphere, where transfer of momentum from these ions to neutrals can remove even heavy atoms. MAVEN does not directly measure sputtering. Sputtering loss is determined through model calculations using measured properties of reimpacting ion fluxes. The inferred average sputtering loss rate from modern Mars is 3 x 10^{24} O s^{-1} (Jakosky et al., 2018). In this study, following Jakosky et al. (2018), we use the functional form from Chassefière et al. (2013) for evolution of the sputtering rate through time, adjusted to fit the modern value.

Table 6.4. Young sedimentary reservoirs on Mars and their estimated O sinks

Unit	Volume (m^3)	Density (kg/m^3)	% Dust[(1)]	Mass dust (kg)	Added O (kg)	Reference
Dunes	9.0E+12	1890	100	1.7E+16	1.54E+15	Hayward (2011); Hayward et al. (2012, 2007)
SPLD	1.6E+15	1220	15	2.9E+17	2.65E+16	Plaut et al. (2007); Zuber et al. (2007)
Duststone	1.2E+14 [(2)]	1500	100	1.8E+17	1.62E+16	Bridges et al. (2010)
Medusae Fossae Formation	1.9E+15	1800	100	3.4E+18	3.10E+17	Watters et al. (2007)
North polar layered deposits, excluding basal unit	8.2E+14	1000	5	4.1E+16	3.72E+15	Grima et al. (2009)
Basal Unit, NPLD	2.7E+14	1960	77	4.0E+17	3.67E+16	Byrne and Murray (2002)

Table 6.4 continued						
Mid latitude mantling deposits	1.3E+15	1960	77	1.9E+18	1.77E+17	Byrne et al. (2009); Schon et al. (2009)
Low latitude glacial ice	6.0E+14	1000	10	6.0E+16	5.43E+15	Shean et al. (2005)
Near-surface ejecta	3.6E+12	2000	100	7.2E+15	6.52E+14	Scott and Tanaka (1986)
Global soil and dust	4.4E+14 (3)	1500	100	6.5E+16	5.91E+15	Warner et al. (2017)
Southern mid latitude icy deposits	2.8E+13	1000	10	2.8E+15	2.54E+14	Holt et al. (2008)
Interior layered deposits	2.4E+14	2400	100	5.8E+17	5.22E+16	Michalski and Niles (2012)
Total O mass (kg)					6.89E+17	
Total O moles						4.30E+19
Added O was calculated assuming modern Fe^{3+}/Fe_{Total}=0.39, and 20 wt% SO_3 derived from 50% H_2S, 50% SO_2						

Table 6.4 continued
[1] Maximum dust content was estimated for formations with <100% dust by the authors, assuming an admixture of silicate-dominated soil material with pure water ice, except in the case of the SPLD where the dust content is taken from the published estimate of Zuber et al. (2007). Only the soil component of dust/ice mixtures represents an oxidative sink for O. [2]Maximum, assuming 4 m thickness on 20.5% of Mars surface [3]Assuming regolith thickness of 3 m

References

Alsaeed, N.R., Jakosky, B.M., 2019. Mars Water and D/H Evolution from 3 Ga to Present. LPI Contrib. 2089, 6059.

Arvidson, R.E., Squyres, S.W., Morris, R.V., Knoll, A.H., Gellert, R., Clark, B.C., Catalano, J.G., Jolliff, B.L., McLennan, S.M., Herkenhoff, K.E., VanBommel, S., Mittlefehldt, D.W., Grotzinger, J.P., Guinness, E.A., Johnson, J.R., Bell, J.F., Farrand, W.H., Stein, N., Fox, V.K., Golombek, M.P., Hinkle, M.A.G., Calvin, W.M., Souza, P.A.D., 2016. High concentrations of manganese and sulfur in deposits on Murray Ridge, Endeavour Crater, Mars. Am. Mineral. 101, 1389–1405. https://doi.org/10.2138/am-2016-5599

Barabash, S., Fedorov, A., Lundin, R., Sauvaud, J.-A., 2007. Martian Atmospheric Erosion Rates. Science 315, 501–503. https://doi.org/10.1126/science.1134358

Basilevskaya, E.A., Neukum, G., the HRSC Co-Investigator Team, 2006. The Olympus volcano on Mars: Geometry and characteristics of lava flows. Sol. Syst. Res. 40, 375–383. https://doi.org/10.1134/S0038094606050029

Bibring, J.-P., Langevin, Y., Mustard, J.F., Poulet, F., Arvidson, Raymond, Gendrin, A., Gondet, B., Mangold, N., Pinet, P., Forget, F., Berthé, M., Bibring, J.-P., Gendrin, A., Gomez, C., Gondet, B., Jouglet, D., Poulet, F., Soufflot, A., Vincendon, M., Combes, M., Drossart, P., Encrenaz, T., Fouchet, T., Merchiorri, R., Belluci, G., Altieri, F., Formisano, V., Capaccioni, F., Cerroni, P., Coradini, A., Fonti, S., Korablev, O., Kottsov, V., Ignatiev, N., Moroz, V., Titov, D., Zasova, L., Loiseau, D., Mangold, N., Pinet, Patrick, Douté, S., Schmitt, B., Sotin, C., Hauber, E., Hoffmann, H., Jaumann, R., Keller, U., Arvidson, Ray, Mustard, J.F., Duxbury, T., Forget, François, Neukum, G., 2006. Global Mineralogical and Aqueous Mars History Derived from OMEGA/Mars Express Data. Science 312, 400–404. https://doi.org/10.1126/science.1122659

Boynton, W.V., Ming, D.W., Kounaves, S.P., Young, S.M.M., Arvidson, R.E., Hecht, M.H., Hoffman, J., Niles, P.B., Hamara, D.K., Quinn, R.C., Smith, P.H., Sutter, B., Catling, D.C., Morris, R.V., 2009. Evidence for Calcium Carbonate at the Mars Phoenix Landing Site. Science 325, 61–64. https://doi.org/10.1126/science.1172768

Cannon, K.M., Parman, S.W., Mustard, J.F., 2017. Primordial clays on Mars formed beneath a steam or supercritical atmosphere. Nature 552, 88. https://doi.org/10.1038/nature24657

Carr, M.H., Head, J.W., 2015. Martian surface/near-surface water inventory: Sources, sinks, and changes with time. Geophys. Res. Lett. 42, 726–732. https://doi.org/10.1002/2014GL062464
Catling, D.C., Kasting, J.F., 2017. Atmospheric Evolution on Inhabited and Lifeless Worlds.

Catling, D.C., Zahnle, K.J., McKay, C.P., 2001. Biogenic Methane, Hydrogen Escape, and the Irreversible Oxidation of Early Earth. Science 293, 839–843. https://doi.org/10.1126/science.1061976

Chassefière, E., Langlais, B., Quesnel, Y., Leblanc, F., 2013. The fate of early Mars' lost water: The role of serpentinization. J. Geophys. Res. Planets 118, 1123–1134. https://doi.org/10.1002/jgre.20089

Cravens, T.E., Rahmati, A., Fox, J.L., Lillis, R., Bougher, S., Luhmann, J., Sakai, S., Deighan, J., Lee, Y., Combi, M., Jakosky, B., 2017. Hot oxygen escape from Mars: Simple scaling with solar EUV irradiance. J. Geophys. Res. Space Phys. 122, 1102–1116. https://doi.org/10.1002/2016JA023461

Cui, J., Wu, X.-S., Gu, H., Jiang, F.-Y., Wei, Y., 2019. Photochemical escape of atomic C and N on Mars: clues from a multi-instrument MAVEN dataset. Astron. Astrophys. 621, A23. https://doi.org/10.1051/0004-6361/201833749

Dickson, J.L., Fassett, C.I., Head, J.W., 2009. Amazonian-aged fluvial valley systems in a climatic microenvironment on Mars: Melting of ice deposits on the interior of Lyot Crater. Geophys. Res. Lett. 36. https://doi.org/10.1029/2009GL037472

Dong, C., Lee, Y., Ma, Y., Lingam, M., Bougher, S., Luhmann, J., Curry, S., Toth, G., Nagy, A., Tenishev, V., Fang, X., Mitchell, D., Brain, D., Jakosky, B., 2018. Modeling Martian Atmospheric Losses over Time: Implications for Exoplanetary Climate Evolution and Habitability. Astrophys. J. 859, L14. https://doi.org/10.3847/2041-8213/aac489

Edwards, C.S., Ehlmann, B.L., 2015. Carbon sequestration on Mars. Geology 43, 863–866. https://doi.org/10.1130/G36983.1

Ehlmann, B.L., Edwards, C.S., 2014. Mineralogy of the Martian Surface. Annu. Rev. Earth Planet. Sci. 42, 291–315. https://doi.org/10.1146/annurev-earth-060313-055024

Ehlmann, B.L., Mustard, J.F., Murchie, S.L., Bibring, J.-P., Meunier, A., Fraeman, A.A., Langevin, Y., 2011. Subsurface water and clay mineral formation during the early history of Mars. Nature 479, 53–60. https://doi.org/10.1038/nature10582

Franz, H. B., Mahaffy, P. R., Stern, J., Archer, P., Jr., Conrad, P., Eigenbrode, J., Freissinet, C., Glavin, D., Grotzinger, J. P., Jones, J., et al., 2015, Isotopic Composition Of Carbon Dioxide Released From Confidence Hills Sediment As Measured By The Sample Analysis At Mars (Sam) Quadrupole Mass Spectrometer, Lunar and Planetary Science Conference 2015.Grant, J.A., Wilson, S.A., 2012. A possible synoptic source of water for alluvial fan formation in southern Margaritifer Terra, Mars. Planet. Space Sci., Mars Habitability 72, 44–52. https://doi.org/10.1016/j.pss.2012.05.020

Greenwood, J.P., Itoh, S., Sakamoto, N., Vicenzi, E.P., Yurimoto, H., 2008. Hydrogen isotope evidence for loss of water from Mars through time. Geophys. Res. Lett. 35. https://doi.org/10.1029/2007GL032721

Grotzinger, J.P., 2013. Analysis of Surface Materials by the Curiosity Mars Rover. Science 341, 1475–1475. https://doi.org/10.1126/science.1244258

Haberle, R.M., Catling, D.C., Carr, M.H., Zahnle, K.J., 2017. The Early Mars Climate System, in: The Atmosphere and Climate of Mars, Cambridge Planetary Science. Cambridge University Press, Cambridge, pp. 526–568.

Halevy, I., Zuber, M.T., Schrag, D.P., 2007. A Sulfur Dioxide Climate Feedback on Early Mars. Science 318, 1903–1907. https://doi.org/10.1126/science.1147039

Hurowitz, J.A., Fischer, W.W., Tosca, N.J., Milliken, R.E., 2010. Origin of acidic surface waters and the evolution of atmospheric chemistry on early Mars. Nat. Geosci. 3, 323–326. https://doi.org/10.1038/ngeo831

Irwin III, R.P., Lewis, K.W., Howard, A.D., Grant, J.A., 2015. Paleohydrology of Eberswalde crater, Mars. Geomorphology, Planetary Geomorphology: Proceedings of the 45th Annual Binghamton Geomorphology Symposium, held 12-14 September 2014 in Knoxville, Tennessee, USA 240, 83–101. https://doi.org/10.1016/j.geomorph.2014.10.012

Jakosky, B.M., 2019. The CO2 inventory on Mars. Planet. Space Sci. 175, 52–59. https://doi.org/10.1016/j.pss.2019.06.002

Jakosky, B.M., 1991. Mars volatile evolution: Evidence from stable isotopes. Icarus 94, 14–31. https://doi.org/10.1016/0019-1035(91)90138-J

Jakosky, B.M., Brain, D., Chaffin, M., Curry, S., Deighan, J., Grebowsky, J., Halekas, J., Leblanc, F., Lillis, R., Luhmann, J.G., Andersson, L., Andre, N., Andrews, D., Baird, D., Baker, D., Bell, J., Benna, M., Bhattacharyya, D., Bougher, S., Bowers, C., Chamberlin, P., Chaufray, J.-Y., Clarke, J., Collinson, G., Combi, M., Connerney, J., Connour, K., Correira, J., Crabb, K., Crary, F., Cravens, T., Crismani, M., Delory, G., Dewey, R., DiBraccio, G., Dong, C., Dong, Y., Dunn,

P., Egan, H., Elrod, M., England, S., Eparvier, F., Ergun, R., Eriksson, A., Esman, T., Espley, J., Evans, S., Fallows, K., Fang, X., Fillingim, M., Flynn, C., Fogle, A., Fowler, C., Fox, J., Fujimoto, M., Garnier, P., Girazian, Z., Groeller, H., Gruesbeck, J., Hamil, O., Hanley, K.G., Hara, T., Harada, Y., Hermann, J., Holmberg, M., Holsclaw, G., Houston, S., Inui, S., Jain, S., Jolitz, R., Kotova, A., Kuroda, T., Larson, D., Lee, Y., Lee, C., Lefevre, F., Lentz, C., Lo, D., Lugo, R., Ma, Y.-J., Mahaffy, P., Marquette, M.L., Matsumoto, Y., Mayyasi, M., Mazelle, C., McClintock, W., McFadden, J., Medvedev, A., Mendillo, M., Meziane, K., Milby, Z., Mitchell, D., Modolo, R., Montmessin, F., Nagy, A., Nakagawa, H., Narvaez, C., Olsen, K., Pawlowski, D., Peterson, W., Rahmati, A., Roeten, K., Romanelli, N., Ruhunusiri, S., Russell, C., Sakai, S., Schneider, N., Seki, K., Sharrar, R., Shaver, S., Siskind, D.E., Slipski, M., Soobiah, Y., Steckiewicz, M., Stevens, M.H., Stewart, I., Stiepen, A., Stone, S., Tenishev, V., Terada, N., Terada, K., Thiemann, E., Tolson, R., Toth, G., Trovato, J., Vogt, M., Weber, T., Withers, P., Xu, S., Yelle, R., Yiğit, E., Zurek, R., 2018. Loss of the Martian atmosphere to space: Present-day loss rates determined from MAVEN observations and integrated loss through time. Icarus. https://doi.org/10.1016/j.icarus.2018.05.030 Jakosky, B.M., Edwards, C.S., 2018. Inventory of CO 2 available for terraforming Mars. Nat. Astron. 2, 634. https://doi.org/10.1038/s41550-018-0529-6

Jakosky, B.M., Phillips, R.J., 2001. Mars' volatile and climate history. Nature 412, 237. https://doi.org/10.1038/35084184

Kite, E.S., 2019. Geologic Constraints on Early Mars Climate. Space Sci. Rev. 215, 10. https://doi.org/10.1007/s11214-018-0575-5

Kite, E.S., Gao, P., Goldblatt, C., Mischna, M.A., Mayer, D.P., Yung, Y.L., 2017. Methane bursts as a trigger for intermittent lake-forming climates on post-Noachian Mars. Nat. Geosci. 10, 737–740. https://doi.org/10.1038/ngeo3033

Kite, E.S., Matsuyama, I., Manga, M., Perron, J.T., Mitrovica, J.X., 2009. True Polar Wander driven by late-stage volcanism and the distribution of paleopolar deposits on Mars. Earth Planet. Sci. Lett. 280, 254–267. https://doi.org/10.1016/j.epsl.2009.01.040

Kite, E.S., Mayer, D.P., Wilson, S.A., Davis, J.M., Lucas, A.S., Quay, G.S. de, 2019. Persistence of intense, climate-driven runoff late in Mars history. Sci. Adv. 5, eaav7710. https://doi.org/10.1126/sciadv.aav7710

Kite, E.S., Williams, J.-P., Lucas, A., Aharonson, O., 2014. Low palaeopressure of the martian atmosphere estimated from the size distribution of ancient craters. Nat. Geosci. 7, 335–339. https://doi.org/10.1038/ngeo2137

Krasnopolsky, V.A., Mumma, M.J., Gladstone, G.R., 1998. Detection of Atomic Deuterium in the Upper Atmosphere of Mars. Science 280, 1576–1580. https://doi.org/10.1126/science.280.5369.1576

Kurahashi-Nakamura, T., Tajika, E., 2006. Atmospheric collapse and transport of carbon dioxide into the subsurface on early Mars. Geophys. Res. Lett. 33. https://doi.org/10.1029/2006GL027170

Kurokawa, H., Sato, M., Ushioda, M., Matsuyama, T., Moriwaki, R., Dohm, J.M., Usui, T., 2014. Evolution of water reservoirs on Mars: Constraints from hydrogen isotopes in martian meteorites. Earth Planet. Sci. Lett. 394, 179–185. https://doi.org/10.1016/j.epsl.2014.03.027

Kurokawa, H., Usui, T., Sato, M., 2016. Interactive evolution of multiple water-ice reservoirs on Mars: Insights from hydrogen isotope compositions. Geochem. J. 50, 67–79. https://doi.org/10.2343/geochemj.2.0407

Lammer, H., Lichtenegger, H.I.M., Kolb, C., Ribas, I., Guinan, E.F., Abart, R., Bauer, S.J., 2003. Loss of water from Mars:: Implications for the oxidation of the soil. Icarus 165, 9–25. https://doi.org/10.1016/S0019-1035(03)00170-2

Lanza, N.L., Fischer, W.W., Wiens, R.C., Grotzinger, J., Ollila, A.M., Cousin, A., Anderson, R.B., Clark, B.C., Gellert, R., Mangold, N., Maurice, S., Le Mouélic, S., Nachon, M., Schmidt, M., Berger, J., Clegg, S.M., Forni, O., Hardgrove, C., Melikechi, N., Newsom, H.E., Sautter, V., 2014. High manganese concentrations in rocks at Gale crater, Mars. Geophys. Res. Lett. 41, 2014GL060329. https://doi.org/10.1002/2014GL060329

Lanza, N.L., Wiens, R.C., Arvidson, R.E., Clark, B.C., Fischer, W.W., Gellert, R., Grotzinger, J.P., Hurowitz, J.A., McLennan, S.M., Morris, R.V., Rice, M.S., Bell, J.F., Berger, J.A., Blaney, D.L., Bridges, N.T., Calef, F., Campbell, J.L., Clegg, S.M., Cousin, A., Edgett, K.S., Fabre, C., Fisk, M.R., Forni, O., Frydenvang, J., Hardy, K.R., Hardgrove, C., Johnson, J.R., Lasue, J., Le Mouélic, S., Malin, M.C., Mangold, N., Martìn-Torres, J., Maurice, S., McBride, M.J., Ming, D.W., Newsom, H.E., Ollila, A.M., Sautter, V., Schröder, S., Thompson, L.M., Treiman, A.H., VanBommel, S., Vaniman, D.T., Zorzano, M.-P., 2016. Oxidation of manganese in an ancient aquifer, Kimberley formation, Gale crater, Mars. Geophys. Res. Lett. 43, 2016GL069109. https://doi.org/10.1002/2016GL069109

Lillis, R.J., Deighan, J., Fox, J.L., Bougher, S.W., Lee, Y., Combi, M.R., Cravens, T.E., Rahmati, A., Mahaffy, P.R., Benna, M., Elrod, M.K., McFadden, J.P., Ergun, R.E., Andersson, L., Fowler, C.M., Jakosky, B.M., Thiemann, E., Eparvier, F., Halekas, J.S., Leblanc, F., Chaufray, J.-Y., 2017. Photochemical escape of oxygen from Mars: First results from MAVEN in situ data. J. Geophys. Res. Space Phys. 122, 3815–3836. https://doi.org/10.1002/2016JA023525

Liu, K.-K., Epstein, S., 1984. The hydrogen isotope fractionation between kaolinite and water. Chem. Geol. 46, 335–350. https://doi.org/10.1016/0009-2541(84)90176-1

Lyons, T.W., Reinhard, C.T., Planavsky, N.J., 2014. The rise of oxygen in Earth's early ocean and atmosphere. Nature 506, 307–315. https://doi.org/10.1038/nature13068

Mahaffy, P.R., Webster, C.R., Stern, J.C., Brunner, A.E., Atreya, S.K., Conrad, P.G., Domagal-Goldman, S., Eigenbrode, J.L., Flesch, G.J., Christensen, L.E., Franz, H.B., Freissinet, C., Glavin, D.P., Grotzinger, J.P., Jones, J.H., Leshin, L.A., Malespin, C., McAdam, A.C., Ming, D.W., Navarro-Gonzalez, R., Niles, P.B., Owen, T., Pavlov, A.A., Steele, A., Trainer, M.G., Williford, K.H., Wray, J.J., Team, the M.S., 2015. The imprint of atmospheric evolution in the D/H of Hesperian clay minerals on Mars. Science 347, 412–414. https://doi.org/10.1126/science.1260291

Mamajek, E.E., Hillenbrand, L.A., 2008. Improved Age Estimation for Solar-Type Dwarfs Using Activity-Rotation Diagnostics. Astrophys. J. 687, 1264–1293. https://doi.org/10.1086/591785
Manning, C.V., Bierson, C., Putzig, N.E., McKay, C.P., 2019. The formation and stability of buried polar CO2 deposits on Mars. Icarus 317, 509–517. https://doi.org/10.1016/j.icarus.2018.07.021

Mansfield, M., Kite, E.S., Mischna, M.A., 2018. Effect of Mars Atmospheric Loss on Snow Melt Potential in a 3.5 Gyr Mars Climate Evolution Model. J. Geophys. Res. Planets 123, 794–806. https://doi.org/10.1002/2017JE005422

Michael, G.G., 2013. Planetary surface dating from crater size–frequency distribution measurements: Multiple resurfacing episodes and differential isochron fitting. Icarus 226, 885–890. https://doi.org/10.1016/j.icarus.2013.07.004

Michalski, J., Niles, P.B., 2012. Atmospheric origin of Martian interior layered deposits: Links to climate change and the global sulfur cycle. Geology 40, 419–422. https://doi.org/10.1130/G32971.1

Morris, R.V., Klingelhöfer, G., Schröder, C., Rodionov, D.S., Yen, A., Ming, D.W., de Souza, P.A., Wdowiak, T., Fleischer, I., Gellert, R., Bernhardt, B., Bonnes, U., Cohen, B.A., Evlanov, E.N., Foh, J., Gütlich, P., Kankeleit, E., McCoy, T., Mittlefehldt, D.W., Renz, F., Schmidt, M.E., Zubkov, B., Squyres, S.W., Arvidson, R.E., 2006. Mössbauer mineralogy of rock, soil, and dust at Meridiani Planum, Mars: Opportunity's journey across sulfate-rich outcrop, basaltic sand and dust, and hematite lag deposits. J. Geophys. Res. Planets 111, E12S15. https://doi.org/10.1029/2006JE002791

Mustard, J.F., Murchie, S.L., Pelkey, S.M., Ehlmann, B.L., Milliken, R.E., Grant, J.A., Bibring, J.-P., Poulet, F., Bishop, J., Dobrea, E.N., Roach, L., Seelos, F., Arvidson, R.E., Wiseman, S., Green, R., Hash, C., Humm, D., Malaret, E., McGovern, J.A., Seelos, K., Clancy, T., Clark, R., Marais, D.D., Izenberg, N., Knudson, A., Langevin, Y., Martin, T., McGuire, P., Morris, R., Robinson, M., Roush, T., Smith, M., Swayze, G., Taylor, H., Titus, T., Wolff, M., 2008. Hydrated silicate minerals on Mars observed by the Mars Reconnaissance Orbiter CRISM instrument. Nature 454, 305–309. https://doi.org/10.1038/nature07097

Niles, P.B., Catling, D.C., Berger, G., Chassefière, E., Ehlmann, B.L., Michalski, J.R., Morris, R., Ruff, S.W., Sutter, B., 2013. Geochemistry of Carbonates on Mars: Implications for Climate History and Nature of Aqueous Environments. Space Sci. Rev. 174, 301–328. https://doi.org/10.1007/s11214-012-9940-y

Poulet, F., Bibring, J.-P., Mustard, J.F., Gendrin, A., Mangold, N., Langevin, Y., Arvidson, R.E., Gondet, B., Gomez, C., 2005. Phyllosilicates on Mars and implications for early martian climate. Nature 438, 623–627. https://doi.org/10.1038/nature04274

Palucis, M.C., Dietrich, W.E., Williams, R.M.E., Hayes, A.G., Parker, T., Sumner, D.Y., Mangold, N., Lewis, K., Newsom, H., 2016. Sequence and relative timing of large lakes in Gale crater (Mars)

after the formation of Mount Sharp. J. Geophys. Res. Planets 121, 472–496. https://doi.org/10.1002/2015JE004905

Putzig, N.E., Smith, I.B., Perry, M.R., Foss, F.J., Campbell, B.A., Phillips, R.J., Seu, R., 2018. Three-dimensional radar imaging of structures and craters in the Martian polar caps. Icarus, Mars Polar Science VI 308, 138–147. https://doi.org/10.1016/j.icarus.2017.09.023

Ramirez, R.M., Kasting, J.F., 2017. Could cirrus clouds have warmed early Mars? Icarus 281, 248–261. https://doi.org/10.1016/j.icarus.2016.08.016

Ramirez, R.M., Kopparapu, R., Zugger, M.E., Robinson, T.D., Freedman, R., Kasting, J.F., 2014. Warming early Mars with CO2 and H2. Nat. Geosci. 7, 59–63. https://doi.org/10.1038/ngeo2000

Ramstad, R., Barabash, S., Futaana, Y., Nilsson, H., Holmström, M., 2018. Ion Escape From Mars Through Time: An Extrapolation of Atmospheric Loss Based on 10 Years of Mars Express Measurements. J. Geophys. Res. Planets 123, 3051–3060. https://doi.org/10.1029/2018JE005727

Ribas, I., Guinan, E.F., Güdel, M., Audard, M., 2005. Evolution of the Solar Activity over Time and Effects on Planetary Atmospheres. I. High-Energy Irradiances (1-1700 Å). Astrophys. J. 622, 680. https://doi.org/10.1086/427977

Sanz-Forcada, J., Micela, G., Ribas, I., Pollock, A.M.T., Eiroa, C., Velasco, A., Solano, E., García-Álvarez, D., 2011. Estimation of the XUV radiation onto close planets and their evaporation. Astron. Astrophys. 532, A6. https://doi.org/10.1051/0004-6361/201116594

Tanaka, K.L., Skinner, J.A., Jr., Dohm, J.M., Irwin, R.P., III, Kolb, E.J., Fortezzo, C.M., Platz, T., Michael, G.G., Hare, T.M., 2014. Geologic map of Mars. U.S. Geological Survey Scientific Investigations Map 3292.

Tu, L., Johnstone, C.P., Güdel, M., Lammer, H., 2015. The Extreme Ultraviolet and X-Ray Sun in Time: High-Energy Evolutionary Tracks of a Solar-Like Star. Astron. Astrophys. 577, L3. https://doi.org/10.1051/0004-6361/201526146

Urata, R.A., Toon, O.B., 2013. Simulations of the martian hydrologic cycle with a general circulation model: Implications for the ancient martian climate. Icarus 226, 229–250. https://doi.org/10.1016/j.icarus.2013.05.014

Usui, T., 2019. Chapter 4 - Hydrogen Reservoirs in Mars as Revealed by Martian Meteorites, in: Filiberto, J., Schwenzer, S.P. (Eds.), Volatiles in the Martian Crust. Elsevier, pp. 71–88. https://doi.org/10.1016/B978-0-12-804191-8.00004-0

Villanueva, G.L., Mumma, M.J., Novak, R.E., Käufl, H.U., Hartogh, P., Encrenaz, T., Tokunaga, A., Khayat, A., Smith, M.D., 2015. Strong water isotopic anomalies in the martian atmosphere: Probing current and ancient reservoirs. Science 348, 218–221. https://doi.org/10.1126/science.aaa3630

Vos, E., Aharonson, O., Schorghofer, N., 2019. Dynamic and isotopic evolution of ice reservoirs on Mars. Icarus 324, 1–7.

Warner, N.H., Golombek, M.P., Sweeney, J., Fergason, R., Kirk, R., Schwartz, C., 2017. Near Surface Stratigraphy and Regolith Production in Southwestern Elysium Planitia, Mars: Implications for Hesperian-Amazonian Terrains and the InSight Lander Mission. Space Sci. Rev. 211, 147–190. https://doi.org/10.1007/s11214-017-0352-x

Warren, A.O., Kite, E.S., Williams, J.-P., Horgan, B., n.d. Through the Thick and Thin: New Constraints on Mars Paleopressure History 3.8 – 4 Ga from Small Exhumed Craters. J. Geophys. Res. Planets n/a. https://doi.org/10.1029/2019JE006178

Webster, C.R., Mahaffy, P.R., Flesch, G.J., Niles, P.B., Jones, J.H., Leshin, L.A., Atreya, S.K., Stern, J.C., Christensen, L.E., Owen, T., Franz, H., Pepin, R.O., Steele, A., Team, the M.S., 2013. Isotope Ratios of H, C, and O in CO2 and H2O of the Martian Atmosphere. Science 341, 260–263. https://doi.org/10.1126/science.1237961

Wernicke, L.J., Jakosky, B.M., 2019. The History of Water on Mars: Hydrated Minerals as a Water Sink in the Martian Crust. LPI Contrib. 2089.

Whitten, J.L., Campbell, B.A., Plaut, J.J., 2018. Defining the material properties of the Dorsa Argentea Formation using MARSIS radar sounder data. LPSC XLIX #2632.

Wordsworth, R.D., 2016. The Climate of Early Mars. Annu. Rev. Earth Planet. Sci. 44, 381–408. https://doi.org/10.1146/annurev-earth-060115-012355

Appendix Table 6.4 References

Bridges, N.T., Banks, M.E., Beyer, R.A., Chuang, F.C., Noe Dobrea, E.Z., Herkenhoff, K.E., Keszthelyi, L.P., Fishbaugh, K.E., McEwen, A.S., Michaels, T.I., Thomson, B.J., Wray, J.J., 2010. Aeolian bedforms, yardangs, and indurated surfaces in the Tharsis Montes as seen by the HiRISE Camera: Evidence for dust aggregates. Icarus, MRO/HiRISE Studies of Mars 205, 165–182. https://doi.org/10.1016/j.icarus.2009.05.017

Byrne, S., Dundas, C.M., Kennedy, M.R., Mellon, M.T., McEwen, A.S., Cull, S.C., Daubar, I.J., Shean, D.E., Seelos, K.D., Murchie, S.L., Cantor, B.A., Arvidson, R.E., Edgett, K.S., Reufer, A., Thomas, N., Harrison, T.N., Posiolova, L.V., Seelos, F.P., 2009. Distribution of Mid-Latitude Ground Ice on Mars from New Impact Craters. Science 325, 1674–1676. https://doi.org/10.1126/science.1175307

Byrne, S., Murray, B.C., 2002. North polar stratigraphy and the paleo-erg of Mars. J. Geophys. Res. Planets 107, 11-1-11–12. https://doi.org/10.1029/2001JE001615

Grima, C., Kofman, W., Mouginot, J., Phillips, R.J., Hérique, A., Biccari, D., Seu, R., Cutigni, M., 2009. North polar deposits of Mars: Extreme purity of the water ice. Geophys. Res. Lett. 36. https://doi.org/10.1029/2008GL036326

Hayward, R.K., 2011. Mars Global Digital Dune Database (MGD3): north polar region (MC-1) distribution, applications, and volume estimates. Earth Surf. Process. Landf. 36, 1967–1972. https://doi.org/10.1002/esp.2219

Hayward, R.K., Fenton, L.K., Titus, T.N., Colaprete, A., Christensen, P.R., 2012. SP_Dune_Pamphlet.doc. Mars Glob. Digit. Dune Database.

Hayward, R.K., Mullins, K.F., Fenton, L.K., Hare, T.M., Titus, T.N., Bourke, M.C., Colaprete, A., Christensen, P.R., 2007. Mars Global Digital Dune Database and initial science results. J. Geophys. Res. Planets 112. https://doi.org/10.1029/2007JE002943

Holt, J.W., Safaeinili, A., Plaut, J.J., Head, J.W., Phillips, R.J., Seu, R., Kempf, S.D., Choudhary, P., Young, D.A., Putzig, N.E., Biccari, D., Gim, Y., 2008. Radar Sounding Evidence for Buried Glaciers in the Southern Mid-Latitudes of Mars. Science 322, 1235–1238. https://doi.org/10.1126/science.1164246

Michalski, J., Niles, P.B., 2012. Atmospheric origin of Martian interior layered deposits: Links to climate change and the global sulfur cycle. Geology 40, 419–422. https://doi.org/10.1130/G32971.1

Plaut, J.J., Picardi, G., Safaeinili, A., Ivanov, A.B., Milkovich, S.M., Cicchetti, A., Kofman, W., Mouginot, J., Farrell, W.M., Phillips, R.J., Clifford, S.M., Frigeri, A., Orosei, R., Federico, C., Williams, I.P., Gurnett, D.A., Nielsen, E., Hagfors, T., Heggy, E., Stofan, E.R., Plettemeier, D., Watters, T.R., Leuschen, C.J., Edenhofer, P., 2007. Subsurface Radar Sounding of the South Polar Layered Deposits of Mars. Science 316, 92–95. https://doi.org/10.1126/science.1139672

Schon, S.C., Head, J.W., Milliken, R.E., 2009. A recent ice age on Mars: Evidence for climate oscillations from regional layering in mid-latitude mantling deposits. Geophys. Res. Lett. 36. https://doi.org/10.1029/2009GL038554

Scott, D.H., Tanaka, K.L., 1986. Geologic map of the western equatorial region of Mars. IMAP. https://doi.org/10.3133/i1802A

Shean, D.E., Head, J.W., Marchant, D.R., 2005. Origin and evolution of a cold-based tropical mountain glacier on Mars: The Pavonis Mons fan-shaped deposit. J. Geophys. Res. Planets 110. https://doi.org/10.1029/2004JE002360

Warner, N.H., Golombek, M.P., Sweeney, J., Fergason, R., Kirk, R., Schwartz, C., 2017. Near Surface Stratigraphy and Regolith Production in Southwestern Elysium Planitia, Mars: Implications for Hesperian-Amazonian Terrains and the InSight Lander Mission. Space Sci. Rev. 211, 147–190. https://doi.org/10.1007/s11214-017-0352-x

Watters, T.R., Campbell, B., Carter, L., Leuschen, C.J., Plaut, J.J., Picardi, G., Orosei, R., Safaeinili, A., Clifford, S.M., Farrell, W.M., Ivanov, A.B., Phillips, R.J., Stofan, E.R., 2007. Radar Sounding of the Medusae Fossae Formation Mars: Equatorial Ice or Dry, Low-Density Deposits? Science 318, 1125–1128. https://doi.org/10.1126/science.1148112

Zuber, M.T., Phillips, R.J., Andrews-Hanna, J.C., Asmar, S.W., Konopliv, A.S., Lemoine, F.G., Plaut, J.J., Smith, D.E., Smrekar, S.E., 2007. Density of Mars' South Polar Layered Deposits. Science 317, 1718–1719. https://doi.org/10.1126/science.1146995

Chapter 7 – Reevaluating the Kinetics of Ferrous Iron UV Photooxidation and its Implications for Chemical Sedimentation in Martian Lakes.

Foreword

In Chapter 6, we considered the role of ferrous iron (Fe^{2+}) as a redox sink at Mars's surface during the loss of its volatile reservoirs, but we did not delve into the mechanisms of Fe^{2+} oxidation themselves. Unlike on Earth, where the Great Oxidation Event (GOE) was ultimately driven by biological production of free O_2 (Catling et al., 2001; Lyons et al., 2014), and Fe-based metabolisms were probably active players in pre-GOE biogeochemical cycles (Kappler et al., 2005; Konhauser et al., 2002, 2005; Walker, 1984), we cannot appeal to life as a mechanism for oxidation of the Martian surface, or any Martian geochemical features; and therefore abiotic processes should be able to provide adequate explanations. Mars has a rich geological record of ancient lakes that saw prolonged sedimentation (Ehlmann et al., 2016; Kite, 2019), including chemical sedimentation; and the chemical environments of some of these water bodies have been interpreted to have been potentially habitable, with defined redox structures (Grotzinger et al., 2014; Hurowitz et al., 2017). To better understand the redox structure of Martian lakes, we need to understand the mechanisms that can oxidize Fe^{2+}, the most abundant redox-active metal at the planet's surface, in these lake environments. Here in Chapter 7, our aim is to better understand one of the main proposed mechanisms for Fe^{2+} oxidation in aqueous environments on Mars; ultraviolet (UV) photooxidation (Hurowitz et al., 2017, 2010; Nie et al., 2017; Schaefer, 1996; Tabata et al., 2021).

UV photooxidation is a photochemical process wherein the absorption of a UV photon by an ion or molecule, in this case, Fe^{2+} or $FeOH^{+}$, causes the ejection of an electron from the now-energetically-excited ion, during some fraction of absorption events. Oxidation of Fe^{2+} by UV

photons is appealing because it has such basic requirements. Other Fe^{2+} oxidation pathways require a chemical oxidant, but UV photooxidation requires only Fe^{2+}, water, and a source of UV radiation, the latter of which is readily supplied by the Sun. Given that all of these components are readily available at Mars's surface (or were, in its wetter early history), some amount of Fe^{2+} photooxidation seems like an inevitability, and its effectiveness as a geochemical process comes down to the rate at which photooxidation could proceed, relative to the lifetime of standing water bodies on Mars. Of course, pre-GOE Earth probably lacked an ozone layer and was also strongly irradiated by solar UV at its surface, and UV photooxidation has also been invoked as a driving mechanism for the deposition of Fe^{3+} in iron formations (IFs) (Anbar and Holland, 1992; Braterman et al., 1983; Cairns-Smith, 1978; François, 1986). However, defining an abiotic baseline rate for Fe deposition on the early Earth has limited value, because biologically influenced geochemical processes can outstrip UV photooxidation rates (Konhauser et al., 2007; Thompson et al., 2019); evidence for primary photosynthesizers, which oxidize the environment during carbon fixation in the marine environment, is overwhelming; and the geochemical (Fe isotopic) imprints of oxidation by biotic and abiotic pathways for Fe^{2+} oxidation appear to be indistinguishable (Bullen et al., 2001; Croal et al., 2004; Nie et al., 2017).

By contrast on Mars, UV photooxidation can almost be considered the baseline assumption for the oxidation of Fe^{2+} in aqueous environments. Other strong oxidants, generated through atmospheric photochemistry and volcanic gas emissions, such as O_2, H_2O_2, and oxychlorine species, could have formed on Mars and been potent oxidizers of Fe^{2+} (Hurowitz et al., 2017; Mitra et al., 2020; Mitra and Catalano, 2019; Schaefer, 1996; Wordsworth et al., 2021). However, is difficult to infer the past abundance of these species from the Mars geochemical record, and therefore interpretations of their role in Fe^{2+} oxidation 3.5 billion years ago require more assumptions than UV

photooxidation, which relies purely on a dissolved Fe^{2+} and relatively well-characterized solar UV flux. In this chapter, to build towards an understanding of the possible role of Fe^{2+} photooxidation on Mars, and whether we find support for this process in the Martian geochemical record, we conducted a multi-part study comprised of the following:

1) We conducted new anoxic experiments designed reevaluate the efficiency of Fe^{2+} photooxidation. Specifically, we calculate a parameter called the quantum yield (denoted with Φ), which is defined as the proportion of photon absorptions by a ferrous Fe species in that results in a photooxidation event. Determining the value of Φ has been the subject of numerous previous experimental studies (Braterman et al., 1984; Jortner and Stein, 1962a, 1962b; Logan, 1990; Nie et al., 2017; Tabata et al., 2021). However, our experimental design incorporates a more favorable geometry for accurately modeling the photon flux to our solutions, and uses a light source that provides the best available solar simulator, which only one previous study has used. By running long-duration experiments, we also determine the extent to which photooxidation can deplete solutions of dissolved Fe(II) at different pH levels, and draw conclusions about the chemical environments on Mars where photooxidation could enable quantitative Fe removal to sediments.
2) We construct a reaction-transport model of a Martian lake and calculate rates of Fe^{3+} chemical precipitation that would be supported by photooxidation, using the new experimental constraints on the kinetic efficiency of this process. We adapted the model from Chapter 3 that was used to determine the Fe isotopic fractionation associated with the marine oxic Fe sink (Czaja et al., 2012; Heard et al., 2020); which emphasizes the benefit of transferring concepts from studies of early Earth to more general understanding of anoxic water columns on other planetary bodies (Schaefer, 1996).

3) We place our model results in the context of ancient lake sediments that have been geochemically characterized by the Curiosity rover at Gale Crater. Secondary Fe mineral abundances and textural observations of sedimentary laminations together provide an independent estimate of Fe^{3+} deposition we can compare to modeled photooxidation rates to infer the viability of this process in explaining ferric mineral deposition on Mars (Hurowitz et al., 2017). Meanwhile, photooxidation-driven Fe deposition also makes predictions iron to manganese (Fe/Mn) ratio systematics, which we can compare to published Fe and Mn data from Gale Crater that have previously been used to argue for the presence of O_2 the Gale Lake aqueous environment (Hurowitz et al., 2017; Lanza et al., 2016; Wordsworth et al., 2021).

Many of the lessons learned from the redox evolution of Earth prior to the GOE can be transferred in useful ways to understanding ancient Martian environments. Towards the end of this chapter, we show how the record of terrestrial IFs and other products of ferruginous ocean from early in Earth history, can provide great value in understanding the geochemical systematics of lake sediments formed in Martian water bodies. The abiotic deposition of IF-like chemical sediments has been both hypothesized (Schaefer, 1996), and inferred directly from Curiosity rover data at Gale Crater (Hurowitz et al., 2017), many concepts developed by studying the huge geochemical archive of terrestrial IFs can still be generalized to Mars, even though it never be possible to disentangle biology from the deposition of IFs on Earth. In particular, we show that the Fe/Mn systematics of IFs formed in the runup to, and during, the GOE (Kurzweil et al., 2016; Thibon et al., 2019; Tsikos et al., 2010), are a useful comparison point when trying to understand Fe/Mn systematics in Gale Crater rocks, and whether they provide evidence for elevated O_2 on Mars coincident with habitable conditions in long-lived lakes.

Abstract

Ferric iron is abundant at the surface of Mars, both in surface dust and ancient lake sediments. The Martian atmosphere is currently thin and contains negligible oxygen, and it is unclear if the Martian atmosphere was ever oxygenated. In the absence of oxygen or biology, UV photooxidation of Fe^{2+} is an appealing mechanism to explain Fe^{3+} deposition in Martian sediments because it requires only water, Fe, and sunlight, all of which were readily available. However, the kinetic viability of UV photooxidation on Mars is unclear because experiments to determine the efficiency of this reaction (the quantum yield, Φ), mostly used inappropriate light sources and/or were not run for sufficiently long durations to quantify how much Fe^{2+} can be permanently removed from solution. Here we report new photooxidation experiments conducted using a Xe lamp that is a good solar simulator. We find Φ values in good agreement with earlier studies, but not with the most recent work that also used a Xe light source. We ran long duration experiments and found that the depletion of Fe^{2+} from solution is effective at near neutral pH, but at pH 2.00, only 25 % of Fe^{2+} was oxidized before further reaction progress tailed off. We suggest that Fe^{3+} photoreduction stabilizes high Fe^{2+} in solution at low pH, and thus Fe^{3+} deposition in low pH environments on Mars like the jarosite-bearing Burns formation is unlikely to have been driven by photooxidation. Using a reaction-transport model of near-neutral Martian lake conditions, and find that photooxidation supports Fe^{3+} deposition rates that can more than adequately explain apparent authigenic mineral accumulation rates in the Murray Formation logged by the Curiosity Rover at the 3.5 billion year old Gale Crater Lake deposits. Last, we show that redox decoupling of Fe and Mn driven by photooxidation of the former and not the latter, can explain Fe/Mn systematics observed in bulk Murray Formation mudstones, and can produce Mn-rich residual fluids from which high-Mn alteration features observed in Gale Crater may have precipitated.

Introduction

Iron (Fe) is the most abundant element that has multiple stable redox states in rocks on the surface of Earth and Mars. Because of this, geochemical processes involving Fe can exert strong controls on the overall redox conditions at planetary surfaces, with Fe acting as a redox buffer. Meanwhile, the geochemical record of Fe in rocks provides a witness of changing redox processes at planetary surfaces. Throughout much of their early planetary history, both Earth and Mars have had reducing atmospheres with vanishingly low levels of free oxygen (O_2) (Catling and Zahnle, 2020; Liu et al., 2021; Lyons et al., 2014; Wordsworth et al., 2021), but sedimentary rocks formed beneath these anoxic atmospheres often contain abundant ferric iron, with striking examples including terrestrial iron formations (Bekker et al., 2010; Konhauser et al., 2017); and Fe^{3+}-rich alteration mineral assemblages observed on Mars via remote sensing and rover instruments (Burns, 1987; Hurowitz et al., 2017; Klingelhöfer et al., 2004; Liu et al., 2021; Morris et al., 2006, 2000). The capacity for Fe to take part in low temperature redox cycling on pre-oxygenation worlds makes it an element of great astrobiological significance, as it can act as an electron donor for autotrophic life when in its reduced form, and as an electron acceptor for respiration of organic matter when oxidized.

As we have yet to observe evidence for life, microbial or otherwise, on modern or ancient Mars, alternative abiotic pathways to Fe redox cycling should be considered the null hypothesis when interpreting geochemical data. Aqueous photooxidation, the process by which dissolved ferrous iron ions absorb solar ultraviolet (UV) photons and some fraction of these absorptions result in the removal of an electron, is one such process (Hurowitz et al., 2017, 2010; Nie et al., 2017; Schaefer, 1996; Tabata et al., 2021). The net reaction for Fe^{2+} photooxidation including subsequent hydrolysis and precipitation of Fe^{3+} oxyhydroxide can be written as

$$Fe^{2+} + 3H_2O \xrightarrow{h\nu} Fe(OH)_3 + 2H^+ + 0.5H_2, \quad \text{(Eq. 1)}$$

This Fe^{2+} oxidation pathway requires minimal assumptions about the chemistry of aqueous environments on Mars, because it relies only on the presence of dissolved ferrous iron; essentially guaranteed given the presence of water and rock under an anoxic atmosphere; and solar UV radiation that has been available throughout the history of the solar system and was more intense when the Sun was younger (Ranjan et al., 2017; Ribas et al., 2010). The challenge for UV photooxidation models for early Earth and Mars boils down to whether the kinetics of this process would allow Fe^{2+} oxidation an sedimentation at rates that are comparable to the accumulation times of authigenic Fe sediments; and, fast enough to outpace the drying of short-lived standing water bodies, on Earth and Mars respectively. The kinetics of iron photooxidation depend on the rate at which UV photons are absorbed, the fraction of absorptions that results in oxidation. This latter parameter is called the quantum yield, commonly denoted Φ, and is calculated as Φ = [number of atoms oxidized/number of photons absorbed].

Experiments to determine Φ have been conducted over a swathe of pH conditions from highly acidic (pH 0.35-3.5) (Jortner and Stein, 1962a, 1962b; Logan, 1990; Tabata et al., 2021), to near-neutral (Braterman et al., 1984, 1983; Nie et al., 2017; Tabata et al., 2021). Jortner and Stein (1962b) found that the quantum yield increased with decreasing pH below 2.5, and that this pH dependence tailed off at higher pH. These authors reason that the photooxidation reaction is facilitated in part by the scavenging of liberated electrons by H^+ and thus favored where more H^+ ions were available. Overall photooxidation rates (not quantum yields) increase at higher pH because the speciation of Fe(II) favors $Fe(OH)^+$, which has a far stronger and broader absorption spectrum (Braterman et al., 1984; François, 1987).

Earlier experiments notably all made use of low- or medium-pressure mercury vapor lamps, which have emission spectra with abundant sharp features in the 200-450 nm wavelength range relevant

to absorption by Fe^{2+} and $FeOH^{+}$ (Braterman et al., 1984; Jortner and Stein, 1962a, 1962b; Nie et al., 2017). A concern with using such light sources is that a few (or even just one), discrete wavelength may dominate the photon absorption integrated over all wavelengths within the range of interest, so that minor inaccuracies in characterizing the amplitude and width of a few sharp features could propagate to systematic under- or overestimates of the quantum yield as a result (Fig. 7.2). High-pressure lamps have smoother output spectra and xenon arc lamps in particular have the added benefit of being good solar simulators in the wavelength range of interest for iron photooxidation (Fig. 7.2). Tabata et al. (2021) recently published a large dataset of new photooxidation experimental results conducted with a xenon lamp that investigated the full pH range encompassed by earlier studies, and proposed a pH-dependent function for Φ_{Fe2+} and a separate value for Φ_{FeOH+} determined at neutral pH by employing a >300 nm cutoff filter. Quantum yields were determined from small early decreases in Fe(II) concentration before inhibiting effects of accumulating Fe^{3+} could be observed. In nature, photooxidation reactions would occur over longer time periods where they might be anticipated to run to completion or reach a steady state within a more complex geochemical system. Therefore, in this study, in addition to making our own determinations of the quantum yield, Φ, we aim to conduct longer timescale photooxidation experiments to determine how low the ferrous Fe concentration can be driven by this process. We will then incorporate these experimental constraints into a geochemical model for Fe (and Mn) deposition in Martian lakes.

Photooxidation in and redox evolution in Martian aqueous environments

Photooxidation has been invoked as an Fe oxidation pathway in multiple locations on Mars (Schaefer, 1996), including the rover exploration sites at Meridiani Planum (Mars Exploration

Rover Opportunity) (Hurowitz et al., 2010), and Gale Crater (Mars Science Laboratory Curiosity) (Hurowitz et al., 2017). At Meridiani Planum, where low-pH acid sulfate alteration conditions prevailed (Clark et al., 2005; Klingelhöfer et al., 2004; Squyres and Knoll, 2005), photooxidation would provide a more efficient aqueous Fe^{2+} oxidation mechanism than oxidation by O_2, which is extremely slow at low pH. Hurowitz et al. (2010) and Nie et al. (2017) both modeled photooxidation in a standing water body at Meridiani Planum in which pH was allowed to evolve to acidic levels following hydrolysis of Fe^{3+}. While employing different model assumptions, these studies qualitatively agreed in finding that photooxidation rates far outstripped O_2-mediated oxidation rates in an acid-sulfate solution for any reasonable estimate of Martian pO_2 (Catling and Moore, 2003). Aqueous photooxidation modeling at Meridiani Planum was prefaced on the existence of relatively long-lived, albeit shallow, standing water bodies rich in Fe^{2+} that could receive prolonged exposure to solar radiation (Hurowitz et al., 2010; Nie et al., 2017). New analog studies and the geologic context of the jarosite-bearing assemblages at Meridiani Planum now suggest that such a setting is somewhat less likely than the formation of jarosite formation in cold, dry environments during ice-dust interaction processes at low water activity (Baccolo et al., 2021; Niles and Michalski, 2009). The diagenetic nature of certain features in the Burns Formation of Meridiani Planum such as hematite spherules also obscure the sequence of events that led to the formation of ferric iron-rich mineral assemblages at this location (Squyres et al., 2006).

Gale Crater on Mars contains a thick siliciclastic sedimentary succession with chemical and textural features consistent with deposition in a long-lived, near-neutral freshwater lacustrine setting (Grotzinger, 2013; Grotzinger et al., 2014). The upward succession indicates deepening of depositional facies from the deltaic sandstones and conglomerates in the Bradbury Group to deposition of laminated mudstones in the Mount Sharp Group, within which the Murray Formation

has been the subject of extensive geochemical investigation (Frydenvang et al., 2020; Grotzinger et al., 2015; Hurowitz et al., 2017; Rampe et al., 2017). The Murray Formation is a fine-grained mudstone succession that features roughly equal detrital (mafic), amorphous, and secondary mineral components (Frydenvang et al., 2020; Hurowitz et al., 2017; Rampe et al., 2017). The prevailing interpretation of the Murray Formation is that deposition occurred in a stratified lake environment featuring distinct facies containing different secondary mineral assemblages (Hurowitz et al., 2017). The distal magnetite-silica (MS) facies is typified by high opaline silica contents and an iron-bearing secondary mineral assemblage dominated by the mixed-valence oxide magnetite, which can form authigenically in an anoxic water column, both through a homogenous reaction (Tosca et al., 2018) and through the interaction of sinking ferric oxyhydroxides with dissolved Fe^{2+}. The hematite-phyllosilicate (HP) facies of the Murray Formation features thicker laminations suggesting a shallower, more proximal depositional environment, and its secondary mineral assemblage is rich in phyllosilicates and fully oxidized secondary iron minerals, predominantly hematite, with jarosite that might be a diagenetic overprint resulting from sulfide mineral breakdown. The observation that the Murray Formation contains a more oxidized shallow water facies led to the redox-stratification model, wherein shallow waters experienced oxidizing conditions provided by surface-derived chemical oxidants and/or UV photons (Hurowitz et al., 2017). Downward attenuation of surface oxidants would allow anoxic conditions to prevail at depth, with high dissolved Fe^{2+} concentrations provided by anoxic groundwaters buffered by subsurface interactions with basaltic bedrock.

Several oxidants have been implicated in early Martian aqueous geochemistry including O_2, chlorate, and UV photons (Burns, 1993; Hurowitz et al., 2017, 2010; Lanza et al., 2016; Mitra et al., 2020; Mitra and Catalano, 2019; Nie et al., 2017; Schaefer, 1996; Tosca et al., 2008;

Wordsworth et al., 2021). The former two require atmospheric photochemical and volcanic sources, respectively, and source fluxes and possible concentration levels for these represent an additional unknown when interpreting the geochemistry of ancient sediments with a quantitative model. This does not diminish the likelihood of these oxidants being present in Gale Crater Lake, but we suggest that oxidation requiring only sunlight should be the baseline against which all other oxidation pathways are compared. We will use a physically realistic model of photooxidation-driven iron cycling in Gale Crater Lake to test whether this process alone can explain features of the iron geochemistry of the Murray Formation, make estimates of deposition rates in the lake, which have paleohydrological and paleoenvironmental implications for Mars at ca. 3.5 Ga. Recent observations of large manganese (Mn) enrichments relative to Fe at Gale Crater and Meridiani Planum have also raised the possibility that Mars saw episodes of high atmospheric O_2, which is the oxidant most capable of oxidizing Mn^{2+} (Arvidson et al., 2016; Lanza et al., 2016, 2014; Wordsworth et al., 2021). Iron and Mn are oxidized at different redox potentials and could become decoupled by photooxidation of Fe^{2+} alone (Anbar and Holland, 1992), therefore we will also incorporate Mn into our modeling to assess whether free O_2 on Mars is required to explain the existing geochemical observations of variable Fe/Mn systematics in bulk rocks, and extreme manganese enrichments in certain geological target materials.

Methods

Experimental setup

The experimental setup consists of a light source and quartz reaction cell (Fig. 7.1). The experiments were conducted in an anoxic environment to minimize unwanted oxidation by atmospheric O_2. We housed the experimental set up in a Coy polymer anoxic chamber (Coy

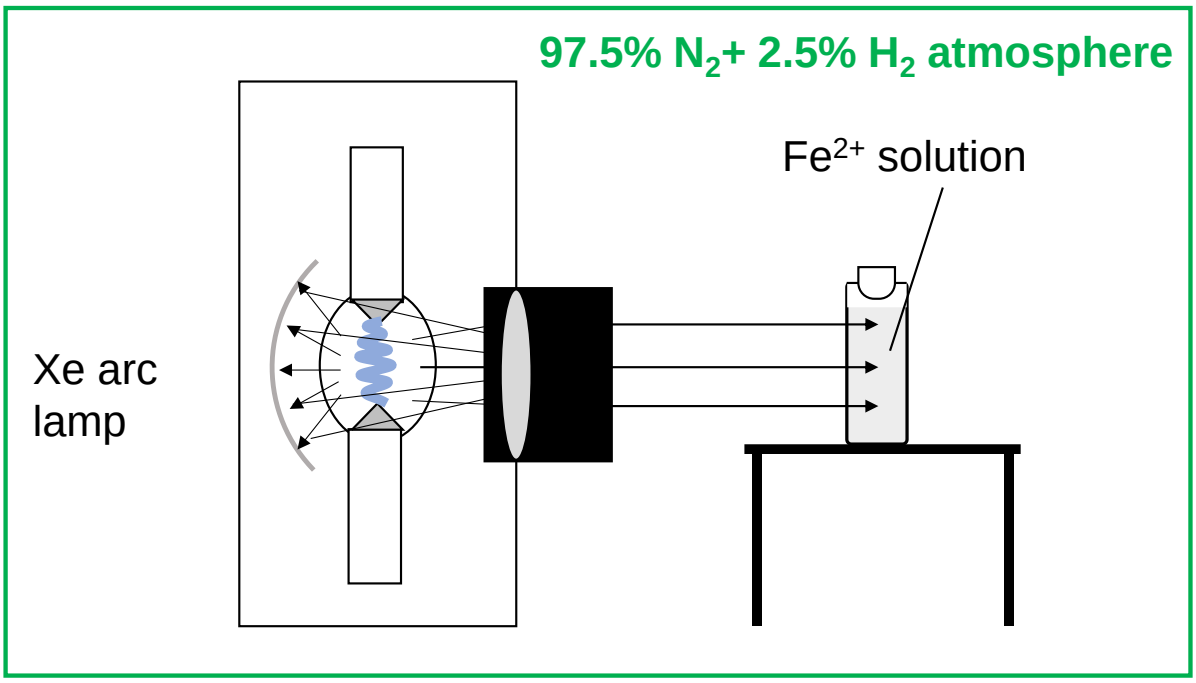

Figure 7.1. Experimental setup for photooxidation. The entire setup is housed in a rigid acrylic anoxic chamber with O_2 maintained at < 1 ppm by recirculation of a 5 % H_2, 95 % N_2 gas mixture that reacts O_2 and H_2 to form water on a palladium catalyst. H_2 levels are automatically maintained between 2.3 % and 2.5 % by a gas analyzer connected to gas infuser. Photooxidation experiments are conducted by irradiating a 1 cm × 1 cm × 3 cm quartz photometry cell containing a solution of known Fe^{2+} concentration. The light source is a 300 W UV-enhanced Xe lamp set to 150 W power that produces a collimated beam for easy calculation of photon absorption rates. Progress of the reaction was determined by periodic sampling of the solution with a micropipette.

Laboratory Products, Inc, USA). The chamber is a glove box that contains removes O_2 by reaction with H_2, supplied by a 5%/95% H_2/N_2 gas mix. A gas analyzer and gas infuser maintain H_2 levels in the chamber between 2.3 and 2.5% H_2. Reaction between H_2 and trace O_2 is promoted by recirculation of the atmosphere inside the glovebox through a palladium catalyst with the resulting H_2O being removed to an alumina desiccator. Assuming Henry's law dissolution of H_2 of ambient into the reaction solution, the contribution of H_2 from the chamber atmosphere is expected to be negligible relative to the H_2 produced as a by-product of photooxidation and is therefore not expected to affect results.

All experiments made use of a 300 W UV-enhanced xenon arc lamp (#6259, Newport Corporation, USA), inside of a lamp housing (#67005, Newport) that outputs a collimated beam. Lamp power was set to 150 W during all experiments, although only a fraction of this power is transmitted via the beam. The reaction cells were a 1 cm × 1 cm × 3 cm fused quartz cuvettes with airtight PTFE stoppers (Thorlabs, Inc, USA). Our approach differs from other studies that irradiate large volume reaction vessels that tend to have curved walls and or relied on top-down illumination from a point source (Braterman et al., 1984; Nie et al., 2017; Tabata et al., 2021). The small cuvettes allow for a more favorable geometry for modeling the irradiation of solutions when calculating the quantum yield, as we do not have to make any simplifying assumptions about the pathlength of incident photons in the reaction vessel. We expect minimal absorption of incoming photons by the glass wall of the cuvette itself, because < 10% absorption of light in the 200-450 nm wavelength range is observed for quartz glass sheets of ~2.8 mm thickness, and the walls of the cuvette are only a fraction of this thickness (Khashan and Nassif, 2001).

Chemical actinometry to determine photon flux

In order to determine the photon flux incident on the reaction vessels we using chemical actinometry, measuring the rate of photoreduction of a solution of potassium ferrioxalate trihydrate; $K_3[Fe(C_2O_4)_3]\cdot 3H_2O$; which has a known quantum yield in the wavelength range 200-460 nm (Hatchard and Parker, 1956). The ferrioxalate was prepared by precipitating solid crystals from a warm (45°C) solution of ferric chloride hexahydrate ($FeCl_3\cdot 6H_2O$) and potassium oxalate monohydrate ($(COOK)_2\cdot H_2O$) in a 1:3 molar ratio (Hatchard and Parker, 1956). The green crystals were reprecipitated 3 times by draining off excess solution with a pipette and replacing it with

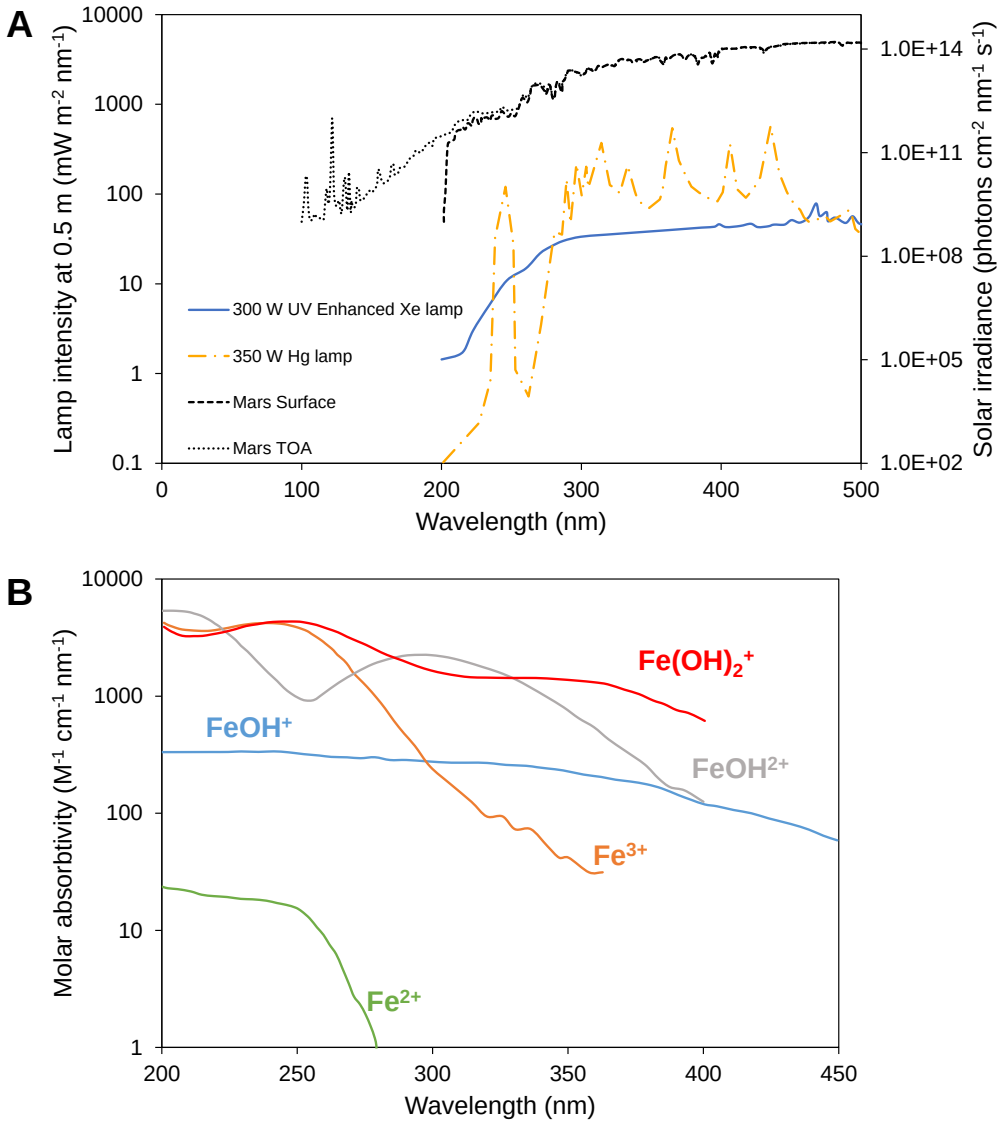

Figure 7.2. Spectra of light sources and chemical absorption relevant to Fe photochemical processes. **A.** Emission spectra of light sources used in various photooxidation experiments (left axis) and modeled early Martian UV irradiation spectra (right axis). The blue solid line is the emission spectrum of the UV-enhanced Xe arc lamp used in these experiments (and similar to that used by Tabata et al., 2021). The yellow dot-dashed line is the emission spectrum of a medium-pressure Hg vapor lamp used by the previous study of Nie et al. (2017) and is typical of the Hg vapor light sources used in many earlier Fe photooxidation studies. The smooth, easier-to-characterize spectrum of the Xe lamp is preferable for accurate determination of quantum yields, and this light source is also a better solar simulator. For the Martian irradiation spectra, the dotted and dashed black lines are the top of atmosphere (TOA) and surface UV fluxes, respectively, for early Mars with a 200 mbar CO_2 atmosphere, from modeling by Ranjan et al. (2017). **B.** Molar absorption spectra for various Fe species in solution. Fe^{2+} and $FeOH^{+}$ are ferrous Fe species that can undergo photooxidation. Fe^{3+}, $FeOH^{2+}$, and $Fe(OH)_2^{+}$ are ferric Fe species that can undergo photoreduction. Absorption data are from Anbar and Holland (1992) and (Stefánsson, 2007) for Fe(II) species and Fe(III) species, respectively.

Milli-Q water. This process removes excess solutes, specifically $KCl_{(aq)}$ which forms during the balanced reaction

$$FeCl_{3(aq)}+3K_2C_2O_{4(aq)}+9H_2O \rightarrow K_3[Fe(C_2O_4)_3]\cdot 3H_2O_{(aq)}+3KCl_{(aq)}+6H_2O,$$

so that only pure $K_3[Fe(C_2O_4)_3]\cdot 3H_2O$ remains. The crystals were then briefly rinsed with a few drops of Milli-Q water and dried on ashless filter paper before use. The potassium ferrioxalate solution was made by dissolving a pre-weighed quantity of the crystal in 0.1 M H_2SO_4 to give a ~6 mM solution (Hatchard and Parker, 1956). The ferrioxalate solution was prepared under a >500 nm safelight to minimize the risk of photochemical artifacts from ambient light and stored in an opaque vessel until use.

Actinometry was performed by irradiating the ferrioxalate solution in the same reaction vessel using the same geometric configuration as photooxidation experiments. During irradiation, ferrioxalate is photo-reduced to ferrous iron and its accumulation is measured by the 1,10 o-phenanthroline method. Pre-prepared 1,10 o-phenanthroline colorimetric solution was made using 1,10 o-phenanthroline monohydrate, ammonium acetate and HCl following Herrera et al. (1989). Small volumes from the reaction cell were sampled with a pipette and added to polypropylene centrifuge tubes containing a pre-measured volume of the colorimetric solution. The samples were transferred out of the glove box and iron was allowed to fully complex with the phenanthroline for 30 minutes. Absorbance at 512 nm was measured with a UV-Vis spectrophotometer. All absorbance measurements were corrected to blank o-phenanthroline solution. $[Fe^{2+}]$ values were determined by comparison to a calibration curve made using solutions with known $[Fe^{2+}]$. The change in $[Fe^{2+}]$ with time was determined relative to small $[Fe^{2+}]$ levels in the unirradiated initial solution.

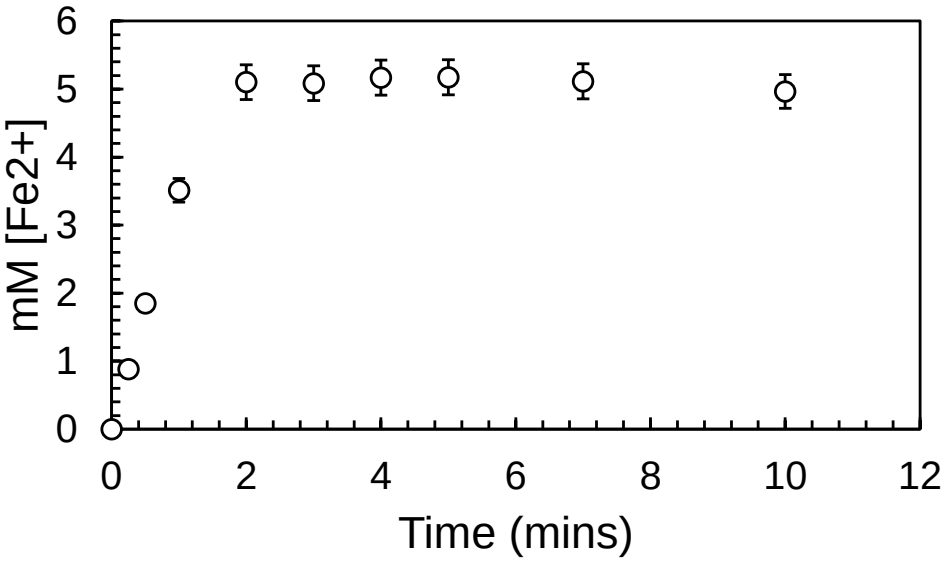

Figure 7.3. Increase in $[Fe^{2+}]$ concentration during irradiation of potassium ferrioxalate solution. The initial maximum rate of increase is taken to estimate photoreduction rates and calculate the irradiation flux assuming a known Φ for the reaction. Error bars are estimated to be 5 % and are dominated by the uncertainty in micropipetted volumes sampled for spectrophotometric $[Fe^{2+}]$ determination.

Due to the geometry of our experimental setup, the photoreduction reaction proceeded very quickly with the solution $[Fe^{2+}]$ reaching an apparent maximum value within 2 minutes and then leveling off (Fig. 7.3), presumably because all ferrioxalate in the solution had been consumed and the photo-oxidation reaction operating in the opposite direction is far less efficient. However, sampling at 15, 30, and 60 seconds into the experiment did indicate a linear increase in $[Fe^{2+}]$ with time while the majority of ferrioxalate was still present, and the maximum initial photoreduction rate was thus determined from the change taking place in the first 15 seconds, giving a value of 0.059 mM/s. The rate of the photochemical reaction is related to the quantum yield and the photon absorption flux by the relation

$$\Delta[Fe^{2+}]/\Delta t = \int_{200\ nm}^{460\ nm} F_{abs,\,X}(\lambda)\ \phi_X(\lambda)\ d\lambda, \qquad \text{(Eq. 2)}$$

where the quantum yield Φ of ferrioxalate (denoted X for simplicity) is well characterized as a function of wavelength (Hatchard and Parker, 1956; Tabata et al., 2021), and $F_{abs,\,X}$, the flux of photons absorbed by ferrioxalate, is given by

$$F_{abs,\,X}(\lambda)=F_0(\lambda)\left(1-10^{-k(\lambda)}\right). \quad \text{(Eq. 3)}$$

F_0 is the incident photon flux, and k is the absorbance of the solution

$$k(\lambda) =\epsilon_X(\lambda)[X]z. \quad \text{(Eq. 4)}$$

where z is the path length of the cell (1 cm), [X] is concentration and $\epsilon_X(\lambda)$ is the absorption spectrum of ferrioxalate. The solution of ferrioxalate is optically thick in the wavelength range of interest over a 1 cm pathlength (such that $10^{-k(\lambda)z}$ is close to zero) (Hatchard and Parker, 1956). We consider $F_0(\lambda)$ as a total incident photon flux F_{tot} multiplied by a normalized wavelength function F_{norm}, that has the shape of the published Xe lamp emission spectrum and is scaled give a value of unity when integrated between 200 and 460 nm. We can thus solve for F_{tot}:

$$F_{tot}=\frac{\Delta[Fe^{2+}]/\Delta t}{\int_{200\text{ nm}}^{460\text{ nm}} F_{norm}(\lambda)(1-10^{-k(\lambda)z})\,\phi_X(\lambda)d\lambda}. \quad \text{(Eq. 5)}$$

From our experiments and published absorption, emission, and quantum yield data, we calculated a total photon flux in the 200-460 nm wavelength range of 3.2×10^{16} photons/cm^2/s, which was used to calculate quantum yields of photooxidation.

Ferrous iron photooxidation

Photooxidation experiments were conducted on ferrous iron solutions consisting of a ferrous iron salt (Mohr's salt, $(NH_4)_2Fe(SO_4)_2(H_2O)_6$) dissolved in a buffer solution designed to prevent the experimental pH changing as the reaction released protons to solution. We investigated photooxidation at pH levels of 2.00, 5.35, and 7.15. For the pH 2 experiment a sulfate buffer solution ($NaHSO_4$-Na_2SO_4) was used, and for pH 5.35 and 7.15, a borate buffer solution (H_3BO_3-

NaOH) was used. All solutions were prepared by dissolving >99% pure reagents in 18.2 MΩ Milli-Q water, and a pH meter (ThermoScientific) was used to determine initial solution pH to within 0.1 unit. Prior to experiments, all solutions were bubbled for at least 30 minutes with pure N_2 to flush out O_2, then transferred to the anoxic chamber in where they were vigorously shaken and reopened at least 3 times, before being left unsealed (thus able to communicate with the H_2-N_2 ambient atmosphere) for at least 24 hours prior to photooxidation experiments. Ferrous iron solutions were made by adding buffer solutions to small (~20 mg) weighted amounts of Mohr's salt in a centrifuge tube prior to experiments. A starting ferrous iron concentration ($[Fe^{2+}]_0$) of approximately 4 mM was used for all experiments, which was sufficient for subsampling small volumes for analysis without having a large effect on UV transmission through the reaction volume.

Photooxidation experiments were run for between 10 and 49 hours (Fig. 7.4). The anoxic chamber was covered, in a room with the lights turned off, during experiments (except during sampling) to minimize the contribution of ambient light to the photooxidation process. The solutions being irradiated by the xenon lamp were not stirred, allowing any precipitates that might form to settle and thus not contribute to absorption within the reaction volume. The progress of the reaction was determined by measuring the decline in $[Fe^{2+}]$ with time, by sampling solution aliquots with a pipette and determining their $[Fe^{2+}]$ with the same 1,10 o-phenanthroline method as described above for the actinometry procedure (Herrera et al., 1989). Samples were measured relative to a blank solution containing the pH buffer without added iron, mixed with the colorimetric reagent in the same proportion as the sample solutions. In order to collect enough samples of sufficient size for accurate photometric analysis, each experiment was run twice with identical conditions

and sampling was done at different time intervals each time (Fig. 7.4). This also serves as a check on the reproducibility of experiments.

The calculation of quantum yields for ferrous iron photooxidation uses similar equations to those above for actinometry, with the quantum yield rather than the photon flux being the unknown to be solved for, such that

$$\Delta[Fe^{2+}]/\Delta t = -\sum_X \int_{200\ nm}^{450\ nm} F_{abs,\,X}(\lambda)\phi_X\, d\lambda \qquad \text{(Eq. 6A)}$$

$$= -\int_{200\ nm}^{300\ nm} F_0(\lambda)\left(1-10^{-k(\lambda)}\right)\frac{\epsilon_{Fe2+}(\lambda)[Fe^{2+}]}{\sum_X \epsilon_X(\lambda)[X]}\phi_{Fe2+}\, d\lambda$$

$$-\int_{200\ nm}^{450\ nm} F_0(\lambda)\left(1-10^{-k(\lambda)}\right)\frac{\epsilon_{FeOH+}(\lambda)[FeOH^+]}{\sum_X \epsilon_X(\lambda)[X]}\phi_{FeOH+}\, d\lambda, \qquad \text{(Eq. 6B)}$$

where $\Delta[Fe^{2+}]/\Delta t$ is the maximum initial rate of decline in ferrous iron concentration due to photooxidation and is negative, and the transmission of photons through the solution is affected by absorption by all species X (Fig. 7.2), but photooxidation of a given species only depends on absorption by that species (Tabata et al., 2021). At pH 2.00, we also considered absorption by accumulated Fe^{3+}, which is soluble at these conditions. We calculated $\Delta[Fe^{2+}]/\Delta t$ from the fastest initial decline between time zero and the first sample, and therefore Φ calculations were made assuming photoabsorption at average value of that prescribed by the solution chemistry at time zero and the first sampling time.

Results

Experiments at all pH levels we investigated saw a decline in $[Fe^{2+}]$ over time during UV irradiation, suggesting that photooxidation to ferric Fe took place (Fig. 7.4; Table 7.1). In the experiments at pH 5.35 and 7.15, a fine layer of orange precipitates was deposited at the base of the reaction cell, but at pH 2.00, no formation of precipitates was observed. Based on comparison

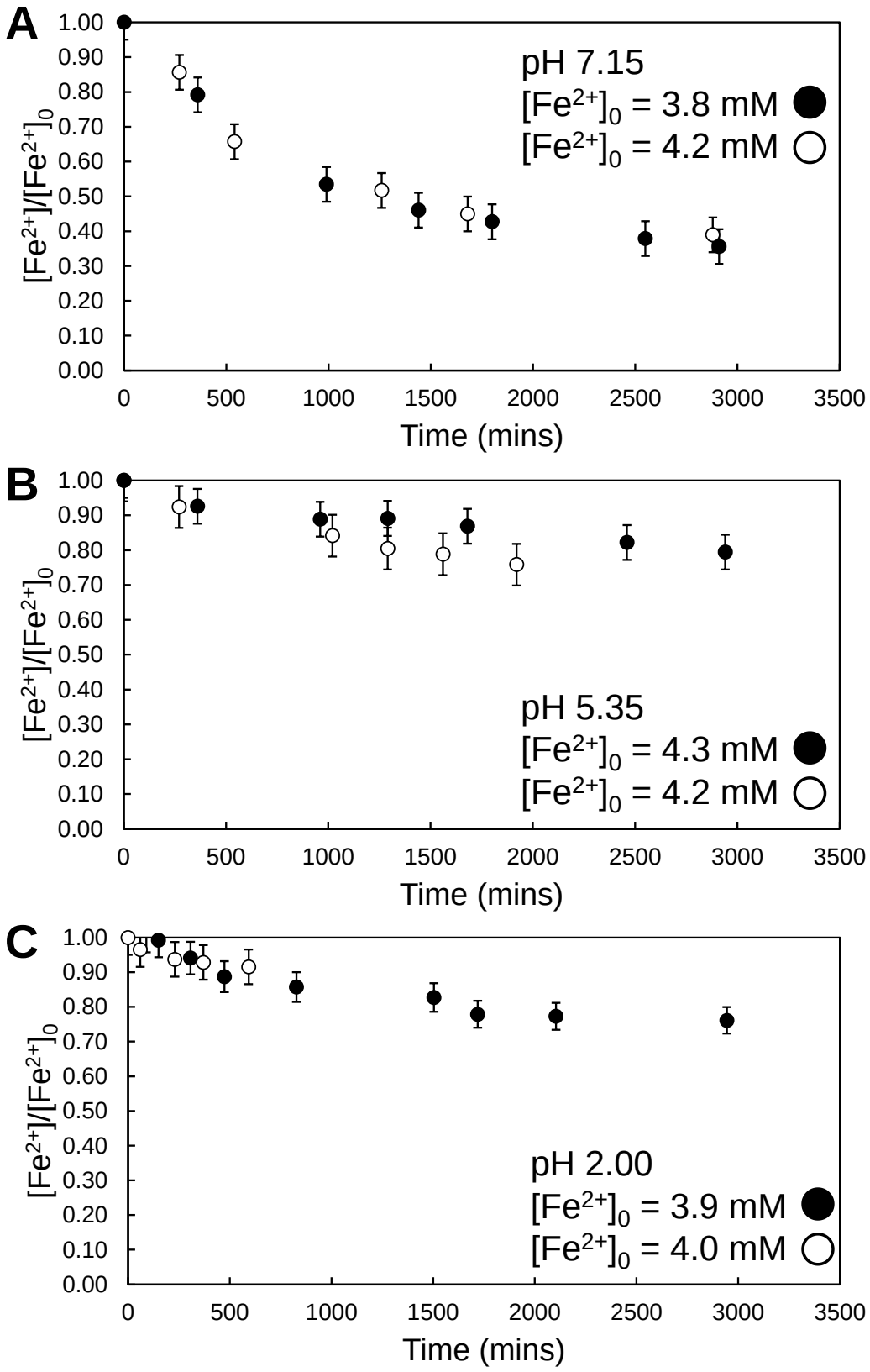

Figure 7.4. Progress of Fe^{2+} photooxidation experiments.

Figure 7.4. continued. Progress of Fe^{2+} photooxidation experiments in solutions at **A.** pH 7.15, **B.** pH 5.35, and **C.** pH 2.00. The decrease in Fe^{2+} concentration over time reflects photooxidation to Fe^{3+}. Photooxidation rates are highest at the beginning of the experiment, and the initial photooxidation rate is used to calculate quantum yields. Black filled and open circles represent separate experimental runs conducted under conditions as close as possible to identical. This allowed us to check reproducibility of experiments and collect more datapoints from solutions with limited volume. Error bars are estimated to be 5 %, which is dominated by the uncertainty in micropipetted volumes sampled for spectrophotometric [Fe^{2+}] determination.

to the study Nie et al. (2017) that investigated photooxidation at near-neutral pH from a similar borate buffer solution, it is most likely that this precipitate was an Fe^{3+} oxyhydroxide, such as lepidocrocite, which was observed in that earlier study. The small quantity of precipitate produced in our experiments was not adequate for detailed characterization. The absence of a solid precipitate in the pH 2.00 experiment can be attributed to the higher solubility of Fe^{3+} in strongly acidic solutions, compared to near-neural pH where Fe^{3+} is highly insoluble and will tend to rapidly precipitate.

In the pH 7.15 experiments (Fig. 7.4A), samples from both runs agree well, showing an initial decline of 40% of the initial [Fe^{2+}] content over the first 500 minutes of irradiation, followed by a noticeable decrease in the rate of decline and flattening of the [Fe^{2+}] change with time through to the ~3000 minute mark when the experiment was terminated, at which point slightly less than 40% of the original [Fe^{2+}] in solution remained. The trend in the datapoints of declining [Fe^{2+}] removal rates over time is consistent with $\Delta[Fe^{2+}]/\Delta t$ being dependent on [Fe^{2+}] in an optically thin solution where not all photons are absorbed**.** In the pH 5.35 experiments (Fig 7.4B), [Fe^{2+}] declined more slowly, reaching 76-79 % of the original [Fe^{2+}] over 2000-3000 minutes, with the two runs diverging in their [Fe^{2+}] evolution after around the 1000-minute mark, although both runs are within error of falling on linear trends due to their small overall decreases in [Fe^{2+}]. The pH 2.00 experiments show a qualitatively similar evolution to the pH 7.15 experiment (Fig. 7.4C),

Table 7.1. Decrease in $[Fe^{2+}]$ over time in photooxidation experiments at different pH levels

pH 7.15			**pH 5.35**			**pH 2.00**	
Time (mins)	**Fe^{2+}/Fe_0**		**Time (mins)**	**Fe^{2+}/Fe_0**		**Time (mins)**	**Fe^{2+}/Fe_0**
Run #1			**Run #1**			**Run #1**	
0	1.00		0	1.00		0	1.00
360	0.79		360	0.93		90	1.01
990	0.53		960	0.89		150	0.99
1440	0.46		1290	0.89		307	0.94
1800	0.43		1680	0.87		474	0.89
2550	0.38		2460	0.82		828	0.86
2910	0.36		2940	0.79		1504	0.83
						1719	0.78
						2104	0.77
						2944	0.76
Run #2			**Run #2**			**Run #2**	
0	1.00		0	1.00		0	1.00
270	0.86		270	0.92		60	0.97
540	0.66		1020	0.84		230	0.94
1260	0.52		1290	0.80		370	0.93
1680	0.45		1560	0.79		593	0.92
2880	0.39		1920	0.76			

Uncertainty is estimated to be 5 % and is dominated by uncertainty in the volume of sample aliquots obtained with the micropipette. $[Fe^{2+}]_0$ was ~ 4 mM in all experiments.

with a faster initial decline that flattens over time as the net [Fe^{2+}] rate declines; however the maximum rate of [Fe^{2+}] decline and the overall decrease in [Fe^{2+}] over the entire experimental run were both smaller in magnitude than in the pH 7.15 experiments, falling to 76% of the initial [Fe^{2+}] after ~3000 minutes.

Using Equation 6A above, taking $\Delta[Fe^{2+}]/\Delta t$ to be the maximum rate of decrease between time zero and first sample after irradiation, 'bulk' Φ values for ferrous Fe in solution (i.e. a single Φ value for Fe^{2+} and $FeOH^{+}$) were calculated at all pH levels. We find bulk Φ values of 0.148, 0.061, and 0.056 at pH 2.00, 5.35, and 7.15, respectively (Fig. 7.5). As multiple studies have observed that Φ_{Fe2+} is effectively independent of pH above values of 3.5, we take the Φ_{Fe2+} determined at pH 5.35 (where photon absorption by $FeOH^{+}$ negligible) and substituted this value into Equation 6B, with fractions of Fe^{2+} and $FeOH^{+}$ reflecting speciation at pH 7.15, to calculate a separate value for Φ_{FeOH+} of 0.053.

Discussion

Comparison to previous studies

In theory, Φ is strictly a function of wavelength. The apparently higher quantum yield of iron photooxidation seen in previous Xe and Cd (Logan, 1990) lamp-illuminated experiments compared to Hg lamp-illuminated experiments was attributed to the greater proportion of higher energy of photons arriving at shorter wavelengths than the 254 nm peak in Hg lamp emission spectra. However, we anticipate that the wavelength-integrated Φ determined using a Xe light source is a fairly accurate representation the wavelength-integrated quantum yield that is applicable to natural geochemical settings, because of the similarity between the Xe lamp spectrum and the solar spectrum.

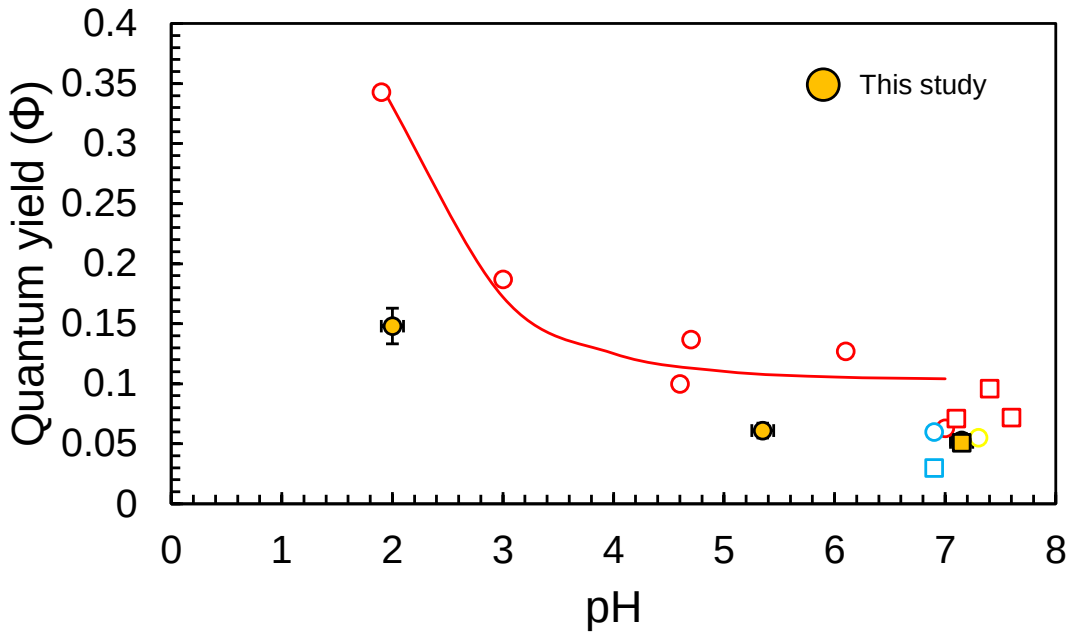

Figure 7.5. Experimentally determined quantum yields (Φ) of Fe(II) photooxidation, *vs*. pH. Circles: bulk Fe(II) or Fe^{2+}. Squares: $FeOH^{+}$. Filled symbols are from this study, with estimated uncertainties of 10% on the quantum yield and 0.1 units on the pH; and open symbols are from previous studies, with uncertainties omitted for clarity. Red: Tabata et al. (2021). Blue: Braterman et al. (1984). Yellow: Nie et al. (2017). The solid red line is a fit to Φ_{Fe2+} data as a function of pH, from Tabata et al. (2021). We observe a qualitatively similar pH dependence in this study.

The bulk Φ values determined at near-neutral pH of 7.15 in the experiments conducted here are in fairly good agreement with the earlier studies of Braterman et al. (1984) (0.06±0.03 for total Fe(II), 0.01-0.05 for $FeOH^{+}$) and Nie et al. (2017) (0.04-0.07), but are approximately a factor of 2 lower than the values determined by Tabata et al. (2021) (Fig. 7.5). That latter study also determined an independent value for Φ_{FeOH+} by using >300 nm filtered light (which eliminated Fe^{2+} photooxidation), of 0.08±0.01, which is also approximately a factor of 2 greater than we value we determined for Φ_{FeOH+}. The finding of this study that Φ_{Fe2+} is considerably higher at pH 2 than at near-neutral pH qualitatively agrees with earlier studies, and the value of Φ_{Fe2+} at pH 2 found here of 0.148 is similar to the values of 0.10 and 0.11 found at pH values of 1.9 and 2.7, respectively by Jortner and Stein (1962a, 1962b), despite very different irradiation conditions (a low-pressure

Hg lamp) used in that study. These values are all considerably lower than the value of 0.34 determined at pH 2.0 by Tabata et al. (2021). The agreement presented by Tabata et al. (2021) between their data and that of Jortner and Stein for low-pH Φ values is not an appropriate like-for-like comparison, because they compared to results from Jortner and Stein that were conducted on oxygenated solutons, not those conducted in anoxic conditions that showed far lower quantum yields, more similar to what we find here.

There are several possible reasons why the quantum yield data reported here differ with the most recent study also conducted with a xenon UV light source (Tabata et al., 2021), but given the use of similar light sources in both studies, any wavelength-dependence in Φ is unlikely to be the source of these discrepancies. One explanation may be that the longer time intervals we used for sampling did not capture the maximum initial rate Fe^{2+} photooxidation when $[Fe^{2+}]$ was at its highest value. As explained above, the maximum rate should occur as soon as the lamp is turned on and the photooxidation rate will decline in proportion with the ferrous iron concentration. While some aspect of this effect is unavoidable and was certainly minimized with the shorter sampling intervals employed by Tabata et al. (2021), the most that $[Fe^{2+}]$ had declined by at the point we first sampled the solution was 14%. Given that the decline to this point should reflect a time-integrated average photooxidation rate at concentrations between 100 and 86% of $[Fe^{2+}]_0$, such an effect cannot be the driver of a factor of 2-3 discrepancy between the two separate studies, and is likely to fall within the overall degree of uncertainty of the Φ values determined here.

Second, we note that unlike previous work, our experiments were conducted in an anoxic glovebox atmosphere maintained by a 2.5 % H_2 atmosphere, providing a source of reducing power that may have inhibited the forward photooxidation reaction. Due to the insolubility of H_2 gas in aqueous solution, and the fact that the photooxidation reaction itself produces H_2, the effect of a H_2-

containing atmosphere is likely to be minor. For example, Henry's law solubility suggests that at most, 0.02 mM of H_2 may be dissolved from the glovebox atmosphere into the experimental solution prior to some degree of heating by the lamp, and likely associated degassing. For comparison, 0.25% photooxidation of the solution with $[Fe^{2+}]_0$ would be required to produce this much H_2. So, very soon after the initiation of the experiment, the H_2 content generated by photooxidation should exceed the amount that could be initially dissolved from the glovebox atmosphere. The experiment will thus quickly accumulate H_2 relative to its surroundings and any H_2 dissolution from the atmosphere into the experiment would be unfavored.

Third, the experiments conducted here, much like the earlier work of Nie et al. (2017), featured a setup with the lamp placed very close to the experimental solution, which enhances photooxidation rates but also makes heating of the solution by the lamp unavoidable. We were not able to do real-time temperature monitoring of out solutions because of the small volume of the experimental cell, but Nie et al. (2017) observed temperatures of up to 45 °C. Our experiments did not form blackish precipitates of magnetite that were observed by Nie et al. (2017) at temperatures of 60-90 °C, so it is unlikely that our experiments reached these temperatures. By contrast, some earlier studies used larger experimental volumes that remained at ~25°C (e.g. Braterman et al., 1984; Tabata et al., 2021). Some temperature dependence in Φ may be expected because higher temperatures provide more energy for chemical reactions to take place. Following this logic, a temperature effect would be expected to lead to higher quantum yields being observed in the present study and that of Nie et al. (2017), compared to Braterman et al. (1984) and Tabata et al. (2021). However, no such systematic difference is observed, with the present study, Nie et al. (2017) and Braterman et al. (1983) all agreeing withing error despite quite different T conditions, and the study of Tabata et al. (2021) alone giving considerably higher values for Φ. Similarly, a

photooxidation study conducted over a controlled temperature range of 277-326 K, which encompasses the range of temperatures reach in the experiments discussed above, showed that there is negligible temperature dependence of the reaction (Logan, 1990).

Fourth, the calculation of Φ is highly sensitive to the way in which the irradiation of the solution is modeled; and this makes standardization between experimental studies particularly difficult. Unlike potassium ferrioxalate actinometer solutions, the millimolar Fe(II) solutions used in photooxidation experiments are optically thin, so that only a fraction of incident photons will be absorbed. As Equation 3 shows shows, the photon absorption in the solution is strongly dependent on the path length z that is assumed for photons passing through the experimental solution. If this average pathlength is difficult to quantify, the assumed value of z represents a source of uncertainty that could potentially be larger than all known analytical uncertainties reported in studies of this kind. The experiments reported on here were explicitly designed to minimize this uncertainty, by directing a collimated beam of light normal to the flat surface of a reaction cell with a uniform 10 mm pathlength within the solution. By contrast, the experimental design of Tabata et al. (2021) would not have allowed easy modeling of the pathlength for photons within the reaction vessel, because they irradiated a large volume cylindrical reaction vessel from the side with uncollimated light. Tabata et al. (2021)'s assumption of an average pathlength of 6.3 cm for a cylinder with an 8 cm diameter can be shown to be reasonable from a pure geometric perspective. However, photons meeting the curved inside surface of the reaction vessel, and meeting the liquid surface at a large angle, may both have been reflected back into the reaction solution, increasing the average pathlength beyond the assumed value, allowing more photon absorption than accounted for and thus resulting in an overestimate of Φ as a result. It is unclear whether this path length uncertainty could account for a large degree of the difference in Φ values observed in the present study and

earlier work, and we have identified some other factors that may have contributed to biasing the calculation of Φ presented here to slightly lower values. It is important to emphasize that a linear irradiation geometry and a uniform path length for photons entering an experimental solution allow the easiest modeling of photon absorption during photochemical experiments and should be employed wherever possible.

Understanding the time evolution of [Fe^{2+}] in experiments

Both the pH 2.00 and pH 7.15 photooxidation experiments featured initially fast photooxidation rates that declined over time, so that the [Fe^{2+}] trend over time tended to flatten out (Fig. 7.4). It is unclear if the pH 5.35 experiment would feature a similar evolution if given long enough to evolve away from the apparently linear trend with time that it fits within error. Qualitatively, flattening of the [Fe^{2+}] evolution with time is expected because the photooxidation rate is directly dependent on [Fe^{2+}] and thus it might be expected to be approximated over time by an exponential decay (provided the solution remains optically thin). However, our experimentally determined trends flatten out at non-zero values, whereas a simple exponential decay should asymptote at [Fe^{2+}] = 0. We hypothesize that this reflects a competing back-reaction of Fe^{3+} photo-reduction, and that the apparent 'equilibrium' level of [Fe^{2+}] is dependent on pH and should be lower as pH increases, because the forward reaction is faster and the back-reaction is hindered by Fe^{3+} being removed by precipitation into insoluble oxyhydroxides. Indeed, the study of Nie et al. (2017), conducted at a slightly higher pH of 7.3, reached greater degrees of fractional Fe^{2+} removal than any of the experiments conducted here.

At low pH, Fe^{3+} remains in solution, and the lack of precipitates in the pH 2.00 experiment confirm this. As photooxidation progresses, [Fe^{3+}] and other Fe(III) species accumulate accumulates in

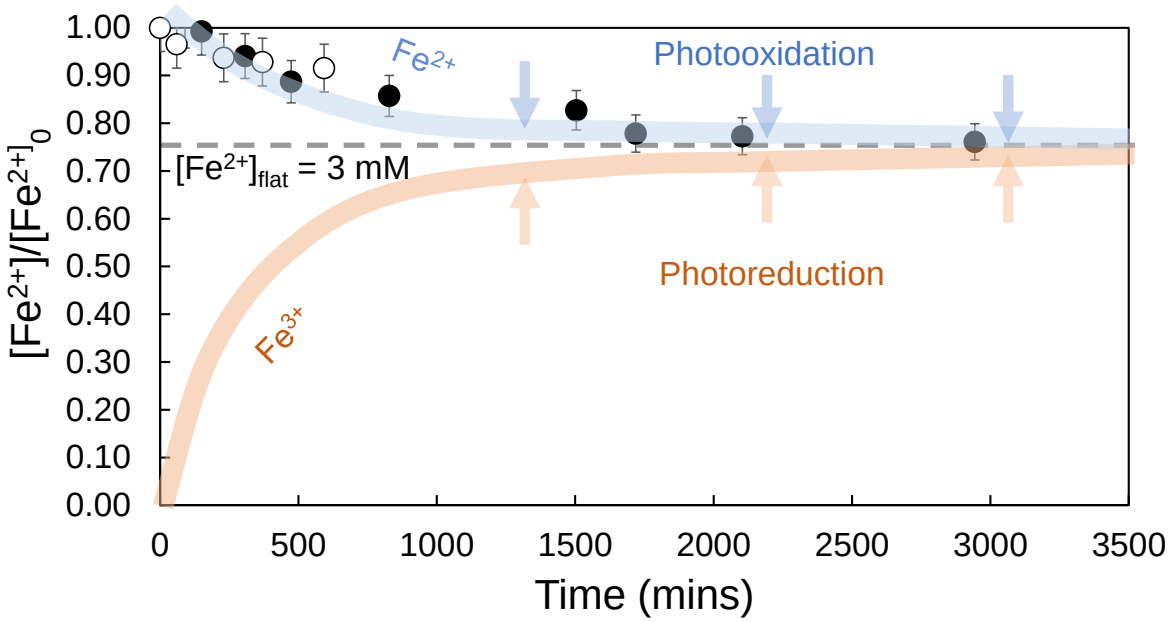

Figure 7.6. Conceptualized interpretation of the leveling out of the $[Fe^{2+}]$ with time in the pH 2.00 photooxidation experiment. $[Fe^{2+}]_{flat}$ is the concentration level, at ~3 mM or 75 % of $[Fe^{2+}]_0$, where further decline in $[Fe^{2+}]$ is not observed. As there is plenty of Fe^{2+} available for photooxidation, this leveling off in the $[Fe^{2+}]$ trend with time is interpreted as reflecting a steady state balance between the forward photooxidation reaction, and Fe^{3+} photoreduction (a documented process), occurring in the opposite direction. The estimated quantum yield for Fe^{3+} photoreduction determined from this experiment is consistent with previous experimental results. The stabilization of high $[Fe^{2+}]$ levels by a balance between photooxidation and photoreduction reactions at low pH where Fe^{3+} can remain in solution (no precipitates were observed in the pH 2.00 experiment), suggests that photooxidation may not be a viable pathways for the quantitative precipitation of Fe^{3+} phases from acidic solutions on Mars. Lower water-rock ratio, or ice-dust reactions, may thus be plausible pathways to forming jarosite-rich materials such as observed at Meridiani Planum on Mars.

solution, and due to their large absorption coefficients in the 200-400 nm range, the transmission of photons through the solution declines. This decrease in availability of photons, combined with lowered $[Fe^{2+}]$, causes the rate of Fe^{2+} photooxidation to decrease. At the same time, absorption of a large number of photons by $[Fe^{3+}]$ allows rates of the photo-reduction back-reaction to increase, until at some balance of $[Fe^{2+}]$ and $[Fe^{3+}]$, rates of the two competing reactions will approximately balance each other and the $[Fe^{2+}]$ evolution with time will flatten (Fig. 7.6). An equation than then be set up where the only unknown is a quantum yield associated with Fe^{3+} photoreduction. The pH

2.00 experiment appears to flatten at $[Fe^{2+}]_{flat} \approx 3$ mM, giving $[Fe^{3+}]_{flat} = [Fe^{2+}]_0 - [Fe^{2+}]_{flat} \approx 1$ mM. At these values we calculate an absorptivity k, and set up the equation:

$$\int_{200\ nm}^{300\ nm} F_0(\lambda)\left(1\text{-}10^{-k(\lambda)}\right)\frac{\epsilon_{Fe2+}(\lambda)[Fe^{2+}]_{flat}}{\sum_X \epsilon_X(\lambda)[X]}\phi_{Fe2+}\,d\lambda = \int_{200\ nm}^{450\ nm} F_0(\lambda)\left(1\text{-}10^{-k(\lambda)}\right)\frac{\epsilon_{FeOH+}(\lambda)[Fe^{3+}]_{flat}}{\sum_X \epsilon_X(\lambda)[X]}\phi_{Fe3+}\,d\lambda. \quad \text{(Eq. 7)}$$

Here we write the term for $[Fe^{3+}]$ as a single species for simplicity, but in our calculation we considered the speciation of Fe(III) between Fe^{3+}, $FeOH^{2+}$, and $Fe(OH)_2^+$, at pH 2.00, using published speciation and absorption data (Fig. 7.2 Stefánsson, 2007). Solving this equation for Φ_{Fe3+} gives a value of ~0.00024. While this calculation is highly simplified and the experiment was not designed *a priori* to investigate photoreduction of Fe^{3+}, we note that this value agrees relatively well with a previously determined range of Φ for Fe(III), from a study on photoreduction of ferric Fe in raindrops, which are both highly uncertain and wavelength-dependent (Kieber et al., 2003). We therefore take this as tentative confirmation of our hypothesis that $[Fe^{2+}]$ levels off at long irradiation times due to the competing effects of photooxidation and photoreduction.

At the higher pH, the competing reactions are more complicated to model, because Fe^{3+} precipitated as ferric oxyhydroxides in our experiments and can no longer be simply considered as a homogeneously distributed solute, and rates of precipitation and/or surface dissolution of oxyhydroxides would need to be considered to approximate a value for $[Fe^{3+}]$. From a qualitative perspective, as pH increases, the speciation of Fe^{3+} into solid precipitates would be increasingly favored, and once bound in a precipitate, ferric iron would be less available for photoreduction. If any photoreduction were able to occur at higher pH, it would balance Fe^{2+} photooxidation when $[Fe^{2+}]$ was far lower, and a larger proportion of the total iron in the system was oxidized, with a fraction of that amount remaining in the aqueous phase. Therefore, our observation that the $[Fe^{2+}]$

evolution at higher pH either starts to flatten out when a far lower percentage of the initial Fe^{2+} remains, supports our interpretations.

These experimental observations could have severe implications for the viability of UV photooxidation in highly acidic settings, such as the environment that deposited the low-pH mineral jarosite at Meridiani Planum on Mars. If Fe^{3+} that remains in solution at low pH is efficiently photoreduced back to Fe^{2+}, then photo-oxidation would not be an effective mechanism of exporting ferric iron to sediments in the shallow, acidic playa-lake setting that forms the basis of the photooxidation model for the Burns Formation at Meridiani (Hurowitz et al., 2010). The saturation of schwertmannite, which is hypothesized to be the metastable precursor to jarosite in this setting (Hurowitz et al., 2010; Nie et al., 2017), requires [Fe^{3+}] levels an order of magnitude higher than the ones used in the experiments reported here (Yu et al., 2002) at the same sulfate concent, and the accumulation of sufficient [Fe^{3+}] to precipitate schwertmannite would thus be inhibited both by photoreduction of [Fe^{3+}] back to [Fe^{2+}], and the strong absorption of photons in the relevant wavelength range by [Fe^{3+}] as it accumulated. For these reasons it seems more likely that alternative atmospherically derived oxidants (Mitra et al., 2020; Mitra and Catalano, 2019), or a different class of model involving dust-ice interactions (Baccolo et al., 2021; Niles and Michalski, 2009), provide a better explanation for the formation of jarosite on Mars during acid alteration activity in the Hesperian.

A Photochemically-Driven Model for Redox Geochemistry in Gale Crater Lake

Model Design

We investigated Martian Fe^{2+} photooxidation rates using 1-D geochemical model that we adapted from studies of iron cycling in early Earth oceans (See Appendix of Chapter 3), where O_2 rather

than UV photons provided the oxidant (Czaja et al., 2012; Heard et al., 2020). The model employs a finite difference approach with discrete layers of thickness Δz =5 cm. In the model, a Mars-relevant solar photon flux (Fig. 7.2; Ranjan et al., 2017) in the wavelength (λ) range 200-450 nm is imposed at the top of a water column containing anoxic, ferruginous rich water, with [Fe(II)] of 0.7 mM fixed at the base of the model (Tosca et al., 2018). The solar photon flux is adjusted to the latitude of Gale Crater (5.4° S) and multiplied by 0.5 to account for diurnal variations. The photon flux $F(\lambda)$ is attenuated with depth in the water column due to absorption by water molecules and dissolved ferrous iron species Fe^{2+} and $FeOH^{+}$ according to the equation

$$F(\lambda, z)= F(\lambda)_0 \times 10^{\left(-\int_0^z k(\lambda)dz\right)}, \quad \text{(Eq. 8)}$$

where $F(\lambda, z)$ and $F(\lambda)_0$ are the photon fluxes at depth z within the water column and at the surface of the water column, respectively, and

$$k(\lambda,z)=\epsilon(\lambda)_{H_2O}+\sum_i \epsilon(\lambda)_{X_i}[X_i](z), \quad \text{(Eq. 9)}$$

where absorption spectra for pure water (ϵ in cm^{-1} nm^{-1}) and ferrous species [X_i] (ϵ in M^{-1} cm^{-1} nm^{-1}) are taken from Smith and Baker, 1981, and Anbar and Holland (1992). We also consider absorption by Cl, with a concentration taken from estimates for Gale Lake waters by Fukushi et al. (2019) and an absorption spectrum from Anbar and Holland (1992). There is uncertainty in the turbidity of the water column and the effect of absorption by other dissolved species. In not including these unconstrained absorbers, model photon fluxes and thus photooxidation rates should be taken as maximum values.

Photooxidation rates $R_X(z)$ for each Fe(II) species (X = Fe^{2+}, $FeOH^{+}$) are calculated within each layer as

$$R_X(z)=\frac{10^3}{N_A \times \Delta z}\int_{200}^{450} \Phi_X \epsilon(\lambda)_X [X(z)]F(\lambda, z)d\lambda, \quad \text{(Eq. 10)}$$

where N_A is Avagadro's number, and the factor $10^3/\Delta z$ cm^3 L^{-1} converts rates to M s^{-1} over a 1 cm^2 irradiated area of water column (done for convenience as concentrations are considered in units of M). We investigated the effects of using Φ values from our experiments and those of Tabata et al. The total photooxidation rate within each layer is calculated as the sum of $R_x(z)$ for X = Fe^{2+}, $FeOH^+$, and oxidized iron is immediately removed as insoluble precipitates (such as $Fe(OH)_3$). In the absence of strong constraints on the depth of Gale Lake during deposition of the Murray Formation, we consider a 100 m deep water column for comparison with Tabata et al. (2021). The large majority of photons involved in UV photooxidation are absorbed over this pathlength, particularly in the wavelength range of Fe^{2+} absorption. Rather than just reporting maximum initial photooxidation rates in a homogenized water column across a spectrum of pH and [Fe^{2+}] conditions (Tabata et al., 2021), we take the assumption of near-neutral pH lake waters (Fukushi et al., 2019; Grotzinger et al., 2014), and initial [Fe^{2+}] ~0.7 mM (Tosca et al., 2018), and focus instead on understanding how the profile of [Fe^{2+}] in the Gale Lake water column, and Fe deposition driven by photooxidation, would evolve over a given period of time (Fig. 7.7). For a given pH and [Fe^{2+}] scenario, this approach is more physically realistic for calculating the time-integrated Fe^{3+}-deposition rate in for Gale Lake that is captured by the geologic record of the Murray Formation.

Based on terrestrial examples, the physical mixing processes that vertically transport solutes in lakes are highly varied, and it is not immediately obvious which type of mixing or stratification regime is the best proxy for the lake at Gale Crater, in part because the depth of the lake water column is unconstrained. Many ferruginous lakes on Earth maintain anoxic, Fe^{2+}-rich deep waters because they are permanently stratified, due to the absence of strong seasonal temperature variations that can drive the necessary changes in buoyancy, efficient enough wind mixing, to

encourage overturning of the entire lake water column. Notable examples of these ferruginous, meromictic lakes include Lake Nyos, in Cameroon, Lac Pavin, in France, and Lake Matano, in Indonesia (Busigny et al., 2014; Crowe et al., 2014, 2008; Teutsch et al., 2009). All have been studied extensively as analogs for ancient marine iron cycling on Earth, and are typified by persistently Fe^{2+}-poor, oxic shallow layers in communication with the atmosphere that can be well-mixed, where oxidation and precipitation rapidly removes upward-diffusing Fe^{2+}, and Fe^{2+}-rich, anoxic deeper waters. Chemical profiles in Martian lakes may differ to terrestrial examples because of the way in which oxidants penetrate into the lake. For example, in the Martian environment, UV photons would be associated with a finite pathlength into the water column. By comparison, dissolved O_2, equilibrated with an O_2-rich atmosphere (which is available on Earth but questionable for ancient Mars) and transported with water parcels, would be expected to follow the physical stratification within the lake.

Alternatively, there are many examples of lakes on Earth that see mixing of their entire water column annually, due to significant seasonal changes in temperature forcing that allow stratification to periodically develop, and then collapse (*e.g.* León et al., 2016). In these lakes, stratification typically develops due to warming following the end of winter, where surface waters receive more thermal energy from solar radiation than they lose due to sensible, radiative, and latent heat loss. Warm surface waters decrease in density and become buoyant relative to cooler deeper waters throughout spring and summer. As surface cooling occurs heading into fall and winter, buoyancy stratification can collapse, causing vertical mixing, potentially from top to bottom, depending on factors including the depth of the lake, and the extent of wind forcing. In contrast to permanently stratified lakes, communication of underlying deep waters with (oxidizing) surface conditions can take place seasonally when stratification collapses, providing the

opportunity for deeper water solutes to efficiently mix throughout the water column. This type of seasonal mixing could be expected for Gale Crater lake because, even though Gale Crater is at near-equatorial latitudes, the eccentricity of Mars's orbit around the Sun could have driven significant annual variations in solar insolation at the and thus radiative heating of the lake surface (Laskar et al., 2004).

To account for the main endmember models for mixing that we can envision, we perform 6 different model runs in total (Fig. 7.7; Table 7.2), with 3 each using our experimental constraints on Φ, and that of Tabata et al. (2021). For each Φ scenario, we run two 1-Mars-year-long models that tracks the evolution of lake [Fe^{2+}] and photooxidation rates. One of these models has vertical transport facilitated by slow eddy diffusion with a representative diffusion coefficient for lakes of 0.1 cm^2 s^{-1} (Hondzo et al., 1991; León et al., 2016). Photooxidation depletes surface and shallow waters of ferrous Fe, so the eddy diffusion facilitates transport of ferrous Fe upwards, down this concentration gradient. The other year-long model represents rapid mixing conditions, where we homogenize the entire lake instantaneously at each time step (the approach taken by Nie et al., 2017). In both these models, if the lake is seasonally mixed then concentration profile would be 'reset' after a maximum timescale of 1 Mars year. If the 100 m depth exceeds the true depth of the lake, this would represent top-to-bottom mixing of the lake. However, if the lake were deeper than the 100 m layer we model, seasonal de-stratification could resupply the upper 100 m with more Fe^{2+}-rich waters (represented by the fixed 0.7 mM [Fe^{2+}] at the base of our model), the next year of photooxidation and Fe^{3+} deposition would proceed in a similar manner.

The third model for each Φ scenario is one in which the [Fe^{2+}] profile is allowed to evolve for multiple model Mars years until it reaches a steady state where no further perceptible change is taking place. Mixing in this scenario was facilitated by the eddy diffusion term, because constant

homogenization of the lake waters by rapid mixing would prevent a steady state being reached and [Fe^{2+}] would continuously decrease until no [Fe^{2+}] remained in the model column.

In all the models, photooxidation rates scale with the photon flux in the absorption wavelength ranges for Fe^{2+} and $FeOH^{+}$, and the local concentration of ferrous iron. This results in a near-surface maximum in photooxidation rates (Fig. 7.7). Below this maximum, the photooxidation rate declines towards the bottom of the lake because the photon flux is so strongly attenuated by absorption. At the shallowest depths the photon flux is not attenuated strongly. However, in the diffusion-only one year and steady state scenarios where a concentration profile can develop, [Fe^{2+}] at shallow depths can be depleted, leaving less Fe^{2+} available to be photooxidized. As we assume that Fe^{3+} oxyhydroxides are insoluble and sink without dissolution, the water column-integrated ferrous iron photooxidation is equal to the burial flux of ferric iron oxyhydroxides in the underlying sediment column.

Ferrous iron supply to Gale Crater Lake.

In modeling an initially ferruginous water column in Gale Lake, we are implicitly assuming that a steady resupplying flux of Fe^{2+} to lake waters would be readily available. Supplying Fe^{2+} to Gale Lake could in one sense be considered trivial, as there is evidence for reducing weathering conditions on early Mars that mobilized Fe^{2+} from the surface crust (Liu et al., 2021), and subsurface weathering fluids in basalt should remain reducing and thus encourage Fe^{2+} mobilization during groundwater flow (Hurowitz et al., 2010; Kite and Melwani Daswani, 2019; Schaefer, 1996; Tosca et al., 2018). However, weathering fluids enriched in Fe^{2+} will also be enriched in other solutes, particularly Na^{+} and Cl^{-} (Kite and Melwani Daswani, 2019) and the

relative concentration of Fe^{2+} to these sources of salinity in fluids delivered to Gale Lake depends on the source of the weathering fluids.

Groundwater transported over long flow paths in basaltic bedrock sees alteration become rock-buffered, a resulting in high pH (>8) levels, and elevated Na/Fe ratios of ≥100 in fluids. This phenomenon is seen for Mars-relevant conditions in both reactive-transport modeling (Kite and Melwani Daswani, 2019) and field studies of cool basaltic aquifers in Iceland (Kristmannsdóttir and Ármannsson, 2004). The elevated Na/Fe ratios, which are orders of magnitude higher than those in the source basalt, are a result of the inability of Fe^{2+} to be transported long distances at high pH, because the precipitation of iron hydroxides, phyllosilicates and clay minerals is thermodynamically favored (Kite and Melwani Daswani, 2019; Tosca et al., 2018). Such high input Na/Fe to Gale Lake is highly problematic because of the implied Na budget for a closed basin with no outflow. For example, assuming that the ~5 wt% of Fe in secondary phases in the Murray Formation reflects authigenic precipitates of groundwater-sourced Fe^{2+} (based on XRD mineralogy from Hurowitz et al., 2017) over the >400m thickness of the Murray, ~5000 kg m^{-2} of Fe must be accounted for by groundwater supply. For a molar ratio ~Na/Fe ratio of 100 for the input groundwater (Kite and Melwani Daswani, 2019; Kristmannsdóttir and Ármannsson, 2004), this equates to ~2×10^6 kg m^{-2}, or ~9×10^7 moles m^{-2} of Na accumulated in Gale Lake, with no obvious Na-enriched sedimentary output indicated by XRD mineralogy of the Murray Formation (Hurowitz et al., 2017). Assuming Cl contents similar to those for Na, saturation for halite (~6 mol kg H_2O^{-1}) in a 1000 m deep lake (a likely maximum estimate) would already be reached when Na in the column reached 6×10^6 moles m^{-2}, just 1/15 of the amount estimated above from Na/Fe ratios. Since there is no evidence for massive accumulation of halite in Gale Crater, this implied 'salinity crisis' suggests that a far-field, rock-buffered groundwater supply for Fe^{2+} to Gale

Lake during deposition of the Murray is not feasible. Far from reaching halite saturation, cation substitution data for the underling Yellowknife Bay formation in Gale Crater suggest that salinities of late-stage lake waters were at-most similar modern Earth seawater, and more likely hyposaline, with salinities on the order of 0.1 M for Na^+ and Cl^- (Fukushi et al., 2019).

While a simple back-of-the-envelope salt balance apparently rules out Fe^{2+}-sourcing from large scale groundwater circulation, there are other ways to generate ferruginous (Fe^{2+}-rich) conditions in lakes, as exemplified by numerous examples on Earth, where stratified, anoxic lakes with Fe^{2+}-rich subsurface waters exist on numerous continents (Busigny et al., 2014; Camacho et al., 2017b, 2017a; Crowe et al., 2008; Lambrecht et al., 2018; Sheppard et al., 2019; Teutsch et al., 2009). These lakes are often established on Fe-rich volcanic bedrock (Busigny et al., 2014; Crowe et al., 2008; Sheppard et al., 2019; Teutsch et al., 2009) and therefore offer good geochemical proxies for Mars. These lakes source their dissolved Fe^{2+} from local surface weathering or the dissolution of Fe-rich sedimentary detritus deposited on the lake floor, including that supplied by microbially-mediated reductive dissolution, such as in the case of Lac Pavin. Iron supply by these means does not require long flow-paths for weathering fluids, and so near-quantitative transfer of Fe^{2+} leached from rocks to the lake water column is a reasonable assumption, in which case input Na/Fe ratios will be reflective of the initial leached fluid and potentially not too different from the bedrock composition. In the case of high degrees of alteration where all Na and Fe are leached (such as the reductive alteration seen in the upper profile of paleosols formed under Earth's anoxic early atmosphere; Heard et al., 2021; Macfarlane et al., 1994; Rye and Holland, 1998), this Na/Fe ratio would be approximated by the ratio in the bulk basalt, ~0.2. This scenario would represent solute supply from locally established by heavily leached weathering profiles. Alternatively, mineral breakdown could be partial, favoring significant dissolution of Fe-bearing olivine (Tosca et al.,

2018) and only minor dissolution of Na-bearing plagioclase. This is supported by XRD-derived mineralogy of the Murray Formation that shows >20 wt% plagioclase and no evidence of olivine surviving in the rocks through deposition, alteration, and diagenesis (Hurowitz et al., 2017). In this alternative model for Fe^{2+}-supply to Gale, solutes could be sourced either during breakdown of sediments on the lakebed interacting with porewaters (Tosca et al., 2018), or from locally-developed weathering profiles with short lifetimes for chemical alteration, such as eroding hillslopes on the crater walls.

To summarize, there are pathways to generating ~0.1-1.0 millimolar concentrations of Fe^{2+} in Gale Lake during deposition of the Murray Formation that do not require large groundwater Fe^{2+} fluxes associated with ≥100× 'Na tax'. These alterative local Fe^{2+}-sourcing scenarios for Gale Lake might be preferable because they are also consistent with the observed mineralogy of the Murray Formation. This type of scenario is consistent with initial [Fe^{2+}] used in our photooxidation without implying high NaCl salinity.

Model Results

Dissolved ferrous Fe profile evolution.

Depth profiles of ferrous Fe concentration developed in our model runs are shown in Figures 7.7A-B. For the long-duration models, steady state was reached in the two Φ scenarios on a timescale of ~5 and ~10 Mars years for Φ values from Tabata et al. (2021) and our experiments, respectively. This steady state model result is the geochemical scenario we would predict if Gale Lake remained poorly mixed year-round, similar to terrestrial lakes like Nyos, Pavin, and Matano. In the bottom half of the model water column, this steady state profile is a linear trend of increasing concentration with increasing depth, but this decreasing trend weakens at shallower depth and the

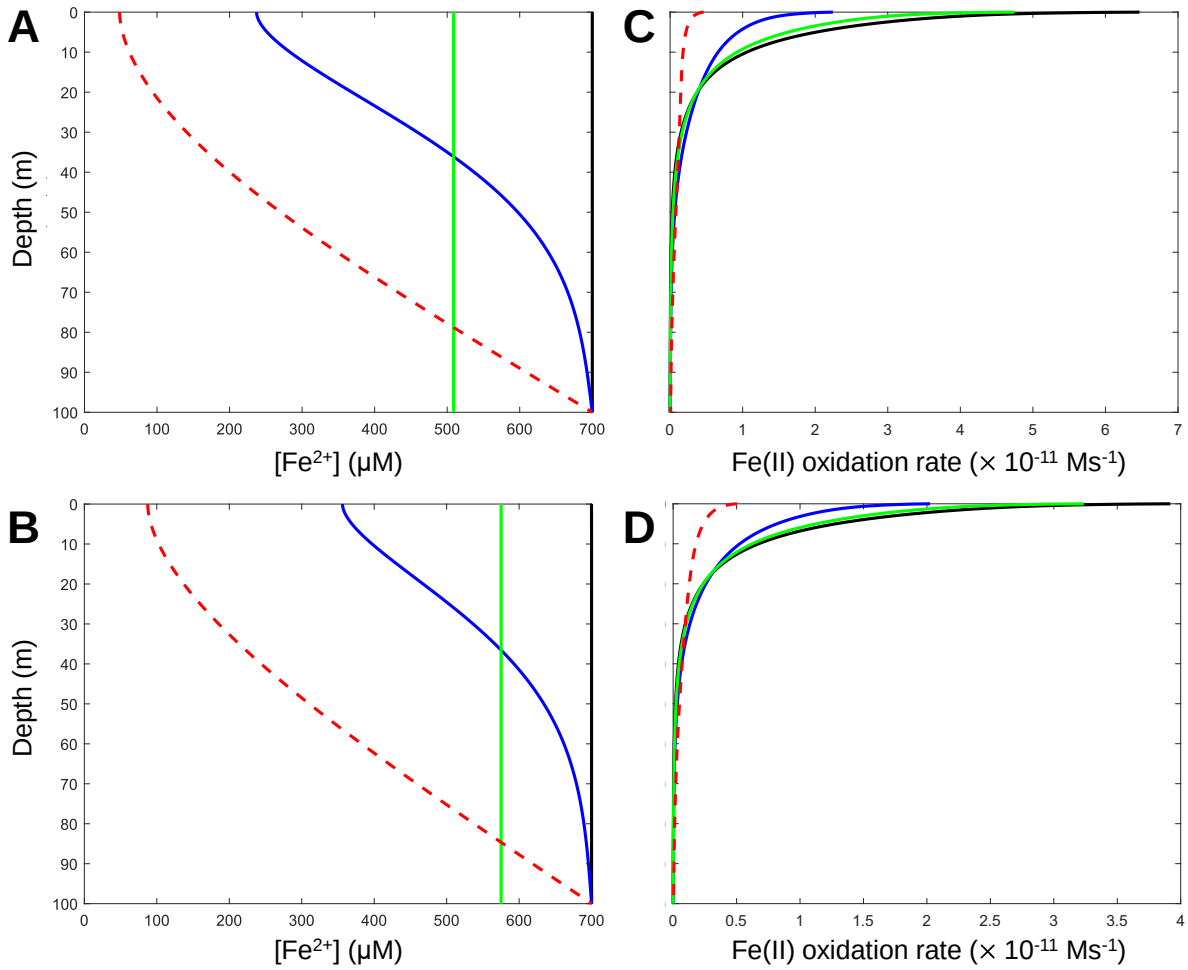

Figure 7.7. Photooxidation model outputs for a 100 m deep, near neutral 7 lake water column on Mars. **A.** and **B.** show $[Fe^{2+}]$ in the lake water column in models using quantum yield (Φ_{Fe2+} and Φ_{FeOH+}) data from **A.** Tabata et al. (2021) and **B.** This study. **C.** and **D.** show corresponding Fe(II) photooxidation rates for model runs shown in **A.** and **B.**, respectively. The different lines correspond to the initial conditions (black), after 1 year in the diffusion-only model (blue), after 1 year in the instantaneously mixed model (green), and steady state in the diffusion-only model (red, dashed).

steady-state $[Fe^{2+}]$ in the surface waters is a low but non-zero value that represents the balance between photooxidation by the unattenuated surface photon flux, and diffusive resupply from deeper waters (Figs. 7.7A-B).

Over the 1 Mars year runtime of the other diffusion-only models, the ferrous Fe concentration profile evolves towards that steady state profile, reaching ~20 % and ~51 % of the bottom water $[Fe^{2+}]$ at the lake surface in the scenarios using Tabata et al. (2021)'s Φ data and our Φ data

respectively (Figs. 7.7A-B). After the 1 Mars year runtime in the rapidly mixed models, no profile in $[Fe^{2+}]$ develops because of the homogenization we prescribed, but the $[Fe^{2+}]$ in the lake water column decreases to ~70 % and ~82 % of $[Fe^{2+}]_0$ in the scenarios using Tabata et al. (2021)'s Φ data and our Φ data respectively (Figs. 7.7A-B).

Ferric Fe burial rates and implications for deposition of the Murray Formation.

Depth profiles of photooxidation rates are shown in Figures 7.7C-D, and column-integrated Fe^{3+} deposition rates are given in Table 7.2. Photooxidation modeling suggests a range of authigenic Fe^{3+} deposition fluxes at the 100m depth base of the model of 0.21-0.92 mm yr^{-1} assuming a density of 3.8 g cm^{-3} for ferrihydrite (Table 7.2). Table 7.2 also shows the burial rate of Fe^{3+} at 5, 10, 20, and 50 m depth in the water column for each model, which provide approximate burial rates in shallower depositional environments. The highest Fe^{3+} deposition rates are seen (in decreasing order) in the initial unevolved water column (equivalent to the calculations of Tabata et al. 2021), followed by the rapidly mixed water column after 1 Mars year, then the diffusion-only water column after 1 Mars year (Figs. 7.7C-D). The lowest Fe^{3+} burial rates are seen in the steady-state water column because this model generates the great ferrous Fe depletion in irradiated near surface waters (Figs. 7.7). Ferric Fe deposition rates are higher when using the larger Φ values of Tabata et al. (2021), and the same inter-model variations are seen in both Φ scenarios.

In the Murray Formation, the authigenic ferric iron flux is only a fraction of the total depositional flux that includes a large fine grained, mafic siliciclastic component. The fraction of secondary mineral components in the Murray Formation were characterized by ChemMin XRD analysis in Hurowitz et al. (2017). The secondary minerals of interest are hematite, magnetite and jarosite because they contain Fe^{3+} and can thus be used to provide an estimate of the authigenic ferric iron

Table 7.2. Modeled photooxidation-driven Fe^{3+} deposition rates in different mixing and Φ scenarios. All models assume a 100 m column at pH 7.

	Φ values from Tabata et al. (2021)				**Φ values from this study**		
z (m)	**Fe^{3+}**	**Fe^{3+}**	**Bulk rock**		**Fe^{3+}**	**Fe^{3+}**	**Bulk rock**
	mol $cm^{-1}s^{-1}$	**mm yr^{-1}**	**mm yr^{-1}**		**mol $cm^{-1}s^{-1}$**	**mm yr^{-1}**	**mm yr^{-1}**
	Initial				Initial		
5	1.59E-11	0.43	9.90		1.01E-11	0.27	6.29
10	2.33E-11	0.63	14.50		1.48E-11	0.40	9.21
20	2.98E-11	0.81	18.55		1.89E-11	0.51	11.76
50	3.37E-11	0.91	20.98		2.14E-11	0.58	13.32
100	3.41E-11	0.92	21.23		2.17E-11	0.59	13.51
	End of one Mars year (diffusion only)				End of one Mars year (diffusion only)		
5	6.3E-12	0.17	3.92		5.73E-12	0.15	3.57
10	1E-11	0.27	6.22		9.00E-12	0.24	5.60
20	1.5E-11	0.41	9.34		1.27E-11	0.34	7.91
50	2.1E-11	0.57	13.07		1.61E-11	0.44	10.02
100	2.10E-11	0.57	13.07		1.65E-11	0.45	10.27
	End of one Mars year (rapid mixing)				End of one Mars year (rapid mixing)		
5	1.22E-11	0.33	7.59		8.58E-12	0.23	5.34
10	1.84E-11	0.50	11.45		1.28E-11	0.35	7.97
20	2.44E-11	0.66	15.19		1.68E-11	0.45	10.46
50	2.87E-11	0.78	17.86		1.95E-11	0.53	12.14
100	2.92E-11	0.79	18.18		1.98E-11	0.54	12.32

Table 7.2 continued

	Steady state burial rates (diffusion only)				Steady state burial rates (diffusion only)		
5	1.39E-12	0.04	0.86		1.54E-12	0.04	0.96
10	2.36E-12	0.06	1.47		2.57E-12	0.07	1.60
20	3.97E-12	0.11	2.47		4.08E-12	0.11	2.54
50	7.42E-12	0.20	4.62		6.62E-12	0.18	4.12
100	9.12E-12	0.25	5.68		7.60E-12	0.21	4.73

Rates at a given depth (z) are the column integrated amounts from the whole water column above this depth. Fe^{3+} burial rates in mm yr^{-1} were calculated assuming a density of 3.8 g cm^{-3} for ferrihydrite, and bulk rock burial rates were calculated assuming a density of 3.0 g cm^{-3} for the bulk mudstone.

flux from the Gale Crater Lake water column. Using XRD mineralogy we calculate average authigenic Fe^{3+} contents in the Murray Formation of ~5.5 wt % in the HP facies. With authigenic Fe^{3+} being diluted by the clastic and amorphous components of the mudstone, the total mudstone deposition rates at 100 m depth implied by our modeling (assuming 3 g cm^{-3} for the bulk rock) are between 4.7-21 mm yr^{-1} (Table 7.2). For comparison, observed laminae thicknesses in the HP facies range from ~0.9-2.2 mm (Hurowitz et al., 2017). If these laminations reflect annual depositional layers (also known as varves), then our model would predict higher rock deposition rates at 100 m depths than implied by the Martian sedimentological record. However, deposition in the steady state models to column-integrated depths of 20 m give Fe^{3+} and thus bulk rock deposition rates that would be consistent with lamination thicknesses seen the HP facies of the Murray Formation Table 7.2). Therefore, one way we could interpret our results is that the authigenic Fe^{3+} in the HP facies resulted from shallow water photooxidation-driven deposition

(potentially permanently) stratified lake mixed by slow eddy diffusion. This interpretation would agree very well with the redox-stratified lake model of Hurowitz et al. (2017).

However, it is also possible that the Fe^{3+} deposition rates from other model runs that are too high to agree with Murray Formation sedimentology, which would indicate instead that we selected conditions that overestimate the photooxidation rate relative to the actual environmental conditions on Mars at 3.5 Ga. For example, beyond chemical absorption by H_2O and dissolved ions, UV photons make have been attenuated in the lake water column by solid material, included suspended fine-grained clastic sediment and water column precipitates. Alternatively, a thicker atmosphere than the 200 mbar pCO_2 assumed in the solar UV model we used (Figure 7.2; Ranjan et al. 2017), or strong cloud cover on Mars, would also decrease the photon flux and thus photooxidation rates within the lake. Last, as shown previously by Tabata et al. (2021), lower dissolved [Fe^{2+}] in deep lake waters, or lower solution pH disfavoring speciation of $FeOH^+$, can also decrease photooxidation rates. The model results presented here do however indicate that UV photooxidation could have supported Fe^{3+} deposition rates that more than adequately account for estimated accumulation rates in the Murray Formation mudstones, so additional chemical oxidants during normal lake deposition may not have been necessary, even if they ultimately were available and played a role in redox geochemistry in Martian lakes.

Iron and Manganese and the Redox State of Gale Crater Lake.

Another important potential redox indicator in Gale Crater rocks investigated by Curiosity is manganese (Mn). Reduced manganese (Mn^{2+}) is soluble and has similar geochemical sources and behaviors to Fe^{2+}. Decoupling of these elements in low-temperature settings typically occurs in more oxidizing conditions because oxidation and precipitation of oxidized minerals occurs at a

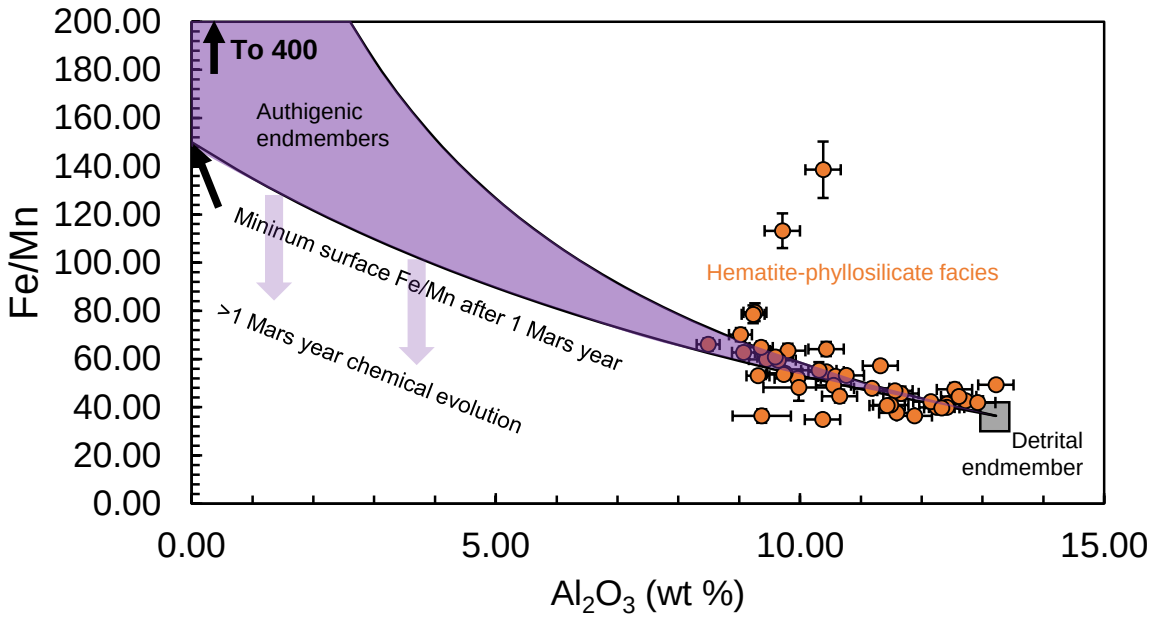

Figure 7.8. Fe/Mn vs. Al_2O_3 systematics in the Murray Formation. Negative covariation of Fe/Mn vs. Al_2O_3 in the hematite-phyllosilicate (HP) facies suggests mixing between an Al_2O_3-rich (detrital) endmember with low Fe/Mn, and an authigenic endmember with high Fe/Mn. The range of authigenic endmember compositions is calculated by multiplying the largest range of dissolved Fe/Mn ratios obtained in one-Mars-year-duration photooxidation models by an adsorption coefficient $D_{Fe/Mn} \approx 0.1$ (see text and Fig. 7.9). The mixing calculation assumes the authigenic endmember containing an Fe^{3+}-oxyhydroxide component equal to the fraction of crystalline secondary minerals (dark shaded area) in the HP facies comprised of hematite + magnetite + jarosite, which is ~0.33 in the Confidence Hills and Mojave 2 samples (Hurowitz et al., 2017). The clastic/detrital endmember is fixed at the lowest Fe/Mn and highest Al_2O_3 observed in the HP facies. Lower authigenic Fe/Mn endmember ratios (purple arrows) could be attained after more prolonged photo-oxidation, assuming, for example, that annual mixing did not re-homogenize the lake water column.

lower redox potential for Fe^{2+} than for Mn^{2+}. As such, conditions that oxidize and remove Fe^{2+} may leave the majority of Mn^{2+} in solution until higher redox potentials commensurate with the presence of free O_2, or and other reactive oxygen compounds, are realized. The Fe/Mn ratio was proposed to trace redox conditions in the redox-stratified model for Gale Crater Lake, with lower Fe/Mn in the shallower-water hematite-phyllosilicate (HP) facies reflecting enrichment of Mn through the oxidation and precipitation of Mn (Hurowitz et al., 2017). Localized high Mn levels in veins, nodules, and hardground surfaces in Gale Crater rocks have been observed with

ChemCam and interpreted as evidence for the past presence of high O_2 levels on ancient Mars (Gasda et al., 2019; Lanza et al., 2014, 2016, 2021). However, ChemCam data from observations of both the Murray Formation and the underlying Bradbury Formation are distinct from bulk rock APXS data in that they come from targeting specific features of interest within rocks, and do not necessarily relate directly to environmental conditions during deposition of bulk Murray Formation lacustrine mudstones.

While the Fe/Mn systematics in the Murray Formation have been taken to qualitatively indicate more oxidizing conditions in the HP facies, the lowest values of this ratio are only slightly lower than the value of ~40 for bulk silicate Mars (BSM) (McSween et al., 2009), and the highest MnO is just 0.53 wt % (Hurowitz et al., 2017). Therefore, low Fe/Mn values could be explained by a dominantly siliciclastic signal with the authigenic component of the mudstones in fact being Mn depleted, and indeed, a plot of Fe/Mn vs. Al_2O_3 supports the notion that detrital input drives the low Fe/Mn values in the HP facies (Fig. 7.8). Assuming congruent behavior of Fe^{2+} and Mn^{2+} during dissolution of basalt, the negative trend vs. Al_2O_3 in the HP facies indicates that the authigenic flux to the Murray Formation had a high Fe/Mn relative to the Gale Lake water column. We suggest that anoxic magnetite precipitation (in the MS facies; Hurowitz et al., 2017; Tosca et al., 2018) and Fe^{2+} photooxidation in shallower waters, could both result in a high Fe/Mn authigenic component where Mn would be deposited solely through minor non-redox adsorption to ferric minerals (Nie et al., 2020). This is entirely consistent with Murray Formation geochemical data and indicates that a high-potential oxidant like O_2 is not required for the redox-stratified lake model.

Removal of a high Fe/Mn authigenic precipitate over time will eventually drive the dissolved Fe/Mn reservoir to sub-BSM values if no other sink flux for Mn^{2+} was present. We incorporated

Fe/Mn ratios into our photooxidation model assuming an initial BSM value for Fe/Mn, modeling the authigenic Mn removal as an adsorption process that scales with the dissolved Fe/Mn ratio:

$$\frac{[Fe(II)]}{[Mn(II)]} = D_{Mn/Fe} \frac{R_{Fe}}{R_{Mn}}, \quad \text{(Eq. 11)}$$

where $D_{Mn/Fe} \approx 0.1$, inferred from Fe/Mn and iron isotopic systematics in Precambrian iron formations (Nie et al., 2020) that are somewhat analogous to the authigenic components of the Murray Formation (Hurowitz et al., 2017). In the model, Fe/Mn in solution (and as a result, in the precipitates) decreases over time as Fe^{2+} removal progresses, so the Fe/Mn ratio is particularly low at shallow depths where Fe^{2+} is most depleted by photooxidation. With a constant input of anoxic weathering fluids and only one exit channel, the dissolved Fe/Mn ratio will continue to decline unless a Mn-enriched authigenic phase starts to be removed. Over ~year-long timescales on which the lake may be anticipated to mix, a depth profile in dissolved Fe/Mn develops, so that the authigenic flux at different depths takes on a range of Fe/Mn ratios between 150 and 400 (Fig 7.9). These values are all far higher than BSM. Using these calculated values to define a range of authigenic endmember compositions, a simple two-component mixing model mixing model between Al_2O_3-rich endmember with a near-BSM Fe/Mn and an authigenic component with negligible Al_2O_3 can explain a much of the variation in the Fe/Mn vs. Al_2O_3 plot for APXS data from the HP facies of the Murray Formation (Fig. 7.8).

The simple adsorption model will become quantitatively incorrect if Fe/Mn continues to decrease unchecked in the entire lake reservoir. However, such prolonged preferential removal of Fe^{2+} relative to Mn^{2+} resulting in extremely fractionated Fe/Mn ratio would have been strictly necessary for oxidative precipitation of Mn to ever take place on Mars (Gasda et al., 2019; Hurowitz et al., 2017; Wordsworth et al., 2021). This is because $Mn^{3+/4+}$ oxides are efficiently reduced and redissolved in the presence of Fe^{2+}. For example, Mn^{2+} photooxidation in Fe^{2+}-free solutions has

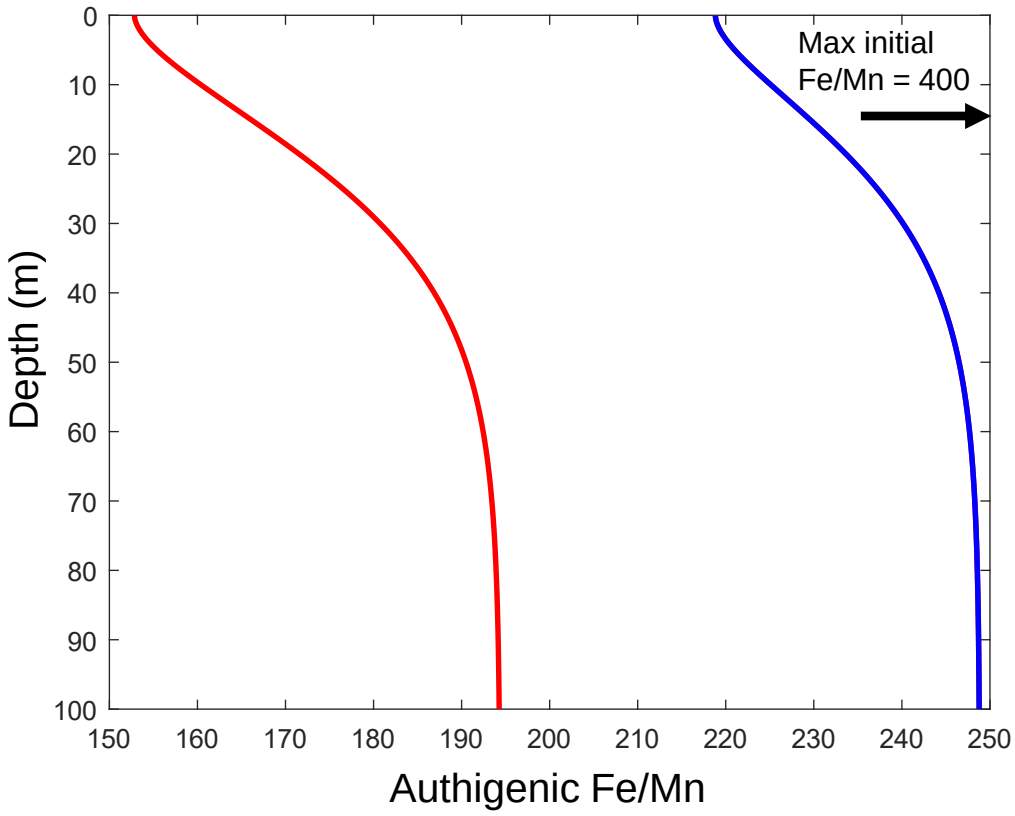

Figure 7.9. Authigenic Fe/Mn ratios developed in precipitates after 1 year model runs in diffusion-only models, assuming an adsorption coefficient $D_{Fe/Mn} \approx 0.1$ (see text, Nie et al., 2020), as a function of depth. The minimum Fe/Mn value is generated in shallow waters that experience the most extensive Fe removal relative to Mn. Ratios at depth reflect the column integrated composition of all authigenic precipitates from the water column above, but the highest possible Fe/Mn in authigenic material is at any location or time in the model is 400 (bulk silicate Mars ratio of 40 × $D_{Fe/Mn}$). The different lines correspond to models run with quantum yield data from Tabata et al. (2021) (red), and this study (blue). More extreme Fe/Mn fractionation relative could be seen if the water column was not mixed on annual timescales.

been observed to be efficient in experiments, but when $[Mn^{2+}] \approx [Fe^{2+}]$, little permanent Mn^{2+} removal from solution can occur because photooxidized manganese immediately oxidizes ferrous iron and is reduced back into solution (Anbar and Holland, 1992). The same principle may apply to Mn^{2+} oxidation by O_2 if the water column is not oxygenated top to bottom and substantial Fe^{2+} remains at depth, as has been suggested for Earth's early oceans (Kurzweil et al., 2016).

The requirement for extensive Fe^{2+} oxidation to decouple Mn and Fe in solution is also important to recognize in the context of localized manganese enrichments observed with ChemCam in Gale

Crater (Gasda et al., 2019; Lanza et al., 2014, 2016). These signatures were initially interpreted as signs of a high atmospheric O_2 episode on ancient Mars (Lanza et al., 2016). This interpretation is based on the strong temporal link between the onset of major Mn deposition and rising atmospheric O_2 in the terrestrial geologic record (Gumsley et al., 2017). An aspect of this comparison that is often overlooked is that widespread Mn^{2+} oxidation must be preceded for a long time by conditions too reducing to oxidize manganese, during which time Fe^{2+} could preferentially react with oxidants and be removed from solution, causing dissolved Fe/Mn ratios to fall (Kurzweil et al., 2016; Tsikos et al., 2010). On Earth, the first major deposition of Mn in the Hotazel Formation, South Africa, was preceded by several millions to tens of millions of years of deposition of Fe-rich, Mn-poor banded iron formations (BIFs) in the same depositional basin, and coupled Fe/Mn and Fe isotope systematics attest to the progressive oxidative removal of Fe from solution and coinciding decrease in Fe/Mn in the seawater reservoir (Beukes, 1984; Beukes and Gutzmer, 2008; Kurzweil et al., 2016; Thibon et al., 2019; Tsikos et al., 2010). If high Fe/Mn authigenic mineral precipitation that took place during 'normal' deposition in Gale Lake approximates on a smaller scale the prolonged period of low-Mn BIF deposition on Earth, then any high-Mn authigenic mineral formation on Mars could only come at the end of a period of high Fe/Mn chemical sedimentation.

On Earth, the Hotazel Formation was formed on the margins of an open basin, and overwhelming atmospheric oxygenation and likely mediation by chemoautotrophic microbes were the biogeochemical switches that initiated unprecedented levels of Mn deposition (Tsikos et al., 2010). On Mars, we hypothesize that an alternative switch would be episodic drawdown of the lake associated with evaporation and retreat of the water table, as this would cut off the resupply of Fe^{2+} with no new fluids being introduced to the lake. Without a steady input of fluids with Fe/Mn close to BSM, closed system evolution of the dissolved Fe/Mn ratio to strongly fractionated values

could be facilitated by the continued preferential removal of Fe^{2+} via photooxidation. A testable hypothesis for this scenario is that high manganese deposits in Gale Crater should be associated with evidence for drying, and/or retreat of lake waters to the subsurface and resulting late-stage fluid interactions. This should be a prerequisite for formation of such Mn-rich materials as observed with ChemCam irrespective of the precipitation mechanism for Mn, whether this was oxidation by O_2 or another strong oxidant, or precipitation of a stable Mn^{2+} phase.

The high-Mn materials documented with ChemCam do in fact show some evidence that they were deposited in very shallow waters, and/or during drying and late fluid circulation, and therefore in environments where the requisite oxidative Fe depletion could be explained. Observations of Mn-rich materials are being continuously updated during the traverse of Curiosity up Mt. Sharp, and to date, observations of high-Mn materials have been observed in fracture-filling veins inferred to be linked to an ancient aquifer (Lanza et al., 2014, 2016), diagenetic nodules formed between sedimentary laminae and hardgrounds (Lanza et al., 2021), and shallow water sandstones inferred to have formed in braided stream networks feeding the open lake basin (Gasda et al., 2019). Similar fracture-filling Mn-rich veins were also observed by MER Opportunity at Endeavor Crater (Arvidson et al., 2016), which reinforces the idea that late-stage fluids in Martian aqueous settings tend to become Mn^{2+}-rich. Other telltale signs of a late-stage fluid origin for Mn enrichments in Gale Crater rocks include a mixing array in ChemCam targets that tracks towards high Mn at low Fe content, and a close association of dark-toned Mn-rich materials with $CaSO_4$ and NaCl that were likely added to rocks during evaporative concentration of the dregs of larger water bodies (Comellas et al., 2021; Lanza et al., 2021). Once concentrated in late-stage fluids, the potential for precipitation of highly soluble Mn^{2+} is enhanced. Thermodynamic modeling has shown that brine evaporation can encourage Mn redox precipitation because reactive chlorine compounds capable

of oxidizing Mn^{2+} likely available on early Mars (Mitra et al., 2020; Mitra and Catalano, 2019) could become highly concentrated coincident with increased [Mn^{2+}] (Berger et al., 2019). It is of course worth noting that 100% evaporation would also necessitate precipitation of Mn^{2+} oxides even in the absence of an oxidant. Indeed, recent experiments conducted with the SAM instrument on Curiosity have suggested that Mn is present as an Mn^{2+} phase (Lanza et al., 2021), rather than previously inferred Mn^{3+}/Mn^{4+} oxides (Lanza et al., 2016).

In summary, the sedimentary rock record at Gale Crater shows evidence that Mn and Fe were decoupled during sedimentary and diagenetic processes (Fig. 7.10). During deposition of the Murray Formation mudstones in a relatively fresh and deep lake environment, there should have been preferential export of Fe^{3+} oxyhydroxides, along with some minor adsorbed Mn^{2+}, out of the lake water column and into the sediment pile (Fig. 7.10A). This would have progressively depleted the Fe/Mn ratio of the lake water reservoir relative to input values, while authigenic sedimentary phases added to mudstone would have had had high Fe/Mn ratios relative to detrital, bulk Mars-like material. This time integrated effect of this process on the Fe/Mn of Gale Lake waters could have been somewhat diminished during favorable climatic conditions by continued hydrologic input, with dissolved Fe/Mn similar to BSM, along with the potential removal of Mn oxides in the shallowest lake waters where Fe^{2+} was entirely removed by photooxidation processes (Gasda et al., 2019). During eventual drawdown of the lake level, with new hydrologic inputs shut off, Mn^{2+} could be further enriched in lake waters, both relative to Fe^{2+} due to continued photooxidation, and in absolute terms due to evaporative concentration (Fig. 7.10B) (Berger et al., 2019). These factors together could have enabled the eventual precipitation of Mn-rich mineral phases in aquifer fractures and diagenetic nodules as late stage fluids retreated to the subsurface (Fig. 7.10C). The ability of high Mn^{2+} late-stage fluids to be mobilized in Gale Crater provides evidence against

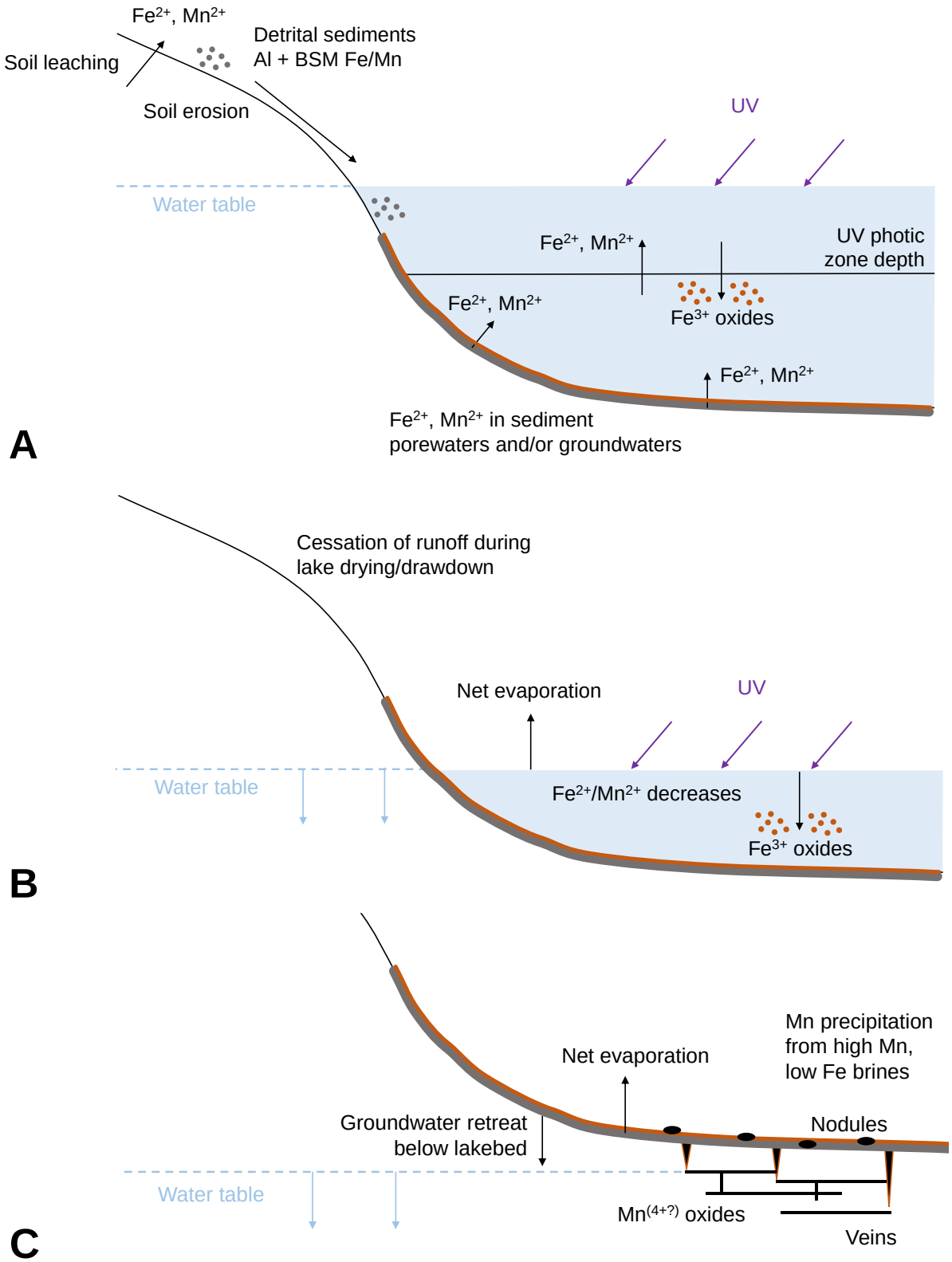

Figure 7.10. Conceptual illustration of Fe and Mn cycling at Gale Crater Lake.

Figure 7.10. continued. Conceptual illustration of Fe and Mn cycling at Gale Crater Lake during the course of a lake event. **A.** During a steady state lake event, runoff and/or groundwater balances evaporation so the water level remains stable. Ferrous iron and Mn^{2+} are delivered from local soil weathering runoff and/or dissolution of olivine in sediment porewaters, in Fe/Mn ratio close to BSM. Solid detrital sediments with Fe/Mn also similar to BSM are eroded from local soil and deposited in shallower facies. UV radiation drives photooxidation of Fe^{2+} and deposition of insoluble ferric oxides in Gale sediments. Preferential removal of Fe due to photooxidation decreases the dissolved Fe/Mn ratio in lake waters. **B.** When climatically-imposed drawdown of the lake level begins, runoff is shut off and net evaporation of the lake takes place. Ferrous iron photooxidation continues, but dissolved Fe/Mn can increase more sharply as the lake water composition is no longer buffered by new fluid with BSM-like composition. **C.** Continued drying of the lake eventually causes lake waters to retreat into the subsurface. Late-stage fluids with low Fe and high dissolved Mn interact with buried sediment to form diagenetic nodules Mn enrichments and Mn-rich fracture filling veins through evaporative precipitation and/or oxidation.

proposed episodes of high atmospheric O_2 on Mars around this time and should motivate further investigation in the Mars geochemistry community into alternative precipitation mechanisms for Mn-rich materials.

Conclusions

Photooxidation has long been considered as a potential pathway to ferrous iron oxidation on Mars because the basic ingredients (liquid water, iron-bearing rocks, solar radiation) required for it to take place were readily available early in Mars's history. Many of the previous experimental constraints on the quantum yield of photooxidation came from studies using UV light sources that are poor solar simulators or featured short reaction timescale that did not determine the effectiveness of photooxidation at quantitatively depleting ferrous iron from solutions. Our new experiments produced quantum yields similar to many previous studies and in disagreement with the most recent published data. We also found that photooxidation of ferrous iron in low pH solutions is ineffective at quantitatively depositing Fe^{3+} from solution, due to the competing effects of Fe^{3+} photoreduction that stabilize Fe^{2+} at high levels. This suggests that aqueous photooxidation

may not have been a viable pathway to jarosite deposition at Meridiani Planum, and recently proposed ice-dust interaction mechanisms may better explain those mineral occurrences.

We simulated ferrous iron photooxidation in Gale Crater Lake with a more realistic reaction-transport model than has previously been applied to the photooxidation question, and find that the range of plausible photooxidation-driven Fe^{3+} deposition rates in a near-neutral pH lake can more than account for the mineral abundances in laminated mudstones in the Murray Formation. Our model results favor shallow water deposition of the hematite-silicate facies of the Murray Formation from a permanently stratified steady-state lake, which support the prevailing hypothesis for this sedimentary succession. Last, we find that redox-decoupling of iron and manganese by photooxidation of ferrous iron, combined with mixing between detrital and authigenic sedimentary phases, can adequately explain the iron and manganese systematics of bulk Murray Formation mudstones without the need to appeal to free O_2 as an oxidant for Mn^{2+} in open lake conditions. We also suggest that the eventual formation of a low Fe^{2+}, high Mn^{2+} late-stage lake fluid resulting from this redox decoupling would produce the necessary parent fluids for the precipitation of manganese-rich mineral assemblages in vein fills and diagenetic nodules observed *in situ* at Gale Crater.

Acknowledgements

Gerry Olack and Thomas Stephan are thanked for providing access to laboratory equipment. Development of the lake model benefitted from discussions about mixing processes Martian hydrology with Edwin Kite and Malte Jansen

References

Anbar, A.D., Holland, H.D., 1992. The photochemistry of manganese and the origin of banded iron formations. Geochim. Cosmochim. Acta 56, 2595–2603. https://doi.org/10.1016/0016-7037(92)90346-K

Arvidson, R.E., Squyres, S.W., Morris, R.V., Knoll, A.H., Gellert, R., Clark, B.C., Catalano, J.G., Jolliff, B.L., McLennan, S.M., Herkenhoff, K.E., VanBommel, S., Mittlefehldt, D.W., Grotzinger, J.P., Guinness, E.A., Johnson, J.R., Bell, J.F., Farrand, W.H., Stein, N., Fox, V.K., Golombek, M.P., Hinkle, M.A.G., Calvin, W.M., Souza, P.A.D., 2016. High concentrations of manganese and sulfur in deposits on Murray Ridge, Endeavour Crater, Mars. Am. Mineral. 101, 1389–1405. https://doi.org/10.2138/am-2016-5599

Baccolo, G., Delmonte, B., Niles, P.B., Cibin, G., Di Stefano, E., Hampai, D., Keller, L., Maggi, V., Marcelli, A., Michalski, J., Snead, C., Frezzotti, M., 2021. Jarosite formation in deep Antarctic ice provides a window into acidic, water-limited weathering on Mars. Nat. Commun. 12, 436. https://doi.org/10.1038/s41467-020-20705-z

Bekker, A., Slack, J.F., Planavsky, N., Krapež, B., Hofmann, A., Konhauser, K.O., Rouxel, O.J., 2010. Iron Formation: The Sedimentary Product of a Complex Interplay among Mantle, Tectonic, Oceanic, and Biospheric Processes. Econ. Geol. 105, 467–508. https://doi.org/10.2113/gsecongeo.105.3.467

Berger, J.A., King, P.L., Gellert, R., Clark, B.C., O'Connell-Cooper, C.D., Thompson, L.M., VanBommel, S.J.V., Yen, A.S., 2019. Manganese Enrichment Pathways Relevant To Gale Crater, Mars: Evaporative Concentration And Chlorine-Induced Precipitation. LPSC L 2847.

Beukes, N.J., 1984. Sedimentology of the Kuruman and Griquatown Iron-formations, Transvaal Supergroup, Griqualand West, South Africa. Precambrian Res. 24, 47–84. https://doi.org/10.1016/0301-9268(84)90069-X

Beukes, N.J., Gutzmer, J., 2008. Origin and Paleoenvironmental Significance of Major Iron Formations at the Archean-Paleoproterozoic Boundary. Rev. Econ. Geol. 15. https://doi.org/10.5382/Rev.15.01

Braterman, P., Cairns-Smith, A., Sloper, R., Truscott, T., Craw, M., 1984. Photooxidation of iron(II) in water between pH 7.5 and 4.0. J. Chem. Soc.-Dalton Trans. https://doi.org/10.1039/dt9840001441

Braterman, P.S., Cairns-Smith, A.G., Sloper, R.W., 1983. Photo-oxidation of hydrated Fe2+—significance for banded iron formations. Nature 303, 163–164. https://doi.org/10.1038/303163a0

Bullen, T.D., White, A.F., Childs, C.W., Vivit, D.V., Schulz, M.S., 2001. Demonstration of significant abiotic iron isotope fractionation in nature. Geology 29, 699–702. https://doi.org/10.1130/0091-7613(2001)029<0699:DOSAII>2.0.CO;2

Burns, R.G., 1993. Rates and mechanisms of chemical weathering of ferromagnesian silicate minerals on Mars. Geochim. Cosmochim. Acta 57, 4555–4574.

Burns, R.G., 1987. Gossans on Mars: Spectral features attributed to jarosite (No. 19870013984), NASA, Washington, Reports of Planetary Geology and Geophysics Program, 1986.

Busigny, V., Planavsky, N.J., Jézéquel, D., Crowe, S., Louvat, P., Moureau, J., Viollier, E., Lyons, T.W., 2014. Iron isotopes in an Archean ocean analogue. Geochim. Cosmochim. Acta 133, 443–462. https://doi.org/10.1016/j.gca.2014.03.004

Cairns-Smith, A.G., 1978. Precambrian solution photochemistry, inverse segregation, and banded iron formations. Nature 276, 807–808. https://doi.org/10.1038/276807a0

Camacho, A., Miracle, M.R., Romero-Viana, L., Picazo, A., Vicente, E., 2017a. Lake La Cruz, an Iron-Rich Karstic Meromictic Lake in Central Spain. Ecol. Meromictic Lakes 187–233. https://doi.org/10.1007/978-3-319-49143-1_8

Camacho, A., Walter, X.A., Picazo, A., Zopfi, J., 2017b. Photoferrotrophy: Remains of an Ancient Photosynthesis in Modern Environments. Front. Microbiol. 8. https://doi.org/10.3389/fmicb.2017.00323

Catling, D.C., Moore, J.M., 2003. The nature of coarse-grained crystalline hematite and its implications for the early environment of Mars. Icarus 165, 277–300. https://doi.org/10.1016/S0019-1035(03)00173-8

Catling, D.C., Zahnle, K.J., 2020. The Archean atmosphere. Sci. Adv. 6, eaax1420. https://doi.org/10.1126/sciadv.aax1420

Catling, D.C., Zahnle, K.J., McKay, C.P., 2001. Biogenic Methane, Hydrogen Escape, and the Irreversible Oxidation of Early Earth. Science 293, 839–843. https://doi.org/10.1126/science.1061976

Clark, B.C., Morris, R.V., McLennan, S.M., Gellert, R., Jolliff, B., Knoll, A.H., Squyres, S.W., Lowenstein, T.K., Ming, D.W., Tosca, N.J., Yen, A., Christensen, P.R., Gorevan, S., Brückner, J., Calvin, W., Dreibus, G., Farrand, W., Klingelhoefer, G., Waenke, H., Zipfel, J., Bell III, J.F., Grotzinger, J., McSween, H.Y., Rieder, R., 2005. Chemistry and mineralogy of outcrops at

Meridiani Planum. Earth Planet. Sci. Lett., Sedimentary Geology at Meridiani Planum, Mars 240, 73–94. https://doi.org/10.1016/j.epsl.2005.09.040

Comellas, J.M., Essunfeld, A., Lanza, N., Gasda, P.J., Delapp, D., Wiens, R.C., Gasnault, O., Clegg, S., Bedford, C., Dehouck, E., Clark, B., Anderson, R., Fisher, W., Lueth, V., 2021. Geologic Interpretations Of Elevated-Mn Chemcam Targets In The Bradbury Rise, Gale Crater, Mars. LPSC LII 2548.

Croal, L.R., Johnson, C.M., Beard, B.L., Newman, D.K., 2004. Iron isotope fractionation by Fe(II)-oxidizing photoautotrophic bacteria 1. Geochim. Cosmochim. Acta 68, 1227–1242. https://doi.org/10.1016/j.gca.2003.09.011

Crowe, S.A., Jones, C., Katsev, S., Magen, C., O'Neill, A.H., Sturm, A., Canfield, D.E., Haffner, G.D., Mucci, A., Sundby, B., Fowle, D.A., 2008. Photoferrotrophs thrive in an Archean Ocean analogue. Proc. Natl. Acad. Sci. 105, 15938–15943. https://doi.org/10.1073/pnas.0805313105

Crowe, S.A., Paris, G., Katsev, S., Jones, C., Kim, S.-T., Zerkle, A.L., Nomosatryo, S., Fowle, D.A., Adkins, J.F., Sessions, A.L., Farquhar, J., Canfield, D.E., 2014. Sulfate was a trace constituent of Archean seawater. Science 346, 735–739. https://doi.org/10.1126/science.1258966

Czaja, A.D., Johnson, C.M., Roden, E.E., Beard, B.L., Voegelin, A.R., Nägler, T.F., Beukes, N.J., Wille, M., 2012. Evidence for free oxygen in the Neoarchean ocean based on coupled iron–molybdenum isotope fractionation. Geochim. Cosmochim. Acta 86, 118–137. https://doi.org/10.1016/j.gca.2012.03.007

Ehlmann, B.L., Anderson, F.S., Andrews-Hanna, J., Catling, D.C., Christensen, P.R., Cohen, B.A., Dressing, C.D., Edwards, C.S., Elkins-Tanton, L.T., Farley, K.A., Fassett, C.I., Fischer, W.W., Fraeman, A.A., Golombek, M.P., Hamilton, V.E., Hayes, A.G., Herd, C.D.K., Horgan, B., Hu, R., Jakosky, B.M., Johnson, J.R., Kasting, J.F., Kerber, L., Kinch, K.M., Kite, E.S., Knutson, H.A., Lunine, J.I., Mahaffy, P.R., Mangold, N., McCubbin, F.M., Mustard, J.F., Niles, P.B., Quantin-Nataf, C., Rice, M.S., Stack, K.M., Stevenson, D.J., Stewart, S.T., Toplis, M.J., Usui, T., Weiss, B.P., Werner, S.C., Wordsworth, R.D., Wray, J.J., Yingst, R.A., Yung, Y.L., Zahnle, K.J., 2016. The sustainability of habitability on terrestrial planets: Insights, questions, and needed measurements from Mars for understanding the evolution of Earth-like worlds. J. Geophys. Res. Planets 121, 2016JE005134. https://doi.org/10.1002/2016JE005134

François, L.M., 1987. Reducing power of ferrous iron in the Archean Ocean, 2. Role of FeOH+ photooxidation. Paleoceanography 2, 395–408. https://doi.org/10.1029/PA002i004p00395

François, L.M., 1986. Extensive deposition of banded iron formations was possible without photosynthesis. Nature 320, 352–354. https://doi.org/10.1038/320352a0

Frydenvang, J., Mangold, N., Wiens, R.C., Fraeman, A.A., Edgar, L.A., Fedo, C.M., L'Haridon, J., Bedford, C.C., Gupta, S., Grotzinger, J.P., Bridges, J.C., Clark, B.C., Rampe, E.B., Gasnault, O., Maurice, S., Gasda, P.J., Lanza, N.L., Olilla, A.M., Meslin, P.-Y., Payré, V., Calef, F., Salvatore, M., House, C.H., 2020. The Chemostratigraphy of the Murray Formation and Role of Diagenesis at Vera Rubin Ridge in Gale Crater, Mars, as Observed by the ChemCam Instrument. J. Geophys. Res. Planets 125, e2019JE006320. https://doi.org/10.1029/2019JE006320

Fukushi, K., Sekine, Y., Sakuma, H., Morida, K., Wordsworth, R., 2019. Semiarid climate and hyposaline lake on early Mars inferred from reconstructed water chemistry at Gale. Nat. Commun. 10, 4896. https://doi.org/10.1038/s41467-019-12871-6

Gasda, P.J., Lanza, N., Sumner, D.Y., Stein, N., Lamm, S.N., Ollila, A., Clark, B.C., Fairén, A.G., Newsom, H.E., Clegg, S.M., Wiens, R.C., Maurice, S., Sabatier, U.P., 2019. High-Mn Sandstone As Evidence For Oxidized Conditions In Gale Crater Lake. LPSC L 2132.

Grotzinger, J.P., 2013. Analysis of Surface Materials by the Curiosity Mars Rover. Science 341, 1475–1475. https://doi.org/10.1126/science.1244258

Grotzinger, J.P., Gupta, S., Malin, M.C., Rubin, D.M., Schieber, J., Siebach, K., Sumner, D.Y., Stack, K.M., Vasavada, A.R., Arvidson, R.E., Calef, F., Edgar, L., Fischer, W.F., Grant, J.A., Griffes, J., Kah, L.C., Lamb, M.P., Lewis, K.W., Mangold, N., Minitti, M.E., Palucis, M., Rice, M., Williams, R.M.E., Yingst, R.A., Blake, D., Blaney, D., Conrad, P., Crisp, J., Dietrich, W.E., Dromart, G., Edgett, K.S., Ewing, R.C., Gellert, R., Hurowitz, J.A., Kocurek, G., Mahaffy, P., McBride, M.J., McLennan, S.M., Mischna, M., Ming, D., Milliken, R., Newsom, H., Oehler, D., Parker, T.J., Vaniman, D., Wiens, R.C., Wilson, S.A., 2015. Deposition, exhumation, and paleoclimate of an ancient lake deposit, Gale crater, Mars. Science 350, aac7575. https://doi.org/10.1126/science.aac7575

Grotzinger, J.P., Sumner, D.Y., Kah, L.C., Stack, K., Gupta, S., Edgar, L., Rubin, D., Lewis, K., Schieber, J., Mangold, N., Milliken, R., Conrad, P.G., DesMarais, D., Farmer, J., Siebach, K., Calef, F., Hurowitz, J., McLennan, S.M., Ming, D., Vaniman, D., Crisp, J., Vasavada, A., Edgett, K.S., Malin, M., Blake, D., Gellert, R., Mahaffy, P., Wiens, R.C., Maurice, S., Grant, J.A., Wilson, S., Anderson, R.C., Beegle, L., Arvidson, R., Hallet, B., Sletten, R.S., Rice, M., Bell, J., Griffes, J., Ehlmann, B., Anderson, R.B., Bristow, T.F., Dietrich, W.E., Dromart, G., Eigenbrode, J., Fraeman, A., Hardgrove, C., Herkenhoff, K., Jandura, L., Kocurek, G., Lee, S., Leshin, L.A., Leveille, R., Limonadi, D., Maki, J., McCloskey, S., Meyer, M., Minitti, M., Newsom, H., Oehler, D., Okon, A., Palucis, M., Parker, T., Rowland, S., Schmidt, M., Squyres, S., Steele, A., Stolper, E., Summons, R., Treiman, A., Williams, R., Yingst, A., Team, M.S., 2014. A Habitable Fluvio-Lacustrine Environment at Yellowknife Bay, Gale Crater, Mars. Science 343, 1242777. https://doi.org/10.1126/science.1242777

Gumsley, A.P., Chamberlain, K.R., Bleeker, W., Söderlund, U., Kock, M.O. de, Larsson, E.R., Bekker, A., 2017. Timing and tempo of the Great Oxidation Event. Proc. Natl. Acad. Sci. 114, 1811–1816. https://doi.org/10.1073/pnas.1608824114

Hatchard, C.G., Parker, C.A., 1956. A new sensitive chemical actinometer - II. Potassium ferrioxalate as a standard chemical actinometer. Proc. R. Soc. Lond. Ser. Math. Phys. Sci. 235, 518–536. https://doi.org/10.1098/rspa.1956.0102

Heard, A.W., Aarons, S.M., Hofmann, A., He, X., Ireland, T., Bekker, A., Qin, L., Dauphas, N., 2021. Anoxic continental surface weathering recorded by the 2.95 Ga Denny Dalton Paleosol (Pongola Supergroup, South Africa). Geochim. Cosmochim. Acta 295, 1–23. https://doi.org/10.1016/j.gca.2020.12.005

Heard, A.W., Dauphas, N., Guilbaud, R., Rouxel, O.J., Butler, I.B., Nie, N.X., Bekker, A., 2020. Triple iron isotope constraints on the role of ocean iron sinks in early atmospheric oxygenation. Science 370, 446–449. https://doi.org/10.1126/science.aaz8821

Herrera, L., Ruiz, P., Aguillon, J.C., Fehrmann, A., 1989. A new spectrophotometric method for the determination of ferrous iron in the presence of ferric iron. J. Chem. Technol. Biotechnol. 44, 171–181. https://doi.org/10.1002/jctb.280440302

Hondzo, M., Ellis, C.R., Stefan, H.G., 1991. Vertical Diffusion in Small Stratified Lake: Data and Error Analysis. J. Hydraul. Eng. 117, 1352–1369. https://doi.org/10.1061/(ASCE)0733-9429(1991)117:10(1352)

Hurowitz, J.A., Fischer, W.W., Tosca, N.J., Milliken, R.E., 2010. Origin of acidic surface waters and the evolution of atmospheric chemistry on early Mars. Nat. Geosci. 3, 323–326. https://doi.org/10.1038/ngeo831

Hurowitz, J.A., Grotzinger, J.P., Fischer, W.W., McLennan, S.M., Milliken, R.E., Stein, N., Vasavada, A.R., Blake, D.F., Dehouck, E., Eigenbrode, J.L., Fairén, A.G., Frydenvang, J., Gellert, R., Grant, J.A., Gupta, S., Herkenhoff, K.E., Ming, D.W., Rampe, E.B., Schmidt, M.E., Siebach, K.L., Stack-Morgan, K., Sumner, D.Y., Wiens, R.C., 2017. Redox stratification of an ancient lake in Gale crater, Mars. Science 356, eaah6849. https://doi.org/10.1126/science.aah6849

Jortner, J., Stein, G., 1962a. The Photochemical Evolution Of Hydrogen From Aqueous Solutions Of Ferrous Ions. Part I. The Reaction Mechanism At Low pH. J. Phys. Chem. 66, 1258–1264. https://doi.org/10.1021/j100813a012

Jortner, J., Stein, G., 1962b. The Photochemical Evolution Of Hydrogen From Aqueous Solutions Of Ferrous Ions. Part II. Effect Of Changing pH. J. Phys. Chem. 66, 1264–1271. https://doi.org/10.1021/j100813a013

Kappler, A., Pasquero, C., Konhauser, K.O., Newman, D.K., 2005. Deposition of banded iron formations by anoxygenic phototrophic Fe(II)-oxidizing bacteria. Geology 33, 865–868. https://doi.org/10.1130/G21658.1

Khashan, M.A., Nassif, A.Y., 2001. Dispersion of the optical constants of quartz and polymethyl methacrylate glasses in a wide spectral range: 0.2–3 μm. Opt. Commun. 188, 129–139. https://doi.org/10.1016/S0030-4018(00)01152-4

Kieber, R.J., Hardison, D.R., Whitehead, R.F., Willey, J.D., 2003. Photochemical Production of Fe(II) in Rainwater. Environ. Sci. Technol. 37, 4610–4616. https://doi.org/10.1021/es030345s

Kite, E.S., 2019. Geologic Constraints on Early Mars Climate. Space Sci. Rev. 215, 10. https://doi.org/10.1007/s11214-018-0575-5

Kite, E.S., Melwani Daswani, M., 2019. Geochemistry constrains global hydrology on Early Mars. Earth Planet. Sci. Lett. 524, 115718. https://doi.org/10.1016/j.epsl.2019.115718

Klingelhöfer, G., Morris, R.V., Bernhardt, B., Schröder, C., Rodionov, D.S., Souza, P.A. de, Yen, A., Gellert, R., Evlanov, E.N., Zubkov, B., Foh, J., Bonnes, U., Kankeleit, E., Gütlich, P., Ming, D.W., Renz, F., Wdowiak, T., Squyres, S.W., Arvidson, R.E., 2004. Jarosite and Hematite at Meridiani Planum from Opportunity's Mössbauer Spectrometer. Science 306, 1740–1745. https://doi.org/10.1126/science.1104653

Konhauser, K.O., Amskold, L., Lalonde, S.V., Posth, N.R., Kappler, A., Anbar, A., 2007. Decoupling photochemical Fe(II) oxidation from shallow-water BIF deposition. Earth Planet. Sci. Lett. 258, 87–100. https://doi.org/10.1016/j.epsl.2007.03.026

Konhauser, K.O., Hamade, T., Raiswell, R., Morris, R.C., Ferris, F.G., Southam, G., Canfield, D.E., 2002. Could bacteria have formed the Precambrian banded iron formations? Geology 30, 1079–1082. https://doi.org/10.1130/0091-7613(2002)030<1079:CBHFTP>2.0.CO;2

Konhauser, K.O., Newman, D.K., Kappler, A., 2005. The potential significance of microbial Fe(III) reduction during deposition of Precambrian banded iron formations. Geobiology 3, 167–177. https://doi.org/10.1111/j.1472-4669.2005.00055.x

Konhauser, K.O., Planavsky, N.J., Hardisty, D.S., Robbins, L.J., Warchola, T.J., Haugaard, R., Lalonde, S.V., Partin, C.A., Oonk, P.B.H., Tsikos, H., Lyons, T.W., Bekker, A., Johnson, C.M., 2017. Iron formations: A global record of Neoarchaean to Palaeoproterozoic environmental history. Earth-Sci. Rev. 172, 140–177. https://doi.org/10.1016/j.earscirev.2017.06.012

Kristmannsdóttir, H., Ármannsson, H., 2004. Groundwater in the Lake Myvatn area, northern Iceland: Chemistry, origin and interaction. Aquat. Ecol. 38, 115–128. https://doi.org/10.1023/B:AECO.0000032067.47495.71

Kurzweil, F., Wille, M., Gantert, N., Beukes, N.J., Schoenberg, R., 2016. Manganese oxide shuttling in pre-GOE oceans – evidence from molybdenum and iron isotopes. Earth Planet. Sci. Lett. 452, 69–78. https://doi.org/10.1016/j.epsl.2016.07.013

Lambrecht, N., Wittkop, C., Katsev, S., Fakhraee, M., Swanner, E.D., 2018. Geochemical Characterization of Two Ferruginous Meromictic Lakes in the Upper Midwest, USA. J. Geophys. Res. Biogeosciences 123, 3403–3422. https://doi.org/10.1029/2018JG004587

Lanza, N.L., Fischer, W.W., Wiens, R.C., Grotzinger, J., Ollila, A.M., Cousin, A., Anderson, R.B., Clark, B.C., Gellert, R., Mangold, N., Maurice, S., Le Mouélic, S., Nachon, M., Schmidt, M., Berger, J., Clegg, S.M., Forni, O., Hardgrove, C., Melikechi, N., Newsom, H.E., Sautter, V., 2014. High manganese concentrations in rocks at Gale crater, Mars. Geophys. Res. Lett. 41, 2014GL060329. https://doi.org/10.1002/2014GL060329

Lanza, N.L., Gasda, P.J., Essunfeld, A., Comellas, J., Caravaca, G., Rampe, E., Williams, A., Meslin, P.-Y., Dehouck, E., Mangold, N., Rapin, W., Hazen, R., Fischer, W.W., Ollila, A.M., House, C., Wiens, R.C., 2021. Chemistry of manganese-bearing minerals at the Groken drill site, Gale Crater, Mars. LPSC LII 2231.

Lanza, N.L., Wiens, R.C., Arvidson, R.E., Clark, B.C., Fischer, W.W., Gellert, R., Grotzinger, J.P., Hurowitz, J.A., McLennan, S.M., Morris, R.V., Rice, M.S., Bell, J.F., Berger, J.A., Blaney, D.L., Bridges, N.T., Calef, F., Campbell, J.L., Clegg, S.M., Cousin, A., Edgett, K.S., Fabre, C., Fisk, M.R., Forni, O., Frydenvang, J., Hardy, K.R., Hardgrove, C., Johnson, J.R., Lasue, J., Le Mouélic, S., Malin, M.C., Mangold, N., Martìn-Torres, J., Maurice, S., McBride, M.J., Ming, D.W., Newsom, H.E., Ollila, A.M., Sautter, V., Schröder, S., Thompson, L.M., Treiman, A.H., VanBommel, S., Vaniman, D.T., Zorzano, M.-P., 2016. Oxidation of manganese in an ancient aquifer, Kimberley formation, Gale crater, Mars. Geophys. Res. Lett. 43, 2016GL069109. https://doi.org/10.1002/2016GL069109

Laskar, J., Correia, A.C.M., Gastineau, M., Joutel, F., Levrard, B., Robutel, P., 2004. Long term evolution and chaotic diffusion of the insolation quantities of Mars. Icarus 170, 343–364. https://doi.org/10.1016/j.icarus.2004.04.005

León, D.A.S. de, Alcocer, J., Gloria, V.A., Quiroz-Martínez, B., 2016. Estimation of the eddy diffusivity coefficient in a warm monomictic tropical Lake. J. Limnol. 75. https://doi.org/10.4081/jlimnol.2016.1431

Liu, J., Michalski, J.R., Tan, W., He, H., Ye, B., Xiao, L., 2021. Anoxic chemical weathering under a reducing greenhouse on early Mars. Nat. Astron. 1–7. https://doi.org/10.1038/s41550-021-01303-5

Logan, S.R., 1990. Effects of temperature and wavelength on the primary process in the photo-oxidation of iron(II) ion. J. Chem. Soc. Faraday Trans. 86, 615–617. https://doi.org/10.1039/FT9908600615

Lyons, T.W., Reinhard, C.T., Planavsky, N.J., 2014. The rise of oxygen in Earth's early ocean and atmosphere. Nature 506, 307–315. https://doi.org/10.1038/nature13068

Macfarlane, A.W., Danielson, A., Holland, H.D., 1994. Geology and major and trace element chemistry of late Archean weathering profiles in the Fortescue Group, Western Australia: implications for atmospheric PO2. Precambrian Res. 65, 297–317. https://doi.org/10.1016/0301-9268(94)90110-4

McSween, H.Y., Taylor, G.J., Wyatt, M.B., 2009. Elemental Composition of the Martian Crust. Science 324, 736–739. https://doi.org/10.1126/science.1165871

Mitra, K., Catalano, J.G., 2019. Chlorate as a Potential Oxidant on Mars: Rates and Products of Dissolved Fe(II) Oxidation. J. Geophys. Res. Planets 124, 2893–2916. https://doi.org/10.1029/2019JE006133

Mitra, K., Moreland, E.L., Catalano, J.G., 2020. Capacity of Chlorate to Oxidize Ferrous Iron: Implications for Iron Oxide Formation on Mars. Minerals 10, 729. https://doi.org/10.3390/min10090729

Morris, R.V., Golden, D.C., Bell, J.F., Shelfer, T.D., Scheinost, A.C., Hinman, N.W., Furniss, G., Mertzman, S.A., Bishop, J.L., Ming, D.W., Allen, C.C., Britt, D.T., 2000. Mineralogy, composition, and alteration of Mars Pathfinder rocks and soils: Evidence from multispectral, elemental, and magnetic data on terrestrial analogue, SNC meteorite, and Pathfinder samples. J. Geophys. Res. Planets 105, 1757–1817. https://doi.org/10.1029/1999JE001059

Morris, R.V., Klingelhöfer, G., Schröder, C., Rodionov, D.S., Yen, A., Ming, D.W., de Souza, P.A., Wdowiak, T., Fleischer, I., Gellert, R., Bernhardt, B., Bonnes, U., Cohen, B.A., Evlanov, E.N., Foh, J., Gütlich, P., Kankeleit, E., McCoy, T., Mittlefehldt, D.W., Renz, F., Schmidt, M.E., Zubkov, B., Squyres, S.W., Arvidson, R.E., 2006. Mössbauer mineralogy of rock, soil, and dust at

Meridiani Planum, Mars: Opportunity's journey across sulfate-rich outcrop, basaltic sand and dust, and hematite lag deposits. J. Geophys. Res. Planets 111, E12S15. https://doi.org/10.1029/2006JE002791

Nie, N.X., Dauphas, N., Greenwood, R.C., 2017. Iron and oxygen isotope fractionation during iron UV photo-oxidation: Implications for early Earth and Mars. Earth Planet. Sci. Lett. 458, 179–191. https://doi.org/10.1016/j.epsl.2016.10.035

Nie, N.X., Dauphas, N., Villalon, K.L., Liu, N., Heard, A.W., Morris, R.V., Mertzman, S.A., 2020. Iron isotopic and chemical tracing of basalt alteration and hematite spherule formation in Hawaii: A prospective study for Mars. Earth Planet. Sci. Lett. 544, 116385. https://doi.org/10.1016/j.epsl.2020.116385

Niles, P.B., Michalski, J., 2009. Meridiani Planum sediments on Mars formed through weathering in massive ice deposits. Nat. Geosci. 2, 215–220. https://doi.org/10.1038/ngeo438

Rampe, E.B., Ming, D.W., Blake, D.F., Bristow, T.F., Chipera, S.J., Grotzinger, J.P., Morris, R.V., Morrison, S.M., Vaniman, D.T., Yen, A.S., Achilles, C.N., Craig, P.I., Des Marais, D.J., Downs, R.T., Farmer, J.D., Fendrich, K.V., Gellert, R., Hazen, R.M., Kah, L.C., Morookian, J.M., Peretyazhko, T.S., Sarrazin, P., Treiman, A.H., Berger, J.A., Eigenbrode, J., Fairén, A.G., Forni, O., Gupta, S., Hurowitz, J.A., Lanza, N.L., Schmidt, M.E., Siebach, K., Sutter, B., Thompson, L.M., 2017. Mineralogy of an ancient lacustrine mudstone succession from the Murray formation, Gale crater, Mars. Earth Planet. Sci. Lett. 471, 172–185. https://doi.org/10.1016/j.epsl.2017.04.021

Ranjan, S., Wordsworth, R.D., Sasselov, D.D., 2017. Atmospheric Constraints on the Surface UV Environment of Mars at 3.9 Ga Relevant to Prebiotic Chemistry. ArXiv170101373 Astro-Ph.

Ribas, I., Mello, G.F.P. de, Ferreira, L.D., Hébrard, E., Selsis, F., Catalán, S., Garcés, A., Jr, J.D. do N., Medeiros, J.R. de, 2010. Evolution Of The Solar Activity Over Time And Effects On Planetary Atmospheres. Ii. K1 Ceti, An Analog Of The Sun When Life Arose On Earth*. Astrophys. J. 714, 384. https://doi.org/10.1088/0004-637X/714/1/384

Rye, R., Holland, H.D., 1998. Paleosols and the evolution of atmospheric oxygen; a critical review. Am. J. Sci. 298, 621–672. https://doi.org/10.2475/ajs.298.8.621

Schaefer, M.W., 1996. Are there abiotically-precipitated iron-formations on Mars? Geochem. Soc. Spec. Publ. 5.

Sheppard, R.Y., Milliken, R.E., Russell, J.M., Dyar, M.D., Sklute, E.C., Vogel, H., Melles, M., Bijaksana, S., Morlock, M.A., Hasberg, A.K.M., 2019. Characterization of Iron in Lake Towuti sediment. Chem. Geol. 512, 11–30. https://doi.org/10.1016/j.chemgeo.2019.02.029
Smith, R.C., Baker, K.S., 1981. Optical properties of the clearest natural waters (200–800 nm). Appl. Opt. 20, 177–184. https://doi.org/10.1364/AO.20.000177

Squyres, S.W., Arvidson, R.E., Bollen, D., Bell, J.F., Brückner, J., Cabrol, N.A., Calvin, W.M., Carr, M.H., Christensen, P.R., Clark, B.C., Crumpler, L., Des Marais, D.J., d'Uston, C., Economou, T., Farmer, J., Farrand, W.H., Folkner, W., Gellert, R., Glotch, T.D., Golombek, M., Gorevan, S., Grant, J.A., Greeley, R., Grotzinger, J., Herkenhoff, K.E., Hviid, S., Johnson, J.R., Klingelhöfer, G., Knoll, A.H., Landis, G., Lemmon, M., Li, R., Madsen, M.B., Malin, M.C., McLennan, S.M., McSween, H.Y., Ming, D.W., Moersch, J., Morris, R.V., Parker, T., Rice, J.W., Richter, L., Rieder, R., Schröder, C., Sims, M., Smith, M., Smith, P., Soderblom, L.A., Sullivan, R., Tosca, N.J., Wänke, H., Wdowiak, T., Wolff, M., Yen, A., 2006. Overview of the Opportunity Mars Exploration Rover Mission to Meridiani Planum: Eagle Crater to Purgatory Ripple. J. Geophys. Res. Planets 111, E12S12. https://doi.org/10.1029/2006JE002771

Squyres, S.W., Knoll, A.H., 2005. Sedimentary rocks at Meridiani Planum: Origin, diagenesis, and implications for life on Mars. Earth Planet. Sci. Lett., Sedimentary Geology at Meridiani Planum, Mars 240, 1–10. https://doi.org/10.1016/j.epsl.2005.09.038

Stefánsson, A., 2007. Iron(III) Hydrolysis and Solubility at 25 °C. Environ. Sci. Technol. 41, 6117–6123. https://doi.org/10.1021/es070174h

Tabata, H., Sekine, Y., Kanzaki, Y., Sugita, S., 2021. An experimental study of photo-oxidation of Fe(II): Implications for the formation of Fe(III) (hydro)oxides on early Mars and Earth. Geochim. Cosmochim. Acta 299, 35–51. https://doi.org/10.1016/j.gca.2021.02.006

Teutsch, N., Schmid, M., Müller, B., Halliday, A.N., Bürgmann, H., Wehrli, B., 2009. Large iron isotope fractionation at the oxic–anoxic boundary in Lake Nyos. Earth Planet. Sci. Lett. 285, 52–60. https://doi.org/10.1016/j.epsl.2009.05.044

Thibon, F., Blichert-Toft, J., Tsikos, H., Foden, J., Albalat, E., Albarede, F., 2019. Dynamics of oceanic iron prior to the Great Oxygenation Event. Earth Planet. Sci. Lett. 506, 360–370. https://doi.org/10.1016/j.epsl.2018.11.016

Thompson, K.J., Kenward, P.A., Bauer, K.W., Warchola, T., Gauger, T., Martinez, R., Simister, R.L., Michiels, C.C., Llirós, M., Reinhard, C.T., Kappler, A., Konhauser, K.O., Crowe, S.A., 2019. Photoferrotrophy, deposition of banded iron formations, and methane production in Archean oceans. Sci. Adv. 5, eaav2869. https://doi.org/10.1126/sciadv.aav2869

Tosca, N.J., Ahmed, I.A.M., Tutolo, B.M., Ashpitel, A., Hurowitz, J.A., 2018. Magnetite authigenesis and the warming of early Mars. Nat. Geosci. 11, 635–639. https://doi.org/10.1038/s41561-018-0203-8

Tosca, N.J., McLennan, S.M., Dyar, M.D., Sklute, E.C., Michel, F.M., 2008. Fe oxidation processes at Meridiani Planum and implications for secondary Fe mineralogy on Mars. J. Geophys. Res. Planets 113, E05005. https://doi.org/10.1029/2007JE003019

Tsikos, H., Matthews, A., Erel, Y., Moore, J.M., 2010. Iron isotopes constrain biogeochemical redox cycling of iron and manganese in a Palaeoproterozoic stratified basin. Earth Planet. Sci. Lett. 298, 125–134. https://doi.org/10.1016/j.epsl.2010.07.032

Walker, J.C.G., 1984. Suboxic diagenesis in banded iron formations. Nature 309, 340–342. https://doi.org/10.1038/309340a0

Wordsworth, R., Knoll, A.H., Hurowitz, J., Baum, M., Ehlmann, B.L., Head, J.W., Steakley, K., 2021. A coupled model of episodic warming, oxidation and geochemical transitions on early Mars. Nat. Geosci. 14, 127–132. https://doi.org/10.1038/s41561-021-00701-8

Yu, J.-Y., Park, M., Kim, J., 2002. Solubilities of synthetic schwertmannite and ferrihydrite. Geochem. J. 36, 119–132. https://doi.org/10.2343/geochemj.36.119

CONCLUDING REMARKS

The dominant theme of this thesis has been to further illuminate the dual roles that iron (Fe) plays as a driver of, and an unmatched geological recorder of, changes in the redox environment of planetary surfaces. Chapters 1 and 6 showed these two roles in the context of weathering of Fe-rich rocks at the surface of Earth and Mars, respectively. In Chapter 1, new trace element and isotopic data are used to overturn an earlier case for atmospheric oxygenation on Earth 2.95 billion years ago (Ga); and the robust isotopic record of Fe, in particular was key to this story. Meanwhile, the late oxidation of iron at the surface of Mars as it was undergoing loss of its surface volatiles was shown in Chapter 6 to have been a non-negligible sink of oxygen separated from water during escape of hydrogen to space. Chapters 2 and 3 provided new perspectives on the Fe isotopic record of the major redox-active Fe sinks in the pre-oxygenation oceans. The role of pyrite Fe isotopes as a passive record of the ocean redox state had been debated for over 15 years. The work presented in this thesis not only brings some clarity to the meaning of this isotope record, but also emphasized the role of the marine iron cycle in a preexisting model for surface oxygenation driven by pyrite burial. In Chapter 4, we presented one example of where the redox buffering power of Fe in the shallow oceans may not have been up to task; with the quantitative oxidation of Fe^{2+} at the site of biological O_2 production allowing the redox state of shallow water environments to take a further step up the redox ladder to the oxidation of manganese and cerium.

Teasing out the geochemical record of Fe can benefit greatly from multiproxy work, and an approach consistently taken in this thesis has been to combine Fe geochemistry with a wide variety of independent proxy data to shore up our interpretations. Chapter 1 showed how measurements of divalent transition metals, Fe isotopes, and Cr isotopes of the same sample materials, can all be used to ground truth one another, and ultimately, they presented an internally consistent story of

anoxic continental weathering in the Mesoarchean. Chapters 2 and 3 demonstrated two very different approaches to tackling the same problem in the Fe isotopic record of pyrites. Chapter 2 showed how long-term trends can be understood through comparison to independent proxy records for different geochemical driving mechanisms. Meanwhile, Chapter 3 showed how even a second isotope ratio of the same element can provide an additional variable that enables quantification of fractionation processes in the pyrite Fe isotope record. Chapter 4 made use of textural characteristics of stromatolitic samples to understand the physicochemical conditions in which they formed, which is crucial for interpreting their geochemical compositions. And in Chapter 6, the use of hydrogen isotopes as an independent proxy for historic water loss from Mars provided a means to deconvolve oxygen escape channels associated with the hydrosphere, and the atmospheric CO_2 reservoir. Arguably, a final example of a 'multiproxy' approach taken in this thesis can be seen in Chapter 7, where we make the case that the geochemical record of Martian lakes can be interpreted best when using the additional context provided by Earth's early geochemical record. Until we finally have access to returned samples from Mars, the models of surface redox evolution on that planet will be restricted by the types of geochemical data that can be collected *in situ* by rovers; while the ancient geologic record of Earth can already be interrogated using the most refined analytical equipment. The Fe isotope and Mn/Fe systematics of terrestrial iron formations provide just one example of how our understanding of redox element behavior in ancient environments can be refined on Earth, and then be cautiously translated to potentially analogous environments on Mars. It cannot be stressed enough how a sound understanding of Earth's geochemical evolution offers one of the best tools available to the Martian scientist's toolbox.

The topic of Martian sample return that was alluded to above is very much a case of looking to the future. So, to conclude this thesis, it seems worthwhile to note very briefly some far more modest ways in which future work may benefit our understanding of ancient Fe geochemistry and the role what it can tell us about Earth surface redox evolution. Chapter 5 emphasized that an immediate goal in low temperature Fe isotope geochemistry should be empirical experiments that target the Fe isotopic fractionation associated with greenalite precipitation under different chemical conditions. The equilibrium Fe isotope behavior inferred in the preliminary work presented in this thesis leaves the question of isotopically viable precursors for Archean IFs less than fully answered. Finally, Chapter 1 provided to our knowledge, the first estimate of the Fe isotope composition of the continental Fe^{2+} flux to the Archean oceans. To date, our assumptions about the isotopic composition of hydrothermal input fluxes of Fe to the pre-oxygenation oceans have been very much grounded in comparison to modern analogs. Modern hydrothermal vent systems show an Fe isotopic diversity that is rarely reflected in the uncertainty of models for the ancient Fe isotopic balance, perhaps in part because the Fe isotopic composition of the seafloor hydrothermal Fe flux is understood at an empirical level, without generalizable concepts that can be applied to different ocean bottom water chemistries. The Fe isotopic balance of hydrothermal vent fluids should represent a balance of oxide and sulfide mineral controls. As such, the triple Fe isotope technique presented in Chapter 3 is well-placed to help us gain a more fundamental and generalizable understanding of the isotopic controls in hydrothermal vent systems, which may ultimately help us place better constraints on the deep water drivers of geochemistry in the oceans of the ancient Earth, and perhaps eventually, the oceans of icy moons in the outer solar system.